UNITED STATES OF AMERICA
DEPARTMENT OF THE INTERIOR
GEOLOGICAL SURVEY

he Soviet-American Exchange in Earthquake Prediction

edited by

HENRY SPALL
U.S. Geological Survey
National Center
Reston, Virginia

and

DAVID W. SIMPSON
Lamont-Doherty Geological Observatory
Columbia University
Palisades, New York

U.S. GEOLOGICAL SURVEY OPEN-FILE REPORT 81-1150

1981

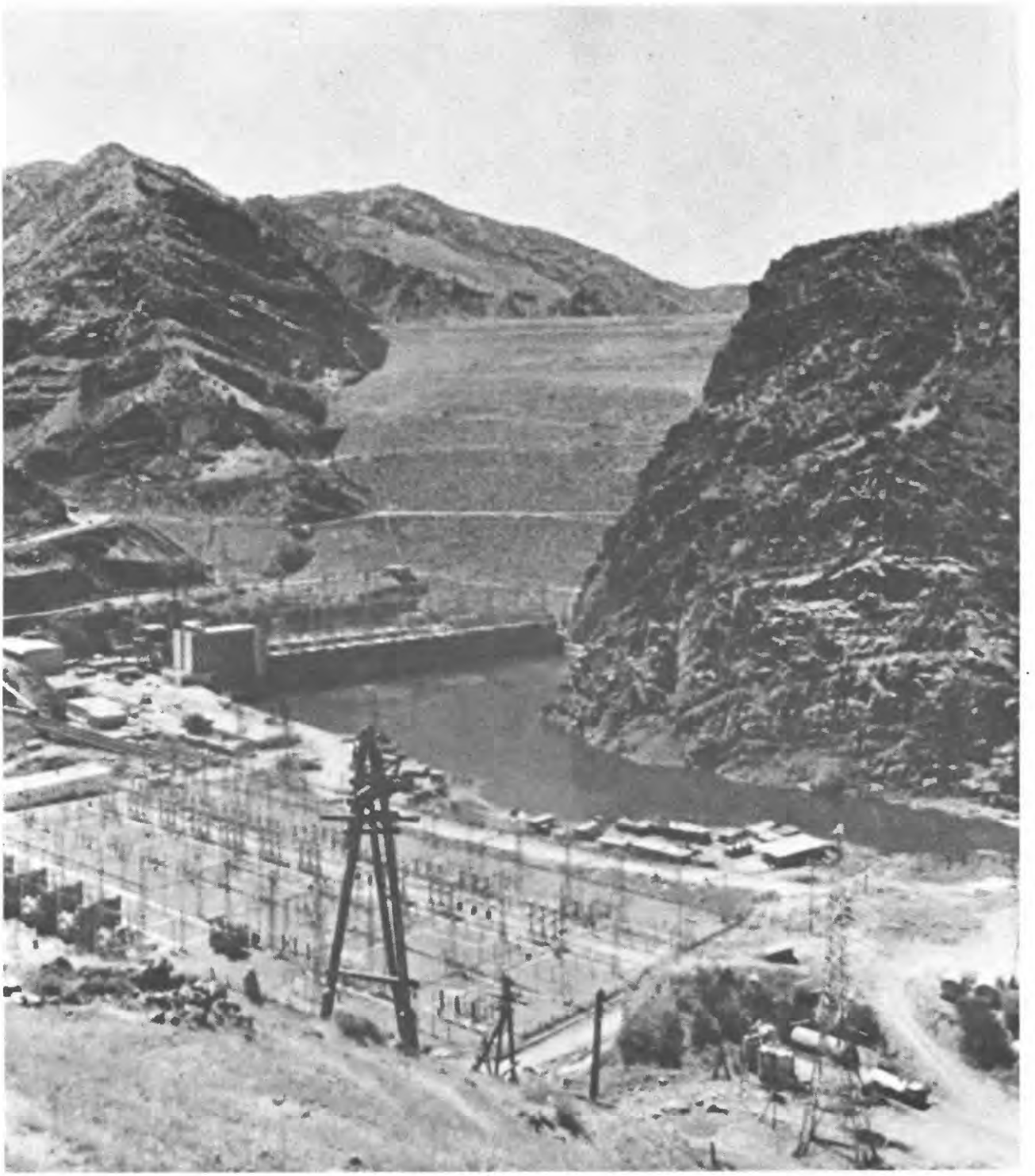

Frontispiece: Nurek Dam in Soviet Central Asia. Photograph by D. W. Simpson.

Table of Contents

Introduction

Following the XV General Assembly of the International Union of Geodesy and Geophysics (IUGG) in Moscow in 1971, a group of US seismologists visited Soviet Central Asia to view the work being done on earthquake prediction in the seismically active areas near Dushanbe, Garm and Tashkent. At the IUGG meeting, reports had been presented on recent Soviet studies of earthquake prediction in these areas that included premonitory variations in velocities prior to earthquakes in the Garm area. While international meetings such as the IUGG General Assembly had traditionally provided a forum for Soviet and American colleagues to exchange ideas in various areas of seismology, the 1971 visit resulted in discussions concerning the development of a more formal exchange program in earthquake prediction studies. At the Nixon-Brezhnev summit in Moscow in May 1972, an agreement was signed which provided the official vehicle for such a program: earthquake prediction was included as Area IX of the US-USSR Agreement on Cooperation in the Field of Environmental Protection. A working group chaired by M. A. Sadovsky of the Institute of Physics of the Earth and R. E. Wallace of the U.S. Geological Survey was formed in 1973 and the first exchange took place in 1974. The members of the working group for Area IX in 1980 are listed below. Working Group protocols have provided for up to 34 man-months of exchange visits per year.

The papers in this volume describe some of the work carried out under the exchange agreement. Other collections of papers have been previously published in Russian (Sadovsky and others, 1976a,b, 1979a,b). In addition to the specific projects described in these reports, many of which have involved continuing laboratory experiments, field programs and collaboration in theoretical studies, the exchange has provided the forum for contacts between scientists in various disciplines during short visits to research centers in both countries.

The earthquake prediction exchange has been cited as one of the more successful programs among the many scientific exchanges between the US and USSR. This success reflects the inherent international nature of seismology. It also reflects the common objective of studies of earthquake hazards mitigation, namely to reduce human suffering. Earthquakes show no respect for international boundaries. Seismology has had and must continue to have a tradition of free exchange of data and ideas in the international scientific community.

One of those deeply committed to both the humanitarian and scientific aspects of seismology was Victor I. Miyachkin, who served as a project leader in the exchange program since its inception. Those of us who knew and worked with him were saddened by his recent death. This volume is dedicated to his memory.

Robert L. Wesson
David W. Simpson

Five project areas are included under the agreement and some of the major areas of research are:

Project 1 - Field investigations of earthquake prediction. Establishment of networks for studies of induced seismicity at Nurek Reservoir, Tadjikistan, and Toktogul Reservoir, Kirgizia; establishment of a network for seismicity, velocity and focal-mechanism studies in the Peter the First ranges near Garm, Tadjikistan; establishment of a network of digital instruments to investigate spectra and strong ground motion in sediment-filled valleys near Garm.

Project 2 - Laboratory and theoretical investigations of the physics of the earthquake source. Laboratory studies in Moscow, Colorado and California on rupture processes and premonitory phenomena in rock and synthetic materials; development of models for earthquake premonitory phenomena; theoretical studies of the earthquake source and fracture processes.

Project 3 - Mathematical and computational prediction of places where large earthquakes occur and evaluation of seismic risk. Studies in Moscow and California of the application of pattern recognition techniques to earthquake prediction; use of seismicity patterns (foreshocks, aftershocks, earthquake swarms) in earthquake prediction; development of algorithms for prediction and risk estimates.

Project 4 - Engineering-seismological investigations. Establishment of a network of 19 strong-motion instruments in Tadjikistan; studies of explosion-induced vibrations in full scale buildings near Dushanbe, Tadjikistan.

Project 5 - Tsunami warning system. Exchange of data related to tsunami-generating earthquakes; recording of tsunami in the open ocean.

Collections of papers (in Russian) on Soviet-American work on earthquake prediction:

Volume 1. M. A. Sadovsky (editor-in-chief)
A. B. Maksimov, V. I. Miyachkin, S.Kh. Negmatullaev,
I. L. Nersesov. Published by Donish. Dushanbe and Moscow.
Book 1. 1976 236 pages
Book 2. 1976 220 pages

Volume 2. M. A. Sadovsky, S.Kh. Negmatullaev, I. L Nersesov,
A. B. Maksimov. Published by Donish. Dushanbe and Moscow.
Book 1. 1979 91 pages
Book 2. 1979 169 pages

US-USSR Environmental Agreement
Co-Chairmen and Project Leaders (1980)

	USSR	USA
Co-Chairman of Agreement	Yu. A. Izrael	Douglas M. Costle
Executive Secretary	Yu. Ye. Kazakov	Linwood R. Starbird
Area IX, Working Group		
Co-Chairman	M. A. Sadovsky	Robert L. Wesson
Project Leaders		
.Field investigations of earthquake prediction	I. L. Nersesov	David W. Simpson
.Laboratory and theoretical investigations	V. I. Miyachkin	Hartmut A. Spetzler
.Mathematical and computational prediction	V. I. Keilis-Borok	Leon Knopoff
.Engineering seismology	S.Kh. Negmatullaev	Charles C. Thiel
.Tsunami warnings	V. M. Popov	Bertrand J. Thompson

AUTHOR ADDRESSES

Union of Soviet Socialist Republics

F. F. Aptikaev
V. A. Dubrovskiy
V. I. Keilis-Borok
A. Koltsov
B. K. Kostrov
V. N. Krestnikov
I. L. Nersesov
M. V. Nevskiy
A. K. Nikolaev
V. D. Pavlov
I. M. Rotvain
M. A. Sadovsky
B. G. Salov
E. N. Sedova
T. M. Sidorenko
G. A. Sobolev
D. V. Stange
A. I. Zolotarev
Institute of Physics of the Earth
Academy of Sciences of the USSR
Moscow, USSR

I. M. Gelfand **Sh.A. Guberman**
Institute of Applied Mathematics
Academy of Sciences of the USSR
Moscow

E.Ya. Ranzman
Institute of Geography
Academy of Sciences of the USSR
Moscow

A. A. Lunëv **K. M. Mirozoyev**
S.Kh. Negmatullaev **O. V. Soboleva**
G. S. Seleznyov
Tadjik Institute of Seismoresistant
Construction and Seismology
Dushanbe, Tadjik SSR

United States of America

F. Press
Department of Earth and Planetary Sciences
Massachusetts Institute of Technology
Cambridge, Massachusetts 02139

C. R. Allen **S. Ashmoll**
Seismological Laboratory
California Institute of Technology
Pasadena, California 91125

Walter Alvarez
Department of Geology
University of California
Berkeley, California 94720

L. Knopoff
Institute of Geophysics and Planetary Physics
University of California
Los Angeles, California 90024

Shamita Das **M. W. Hamburger**
C. M. Keith **William Leith**
D. W. Simpson
Lamont-Doherty Geological Observatory
Palisades, New York 10964

H. A. Spetzler
Cooperative Institute for Research in Environmental Sciences
and Department of Geological Sciences
University of Colorado/NOAA
Boulder, Colorado 80309

I. C. Getting **C. H. Sondergeld**
Cooperative Institute for Research in Environmental Sciences
University of Colorado/NOAA
Boulder, Colorado 80309

Fred Fischer **A. G. Lindh**
R. B. Matthiesen **Jack Pelton**
C. Rojahn
U. S. Geological Survey
Menlo Park, California 94025

Henry Spall **R. L. Wesson**
U.S. Geological Survey
National Center
Reston, Virginia 22092

Urban Development in Relation to Earthquakes, Landslides, and Unstable Ground

I. L. Nersesov and F. F. Aptikaev
Institute of Physics of the Earth, USSR

At the beginning of this century the population of this globe was 1.6 billion. By the end of the century it is estimated that the population will reach 6 to 7 billion. Urban areas are growing especially rapidly. Whereas in 1900 about 10 percent of the people in the world lived in urban areas, by the year 2000 half of these will live in cities. Even now, in many developed countries, urban inhabitants make up about three-quarters of the population.

Coincident with this trend toward urban population growth, we also observe a more rapid development of large cities. This phenomenon occurs in every climatic zone and in countries at different levels of development. From 1960 to 1970, the number of cities in the tropics with populations of more than 1 million grew from 4 to 14. During the same period in the Union of Soviet Socialist Republics, the number of cities with more than 1 million inhabitants grew from 4 to 10, and by 1980 that number will increase to 22.

This includes not only the simple growth of preexisting cities and towns, but also the establishment of completely new urban areas. So, in the Soviet Union every year more than 20 new towns come into being; half of them are in previously uninhabited areas. The same tendency is observed in other countries.

Towns, transport lines, and industrial complexes take away from agriculture enormous areas, amounting to millions of hectares per year. During recent times areas under development of different kinds have been redoubling each 15 years. In many cases this development of new lands occurs spontaneously, often without necessary geological investigations.

Naturally, urban growth is more intensive in areas with the greatest increase in population, generally between 40 degrees North and South latitude. Almost three-quarters of the world's population lives in this region. And in this same area, geological processes are the most active. Thus, geologic hazards such as earthquakes, landslides, and mud flows annually account for serious losses of life and property.

*Paper presented at 1979 International Centennial Symposium "Resources for the Twenty-first Century," to be published in U.S. Geological Survey Professional Paper 1193 (in press).

It sounds paradoxical, but recent technical developments are actually capable of increasing geologic hazards if they are not properly applied. In fact, every year man's interference with nature increases. Already, the large-scale production and burning of fuel, the subsequent pollution of the atmosphere, the constant reduction of forest areas, the modification of rivers and lakes as well as subsoil waters, which are in turn connected with the enormous consumption of fresh water for agriculture and industry, and other of man's activities have adversely affected geological processes. The mining industry is developing one and a half times faster than other branches of industry. According to estimates by experts, disturbances caused by opencut mining can affect an area up to ten times larger than the area of quarry operation itself, changing the hydrological regime and natural geochemical processes, depositing erosion products, and otherwise altering the landscape. Dumps and waste heaps are not carefully monitored, they can give rise to landslides that endanger neighbouring settlements. It is sufficient to remember the tragic case of Aberfan in South Wales. Likewise, demands for fresh water and for energy have caused a sharp rise in the number of large dams. Dam heights continue to increase and reservoir volumes continue to grow. Naturally, dams are erected in the places with large reserves of energy, mainly in mountainous regions where geologic hazards are high. Besides natural geologic hazards it is necessary to take into account the possibility of manmade earthquakes, connected with the impounding of the reservoir itself. Unfortunately, destruction has resulted from such earthquakes. The enormous potential danger of the failure of a large dam for downstream towns can scarcely be exaggerated. Moreover, building and development in highland areas can disturb slope stability, thus causing rockfalls and landslides. Often these phenomena are observed not only in highland regions, but also near rivers, lakes and coastal areas.

To reduce the losses due to geologic hazards it is necessary to plan future population expansion in regions chosen for this purpose. Firstly, they should be areas with low geologic hazards, and second, areas of little use for agriculture. It is vital that we provide the legislation necessary to ensure that both the estimation of geologic hazards and the consideration of suitability are included in the development of new lands set aside for civil and industrial construction. In the Soviet Union legislation for protecting lands and the environment has been issued during the past 10 years to pursue just these goals—land recultivation after mining exploitation, control of water pollution, protection against soil erosion, and the development of lands useless for agriculture.

Of all geologic hazards, earthquakes can cause the greatest loss of life and the largest property damage. Some numbers can illustrate this. Landslides affecting an area of one square kilometre are considered serious. However, an earthquake with magnitude M = 7.5 on the Richter scale (not the largest possible) can destroy an area of as much as one thousand square kilometres—an area large enough to include a city with a population of several million. Thus

the rapid spread of population in active earthquake belts has resulted in the presence of more settlements near zones in which destructive earthquakes may occur. Not only are the direct effects of seismic vibration most serious in such built-up areas but so also are the secondary geological phenomena—rockfalls, landslides, soil subsidence and soil liquefaction.

Earthquake hazard is especially great in large urban areas where there is not only a high concentration of structures and goods, but where the disruption of the normal course of the urban economy—water supply, gas lines, electricity, telephone lines, computer systems—can also provoke additional economic problems.

In figure 1 we have plotted some of the summary data on hazards in order to assess the possible strongest effects of earthquakes according to the following factors: (*A*) intensity versus magnitude (mean and maximum values); (*B*) areas shaken at different levels of intensity (mean values), (*C*) monetary losses; and (*D*) loss of lives (maximum values). Maximum estimates correspond to the effects

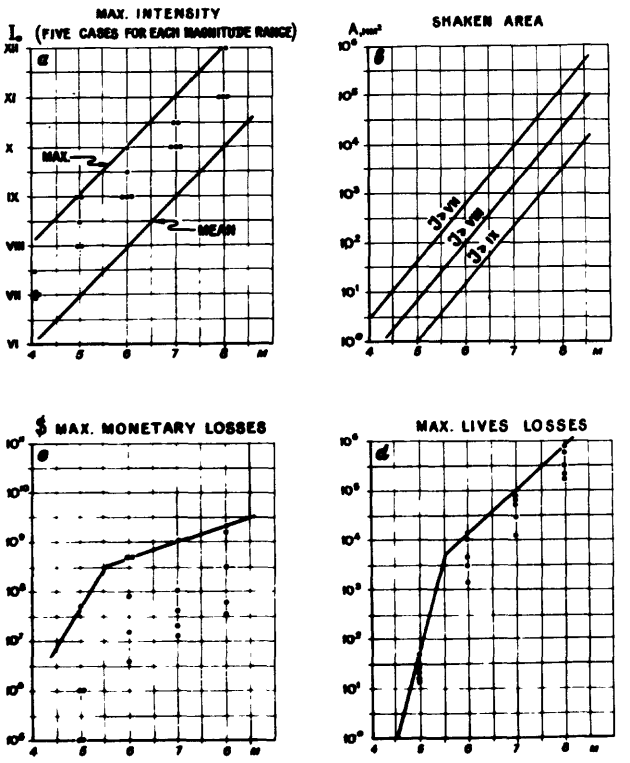

Figure 1 Some earthquake characteristics versus magnitude (*M*): A, Maximum and mean intensity (*I*). B, Area (in km²) shaken at different levels of intensity (*I*). C, Maximum monetary loss, in dollars. D, Maximum loss of lives.

observed during the five most severe earthquakes in each magnitude range. According to these data, the lives lost during the strongest earthquake could reach up to one million. This estimate is based upon the most unfavourable conditions: (1) demographic (high population density); (2) social (low level of economic development resulting in non-antiseismic construction), and (3) geological (unconsolidated substrate, location relative to active faults). For

earthquakes greater than magnitude 5.5 an increase of one magnitude unit causes a tenfold increase in the number of fatalities; however, equivalent decreases in fatalities for earthquakes of magnitude less than 4.5 are not observed as a rule. Antiseismic construction could reduce these estimates of lives lost by a factor of ten. In urban areas each fatality is accompanied by about one million dollars loss to the economy. Furthermore, the growing concentration of material values in large cities will in the future increase both the absolute and relative values of monetary losses when geological catastrophes occur. The relatively rare occurrence of the strongest geological catastrophes, especially seismic ones, and the use of mean values in loss estimates, can result in underestimation of geologic hazards.

First and foremost, these examples clearly illustrate the practical necessity for estimates of the seismic hazard for new lands, and for estimates of accompanying geological phenomena before civil and industrial construction. The wide complex of geological and geophysical methods used in seismic zoning indicates the breadth and importance of this technique. Seismic zoning includes estimating the danger not only from vibration but from other geological phenomena as well—creep, landslides, snow slides, flash floods, and soil deformation.

Seismic zoning as a complex geological-geophysical method has been under development in the Soviet Union since 1930 (Seismic Zoning of the USSR, 1978 [trans. 1980]). The earliest seismic zoning maps were made at a scale of 1:2.5 million. This scale is still being used. Every 10 to 15 years these maps are revised on the basis of new experimental data and further development of the zoning method. In addition to seismic intensity estimates, maps that were completed in 1978 include possible strong earthquake zones, probability of different magnitudes, and the mean isoseismal lines for large earthquakes. These maps show the isoseismal areas up to intensity 9 (fig. 2*A*). Higher intensities may occur in source zones and these areas should be excluded from areas for development (fig. 2*B*). As general seismic danger estimates our general seismic zoning maps receive government approval and are the legislative basis for all planning, design and building organizations of the State.

In the Soviet Union, legal codes regulate detailed investigations of local conditions: engineering geology; local tectonics; geodetic estimates of small scale crustal deformation; hydrogeology; soil characteristics and their influence on seismic vibration. Investigations of this kind are called "seismic microzonation."

However, in many cases of civil and industrial development, general zoning cannot answer questions about geologic hazards with the required accuracy, nor can microzonation, which provides information on a small area of only local interest. For these reasons special methods for more detailed estimations of geologic hazards are being developed. This large-scale detailing is necessary for large hydrotechnical projects, nuclear power plants, urban design, and long-term planning of new land developments. This new direction in planning is called "detailed seismic zoning."

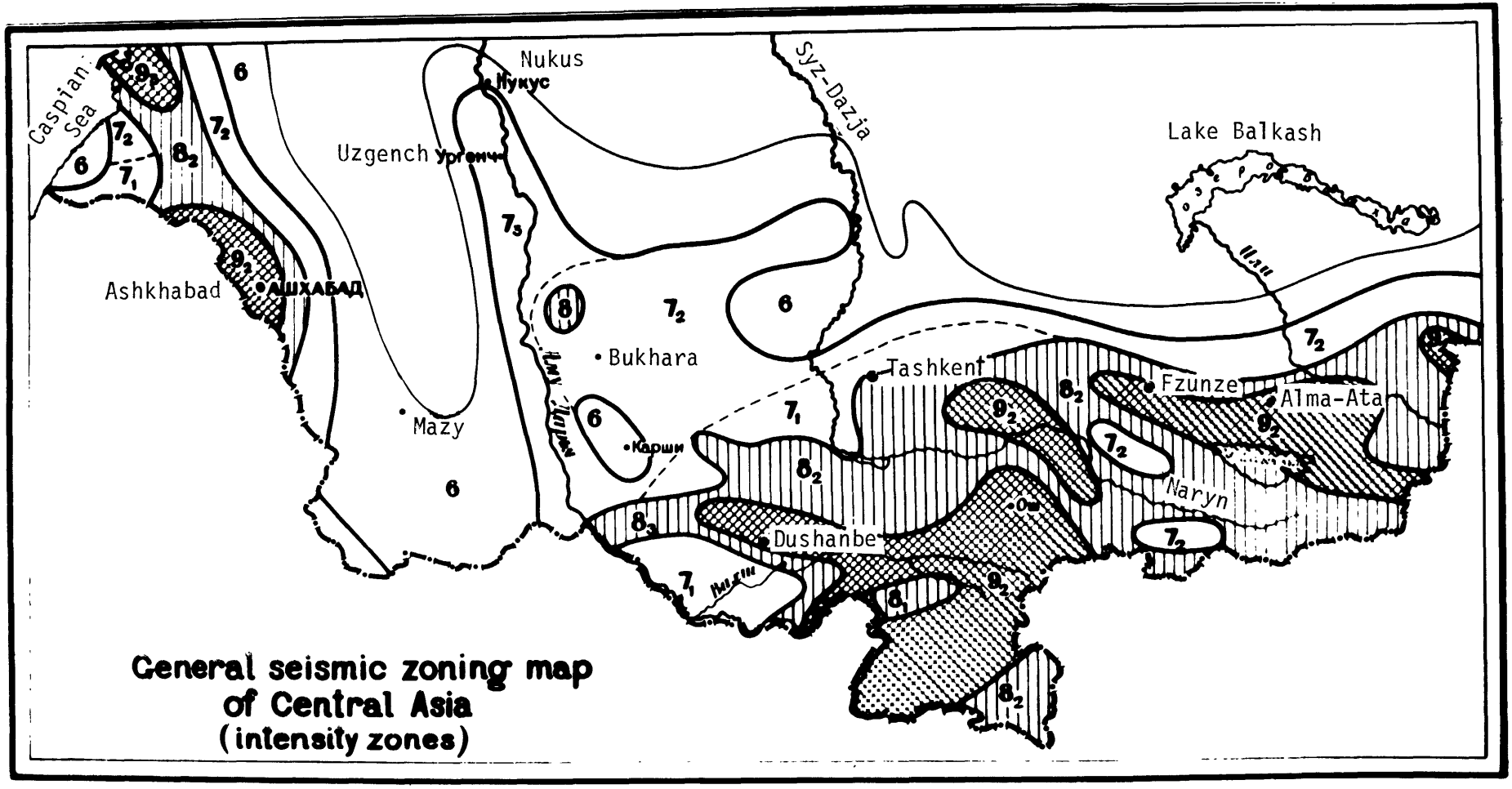

Figure 2a General seismic zoning map of Central Asia showing intensity zones. The numbers 6, 7, 8 and 9 refer to intensity zones (on the Soviet scale). The subscripts $\mathcal{E}_1, \mathcal{E}_2, \mathcal{E}_3$ refer to the average recurrence time in terms of 1 in 100 years, 1 in 1000 years and 1 in 10,000 years respectively.

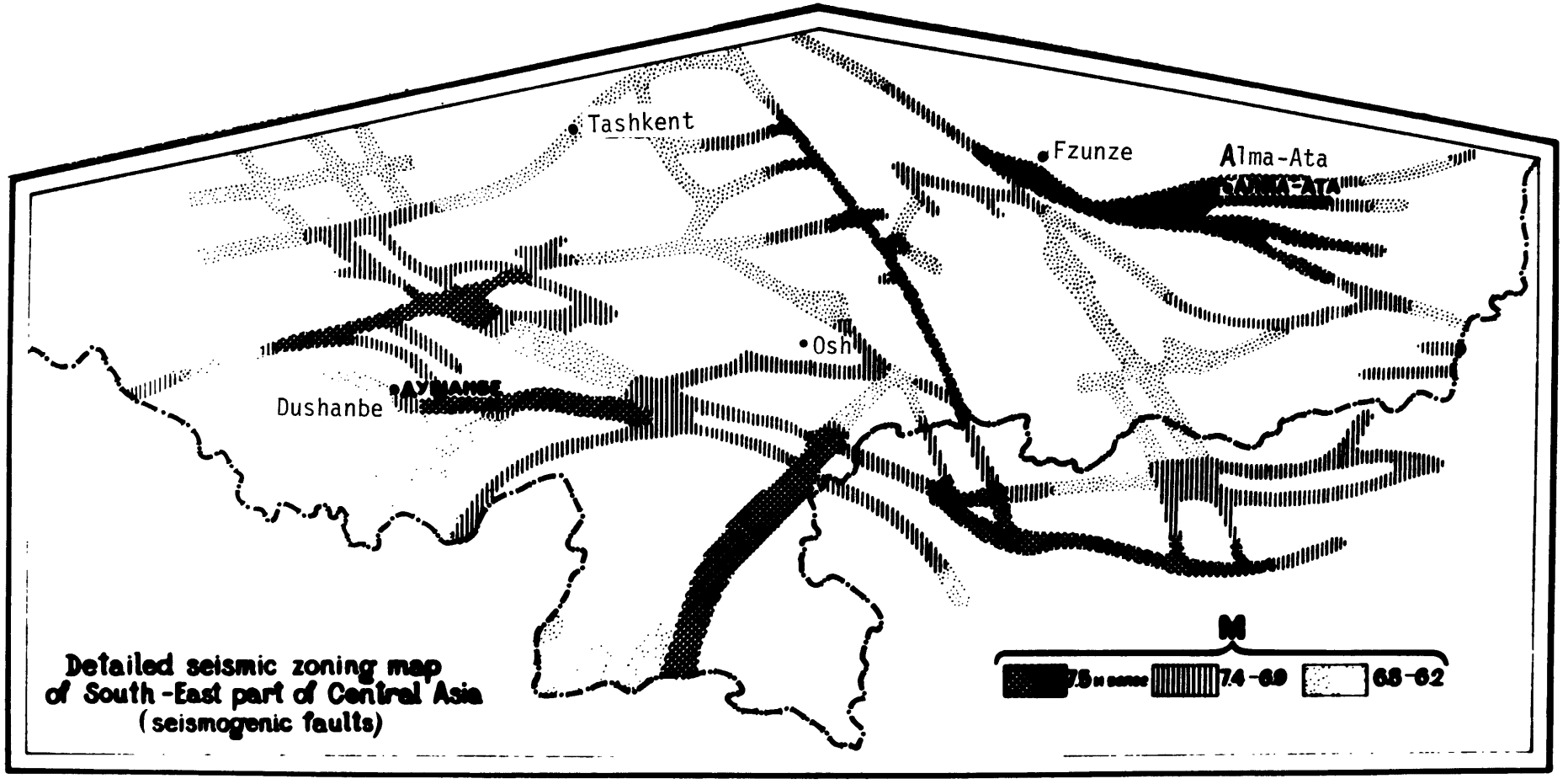

Figure 2b Detailed seismic zoning map of the southeast part of central Asia showing seismogenic faults. The shading shows the magnitude of earthquakes expected on those faults.

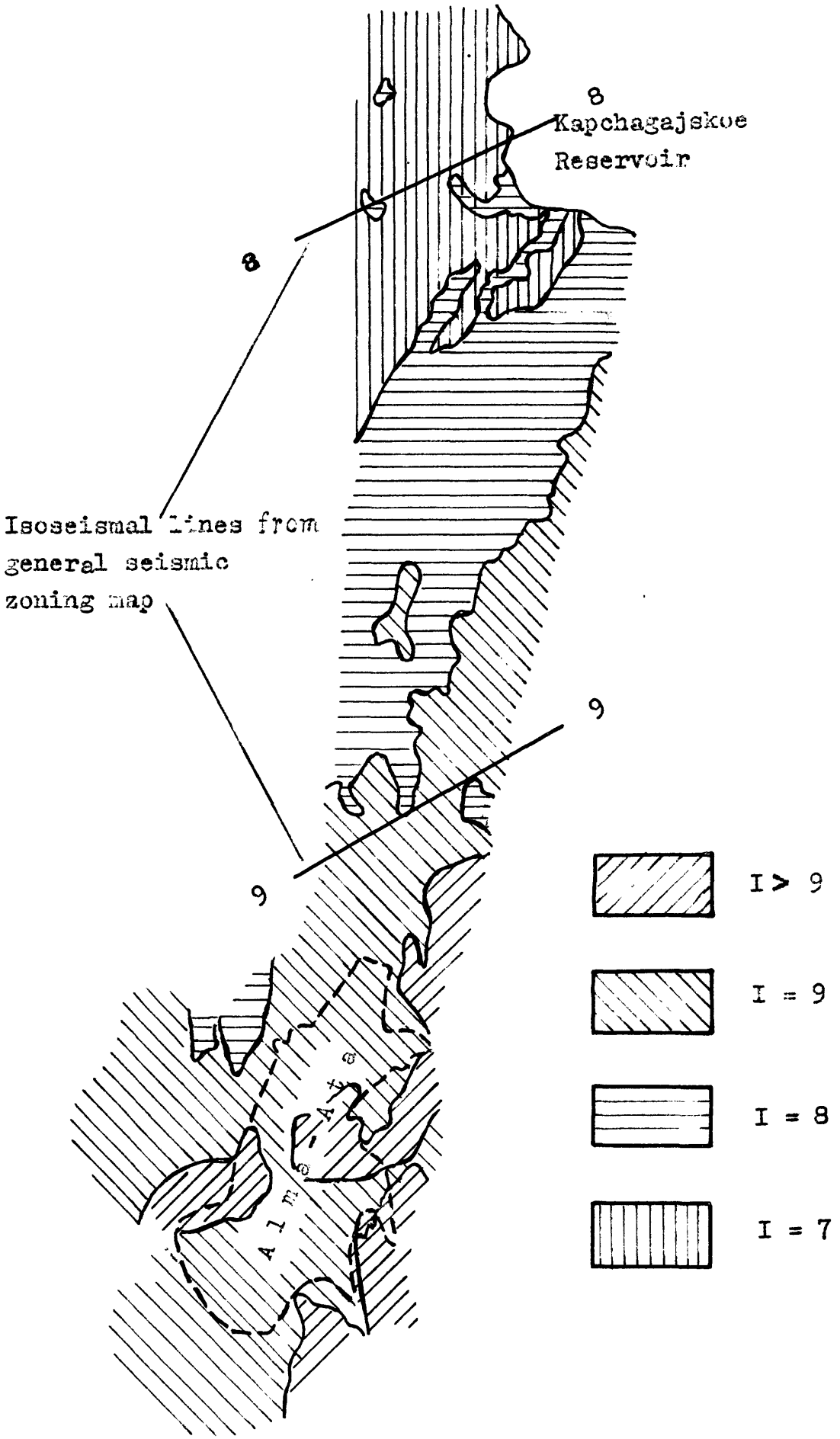

Figure 2c Microzonation map of Alma-Ata region (using data of Gosstroy and Academy of Science of Kazakhstan). Shading reflects intensity zones (on the Soviet scale).

Thus, engineering seismology investigations for specific building sites naturally separate into two types—detailed seismic zoning and seismic microzonation. The first is aimed at investigation of seismic events, the second at the influence of local conditions upon seismic effects. While microzonation in the Soviet Union already has a long tradition, detailed seismic zoning work has only begun. Currently a special commission is developing recommendations to implement this technique.

The basic principles of detailed seismic zoning are

1. For seismically active areas detailed seismic zoning is obligatory and is based on data plotted on the general seismic zoning map.
2. Maps of detailed seismic zoning are overlaid on topographic base maps with scales from 1:200,000 up to 1:1,000,000. Engineering geology maps may be more detailed. The mapping scale depends on the level of hazard. The size of the mapped area depends on specific conditions, but as a rule a mapped area will include a radius of 50 to 100 kilometers from the building site.
3. Selection of the building site and estimation of possible seismic forces affecting this site are made on the basis of both detailed seismic zoning and microzonation. Site selection is also based on estimates of geologic hazards of non-vibration character.

Detailed seismic zoning is carried out by using different scientific methods to obtain the needed data. Those data are then examined in an integrated fashion, and on this basis, the final conclusions—including earthquake predictions if possible—are drawn about the geologic hazards of the region.

Seismological methods, both macroseismic and instrumental, are used to determine the distribution of events in time and space, the nature of focal mechanism, the maximum magnitude and intensity, the wave attenuation and estimates of the probable characteristics of seismic motions.

Geological methods are used to estimate the places of possible earthquakes, their magnitude and focal mechanism, and to determine places unfavourable for use because of geological conditions.

Engineering geology is used to identify locations with high geologic hazards, such as landslides and rockfalls, and to estimate the specific effect upon construction of materials beneath the site.

Correlations between seismic activity and geophysical parameters are used to find the places of possible earthquake origin. In addition, geophysical methods are used to investigate geological structures.

Geodetic observations are used to estimate recent crustal movements and the tectonic strain field.

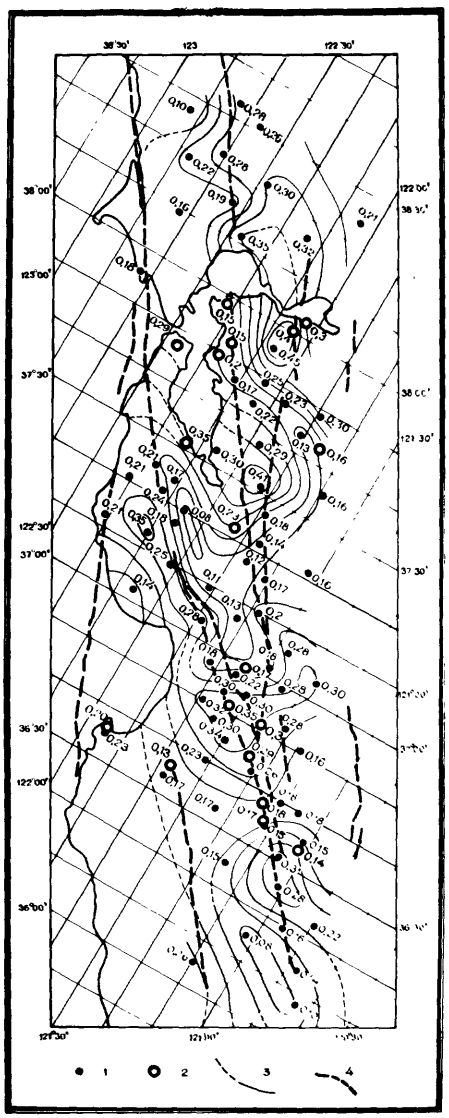

Figure 3 Expected predominant period of acceleration for California earthquakes: 1. Solid circle, high sensitivity station. 2. Open circle, strong motion station. 3. Solid line, isoline of periods. 4. Dashed line, main faults.

Finally, the basic results of detailed seismic zoning investigations are summarized on four types of maps, which must show the probability ranking of all the mapped values:

1. Tectonic map showing the various seismogenic structures and epicentral areas.
2. Engineering geology map.
3. Map of expected seismic intensity.
4. Map of expected seismic motion characteristics.

In addition to these final maps, working maps compiled during a detailed investigation show different geological and geophysical characteristics of the area such as its geomorphology, epicenters, and isoseismal lines of former earthquakes. Working maps show the basic data used in preparing the final zoning maps.

Within the bounds of joint Soviet-American work on earthquake prediction we have together studied the development of detailed seismic zoning and have investigated methods for quantitative estimation of seismic motion. The essence of this latter approach is its assessment of quantitative characteristics in specific places, using both instrumental records of strong and weak local earthquakes and those of distant shocks (Aptikaev and others, 1976, 1979).

As an example we show some results for California. Figure 3 is a map of predominant periods of acceleration during local earthquakes in California. Any other parameters of strong motion, such as peak amplitude or relative duration, could be mapped in the same manner. By comparing a map of general seismic zoning with a map of quantitative characteristics it is possible to see clearly some difference in motion within the same intensity zones. Such knowledge of seismic motion characteristics allows engineers to take into account local peculiarities of vibration and to choose for designs employing the most earthquake-resistant construction methods. We have so far described in a general way the seismic zoning methods used in the Soviet Union.

The American school of seismology, geology, geophysics and earthquake engineering has made valuable contributions to methods of earthquake-hazard estimation. Most zoning maps in the United States, just as in the Soviet Union, show the expected seismic intensity (fig. 4). These maps are usually based on historic data and on fault tectonics (fig. 5). U.S. microzonation includes mapping of the existing or potential geologic hazards at a given location and of the ground amplification factor. To estimate quantitative characteristics of seismic motion the United States has also developed the world's best strong-motion array.

The U.S. Government initiated and has supported major research in earthquake-hazard estimation and earthquake prediction. At the time of its passage, the enabling Field Act was a great event, and not only for America. By 1978 Congress had also approved the Earthquake Hazard Reduction Program. Generally speaking, this program is similar to the Soviet national program. It further indicates that such programs are the only true way to solve this dangerous problem and thus save thousands of lives.

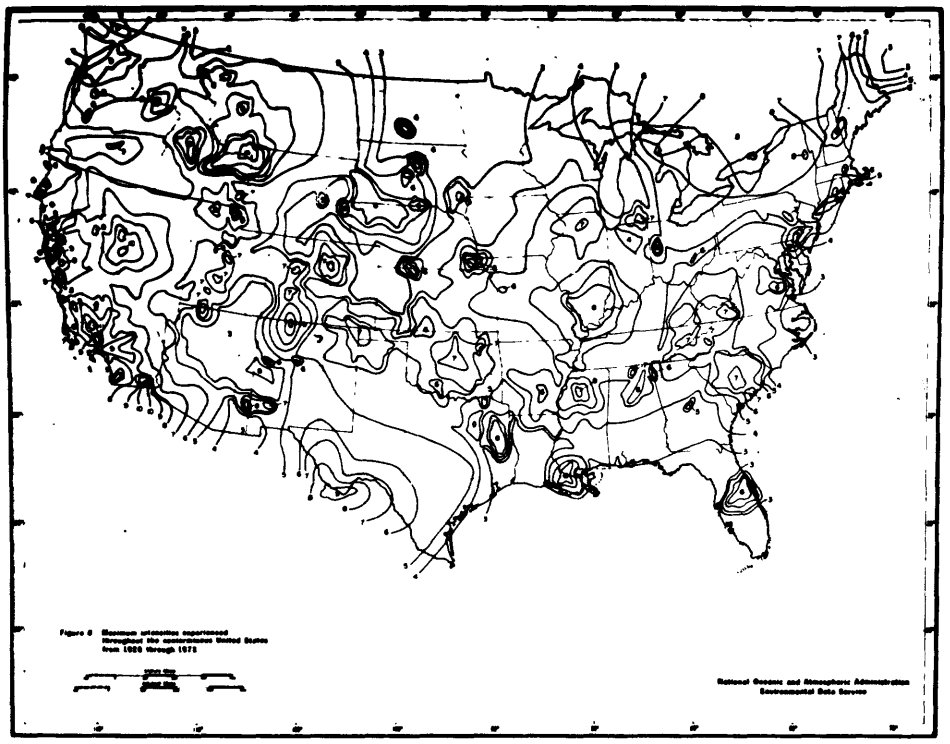

Figure 4 Maximum intensities experienced through the 48 conterminous States of the United States from 1928 through 1973 (from R. J. Brazee, 1976).

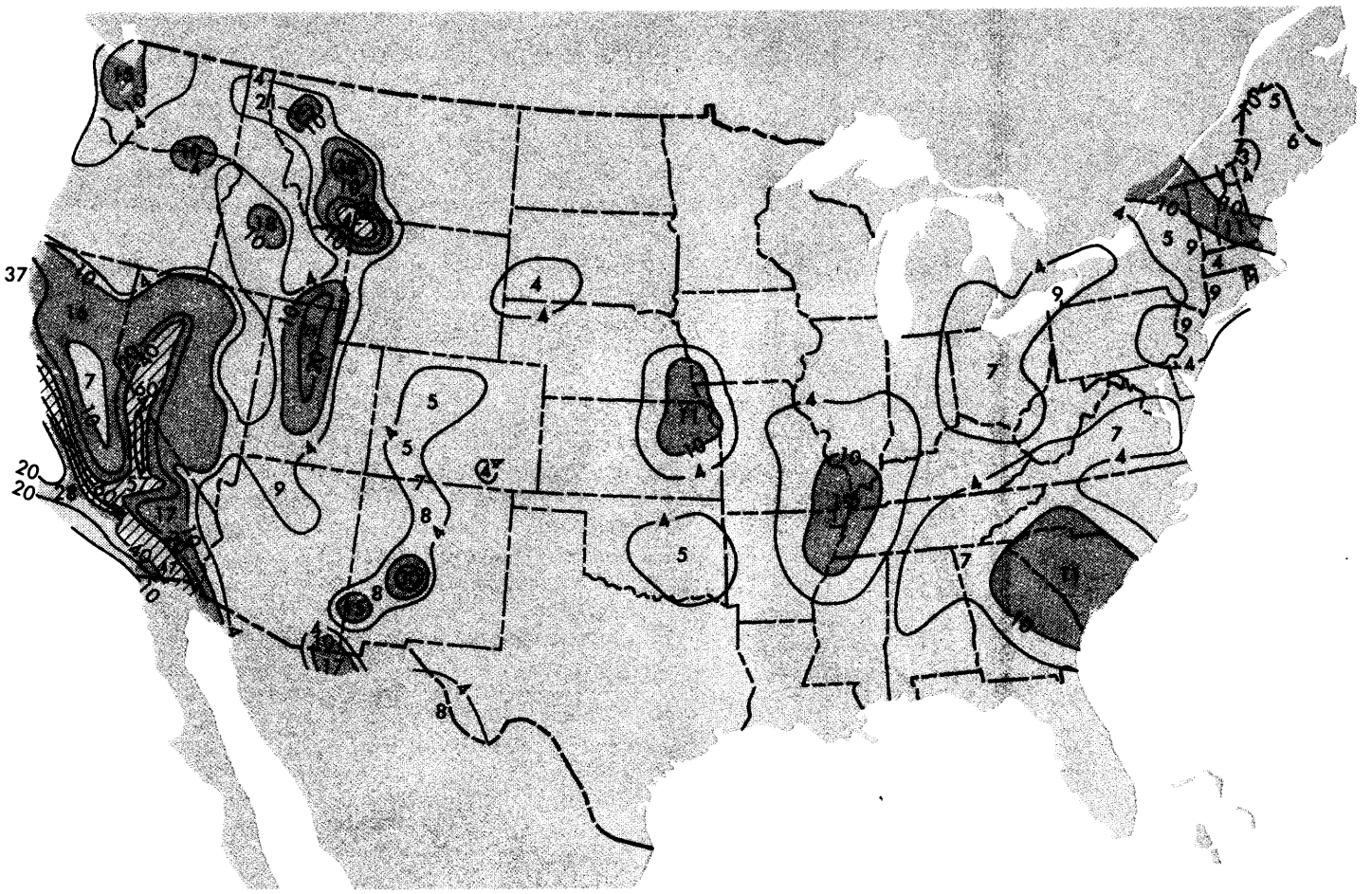

Figure 5 Preliminary map of expected horizontal acceleration (expressed as percent of gravity) in rock with 90 percent probability of not being exceeded in fifty years. Maximum acceleration within the 60 percent contour along the San Andreas and Garlock faults in California is 80 percent of gravity (using the attenuation curves of Schnabel and Seed, 1973.) The 48 conterminous States of the United States (from S. T. Algermissen and D. M. Perkins, 1976).

REFERENCES CITED

Algermissen, S. T., and Perkins, D. M., 1976, A probabilistic estimate in maximum acceleration in rock in the contiguous United States: U.S. Geological Survey Open-File Report 76-416.

Aptikaev, F. F., Gladysheva, G. S., Iton, Dzh., Nersesov I. L., 1979, Sviaz' parametrov seismicheskikh kolebanii pri sil'nykh i sliabykh zemletriaseniiakh [Connection of parameters of seismic vibrations for strong and weak earthquakes]: Sb. sov.-amer. rabot po prognozu zemletriasenii, t. 2., kn.2.

Aptikaev F. F., Iton, Dzh., Nikolaev, A. V., and Sedova, E. N., 1979, Korelliatsiia parametrov seismicheskikh kolebanii pri mestnykh i udalennykh zemletriaseniiakh [The correlation of parameters of seismic vibration for local and remote earthquakes]: Sb. sov.-amer. rabot po prognozu zemletriasenii, t.2, kn.2.

Aptikaev, F. F., Matissen, R. B., Negmatullaev, S. Kh., Nersesov, I. L., Rodzhan, K., and Uelles, R. E., 1976, Prognoz seismicheskogo dvizhenie grunta [Forecasting seismic movement of the Earth. A collection of Soviet-American works on earthquake forecasting]: Sb sov.-amer. rabot po prognozu zemletriasenii, t.1, kn. 2., Dushanbe-Moskva, Izd. Donish.

Brazee, R. J., 1976, Final report on analysis of earthquake intensities with respect to attenuation, magnitude and rate of recurrence: NOAA Technical Memorandum EDS NGSDS-2 Boulder, Colorado.

Schnabel, P. D., and Seed, H. B., 1973, Acceleration in rock for earthquakes in the Western United States: Seismological Society of America Bulletin, v. 63, p. 501-516.

Seismicheskoe raionirovanie SSSR, Izd. Nauka moskva, 1978, [Seismic Zoning of the USSR (translated from Russian). Jerusalem, 1980.]

I. L. Nersesov
Institute of Physics of the Earth
Academy of Science, USSR
B. Bruzinskaya 10
Moscow D242, USSR

(page 13 follows)

Reprinted from Proceedings of the Second International Conference on Microzonation for Safer Construction-Reseach and Application, p.681-691, 1978.

ENGINEERING AND SEISMOLOGICAL OBSERVATIONS AT DAMS

by

S. Kh. Negmatullaev[I], G. S. Seleznyov[II], D. W. Simpson[III] and C. Rojahn[IV]

ABSTRACT

Seismological studies related to dams must investigate the pre-impounding seismic regime and monitor any changes in seismicity during and after filling of the reservoir. Engineering seismological studies must investigate the kinematics of ground motion in and around the dam during earthquakes, the dynamic stresses and pore pressure within the body of the dam and any residual deformation. Depending on the size of the dam and seismic hazard, three levels of investigation are recommended:

1) For dams less than 100 meters high in areas of low seismicity, continuous operation of 1 to 3 seismograph stations in the reservoir region and 1 or 2 strong-motion instruments on or near the dam.
2) For dams more than 100 meters high in areas of moderate to high seismicity, continuous operation of 4 to 6 seismograph stations around the reservoir and 4 to 6 sets of instruments for measuring strong-motion, stress, pore pressure and residual deformation within the dam.
3) For dams of special interest, such as the 315 meter high earth-fill Nurek Dam in Tadjikistan, continuous operation of more than 6 seismograph stations around the reservoir including at least 5 years of pre-impounding monitoring; and a more complete complex of instruments for measuring strong-motion and stress deformation conditions within the dam.

INTRODUCTION

In order to satisfy increased demands for hydroelectric power, irrigation, flood control and water supply, the number of large reservoirs, especially those with very high dams, has increased rapidly over the last two decades. There are now more than 400 dams higher than 100 meters of which 93 have heights greater than 150 meters (1). The highest dams are: Ragoun (USSR, 340 m), Nurek (USSR, 317 m), Grande Dixence (Switzerland, 285 m), Inguri (USSR, 272 m), Rossella (Italy, 265 m), Vajont (Italy, 261 m), Mica (Canada, 242 m), Sayano-Shushenskoe (USSR, 242 m), Mauvoisin (Switzerland, 236 m) and Oroville (USA, 236 m). These dams produce reservoirs with capacities (for the largest dams) from 10 to 169 km^3. About half of these reservoirs are located in seismically active regions. These unique structures demand special attention, not only during the planning and construction stages, but also during utilization.

I Institute Director, Institute of Seismoresistant Construction and Seismology, Dushanbe, Tadjikistan, USSR.
II Chief, Department of Hydrotechnical Structures, Institute of Seismoresistant Construction and Seismology, Dushanbe, Tadjikistan, USSR.
III Research Associate, Lamont-Doherty Geological Observatory of Columbia University, Palisades, New York 10964.
IV Research Civil Engineer, U.S. Geological Survey, Menlo Park, California 94025.

Large dams must be constructed to withstand the strongest earthquake shaking expected at the site. This requires information on both the expected maximum earthquake and the response of the dam to this ground shaking. In the design of most critical engineering structures, seismic risk is evaluated assuming that future seismicity can be estimated from the seismic history of the area. This assumes that the structure is passive and has no effect on the local seismicity. With dams and large reservoirs this may not be true. The impounding of large reservoirs has, in a number of cases, severely modified the local seismic regime (1, 2). Estimates of seismic risk for large dams must, therefore, include the effect of natural seismicity and also the potential for induced seismicity.

To insure the seismic safety of a large dam requires the integration of geological, seismological and engineering studies of the reservoir area, the dam site and the dam structure. These studies, and a close coordination between them, must extend throughout the planning, construction and utilization of the project. In the following, we will discuss some of the techniques and instrumentation required for monitoring the seismic safety of a dam, with special reference to existing and proposed studies at the Nurek Dam in Tadjikistan, USSR.

SEISMOLOGICAL OBSERVATIONS

Seismicity studies at reservoirs, as with any large engineering structure, must include studies of regional seismicity in order to estimate the maximum expected earthquake for which the structures must be designed. In the early planning stages for a large dam project, estimates must be made of the seismic risk. This requires a knowledge of the regional seismicity, active geological structures and historical earthquake activity within the region. From these data, standard techniques are used to estimate the expected size and location of the maximum natural earthquake. Unlike other types of structures, however, studies of seismicity at large reservoirs must also take into consideration the effect which the reservoir may have on changing the seismic regime (1).

The initial basis for evaluating the seismic requirements for a dam is the regional seismicity. In most areas of moderate to high seismicity, such information is available from regional or national seismograph networks. These provide an indication of the general level of seismicity in the project area. Early in the planning stages for the dam, special studies should be initiated, increasing the number of stations and improving the coverage of the reservoir area. If there is seismicity near the reservoir, seismological and geological information should be integrated to identify the extent of active or potentially active faults. As the time of impounding approaches, the station coverage should be further increased to provide detailed observations during the initial filling cycles.

How many stations are required will depend on a number of factors, including the background level of seismicity, the size of the dam and reservoir, the potential for induced seismicity and the hazard posed to populated areas (5). For any large dam, 1 to 3 sensitive seismograph stations should be included in the standard monitoring equipment for the project. For dams more than 100 meters high in areas of moderate to high seismicity, 4 to 6 stations should begin operation at least 5 years prior to first impounding and continue to operate throughout the lifetime of the

dam. These stations should be located within an area, centered on the reservoir, with a diameter of less than twice the maximum dimension of the reservoir.

For those dams which are of special interest, either because of their size or specific seismic hazards, a temporary network of stations should supplement the long-term observations during, and for 5 years following, the first filling of the reservoir. This network, consisting of 6 to 10 stations, should be located in the immediate vicinity of the reservoir, with special emphasis near areas of active faulting and near the deepest part of the reservoir.

Studies of reservoirs with potential for induced seismicity require monitoring of both temporal and spatial changes in seismicity. In order to positively identify changes in the seismic regime caused by filling of a reservoir, it is necessary to have stable observations of seismicity over many years. At most of the reservoirs where large induced earthquakes have occurred (e.g., Kariba, Koyna, Kremasta, Hoover, Hsinfengkiang) (1, 2), networks of seismograph stations were installed only after the onset of increased seismicity, so that it has been difficult to compare pre- and post-impounding seismicity and to define the exact nature of changes caused by the reservoir.

When induced or natural earthquakes occur near a reservoir, it is important to be able to locate hypocenters with sufficient accuracy to associate activity with specific faults. Migration of activity and changes in the level of activity associated with variations in water level in the reservoir may be important in predicting future patterns of seismic activity. A dense network of high-magnification stations close to the reservoir is necessary to provide the accuracy and detection of microearthquakes required for such studies.

As an example of a combination of regional, local and intensive seismicity surveys for observation at a large reservoir where induced seismicity is occurring, we will use the case of Nurek Reservoir on the Vakhsh River in Tadjikistan (3). When completed in 1979, the earth-fill Nurek Dam will be 315 meters high and impound a reservoir volume of 10.5 km^3. The reservoir first filled to 100 meters in 1972 and the second stage of filling, to 200 meters, was in 1976 (Figure 1).

The southern part of Tadjikistan is a region of moderate to high seismicity. Instrumental observations of seismicity began in Tadjikistan in 1920. Since 1955, regional seismic stations have operated around the reservoir, and the catalog of earthquakes greater than magnitude 2.5 is complete from 1955. The maximum expected earthquake for the area has been estimated as magnitude 6.5 (3).

As shown in Figure 1, there have been pronounced increases in seismic activity during the first two stages of filling of the reservoir. Before filling, approximately 10 earthquakes per year greater than magnitude 1.5 occurred within 10 km of the reservoir. During the early filling stages, this number rose to more than 100 per year. The largest earthquakes following impounding were two of magnitude 4.5 near the southwest end of the reservoir, at the end of the first stage of filling in 1972 (4).

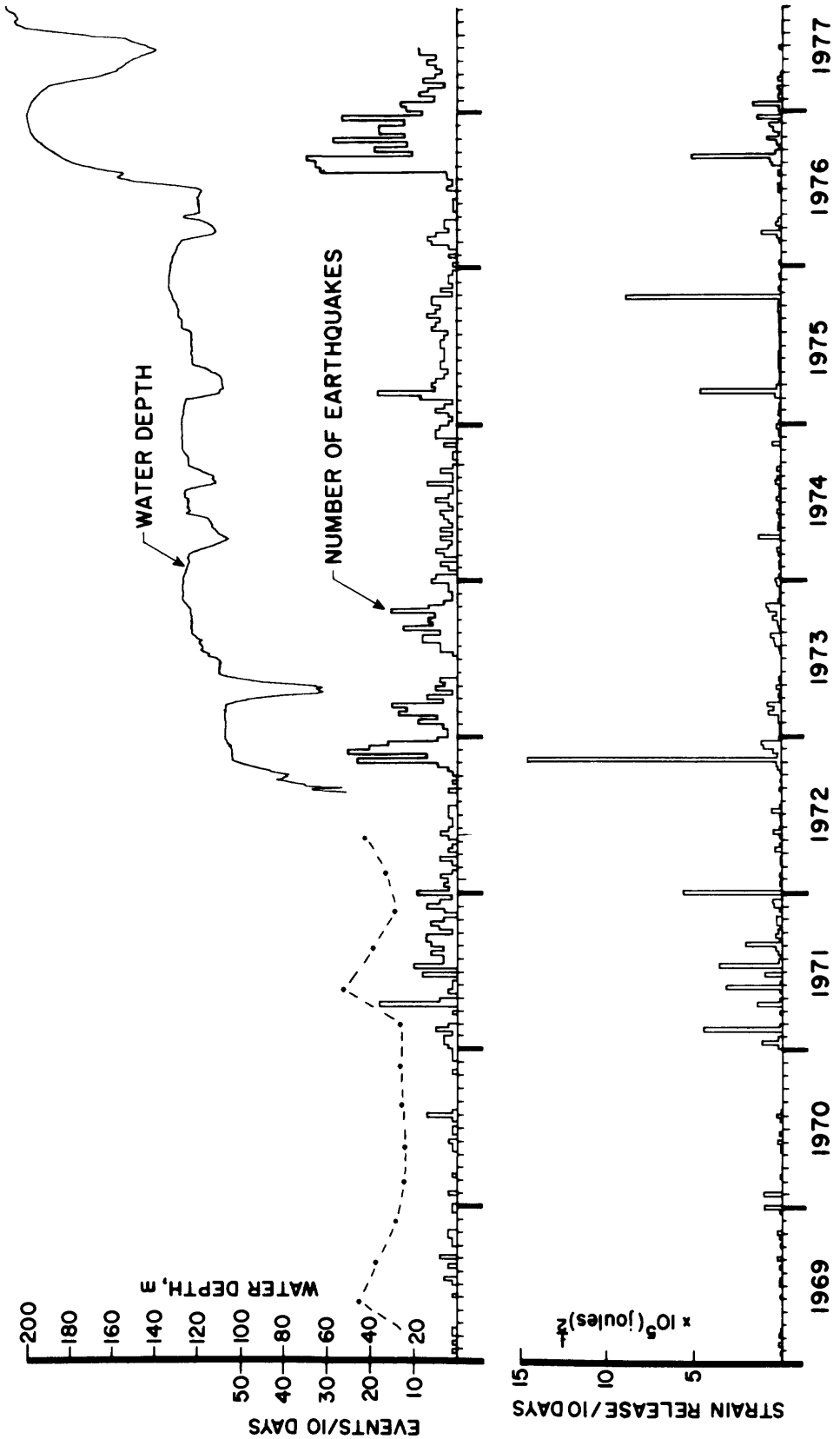

Figure 1: Water level, number of earthquakes per ten days and strain release per ten days for earthquakes within 10 km of Nurek Reservoir.

When the dam began filling in 1971, there were five stations within 40 km of the reservoir operated by the Tadjik Institute of Seismoresistant Construction and Seismology and four additional stations were added before 1976. In 1975, as part of a joint Soviet-American program in earthquake prediction, a radio-telemetered network of 10 stations was installed around the reservoir. Figure 2 shows the location of the two sets of stations. The combined network of Soviet and American stations is well-suited for studying both temporal and spatial variations in seismicity. The Soviet stations have provided a stable and complete catalog of earthquakes for the 10-15 year period prior to and during filling of the reservoir. Each of the Soviet stations is manned and operates independently, recording three components of ground motion at magnifications of 10,000-20,000. Because of the relatively wide spacing between stations, the location accuracy is not high, but the temporal stability provides a clear indication of the changes in seismicity caused by filling of the reservoir (Figure 1).

The stations of the American network installed in 1975 operate unattended, continuously telemetering data to a central recording location. Station magnifications are 200,000-500,000. The network is concentrated near the central part of the reservoir, where most of the induced seismicity is occurring. Within this area, location accuracy has improved by an order of magnitude and the detection threshold has decreased by 2 magnitude units.

Figure 1 shows that increased seismicity at Nurek is closely related to times of rapid change in water level (e.g., November 1972, March 1975, August 1976). There are also indications that the level of seismicity is also related to the rate at which the water level is changed. Thus, it is possible that careful control of the way in which the water level is changed can be used to control the level of seismic activity. In order to monitor such controlled changes in seismicity, or to observe changes in microearthquake activity preceding larger natural or induced earthquakes, a sensitive network of seismograph stations is required in the immediate reservoir area.

ENGINEERING INVESTIGATIONS

Many of the parameters necessary to study the seismic response of a large dam are included in the standard observations for the control and monitoring of the dam structure. These "static" observations include the monitoring of residual deformation (settlement and displacement), stress, pore pressure (especially in the core, in the upstream face and in the foundation), filtration rates through the dam and water levels upstream and downstream from the dam. These observations, some obtained by passive measurement and some through active experiments, are traditional and well known, and will not be discussed here. Usually, the extent to which these static observations are made depends on the size and importance of the structure.

When dams are constructed in seismic regions, these static observations must be supplemented with equipment for monitoring "dynamic" processes (5, 6, 7), especially the kinematic parameters of motion: displacement, velocity and acceleration. A detailed study of the dynamic processes taking place in dams during earthquakes also requires observation of

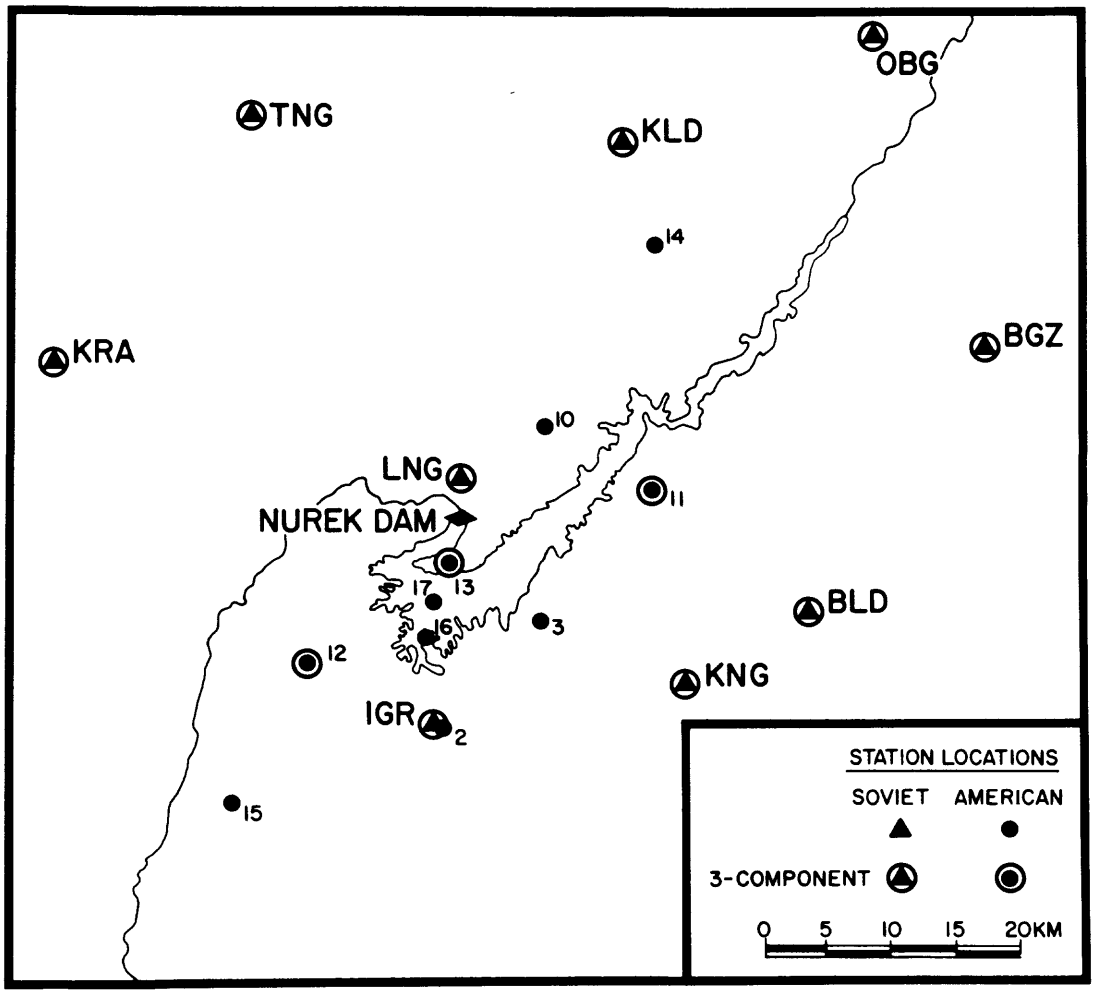

Figure 2: Seismograph stations in the vicinity of Nurek Reservoir.

the dynamic deformation, stresses and pore pressure within the dam and its foundation. Such observations can lead to improved design techniques and predictions of the behavior of specific structures during severe ground shaking.

Following is a general description of proposed instrumentation for monitoring "dynamic" processes in Nurek Dam. The proposed schemes have been recommended by the Tadjik Institute of Seismoresistant Construction and Seismology. They are based on experience gained from studies of other large dams in the Soviet Union (6, 7).

The earth-fill Nurek Dam will have a height of 315 meters and a crest length of 700 meters; it will extend 1500 meters along the river channel (Figure 3). The body of the dam consists of a central water-resistant core, transition zones, supporting prisms of gravel and rockfill on the upstream and downstream faces. The gradients of the slopes are 1:2.25 for the upstream face and 1:2.20 for the downstream face. The dam will form a reservoir with a total capacity of 10.5 km^3 and an area of 100 km^2, which will extend 70 km upstream from the dam. Annual variations in water level will be 50 to 60 meters (a volume of 4.5 km^3).

Shown in Figure 3 is the proposed system for measuring kinematic parameters in the dam. The system will consist of 29 measuring points (13 permanent and 16 temporary); its purpose is to record the movement of the foundation, the walls of the canyon and the body of the structure during small and strongly felt earthquakes. The thirteen measuring points designed for long-term use are equipped with apparatus for recording strong and destructive earthquakes. The other 16 measuring points are to be used for short-term experiments (3 to 5 years). Their purpose is to obtain data for special projects such as the study of spatial variations in the vibration of the body of the dam, variations in the dynamic behavior of the rock canyon and/or the interaction of the structure with the rock foundation.

Shown in Figure 4 is a proposed system for observing dynamic stresses in the core and downstream prism, which is the most stressed element within the body of an earth-fill dam. The three-component dynamic stress cells are to be located at three levels with a total of 5 measuring points in the prism and 2 in the central core.

Also shown in Figure 4 are proposed locations for pore pressure measurements in the core of the dam and in the water-saturated upper prism. The instruments are to be located at the levels of the main viewing galleries, i.e., at 1/2 and 3/4 of the height of the dam.

Strainmeters for measuring residual deformations during earthquakes are proposed at 5 points along the transverse profile (maximum section) of the dam (Figure 4). These observations will be made at the crest on both slopes and in the viewing galleries at approximately 1/2 and 3/4 of the dam height.

Continuous observations will also be made of the variations in water level upstream and downstream of the dam. Locations of the proposed gauges are shown in Figure 4. The range of these observations must include variations in the reservoir level during normal use and also take into

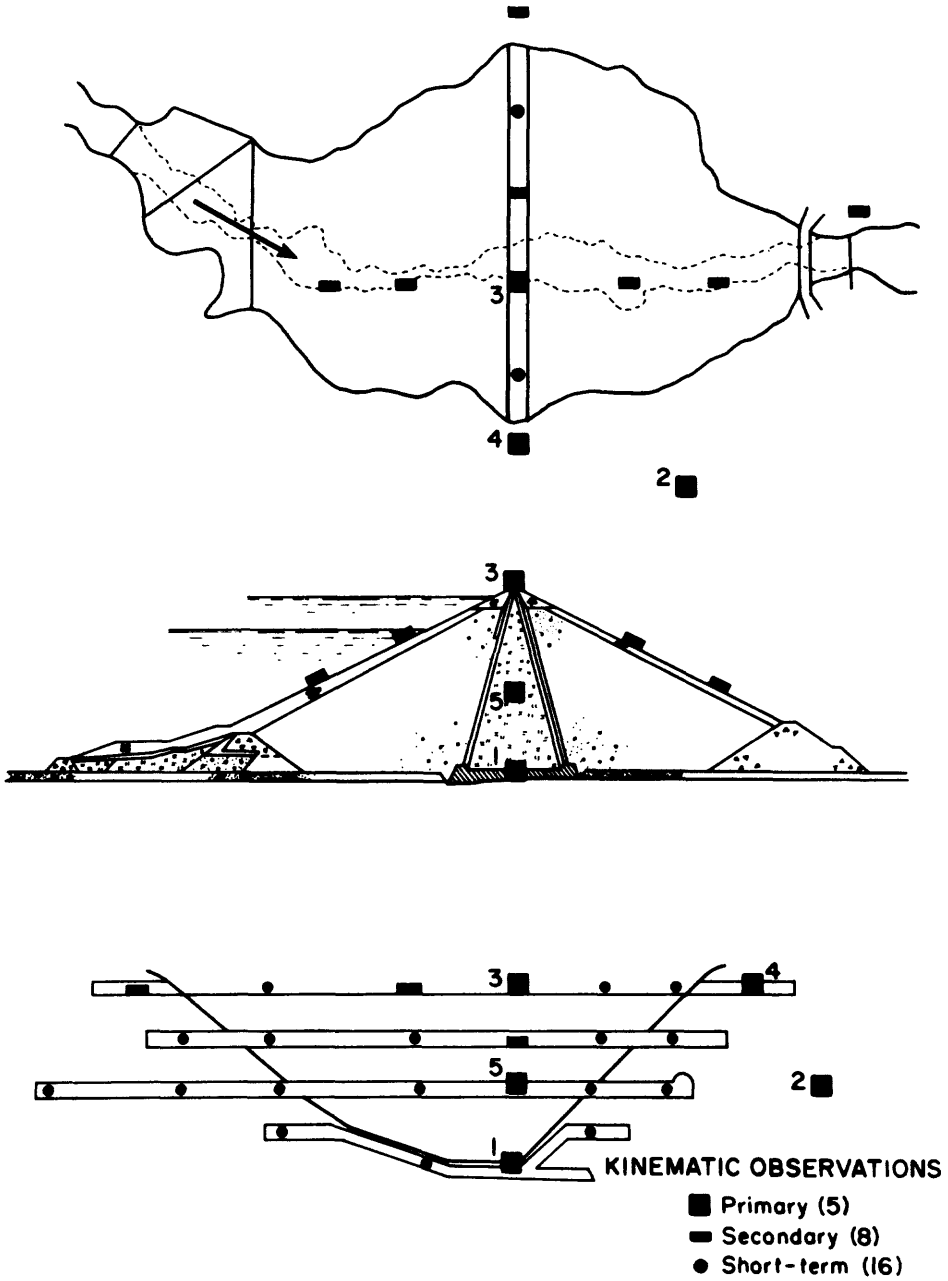

Figure 3: Plan view, transverse section and longitudinal section of Nurek Dam showing proposed system for measuring strong-motion.

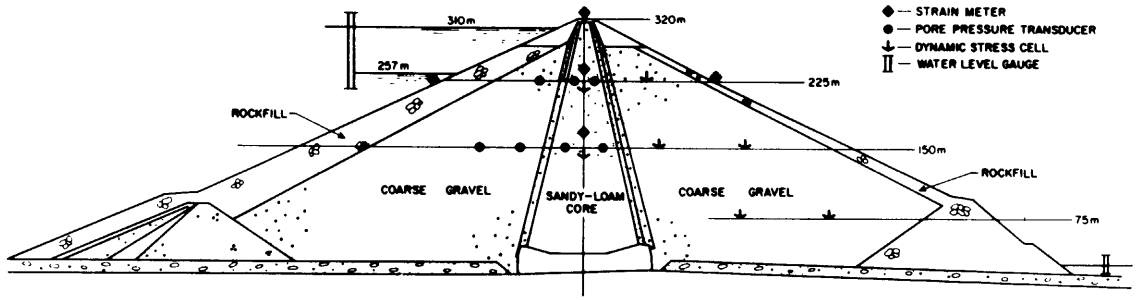

Figure 4: Transverse section of Nurek Dam showing proposed system for measuring dynamic stress and pore pressure.

account possible disturbances as the result of a strongly felt earthquake (e.g., seiches, increased filtration).

For monitoring and control of the dam structure, it is proposed that the following 24 channels of data be continuously recorded at a central site: residual displacements at the crest and on the slopes (6 channels); acceleration of the foundation and crest at the maximum section (6 channels); pore pressure in the upper prism and in the central core at 2 levels (4 channels); water level upstream and downstream of the dam (2 channels); and dynamic stress at one point in the core and at one point in the lower prism (6 channels).

The extent of instrumentation for measuring the dynamic response of Nurek Dam is based on the fact that the dam is unusually large and is located in a moderately active seismic zone. The degree to which smaller dams should be instrumented depends on the relative size and type of dam as well as the expected level and occurrence of seismic activity. A survey of instrumented dams in the U.S. (8) suggests that most instrumented dams fall into one of the following two categories: 1) dams where 1 or 2 strong-motion accelerographs have been installed to record site response; and 2) dams where 4 to 6 strong-motion accelerographs have been installed to measure site response and structural response. It is assumed that the extent of instrumentation at each of these dams is dependent upon the availability of funding, size and type of dam and extent of expected seismic activity. Considering such factors in general as well as experience with dam instrumentation in the USSR, the following instrumentation schemes are recommended: 1) for dams less than 100 meters high in areas of low seismicity 1 or 2 strong-motion instruments near and/or beneath the dam; 2) for dams more than 100 meters high in areas of moderate to high seismicity, 4 to 6 sets of instruments for measuring strong-motion on and near the dam as well as stress, pore pressure and residual deformation within the dam; and 3) for dams of special interest such as the 315 meter high earth-fill Nurek Dam, a more complete complex of instruments for measuring strong-motion and stress deformation conditions within the dam.

ACKNOWLEDGEMENTS

This work is supported in part by National Science Foundation Grants ENV 77-01092, AEN 75-22996, U.S. Geological Survey Contract 14-08-0001-15279 and Earth Science Section, National Science Foundation Grant GA 43650. We wish to thank Michael Hamburger for assistance in translation.

Lamont-Doherty Geological Observatory Contribution Number 2713.

BIBLIOGRAPHY

(1) Simpson, D.W., 1976. Seismicity changes associated with reservoir loading; In "Induced Seismicity", edited by W.G. Milne, Eng. Geol., 10(2-4), 123-150.

(2) Gupta, H.K. and B.K. Rastogi, 1976. Dams and Earthquakes, Elsevier, Amsterdam, 229 pp.

(3) Negmatullaev, S.Kh. (ed.), 1975. Induced Seismicity near Nurek Reservoir; Donish Publishing House, Dushanbe, 88 pp. [in Russian].

(4) Soboleva, O. and U.A. Mamadaliev, 1976. The influence of the Nurek Reservoir on local earthquake activity; Eng. Geol., 10, 293-305.

(5) Bolt, B.A. and D.E. Hudson, 1975. Seismic instrumentation of dams; J. Geotechnical Engineering Division, Proc. Amer. Soc. Civil Engineers, 10, 1095-1104.

(6) Sagdiev, T.G., R.S. Shuser and G.S. Seleznyov, 1966. On the establishment of engineering-seismological observations at dams; Eng. Seismol., No. 3-4, Donish Publishing House, Dushanbe, pp. 82-86 [in Russian].

(7) Sagdiev, T.G., G.S. Seleznyov and U.L. Zaslavckii, 1968. Questions on the Organization of Engineering-Seismological Surveys at Dams; Donish Publishing House, Dushanbe, 41 pp. [in Russian].

(8) Western Hemisphere Strong Motion Accelerograph Station List, 1976; USGS Open File Report N77-374, 1977, 112 pp.

(page 25 follows)

Bulletin of the Seismological Society of America, Vol. 71, No. 5, pp. 1561–1586. October 1981

INDUCED SEISMICITY AT NUREK RESERVOIR, TADJIKISTAN, USSR

By D. W. Simpson and S. K. Negmatullaev

ABSTRACT

More than 1800 earthquakes ($1.4 > M > 4.6$) have occurred during the first 9 yr of filling of the 300-m deep Nurek Reservoir in Tadjikistan. This is more than four times the average rate of activity in the region prior to the start of filling. The increased seismicity has occurred in a series of bursts, the two most intense of which were related to rapid increases in water level during the first two stages of filling—to 105 m in 1972 and to 205 m in 1976. All periods of high seismicity take place when the water level is higher than it has been previously or within 10 m of its previous maximum. If the water level drops more than 10 m below its previous maximum, the level of seismicity decreases. All of the largest earthquakes and most of the bursts of activity are triggered by decreases in the rate of filling of the reservoir. Once the water level is more than 10 m above the previous maximum, the potential for increased seismicity is high. Extremely small changes in filling rate can then trigger the onset of activity. For example, the largest earthquakes all followed decreases in filling rate of approximately 0.5 m/day; and in a number of cases, increased seismicity began soon after the reservoir started to empty by rates as small as 0.2 m/day^2. The response in seismicity to decreases in the filling rate is rapid. Increased activity follows abrupt decreases in filling rate with delays as short as 1 to 4 days.

As the reservoir has approached its maximum size, extending 40 km upstream from the dam, the area of induced seismicity has increased as well. The first induced earthquakes in 1971 were located 10 to 15 km southwest of the reservoir. From 1972 to 1978, activity migrated into the immediate reservoir area and followed the growth of the reservoir upstream. The first stage of activity in 1971 to 1972 was characterized by low b values and included the largest earthquakes of $M = 4.6$ and $M = 4.3$ in November 1972, when the water level first exceeded 100 m. From 1973 to 1979, activity was confined to the immediate reservoir area and b values were higher. Although the water level has risen to over 250 m, no induced earthquakes larger than $M = 4.1$ have occurred since November 1972.

Introduction

The filling of Nurek Reservoir in the Tadjik SSR, USSR has been accompanied by significant levels of induced seismicity. In 1981, the level of the reservoir will be raised to its maximum depth of 300 m, making it the deepest man-made reservoir in the world. Central Tadjikistan is a region of complex tectonics and experiences a high level of natural earthquake activity. Because of this, seismological and geological studies of the reservoir area began in the early planning stages for the project. Since 1955, the Tadjik Institute of Seismoresistant Construction and Seismology (TISSS) has been monitoring seismicity in the Nurek area, so that Nurek is one of the few reservoirs with induced seismicity where there is a detailed knowledge of the seismological conditions existing around the reservoir prior to impounding. This has made it possible to determine the extent of changes in the rate of seismic activity related to filling of the reservoir, and to study changes in other aspects of the seismic regime. Geological and seismological studies carried out prior to construction of the dam are described by Baratov and Gaiskii (1962). Descriptions of induced seismicity during the initial stages of filling of the reservoir are found in

Negmatullaev (1975), Soboleva and Mamadaliev (1976), and Simpson and Negmatullaev (1978).

Under the auspices of the US-USSR Exchange in Earthquake Prediction, a joint study of induced seismicity at Nurek Reservoir began in 1975. As part of that project, a 10-station American telemetered network was installed around the reservoir. This network complements the permanent set of 10 Soviet stations within 50 km of the reservoir. The American stations cover a 15- by 60-km area, concentrating on the region showing the highest level of induced seismicity. The combined network of Soviet and American stations is well suited to studying temporal and spatial variations in seismicity related to filling of the reservoir—the Soviet stations providing a stable long-term data base for studying temporal variations in seismicity and their relation to changes in water level; the American stations providing the precision necessary to map spatial patterns in seismicity and their relationship to geological structure. The results of studies using the telemetered network are presented elsewhere (Keith *et al.*, 1981). In the present work, we describe the spatial and temporal patterns of induced seismicity at Nurek and their relationship to water level in the reservoir, basing our study entirely on two sets of data: the TISSS catalog of earthquakes in the Nurek area, 1955 to 1979, and daily water levels in the reservoir, 1972 to 1979. A monograph presenting tabulations of these two sets of data is being prepared.

Location and Tectonic Setting

Nurek Dam is located in the northern part of the Tadjik Depression in a narrow gorge of the Vakhsh River, a tributary of the Amu Dary'a (Figure 1). The waters of the Vakhsh rise in the snow fields and glaciers of the Pamir and Alai Mountains as the Surkhob and Obi Khingau rivers, which meet to form the Vakhsh River at the northeastern extremity of the Tadjik Depression in the vicinity of Garm. The Vakhsh follows the structural trend of the Tadjik Depression, flowing southwestward through the northern portion of the depression, changing direction at Nurek to run southward for 200 km before joining the Amu Dary'a at the Afghanistan border. General features of the Nurek area and the Tadjik Depression can be seen in the LANDSAT photograph in Figure 1.

Reviews of regional geology and tectonics can be found in Gubin (1960, 1967), Academy of Sciences, Tadjik SSR (1968), Bekker *et al.* (1974), and Negmatullaev (1975). We present here a general outline of the regional tectonics as it relates to seismicity at Nurek. Separate publications discuss how the seismicity at Nurek relates to the style of deformation in the depression (Keith *et al.*, 1981) and how the local reservoir geology actively controls the spatial distribution of induced earthquake activity (Leith *et al.*, 1981).

The Tadjik Depression is a post-Paleozoic sedimentary basin which has been syndepositionally deformed during the Alpine orogeny. The depression is bounded on the north by the Gissar Ranges, a spur of the southern Tien Shan Mountains; on the east by the Pamir Mountains; on the south by the Hindu Kush and Kopet-Dag; and on the west by the Turan platform. Major seismicity is associated with parts of the northern, eastern, and southern boundaries, and scattered seismicity up to magnitude $5\frac{1}{2}$ occurs throughout the interior of the depression. The Gissar-Kokshal and Vakhsh-Illiak faults form a major boundary between the Caledonian- and Hercynian-deformed structures of the Tien Shan to the north and the Alpine-deformed structures to the south. Recent deformation throughout the region shows a general north to northwest compression which is primarily related to the India-

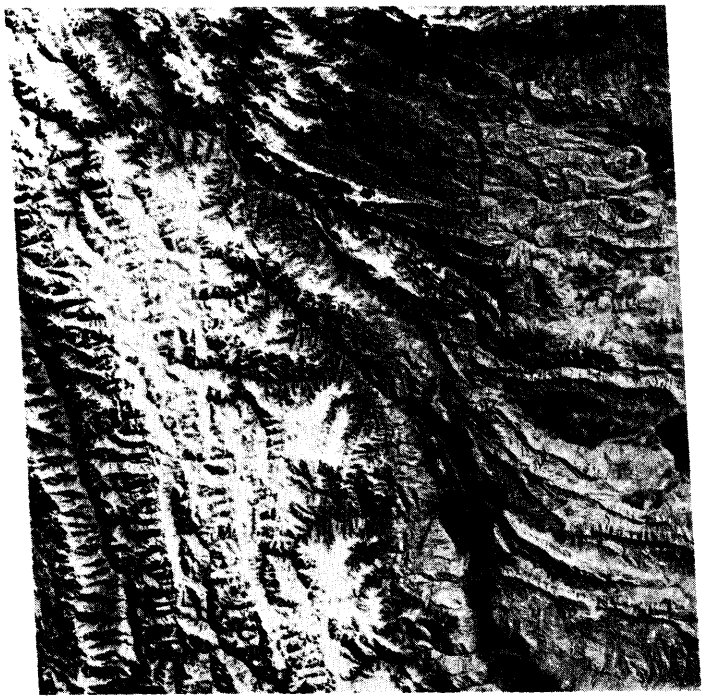

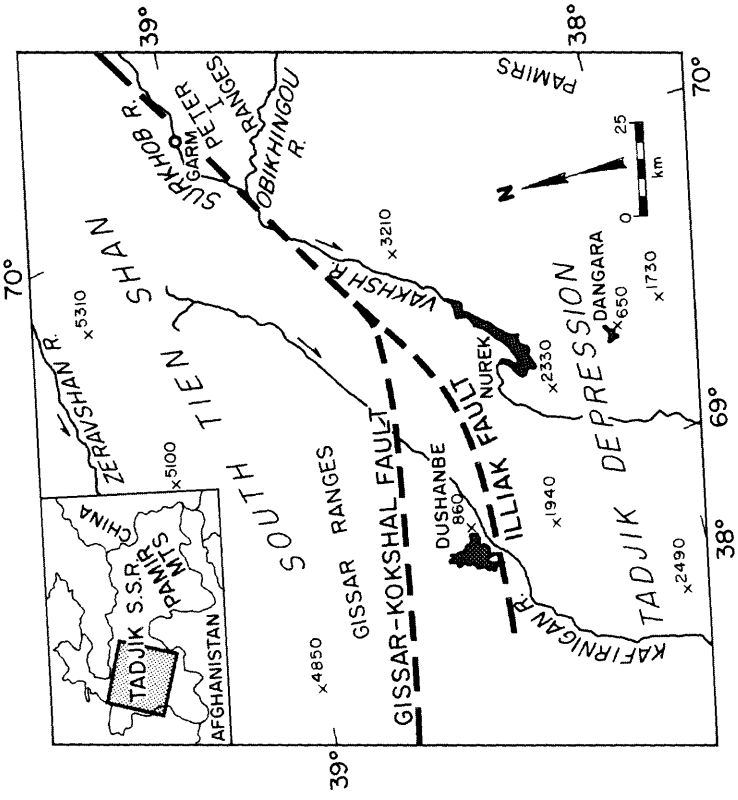

FIG. 1. LANDSAT image of the Nurek area (*right*) and location map (*left*). Elevations of major ranges and cities are given in meters. The east-west trending structures and high topography of the Paleozoic granites of the South Tien Shan contrast with the northeasterly trend of the lower but more intensely folded structures in the Mesozoic and Cenozoic sediments in the Tadjik Depression.

Eurasian collision (Molnar and Tapponnier, 1975). Numerous earthquakes, as large as magnitude 8, have occurred along the Gissar-Kokshal fault zone north of the Depression and the Pamir Mountains in this century (Kristy and Simpson, 1980). To the east, the Darvaz-Kara-Kul fault separates the depression from the Pamir Mountains. Both shallow and intermediate depth seismicity here and to the south of the depression are related to subduction in the Hindu Kush and Pamirs (Billington *et al.*, 1977; Chatelain *et al.*, 1980).

Nurek Dam and Reservoir

Nurek Dam is an earth and rock fill structure 315 m high with a crest length of 800 m, extending 1.5 km along the river at its base (Negmatullaev *et al.*, 1978). The dam is a major part of the development of water resources on the Vakhsh River. Seventy kilometers upstream from Nurek, construction has now started on Ragoun Dam, which has a planned height of 350 m. Nurek drives eight hydroelectric generators providing 2.7×10^6 kW of electric power and the dam provides control of water for use in irrigation. The reservoir formed behind the dam extends 40 km upstream, with a maximum width of 6 km and a maximum volume of 10.5 km^3. The approximate outline of the reservoir at maximum extent is shown in Figure 2.

Filling of the reservoir has taken place in a number of stages (see Figure 5), the water level rising as construction increased the height of the dam. The two major stages of filling occurred in late 1972 (to 105 m) and late 1976 (to 215 m). Large fluctuations in water level result from construction practices at the dam and demands for reservoir water. Maximum water usage occurs in the spring for cotton irrigation, accounting for the rapid decreases in water level starting in early March of each year. Following each of the major filling episodes, the water level was reduced to the prefilling level for inspection and resurfacing of the upstream face of the dam. The minor fluctuations in water level, superimposed on the general filling trend, in September 1972 and August 1976, resulted from the testing of new tunnel structures.

Daily water levels, measured to 0.01 m, are available from mid-August 1972. No data are available prior to August 1972. A coffer-dam, approximately 80 m high (see Negmatullaev *et al.*, 1978), existed immediately upstream of the main dam during the early construction phase (1967 to 1972). The maximum water depth behind the coffer-dam, before it was covered during the first major stage of filling in 1972, occurred in 1971 and was at least 50 m (see Figure 5 in Soboleva and Mamadaliev, 1976).

Seismicity Catalog

The TISSS has operated up to 15 seismograph stations within 100 km of Nurek since 1955. The TISSS catalog of earthquakes for the Nurek area 1955 to 1979 contains over 7000 events (Figure 2). We will refer to the entire region shown in Figure 2 as the Nurek area, and to the rectangular area shown in Figure 2 as the reservoir area. Hypocenters are determined using the graphical methods described by Riznishenko (1960). The catalog contains information on the time, location, depth, and size of each event. Earthquake size is given in terms of the Soviet scale of energy class, K (where K is the logarithm of energy in joules). In the following discussion, we convert the magnitude using the relationship

$$M = (K - 4)/1.8 \qquad \text{(Rautian, 1960).}$$

Earthquakes as small as $K = 5.5$ ($M = 0.8$) are listed in the catalog, which appears to be relatively complete, especially after 1965, above $K = 7.0$ ($M = 1.7$). Before 1965, energy class was given to the nearest 1.0 units and from 1965, to 0.1 units. Epicentral coordinates are given to 0.5 min, accounting for the regular grid pattern of locations in Figure 2.

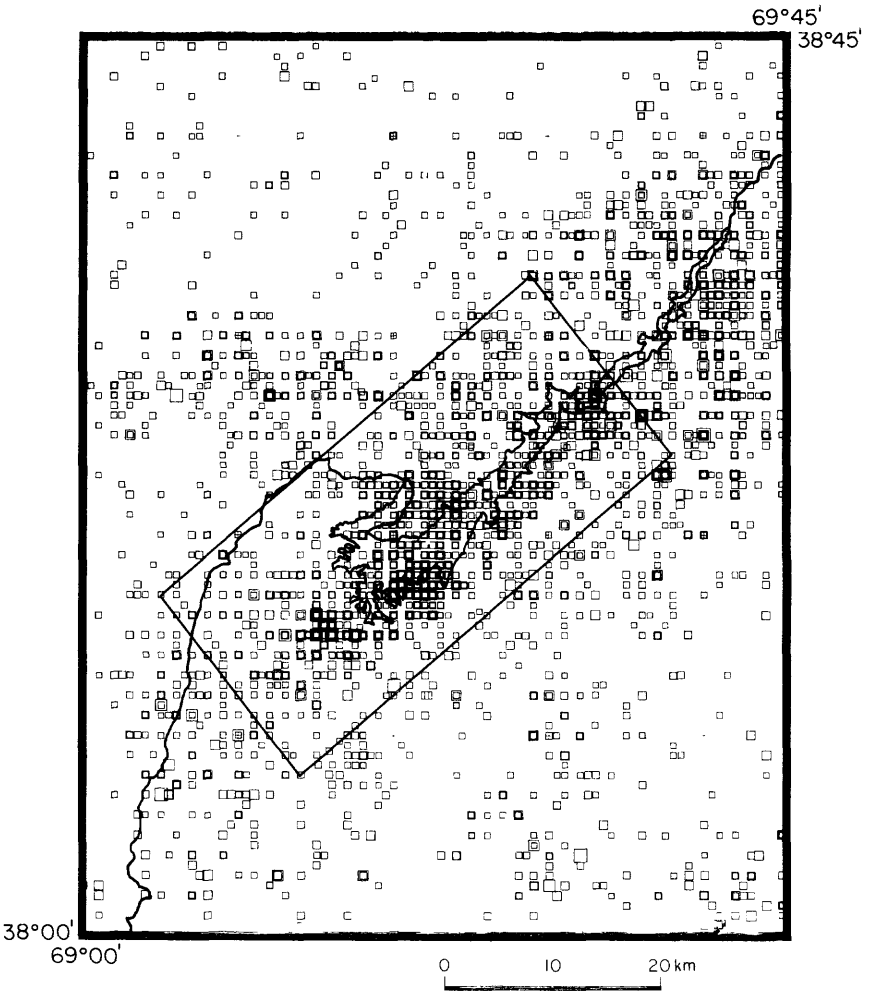

FIG. 2. Earthquakes of $K \geqq 6.5$ ($M \geqq 1.4$) in the Nurek area 1955 to 1979. Epicentral data are from the TISSS catalog. The rectangle outlines the region referred to in the text as the reservoir area. The outline of the reservoir used in all figures is the 1000-m topographic contour and is approximately the limit of the full reservoir.

The accuracy of epicentral location has improved since 1955 and especially after 1968, when additional stations were installed near Nurek. We estimate most early epicenters to be located with a relative precision of ±5 km and more recently of ±2 km. A comparison of TISSS locations with those obtained using the dense network of stations installed around the reservoir in 1975 indicates that there exists a consistent bias of up to 5 km to the northeast in the TISSS locations, but confirms that most of the relative locations are precise to ±2 km. Data from the American

network have not been used in compiling the TISSS catalog, so that the installation of the additional stations in 1975 has not altered the magnitude threshold or location accuracy of the data described in this paper.

There is not sufficient accuracy in depth determinations (±2 km) to resolve any pattern in depth distribution. Except for some of the early events in 1971 (see Figure 9), which are ascribed depths of 10 km, all of the induced seismicity is less than 10 km deep. This is confirmed by studies with the telemetered network, which show most of the post-1976 activity to lie between depths of 2 and 8 km (Keith *et al.*, 1981).

The largest earthquakes, 1955 to 1978, are shown in Figure 3. The largest

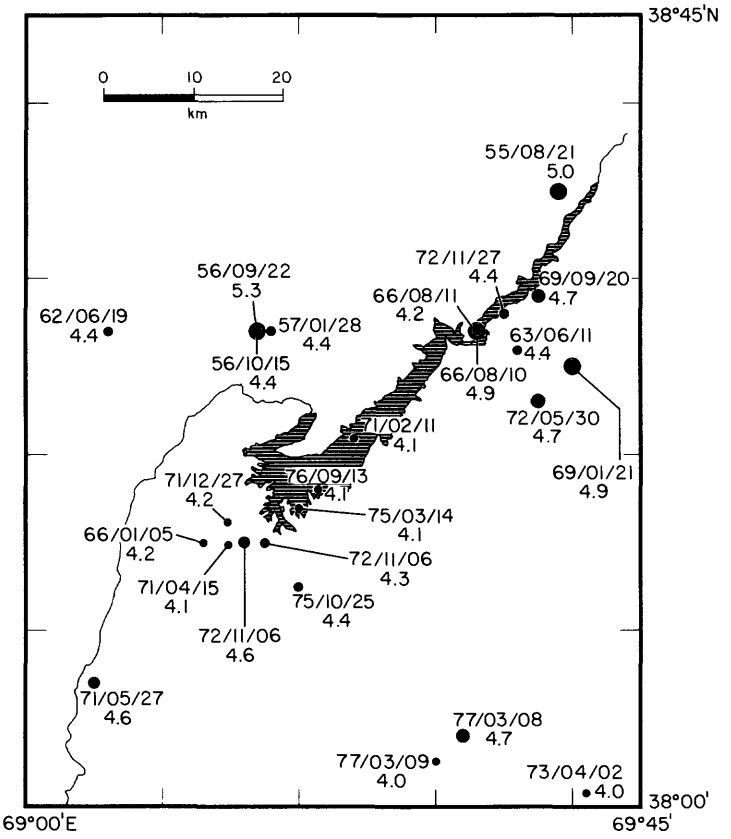

FIG. 3. Earthquakes with $M \geqq 4.0$ in the Nurek area 1955 to 1979.

preimpounding earthquakes near Nurek were the 1956 "Nurek" earthquake of magnitude 5.3, approximately 10 km north of the dam site and events of magnitude 5 in 1966 and 1969 in the far northern end of the future reservoir area.

INDUCED SEISMICITY

In Figure 4, the data of Figure 2 have been divided into two time periods and plotted in a three-dimensional format, showing the number of earthquakes/min^2 of area in the z direction. The 11-yr period, 1960 to 1970, before the filling of the reservoir, shows clusters of activity along the Vakhsh-Illiak fault, north of the reservoir area and a general increase in activity toward the northern end of the reservoir where the Vakhsh-Illiak and Gissar-Kokshal faults merge. Some clustering

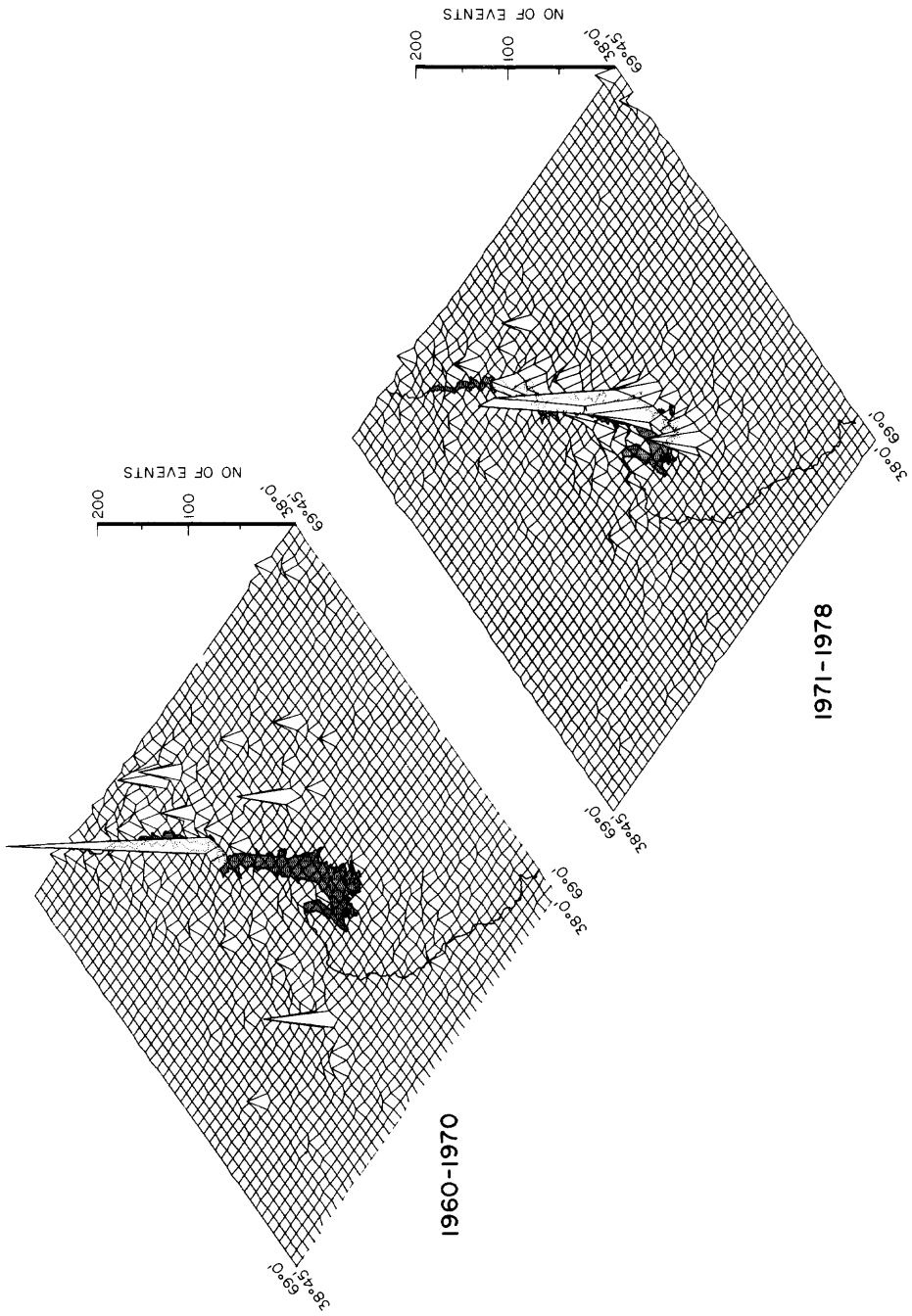

FIG. 4. Three-dimensional representation of seismicity at Nurek before (1960 to 1970) and after (1971 to 1978) impounding of the reservoir. Number of earthquakes with $K \geqq 6.5/1$ min^2 of latitude and longitude is given in the z direction. The outline of the full reservoir is *shaded* in both parts of the diagram. The induced seismicity is clearly seen as the zone of high activity near the reservoir 1971 to 1978.

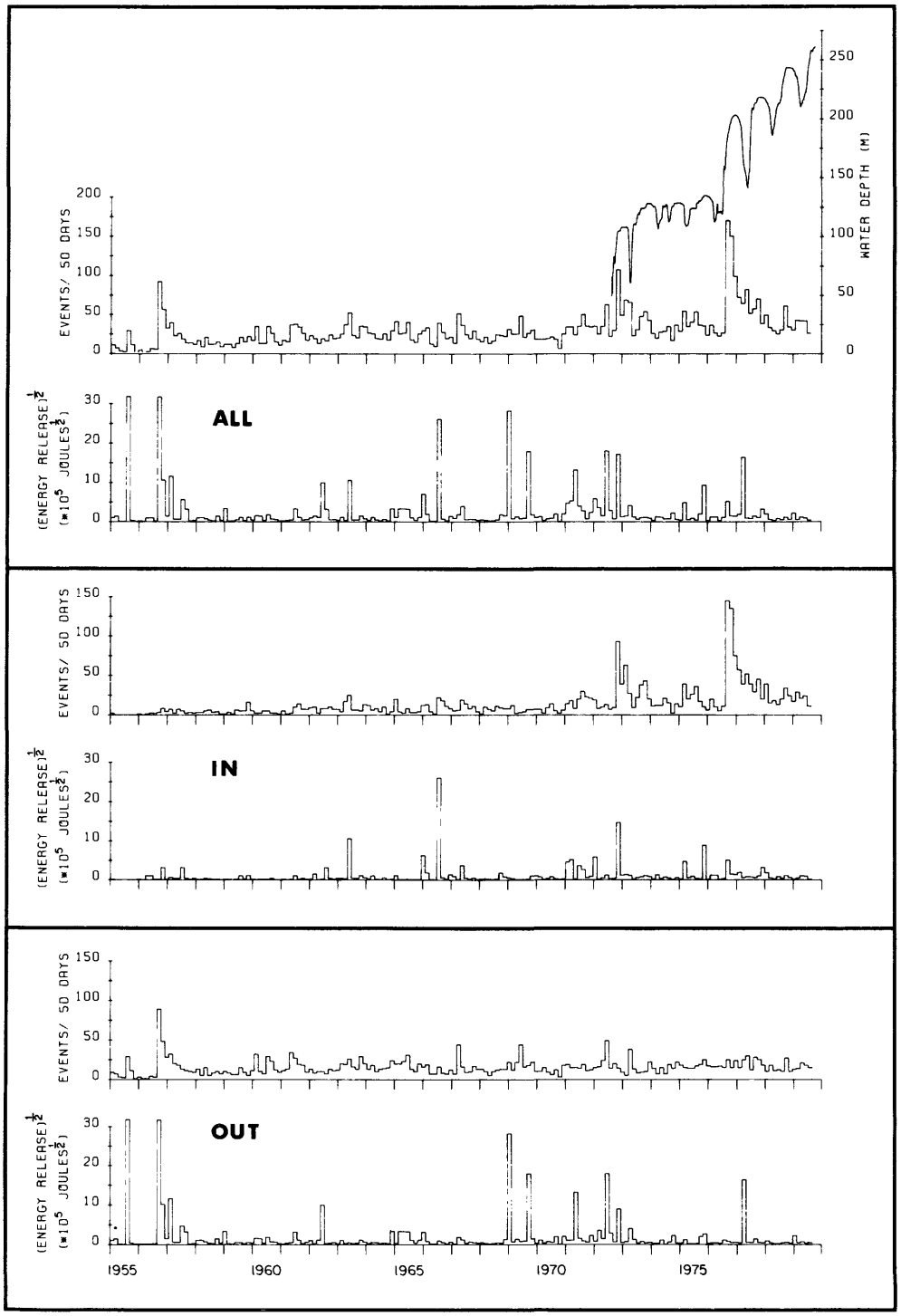

FIG. 5. Temporal variations in seismicity in: (*top*) the entire Nurek area shown in Figure 2; (*middle*) the reservoir area outlined in Figure 2; and (*bottom*) the region outside the reservoir area. Each section shows the number of earthquakes with $K \geqq 6.5$ and the square root of the energy release $\sqrt{\Sigma\ 10^K}/50$ days where K is the Soviet energy class (log of the energy release in joules). The number of earthquakes provides a measure of the rate of activity while the energy release accentuates the larger earthquakes. Water level in the reservoir is given at *top right*. The vertical scales in all three sections are equal. Since the reservoir area (1000 km^2) is 18 per cent of the entire Nurek area (5500 km^2), the vertical scales in the "IN" section should be expanded by a factor of 4.5 to compare the density of activity with the "OUT" section.

of activity can also be seen southwest of the reservoir area. There is very low activity, however, over most of the immediate area of the future reservoir. The 8-yr period following impounding (1971 to 1978) clearly shows a pronounced increase in seismicity, concentrated near the main body of the reservoir. The induced seismicity stands out as an even more pronounced feature than activity on the Vakhsh-Illiak fault, north of the dam (compare with Figure 1).

The area of increased seismicity following filling of the reservoir is outlined in Figure 2. In Figure 5, temporal variations in seismicity for 1955 to 1979 are shown

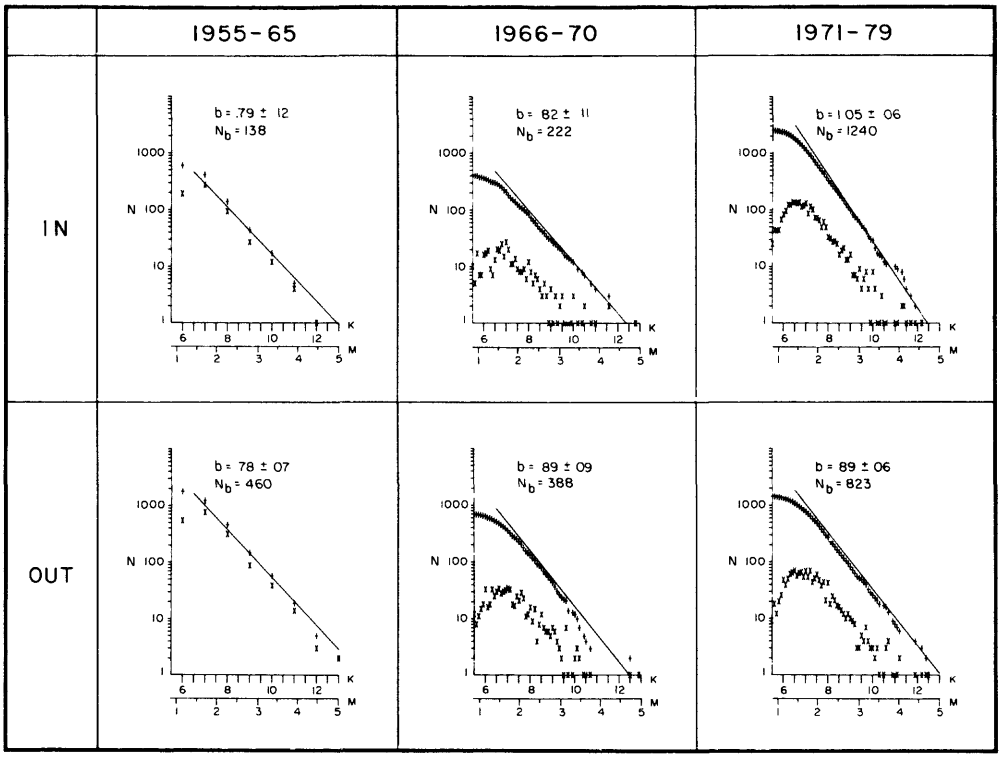

FIG. 6. Recurrence graphs for the reservoir region (IN) and Nurek area outside the reservoir region (OUT) for 1955 to 1965, 1966 to 1970, and 1971 to 1979. Prior to 1966, earthquake size is reported in intervals of 1.0-energy class units and from 1966 to 0.1 units. In each graph, X's are the interval numbers of earthquake (i.e., the number at each K value) and +'s are the cumulative number (i.e., the number greater than or equal to K). N_b is the number of earthquakes used in calculating b, using the maximum likelihood method. Earthquakes with $K \geqq 8$ were used to determine b for the 1955 to 1965 segments and $K \geqq 7$ for time periods after 1965. The b value for the reservoir area after impounding (1971 to 1979) is significantly higher than all of the other noninduced groups.

for the entire Nurek area, for the reservoir area, and for the Nurek area outside of the reservoir area. The number of earthquakes with $K \geqq 6.5$, and the square root of energy release/50 days are shown for each area. The most pronounced changes in seismicity in the reservoir area are the increases beginning in 1971 and 1976. Preimpounding seismicity in the reservoir area is relatively low and stable except for large earthquakes in the northern end of the area in 1963 and 1966 and in the southern end in 1966 (Figure 3). Outside the reservoir area, the Nurek region shows more variability in activity. The most notable burst of activity is related to the 1956 Nurek earthquake. Most of the other activity is concentrated just northeast of the reservoir area or in the very southern part of the region (Figure 3). The induced

seismicity, however, remains as one of the dominant features of the seismicity of the entire region.

Following impounding, the annual rate of seismicity in the reservoir area rises by a factor of more than 4, from an average of 50 earthquakes/yr, 1955 to 1970 to 200 events/yr, 1971 to 1979; with relative rates scaling as high as 400 events/yr in late 1972 and 700 events/yr in late 1976 (Figures 5 and 7).

b Values

Figure 6 shows cumulative and interval numbers of earthquakes as a function of energy class for the areas inside and outside the reservoir region, with associated *b* values, calculated using the maximum likelihood method (Utsu, 1971). Below $K =$

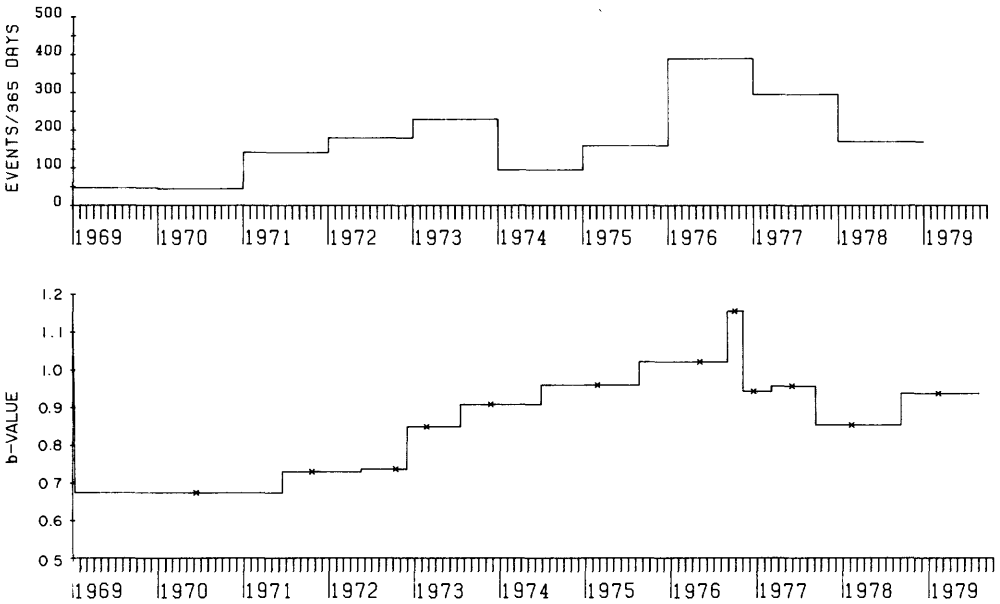

FIG. 7. Temporal variation of *b* value within the reservoir area, 1969 to 1979 (*bottom*) and number of earthquakes/year (*top*). The time inteval over which the *b* values are determined is adjusted so that each interval contains 100 events. The 95 per cent confidence limits for estimates of *b* using samples of 100 earthquakes are ±0.196 *b* (Aki, 1965). For the range of *b* shown here the 95 per cent confidence limits vary from ±0.14 ($b = 0.7$) to ±0.22 ($b = 1.1$). Although the induced seismicity began with the increase in activity in 1971, the *b* value did not increase significantly until 1973.

6.5, the departure from a linear increase in the interval number of events with decreasing energy class indicates the catalog to be relatively complete down to $K = 7$ ($M = 1.7$). All *b* value determinations have, therefore, been made using only events with $K \geqq 7.0$. In Figure 7, *b* values for the reservoir region are shown as a function of time, with *b* values determined using groups of 100 earthquakes. In this way, the error in the maximum likelihood estimate of *b*, which depends on the number of events in the group, remains constant (Aki, 1965; Gibowicz, 1973). Before 1973, the *b* value is approximately 0.8, similar to the value for the entire region outside of the reservoir area (Figure 6). Starting in 1973, *b* values rise to an average value near 1.0 in 1975 to 1976. This increase in *b* value occurs after the start of the induced seismicity, which began in 1971 as shown by the increase in the annual numbers of earthquakes in Figure 7. As discussed below, most of the 1971 and early 1972 seismicity was also located in a different area than the later induced seismicity.

The Rautian (1960) relationship between energy class and magnitude (given earlier) has been used in determining the b values in Figures 6 and 7. The b value is directly proportional to the slope of the function used to convert from energy class to magnitude and any systematic bias in the Rautian relationship would thus cause corresponding changes in b values. Any difference between the b values shown here and values determined for other areas, using different magnitude scales, may not be significant. The increase in b value for the induced seismicity after 1972 appears to be real, however, since it is based on an internally consistent magnitude scale. The increase in b value is also apparent from a comparison of the energy release and number of earthquakes in Figure 8. After 1972, there is a substantial increase in the number of small earthquakes in relation to the larger events.

Migration of Postimpounding Seismicity

Figures 4 and 5 have shown the general increase in seismicity accompanying the two major stages of filling in 1972 and 1976. We now investigate, in more detail, the shorter term spatial and temporal variations in seismicity within the reservoir area.

As Figure 8 shows, most of the induced activity has occurred in bursts, the two most obvious ones being related to the major stages of filling in late 1972 and 1976. The largest postimpounding earthquakes occurred in November 1972 ($M = 4.6$ and $M = 4.3$), March 1975 ($M = 4.1$), September 1976 ($M = 4.1$), December 1977 ($M = 3.9$), and throughout mid-1971 ($M = 4.2, 4.1, 3.9$). As discussed below, there is evidence to suggest that the $M = 4.4$ event in October 1975 is not induced. The epicentral maps in Figure 9 show that the activity has migrated in time, beginning to the southwest of the reservoir in 1971 and migrating to the northeast along the axis of the reservoir. The space-time diagram in Figure 10 shows the details of this migration.

Activity during 1971 was concentrated on the southwest and northeast sides of the reservoir (Figure 9b) with most of the epicenters on the southwest side. Virtually no activity occurred directly beneath the reservoir. Earthquakes during the first major burst of activity in November–December 1972 (Figure 9c) occurred in two groups (Soboleva and Mamadaliev, 1976). The first group, most of which occurred within 10 days following the larger earthquakes on 6 November, was located in the same area as the activity in 1971. The second group, following in late December, occurred 5 to 10 km closer to the reservoir, in an area where no activity had been observed in 1971 and early 1972 (Figure 10).

During 1973 and 1974, activity gradually migrated northeastward, while the level of seismicity decreased in the southwest. In 1975, a concentrated burst of activity occurred in March near the southern edge of the reservoir. Scattered activity occurred throughout the year on the northern edge, with a cluster of events at the northeastern end of the reservoir during June and August.

During the first half of 1976, the whole region was quiet, except for a minor burst of activity in early March, north of the reservoir. The major activity in 1976 began in August and was concentrated in two areas, most of it in the central reaches of the reservoir, with a secondary cluster of activity farther to the northeast. Activity in the central region continued throughout 1977 to 1979, while the second group spread farther to the northeast.

Figures 9 and 10 show that from 1971 to 1979, seismicity had almost completely filled an area 40 km long and 10 km wide. Throughout that period activity gradually migrated toward the northeast and formerly active areas became quiet. In order to check whether the migration to the northeast between 1971 and 1976 could be the

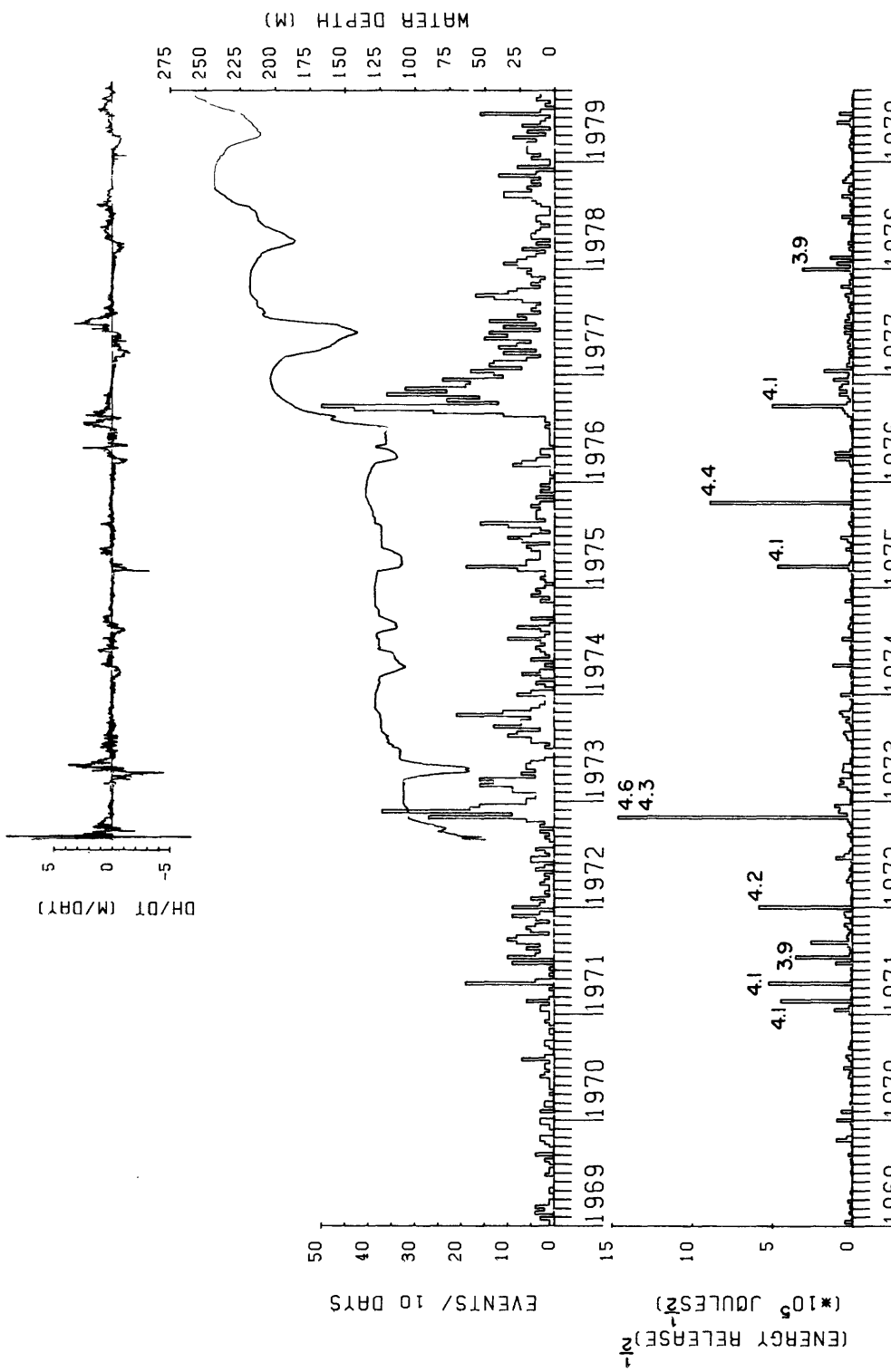

FIG. 8. Temporal variations in seismicity within the reservoir area and daily water level at Nurek. The number of earthquakes and square root of energy release/10 days are given in the same manner as in Figure 5. Numbers in the *lower section* are the magnitudes of the larger earthquakes. Water level gradient (dH/dt) is the daily change in the water level, calculated from the water level data. Positive gradient represents filling, and negative gradient emptying, of the reservoir.

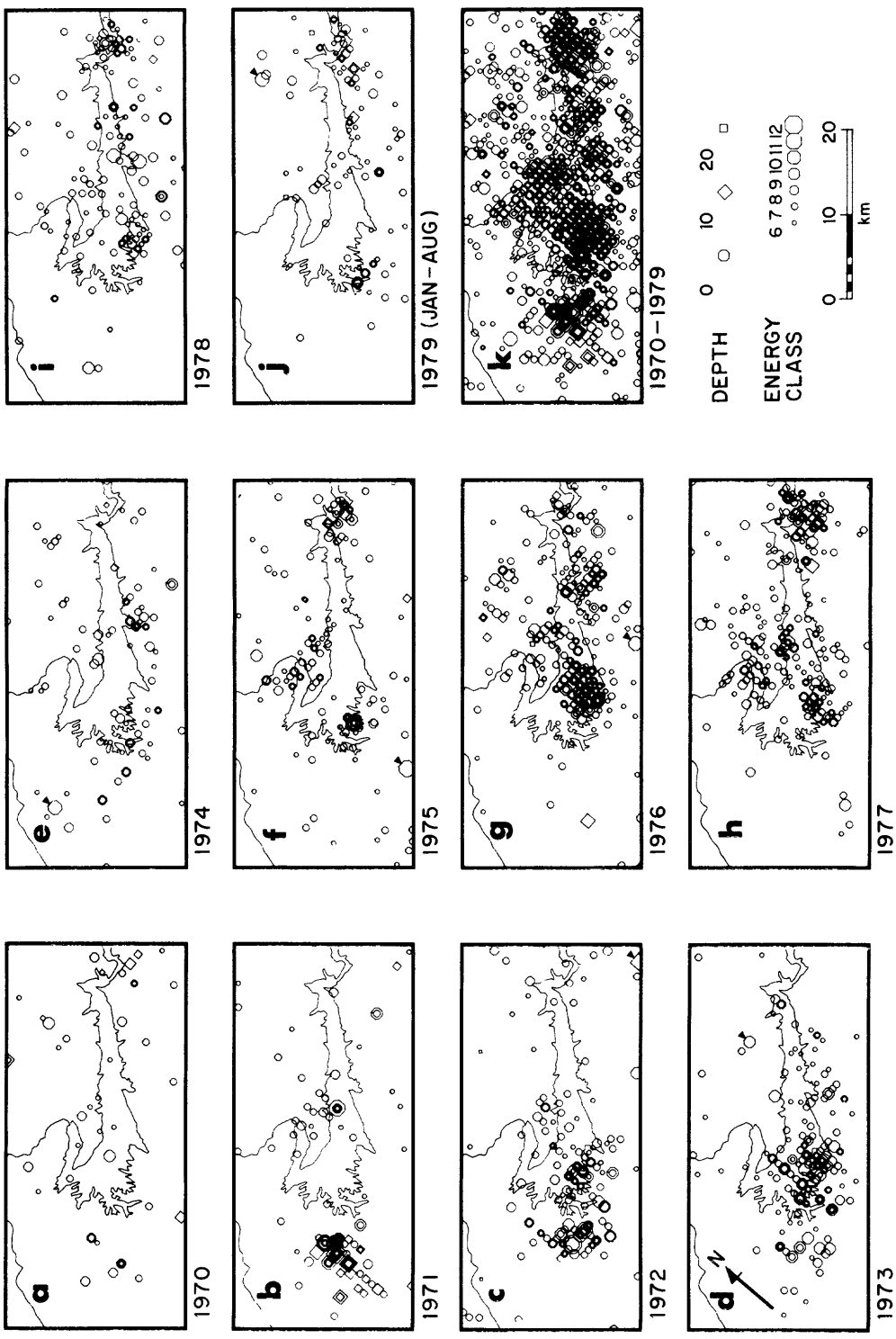

FIG. 9. Yearly epicenter maps of earthquakes with $K \geqq 6.5$ in the reservoir area (see Figure 2) 1970 to 1979. Epicenters marked with *tics* are those larger events that lie outside the main area of induced seismicity, have relatively few aftershocks, and are assumed not to be induced (see text).

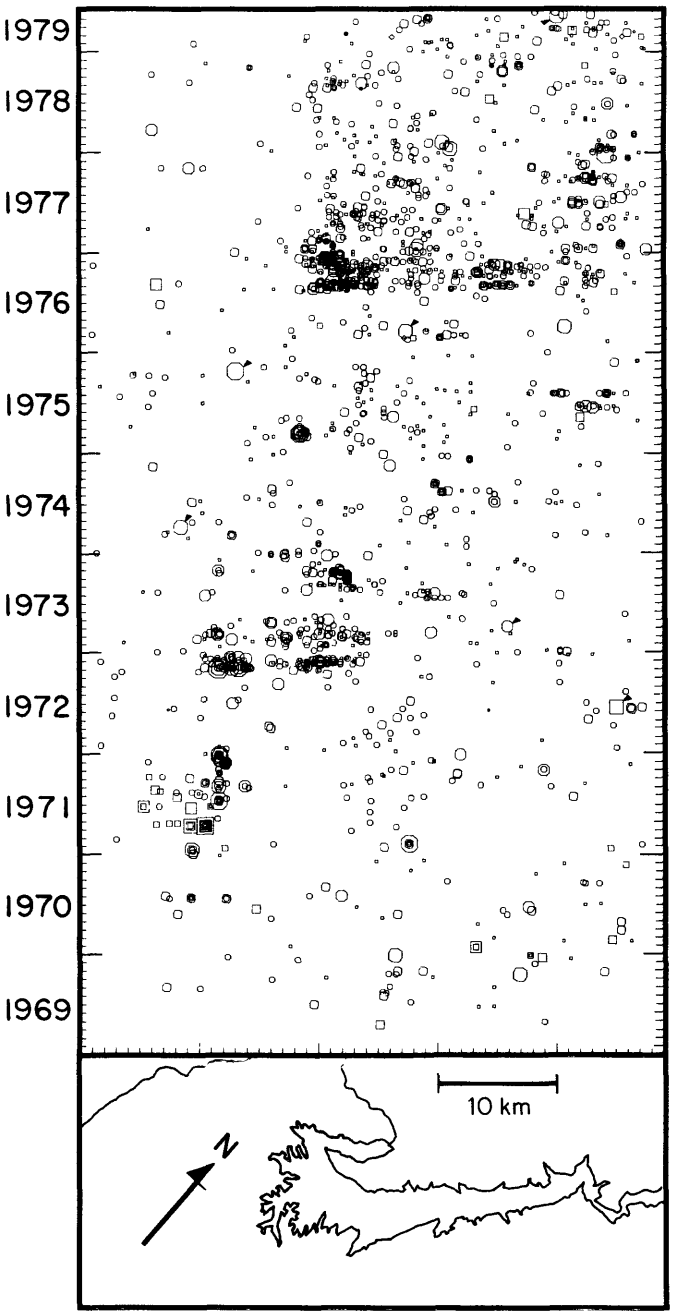

FIG. 10. Space-time graph of migration of activity within the reservoir area 1969 to 1979. Compare with Figures 8 and 9. Symbol sizes depend on earthquake size as shown in Figure 9. The six events with $M \geqq 3.0$, assumed not to be induced (Figure 9), are indicated by *tics*.

result of change in location procedure or station distribution, we show in Figure 11 *S-P* times at Soviet stations for selected earthquakes. Earthquakes have been divided into five groups based on time of occurrence and their locations as given in the TISSS catalog. Stations OBG, BGZ, and KLD, which lie approximately along

the line of migration of activity, show clear decreases in *S-P* times consistent with the TISSS locations. Stations KUL and CGT, which lie transverse to the direction of migration and are approximately the same distance from all groups of activity, show only small changes in *S-P* times, while LNG, which is closer to the reservoir, shows a decrease in *S-P* times as activity moved northeastward in 1972 to 1973. Thus, although the exact path of migration from 1971 to 1976 cannot be determined to better than ±5 km, the two major features of the migration—that it did occur and that activity stopped in areas that were previously active—appear to be real.

At least part of the migration in seismicity can be explained by the growth in the

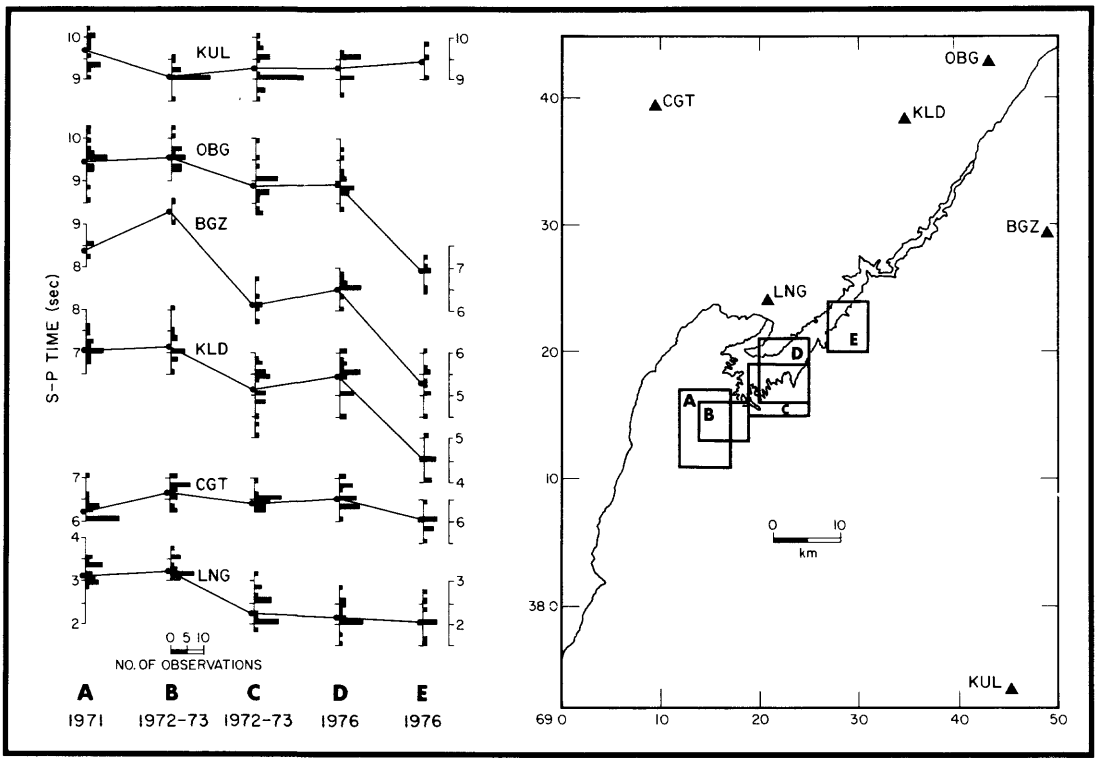

FIG. 11. *S-P* times at stations shown in *right part* of diagram for five groups of earthquakes grouped by their time of occurrence and location as given in the TISSS catalog. Histograms give the number of observations in 0.1-sec intervals and the lines connect the average *S-P* time observed at each station. Only earthquakes with $K \geqq 9$ have been used. The locations of the five groups are shown on the *right* and the time periods covered are given on the *left*. The distribution of events within each group can be seen by comparison with Figures 9 and 10.

area of the reservoir as it filled. Between 1972 and 1976, when the water level was less than 130 m, the reservoir did not extend farther upstream than the area of high seismicity shown in Figure 9 and 10. After 1976, when the water level exceeded 200 m, the reservoir had extended upstream to include the region showing high seismicity beginning in late 1976.

TEMPORAL VARIATIONS IN POSTIMPOUNDING SEISMICITY

The most obvious relationship between water level and seismicity is that the most seismically active periods are related to the two major stages of filling in 1972 and 1976. Closer analysis of short-term changes reveals that more subtle relationships

exist. Therefore, we will now take a closer look at the data from Figure 8, using an expanded time scale and the number of earthquakes per day rather than per 10 days (Figure 12).

From August to November 1972, as the water level rose from 50 to 104 km, seismicity in the reservoir area was low, with only six events occurring during August and September. In October, the water level rose at an almost constant rate of 1 m/day until 2 November when the level had reached 104 m and filling was abruptly stopped. Four days later, on 6 November, there occurred the two largest earthquakes of the entire induced seismicity sequence (magnitudes 4.3 and 4.6, see Figure 3). Two clusters of aftershocks followed these earthquakes (Soboleva and Mamadaliev, 1976), with activity gradually decreasing throughout December.

In early 1973, the water level remained constant until it began to drop slowly in February and rapidly in mid-March. There was an increase in seismicity starting in early February which decreased as the water level approached a minimum in early April. In late April the water level began increasing again and by mid-May had reached its former maximum and it continued rising in short stages throughout the rest of 1973. Seismicity had reached a minimum in June but increased again in July and continued to increase until November when the water level had reached a new maximum.

Seismicity remained relatively low throughout 1974, with only minor peaks in March, July, and August. The level did not increase substantially until March 1975, when a cluster of earthquakes occurred near the southern edge of the reservoir (Figure 9). On 1 March 1975, the water level had started to drop during one of the spring irrigation cycles. Two similar irrigation cycles had occurred in 1974. The 1975 cycle, however, began much more abruptly (a drop of 3 m in the first day) and the average rate over the first part of the draw-down (1.5 m/day) was more rapid than either of the 1974 cycles (less than 1 m/day). In the 6 months from September 1974 to the end of February 1975, there had been only four earthquakes located near the central basin of the reservoir (see Figures 9 and 10). On 2 March 1975, the day following the start of the rapid draw-down, a sequence of earthquakes began near the central basin, culminating in a magnitude 4.1 event on 14 March. This burst of activity was the most pronounced since the end of 1973 and included the largest earthquake (magnitude 4.1) since November 1972. Only minor increases in seismicity had occurred during the two more gradual draw-downs in 1974.

In June and August 1975 the water level again increased in abrupt stages, followed by minor increases in seismicity. A more gradual increase in water level from October to December 1975 does not show any corresponding increase in seismicity near the reservoir. The largest earthquake in 1975 was the magnitude 4.4 event on 25 October. Its location (see Figures 3 and 9f) is outside the main area of high-induced seismicity (Figure 9k). Unlike all the other large induced earthquakes, which are accompanied by high levels of aftershock activity, this earthquake was followed by only two small aftershocks (compare the energy release and number of earthquakes for the larger events in Figures 8 and 12). As shown by the number of events following the larger earthquakes outside of the reservoir area (Figure 5), lower levels of aftershock activity are characteristic of the natural background seismicity of the region. It thus appears that the October 1975 earthquake was part of the natural seismicity of the region and it will not be considered in the following discussions of the induced activity. Although they are smaller and of less significance in the ideas to be developed below, five of the other earthquakes with $M \geq 3.0$ indicated in Figure 12 also are outside the main area of induced seismicity and have

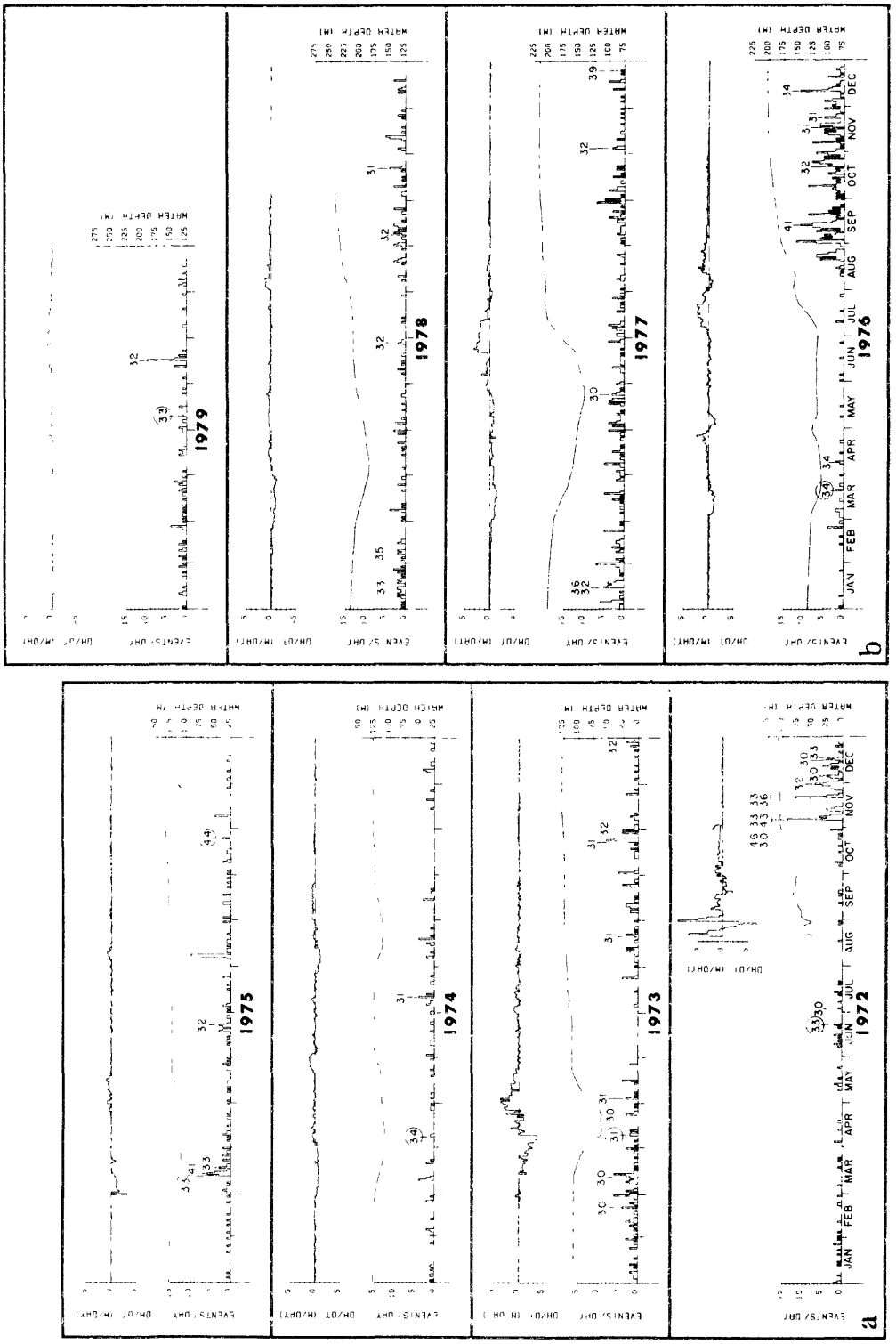

FIG. 12. Temporal variations in seismicity and water level. Data and presentation are the same as in Figure 8 except that the number of events/day is used. Magnitudes of all earthquakes with $M \geq 3.0$ are indicated and the six events assumed not to be induced are *circled*.

little or no aftershock activity (June 1972, April 1973, April 1974, March 1976, and May 1979). These are identified in Figures 9 and 10 and it is assumed that they also are not induced. Note that the events of 27 May 1971, 30 May 1972, and 27 November 1972, which are outside of the reservoir area, but occurred after the start of filling, also have relatively low numbers of aftershocks (Figures 3 and 5).

From December 1975 to the end of February 1976, the water level decreased slowly until 1 March 1976, when the spring irrigation cycle began again. Like the one in 1975, the decrease began abruptly and was accompanied by a minor increase in seismicity. In late April and early May 1976, a rapid fluctuation in water level occurred, but the water depth was well below its former maximum and no increase in seismicity was observed.

The second major stage of filling began in early July 1976. As a result of observations from 1972 to 1975, we had concluded that increased seismicity at Nurek was related to rapid decreases in the filling rate: either an abrupt stop in filling (as in November 1972) or a rapid decrease in water level (as in March 1975). We therefore recommended that the second stage of filling be carried out as slowly and smoothly as possible. As Figures 5 and 8 show, except during a period of rapid fluctuation in mid-August for testing of a tunnel, the filling curve for late 1976 was much smoother than in 1972, especially as the water level peaked at 205 m in December. The filling cycle began on 1 July, when the water level was 120 m, 20 m below its former maximum of 140 m which occurred in November 1975. This former maximum was exceeded on 20 July and the water level continued to rise at approximately 3 m/day until 2 August when a tunnel was tested. On 2 August, a level of 160 m was reached, following which the level decreased to 157 m on 11 August and then continued to rise.

From April to July 1976, the water level was approximately 15 m below the former maximum and the level of seismicity was lower than for most of the postimpounding period. Activity remained low during the first part of the renewed filling cycle, until it increased sharply in mid-August, immediately following the rapid decrease in water level for testing of the tunnel. The seismicity rose to a peak in early September, including an earthquake of magnitude 4.1 on 13 September, and then gradually decreased, even though the water level continued to rise at a gradually decreasing rate until 21 December, when it peaked at 203 m. The water level immediately began a gradual decline accompanied by a slight increase in seismicity, including the second largest earthquake of the 1976 to 1977 swarm (M = 3.6) on 15 January 1977. In early March, when the water level was 30 m below the December peak, the annual irrigation cycle began and the rate of emptying increased. A seismicity increase in March is partially masked by the continuing decay in the activity which began earlier (Figure 8). The water level started to increase again in late May and the seismicity gradually decreased and remained low until September, when the water level had again exceeded its previous maximum.

From 15 October to 1 December 1977, the water remained at a very stable level (ranging less than 20 cm, between 217.8 and 218.0 m) and the seismicity was low. The water level began to decrease on 1 December, with the rate of emptying increasing slightly in early January. A magnitude 3.9 earthquake occurred on 25 December and events of magnitudes 3.3 and 3.5 occurred on 15 January and 7 February 1978. The 25 December event was at the northeastern end of the most northeasterly group of induced activity and the 15 January and 7 February events were at the northeastern end of the group of earthquakes in the central part of the reservoir (Figures 9 and 10). On 1 March, when the water level had dropped to 10

m below the November peak, the level began to decrease more rapidly, and there was a minor increase in seismicity.

Except for a short burst in mid-November 1978, the pattern of seismicity during the 1978 to 1979 filling cycle was similar to that in 1977 to 1978, but at a reduced level of activity. The seismicity was low during the start of filling from May to August; increased in September after the water level had exceeded the previous maximum; was low while the water level remained constant from early October to mid-January 1979; and increased as the water level began to drop in late January and February.

As the water level began to rise in mid-1979, a burst of activity occurred in June, including an event of magnitude 3.2, in an area to the southwest that had not been active since 1972 (Figure 9j).

Water Level and Seismicity

Induced seismicity can be considered as the response of the crust beneath the reservoir to the application of an external load. The forcing function of the load is the water level in the reservoir. This load alters the seismicity by changing, through some transfer function, the stress conditions in the crust, both by increased elastic stress and increased pore pressure (Snow, 1972; Simpson, 1976). A number of factors may control whether and where induced seismicity occurs (Simpson, 1976). Many of these factors are external to the reservoir system (e.g., preexisting stress, geological and hydrological conditions, fault strength, etc.). Once induced seismicity does occur, factors depending on feedback within the response of the crust to the reservoir can also control whether and where future activity will occur (e.g., changes in stress and fault strength resulting from earlier induced earthquakes). Although many of these external and feedback factors may play an important role in determining the size and location of induced earthquakes, changes in water level alone appear to explain most of the general features of the temporal variations in induced seismicity at Nurek. The manner in which Nurek Reservoir has been filled, involving various stages of construction, with extensive annual variations in water level, provides a variety of different filling rates and excursions in water level which can be compared with the level of seismicity.

The induced seismicity at Nurek is not a direct function of the absolute water level. Neither the number of earthquakes nor their size increases in proportion to the depth of water. Although the number of earthquakes was higher in 1976, during the second stage of filling, than it was in 1972, during the first stage, the level of activity did not increase as the water level rose higher in 1978 and 1979. In addition, the peak in activity in 1976 occurred early in the filling cycle, well before the peak in water level was reached.

The seismicity does depend on the absolute water level to the extent that virtually all of the major bursts of seismicity occur when the water level is near or above any previous maximum. Figure 13 shows the periods of increased activity and times at which the water level was higher than it had been previously. The major increases in activity in 1972, 1973, 1976, and 1977 all occur after the water depth had reached a new maximum. Periods of relatively low activity tend to follow times of lower water level.

The correlation of increased activity with high water level and low activity with low water level is improved if we introduce a delay between the change in water level and the response in the seismicity. In Figure 13 we define periods in which the system is "highly primed" as beginning when the water level exceeds its previous

maximum by 10 m and remaining in effect until the level drops 10 m below the new maximum. Periods in which it is "primed" are any other times when the level is within 10 m of its previous maximum. Although we have used ±10 m as the criterion for delay, a constant time delay after the water level enters or leaves a new maximum

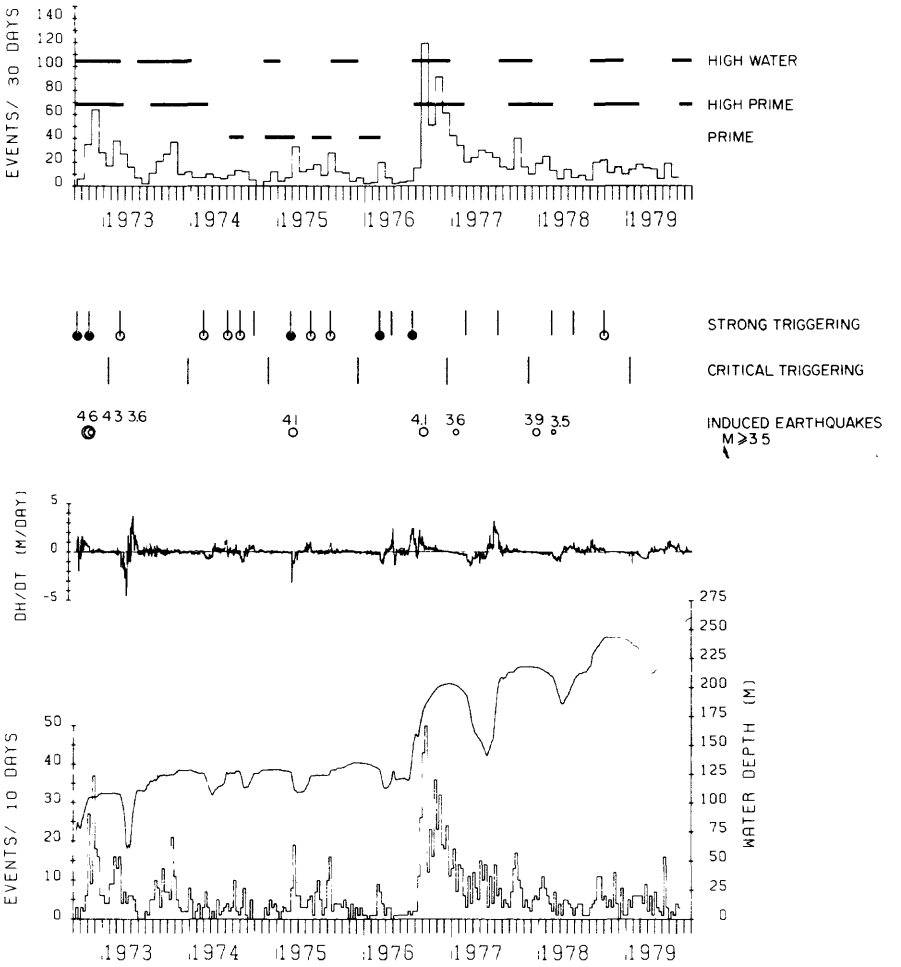

FIG. 13. Comparison of seismicity with primed states and triggering. The level of activity, as measured by the number of earthquakes $K \geqq 6.5/30$ days, is compared to times of "high water," "high prime," and "prime" in the *upper* section. "High water" is any time when the water level is higher than it has been previously. A state of "high prime" is entered when the water level exceeds a previous maximum by 10 m and remains in effect until the level drops 10 m below the new maximum. A state of "prime" begins at any other time when a major peak in water level occurs and remains in effect until the water level drops 10 m below the maximum or begins to rise again. All the major bursts in seismicity start when the system is highly primed and most minor bursts begin when it is primed. Unprimed states usually correspond to periods of relatively low activity.

In the *lower section*, shorter term changes in seismicity and the times of the largest induced earthquakes are compared with times of "strong" and "critical" triggering. "Strong triggering" is a rapid and sustained decrease in the rate of filling. "Critical triggering" exists when the water level is at a peak and the transition occurs from filling to slow and sustained emptying. Those times of strong triggering that occur during primed periods are indicated by circles and those cases in which the drop in filling rate is very large ($d^2H/dt^2 < -0.5$ m/day^2) are indicated by solid circles. All the largest induced earthquakes occur during bursts that start with strong or critical triggering during primed states.

would have a similar effect. At this stage it is only important that the system appears to display some hysterisis—the response in increased seismicity lagging behind the increase in water level and states of high seismicity persisting after the water level begins to drop.

Although the increased seismicity consistently occurs when the system is primed, the timing of when the earthquakes occur within the primed period is not always the same. In some cases, the highest activity occurs at a new peak in water level (e.g., November 1972); in others, it occurs before the peak is reached (e.g., September 1976) and in yet others, it occurs when the water level begins to drop (e.g., March 1975).

The times at which increases in seismicity occur at Nurek appear to be controlled by the rate of change in the water level. As stated earlier, most of the activity is related to decreases in the rate of filling. In Figure 13, we define times of "strong triggering" as when the water level gradient drops rapidly to zero or less (i.e., $dH/dt < 0$ and $d^2H/dt^2 \ll 0$). Times of "critical triggering" are when dH/dt passes gradually through zero (i.e., a change, at a major peak in water level, from slow filling to slow emptying).

All of the earthquakes greater than magnitude 3.5 are related to times of high or intermediate prime and strong or critical triggering. The largest induced earthquakes, of magnitude 4.3 and 4.6 in November 1972, followed immediately after the strong triggering related to the abrupt stop in filling. The magnitude 4.1 earthquake in March 1975 was the largest of a sequence that began with a rapid drop in water level. The swarm culminating in the magnitude 4.1 earthquake in September 1976 began with the strong triggering caused by the testing of the tunnel in August 1976. The magnitude 3.6 event in January 1977 and the magnitude 3.9 event in December 1977 both followed times of critical triggering.

All the other pronounced increases in seismicity, except for the minor bursts in August 1975 and June 1979, happen when the system is primed and the water level is either decreasing rapidly (e.g., March 1976) or dH/dt is fluctuating about zero (e.g., July to October 1973). When weak triggering exists but the system is not highly primed, or when strong triggering exists but the system is not primed at all, increases in seismicity are either minor or not present (e.g., March 1974, August 1974, April 1976, and July 1977).

Of special interest are the four similar draw-downs in water level between 1974 and 1976. All four cycles began when the water level was near 125 m and involved decreases of approximately 20 m. Of the four, the one in March 1975 began most rapidly, started when the water level was closest to its former maximum, and had the largest earthquake associated with it. The cycle beginning in March 1976 was almost as rapid but it began when the water level had already dropped slowly by 6 m. In this case the increase in seismicity was small and more scattered in location than that in 1975 (see Figure 9). The two draw-downs in 1974 were more gradual, but began closer to the previous maxima. The slight increases in seismicity that occured were more concentrated in location (Figure 9).

The responses in seismicity to the six peaks in filling in 1972 to 1973, 1973 to 1974, 1976 to 1977, 1977 to 1978, and 1978 to 1979 present interesting variations on a similar theme. The general pattern is one of a burst of activity at or before the peak in water level; relatively low activity if the water level remains constant at the peak; and increased activity as the water level begins to decrease. In 1972, no strong triggering occurred after the water level exceeded 80 m, and the first peak was reached without any increase in seismicity. The major seismicity (on 6 November, 1972) followed the rapid decrease in filling rate as the water level reached 104 m on 2 November. The water level remained relatively stable for 2.5 months with a low level of seismicity which did not increase until the water level began to decrease slowly in late January 1973. The new maximum water level in October 1973 was reached in a series of short increases, accompanied by short bursts of minor

seismicity. The peak in water level was maintained with low seismicity for 1.5 months from mid-November until the water level began to decrease at the end of December. In 1976, the major swarm began with the strong trigger in August, well before the maximum water level was reached. There was no holding of water level at its peak and no local minimum in seismicity is observed. The 1977 to 1978 filling cycle raised the water level only 15 m above the 1976 peak. The level of seismicity is lower but the general pattern is clearly seen. Unlike 1976 to 1977, the maximum earthquake occurred at the start of the emptying cycle, after the peak in water level (with correspondingly low seismicity) had been maintained for 2 months. The 1978 to 1979 filling cycle increased the maximum water depth by 25 m. Although broader and less intense than the 1977 to 1978 effect, the same pattern in seismicity can be seen with increased activity beginning in September 1978 and February 1979 and relatively low activity during the peak in water level from October to January. The lower level of activity compared to 1977 to 1978, in spite of the greater increase in maximum water level, may be due to the more gradual increase in water level in 1978 or related to a general decrease in stress level caused by the larger earthquakes in 1976 to 1978.

When the water level is at a maximum, the difference between a stable level and an emptying rate sufficient to cause increased seismicity, is extremely small. The increased seismicity in February 1973, January 1977, December 1977 and February 1979 occurred when the water level was decreasing at rates between 0.02 and 0.10 m/day and when the water level was only 1 to 2 m below its peak value.

Discussion

The filling of a large reservoir changes the stress regime by increasing vertical stress caused by the weight of water and by decreasing effective stress due to increased pore pressure. Whether the net effect on fault zones is one of increased or decreased stability depends strongly on the orientation of preexisting stresses and the geometry of the reservoir/fault system (in particular, the location and dip of faults with respect to the reservoir). Snow (1972), Simpson (1976), Gupta and Rastogi (1976), and Bell and Nur (1978) show how load and pore pressure tend to decrease stability in cases of normal faulting (maximum compressive stress vertical); whereas the net effect is one of increased stability in regions of thrust faulting (maximum compressive stress horizontal).

The Tadjik Depression is in a broad zone of horizontal compression related to the India-Eurasia collision. Focal mechanisms for the region are generally of thrust type (Soboleva *et al.*, 1974). Keith *et al.* (1981) show the induced seismicity at Nurek to be occurring on a series of thrust or reverse faults connected by short segments showing strike-slip motion.

Simpson (1976) and Bell and Nur (1978) suggest that temporal changes in water level and lateral variations in permeability may be an important factor in explaining the occurrence of induced seismicity in regions of thrust faulting. Raising the water level immediately increases the vertical stress which opposes the natural horizontal compression and stabilizes faults. The diffusion of increasing pore pressure into fault zones gradually decreases the effective stress, weakening the faults. As long as the water level continues to rise and the load effect exceeds the pore pressure, the net effect is one of increased stability. If the water level decreases rapidly, however, the stabilizing effect of the increased vertical stress is removed immediately, whereas high pore pressure persists until it can diffuse away. Thus, rapid decreases in water level can lead to immediate instability (Simpson, 1976). Lateral variations in

permeability (e.g., along faults) can produce zones of increased pore pressure where net weakening can occur (Bell and Nur, 1978).

The opposing nature of the effects of load and pore pressure in regions of maximum horizontal compression can explain the relationship between loading rate and seismicity at Nurek. As the water level rises, the load effect initially dominates causing lower seismicity. When the filling rate decreases, rising pore pressure exceeds the load effect, resulting in increased seismicity as a peak in water level is reached. If the water level remains constant, pore pressure and load equilibrate and seismicity decreases. When the water level drops, the load is removed before pore pressure can disperse and activity increases with little or no time delay. If changes in the rate of filling take place slowly compared to the diffusion time constant, the effect is small. When they occur rapidly the effect on seismicity is much greater.

There is a very short time delay between decrease in filling rate and the onset of increased activity. In March 1975, when the water level dropped rapidly after an extended period of relatively constant water level, seismicity increased within 1 day. When the decrease in filling rate follows a period of rising water level, the time delay is longer (e.g., 4 days in November 1972 and 8 days in August 1976) because of the initial stablizing effect of the increased load.

The area where induced seismicity began in 1971, 10 to 15 km southwest of the reservoir, had shown a higher level of seismicity prior to impounding (including an $M = 4.2$ earthquake in 1966) than the region immediately surrounding the reservoir, where most of the post-1972 activity occurred (Figures 3 and 4). The b value for the 1971 to 1972 induced seismicity was lower than for the later stages of activity and was closer to the average for the noninduced seismicity both before and after impounding (Figures 6 and 7). Because of the higher seismicity in the southwest before 1971, it can be assumed that faults in that area were less stable than elsewhere in the reservoir region and hence more susceptible to triggering by small changes in stress.

Mogi (1963) shows that high b values are associated with spatially heterogeneous stress distributions, while more homogeneous stresses produce lower b values. Scholz (1968) relates high b values to low mean stresses. Gupta *et al.* (1972) explain the high b values observed in some cases of induced seismicity as resulting from the heterogeneous nature of stresses induced by a reservoir.

As suggested by Simpson (1976), a gradual rise in pore pressure, which exceeded the load effect, may have been the dominant factor in triggering the earthquakes southwest of the reservoir in 1971. Since they were at distances of 10 to 15 km from the reservoir, any short wavelength changes in stress (temporal and spatial) would have been filtered out before reaching these distances. Thus, the weakening of faults in this area resulted from a diffuse and relatively homogeneous rise in pore pressure. The resulting increase in seismicity was the triggered release of preexisting stress which took place at an accelerated rate, but in a manner that retained the relative distribution of large and small shocks and hence gave a b value similar to the regional average. In contrast, once the seismicity had migrated into the immediate reservoir area, it was responding to higher stress gradients in a more heterogeneous stress system (i.e., without the filtering effect of distance from the source) giving rise to higher b values.

The northeastern end of the reservoir region also exhibited a relatively high level of seismicity prior to impounding (Figures 3 and 4). This may explain why, as the induced seismicity migrated into this area in 1977 to 1978 (Figure 10), b values began to decrease (Figure 7). The minor bursts of activity in the northeastern end of the

reservoir region from May to August 1975 and the larger event in March 1976 (Figures 9 and 10) took place before the water level had increased in that area. The occurrence of these events outside the immediate area of increased water depth may be explained in the same manner as the early activity at the opposite end of the reservoir in 1971.

The activity at the southwestern (1971 to 1972) and northeastern (1975 to 1978) ends of the reservoir region (outside of the main body of the reservoir; in regions of high prior seismicity; and showing low b values) thus represent a "triggered" release, on relatively unstable faults, of preexisting stress conditions. The activity in the central region (in the immediate vicinity of the deepest parts of the reservoir; in a region of low prior seismicity; and showing high b values) may more strongly reflect true "induced" seismicity, with the elastic load of the reservoir playing a significant role in raising the stresses to a critical level as well as triggering the release of these stresses.

Conclusions

Earthquakes as large as magnitude 4.6 have been induced by the filling of Nurek Reservoir to 250 m. Activity began when the water depth was less than 80 m and the largest earthquakes occurred as the water level first exceeded 100 m. Raising the water level above its previous maximum primes the area near the reservoir to a state of high potential for increased seismicity. Once in the primed stated, the timing of the occurrence of activity is controlled by changes in the rate of filling of the reservoir. If the rate of filling remains high, seismicity remains low. Decreases in filling rate cause bursts of increased seismicity. The more rapid and sustained the decreases in rate, the more intense the resulting increases in seismicity. The difference between stable water level and a sustained emptying rate as slow as 0.02 m/day is sufficient to initiate increased activity. The largest earthquakes follow times when the rate of filling was decreased by more than 0.5 m/day^2. The time delay between the change in filling rate and increased seismicity can be as short as 1 day.

Nurek is located in a region of high-horizontal compressive stress. In such an environment, the increased vertical stress from the weight of the reservoir tends to increase stability; while increased pore pressure lowers effective stress and decreases stability. The close correlation between rates of loading and seismicity at Nurek may be related to the opposing nature of these two effects.

Induced seismicity appears to be a transient phenomenon. In most of the reported cases of induced seismicity, activity has gradually decreased with time and none of the largest induced earthquakes throughout the world occurred more than 10 yr after the reservoir was first filled (Simpson, 1976). After a sufficient length of time, perhaps on the order of tens of years, the region around a large reservoir must reach a new equilibrium and, if the water depth in the reservoir remains relatively constant, the reservoir should have no more effect on the seismic regime than a natural lake. In cases, such as Nurek, where the seismicity is clearly related to variations in water level, control of the rate of filling may regulate the release of seismic energy as this new equilibrium is reached. Changes in the rate of filling, and rapid decreases in rate in particular, are largely controlled by artificial manipulation of the outflow from the reservoir. The Nurek data clearly show that rapid decreases in filling rate, when the water level is significantly above the previous maximum, should be avoided. It is not obvious however whether the "safest" way to reach a desired peak in water level is by a series of small steps, releasing accumulated stress in minor bursts by artificial triggering at each stage; or by a slow and smooth filling

without any rapid changes in filling rate. The extremely small changes in rate that are sufficient to cause increased activity at Nurek suggest that it may be difficult to maintain "slow and smooth" filling to within the required limits.

Acknowledgments

We wish to thank members of the Tadjik Institute of Seismoresistant Construction and Seismology who have been responsible for collection and analysis of data for the seismicity catalog. In particular we wish to thank V. K. Kulagin, U. A. Mamadaliev, K. M. Mirzoev, and O. V. Soboleva. Many useful discussions have been held with M. Hamburger, C. Keith, M. Kristy, W. Leith, C. Scholz, and O. V. Soboleva. The manuscript was reviewed by L. Sykes, C. Scholz, and W. Leith. The work is carried out as part of a joint program in earthquake prediction under Area IX of the US-USSR Agreement in the Field of Environmental Protection. The American part of the work is supported by the National Science Foundation under Grants ENV 77-01092 and PFR 79-26698 and the U.S. Geological Survey under Contracts USGS 14-08-0001-17707 and USGS 14-08-0001-19743.

References

Academy of Sciences, Tadjik SSR (1968). *Atlas of the Tadjik SSR*, Central Office of Geodesy and Cartography, Dushanbe, 200 pp.

Aki, K. (1965). Maximum likelihood estimate of b in the formula $\log N = a - bM$ and its confidence limits, *Bull. Earthquake Res. Inst., Tokyo Univ.* **43,** 237–239.

Baratov, R. B. and V. N. Gaiskii (Editors) (1962). *The Geology and Seismicity of the Nurek Hydroelectric Station District* (in Russian), Tadjik Academy of Sciences Press, Dushanbe, 87 pp.

Bekker, Y. A., G. V. Koshlakov, and Y. S. Kuznetsov (1974). The deep structure of southwest Tadjikistan according to geological-geophysical data, in *Searches for Earthquake Precursors in Prediction Polygons*, M. S. Asimov, Editor, Nauka, Dushanbe, 16–24.

Bell, M. L. and A. Nur (1978). Strength changes due to reservoir-induced pore pressure and stresses and application to Lake Oroville, *J. Geophys. Res.* **83,** 4469–4483.

Billington, S., B. L. Isacks, and M. Barazangi (1977). Spatial distribution and focal mechanisms of mantle earthquakes in the Hindu-Kush-Pamir region: a contorted Benioff zone, *Geology* **5,** 699–704.

Chatelain, J. L., S. W. Roecker, D. Hatzfeld, and P. Molnar (1980). Microearthquake seismicity and fault plane solutions in the Hindu Kush region and their tectonic implications, *J. Geophys. Res.* **85,** 1365–1387.

Gibowitz, S. J. (1973). Variation of frequency-magnitude relationship during Taupo earthquake swarm of 1964–65, *N. Z. J. Geol. Geophys.* **16,** 18–51.

Gubin, I. E. (1960). *Properties of Seismic Manifestations in the Territory of Tadjikistan*, Academy of Science Press, Moscow, 464 pp.

Gubin, I. E. (1967). *Lecture Notes on Basic Problems in Seismotectonics*, International Institute Seismology and Earthquake Engineering, Tokyo, 195 pp.

Gupta, H. K. and B. K. Rastogi (1976). *Dams and Earthquakes*, Elsevier, Amsterdam, 229 pp.

Gupta, H. K., B. K. Rastogi, and H. Narain (1972). Some discriminatory characteristics of earthquakes near the Kariba, Kremasta and Koyna artificial lakes, *Bull. Seism. Soc. Am.* **62,** 493–507.

Keith, C., D. W. Simpson, and O. V. Soboleva (1981). Induced seismicity and style of deformation at Nurek Reservoir, Tadjik SSR (submitted for publication).

Kristy, M. J. and D. W. Simpson (1980). Seismicity changes preceding two recent central Asian earthquakes, *J. Geophys. Res.* **85,** 4829–4837.

Leith, W. S., D. W. Simpson, and W. Alvarez (1981). Structure and permeability: geologic controls on induced seismicity at Nurek Reservoir, Tadjikistan USSR, *Geology* (in press).

Mogi, K. (1963). Some discussions on aftershocks, foreshocks and earthquake swarms—The fracture of a semi-infinite body caused by an inner stress origin and its relation to the earthquake phemonena (third paper), *Bull. Earthquake Res. Inst., Tokyo Univ.* **41,** 615–658.

Molnar, P. and P. Tapponnier (1975). Cenozoic tectonics of Asia: Effect of a continental collision, *Science* **119,** 419–426.

Negmatullaev, S. K. (Editor) (1975). *Induced Seismicity in the Region of Nurek Reservoir* (in Russian), Donish Press, Dushanbe, 89 pp.

Negmatullaev, S. K., G. A. Selezynov, D. W. Simpson, and C. Rojahn (1978). Seismological and engineering observations at dams, *Proc. 2nd Internat. Conf. on Microzonation,* **2,** 681–691.

Rautian, T. G. (1960). Earthquake energy (in Russian), in *Methods of Detailed Investigations of Seismicity*, U. V. Riznishenko, Editor, Academy of Sciences USSR, Moscow, 75–113.

Riznishenko, U. V. (Editor) (1960). *Methods of Detailed Investigations of Seismicity* (in Russian), Academy Sciences USSR, Moscow, 327 pp.

Scholz, C. H. (1968). The frequency-magnitude relation of microearthquakes in rocks and its relation to earthquakes, *Bull. Seism. Soc. Am.* **59,** 399–415.

Simpson, D. W. (1976). Seismicity changes associated with reservoir loading, *Eng. Geol.* **10,** 123–150.

Simpson, D. W. and S. K. Negmatullaev (1978). Induced seismicity studies in Soviet Central Asia, *Earthquake Information Bull.* **10,** 208–213.

Snow, D. T. (1972). Geodynamics of seismic reservoirs, *Proc. Symp. on Percolation through Fissured Rocks*, Dtsch. Ges. Erd-Grundbau. Stuttgart, T2-J:1–19.

Soboleva, O. V. and U. A. Mamadaliev (1976). The influence of the Nurek Reservoir on local earthquake activity, *Eng. Geol.* **10,** 293–305.

Soboleva, O. V., G. P. Schklyar, and E. E. Blagovestchenskaya (1974). Investigations of stress field in earthquakes foci in connection with the predicition of place and time of large earthquakes (in Russian), in *The Search for Earthquake Forerunners at Prediction Test Fields*, Nauka, Moscow, 65–70.

Soboleva, O. V., U. A. Mamadaliev, and D. W. Simpson (1975). Seismicity changes during the first stage of filling of Nurek Reservoir, Tadjikistan, USSR (abstract), *EOS, Trans. Am. Geophys. Union* **56,** 1025.

Utsu, T. (1971). Aftershocks and earthquake statistics (III): analyses of the distribution of earthquakes in magnitude, time and space with special consideration to clustering characteristics of earthquake occurrence (1), *J. Faculty Sci., Hokkaido Univ.*, Ser. III. **3,** 379–441.

LAMONT-DOHERTY GEOLOGICAL OBSERVATORY
COLUMBIA UNIVERSITY
PALISADES, NEW YORK 10964 (D.W.S.)
CONTRIBUTION NO. 3205

TADJIK INSTITUTE OF SEISMORESISTANT CONSTRUCTION AND SEISMOLOGY
DUSHANBE, TADJIK SSR, USSR (S.K.N.)

Manuscript received August 15, 1980

INDUCED SEISMICITY AND STYLE OF DEFORMATION AT NUREK RESERVOIR, TADJIK SSR

C. M. Keith*, **D. W. Simpson**

Lamont-Doherty Geological Observatory of Columbia University

Palisades, New York 10964 USA

and

O. V. Soboleva

Tadjik Institute of Seismoresistant Construction and Seismology

Tadjik SSR, USSR

Submitted to the Journal of Geophysical Research

August 1981

*Now at: ESSO Resources Canada Ltd., 500 6th Avenue, S.W., Calgary, Alberta, Canada

Abstract. Induced seismicity is occurring at the 315 m high Nurek dam in Tadjikistan, USSR. An intense burst of seismicity accompanied the second stage of filling of the reservoir from 120 to 200 m during August to December 1976. Hypocentral locations and fault-plane solutions determined using data from a ten-station telemetered network surrounding the reservoir show the activity to be concentrated on a series of narrow, planar fault zones near the central basin and on more diffuse zones along the upstream edges of the reservoir. The activity extends to depths of 8 km and appears to be confined within the upper plate of the Ionakhsh thrust, a listric fault which outcrops 1 km north of the dam. The dominant mode of deformation in the post-Paleozoic sediments of the Tadjik Depression is thrusting. Fault-plane solutions for the induced seismicity show short segments of strike-slip and thrust faulting for the most intense activity near the central basin, and normal and thrust faulting along the upstream edges of the reservoir. None of the fault zones delineated by the induced seismicity corresponds to faults mapped at the surface, while none of the surface faults mapped in the reservoir area has shown an increase in seismicity. The spatial distribution of seismicity within the active zones is in general agreement with that expected from models of the changes in strength associated with reservoir loading. The temporal distribution of seismicity shows a migration outward from the center of the reservoir, probably associated with diffusion of pore pressure.

Introduction

Seismicity induced by reservoir impoundment has been clearly established at many dam sites [for reviews see Gupta and Rastogi, 1976; Simpson, 1976]. The economic and social importance of a proper understanding of the phenomenon is obvious. The threat to the integrity of a dam posed by induced seismicity constitutes a major portion of the seismic risk to the structure [Packer et al., 1978]. In addition this phenomenon has some importance for earthquake prediction research. The ability of fluid pressure increases to induce seismicity has been demonstrated with the injection of fluids in deep wells [Raleigh et al., 1976]. An understanding of the effects on reservoir seismicity of small stress changes, due to water load and pore pressure could lead to significant insight into dilatancy and earthquake precursory phenomena [Scholz et al., 1973]. Reservoir impoundment can provide a semi-controlled laboratory for prediction studies, provided an adequate description of the structure and deformation of the region beneath the reservoir can be obtained.

Whilst seismograph networks have been installed around many reservoirs, they have rarely been dense enough to provide adequate resolution of the seismically active areas. Nor have they usually been installed for a sufficient length of time prior to impoundment for the background seismicity level to be properly defined. Consequently, the relationships between the induced seismicity, the active geological structures and the regional tectonics have not been

adequately resolved. Such resolution is important for an accurate description of the response of the crust beneath the reservoir to the applied load.

At Nurek Reservoir in the Tadjik Republic of Soviet Central Asia, we have an example which provides a reasonably adequate degree of resolution and where (i) the induced seismicity defines several distinct fault zones, (ii) composite fault plane solutions are consistent with the regional and reservoir-induced stresses but differ between the distinct fault zones, and (iii) the seismicity exhibits space-time variations in activity along the fault zones.

In 1975 a high-gain seismograph network with a central recording facility was installed around Nurek Reservoir by Lamont-Doherty Geological Observatory and the Tadjik Institute of Seismoresistant Construction and Seismology (TISSS) as part of the Joint Soviet-American Program in Earthquake Prediction. The network is similar to that described by Simpson et al. [1981]. This network and the reservoir outline are shown in Figure 1. Also shown in Figure 1 are the current stations of a separate network operated by TISSS since 1955. The two networks complement one another. The TISSS network provides a reasonably homogeneous catalog of seismicity from 1955 to the present, with about 15 years of pre-impoundment seismicity data. The American network provides the spatial resolution needed to determine the active geological features. Simpson and Negmatullaev [1981], using data from the TISSS network, describe the increase in seismicity associated with the filling of the reservoir and the relationship between changes in water depth and the level of seismicity. In this paper, using data from the telemetered network, we will concentrate on the three-

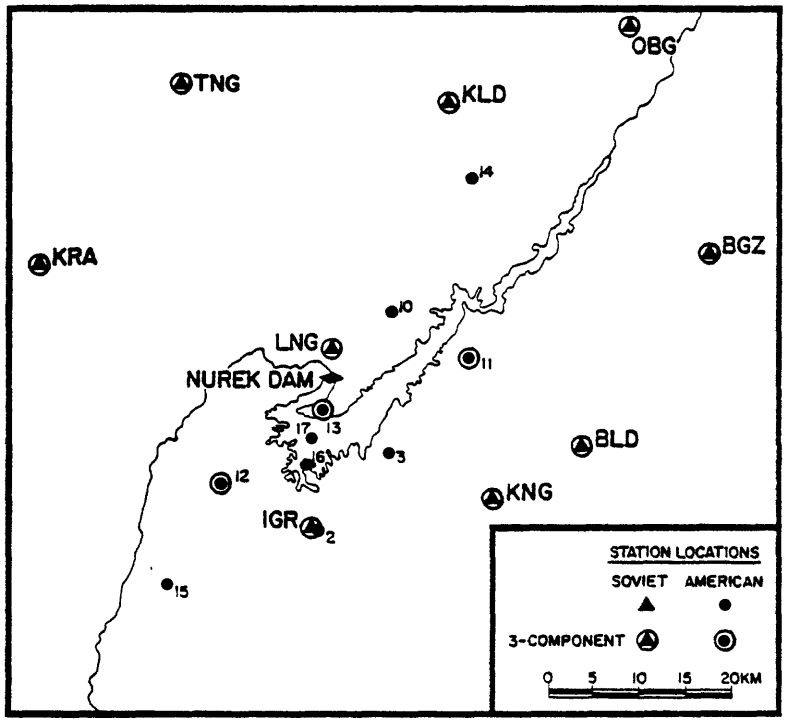

Fig. 1. Seismic stations of the TISSS and American networks at Nurek.

dimensional spatial configuration of the seismicity during the 1976 swarm, the deformation as indicated by composite fault plane solutions, and the relationship between the seismicity and the inferred geological structure and regional tectonics.

Induced Seismic Episodes

The number of earthquakes ($M > 1.5$) from the TISSS catalog and water levels for the period 1969-1979 are shown in Figure 2. The reservoir first began to fill in 1968, but the first sustained filling occurred in 1972 when a water depth of 100 meters was achieved for the first time. A second major filling episode occurred in 1976 when the water level reached 200 meters. In 1981 the reservoir is due to reach its final level of 300 meters which will make Nurek the deepest reservoir in the world. Both the filling episodes in 1972 and 1976 were accompanied by a five to ten-fold increase in seismicity over the background level (Figure 2). The largest earthquakes (magnitude 4.6 and 4.3) occurred on November 6, 1972 during the first stage of filling of the reservoir. The largest earthquake during the second major filling episode occurred on September 13, 1976 and was of magnitude 4.1.

The telemetered American network runs at a much higher gain than the TISSS network and consequently has a much lower detection threshold. Beneath the main body of the reservoir, this threshold is less than magnitude zero. Howerver, to keep the number of events within practical limits and to insure consistent location accuracy, the effective threshold is about magnitude 0.5. Approximately 1500 events were located during the late 1976 induced episode.

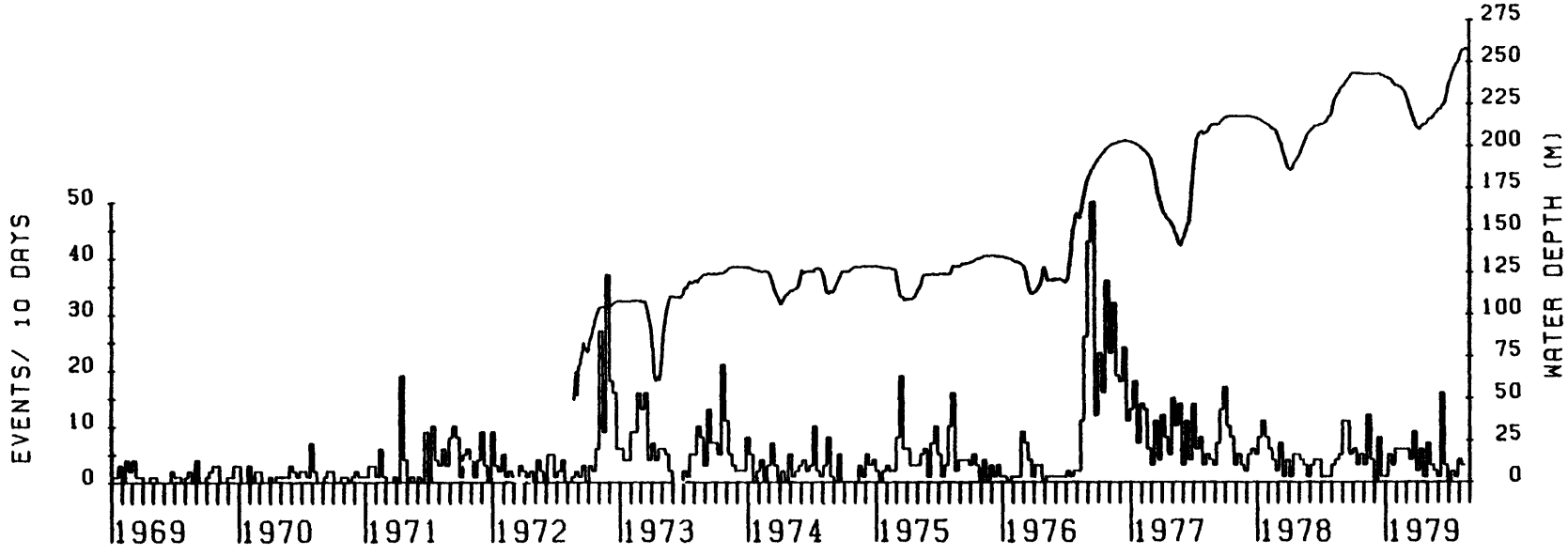

Fig. 2. Water level and number of earthquakes M > 1.5 per ten days within 10 km of Nurek Reservoir located by the TISSS network [from Simpson and Negmatullaev, 1981].

The second stage of filling began on July 15, 1976 and the level of seismicity began to increase on August 15 [Simpson and Negmatullaev, 1981]. Unfortunately, only six stations in the telemetered network were installed at the beginning of filling cycle and some of these operated only intermittently. The data for this period are incomplete and of inferior quality in comparison with those recorded after mid-October 1976, when the network was made fully operational and reconfigured as shown in Figure 1.

Regional Tectonics

The Tadjik Depression is one of many structural blocks involved in the collision between the Indian and Eurasian plates which started about 40 m.y. ago. It is bounded on three sides (Figure 3) by major active features: the Gissar-Kokshal fault to the north (right-lateral strike-slip to oblique reverse), the Darvaz-Karakul to the east (left-lateral strike-slip and thrust) and the Hindu Kush zone to the south. Major deformation is occurring within the sediments of the Depression itself, indicating that it is not simply acting as a rigid block with deformation located at its edges.

The Depression was a shallow sea during the Mesozoic, with widespread deposition of Jurassic evaporites and carbonates [Gubin, 1967; Loziyev, 1970; Leith et al., 1981] followed since then by nearly continuous sediment influx from the surrounding Tien Shan and Pamir regions. Total post-Jurassic sediment thicknesses are quite variable - from upwards of 12 km near the eastern margin with the Pamirs to as little as 3 km in parts of the central Depression [Loziyev, 1974].

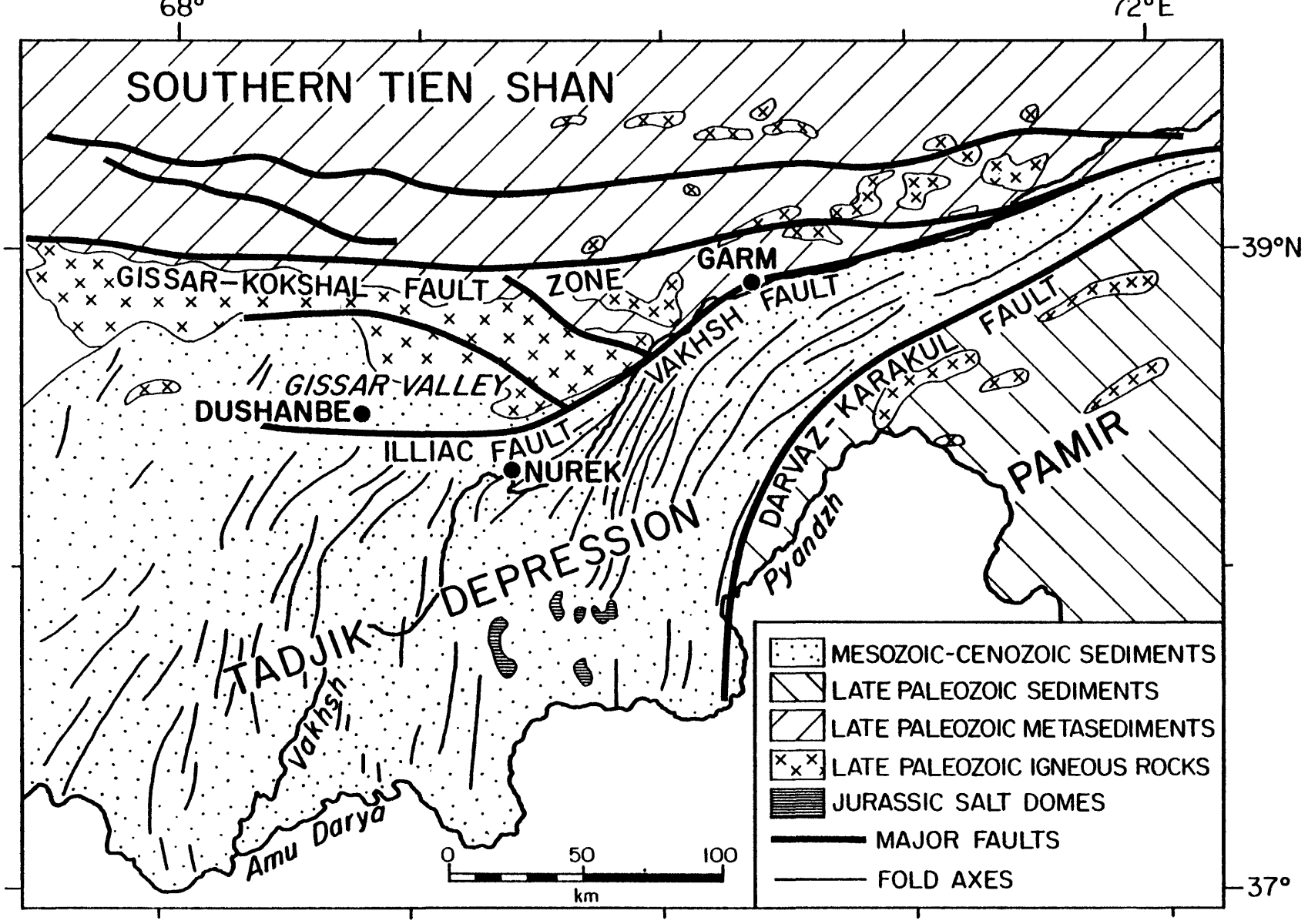

Fig. 3. Generalized geology of the Tadjik Depression, southern Tien Shan and northwestern Pamir. Intense deformation is occurring in the sediments of the Tadjik Depression, being compressed between the more rigid blocks of the Pamir and Tien Shan. Fold axes in the Depression indicate the change in orientation of this deformation, from north-easterly strike in the northeastern part of the Depression to more northerly strike in the central Depression. Based on geological and tectonic maps in the 'Atlas of Tadjikistan' (Academy of Sciences, Tadjik SSR, 1968).

The sedimentary cover has deformed since the Paleogene by large-scale folding and thrusting, with up to 50 km of displacement along individual thrusts (e.g., the Vakhsh thrust in the northeast of the Depression [Gubin, 1960, 1967]). Deformation is more intense in the northeast, where folds become isoclinal and thrusts stack the section imbricately. The highest rate of seismicity takes place along the Vakhsh thrust northeast of Nurek Reservoir. Thrusts in general are listric and cut up-section from the decollément surfaces in the Jurassic evaporites. Salt domes to the south of the reservoir region (Figure 3) and the outcropping of salt at the surface immediately north of the dam also attest to the importance of salt on the tectonics in the area. Vertical and overturned bedding planes observed in Neogene sediments on the northwest shore of the reservoir indicate the large amount of deformation to which the reservoir area has been subjected.

The Illiac fault, north of Nurek (see Figures 3 and 4), is a major structure separating the less deformed and less seismic Gissar Valley from the highly deformed and highly seismic northern part of the Depression. This fault appears to have some controlling influence on the orientation of deformation [Leith et al., 1981]. At its western end it is the northern termination of N-S to NNE-SSW trending folds and mountain ranges. At its eastern end, where it strikes NE-SW, folds and thrusts are sub-parallel to it. The Nurek area appears to be acting as a knot where major features change strike from the NE-SW trend of the northeastern part of the Depression to the more N-S trend typical of the southern and western part of the Depression.

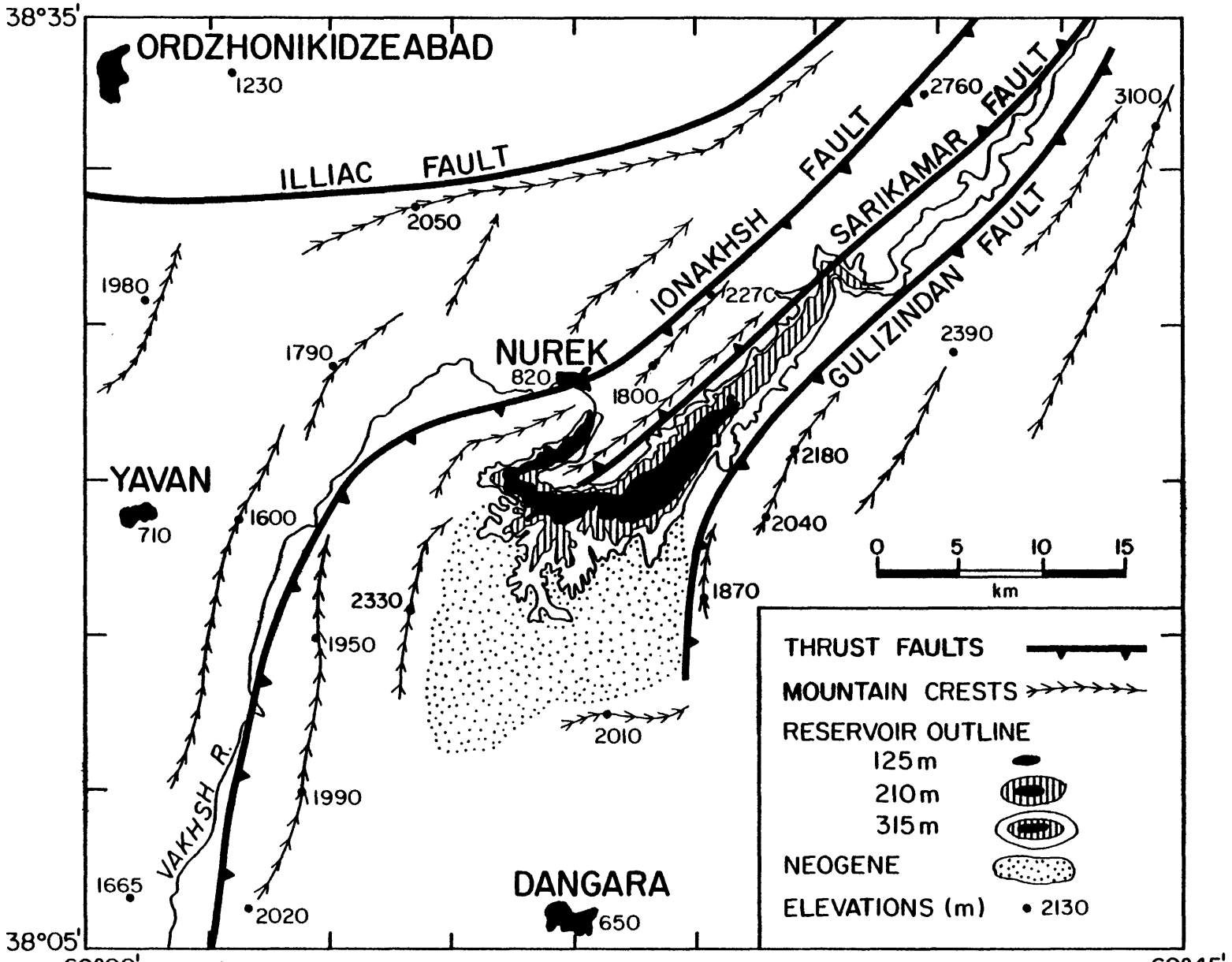

Fig. 4. Main faults and topographic features of the Nurek area. Mountain crests, traces of the Ionakhsh and Gulizindan faults and the course of the Vakhsh River change from a northeasterly orientation in the north to a north-south orientation in the south. The Neogene sandstones which form a basin south of the reservoir are indicated. The outline of the reservoir, taken from Landsat images, is shown at the approximate levels at the beginning of the 1976 filling cycle in August (120 m) and at the maximum level during that cycle in December (203 m). The largest contour (also used in other diagrams) is the 1000 m topographic contour and approximates the reservoir at its maximum extent (315 m.)

The Ionakhsh fault (Figure 4) is one of four thrusts in the Surkhu Mountains described by Gubin [1960, 1967] that have recently been seismically active. From a study of six earthquakes on these faults, Gubin infers that they dip to the southeast. He states further that these thrusts consist of sheets of Cretaceous sediments with Juraasic gypsum at the base. Only one of the events studied by Gubin was deeper than 6 km. This event occurred just to the northeast of the reservoir area, at a depth of 10 km on a nearly horizontal fault plane, indicating that the decollément surface is near 10 km in this area.

The structures and deformation of the Tadjik Depression and in the Nurek area in particular thus have some of the characteristics of a fold and thrust belt at least partially controlled by salt tectonics. Added to this is the complexity caused by the nearby boundary provided by the Illiac fault (Figure 3). The late-Paleozoic crystalline rocks north of the Illiac fault act as a rigid block to concentrate the deformation to the south of it.

Fault plane solutions for earthquakes in the Tadjik Depression [Soboleva et al., 1976] and in the Nurek area prior to the impounding of the reservoir [Soboleva and Mamadaliev, 1976] are characterized by sub-horizontal P-axes oriented northwest. Both thrusting and strike-slip mechanisms are observed; thrust motion occurs on northeasterly trending structures and strike-slip motion takes place on east-west features, such as the Illiac fault (right-lateral), and on north-south features in the central and western part of the Depression (left-lateral).

The sketch map of the reservoir area in Figure 4 shows how the course of the Vakhsh River, the trend of the main ranges and the strike of the main geological faults change from a northeasterly orientation in the upstream end of the reservoir to a more north-south orientation in the southern part of the region. The main body of the reservoir lies in a basin contained on the east, north and west by the high topography of the Gulizindan, Sarikamar and Sanglok Ranges (2000-3000 m). To the south and southeast, the irregular outline of the reservoir reflects the more gentle topography of the fertile Dangara Valley. The main faults in the reservoir area are the Ionakhsh, the Gulizindan and the Sarikamar. Both the Ionakhsh and Gulizindan dip to the southeast. The Sarikamar is a young thrust fault dipping to the northwest and is clearly exposed on the ranges along the northern edge of the reservoir. At its southern termination near the bend in the reservoir, Cretaceous rocks are thrust over Quaternary deposits, attesting to the extensive recent movement on this structure [Reiman et al., 1961]. Beneath and south of the central basin of the reservoir, thick, massive deposits of Neogene sandstone and Quaternary loess cover the Mesozoic formations and no surface expression of faulting has been found.

Seismicity Patterns

Seismicity for the period August 1976 to February 1977, determined with data from the telemetered network, is shown in Figure 5. Hypocenters have been determined using the program HYPOINVERSE [Klein, 1978] with a velocity structure and station corrections determined

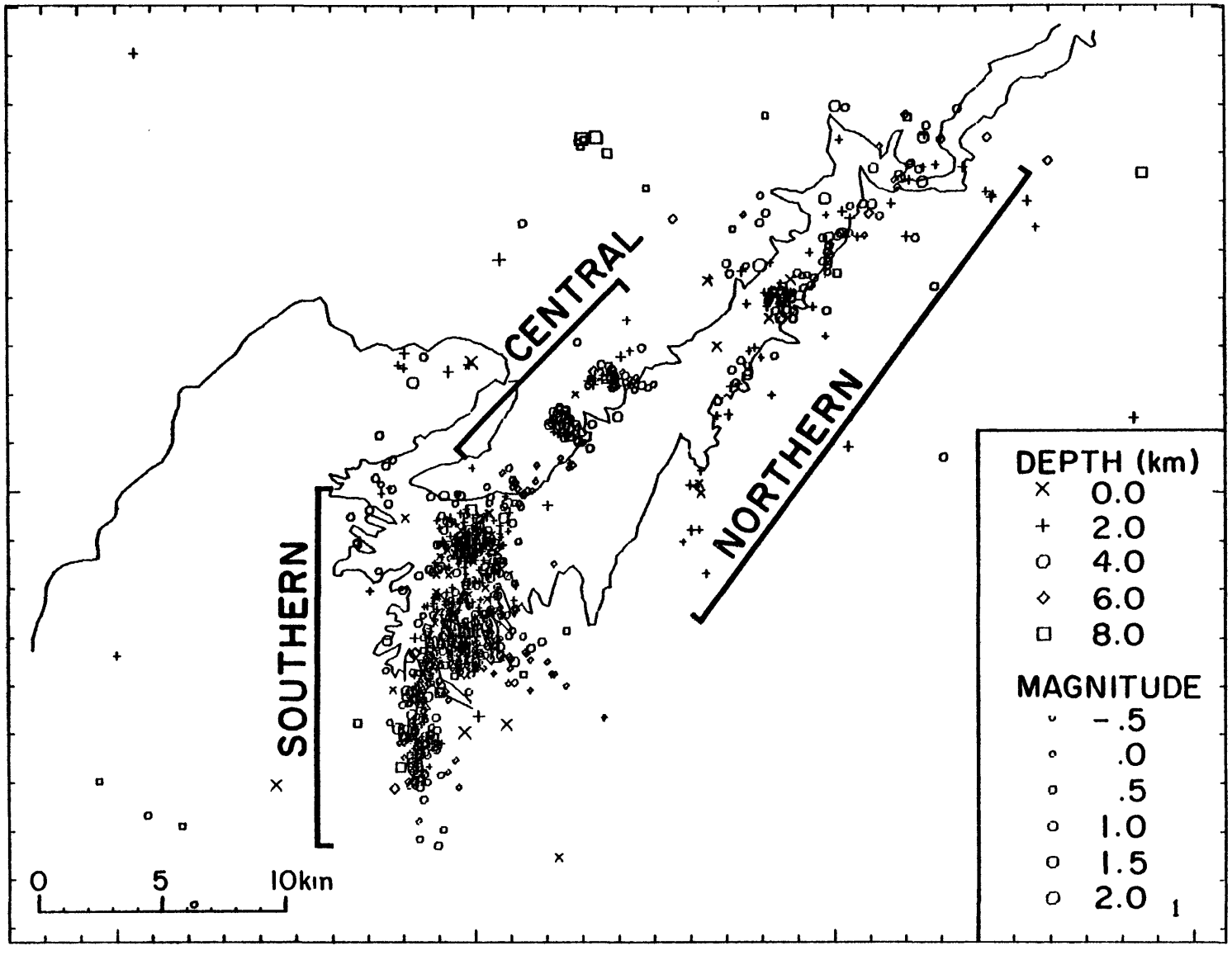

Fig. 5. Epicenter map of a, b, and c quality solutions for data from the telemetered network September 1976 to February 1977.

from an inversion study using the techniques of Crosson [1976]. All locations of quality a, b and c as defined by HYPOELLIPSE [Lahr, 1979] are included in Figure 5. In this paper, a, b and c quality locations are used when displaying temporal changes in seismicity and gross spatial patterns, and only a and b quality solutions are used in cross-sections and fault plane solutions.

The seismicity in the reservoir area can be divided into three general zones (Figure 5). The southern and most active zone begins directly beneath the central basin of the reservoir and extends southward for almost 15 km. The central zones extends northeast for 8 km along the northern shore of the reservoir. In the northern zone, activity is concentrated mainly along the southern edge of the reservoir, with one cluster of activity near the northern shore.

The distribution of seismicity in depth and time is shown in Figure 6. Hypocenters are projected onto the line II' (Figure 7) and plotted as functions of depth and time. The induced seismicity is mainly confined to the depth range 1 to 8 km with the highest level of activity between 2 and 7 km. The widths of the well-defined cross-sections are less than 1 to 2 km. We estimate that the relative accuracies of the best constrained hypocenters (a and b quality) within the network are about 200 to 300 m horizontally and about twice this vertically. For c quality solutions, the horizontal error is up to 1 km and the error in depth determination can be considerably larger. Within the network, the epicenters are constrained primarily by azimuthal control of station location and are insensitive to the assumed velocity structure. The average depth of the earthquakes can be shifted by approximately 1 km by changes in the velocity structure

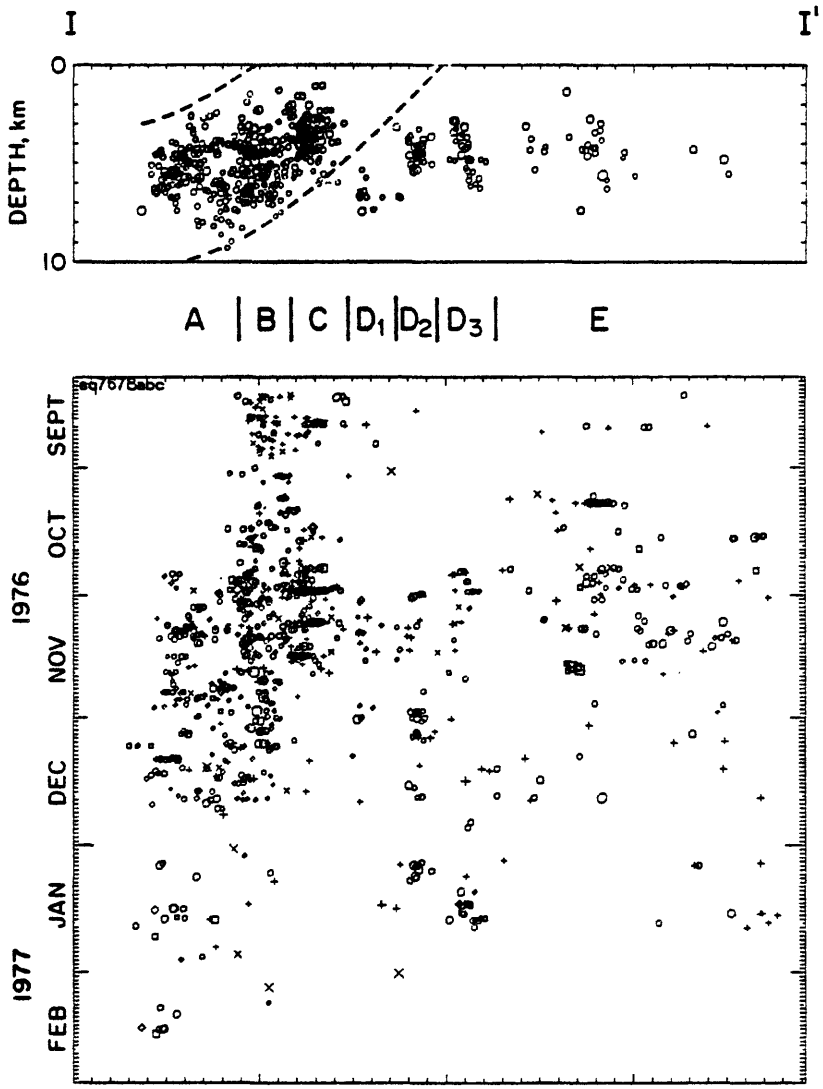

Fig. 6. Vertical cross-section (top) and space-time diagram (bottom) along the line II' shown in Figure 7. Only A and B quality solutions are used in the depth section and a, b, and c quality solutions are used in the space-time diagram. Segments A-E correspond to the groups in Figure 7. Dashed lines in the cross-section indicates the inferred extent of the Ionakhsh thrust sheet. Note that although the operation of the network was improved and new stations were added in mid-October 1976, the detection level in regions A and D was not sufficiently different than for region B and C in September and October, so that the lower levels of activity in A and D before mid-October are real.

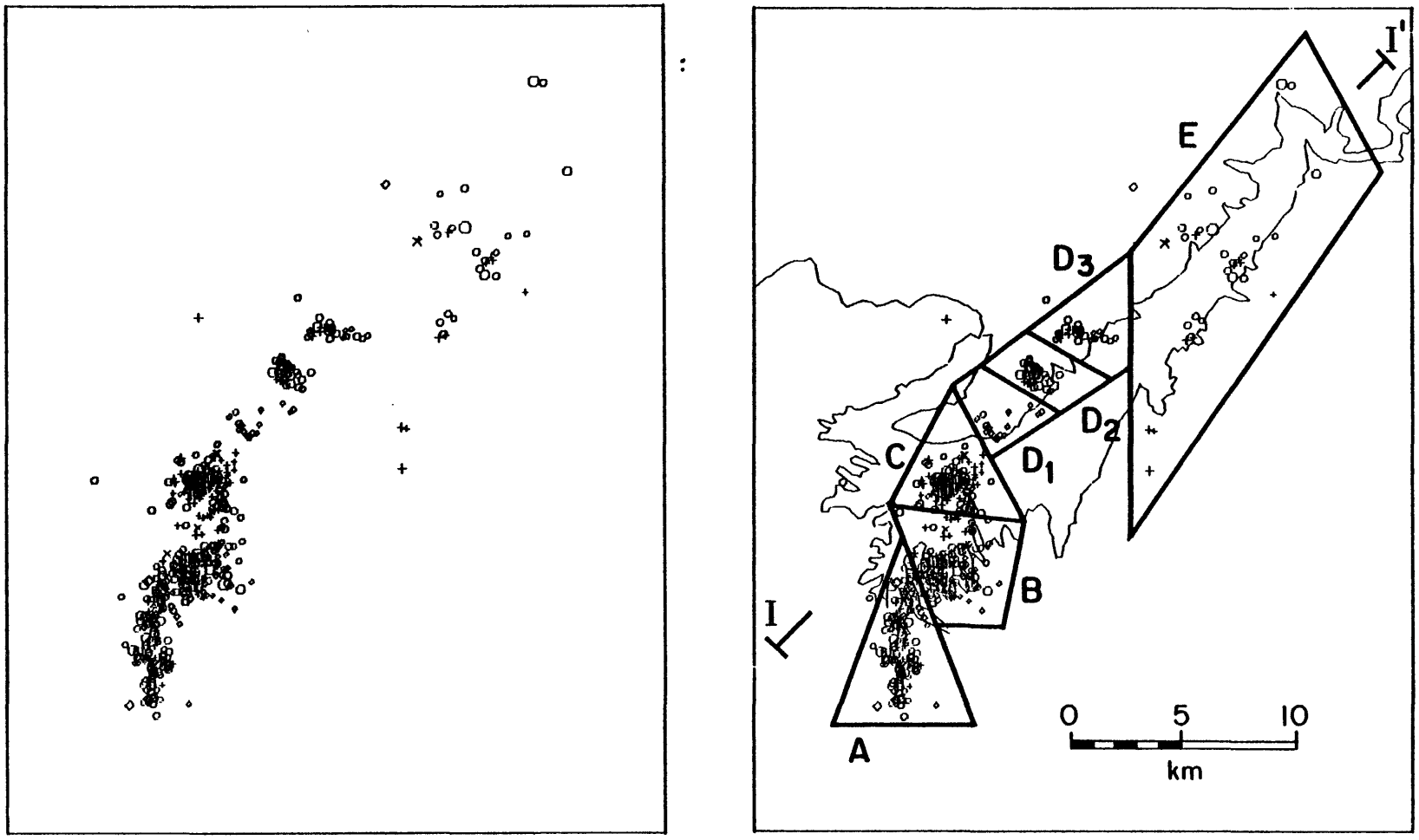

Fig. 7. Epicenters of a and b quality solutions from October 25, 1976 to February 28, 1977. Groups A-E as described in text are shown to the right. The line II' is the projection line used in the cross-section and space-time diagram in Figure 6.

and/or station corrections. The depths cannot be altered sufficiently, however, to invalidate the conclusion that the near surface continuation of the active zones are characterized by low seismicity.

The best located events (a and b quality) for the period October 26, 1976 to February 28, 1977 are shown in Figure 7. Especially in the southern zone, lineations appear in these data which are not obvious in Figure 5. These lineations, coupled with depth cross-sections and composite fault plane solutions, have been used to divide the seismicity into groups A to E as shown in Figure 7. Initial attempts to interpret the southern zone in Figure 5 as a single feature resulted in a broad zone of seismicity, 3 to 4 km wide, with no apparent pattern in depth distribution and entirely inconsistent first motion data in composite fault plane solutions. Similar problems arose in trying to interpret the central and northern zones as a single feature parallel to the axis of the reservoir. Only when sufficient high quality locations were available to resolve the narrow zones shown in Figure 7 did there emerge a pattern of planar fault segments with internally consistent fault plane solutions.

There is a gradual northward decrease in the maximum and minimum depth of the activity along the southern zone (A, B, C in Figure 6). In group A (Figure 8), at the southern end, the main activity is from 4 to 8 km. In group B (Figure 9), most activity is between 3 and 7 km while in group C (Figure 10) the activity extends from 2 to 5 km depth. There is a distinct break in the depth of seismicity between the southern and central zones (Figure 11). In the southern part of the central zone, all earthquakes in group D1 are at depths greater than 6 km. Farther north along the central zone (D2 and D3) and in the northern zone, activity occurs between depths of 3 and 6 Km.

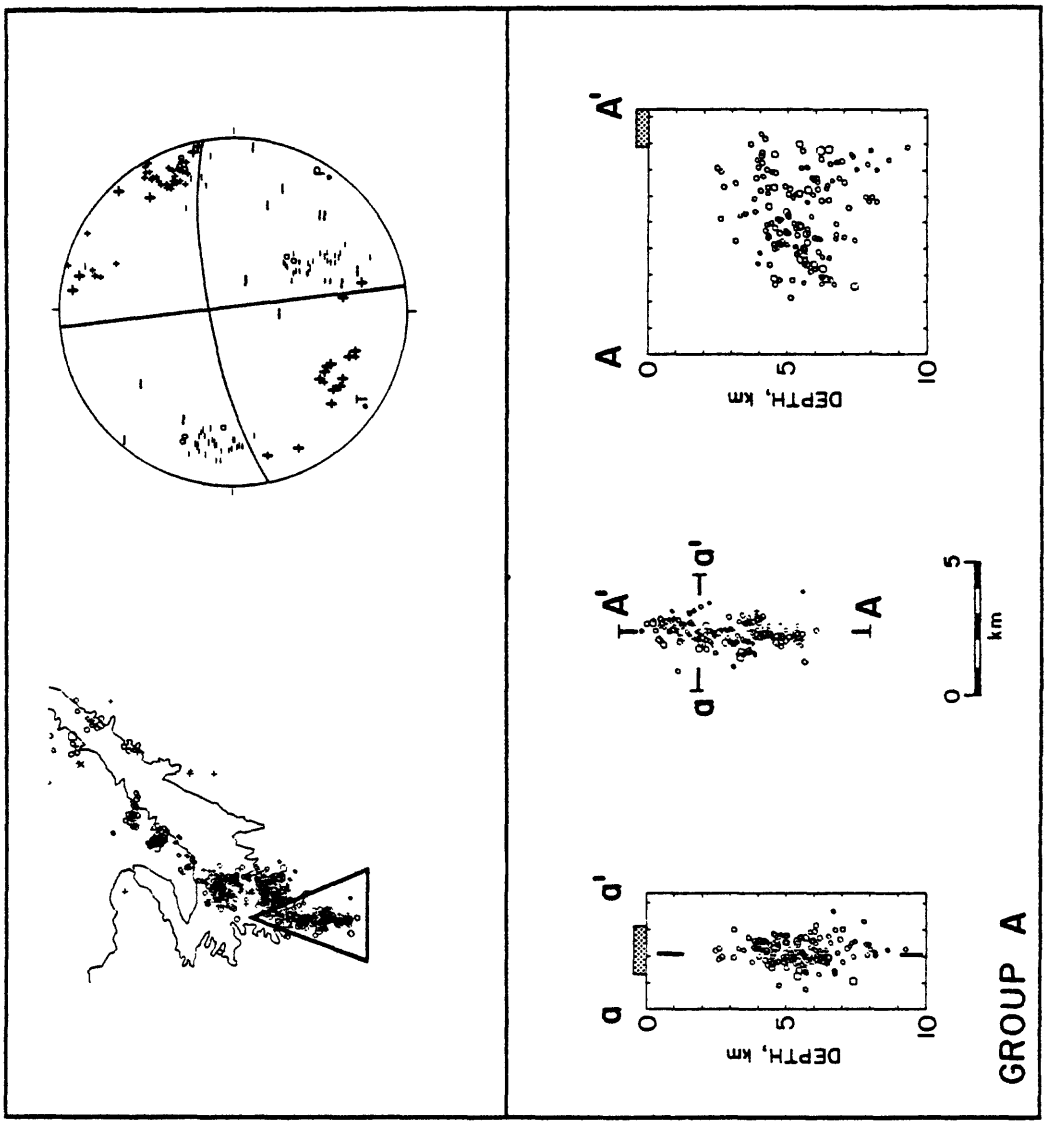

Figure 8

Figure 8

Epicenter map, cross-sections and composite fault plane solutions for group A. Only a and b quality locations are used throughout. Map in the upper left shows location of group A relative to other seismicity. Map view in the bottom center shows events in group A at a larger scale and indicates the projection line used for the depth cross-sections shown in the bottom left and bottom right. Short line segments in the cross section looking along strike (bottom left) indicate the dip of the fault plane as inferred from the composite fault plane solution. The stippled bar over the cross-section indicates the location of the reservoir. Note in this and Figures 9-11 the thin planar nature of the fault zone and the close agreement between the strike and dip of the seismicity patterns and fault plane solution. The composite fault plane solution in the upper right is an upper hemisphere equal area stereographic projection. First motions from both American stations (light symbols) and Soviet stations (heavy symbols) are used; pluses are compressions, minuses are dilations and zeros and nodal arrivals.

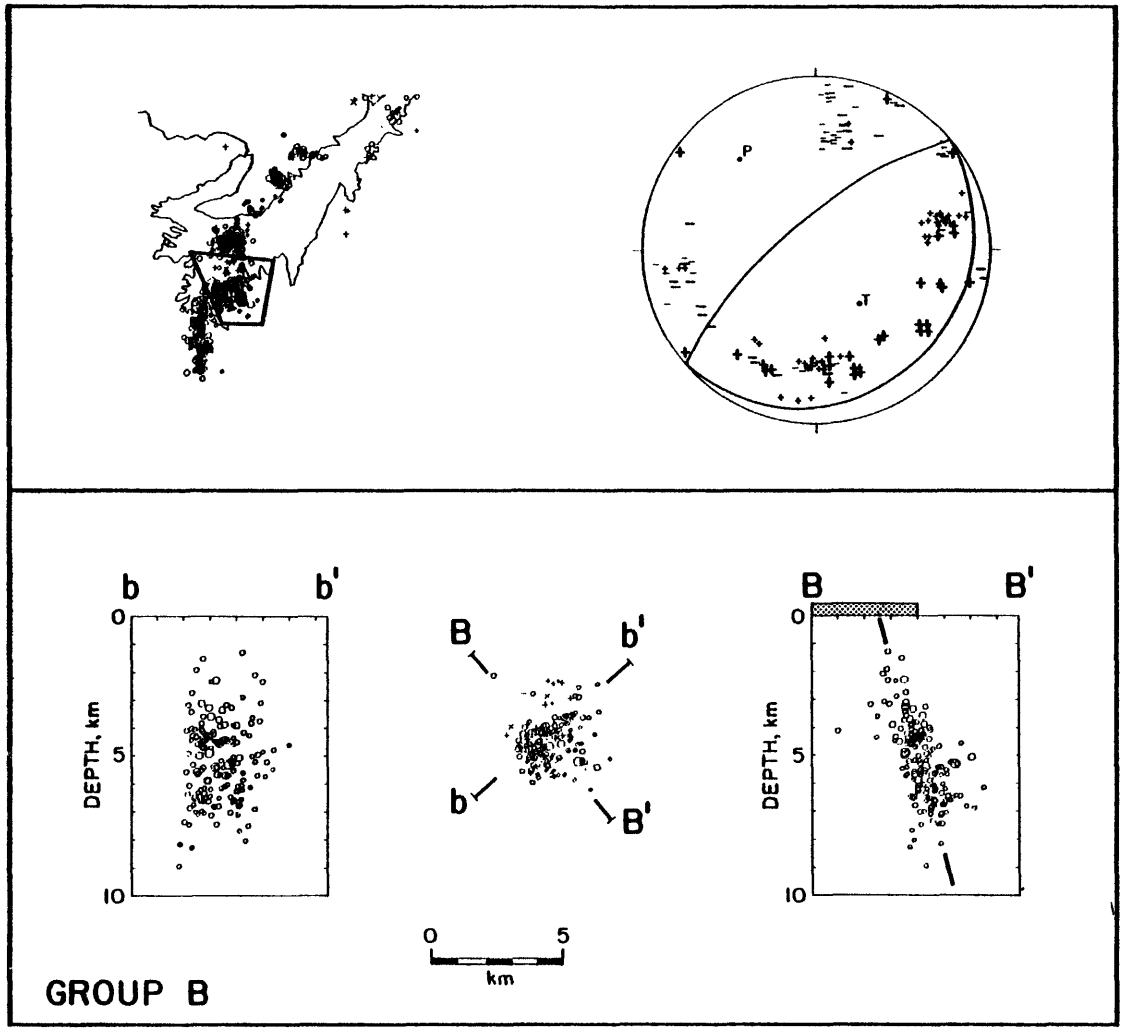

Fig. 9. Epicenter maps, cross-sections and composite fault plane solutions for group B. Symbols and conventions are the same as used in Figure 8.

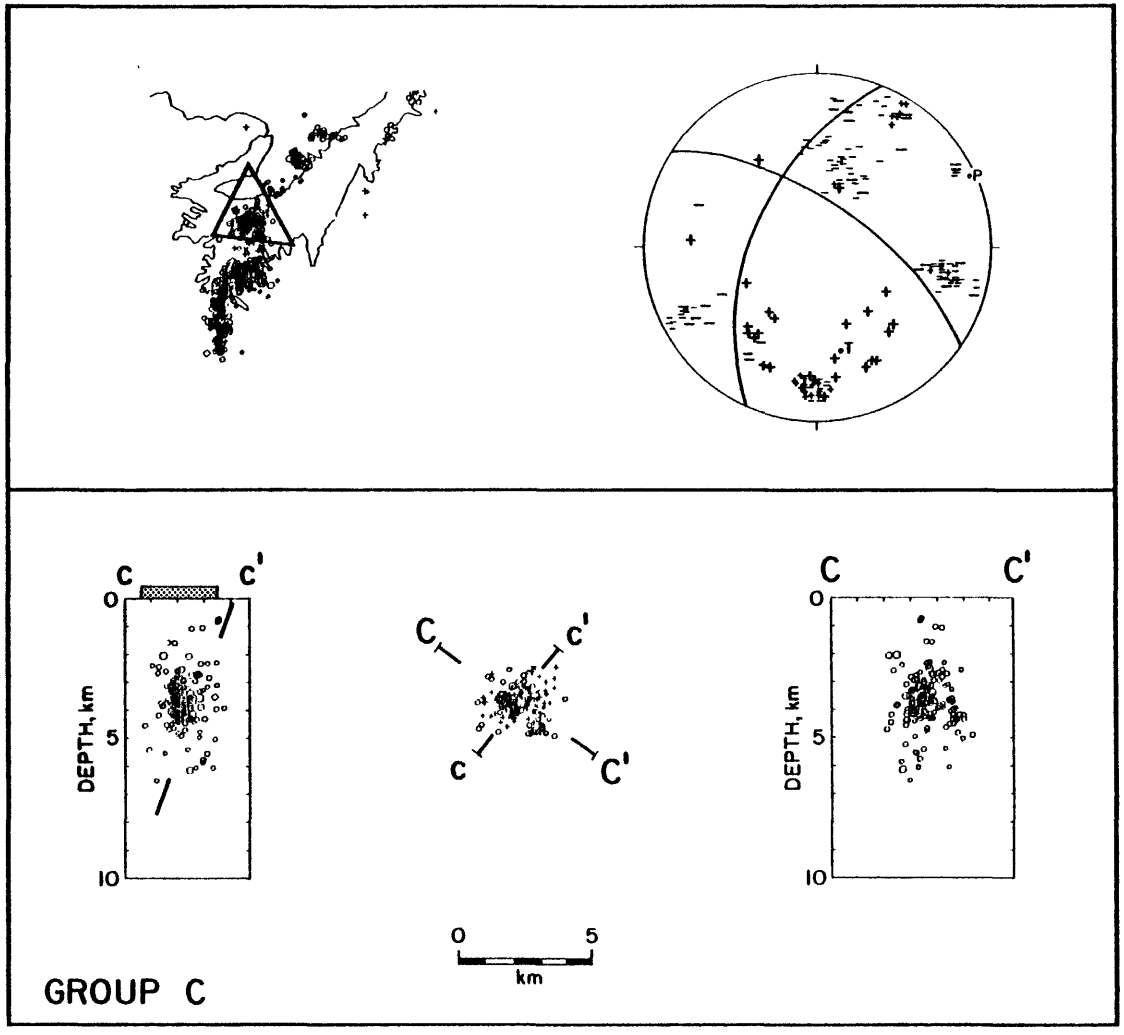

Fig. 10. Epicenter maps, cross-sections and composite fault plane solutions for group C. Symbols and conventions the same as in Figure 8.

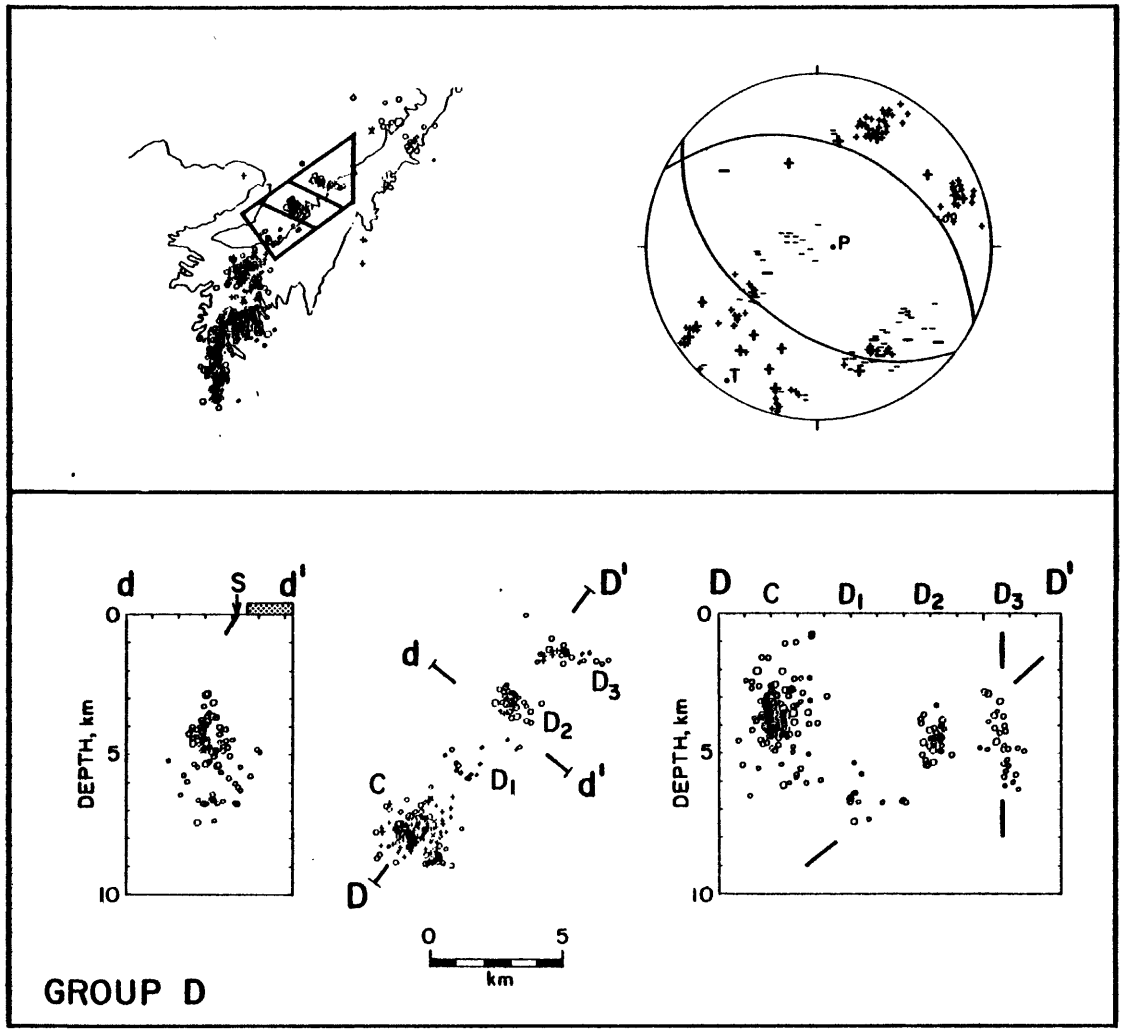

Fig. 11. Epicenter maps, cross-sections, and composite fault plane solutions for group D. In the map view (bottom center) and depth section looking along strike (bottom right) events from group C have been included to show the abrupt change in depth between groups C and D1. The two sets of line segments in the bottom right show the dips for the entire zone as inferred from the fault plane solution in this figure (dipping 50° to the southwest) and for the vertical segment of seismicity in group D3 as shown in Figure 12. S = Sarikamr fault.

The space-time diagram in Figure 6 shows that during September 1976, most of the induced seismicity was confined to the northern section of the southern zone. Although locations during this time are less reliable than after mid-October, the activity appears to be mainly in groups B and C. At the end of October activity began to migrate southward into group A. Except for a short burst of activity on October 9 near the northern shore of the reservoir, seismicity did not increase in the central and northern zones until late in October. The central zone is characterized by short, concentrated bursts of activity which begain in group D3 and migrated southward into groups D2 and D1. In mid-November, group C became quiet and the level of seismicity decayed throughout the entire region. Activity decreased abruptly on December 20 when the water level in the reservoir reached a maximum of 203 m and began to slowly recede.

Mode of Faulting

Composite fault plane solutions have been detemined using data from both the American telemetered network and the Soviet stations. Since significantly different mechanisms are found for relatively short fault segments, only a small portion of the focal sphere is sampled by any one station for earthquakes within each group. By combining data from many events recorded on the high-gain stations of the telemetered network with larger earthquakes recorded on the more distant Soviet stations, a greater portion of the focal sphere is sampled. In most cases, the telemetered network sampled the upper hemisphere, while the Soviet stations received P waves emerging from the lower hemisphere.

Southern Zone

The southern zone contains the most active area of induced seismicity. Because of the station distribution, both hypocenters and composite fault plane solutions are best controlled in this region. As shown in Figure 8, the most southerly segment, group A, shows a narrow vertical zone of seismicity oriented north-south with left-lateral strike-slip motion. Group B (Figure 9) shows a narrow zone oriented in a northeasterly direction dipping steeply to the southeast, and the fault plane solution indicates high angle reverse faulting. Group C (Figure 10) shows an almost vertical zone with a northwesterly strike, and the fault plane solution shows predominantly left-lateral strike-slip motion with a strong thrust component. Groups A and B exhibit very close correlation between the strike and dip of the seismic zone and the orientation of the nodal planes in the fault plane solution. The first motion data are consistent within each group, but there are substantial differences in the distribution of compressions and dilatations between different groups.

Central Zone

The central zone of seismicity is made up of three concentrated clusters labelled D1, D2 and D3 in Figure 7. Taken together, these clusters define a patchy zone of activity 7 km long and 2 to 3 km wide oriented in a northeasterly direction (Figure 11). Individually, they are zones 2 to 3 km long and less than 1 km wide oriented in a north-

westerly direction. The cluster D1 is considerably deeper than the other two. The composite fault plane solution for the entire group can be interpreted as indicating normal faulting with a northwesterly strike (Figure 11). With the southwesterly dipping plane as the fault plane, this interpretation is consistent with the deepening of activity from D2 to D1. Each cluster individually can be interpreted as showing left-lateral strike-slip motion with west-northwest to north-northwest strike (Figure 12). A strike-slip mechanism may be the best interpretation of the vertical segment shown in the cross section in Figure 11 for part of the group D3. Within the limitations of the data, our preferred interpretation of the seismicity in the central zone is that clusters D1 and D2 form a narrow segment of a normal fault dipping to the southwest. The activity in D3 is on an easterly trending strike-slip fault. The eastward extension of the strike-slip segment of D3 coincides with a decrease in the level of activity and change in strike of the seismicity on the opposite side of the reservoir (see Figure 5).

Northern Zone

Northeast of D3 there is a break in seismicity before activity increases again in a concentrated cluster in group E. The most intense activity in the northern zone occurs along the southeastern edge of the reservoir. Figure 13 shows a relatively narrow and linear zone beginning at the upstream bend in the reservoir and extending southwest approximately 15 km before assuming a more southerly strike opposite the D3 cluster. The first motion data are consistent with a

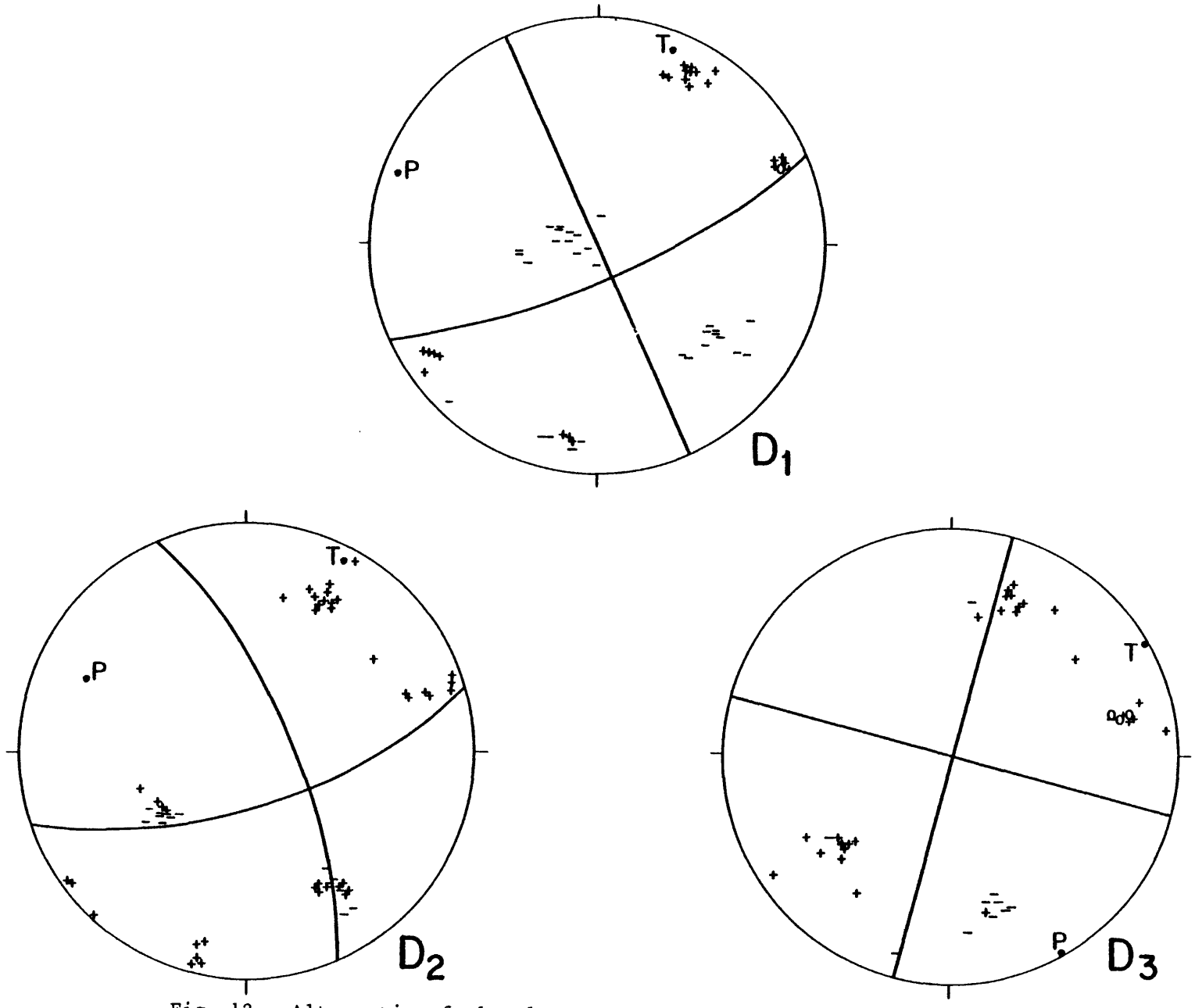

Fig. 12. Alternative fault plane solutions for groups D1-D3. Convention same as used in Figure 8.

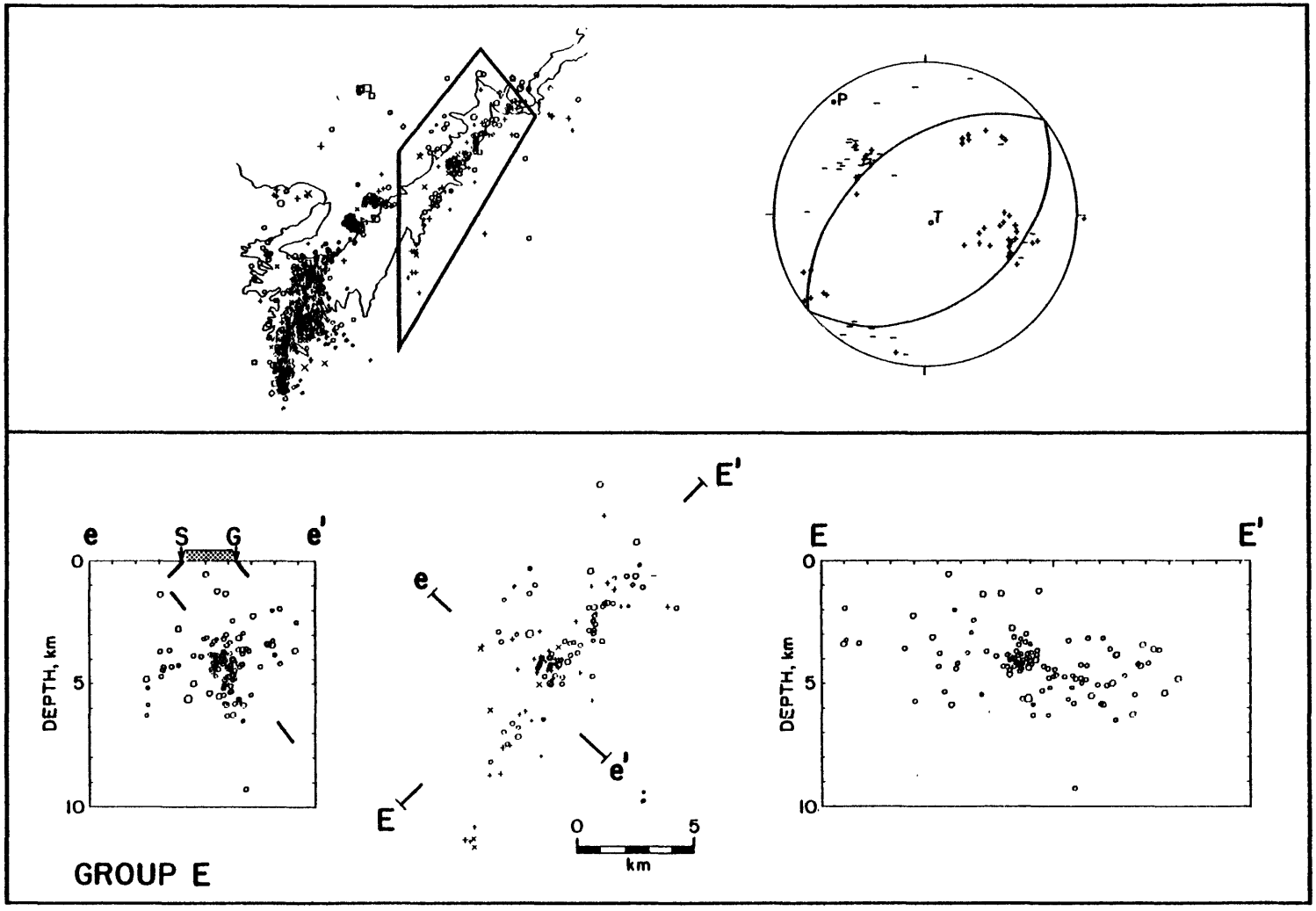

Fig. 13. Epicenter maps, cross-sections, and composite fault plane solution for group E. Symbols and conventions the same as in Figure 8 except that, because of the lower level of activity in this region, a, b, and c quality solutions have been used. S = Sarikimar fault, G = Gulizindan fault.

thrust mechanism with a strike similar to the trends in seismicity. The depth cross-section shows the seismicity to lie mainly beneath the southeastern edge of the reservoir. Although the station distribution is not sufficient to provide the same depth resolution as in the southern zone, there does not appear to be any single planar feature in the cross-section corresponding to the dips of the nodal planes.

Induced Seismicity, Local Geology and Induced Stresses

The fault patterns inferred from the induced seismicity are summarized in Figure 14 along with the mapped faults in the reservoir area. In a broad sense, the patterns of induced seismicity near the reservoir show many features in common with the regional tectonic and geological trends. The change in orientation from northeasterly to northerly strike of the active zones follows the general pattern of the faults, folds and topography in the northeastern Tadjik Depression (Figure 4). The focal mechanisms for the most active zones (groups A, B and E) show maximum horizontal compression in a northwesterly direction, consistent with the trend throughout the Depression. The mode of deformation observed in the induced seismicity, with short segments of alternating thrust and strike-slip motion, may be representative of a more general mechanism by which the change in strike throughout the Depression is accommodated. The pattern formed by groups A, B and C is kinematically similar to trench-trench transform fault systems in plate tectonics. Strike-slip motion along segments A and C is connected to, but does not extend beyond, the thrusting in group B.

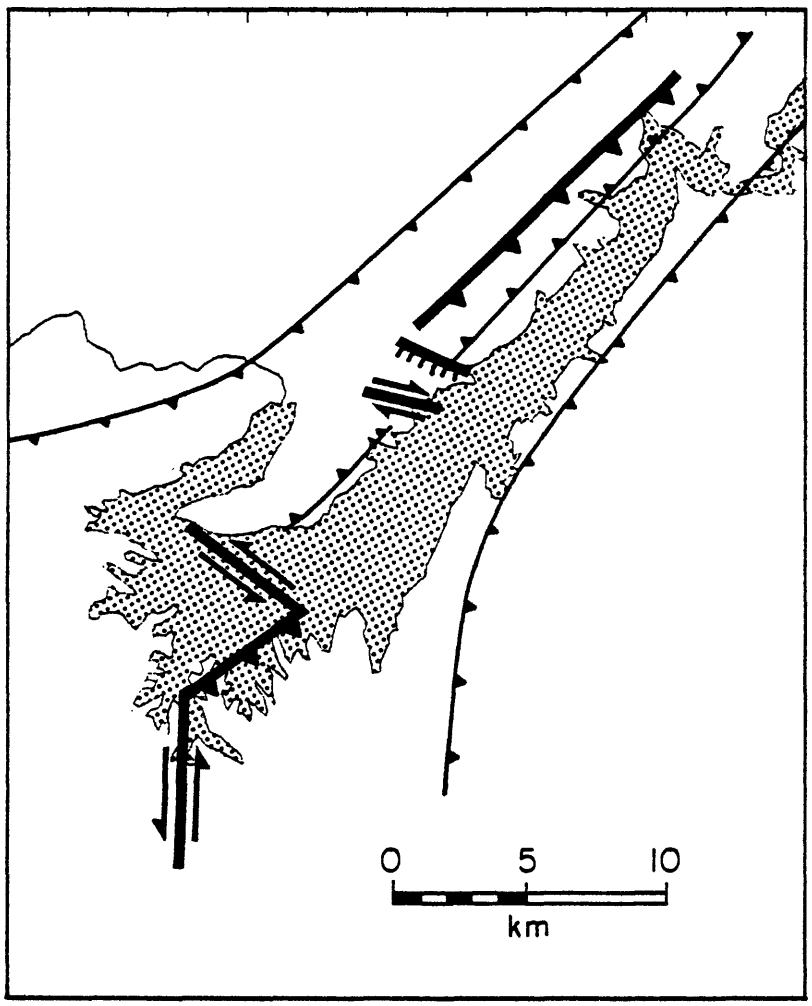

Fig. 14. Summary of the surface outcrop of fault zones and sense of motion inferred from the induced seismicity (heavy lines) and mapped faults (light lines).

In detail, however, there is virtually no one-to-one correspondence between the zones of induced seismicity and mapped faults of the reservoir area (Figure 14). None of the major mapped faults has shown any increased activity since impoundment of the reservoir, and none of the faults showing induced seismicity is evident as a surface geological feature. The seismicity along the northern edge of the reservoir (group D) follows closely the Sarikamar thrust, but hypocenters lie directly beneath the surface trace of the NW dipping fault and both the depths and focal mechanism show the seismicity to be unrelated to the surface fault (Figure 11). On the opposite shore of the reservoir, the trend in seismicity, including the gradual bending away from the reservoir, closely parallels the surface trace of the Gulizindan fault. In this case, the fault plane solution agrees with the thrusting expected on the Gulizindan fault, but, again, the depth of the activity beneath the surface trace of the fault and the absence of any down-dip extension away from the reservoir indicates that these earthquakes are not occurring on the Gulizindan fault (Figure 13). The Gulizindan and Sarikamar faults outcrop on the slopes of the ranges that bound the northern section of the reservoir. For most of their length they lie above the surface of the reservoir and in 1976 they were never beneath more than 20 m of water. The inability of water to penetrate directly into the fault zones may be one of the major reasons for the absence of induced seismicity on these structures.

Leith et al. [1981] suggest that all of the induced seismicity is occurring in the upper plate of the Ionakhsh thrust. Although no induced seismicity can be directly related to the Ionakhsh itself, all of this seismicity lies above a down-dip projection of this fault as

indicated by the gradual increase in the maximum depth of earthquakes from north to south (cross-section I-I' in Figure 6). The corresponding increase in depths of the shallowest earthquakes along the same profile may result from the southward thickening of the Neogene sandstones (Figure 4), confining the seismicity to the Mesozoic rocks of the main Ionakhsh thrust sheet. Salt outcrops along the Ionakhsh fault near Nurek dam and aseismic deformation within the salt may account for the absence of seismicity at the base of the thrust sheet. Seeber and Armbruster [1979] show a similar arrangement of seismicity near Tarbela dam in Pakistan. A concentration of seismicity between 5 and 17 km lies within a slab of rigid rock riding above an aseismic detachment which is the downdip extension of the salt layer under the Salt Ranges.

Geological structures on a scale much smaller than those indicated in Figure 4 must play an imporant role in controlling the induced seismicity at Nurek. Leith et al. [1981] propose that one such factor may be structurally determined differences in permeability that control the access of reservoir water to fault zones. Without a more detailed knowledge of the geology of the reservoir area, we will not at this stage pursue the reasons for the disparity between major surface faults and the zones of induced seismicity. We simply state that this underscores the problems involved in attempts to estimate the potential for induced seismicity at a reservoir site on the basis of prior seismicity and gross geological structures.

Regardless of the absence of their surface expression, faults at depth in the Nurek region are clearly indicated by the post-impoundment seismicity. It is fruitful to investigate how the

activity on these features is related to the regional stress regime and the influence of the reservoir. Given the presence of zones of weakness (faults) which are activated by a reservoir there are a number of factors which can control the resulting type of motion and level of activity [Simpson, 1976; Bell and Nur, 1978]:

1. The orientation of the faults with respect to the existing tectonic stress field. In the Tadjik Depression the regional stress field as indicated by seismicity and Quaternary structures, is dominated by horizontal compression in a northwesterly direction. The preferred sense of motion will be thrusting on northeasterly faults and strike-slip on north-south or east-west faults.
2. The orientation and location of the faults with respect to the additional stresses imposed by the reservoir. The greatest influence of the reservoir is expected near the maximum depth of water. In general, fault zones will be most weakened if the center of mass of the reservoir lies on the foot wall of a thrust fault or the hanging wall of a normal fault.
3. The accessibility of reservoir water to the fault zones. Highly permeable fault zones intersecting the reservoir may allow concentrations of excess pore pressure, decreasing the effective stress and weakening the fault.

Bell and Nur [1978] have modelled the strength changes caused by reservoir-induced pore pressure and stresses. They calculate the relative strengthening or weakening of various simple fault configur-

ations in different tectonic environments. Their main results for a thrust environment are summarized in Figure 15. Many of the spatial features of the Nurek seismicity strongly agree in a qualitative sense with the results presented by Bell and Nur.

The fault plane solutions for groups A and B show P-axes parallel to the regional stress direction (Figures 8 and 9). In group B, the strike of the zone is perpendicular to the regional maximum compressive stress and thrust faulting occurs. In addition, an updip extension of this zone would reach the surface directly beneath the reservoir, the fault dips away from the reservoir and the reservoir lies on the foot wall (down-dropped) block. Bell and Nur show that such a situation results in the strongest weakening in a thrust environment (Figure 15e). During the 1976 swarm, group B experienced the highest level and most persistent seismicity, including the largest earthquakes. The seismicity in zone A is on a vertical plane oriented north-south. The right-lateral strike-slip motion is consistent with the regional maximum compressive stress. Migration of activity along this zone (Figures 6 and 14) suggests pore pressure diffusion, possibily along a permeable zone connected to the reservoir.

The activity in group C lies beneath the central basin of the reservoir. This zone and group B were most active during the early part of the 1976 swarm (Figure 14) when the water load was mainly confined north of the activity, on the foot wall of the presumed fault (see Figures 4 and 10). The focal mechanism shows this fault to have a thrust component. As the water level rose and the reservoir expanded southward (Figure 4), the water load increased over the hanging wall of the fault and the level of seismicity in this zone decreased and had essentially ceased by mid-November (Figure 14).

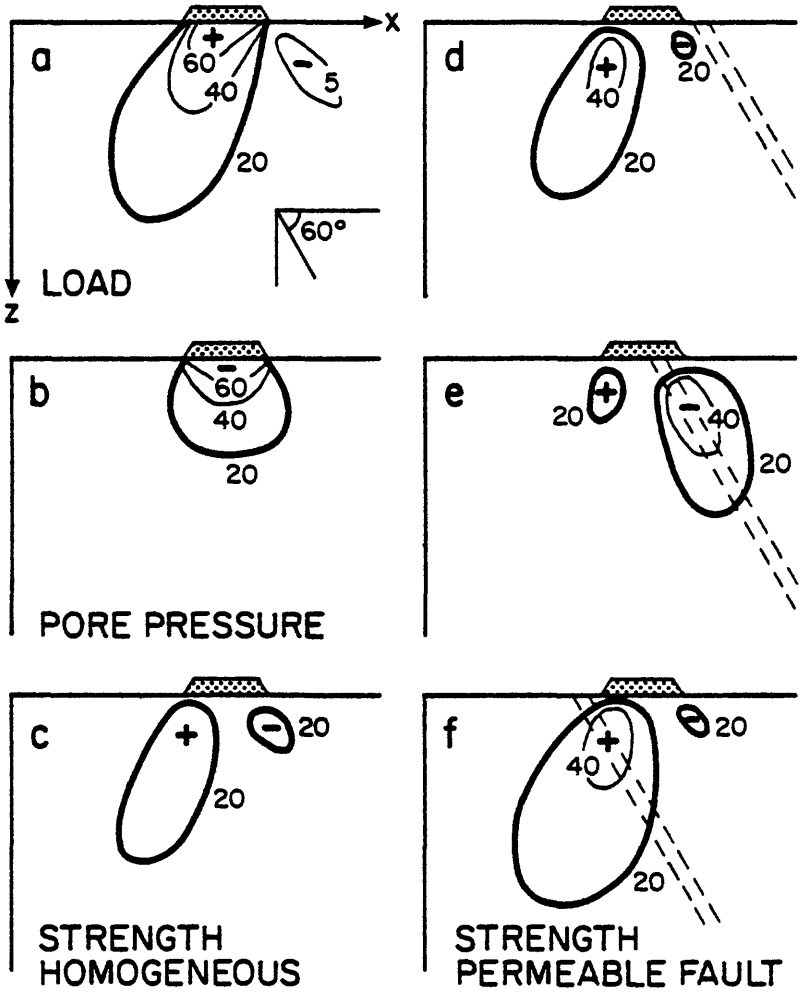

Fig. 15. Changes in (a) stress, (b) pore pressure and (c-f) strength after a characteristic time t' = 20 on planes dipping at 60° beneath a reservoir (a) where the tectonic shear is in the thrust direction [from Bell and Nur, 1978]. In b and c the half-space beneath the reservoir has homogeneous premeability and in d, e and f a fault zone (dashed lines) with permeability 100 times higher than the half-space is included. Contours of stress changes are given in percentage of the maximum load of the reservoir. Dimensions are normalized to the characteristic dimension of the reservoir indicated by the trapozoid at the surface. For a characteristic width of Nurek Reservoir of 3 km, the length of the z axis in these figures would correspond to a depth of 10 km. Negative values of strength (-) indicate net weakening. The case where a permeable fault zone intersects and dips away from the reservoir (e) shows the greatest weakening and is similar to group B at Nurek (Figure 9).

Since the more obvious lineation in epicenters in group D parallels the strike of one of the most active and conspicuous thrust faults in the reservoir area (Sarikamar), we had expected that these events would show a thrust mechanism striking northeast. The first motion data, however, whether taken together as in Figure 11 or in three groups as in Figure 12, show dilatations near the center of the stereographic projection and compressions near the edge and are incompatible with a thrust mechanism. In addition, the cross-section dd' in Figure 11 shows the hypocenters to lie beneath a down-dip extension of the surface trace of the Sarikamar fault. The Sarikamar fault, like the Ionakhsh, is bounded by a gypsum layer and aseismic slip may account for the absence of induced seismicity on these faults [Leith et al., 1981; Reiman et al., 1961]. The predominant stress system in the Tadjik Depression is thrusting, with maximum horizontal compression (σ_1) in a northwest direction, minimum stress (σ_3) vertical and intermediate stress (σ_2) northeast. In the normal faulting mechanism for group D, the relative magnitudes of the two horizontal components of stress agree with the regional stress system (northwest greater than northeast) but the vertical stress is the maximum while it is the minimum for the regional stress field. This increased vertical stress may result both from the increased load of the reservoir (lying mainly on the hanging wall of the normal fault) and from uncompensated vertical stress from the recent overthrusting of the Sarikamar fault [Reiman et al., 1961].

In group E the P-axis, the strike of the zone and the thrusting mechanism are consistent with regional trends. Because of the gradient of the river bed, the water level in this upstream area is almost

100 m less than it is near the southern group and this may, in part, be responsible for the lower level of seismicity. Unlike group B, no planar zone of activity surfacing beneath the reservoir can be seen in the cross-sections for this region (Figure 13). In the absence of a highly permeable zone, Bell and Nur show that, on planes dipping beneath the reservoir, a minor zone of weakening occurs directly beneath the edge of the reservoir on the down-dip side (Figure 15c). The activity in group E, concentrated on the southeastern edge of the reservoir, may therefore be occurring within such a zone of weakening on a series of minor structures parallel to the main Gulizindan fault.

Thus, for the zones indentified by the presence of induced seismicity as zones of weakness, the highest levels of activity (A, B, C) occur on those that are: near the maximum water depth; in apparent hydraulic connection with the reservoir; and oriented in a manner conducive to activation by the tectonic stress field and stresses imposed the reservoir. Those zones that do not satisfy all of these criteria show lower levels of activity (D, E).

Migration of Seismicity

Simpson and Negmatullaev [1981] show that from 1971 to 1979 the area of induced seismicity at Nurek gradually expanded; beginning in the area west of group A and eventually extending 40 km upstream to group E. This long-term migration can be related to the expansion of the surface area of the reservoir as the water level increased (Figure 4). Within the 1976 sequence, however, short-term migration of seismicity occurs, at least part of which appears to be related to diffusion of pore pressure.

During September and early October, 1976 seismicity was confined to groups B and C (Figures 6 and 16). Starting in late October, seismicity began to migrate southward into group A and by the end of November group C had become inactive. The increase in seismicity in group A began October 25-29 with a cluster of six events in the central part of this zone (Figure 6). In addition to these isolated events, the general level of activity throughout the zone gradually extended southward and deeper from October 25 to mid-December. It is not clear why the initiation of seismicity in group A began so abruptly. The water level in late October was more than 75 m above the level at the start of filling in August (see Figure 2) and was continuing to rise. Leith et al. [1981] suggest that the start of this migration may be related to the expanding shoreline of the reservoir. As the water level rose, significant water depths gradually moved southward reaching higher units in an anticline plunging to the south through the active area.

If the migration of activity is related to increasing pore pressure due to the diffusion of water, the rate of migration can provide some bounds on the hydraulic diffusivity and hence the porosity of rocks in the active zone.

The changes in strength caused by the filling of a reservoir involve an instantaneous change in elastic stress and a time-dependent change in pore pressure. The change in pore pressure results both from a coupled response to the changes in elastic stress and from the increased water pressure at the base of the reservoir [Bell and Nur, 1978].

If we consider the time-dependent change in pore pressure to be controlled only by the diffusion resulting from the application of pressure, P_o, at the surface (x = 0) of a homogeneous half-space at time, t = 0, then the solution of the diffusion equation [Carslaw and Jaeger, 1959; Howells, 1974] has the form:

$$P(x,t) = P_o[1-\mathrm{erf}(x/2\sqrt{ct})] \qquad (1)$$

where erf is the error function and c is the hydraulic diffusivity.

The pressure, P(x,t) in (1) depends only on the dimensionless parameter $x/\sqrt{ct}$. The time required to reach a given pressure should thus be proportional to the square of the distance from the source. In Figure 16, the times of earthquakes in groups A, B and C are plotted against the square of the distance from the hypocenter to a point near the center of the reservoir. The gradual migration of activity away from the center of the reservoir can be seen in the x^2 -t diagram and also in the maps in Figure 16. The initiation of seismicity with increasing distance is not abrupt. Scattered earthquakes occur at relatively early times, presumably the result of variations in the strength along the fault zones. The general increase in activity, however, migrates outward with a slope on the x^2-t diagram of 2 km^2/day (approximately 2 x 10^5 cm^2/sec). Note that since the square of distance has been used, this slope depends on the origin used to calculate the distance. Moving the origin (x = 0) within the central basin of the reservoir does not change the slope by more than a factor of 2.

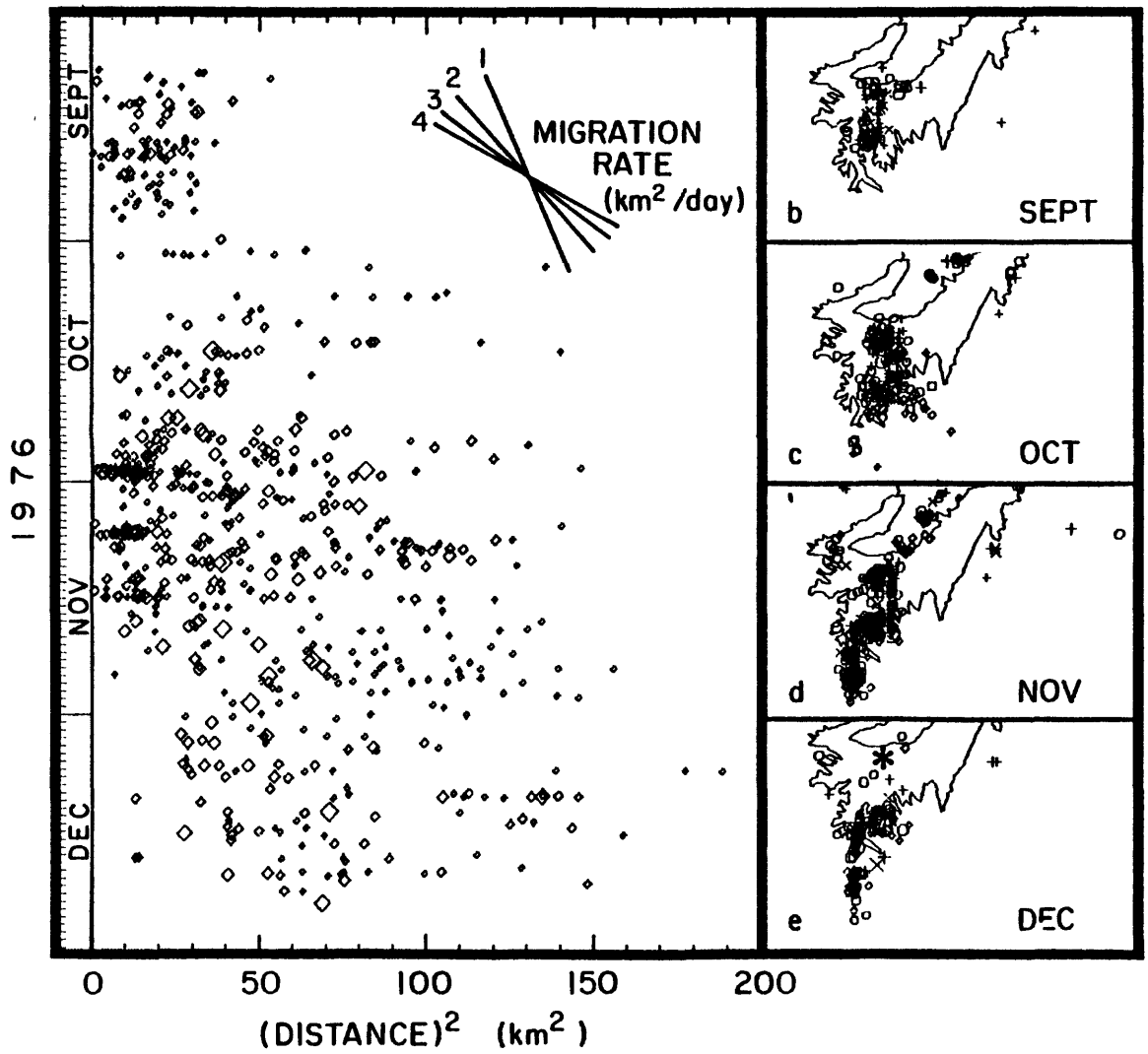

Fig. 16. Time of earthquakes of a, b, and c quality from groups A, B and C plotted against the square of the hypocentral distance from a point near the center of the reservoir (the star in e). Both the migration southward starting in early October at a rate of approximately 2 km^2/day and the cessation of activity near the center of the reservoir in December can be seen in the x^2-t diagram (a) and in the epicenteral maps for one month periods (b-e).

The slope of the migration front on the x^2-t diagram in Figure 16 is related to the hydraulic diffusivity, c, in (1). If we assume that: 1) the initiation of seismicity at a given point indicates that the pore pressure has risen to a critical value; 2) this value is the same for the entire fault zone; 3) the water pressure at the surface can be approximated by an instantaneous increase of P_o at t = 0; and 4) the diffusion of pore pressure is described by (1); then the migration front follows constant values of $x/\sqrt{ct}$ or, using the notation of Bell and Nur [1978], constant values of the dimensionless time:

$$t' = ct/x^2 \qquad (2)$$

The slope of the migration front on the x^2-t diagram is, therefore:

$$dx^2/dt = c/t_c' \qquad (3)$$

where t_c' is the dimensionless time required to achieve an increased pore pressure sufficient to initiate seismicity. Thus, in order to determine c from the migration of hypocenters requires an estimate of the pressure change necessary to trigger seismicity. Since the maximum pressure change available at the surface is small (on the order of 5 bars for a 50 m increase in water level) and since there is not any substantial increase in either the size or number of earthquakes with

increasing time after the main onset of activity in Figure 16, it may be resonable to assume that the onset of seismicity indicates a pore pressure increase close to the maximum possible and occurs close to the attainment of steady state.

If the pore pressure rise were controlled only by the simple diffusion process described by (1), then values of t' of 0.1, 1.0 and 10 would correspond to pore pressure increases of 2.5, 48 and 87 percent of the pressure change P_o, imposed at the surface. In such a model, therefore, steady state is not approached until t' is close to 10. In the more realistic case described by Bell and Nur [1978], where the coupling between the elastic stress and pore pressure is also considered, steady state is achieved at much earlier times, with t' = 0.1. Assuming $t_c' = 0.1$ gives $c = 2 \times 10^4$ cm^2/sec which, using the constants used by Bell and Nur [1978], correspnds to a permeability of 84 millidarcy. Without a more specific estimate of the pore pressure change required to initiate failure and more exact models for the coupling between pore pressure and elastic stress under the conditions existing at Nurek, these values can, at best, be considered only order of magnitude estimates of the diffusivity and permeability.

Conclusions

During an increase in the water level from 120 to 200 m in late 1976, a swarm of induced seismicity, including five earthquakes greater than magnitude 3.0, occurred at Nurek Reservoir. The earthquakes are concentrated on a series of narrow, planar zones, up to

8 km deep, within the post-Paleozoic sediment of the Tadjik Depression. The maximum depths of the earthquake are controlled by the Ionakhsh thrust, with all of the seismicity ocurring in the upper sheet of the thrust. The seismicity did not occur on any of the major faults mapped in the reservoir area and the spatial distribution of the induced seismicity would have been difficult to predict based on geological studies prior to impoundment. The distribution of the active zones, however, is not inconsistent with the regional stress field and the change in strength expected from models of the influence of a reservoir. Whether or not water from the reservoir has direct access to fault zones, rather than the mere presence of faults, is the major factor controlling where induced seismicity will occur. The most active of the zones showing induced seismicity are those where the upward extension of the fault plane reaches the surface directly beneath the reservoir. In contrast, the surface outcrops of the major faults, which have not shown induced seismicity, lie above the level of the reservoir. The importance of fluids in controlling the induced seismicity is also shown by the migration of seismicity outward from the center of the reservoir. The active region expands at a rate in which the square of distance is proportional to time, indicating that a diffusion process is responsible.

Acknowledgments. We wish to thank the many people who have assisted in the operation of the Nurek network. S. Kh. Negmatullaev, Director of the Tadjik Institute of Seismoresistant Construction and Seismology, and O. K. Abramov are responsible for the Soviet support of the network operation. T. A. Koczynski assisted in the instal-

lation of the network. Preliminary reading of network data is done by a group at TISSS under the direction of V. V. Maisooradze. E. Keith assisted in final analysis of the data at Lamont-Doherty Geological Observatory. Most of the credit for the high quality of the data obtained during the 1976 swarm goes to S. T. Morrissey of St. Louis University who performed minor miracles during a major overhaul and expansion of the network in September-October 1976. We have had many useful and stimulating discussions with W. Leith, M. Hamburger, I. E. Gubin, I. L. Nersesov, V. K. Kulagin and W. Alvarez. The manuscript was reviewed by C. Scholz, L. Seeber and R. Stein. The work was carried out as part of a joint US-USSR Exchange in Earthquake Prediction under Area IX of the Joint Soviet-American Agreement for Cooperation in the Field of Environmental Protection. The US part of the work was supported by the National Science Foundation under grants GA43650, ENV 77-01092 and PFR 79-26698 and the U.S. Geological Survey under contracts USGS-14-08-0001-17707 and USGS-14-08-0001-19743.

References

Academy of Sciences, Tadjik SSR, Atlas of the Tadjik SSR (in Russian), Central Office of Geodesy and Cartography, Dushanbe, 200 pp., 1968.

Bell, M L., and A. Nur, Strength changes due to reservoir-induced pore pressure and stresses and application to Lake Oroville, J. Geophys. Res., 83, 4469-4483, 1978.

Carslaw, H. S., and J. C. Jaeger, Conduction of Heat in Solids, 2nd ed., Oxford at the Clarendon Press, Oxford, 510 pp., 1959.

Crosson, R. S., Crustal structure modeling of earthquake data. 1. Simultaneous least-squares estimation of hypocenter and velocity parameters, J. Geophys. Res., 81, 3036-3046, 1976.

Gubin, I. E., Properties of Seismic Manifestation in the Territory of Tadjikistan (in Russian), Academy of Sciences Publishing House, Moscow, 464 pp., 1960.

Gubin, I. E., Lecture Notes on Basic Problems in Seismotectonics, International Institute of Seismology and Earthquake Engineering, Tokyo, Japan, 195 pp., 1967.

Gupta, H. K., and B. K. Rastogi, Dams and Earthquakes, Elsevier, Amsterdam, 229 pp., 1976.

Howells, D. A., The time for a significant change in pore pressure, Eng. Geol., 8, 135-138, 1974.

Klein, F., Hypocenter location program: Hypoinverse. Part 1. Users guide to Versions 1, 2, 3, and 4, U.S. Geol. Surv. Open File Report 78-694, 113 pp., 1978.

Lahr, J. C., Hypoellipse: A computer program for determining local earthquake hypocentral parameters, magnitudes and first motion patterns, U.S. Geol. Surv. Open File Report 79-431, 239 pp., 1979.

Leith, W. S., D. W. Simpson, and W. Alvarez, Structure and permeability: Geologic controls on induced seismicity at Nurek Reservoir, Tadjikstan, USSR, accepted by Geology, 1981.

Loziyev, V. P., Origin of deformation in the sedimentary mantle of the south Tadjik Depression, Geotectonics, 6, 226-232, 1970.

Loziyev, V. P., Present structures and types of local deformations in the south Tadjik Depression, Geotectonics, 10, 291-297, 1974.

Packer, D. R., L. S. Cluff, D. P. Schwartz, F. H. Swan, and J. M. Indriss, Auburn Dam - a case history of earthquake evaluation for a critical facility, Proceedings of the Second International Conference on Microzonation, San Francisco, vol. I, 457-470, 1977.

Raleigh, C. B., J. D. Healy, and J. D. Bredehoeft, An experiment in earthquake control of Rangely, Colorado, Science, 191, 1230-1237, 1976.

Reiman, V. M., S. A. Morozov, and A. M. Babaev, Geomorphologic and structural features of the Dzhangou Range (in Russian), Transactions (Trudy) Geol. Inst., Acad. Sci. Tadjik SSR, 4, 113-125, 1961.

Scholz, C. H., L. R. Sykes, and Y. P. Aggarwal, Earthquake prediction: A physical basis, Science, 181, 803-810, 1973.

Seeber, L., and J. Armbruster, Seismicity of the Hazara arc in northern Pakistan: decollement vs. basement faulting, in Geodynamics of Pakistan, A. Farah and K. A. DeJong (eds.), Geol. Surv. of Pakistan, Quetta, 361 pp., pp. 131-142, 1979.

Simpson, D. W., Seismicity changes associated with reservoir loading, Eng. Geol., 10, 123-150, 1976.

Simpson, D. W., M. M. Hamburger, V. D. Pavlov, and I. L. Nersesov, Tectonics and seismicity of the Toktogul reservoir region, Kirgizia, USSR, J. Geophys. Res., 86, 345-358, 1981.

Simpson, D. W., and S. Kh. Negmatullaev, Induced seismicity at Nurek Reservoir, Tadjikistan USSR, accepted by Bull. Seismol. Soc. Am., 1981.

Soboleva, O. V., and U. A. Mamadaliev, The influence of the Nurek Reservoir on local earthquake activity, Eng. Geol., 10, 293-305, 1976.

Soboleva, O. V., G. P. Schklyar and E. E. Blagovestchenskaya, Investigations of stress field in earthquakes foci in connection with the prediction of place and time of larger earthqukaes (in Russian), in The Search for Earthquake Forerunners at Prediction Test Fields, Nauka, Moscow, 65-70, 1974.

Structure and permeability: Geologic controls on induced seismicity at Nurek reservoir, Tadjikistan, USSR

William Leith
Lamont-Doherty Geological Observatory, Palisades, New York 10964 and
Department of Geological Sciences, Columbia University, New York, New York 10027
David W. Simpson
Lamont-Doherty Geological Observatory, Palisades, New York 10964
Walter Alvarez
Department of Geology and Geophysics, University of California, Berkeley, California 94720

ABSTRACT

Induced seismicity at Nurek, Tadjik S.S.R., is occurring within the upper plate of the Ionakhsh thrust, which passes at depth directly beneath the reservoir. Within the immediate vicinity of the reservoir one can contrast two distinct areas, one seismic and the other aseismic. Both consist of rocks that can be shown to have a highly anisotropic permeability due to alternating permeable and impermeable strata. Water flow is favored along bedding while essentially prohibited across bedding. However, because the two areas differ in structure, they also differ in their vertical component of permeability, as a direct result of the different attitudes of the bedding. In the aseismic area, vertical fluid flow is blocked by a syncline that cups the base of the reservoir. In the seismic area, a plunging anticline that crops out beneath the reservoir allows water to flow to depth in the high-permeability direction—along bedding. Because effective stress changes at depth are dependent on permeability characteristics, knowledge of subsurface permeability or permeability anisotropy can serve as a means by which to predict the distribution of induced seismic activity. Thus, while regional geologic studies may indicate the presence of lithologies that are conducive to the transmission of pore-water pressure, access of water to these units depends on the structural arrangement beneath the reservoir, on a very local scale.

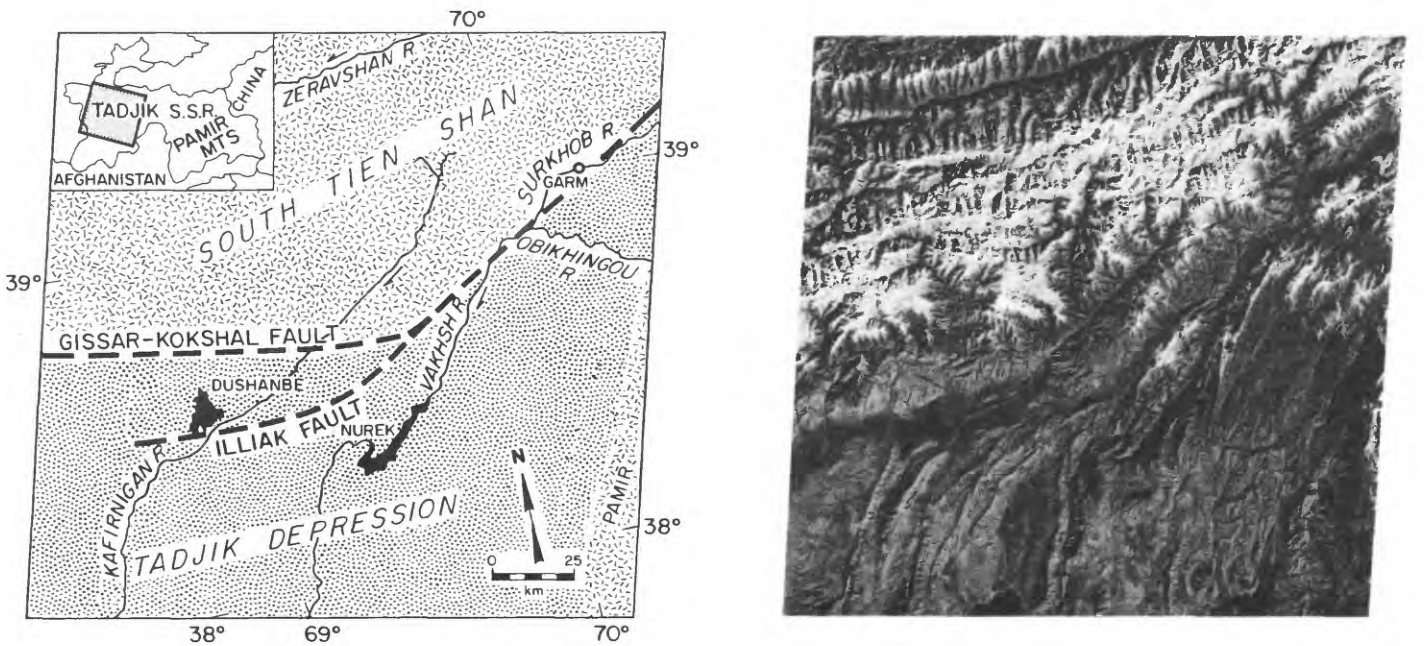

Figure 1. Schematic location map (left) for LANDSAT image E 1500-05315-5 (right), showing Nurek reservoir in relation to regional geography. Dotted pattern marks areal extent of post-Paleozoic sediments of Tadjik Depression. Dashed pattern marks Paleozoic and older rocks of Tien Shan and Pamir. Inset shows present political boundaries.

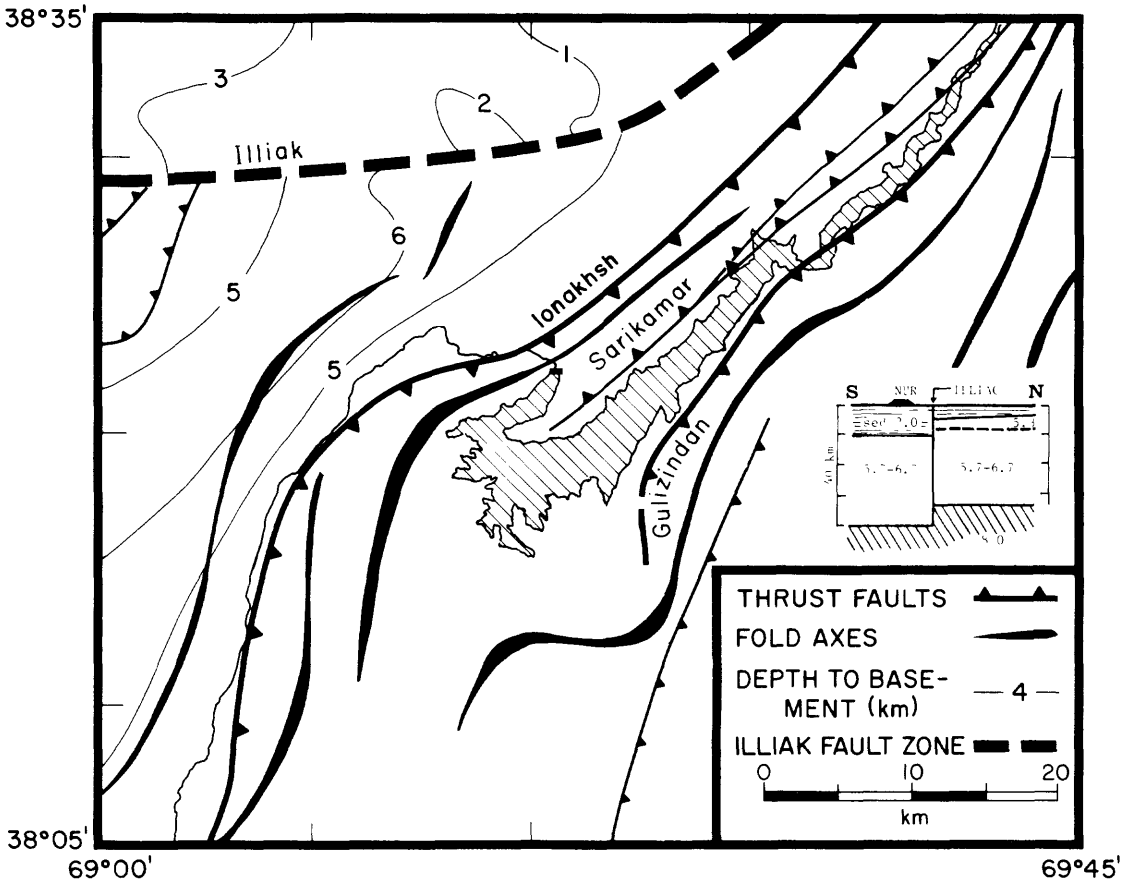

Figure 2. Generalized structural map of Nurek area (modified after Loziyev, 1968, and Zakharov and others, 1968). Inset shows interpreted results of seismic-refraction line running north-northwest-south-southwest near Nurek (after V. K. Kulagin, 1979, personal commun.). Velocities in kilometres per second. No vertical exaggeration.

RESERVOIR-INDUCED SEISMICITY

The filling of a large reservoir changes the local stress regime both by increasing the vertical stress due to the weight of water and by decreasing the effective stress due to increased pore pressure. The load acts immediately, whereas the timing of the decrease in effective stress depends both on the pore water saturation before loading (Jaeger and Cook, 1969) and on the permeability. In addition to stress considerations, water acts to reduce the coefficient of initial friction (Byerlee, 1978; Stesky, 1978), and it has some long-term chemical rock-weakening effects (Orowan, 1944; Griggs, 1967). However, despite such effects, reservoir-induced stresses (order of bars at depth) are probably not of sufficient magnitude to initiate fracturing in the absence of a tectonic or a residual stress [see reservoir stress modeling by Withers, 1977) and Bell and Nur (1978)].

The existence of a relatively high state of tectonic stress near Nurek reservoir is evidenced by historic records of seismicity, which show a high frequency of earthquakes in the region well before the impoundment of the reservoir (Simpson and Negmatullaev, 1981). Induced seismic activity, which has occurred at Nurek since early stages of filling in 1971, is not directly related to absolute water level (that is, total water load or effective stress change). Instead, Simpson and Negmatullaev (1981) showed that the level of seismicity is strongly controlled by the rate of change of water level, which is some measure of the rate at which the stress system moves away from a state of dynamic equilibrium. The 300-m-deep reservoir seems to act primarily to perturb the tectonic stress system, with rapid rates of change of water level serving as the trigger for bursts of local seismic activity.

Although the temporal distribution of Nurek seismicity can be understood in the above terms, the spatial distribution cannot. In a homogeneous medium the greatest departures from equilibrium will occur beneath the center of the reservoir, independent of tectonic stress-axis orientation. Any distribution of hypocenters that does not reflect this indicates inhomogeneity—variation of rock properties from one part of the reservoir to another—and hence becomes dependent on local geologic structure.

STRUCTURAL FRAMEWORK

Nurek reservoir is located in an area of complex folding and thrust faulting of the post-Paleozoic sediments that make up the Tadjik Depression (Fig. 1). Specifically, it lies at a major change in azimuth of fold axes to east-northeast from a regionally consistent north-northeast to south-southwest trend. Accommodation for the rotation of the fold axes appears to have been made in great part by variation in horizontal displacement along individual thrusts and by imbricate thrusting.

Thrusts presumably rise from a basal decollement surface in Jurassic evaporites, which are the oldest rocks seen or drilled in the Tadjik Depression. The existence of an evaporite decollement is supported by several facts: (1) there is evidence of salt and/or gypsum on every thrust surface in the reservoir area; (2) salt domes are found throughout the depression (salt is currently rising along the Ionakhsk thrust at Nurek); and (3) evaporites are commonly the basal unit encountered before repeated section in the numerous boreholes that have been drilled throughout the depression. The Shar-Shar borehole (Figs. 2, 5), which was drilled 5 km west of the Nurek dam, penetrates the Ionakhsh thrust at a depth of 2 km (Korovka and others, 1972; Bekker and others, 1974).

The Ionakhsh is a major thrust whose trace can be followed for perhaps 100 km to the south and northeast of Nurek. It is one of four northeast-striking thrusts northeast of Nurek that

were described by Gubin (1960, 1967) as being seismically active. From a study of six earthquakes occurring on these faults, Gubin inferred that they dipped to the southeast, and he placed the decollement horizon at a depth of 10 km. The induced seismicity at Nurek lies at depths of less than 10 km.

The northern margin of the Tadjik Depression is defined by the Gissar-Kokshal fault zone, which separates the post-Paleozoic sediments of the depression proper from the late Paleozoic igneous complex of the southern Tien Shan. In the Nurek region, the southern spur of the Gissar-Kokshal system is the Illiac fault, which passes about 20 km north of Nurek dam (see Fig. 2). Seismic refraction studies (Kulagin and Kulagina, 1977; V. K. Kulagin, 1979, personal commun.) indicate several kilometres of block uplift of the basement from south to north across the Illiac fault. Although most of the large earthquakes of the region are associated with the Gissar-Kokshal fault zone (Kristy and Simpson, 1980), regional seismicity studies of lower magnitude events ($M < 5$) indicate a marked decrease in the shallow seismicity north of the fault (Negmatullaev and Mirzoev, 1974). The sedimentary section just north of the Illiac fault appears to be complete, although thinner, yet sediments deposited north of the Illiac fault are relatively undeformed.

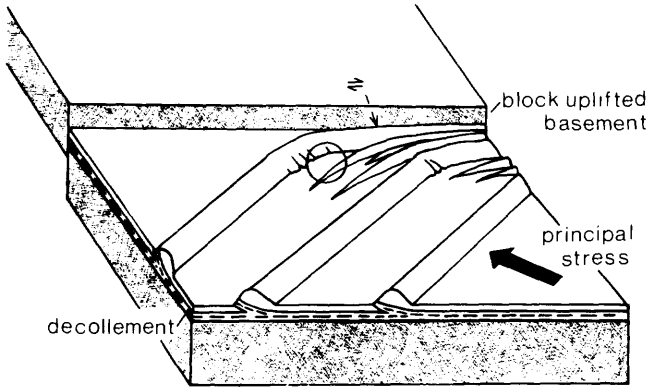

Figure 3. Interpretative tectonic model for structure and evolution of Tadjik Depression. Decollement plates move obliquely to pre-existing basement uplift (exaggerated). Deformation intensity increases where anticlines pile up against block uplift. Circle would correspond to location of Nurek and block uplift to that of Illiac fault.

The deformational complexity seen in the reservoir area can be genetically related to the decollement mode of shortening and to the proximity of the reservoir area to this northern margin of the depression. Apparently, the block uplift along the Illiac fault (and the entire northern margin of the depression) acts as a boundary to the horizontal translation of decollement thrust plates and, as such, concentrates deformation to the south of it. Since the maximum horizontal stress direction is inferred to be in a northwest-southeast direction on the basis of focal-mechanism solutions for earthquakes throughout the depression (Soboleva and others, 1974) and is thus oblique to the trend of the uplifted block, varying amounts of strain occur in the sedimentary section to the south. In the sediments south of the Illiac fault, this results in a complex geometry with increased displacement, imbricate thrusting, and decreased fold wavelength as one progresses along structural trend northeast of the Nurek area, parallel to the Illiac fault. A model for this situation is presented in Figure 3. An example of the resulting geometry is noted along the Sarikamar thrust, which runs along the northern boundary of the reservoir. This thrust has a rotational component about

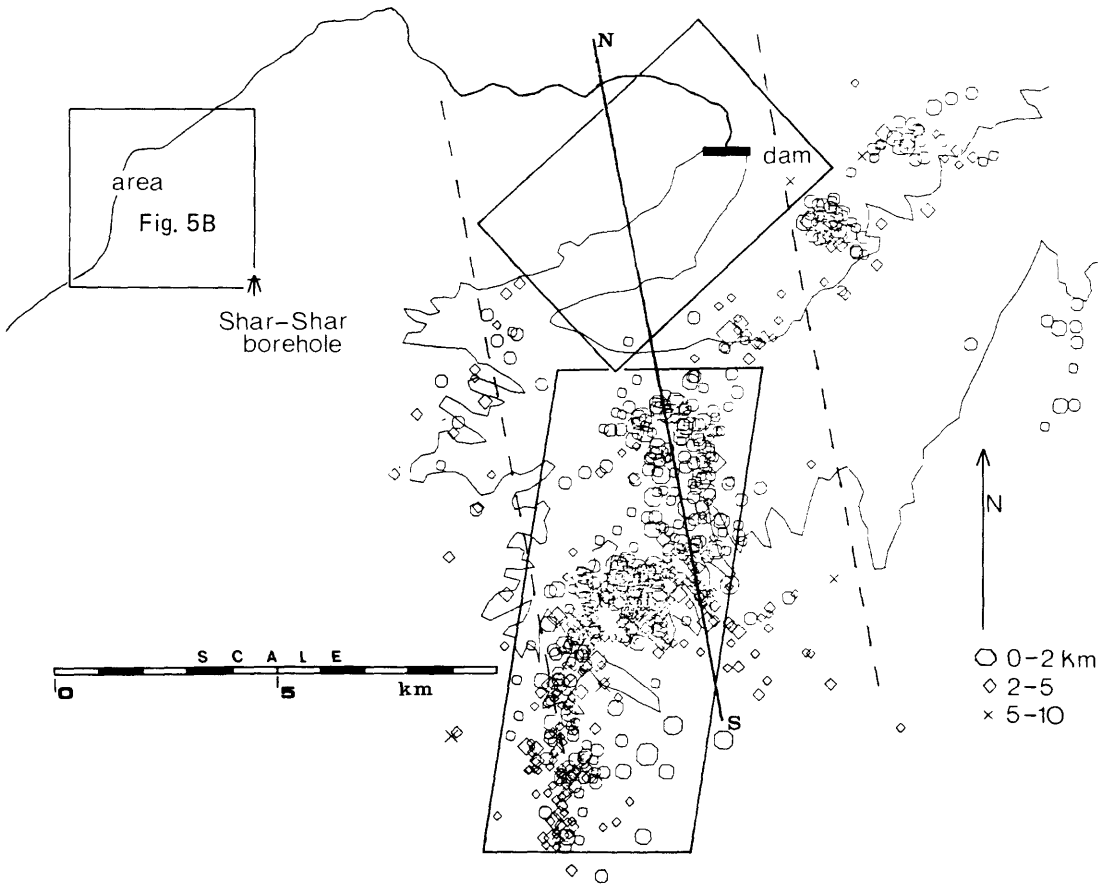

Figure 4. Epicenter map of main body of Nurek reservoir, with boxes emphasizing seismic and aseismic areas considered in text. Location of cross section of Figure 5 is shown for reference. Hypocenters between dashed lines are projected onto section in Figure 5. Symbols indicate depth; size of symbol is proportional to magnitude.

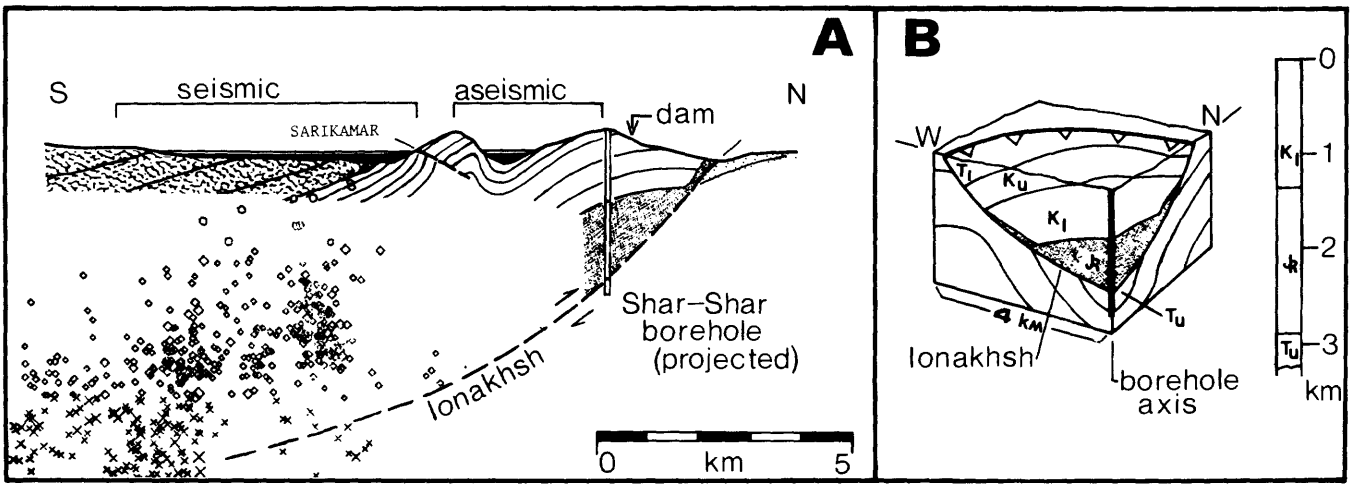

Figure 5. A. Cross section along line N-S of Figure 4, with projected seismicity. B. Interpretation from surface mapping and Shar-Shar borehole data for structure of northwest margin of reservoir and projection of Ionakhsh thrust (adapted from Korovka and others, 1972).

an axis normal to the thrust plane, appearing as if the southwest end of the thrust were "pinned," with relative displacement along the fault trace increasing in the northeasterly direction.

Using data from a high-resolution seismograph network installed at Nurek in 1975, C. M. Keith, D. W. Simpson, and O. V. Soboleva (in prep.) show that the induced seismicity during the second stage of filling of the reservoir in 1976 was confined mainly to a series of narrow zones beneath and south of the central part of the reservoir (Fig. 4). These seismic zones are not related to any fault observed at the surface. Lower levels of seismicity occur upstream of this central basin, whereas the region of the arm of the reservoir immediately behind the dam is essentially aseismic. In cross section, the induced seismic activity defines a zone about 4 to 6 km thick which gradually deepens to the south (Fig. 5A). The upper boundary of this zone appears to follow the base of the Neogene sandstones that fill the basin. The lower surface of the active zone corresponds to the down-dip extension of the Ionakhsh thrust. Borehole data (Fig. 5B), along with evidence cited above for displacement and geometry, require the extension of the thrust beneath the reservoir. The presence of evaporites on the thrust surface indicates that the Ionakhsh thrust itself may be aseismic, due to the low shear strength of the evaporite decollement layer. The induced seismic activity therefore appears to be confined to the pre-Neogene rocks within the Ionakhsh thrust sheet. Because these rocks exist elsewhere around the reservoir, the question arises why this particular section has such a markedly high level of seismicity.

STRUCTURE AND PERMEABILITY

The reasons for an inhomogeneous distribution of seismicity at Nurek may be best understood by contrasting the seismic and the aseismic parts of the reservoir (Fig. 4). Lithologically, both areas consist in part of Upper Cretaceous through Paleogene shallow-water limestones with interbeds of mixed components of shale and gypsum. Generally, the limestone units are highly fractured and may be expected to be relatively permeable. However, the permeability of the shale and gypsum units may be quite low; in a syncline forming the range that bounds the reservoir on the north, gypsum layers form the basal unit from which a series of artesian salt-water springs are generated. This attests to the impermeability of the gypsiferous beds to the downward migration of surface waters.

The alternation of permeable and impermeable strata causes the Upper Cretaceous–Paleogene rocks to have a strongly anisotropic or directional permeability, with the high-permeability direction parallel to bedding. Furthermore, when these strata were folded, the anisotropic permeability inherent in the bedding was folded into the structure. Wood (1974), in a discussion of pressure solution, suggested that bedding may play an important role in determining the boundaries of a fluid system. It is commonly noted that such solution occurs in a single formation, with no evidence for either solution or precipitation in the bounding formations. This suggests that a formation may be a relatively homogeneous fluid system *laterally*, but that it is closed to fluid migration *vertically* (that is, across bedding, at some point). This is consistent with the conclusions of Anderson and Laney (1975), in their study of induced seismicity at Lake Mead, where the distribution of seismicity seems to be controlled by the distribution of a large salt formation.

In the aseismic area, the Upper Cretaceous–Paleogene rocks are folded into a tight but very shallowly plunging syncline. As a result of this structure, water diffusing to depth must move normal to bedding (Fig. 6A). Because the strata are essentially impermeable in this direction, diffusion of water to depth is restricted, and effective stress ceases to be an important variable. The reservoir in this area acts essentially as a load.

In the seismic area, the Upper Cretaceous–Paleogene rocks are conformably overlain by coarsely bedded Neogene sandstones. The strata in this area are folded into a moderately plunging open anticline, which is a subsidiary feature on a generally south-dipping major fold limb. This anticline plunges to the south, away from the reservoir, and the Paleogene core of the anticline crops out in the wide central part of the reservoir, giving reservoir water access to various stratigraphic levels. The plunging anticlinal structure provides no obstacle to the downward diffusion of reservoir water, because water can migrate to depth by traveling in the high-permeability direction—along bedding (Fig. 6B), both down-axis and down-limb.

Support for this model comes from several empirical facts: (1) seismicity in this area roughly parallels the axial surface of the fold; (2) the depth to the seismic zone increases to the south, away from the reservoir (see Fig. 5), and the top of the seismic zone approximates the projected depth to the top of the Paleogene rocks; and (3) during the filling of the reservoir, seismicity migrated with time away from the reservoir. This pattern of

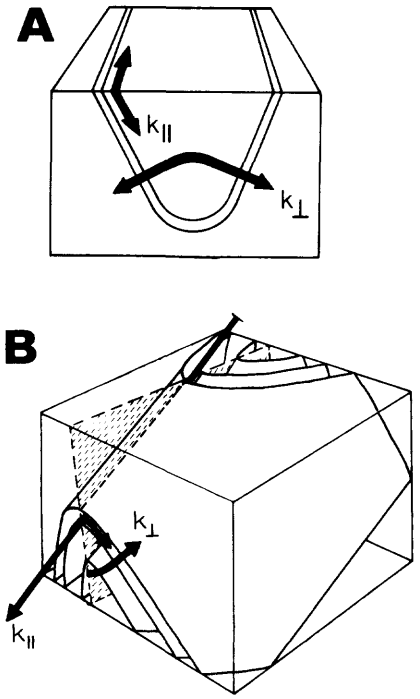

Figure 6. Schematic representation of strata with highly directional permeability, deformed, as at Nurek, into (A) upright syncline, and (B) plunging anticline. Permeability parallel to bedding is much greater than permeability perpendicular to bedding.

seismicity may be attributed to diffusion of pore pressure, but, alternatively, it may also indicate that water was reaching consecutively higher stratigraphic levels in the core of the anticline (see Fig. 6B), as the shoreline of the reservoir expanded to the south. This would allow water moving along bedding planes to extend farther away from the reservoir. Because of the close correspondence to the axial surface of the fold and the general trend of the seismic zone, it may be that water is flowing away from the reservoir along joints dominating the hinge of the fold in the lower units.

CONCLUSIONS

This hypothesis for the distribution of induced seismic activity at Nurek places the seismicity in the upper plate of the Ionakhsh thrust, possibly as a result of the flexure of this upper plate in response to a generally aseismic slip along the decollement surface. If such assertions about the existence of motion along the Ionakhsh are correct, then the horizontal displacements from thrust movement either may continue to be accommodated by deformation in the upper plate or may result in movement along the surface fault trace, which passes within several hundred metres of the dam. Within this framework, the locus of induced activity is determined by the combination of local structure with strata with a highly directional permeability.

Nurek is not in an unusually inhomogeneous lithologic environment, when examined on a *regional* scale. However, detailed geologic information on a subreservoir scale has been necessary for interpreting the seismic distribution and tectonic mechanism for seismicity at Nurek. Such detail may be necessary to assess the potential for induced seismicity imposed by the filling of any reservoir. While regional studies may indicate the presence of lithologies that are conducive to the transmission of pore pressure, whether water has access to these units will depend on the structural arrangement within the immediate environs of the reservoir.

REFERENCES CITED

Anderson, R. E., and Laney, R. L., 1975, The influence of late Cenozoic stratigraphy on distribution of impoundment-related seismicity at Lake Mead, Nevada-Arizona: U.S. Geological Survey Journal of Research, v. 3, p. 337-343.

Bekker, Ya. A., Kushlakov, G. V., and Kuznetsov, Ye. S., 1974, The deep structure of southwest Tadjikistan according to geological and geophysical data, *in* Searches for earthquake precursors in prediction polygons: Moscow, Nauka, p. 16-24 (in Russian).

Bell, M. L., and Nur, A., 1978, Strength changes due to reservoir induced pressure and stresses and application to Lake Oroville: Journal of Geophysical Research, v. 83, p. 4469-4483.

Byerlee, W., 1978, Friction of rocks: Pure and Applied Geophysics, v. 116, p. 615-626.

Griggs, D. T., 1967, Hydrolitic weakening of quartz and other silicates: Royal Astronomical Society Geophysical Journal, v. 14, p. 19-31.

Gubin, I. E., 1960, Regularities of seismic activity in the territory of Tadjikistan: Moscow, Academy of Sciences, 464 p. (in Russian).

———1967, Lecture notes on basic problems in seismotectonics: Tokyo, International Institute of Seismology and Earthquake Engineering, 195 p.

Jaeger, J. C., and Cook, N.G.W., 1969, Fundamentals of rock mechanics: London, Chapman and Hall, 585 p.

Korovka, V. S., Condur, V. P., Saffyan, L. M., and Chyernikov, P. V., 1972, Several features of the deep structure of the Sanglok anticline according to borehole data, *in* Problems of the petroleum capacity of Tadjikistan, Sbornik 4: Dushanbe, USSR, Donish Publishers, p. 335-338 (in Russian).

Kristy, M. K., and Simpson, D. W., 1980, Seismicity changes preceding two recent Central Asian earthquakes: Journal of Geophysical Research, v. 85, p. 4829-4837.

Kulagin, V. K., and Kulagina, M. V., 1977, Surface relief and the thickness of the basalt layer in Tadjikistan: Sbornik 1: Moscow, Izvestiya, p. 103-107 (in Russian).

Loziyev, V. P., 1968, Geological structure, *in* Atlas of the Tadjik SSR: Dushanbe, USSR, Academy of Sciences Tadjik SSR Publishers, p. 13-15 (in Russian).

Negmatullaev, S., and Mirzoev, K., 1974, Present seismological and geologeophysical changes in the territory of the Dushanbe geophysical polygon, *in* Searches for earthquake precursors in prediction polygons: Moscow, Nauka, p. 13-16 (in Russian).

Orowan, E., 1944, Fatigue of glass under stress: Nature, v. 154, p. 341.

Simpson, D. W., and Negmatullaev, S., 1981, Induced seismicity at Nurek reservoir, Tadjikistan, USSR: Seismological Society of America Bulletin (in press).

Sobolexa, O. V., Shklyar, G. P., and Blagoveshchenskaya, Ye. E., 1974, The change in structure of the stress field in earthquake foci in connection with the prediction of the place and time of a strong shock, *in* Searches for earthquake precursors in prediction polygons: Moscow, Nauka, p. 65-70 (in Russian).

Stesky, R. M., 1978, Rock friction effect of confining pressure, temperature and pore pressure: Pure and Applied Geophysics, v. 116, p. 690-704.

Withers, R. J., 1977, Seismicity and stress determination at man-made lakes [Ph.D. dissert.]: Edmonton, University of Alberta, 241 p.

Wood, D. S., 1974, Current views on the development of slaty cleavage: Annual Reviews of Earth and Planetary Sciences, v. 2, p. 369-401.

Zakharov, S. A., Kukhtikov, M. M., Lovgyn, E. Ya., and Villichenko, G. P., 1968, Tectonics, *in* Atlas of the Tadjik SSR: Dushanbe, USSR, Academy of Sciences Tadjik SSR Publishers, p. 17-19 (in Russian).

ACKNOWLEDGMENTS

Reviewed by R. Wallace, C. Bufe, T. Engelder, and W. Snyder. Supported by Department of the Interior, U.S. Geological Survey under contracts 14-08-0001-17707 and 14-08-0001-19743 and National Science Foundation Grants ENV-77-01092 and PFR-79-26698. We thank Soviet geologists A. M. Babaev and L. M. Lyeskov for their assistance in the field and generous application of their knowledge of reservoir area geology to our studies. We also thank Michael Hamburger for expert translations and field help, and Peter Geiser for his field work, discussion, and application of his knowledge of foreland geology. The work is part of an exchange in earthquake prediction under Area IX of the Joint U.S.-USSR Agreement in the Field of Environmental Protection. Lamont-Doherty Geological Observatory Contribution No. 3188.

MANUSCRIPT RECEIVED MARCH 26, 1981

REVISED MANUSCRIPT RECEIVED JULY 10, 1981

MANUSCRIPT ACCEPTED JULY 21, 1981

(page 103 follows)

TECTONICS AND SEISMICITY OF THE TOKTOGUL RESERVOIR REGION, KIRGIZIA, USSR

M. W. Hamburger, D. W. Simpson,

Lamont-Doherty Geological Observatory of Columbia University

Palisades, New York 10964

USA

V. D. Pavlov and I. L. Nersesov

Institute of Physics of the Earth

Moscow

USSR

ABSTRACT

The 214 m high Toktogul Dam will impound a 19.5 km^3 reservoir on the Naryn River in central Kirgizia. The reservoir lies along the Talas-Fergana fault, a major tectonic feature of Central Asia. The nature of Cenozoic movements along the fault is in debate; however, there is considerable evidence of present-day right-lateral movement. The region is one of moderate seismicity. A magnitude 7.6 earthquake occurred in 1946, approximately 65 km from the dam, and was probably associated with the Talas-Fergana.

Construction of the dam was completed in 1975 and by late 1979 the water level in the reservoir has reached three-fourths its final planned depth. Low-magnitude, induced earthquakes began as the water level first

exceeded 100 m in late 1977. A microearthquake survey using portable instruments was carried out in July-August 1978 and a seven-station telemetered network was installed in October 1978. Although the largest of the induced earthquakes has been of magnitude 2.5, the activity is in the immediate vicinity of the dam, is very shallow and is clearly related to water level. Preliminary analysis of data gathered during 1978-1979 shows a zone of activity, extending to 5 km depth, supporting evidence for an active reverse fault beneath the dam and parallel to the canyon of the Naryn River. The water level where the reservoir crosses the Talas-Fergana fault, 15 km upstream from the dam, has not yet reached 100 m and seismicity along the Talas-Fergana has not shown any change related to filling of the reservoir.

INTRODUCTION

One of the most tectonically and seismically active areas of the Soviet Union is the mountainous region of Central Asia. It is part of the broad zone of Eurasia deformed by the northward movement of India, since their collision in the Eocene. The Pamirs, the southernmost of the major mountain ranges in Soviet Central Asia, are part of the Mediterranean-Alpine-Himalayan system (Nalivkin, 1973). They form a convex-northward arc, impinging on the generally east-west ranges of the Tien-Shan to the north. The Tien-Shan themselves are a continuation of the Urals Geosyncline, strongly deformed during the late Paleozoic (Nalivkin, 1973; Burtman, 1975). Their high altitude, the presence of active Quaternary faulting (Tapponnier and Molnar, 1979) and high seismicity all attest to their present reactivation.

Within this tectonic setting, Soviet engineers are constructing a series of major hydroelectric projects, providing irrigation water and electricity for the Central Asian republics. Toktogul Dam is of particular interest because of its proximity to the major Talas-Fergana fault and because of its potential for induced seismicity. Regional seismicity studies have been carried out by Soviet investigators (Nersesov et al., 1960; Grin, 1964). Under the US-USSR Exchange in Earthquake Prediction, a dense telemetered seismic network has been established for detailed examination of the seismicity of the Toktogul region and tectonics of the Talas-Fergana fault.

TOKTOGUL DAM AND RESERVOIR

Toktogul Dam (Figure 1) is a reinforced concrete structure, 214 m high, located in a steep, narrow gorge of the Naryn River in central Kirgizia (Figures 2, 3). The dam was completed in 1975 but, because of low rainfall, by early 1979 the water level at the dam was only 125 m. The maximum capacity of the reservoir will be 19.5 cubic kilometers. The dam lies about 4 km above the Kara Kul' fault, which strikes northeast and meets the Talas-Fergana fault approximately 10 km southeast of the reservoir (Figure 3). Geological evidence also suggests that the Naryn River itself lies along strike of an active reverse fault extending from the dam northward to the Talas-Fergana. From the dam, the reservoir follows the Naryn River northward through a narrow gorge, until it crosses the Talas-Fergana fault and opens into the main body of the reservoir (Figure 2). The main body of the reservoir will be 60 km long and 20 km of the southwestern edge of the reservoir will front directly on the scarp of the Talas-Fergana fault.

THE TALAS-FERGANA FAULT

The Talas-Fergana fault system comprises one of the major tectonic features of Central Asia. The fault extends for over 800 km from Kazakhstan in the northwest through Kirgizia into western China. The fault separates the central Tien Shan range from the western Tien-Shan (Rozova et al., 1968). Along with a series of related faults extending into the Kun Lun range in western China, the Talas-Fergana system comprises the Tien

Figure 1 Toktogul Dam, Kirgizia, USSR. The dam, shown near completion, is a 215 m reinforced concrete structure. The photograph is taken downstream of the dam, within the gorge of the Naryn River.

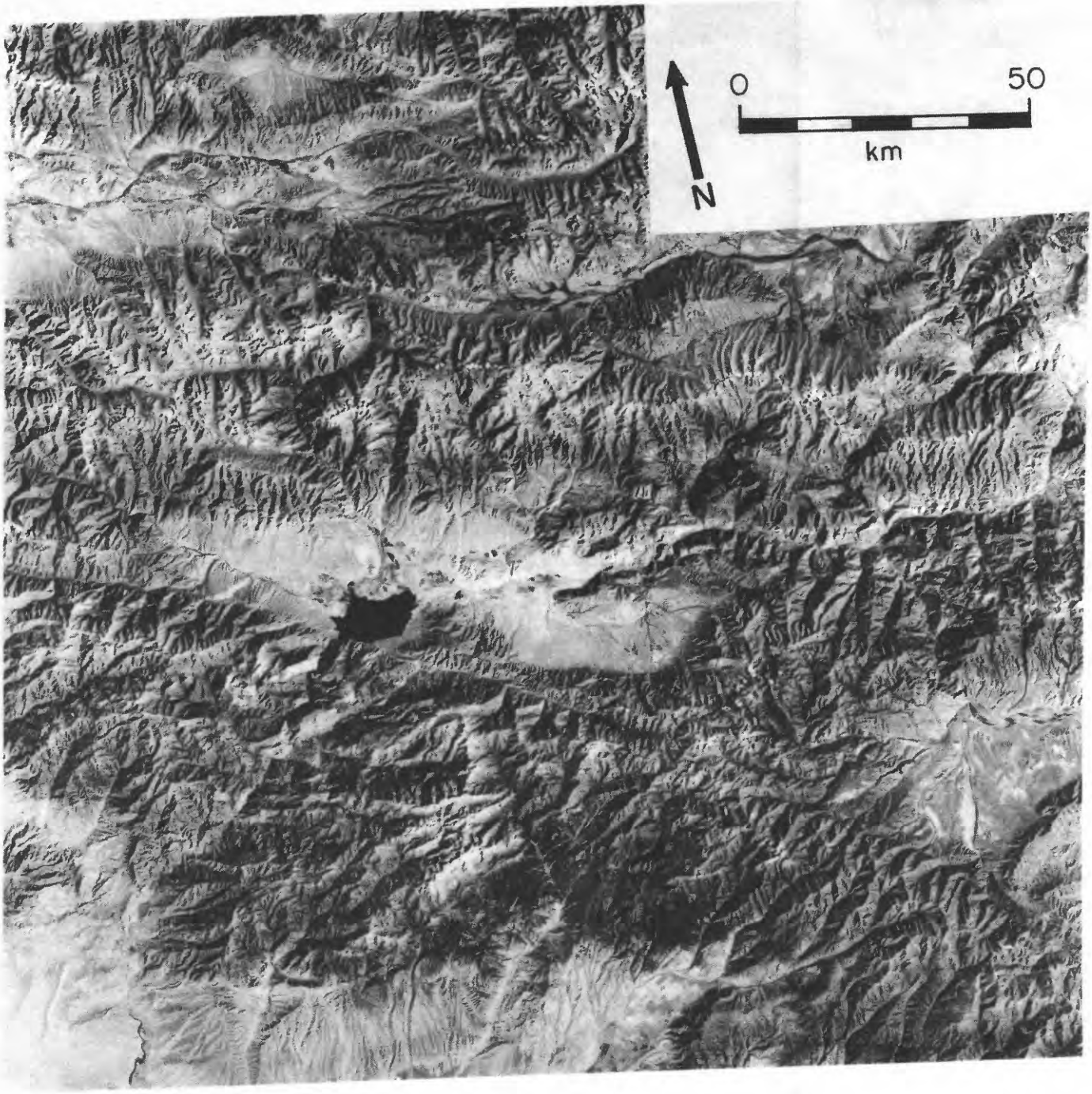

Figure 2: LANDSAT photograph of Toktogul region. Reservoir is center left. It will eventually fill most of the light area at center of photograph. Talas-Fergana and Kara Kul' faults are visible (compare with Figure 3). Northern edge of Fergana basin is at lower left.

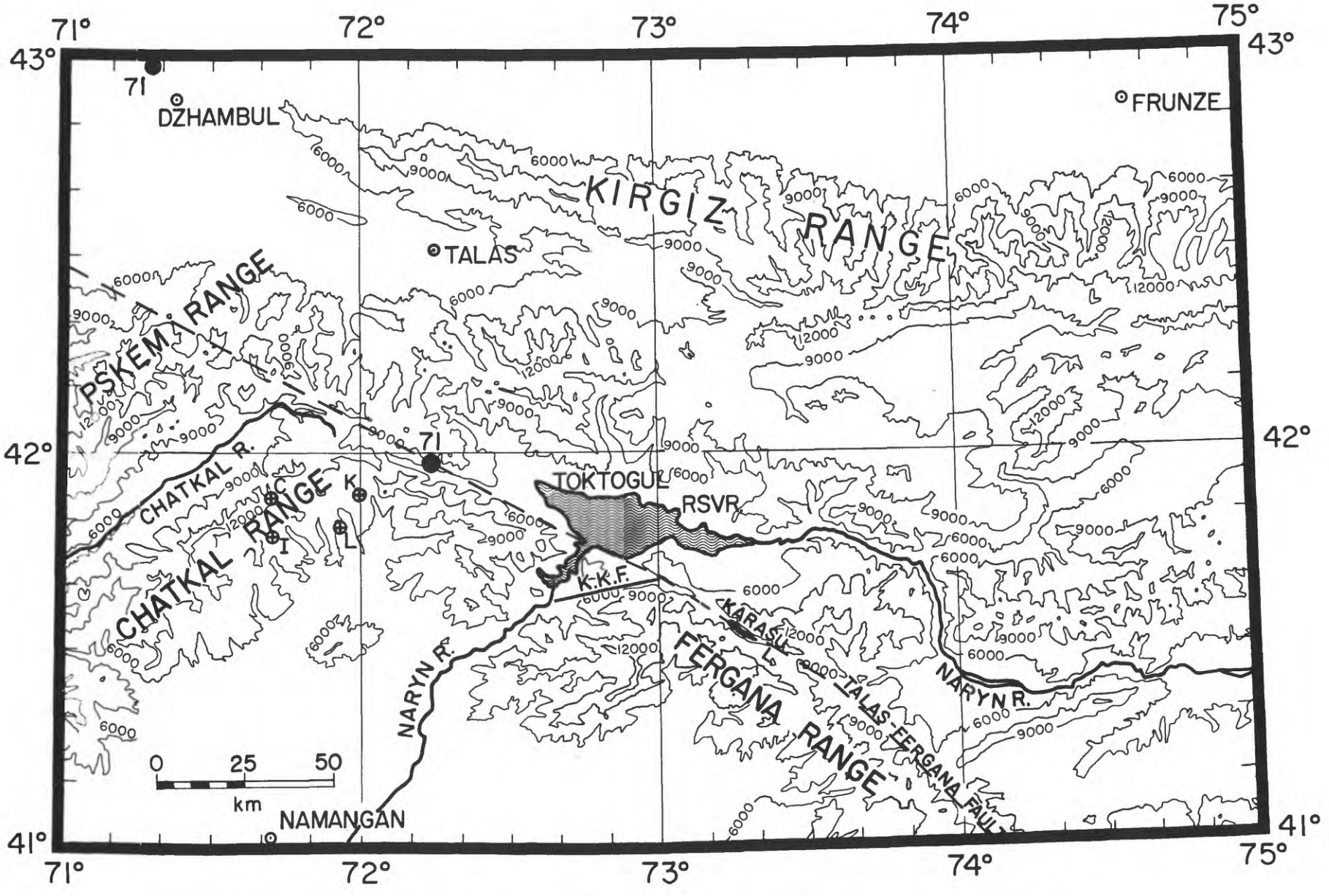

Fig. 3. The Toktogul Reservoir area. Elevation contours at 6000, 9000 and 12,000 feet are shown. Four different locations for the 1946 Chatkal earthquake (M = 7.6) are indicated by circles of crosses: K = Kondorskaya and Shebalin (1977), L = Lamont-Doherty computer relocation, I = International Seismological Summary location, C = Caloi and Peronaci (1948). Solid circles show locations (Kondorskaya and Shebalin, 1977) for the two 1971 events. K.K.F. = Kara Kul' fault.

Shan-Kun Lun fault system (Figure 4), which extends for up to 1200 km, and acts as a first order tectonic feature, dividing the region into discrete tectonic blocks (Burtman et al., 1963).

In the northwest, the fault marks the boundary between the Caledonian (early Paleozoic) geosyncline of the northern Tien Shan and the central Tien Shan Hercynian (late Paleozoic) geosyncline. The junction between the Caledonian and Hercynian structures has been called the "Nikolaev line" (Yakubov et al., 1976). At Toktogul, the Nikolaev line leaves the Talas-Fergana fault, extending eastward along the Main Tien-Shan (or Terskei-Karatau) fault (Rozova et al., 1968). The Toktogul basin is thus located at the junction between these two major "deep faults". Southeast of Toktogul, the Talas-Fergana divides Paleozoic formations deformed during the Hercynian orogeny. In the Arpa depression, near the Chinese border, the fault is obscured by Jurassic deposits, continuing farther south as the Terektin fault along the same strike (Burtman et al., 1963). This fault cuts the Precambrian crystalline rocks of the Tarim massif and the western Kun Lun Hercynian folded region. The fault is near vertical for most of its length (Burtman, 1963).

There is disagreement as to the type and extent of movement along the fault. Ulomov (1973) and Molnar and Tapponnier (1975) interpret the fault as a right-lateral strike-slip feature along which lateral displacements have taken place during crustal shortening in response to the India-Eurasian collision (see Figure 4, Molnar and Tapponnier, 1975). To the north and northeast of the Indian subcontinent, Molnar and Tapponnier suggest that the Indian-Eurasian collision has resulted in a broad zone of deformation including thrusts, strike-slip faults and rift systems extending 2000 km into China. To the northwest of the Indian subcontinent, the

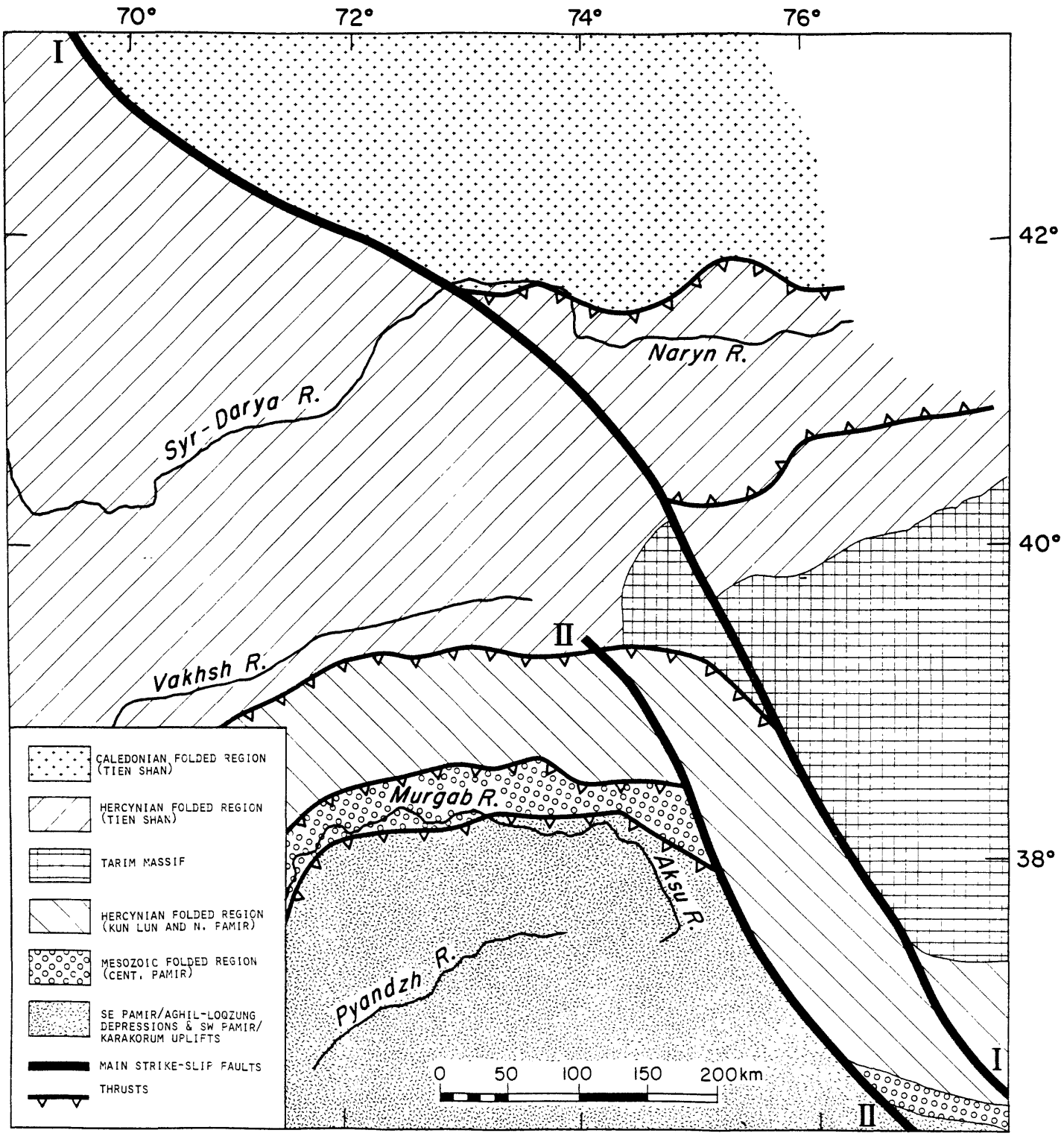

Figure 4: Main structural units of the Central Tien Shan and northern Pamirs: I-I and II-II represent major strike-slip faults, the "Tien Shan-Kun Lun" and the "Pamir-Karakorum", respectively. (After Burtman et al., 1963).

zone of deformation appears much more concentrated, occurring mainly in thrusts in the Hindu-Kush, the Pamirs and the southern Tien Shan. Strike-slip motion in this area may not be as important as it is to the east, but the seismicity indicates that there is present-day activity along the Talas-Fergana and associated faults (Figure 10).

In a detailed lithofacies study of the Paleozoic formations of the central Tien Shan, Burtman (1960) notes up to 200 km of right-lateral offset of the lithologic complexes, with an additional 50 km offset taken up by plastic deformation in the near-fault zone (Figure 5). Much of the offset of these formations took place in the Permo-Triassic, as the final phase of the Hercynian episode of folding and magmatism. After a quiescent period, the fault became reactivated in the Quaternary as part of the Alpine orogeny (Burtman, 1963; 1975). Horizontal movement along the fault is also demonstrated by a 225 km offset of a well-identified gneissic granite intrusive body (Burtman, 1963). The offset limbs of the intrusive are observed in 100 km wide exposures approximately 125 km northwest and 100 km southeast of Toktogul. Kravchenko (1979) cites paleomagnetic data supporting a 60° counterclockwise rotation of the Chatkal block (a set of northeast trending ranges sharply truncated by the Talas-Fergana; see Figure 3) associated with post-Hercynian movements along the fault.

Offsets of several major river valleys suggest up to 3 km of right-lateral displacement since the middle Quaternary (Rantsman, 1963). The present-day activity of the fault is indicated by lineations visible in LANDSAT images, offsets of ephemeral streams, glacial moraines and water divides, as well as by earthquake-induced landslides and lineations in seismic activity along much of the fault (Wallace, 1976; Rantsman, 1973; Burtman, 1963; Grin, 1964).

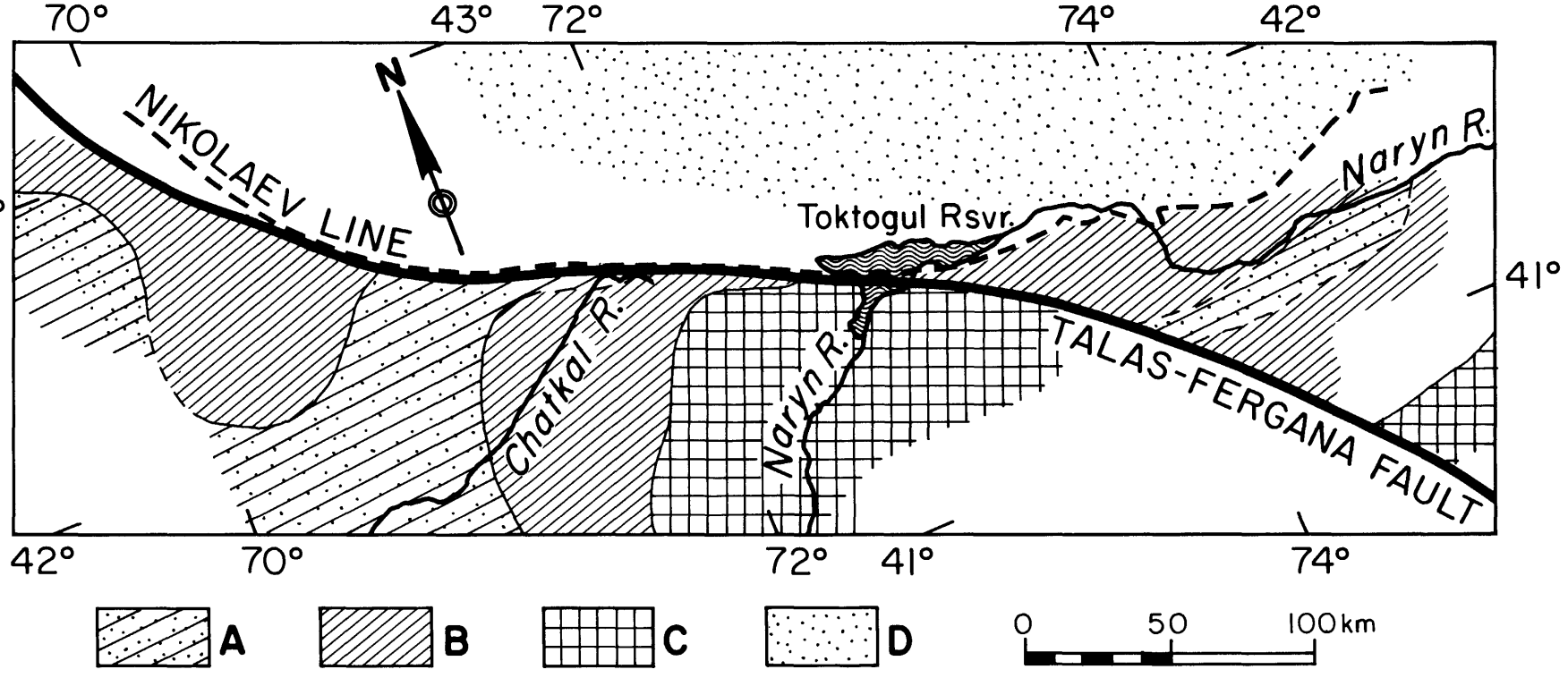

Figure 5: Distribution of upper Devonian lithologic units of the Toktogul region. A) Carbonate-terrigenous rocks; B) argillaceous and arenaceous limestones; C) limestones and dolomites; D) areas of denudation. (After Burtman, 1960).

REGIONAL SEISMICITY

Earthquake locations for the central part of the Tien Shan and surrounding areas for 1900-1977 are shown in Figure 7. The November 2, 1946 Chatkal earthquake (M = 7.6) occurred near the intersection of the Talas-Fergana and Chatkal faults, approximately 65 km northwest of Toktogul Dam. It was the largest in the Toktogul region in this century. It was destructive over a large area of central Kirgizia, and shaking of intensity V was experienced as far as 250 km away in Tashkent (see Figure 6a). The maximum intensity (IX) occurred over a elongate zone extending southeast (parallel to the Talas-Fergana fault) 80-100 km to Toktogul (Rozova et al., 1968). A large landslide measuring 300 x 200 x 10 m temporarily dammed the Naryn River, upstream from the present site of the Toktogul Dam. The intermediate isoseismals form a peculiar L-shaped area, elongated along the Talas-Fergana, as well as perpendicular to it, along the northeast striking Chatkal range. The fourth and fifth isoseismals smooth out to form a large ellipse, its long axis parallel to the Chatkal ranges (Rozova et al., 1968). This effect could be produced by greater attenuation along the strike of the Talas-Fergana.

There has been considerable debate as to the location and type of faulting for the Chatkal earthquake. Ulomov (1974) suggests this earthquake represents a right-lateral strike-slip offset along the "Talas-Fergana zone of deep faults". Others (e.g., Nersesov et al., 1960) suggest the earthquake is associated with the transverse faults of the Chatkal ranges. Computer relocation of the event, using times reported in the 1946 Catalog of Epicentres of the International Seismological Summary, places the epicenter at 41°46.8'N, 71°55.8'E, 25 km southwest of the Talas-

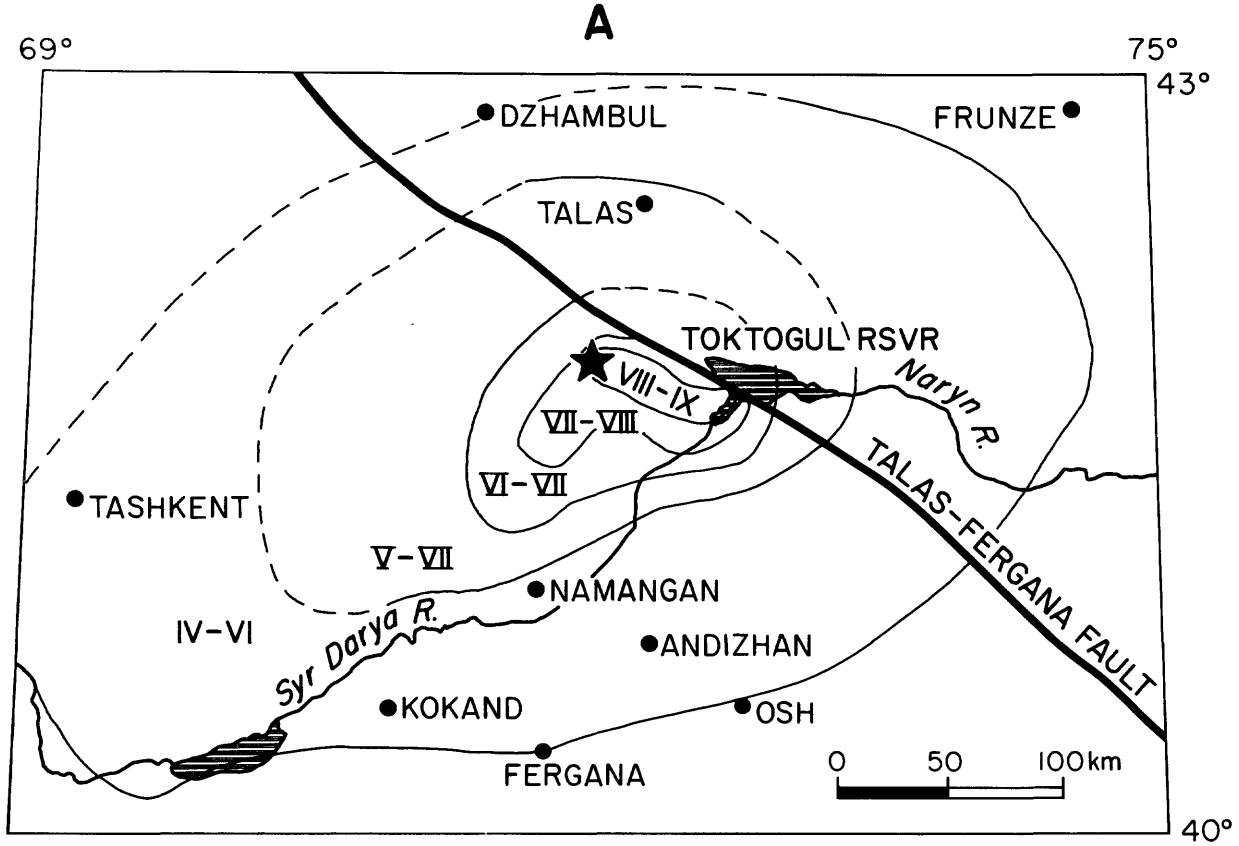

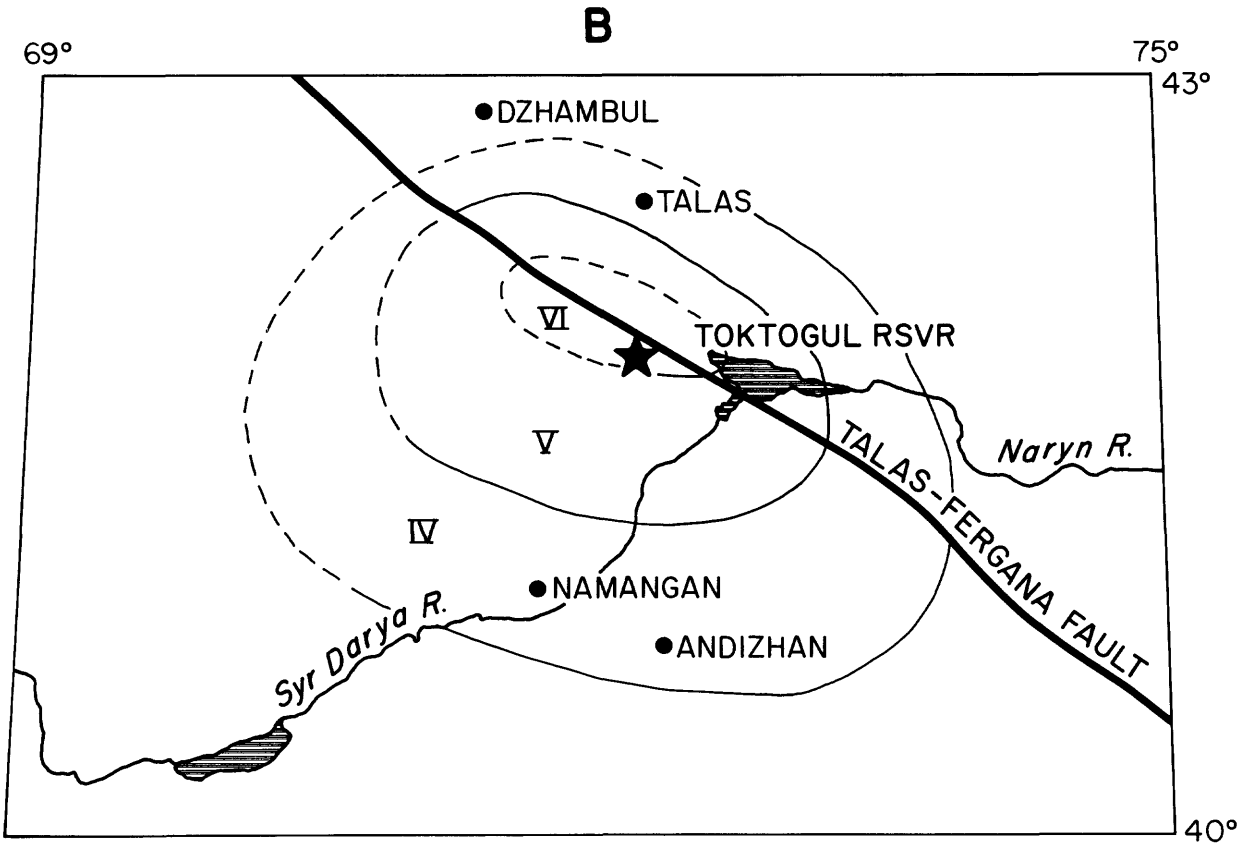

Figure 6 Isoseismals of (A) the Chatkal earthquake (2 November 1946, M = 7.6) and (B) the Toktogul earthquake (28 October 1971, M = 5.6). Intensity values are from the Soviet 12-point scale. Dashed isoseismals indicate incomplete data. Star shows Kondorskaya and Shebalin (1977) locations of the main shocks. (A) from Rosova et al. (1968), (B) from Astaf'eva et al. (1972).

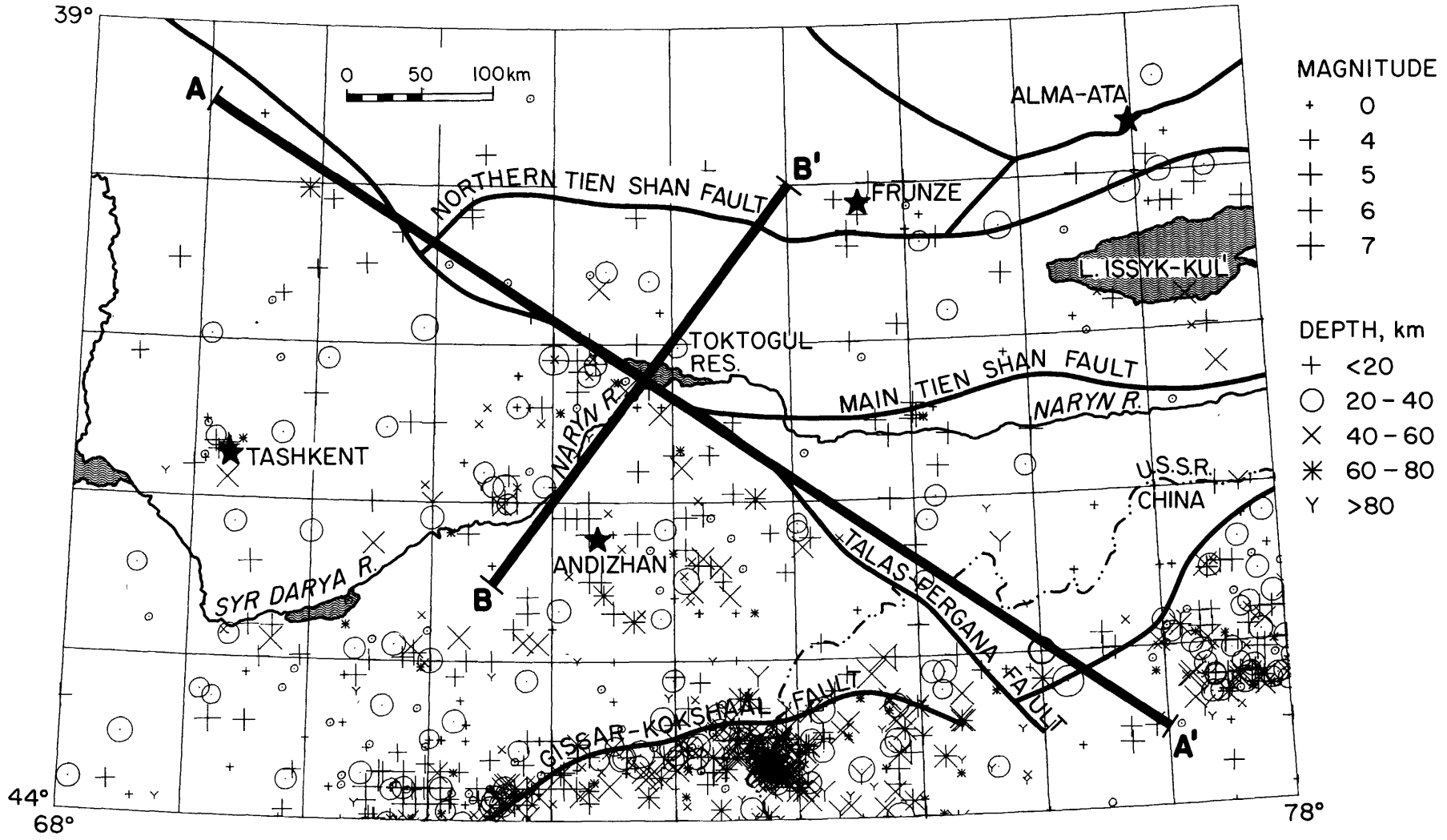

Fig. 7. Seismicity of the central Tien Shan and northern Pamirs, 1900-1977. Data are from the Soviet catalog (Kondorskaya and Shebalin, 1977), the International Seismological Centre (ISC) and National Oceanic and Atmospheric Administration (NOAA) catalogs. Major faults are show, as well as locations of the cross-sections used in Figures 8 and 9.

Fergana. Insufficient data were available to determine the depth. Several other studies (Kondorskaya and Shebalin, 1977; Nersesov et al., 1960; Caloi and Peronaci, 1948) also place the epicenter southwest of the fault at distances of 10-30 km. On the basis of presumed depth phases, Caloi and Peronaci (1948) suggest a depth of 73 km. This, however, is at odds with the shallow depths (less than 20 km) determined for recent weak earthquakes along the fault.

Various epicenters reported for the earthquake are shown in Figure 3. The earthquake was followed by a long series of aftershocks; it was not until 1950 that the activity returned to its "normal" level (Nersesov et al., 1960). Aftershocks show a strong lineation along the Talas-Fergana (Figure 10), with a less pronounced trend transverse to this, along the strike of the Chatkal range. The most reliable epicenter (Kondorskaya and Shebalin, 1977), determined using data from regional and teleseismic stations, lies near the intersection of these two trends, approximately 10 km southwest of the surface trace of the Talas-Fergana.

A focal mechanism for the 1946 earthquake (Shirokova, 1974) suggests pure right-lateral strike-slip motion along a plane subparallel to the Talas-Fergana. The alternate plane could be construed as subparallel with the northeast striking Chatkal faults.

A recent event (October 28, 1971, M 5.6; see Figure 3) occurred within the aftershock zone of the 1946 earthquake. Intensity data (Figure 6b) suggest an elongation along the Talas-Fergana, with a center close to the 1946 event. Focal mechanisms for this earthquake presented by Ni (1978) and Tapponnier and Molnar (1979) show pure thrusting along an easterly or ENE striking plane, approximately parallel to the Chatkal zone. As pointed out by Tapponnier and Molnar, however, a component of strike slip cannot be

ruled out. An alternate mechanism, consistent with the available data, could incorporate a significant component of right-lateral strike-slip, along a plane aligned with the strike of the Talas-Fergana and dipping northeast. The epicenters of the active zone already lie southwest of the Talas-Fergana and the extension of this zone up-dip along such a northeasterly dipping plane would, therefore, reach the surface even farther from the fault. This supports the contention by Tapponnier and Molnar (1979) that the earthquake occurred on a fault parallel to, but southwest of the Talas-Fergana. Systematic errors in epicenter locations, however, may be responsible for the apparent offset between the epicentral zone and the fault trace.

Although the available data are insufficient to identify the exact source of the Chatkal earthquake, it is clearly associated with the complex zone at the oblique intersection of two major features, the Talas-Fergana and Chatkal ranges. Many Soviet workers stress the importance of such junction zones in assessing seismic risk (e.g., Rozova et al., 1968; Nersesov et al., 1960). It is possible that the 1946 event was a multiple rupture, involving both strike-slip and thrust motion along the Talas-Fergana and Chatkal trends, respectively. A similar complex rupture has been suggested by Jackson et al. (1979) for the 1974 Markansu earthquake, north of the Pamirs.

The only other recent event near Toktogul, large enough for fault-plane analysis using teleseismic data, occurred on May 10, 1971 near Dzhambul, approximately 150 km northwest of Toktogul. The epicenter lies on the northern Tien Shan fault, 60 km northeast of the intersection of that fault with the Talas-Fergana (see Figure 3). Ni (1978) incorrectly assumes this earthquake to be on the Talas-Fergana and shows a mechanism

with right-lateral strike-slip. A more probable mechanism given by Tapponnier and Molnar (1979) shows pure thrust on an ENE plane, the approximate strike of the northern Tien Shan fault in this area.

Apart from the Chatkal event and its aftershocks, Figure 7 does not show any clear association of the major seismicity of this century with the Talas-Fergana fault. Smaller earthquakes, however, do show a higher level of activity along the Talas-Fergana (Figure 10). Earthquake activity rapidly decreases along the fault northwest of the Chatkal zone (Figures 7 and 8). This corroborates the conclusion by Tapponnier and Molnar (1979) on the basis of observations of topography from LANDSAT imagery, that the northern portion of the fault is less active than the southern.

Figures 7 and 9 show a striking pecularity of the Talas-Fergana fault. The seismicity is markedly lower northeast of the fault. This pattern is most likely not produced by unequal station distribution, and is confirmed by several other regional studies (Nersesov et al., 1960; Rozova et al., 1968; Grin, 1964). If there is some component of thrusting, the seismicity southwest of the fault would be consistent with greater deformation within an overthrusting block. It may simply be that the fault separates rocks with greatly dissimilar rheological properties.

An alternative model, consistent with more strike-slip motion along the Talas-Fergana, might also explain this phenomenon. The northwestward movement of the southern block appears to be abruptly diminished by thrusting along a series of transverse faults in the Chatkal-Pskem ranges northwest of Toktogul. There, the crust rapidly thickens to 65 km by underthrusting along a series of northeast-trending faults (Ulomov,1973). Relative movement between the blocks drops off sharply northwest of the Chatkal region. Thus, much of the movement of the southern block must be

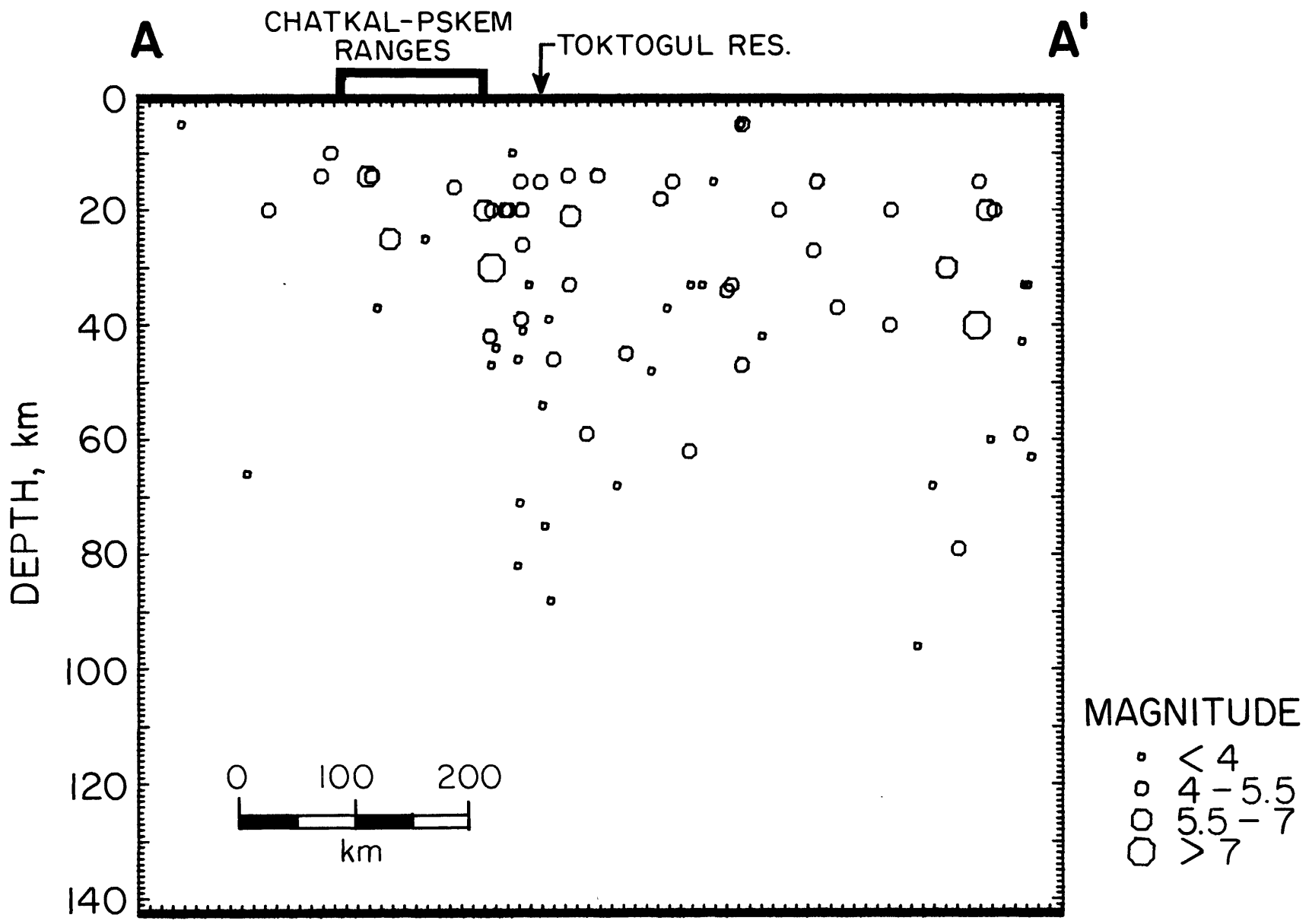

Figure 8: Cross-section along profile AA' in Figure 7. Vertical exaggeration = 5.0. Earthquakes within 50 km of AA' were used in the cross-section.

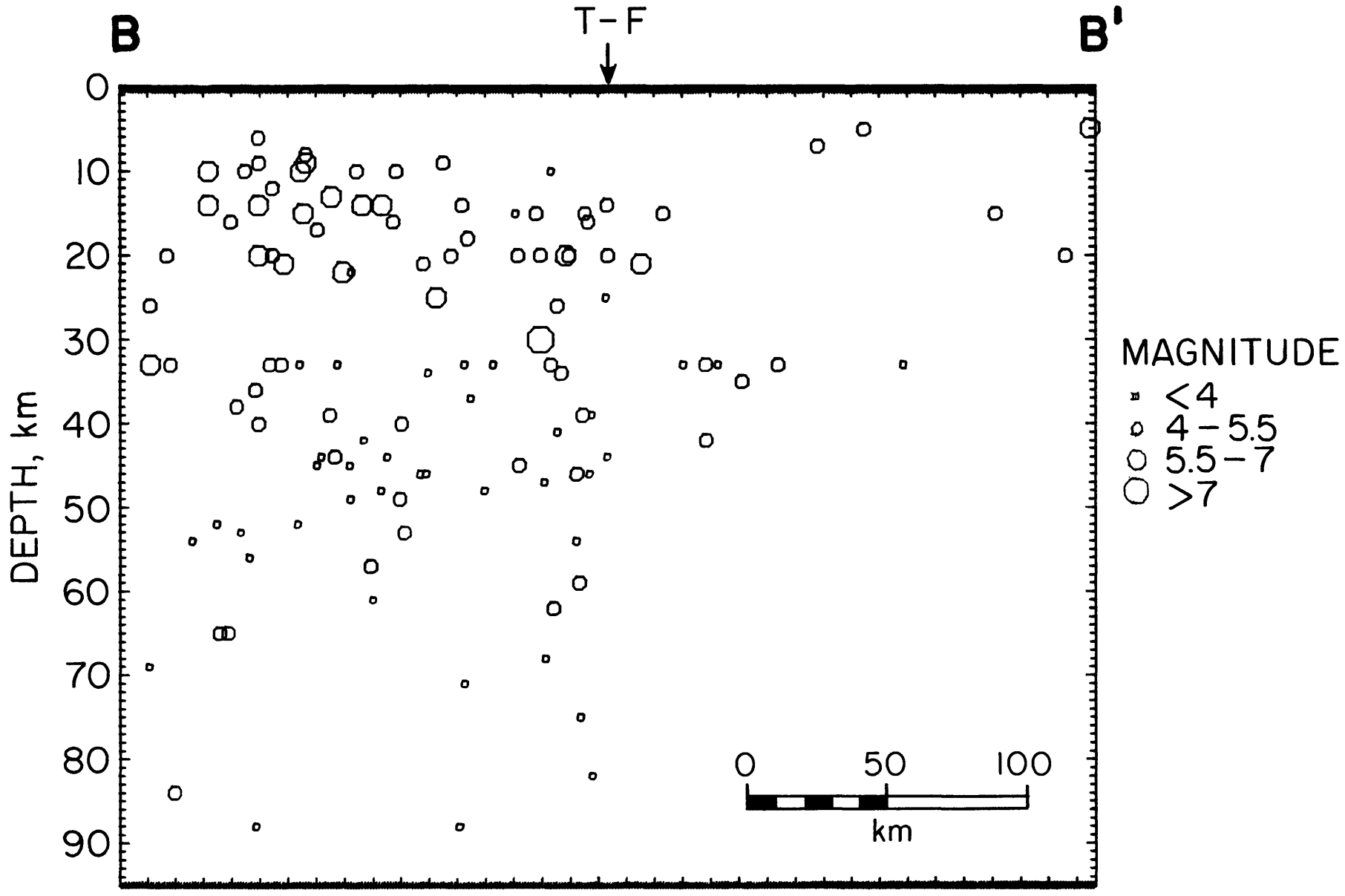

Figure 9: Cross-section along profile BB' in Figure 7. Vertical exaggeration = 3.0. Earthquakes within 150 km of BB' were used in the cross-section.

taken up by underthrusting along the Chatkal faults. Transmission of these compresive stresses throughout the block would result in seismic activity along a series of secondary faults within the southern block. It may be this activity which we see along the Kara Kul' and other transverse faults in the Toktogul region. The northern block, stable relative to the southern, might not be subject to this internal deformation. Focal mechanism data should shed light on this problem.

The Toktogul region itself is of particular seismological interest. It is unusual in that:

1. It is located at the intersection of two major active tectonic features: the Talas-Fergana fault and the Main Tien Shan fault.
2. It is characterized by a very high seismic activity. The activity, represented in Soviet literature by the parameter A_{10}, is the highest in the northern and central Tien Shan (Nersesov et al., 1960).
3. Just northwest of Toktogul, approaching the Chatkal zone, maps of depth to the Moho show a marked step, perhaps related to the underthrusting discussed above. Riznichenko et al. (1975) suggest large earthquakes in this area are associated with such high gradients ("terraces") in the relief of subsurface discontinuities.
4. Burtman (1963) points out significant changes in the strike of the Talas-Fergana fault. These result in the development of elongated tensional fractures in the Leontiev and Arpa depressions, likened to sedimentary basins associated with the San Andreas fault in California. The strike of the fault near

Toktogul changes from northwest to west-northwest; it may be that the stress in this zone is characterized by the greatest component of compression across the fault, allowing greater stress accumulations and, hence, greater earthquakes.

5. Geomorphological evidence supports the occurrence of major earthquake-induced landslides in the Holocene near Toktogul: a) at Karasu Lake, about 40 km southeast of Toktogul; b) at Lake Sarychelek, about 65 km to the northwest; and c) at Kara Kul', in the immediate vicinity of the Toktogul Dam (Krestnikov et al., 1979). Recurrence intervals in this area are long, but the absence of major earthquakes at Toktogul in the last century suggests high accumulated stress.

SEISMICITY NEAR TOKTOGUL RESERVOIR

The Institute of Physics of the Earth (IPE), Moscow, and the Kirgiz Institute of Seismology (KIS), Frunze, have been operating a network of 4 to 11 stations near Toktogul since 1965. Temporary expeditions had also studied the seismicity of the area in greater detail during 1957-1959 and 1962-1963 (Grin et al., 1964). Epicenters for the Toktogul area from 1965 to 1977 are shown in Figure 10. Clusters of activity near the Talas-Fergana can be seen in the aftershock zone of the 1946 Chatkal earthquake, near Toktogul Dam and near Karasu Lake southeast of Toktogul. In this figure, the higher level of activity southwest of the fault is even more apparent than in Figure 7. As was shown for the locations of the Chatkal event in Figure 3, the seismicity is offset to the southwest from the surface trace of the Talas-Fergana. A velocity contrast or significant

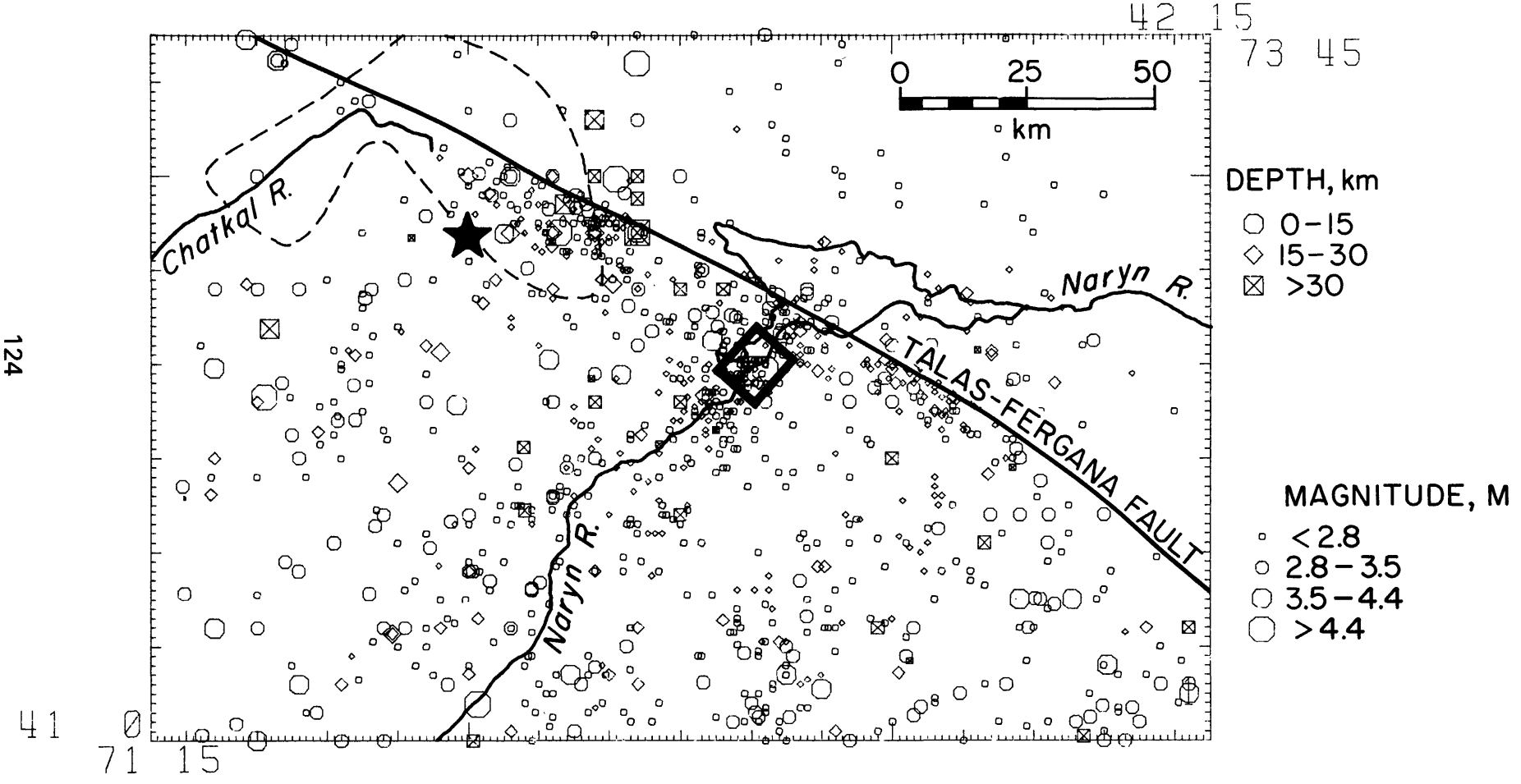

Fig. 10. Seismicity in the Toktogul Reservoir region, 1965-1977. Data are from the I.P.E. catalog. Star indicates location (Kondorskaya ans Shebalin, 1977) of the 1946 Chatkal earthquake (M = 7.6). Dashed line indicates aftershock zone of the Chatkal event, approximated from Nersesov et al. (1960) aftershock locations. Rectangle shows "dam area" used in Figure 12.

differences in crustal thickness across the fault may be sufficient to cause systematic errors in epicentral locations of several kilometers, as shown by Ellsworth (1975) for earthquakes on the San Andreas. Most of the stations used to locate earthquakes in this region lie to the south and southwest of the active area and if the velocities used in the location procedure are too low, epicenters could be severely biased to the southwest.

Temporal variations in seismicity are shown in Figure 11. The largest earthquake during this time period was the magnitude 5.6 event in the Chatkal zone in 1971. The largest earthquake near the reservoir was of magnitude 4.6 in 1966, close to the dam site. Since 1974, there has been a substantial decrease in the energy release shown in Figure 11. This gradual decrease in energy over the past five years appears to be typical of the entire area surrounding the Talas-Fergana.

Temporal variations in the number of earthquakes in the immediate area of the dam (outlined in Figure 10) during the first stage of filling of the reservoir are shown in Figure 12. An increase in the number of earthqukes was observed in early 1977, when the water level at the dam first approached and maintained a value of over 90 m. Only events greater than magnitude 1 are included in Figure 12. In late 1977, a significant increase was observed in the number of smaller earthquakes recorded by a seismic station approximately 7 km east of the dam site. Most of these events were too small to be located and hence do not appear in the catalog used in Figure 12. Data are available on the time of these events, their size and the S-P time at Station S5 (see Figure 14). As more recent data described below have confirmed, these earthquakes are located very close to the dam. The number of events per five days is shown in Figure 13, along

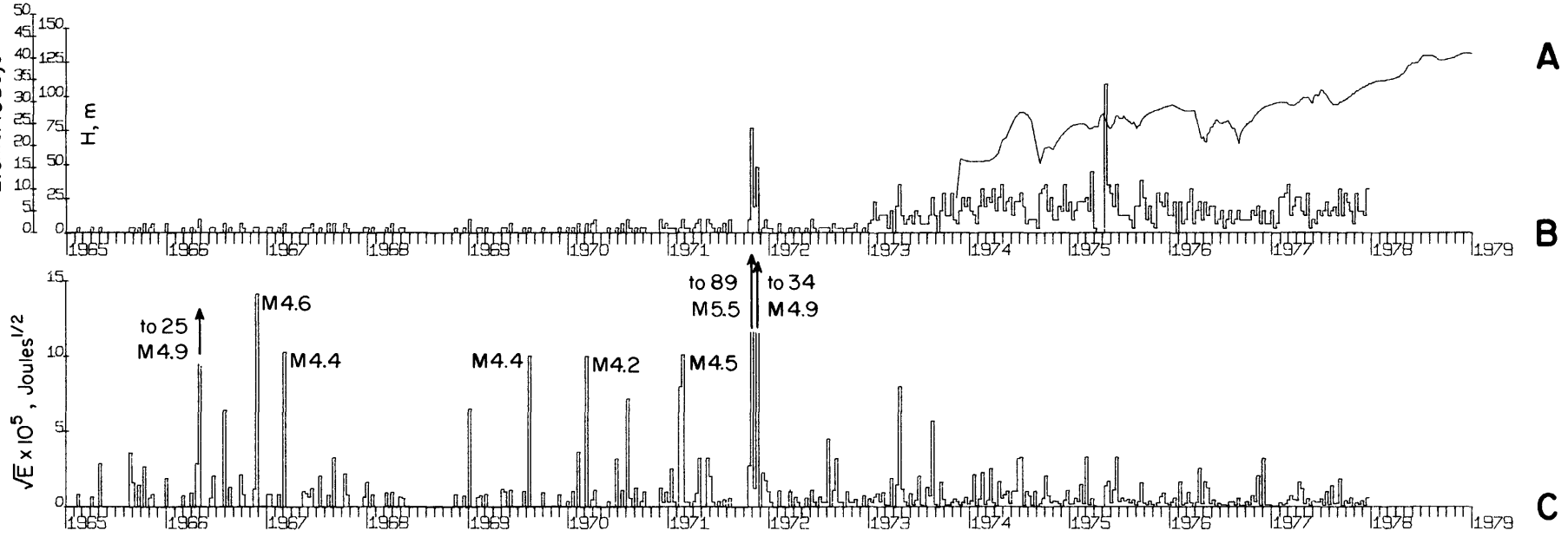

Figure 11: Variation of seismicity with time in the Toktogul Reservoir region (Figure 10), 1965-1977. Data are from I.P.E. catalog. (A) reservoir water level in meters; (B) number of events per 10 days; (C) strain release, E x 10^5 in joules$^{1/2}$. The abrupt increase in the number of events at the beginning of 1973 is produced by a change in threshold from K 9.5 to K 6.

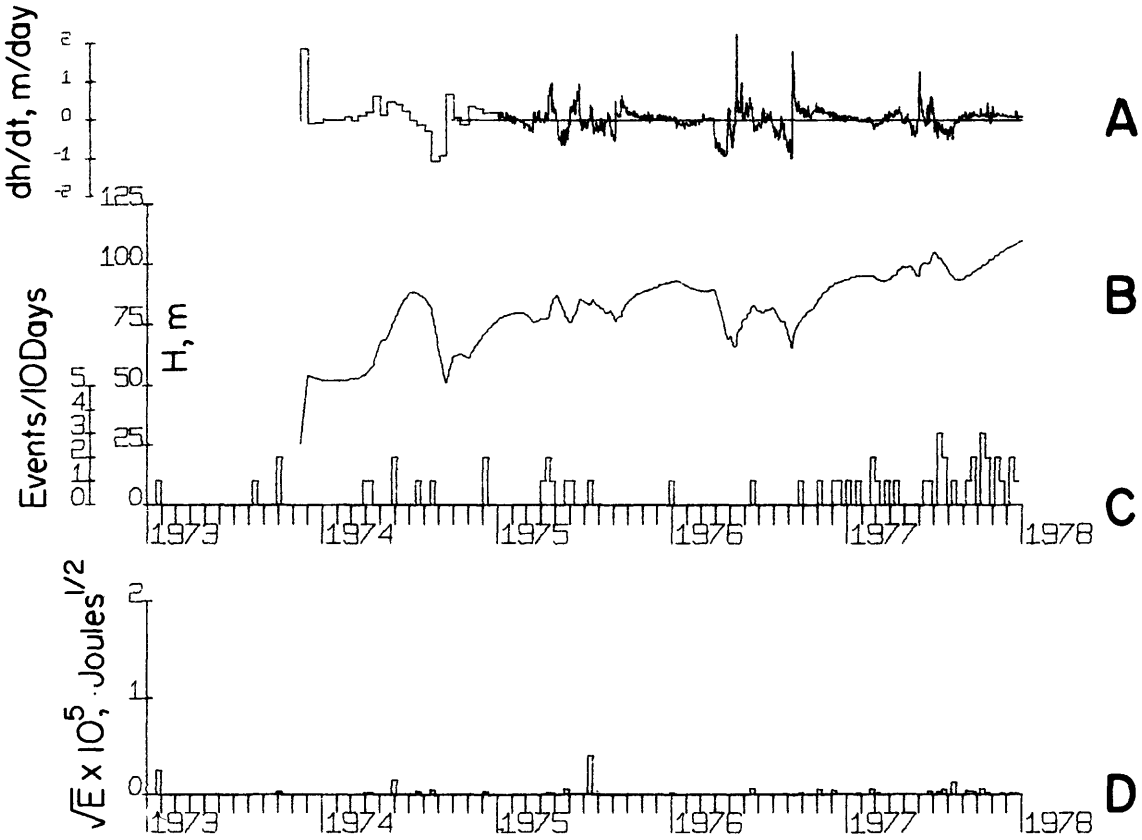

Figure 12: Variation of seismicity with time in the dam area (small rectangle in Figure 10), 1973-1977. Data are from I.P.E. catalog. (A) reservoir water level gradient in meters/day; (B) reservoir water level in meters; (C) number of events per 10 days; (D) strain release, E x 10^5 in joules$^{1/2}$.

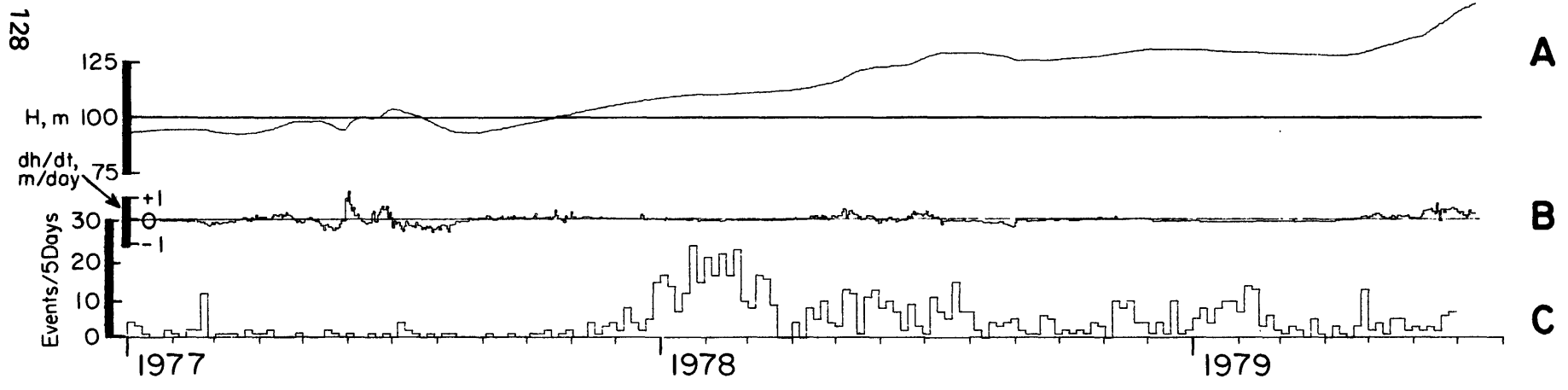

Figure 13: Number of earthquakes near the dam (not located) per 5 days, 1977-1979. Events were recorded at station S5 (Figure 14). (A) reservoir water level in meters;(B) reservoir water level gradient in meters/day;(C) number of events per 5 days. NB: seismic data begins January 1977.

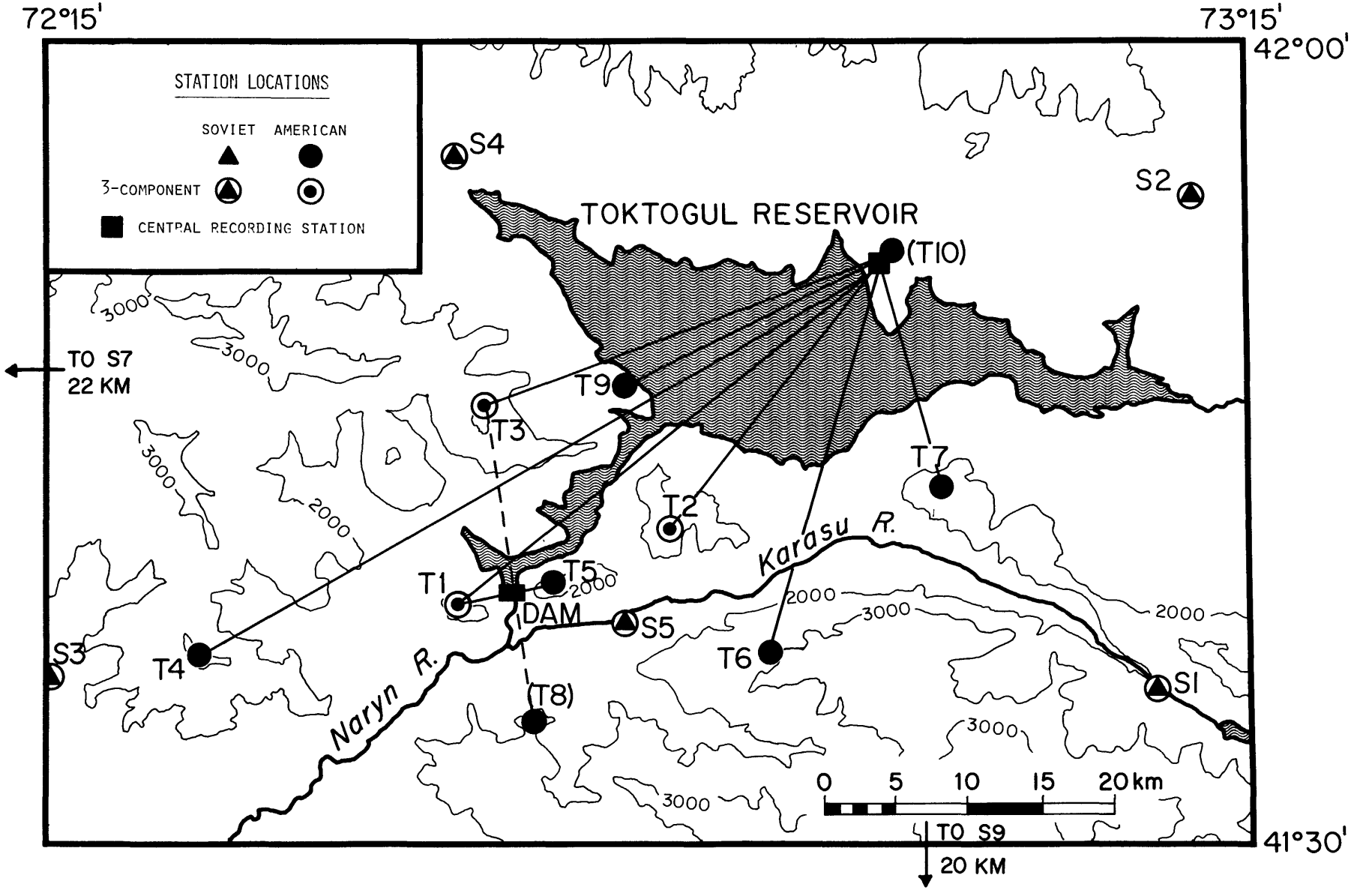

Fig. 14. Toktogul Reservoir region and locations of seismic stations: permanent Soviet stations (S1-S9) and American Telemetered stations (T1-T10). Straight lines show radio telemetry links. Dashed lines and station names in parentheses indicate proposed stations to be installed in 1979. Elevation contours in meters.

with the water level and daily change in water level. A slight increase in the seismicity in July 1977 may be related to a brief period when the water level first exceeded 100 m. A very clear increase in the number of earthquakes followed the first sustained filling to over 100 m in October 1977. As the water level increased to approximately 115 m in mid-January 1978, the number of events increased to an average of five per day. At that time the water depth leveled off as the filling rate decreased, and the rate of seismicity also decreased. The seismicity also abruptly increased again as the water level reached a new maximum of 150 m in early July 1979.

The largest of the earthquakes near the dam since October 1977 has been magnitude 2.5. The activity, however, is in the immediate vicinity of the dam, is very shallow and is clearly related to water level. Previous activity has shown the immediate area to be capable of sustaining events of magnitude 4 1/2 - 5 and the region is capable of events as large as magnitude 7 1/2. The water level in the currently active area will increase a further 40 m before the reservoir is filled. The water level where the reservoir crosses the Talas-Fergana fault, 15 km upstream from the dam, has not yet exceeded 100 m, and induced activity could begin along the Talas-Fergana as the water level increases further. The occurrence of low-magnitude activity near the dam indicates that at least part of the region is in a state susceptible to failure triggered by loading of the reservoir.

SEISMICITY STUDIES 1978-1979

A joint Soviet-American project to study induced seismicity at Toktogul began in 1978 with a microearthquake survey using portable instruments in July-August and the installation of a seven-station tele-

metered network in October. Three additional stations are being installed in 1979. Locations of the ten stations of the telemetered network and the seven Soviet stations in the Toktogul area are shown in Figure 14. Three of the telemetered stations are equipped with three orthogonal components and one low-gain vertical channel. The low-gain channel operates with constant displacement response and the three high-gain channels with constant velocity response. The geometry of the network is such that the three multi-component stations surround the main active area, with the four single component stations providing better azimuthal and distance coverage for earthquakes in this area. The combined network of Soviet and American stations provides good coverage of the reservoir area; the Soviet stations provide widespread monitoring of larger events in the region, the American stations provide dense coverage of events in the most active region, close to the dam and deepest part of the reservoir.

The recording system shown in Figure 15 uses standard, 1/4 inch quadraphonic tape recorders as the primary recording medium. This system provides the timing resolution and dynamic range necessary for a study of local earthquakes with a small network, yet the system is inexpensive, reliable and simple to operate in a remote environment. Up to eight multiplexed FM seismic signals can be recorded on each of three tape channels, with timing information on the fourth channel. Recording occurs only when the system is triggered by an event detector. A tape recorder, operating continuously with a tape loop, provides the delay necessary to capture the first P arrival on all stations. The event detector also controls a multi-channel oscillograph which provides a visible record of events for immediate analysis. Off-line playback from tape can be used for more detailed study of events of interest. Three channels (the vertical

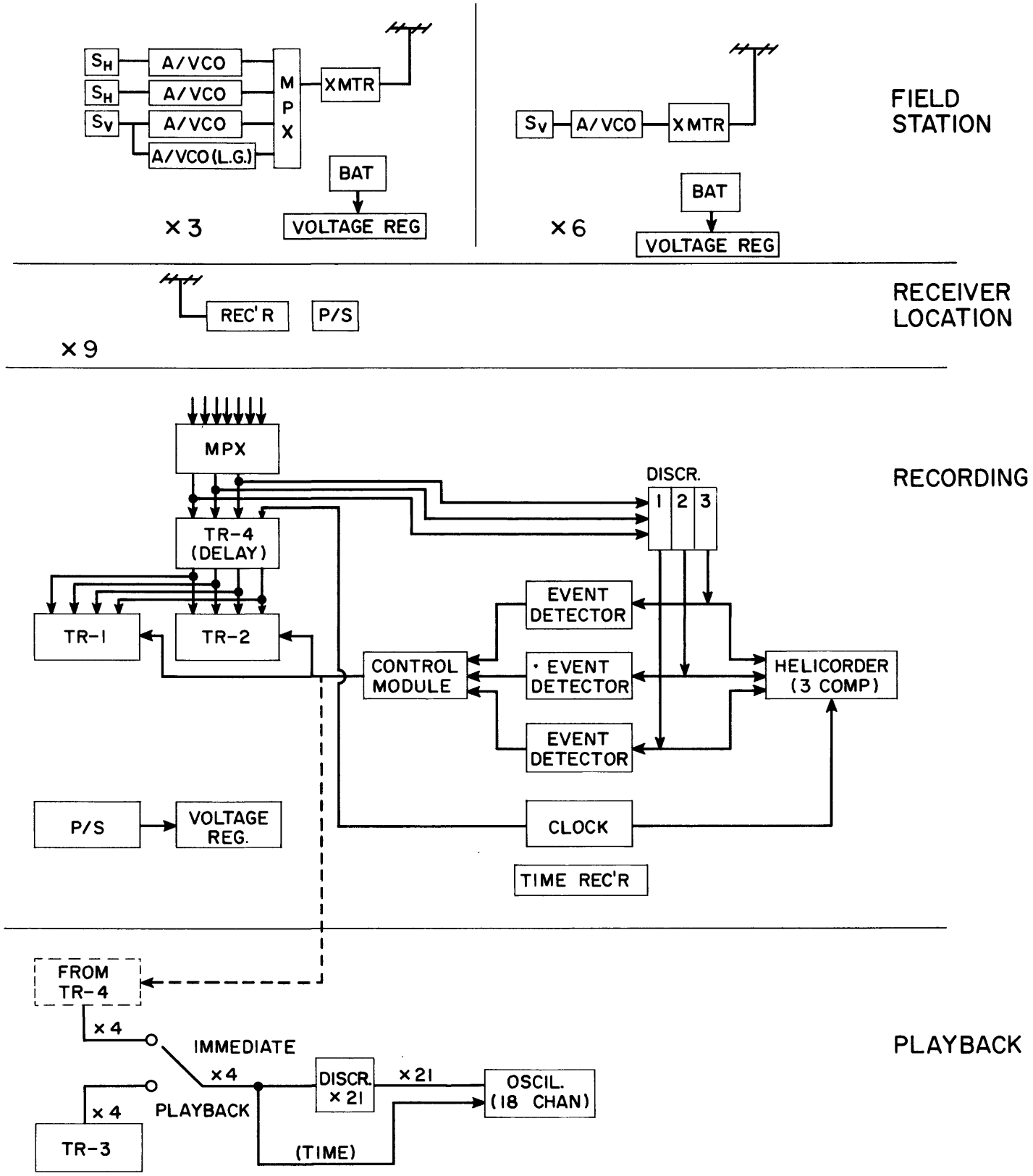

Figure 15: Block diagram of Toktogul telemetered seismic network. S_v = vertical seismometer; S_h = horizontal seismometer; A/VCO = amplifier/voltage controlled oscillator; L.G. = low gain; MPX = multiplexer; XMTR = transmitter; BAT = batteries; REC'R = receiver; P/S = power supply; TR = tape recorder; DISCR = discriminators; OSCIL = oscillograph.

component of the multi-component stations) are continuously recorded on paper seismograms to provide visible monitors. Examples of events recorded on the network are shown in Figure 16.

Three MEQ-800 recorders were used during the microearthquake survey in July-August 1978. Seven station sites where occupied, and more than 250 local earthquakes were recorded during the 35-day recording period. Data from seven permanent Soviet stations were provided, and approximately 150 earthquakes were recorded on sufficient stations to be located. Between November 1978 and May 1979, 270 events were located using the telemetered network. Preliminary locations of all earthquakes from the portable stations and telemetered network are shown in Figure 17. These locations were determined using the program HYPOINVERSE (Klein, 1978) and the velocity model from Nersesov et al. (1960). The velocity structure is an average model based on explosion and earthquakes studies in the Toktogul region. The location accuracy for events within the Toktogul network should improve as earthquake and explosion data are used to refine the velocity model and determine station time corrections for the network.

The strongest concentration of events in Figure 17 occurs in a narrow zone, approximately 10 km long, centered directly beneath the dam. The epicenters form a northeast-southwest lineation, parallel to the strike of the Naryn River canyon. The cross-section in Figure 18 shows this activity to be mainly confined to the 2-5 km depth range. This activity corresponds to the events with S-P times of less than 1.5 s recorded at Soviet station S5, the temporal history of which was shown in Figure 13. All of the activity in this area since 1977 has been less than magnitude 2.5 The proximity of these events to the deepest part of the reservoir and the correspondence of the onset of activity with the time when the reservoir

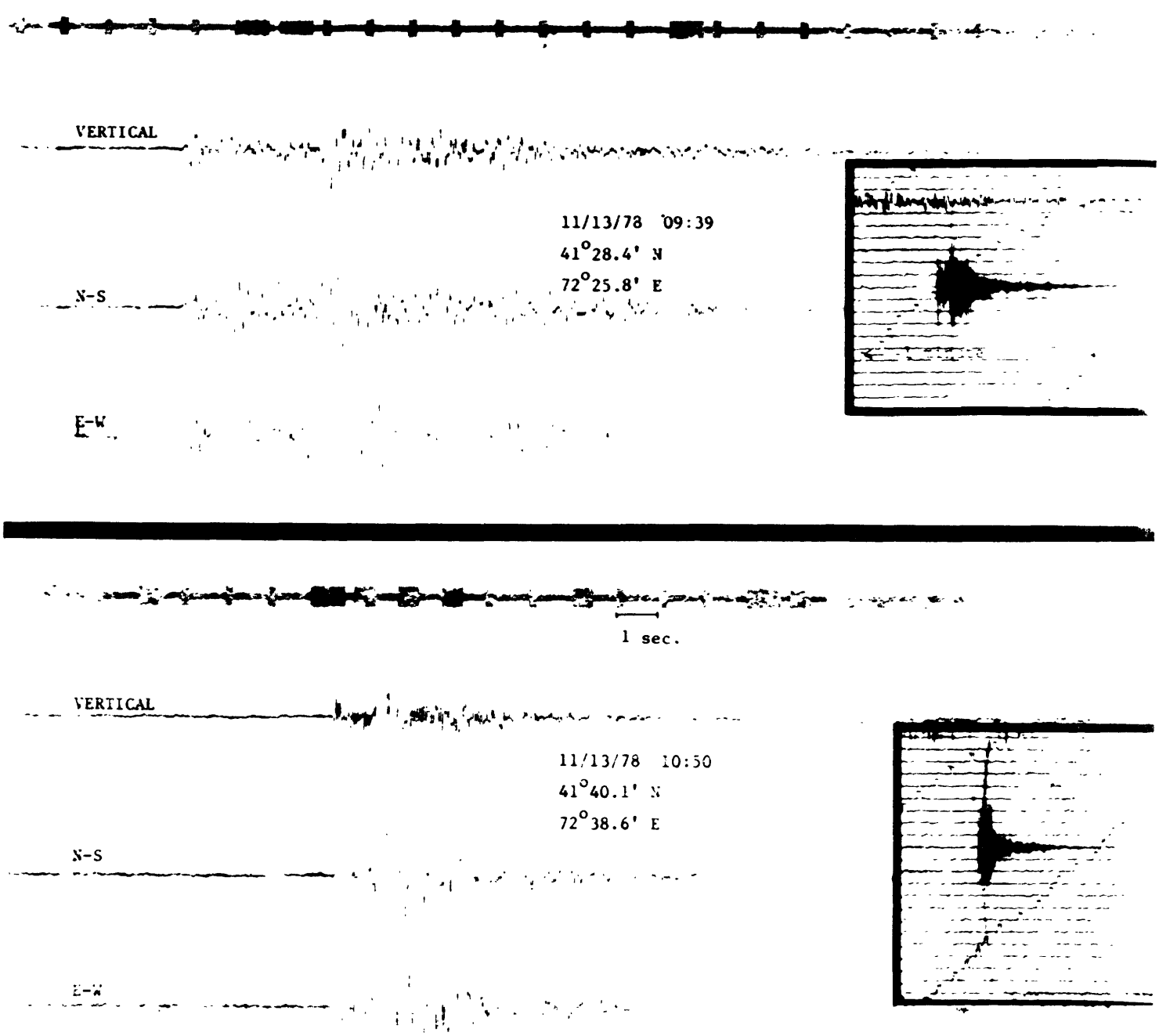

Figure 16: Seismograms from three-component telemetered station T1 for events at epicentral distances of 23.6 km (top) and 4.8 km (bottom). Played back from secondary tape (TR-1 in Figure 15) with tape speed compensation and no filtering. Insets show helicorder records of vertical channel.

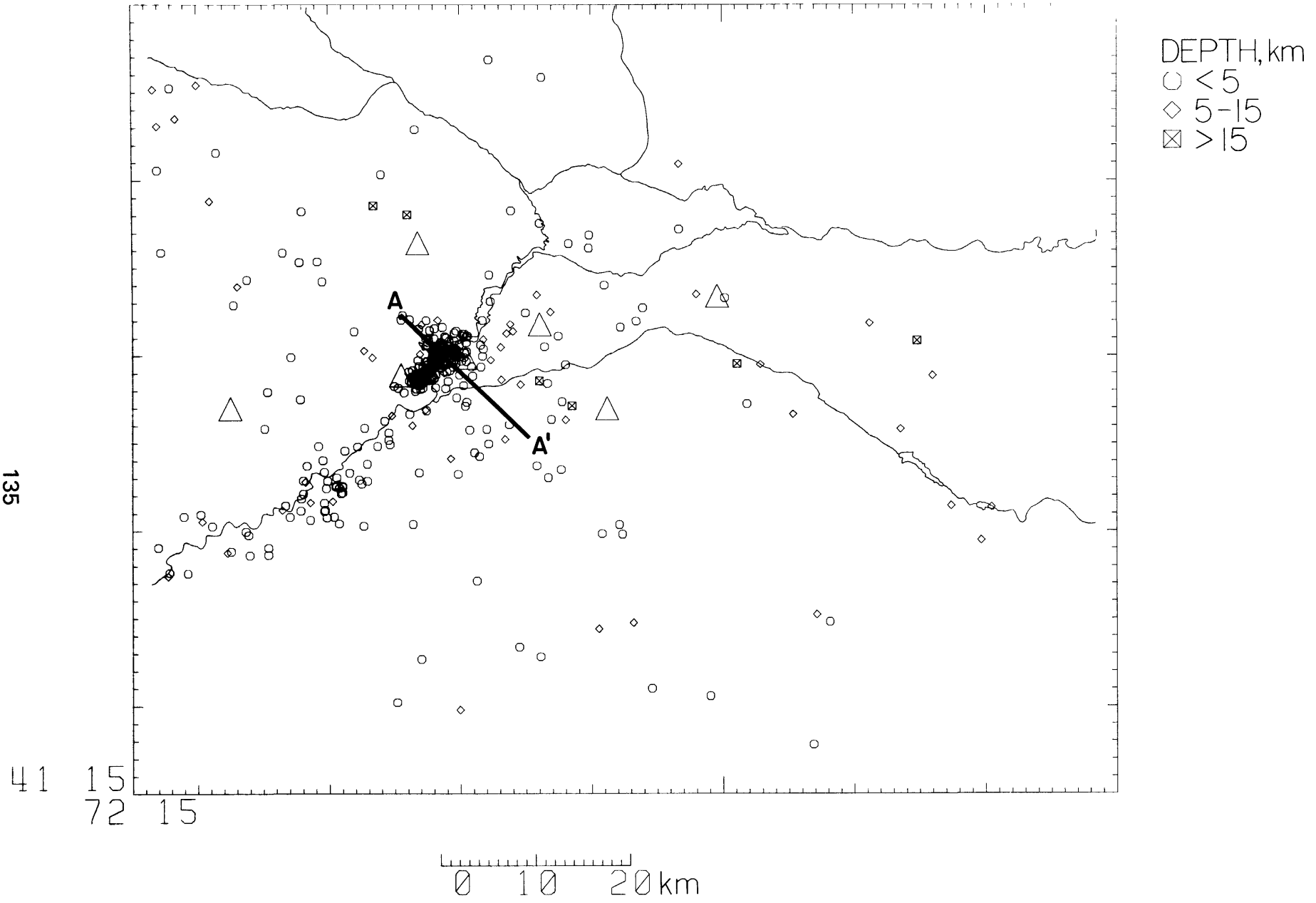

Fig. 17. Preliminary earthquake epicenters from microearthquake survey, July-August 1978 and from telemetered network data, October 1978-May 1979. Events were located using program HYPOINVERSE (Klein, 1978) and velocity structure from Nersesov et al. (1960). Probably road blasts have been removed. Large triangles indicate telemetered seismic stations. Major rivers and outline of reservoir from July 1978 LANDSAT image when water level was 130 m, as well as location of the cross-section shown in Figure 18 are shown.

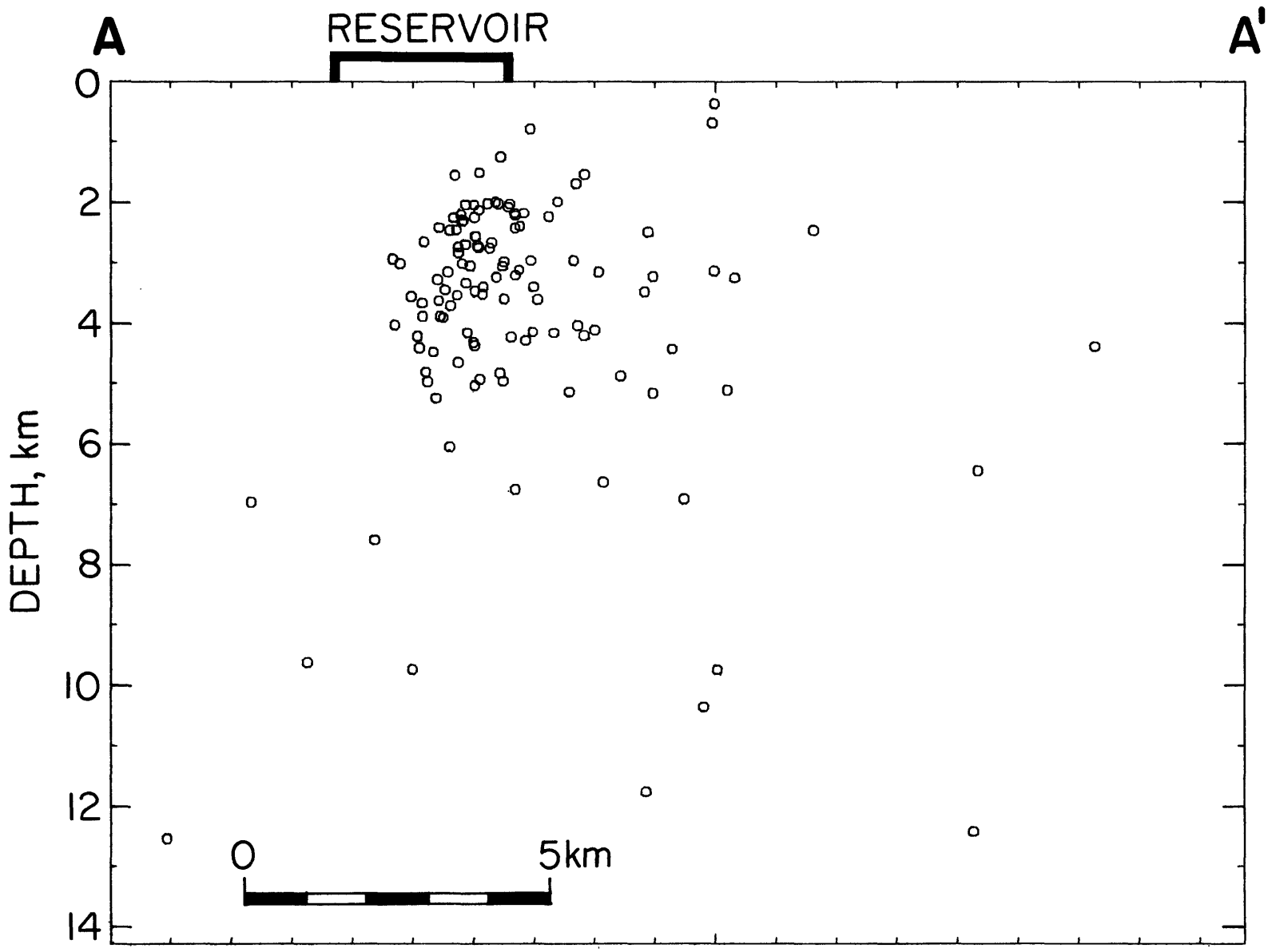

Figure 18: Cross-section along AA' in Figure 17. No vertical exaggeration. Earthquakes within 10 km of AA' are used in the cross-section. Events whose depth could not be constrained have been removed.

first exceeded a depth of 100 m (Figure 13), clearly indicate that this seismicity is reservoir-induced.

The activity near the dam and the more diffuse activity along the Naryn River downstream from the dam suggest the river course may be fault-controlled, supporting geological evidence for a reverse fault along the river canyon. Up to mid-1979, there has been no increase in seismicity where the Talas-Fergana fault crosses the reservoir, approximately 15 km upstream from the dam.

CONCLUSIONS

Toktogul Reservoir, due to its size, tectonic setting and proximity to major faults, was considered likely to produce induced seismicity during filling. The initial stage of filling to 100 m produced a burst of seismicity beginning October 1977 that continued until the rate of filling began to decrease in the fall of 1978. The epicenters form a linear trend along the strike of the Naryn River canyon, near the dam and the deepest portion of the reservoir. They are shallow (< 5 km), of low energy and have produced no damage. As the water level rises to its final height within the next several years, it will be critical to note any migration of this activity northward along the canyon. Any involvement of the Talas-Fergana fault, which may be in a state susceptible to failure, in the reservoir induced seismicity could present a significant seismic hazard.

ACKNOWLEDGEMENTS

This work was supported by the U.S. Geological Survey under contract USGS-14-08-0001-16844.

REFERENCES

Astaf'eva, Ye.G., A.I. Zakharova and others (1972). Earthquakes of Central Asia [in Russian]; in Earthquakes in the USSR in 1971, Moscow, Nauka, 52-93.

Burtman, V.S. (1960). The Talas-Fergana lateral displacement; Izv. Akad. Nauk SSSR, Ser. Geol., no. 12, 31-40.

Burtman, V.S. (1963). Talas-Fergana fault and San Andreas fault; in Faults and Horizontal Movements of the Earth's Crust, Akad. Nauk SSSR, Inst. Geol., Issue 80, 128-151.

Burtman, V.S. (1975). Structural geology of the Variscan Tien Shan; Am. J. Sci., 275-A, 157-186.

Burtman, V.S., A.V. Peive and S.V. Ruzhentsev (1963). The main strike-slip faults of the Tien Shan and Pamir; in Faults and Horizontal Movements of the Earth's Crust, Akad. Nauk SSSR, Inst. Geol., Issue 80, 152-172.

Caloi, P. and F. Peronaci (1948). The Turkestan earthquake of 2 November 1948 [in Italian]; Annali de Geofisica, 1, 246-252.

Ellsworth, W.L. (1975). Bear Valley, California, earthquake sequence of February-March 1972; Bull. Seism. Soc. Am., 65, 483-506.

Grin, V.P. (1964). The seismicity of the lower Naryn River basin [in Russian]; in Problems in the Regional Seismicity of Central Asia, Frunze, "Ilim", 34-48.

Jackson, J., P. Molnar, H. Patton and T. Fitch (1979). Seismotectonic aspects of the Markansu Valley, Tadjikistan earthquake of August 11, 1974; unpublished preprint.

Klein, F.W. (1978). Hypocenter location program HYPOINVERSE, U.S.G.S. Open File Report 78-094.

Kondorskaya, N.V. and N.V. Shebalin (1977). New Catalog of Strong Earthquakes in the USSR from Ancient Times to 1975 [in Russian]; Moscow, Nauka.

Kravchenko, K.N. (1979). Tectonic evolution of the Tien Shan, Pamir and Karakorum; in Geodynamics of Pakistan, Abul Farah and Kees A. DeJong, eds., Quetta, Geol. Surv. of Pakistan, 25-40.

Krestnikov, V.N., T.P. Belousov, V.I. Yarmilin, N.V. Chigaryov,and D.V. Shtange (1979). Quaternary Tectonics of the Pamir and Tien Shan [in Russian]; Moscow, Nauka.

Molnar, P. and P. Tapponnier (1975). Cenozoic tectonics of Asia: effects of a continental collison; Science, 189, 419-426.

Nalivkin, D.V. (1973). Geology of the USSR; Trans. by N. Rast, Toronto, Univ. of Toronto Press.

Nersesov, I.L., V.P. Grin and K. Dzhanuzakov (1960). Seismic Zoning of the Naryn River Basin [in Russian]; Frunze, Akad. Nauk Kirgiz SSSR, 176 pp.

Ni, J. (1978). Contemporary tectonics in the Tien Shan region; Earth Planet. Sci. Lett., 41, 347-355.

Rantsman, Ye.Ya. (1963). Quaternary horizontal movement along the Talas-Fergana fault; Akad. Nauk SSSR Doklady Earth Science Sections, 149, no. 3, 666-668.

Riznichenko, Yu.V., Ye.M. Butovskaya, A.I. Zakharova, M.G. Flenova and Kh.A. Atabaev (1975). Correlations of the elements of the seismic regime with inhomogeneities of the earth's crust in Eastern Uzbekistan [in Russian]; in Questions on Quantitative Analysis of Seismic Risk, Moscow, "Nauka", 73-81.

Rozova, E.A., K. Dzhanuzakov and V.G. Korolev (1968). Kirgizia; in Seismic Zoning of the USSR, S.V. Medvedev, ed., Moscow, Nauka, 335-346.

Shirokova, E.I. (1974). Detailed study of the stresses and fault planes at earthquake foci of Central Asia; Izv. Akad. Nauk SSSR, Fizika Zemli, no. 11, 22-36.

Tapponnier, P. and P. Molnar (1979). Active faulting and Cenozoic tectonics of the Tien Shan, Mongolia and Baykal regions; J. Geophys. Res., 84, 3425-3459.

Ulomov, V.I. (1973). Dynamics of the earth's crust in Central Asia and methods of investigation of horizontal movements; Academy of Sciences of Uzbek SSR, Inst. of Seismology, Information Rept. no. 81, 1-20.

Ulomov, V.I. (1974). Dynamics of the Earth's Crust in Central Asia and Earthquake Prediction [in Russian]; Tashkent, "FAN", 214 pp.

Wallace, R.E. (1976). The Talas-Fergana fault, Kirgiz and Kazakh, USSR; Earthquake Information Bulletin, 8, 4-13.

Yakubov, D.Kh., M.A. Akhmedzhanov and A.M. Borisov (1976). Regional Faults in the Interior and Southern Tien Shan [in Russian]; Tashkent, "FAN".

TEMPORAL VARIATION OF P-WAVE VELOCITIES IN NORTHERN CALIFORNIA

by

I. L. Nersesov, A. V. Nikolaev, E. N. Sedova and R. L. Wesson

Abstract

P-wave travel times of nuclear explosions in Nevada toward seismic stations in northern California have been studied. The small-scale fluctuations in δt travel time were statistically analyzed according to methods published elsewhere (1-3). Temporal anomalies found in the δt field, maybe due to structural changes in horizontal inhomogeneities in the Earth's crust or perhaps in the upper part of the mantle. The most significant variations in δt have a time correlation interval of about 15 days, and their areal extent is some dozens of kilometres. The σt standard value of δt is 0.15 s. for northern California, 0.04 s. for the Oroville region from Bolt's data (4), and 0.13 s. for the relatively small Bear Valley region. An estimate of 0.5% - 2% is obtained for the corresponding contrast in the time variations in P-wave velocity. These short-period variations compare with a more smooth change in the background, characterized by a correlation interval of 100-200 days, with a σt variation of 0.1 s. for California as a whole. A partial restoration of the fluctuation is observed in 500-700 days, which indicates rhythms in the variation of P-wave velocity and in the stress field in the Earth's crust. Some generalizations in the development of geodynamic processes can be made, on the basis of spatial and temporal variations in seismic velocities as observed at California stations from local and distant earthquakes, and from quarry and nuclear blasts.

Introduction

Currently, a large number of data indicate that the velocities of seismic waves and their ratios change significantly in the course of rather short periods of time--that, is several months to several years. These changes are especially noted before large earthquakes (References 1, 2, 5, 6, 7 and 8). In spite of this, it still has not become fully clear what are the basic characteristics of the process of velocity change--namely its areal extent, its contrast, and its characteristic periods.

Northern California appears as a region of high tectonic and seismic activity. It represents the edge of two lithospheric plates, the Pacific and North American plates, with relative motion along the San Andreas fault. Intense horizontal movements occur along this fault with consequent high seismic activity. The dense network of seismographic observations and high quality geophysical investigations, contribute to making this region uniquely suited for the investigation of temporal variation in propagation times and velocities of seismic waves and their connection with seismicity and other geophysical characteristics.

Investigations previously carried out in this region of the temporal variations in seismic velocity are not very conclusive and, in fact, have yielded contradictory results. Data on the propagation time of P-waves from quarry blasts, nuclear explosions from Novaya Zemlya and the Nevada test site to the Oroville region and to distant earthquakes have not demonstrated the existence of the effect at the accuracy level of the measurements (that is, about 0.05 seconds) (9,4, 2). In spite of this, the temporal variations of fluctuations in amplitude of waves from earthquakes from the region of Kamchatka

indicate changes in the elastic layers for waves penetrating the Earth's crust of California. In agreement with these amplitude variations are changes in the time of propagation carried out with somewhat smaller areas of individual measurements. Nonetheless, these can be elucidated through study of the temporal correlation of anomalies in the travel time of waves across a group of stations. This method has already made possible similar studies of small changes in the structure of the field of fluctuation of δt in the northern Tien-Shan and in the Garm regions. (Reference 3).

Data and processing

Our study is based on P-wave travel times from explosions in Nevada to recording stations in northern California. Figure 1 shows the stations that were involved: figure 2 shows the location of the individual explosions, and table 1 lists the details. For the 6-year time interval (1970 to 1976), the data from 32 explosions were used. As can be seen from figure 2, 22 explosions occurred in the southeastern part of the location area, and 10 occurred in the northwestern part: the entire zone in which the explosions were detonated is small. The maximum separation of the sources is 70 km, while the distances to the recording stations are in the 400-600 km interval. Only sharp, first arrivals of the P-wave were used which permitted the arrival time to be recorded with an error of not more than 0.05 s. Typical examples are shown in figure 3: in all, 663 records were used.

Of significant importance to our study is the possible dependence of T, the time intervals between explosions and Δ, the distances between their epicenters. These values are given in figure 4, distinction being made between explosion pairs from the southeast zone, the northwest zone and combined. There is a regular distribution of the ordinate for the entire time interval, except for the period 1300 days $< T <$ 2000 days, where the distance between sources in the southeast zone proved to be appreciably smaller than for T less than 1300 days. This fact should be kept in mind when considering the temporal variations in the wave characteristics in this time interval. It is clear that there is no correlation between Δ and T among the other data points.

We shall study the stability with time of P-wave travel time from the focus to the seismic station. Let t_{im} and t_{jm} be the travel times of the first arrival from the i-th and j-th sources to the m-th seismic station. The difference $\delta t_{ijm} = t_{im} - t_{jm}$ of these times is caused by the source location and the possible variation in seismic wave velocities in the medium during the time interval between the i-th and j-th explosions. This difference also includes the error in determining the first arrival time. To minimize this and to obtain a more stable estimate of the time difference for wave travel from the i-th and j-th sources, it was necessary to standardize the two-station residuals as

$$\sigma t_{ij} = \left(\frac{1}{M} \sum_m \left(\delta t_{ijm} - \frac{1}{M} \sum_m \delta t_{ijm} \right)^2 \right)^{1/2}$$

The summation is carried out for all M stations where signals from the i-th and j-th sources are clearly recorded. This method of processing is suitable only when the explosion time is exactly known. Its advantage is that the arrival times are recorded at the same stations, if not exactly, then with similar errors. During the calculations these errors, as well as station residuals are eliminated.

A second advantage of this method is that the foci and the stations form rather compact and well scattered groups with long distances between them. The azimuth interval from the group of foci toward the seismic station is about 35°: therefore

$$\Delta_{i1} - \Delta_{j1} \approx \Delta_{i2} - \Delta_{j2} \approx \cdots\cdots$$

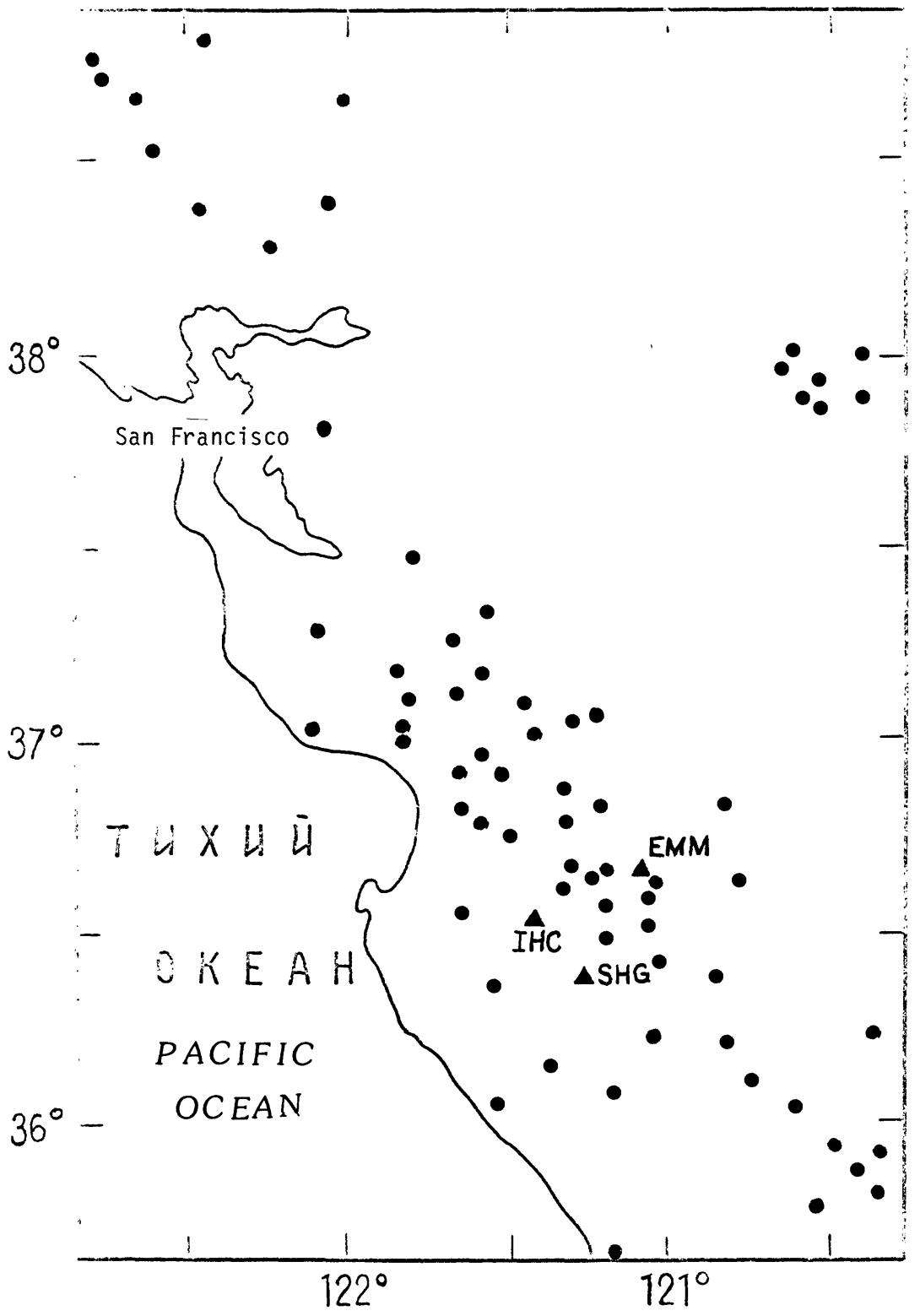

Figure 1 Schematic map showing distribution of seismic stations.

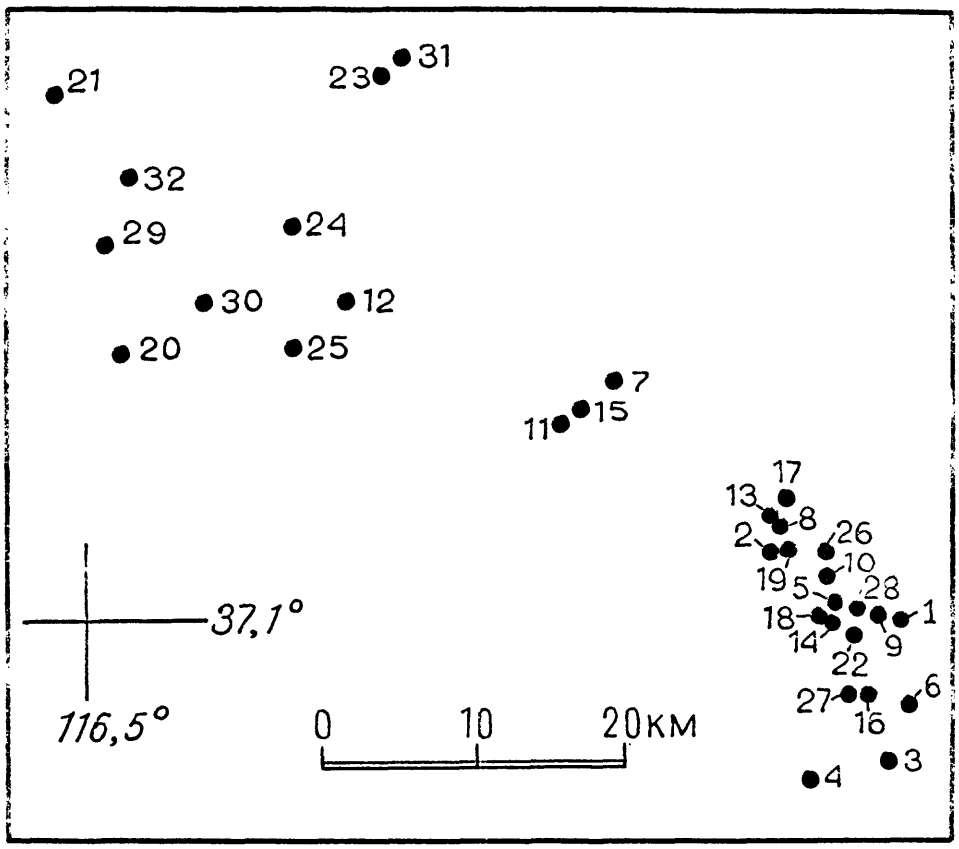

Figure 2 Epicenter map: numbers correspond to data in Table I.

Table 1 Listing of explosions used

Event	Date Day	Mth.	Year	Time Hr.Min.Sec	Latitude °North	Longitude °West	H	Magn. M	Number of arrivals
1.	16.	12.	70	16 00	37.100	116.008		5.1	
2.	17.	12.	70	16 05	37.128	116.083		5.7	13
3.	16.	06.	71	14 50	37.088	116.018		4.5	6
4.	23.	06.	71	15 30	37.021	116.066		4.5	13
5.	08.	07.	71	14 00	37.110	116.051		5.2	14
6.	19.	05.	71	17 00	37.065	116.001		4.9	6
7.	20.	07.	72	17 16	37.215	116.183		4.8	9
8.	21.	12.	72	20 15	37.140	116.083		4.8	12
9.	08.	03.	73	16 10	37.103	116.026		5.4	8
10.	26.	04.	73	17 15	37.123	116.058		5.8	8
11.	05.	06.	73	17 00	37.185	116.215		4.8	7
12.	06.	06.	73	13 00	37.245	116.345		5.9	60
13.	28.	06.	73	19 15	37.148	116.085		4.8	14
14.	27.	02.	74	17 00	37.105	116.053		5.4	17
15.	19.	06.	74	16 00	37.200	116.200		4.7	9
16.	10.	07.	74	16 00	37.068	116.032		5.6	29
17.	30.	08.	74	15 00	37.151	116.083		5.8	26
18.	28.	02.	75	15 15	37.106	116.056		5.6	32
19.	07.	03.	75	15 00	37.133	116.084		5.2	5
20.	14.	05.	75	14 00	37.220	116.473		5.8	18
21.	03.	06.	75	14 20 00.2	37.340	116.516	731	6.0	18
22.	03.	06.	75	14 40 00.1	37.095	116.036	637	5.6	11
23.	19.	06.	75	13 00 00.1	37.350	116.320	912	5.9	20
24.	24.	06.	75	12 30 00.2	37.279	116.370	1311	6.1	19
25.	20.	11.	75	15 00 00.1	37.220	116.370	817	6.0	33
26.	20.	12.	75	20 00 00.2	37.127	116.062	716	5.7	22
27.	04.	02	76	14 20	37.069	116.027		5.4	35
28.	04.	02.	76	14 40	37.107	116.088		5.6	26
29.	12.	02.	76	14 45	37.271	116.488		6.3	44
30.	14.	02.	76	11 30	37.242	116.420		5.7	58
31.	09.	03.	76	14 00	37.310	116.364		5.9	41
32.	14.	03.	76	12 30	37.306	116.472		6.3	45

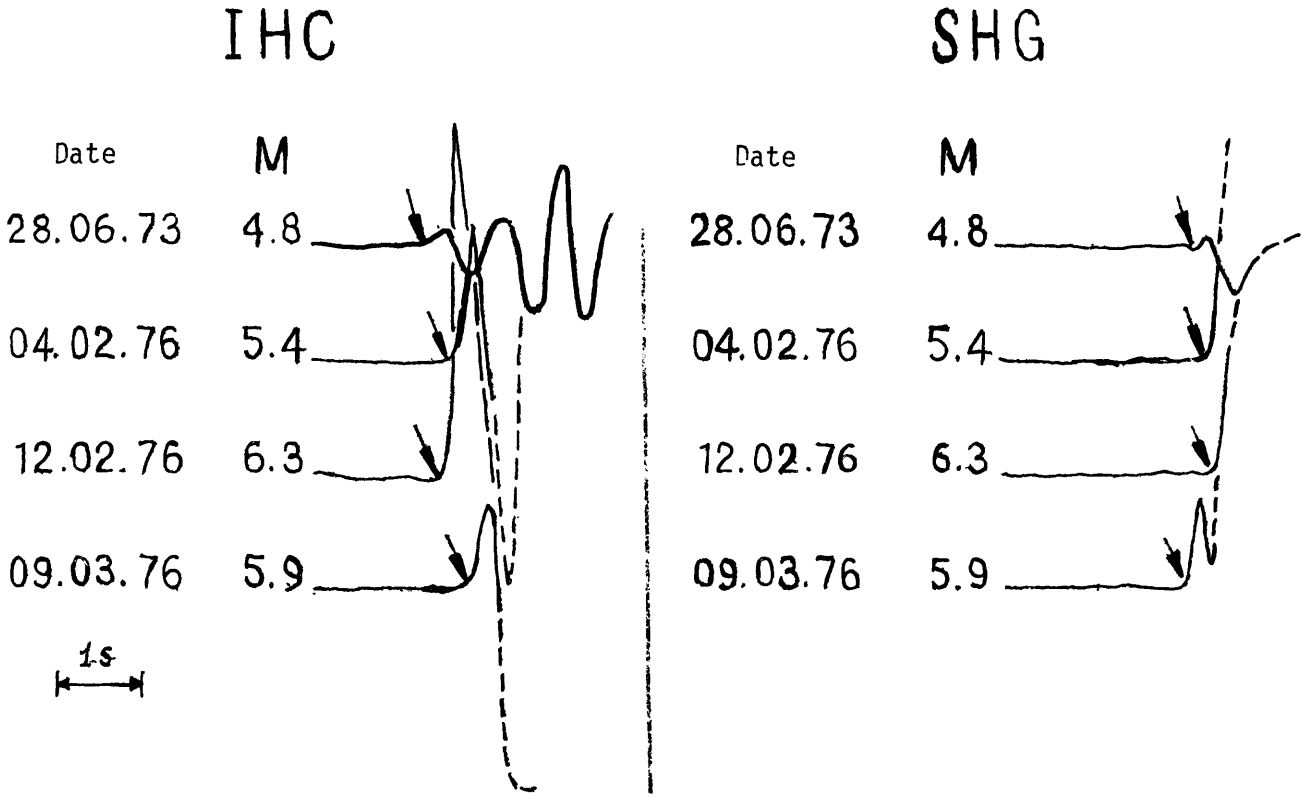

Figure 3 Examples of seismic records.

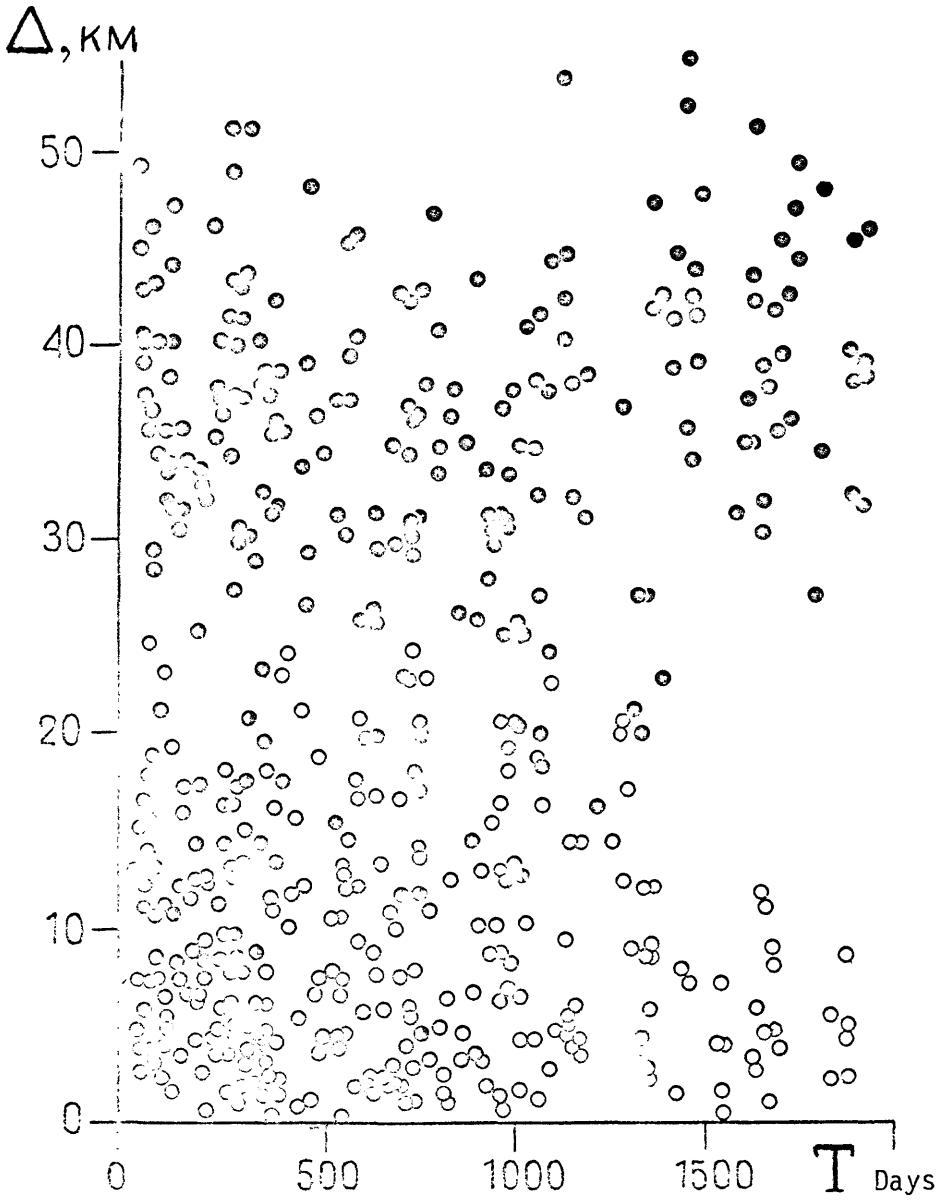

Figure 4 Relation of distances between epicenters and the time interval between blasts.

That is, the difference in epicentral distances between the i-th and j-th sources is approximately equal for all the seismic stations. Thus in the absence of temporal variations the following requirement must be met: the mean value of σt_{ij} for any combination of pairs of foci is approximately equal; in addition there is a comparatively small dependence of σt_{ij} on the epicentral distance. The methods described for analyzing the δt_{ij} fluctuation are suitable for studying the data on P-wave travel times to all the stations in central and northern California shown in figure 1.

The other method of investigating travel time anomalies is to analyze the differences in arrival time from the i-th source to pairs of seismic stations, the n-th and m-th ones $\delta t_{im} - \delta t_{in}$

This two station residual contains a stable part

$$\langle \delta\delta t \rangle_{m,n} = \frac{1}{I} \sum_{I} \delta t_{in}$$

where summation is carried out by all I-sources: its deviations result from measurement errors, the time variation in seismic wave velocities, and the dependence on the location of the focus. This latter value is negligible if the stations being compared are not far from each other.

We paid particular attention to three stations, EMM, IHC, and SHG, which are shown in figure 1. They are in the region of high seismicity and intensive displacement along the San Andreas fault. In this area a series of earthquakes occurred in February and March 1972. The most significant were on February 22 (M=3.5) and on February 27 (M=4.6). For eighteen months afterwards, a series of aftershocks occurred, as well as a general increase in microearthquake activity (16). The next noticeable event was the M=4.9 San Juan Batista earthquake of October 4, 1974, 40 km northwest of the array. Feb 24 (M=5.0)

The spacing between the stations chosen is 20 km and 30 kms, which, according to our experience of δt time fluctuations, should be sufficient to notice the difference in the travel time anomaly at individual points, and thus to determine any temporal trend in the two-station residuals.

$$t_{EMM} - t_{IHC}\ ,\quad t_{EMM} - t_{SHG}\ ,\quad t_{IHC} - t_{SHG}$$

These stations form a compact triangle: all three points are practically in one azimuth with respect to the foci. Thus any differences must be practically independent of the epicenter. The absolute difference in interstation residuals, the so-called "second derivative" or two-station/two-event residual (9), was then derived for each station pair of m and n stations.

$$|\delta\delta t_{m,n}(EMM, IHC)| = t_{n,EMM} - t_{n,IHC} - t_{m,EMM} + t_{m,IHC}$$

Mean values of the first derivative are eliminated during the "second derivative" calculation: thus the values obtained depend on only two factors--measurement inaccuracy and temporal variations in the seismic wave travel time.

Temporal variations of σt at stations in northern and central California

Temporal fluctuations in δt are supposed to be a stationary random process, and studies of temporal variations in seismic wave travel times are based on this assumption. The time differences for wave travel from the focus to the station will generally increase as the interval of time between actual basts increases. When this interval exceeds that of the time corrlation of the fluctuations, then the travel times approach some asymptotic value.

The graph in figure 5 shows the dependence of σt on the explosion time interval for stations in northern California. Data from the south-eastern and north-western platform

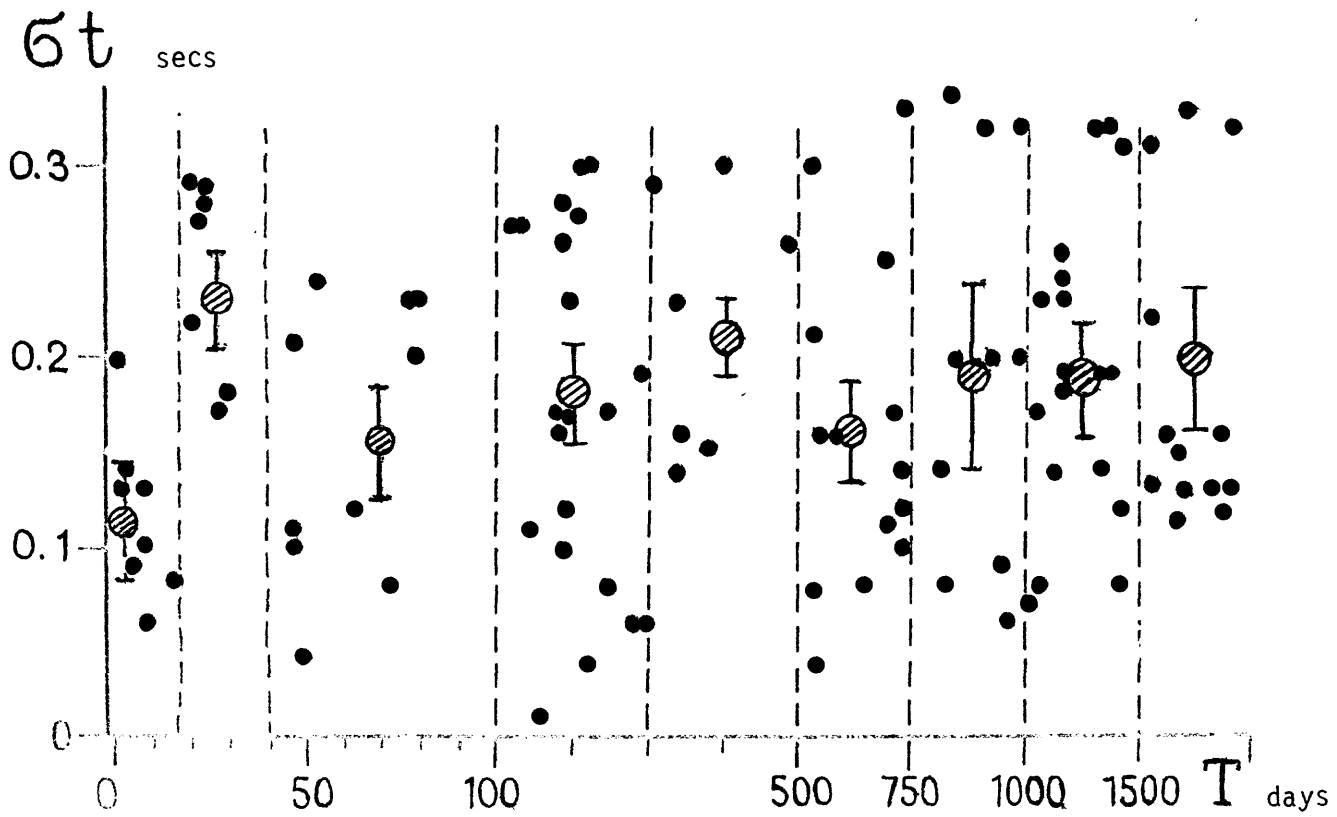

Figure 5 Relation of root mean square value of the time fluctuations of the P-wave travel time and the interval between blasts.

are marked by different symbols: data from foci pairs on different platforms were not processed. As can be seen from the graph, data from the most compact south-eastern platform are predominant. Mean values of σt were determined for unequal time intervals between events marked by the dotted lines: the vertical bars denote the standard deviation about each mean.

All the mean values are confined to a comparatively narrow range of 0.16-0.21 secs. Although their resolution is low, the following generalizations can be made about the mean value variations: an increase from 0.16 to 0.21 secs as T increases from 0-100 to 300-500 days; a decrease to 0.16 secs in the interval from 500-750 days; and then an approximately constant level of 0.18 to 0.20 secs is approached during the 750-2000 day interval. Such characteristics are in qualitative agreement with the results from studies of temporal variations in P-wave travel times from distant earthquakes recorded at seismic stations in the Northern Tien-Shan and Garm network, where σt graphs are generally of a similar appearance (3).

The individual points in figure 5 are distributed regularly in the range 0.04 to 0.32 sec. with no single point exceeding the value 0.34 sec: nevertheless several are near this limiting value. Such large values of σt indicate travel time changes, as they evidently exceed the limit of individual record errors as well as those caused by differences in epicenter (not more than 0.1s. for the southeast zone). It should be noted that those data points corresponding to $T > 1300$ days are typical of travel time differences between closely situated sources in the southeast platform (figure 2). In the absence of any decay in σt after $T \approx 1500$ days, one can see signs of an increase in the time changes in the fluctuations.

Comparatively weak variations in the σt mean values as T increase in the presence of large values of σt =0.2 to 0.3 secs, which exceed the natural limit denoted by measurement inaccuracy and by the effect of epicenter locations, can be explained by the presence of comparatively contrasting variations (of the order of 0.1 secs) and short-period variations of the seismic wave velocities for which the correlation interval ranges from several days to several tens of days. Furthermore, we can draw attention to the group of eight points in the range T = 0 to 15 days. Their center is at 0.11 secs., and the range in variation of σt is 0.06-0.20 secs. Thus the interval of the time correlation of the fluctuations is about 15 days, this short period component being the most intensive. If 0.11s. is considered to correspond to the $\langle \sigma t_N \rangle$ noise level associated with from the inaccuracy in determining the arrival time and the effect of the source, then the average level of the next group of data points where $\langle \sigma t \rangle$= 0.23s. will correspond to the effect of two independent factors. One is the temporal variation $\langle \sigma t_p \rangle$ and the other is noise $\langle \sigma t_N \rangle$. The temporal variation is calculated from the equation:

$$\langle \sigma t \rangle^2 = \langle \sigma t_p \rangle^2 + \langle \sigma t_N \rangle^2 = (0,23)^2 s^2$$

By this means $\langle \sigma t_p \rangle$= 0.20s. This is a comparatively high value that exceed the amplitude of the slow fluctuations for T 100 days. The maximum change, corresponding to the values of $\langle \sigma t \rangle$ = 0.23s. for T=300-500 days and $\langle \sigma t \rangle$ 0.16s. for T = 500-750 days, depends on the time anomaly, whose root mean square value is $(0.21^2 - 0.16^2)^{1/2} = 0.15$. This time anomaly depends on partial restoration of the δt fluctuation field in 500-750 days, that is, with the cyclic component of the change.

Temporal variations in $\delta\delta t$ in the Bear Valley region

In figure 6 are plotted the centered values of the second derivative of the travel time from pairs of the stations EMM, IHC and SHG: the pair IHC-SHG has the most complete

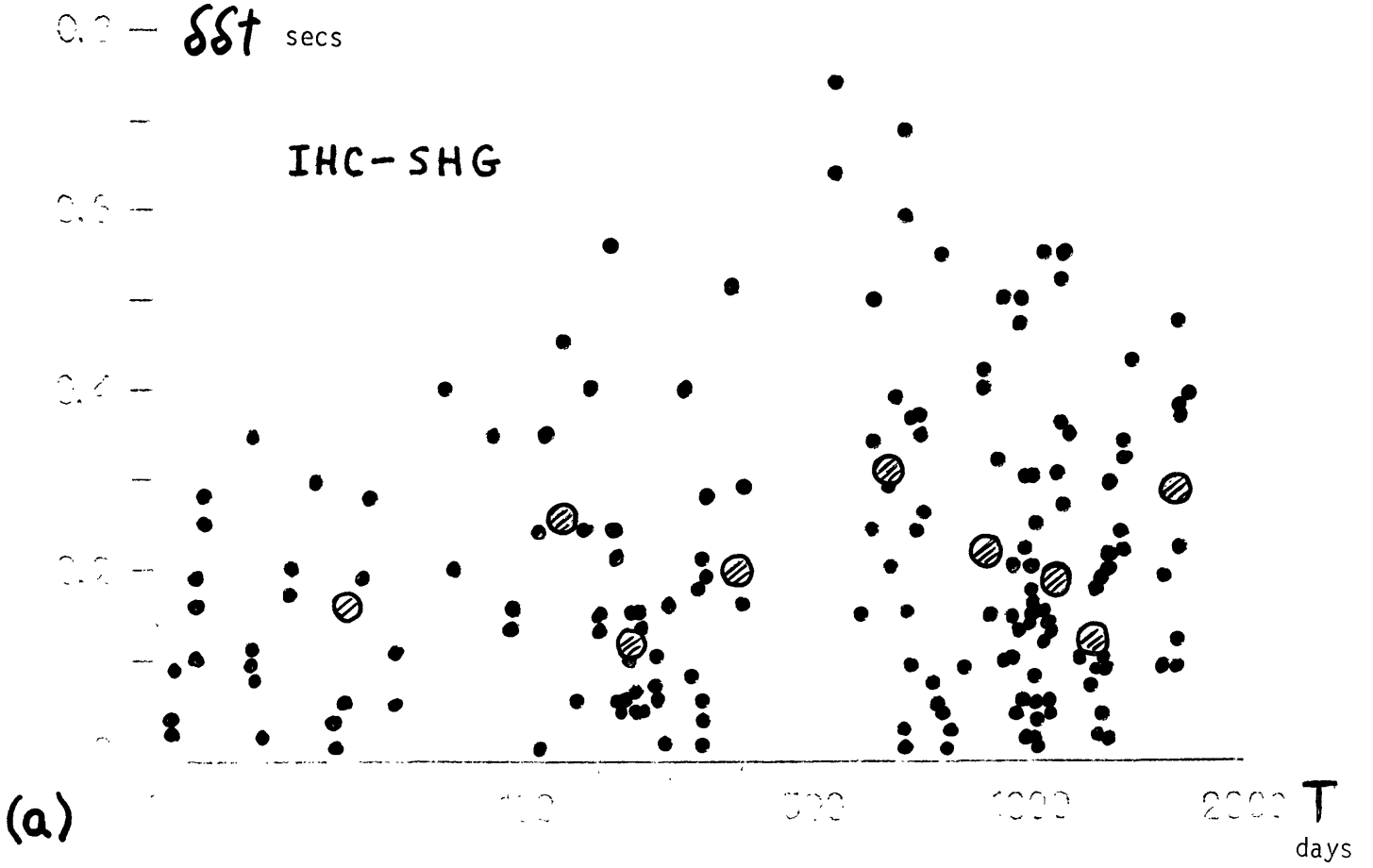

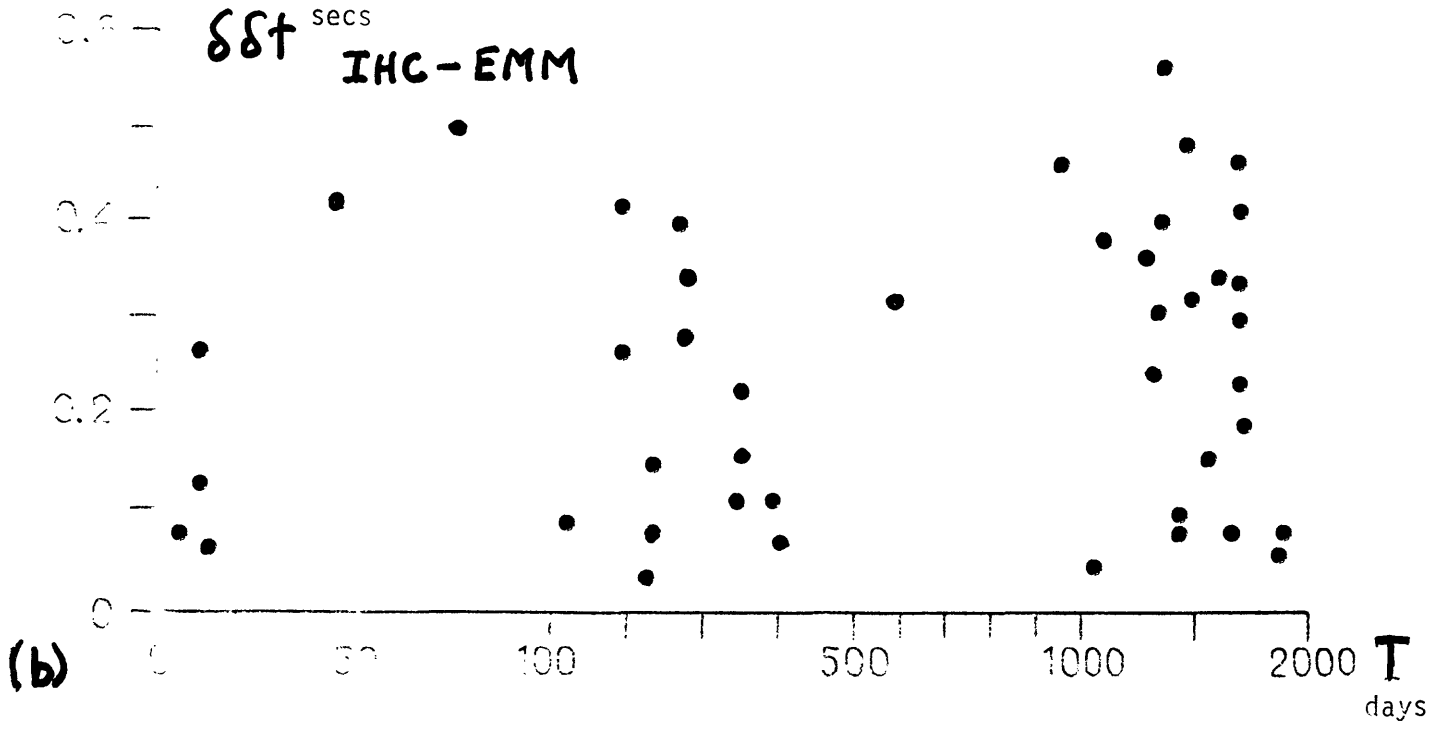

Figure 6 Relation of second derivative to the time interval between blasts (a) stations IHC-SHG (b) IHC-EMM (c) EMM-SHG and (d) overall graph.

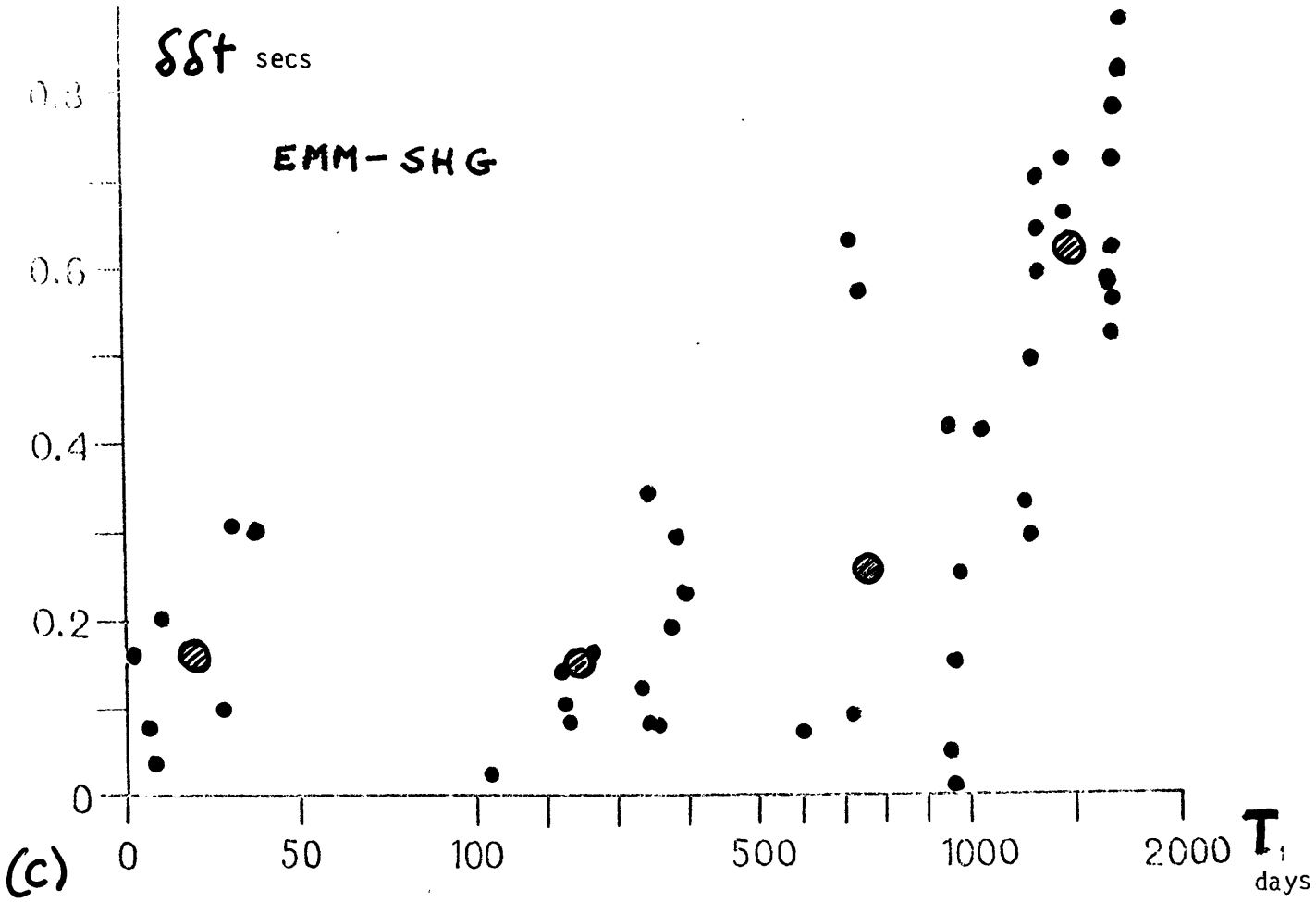
δδt secs
EMM-SHG
0.8
0.6
0.4
0.2
0
0
50
100
500
1000
2000
T
days
(c)

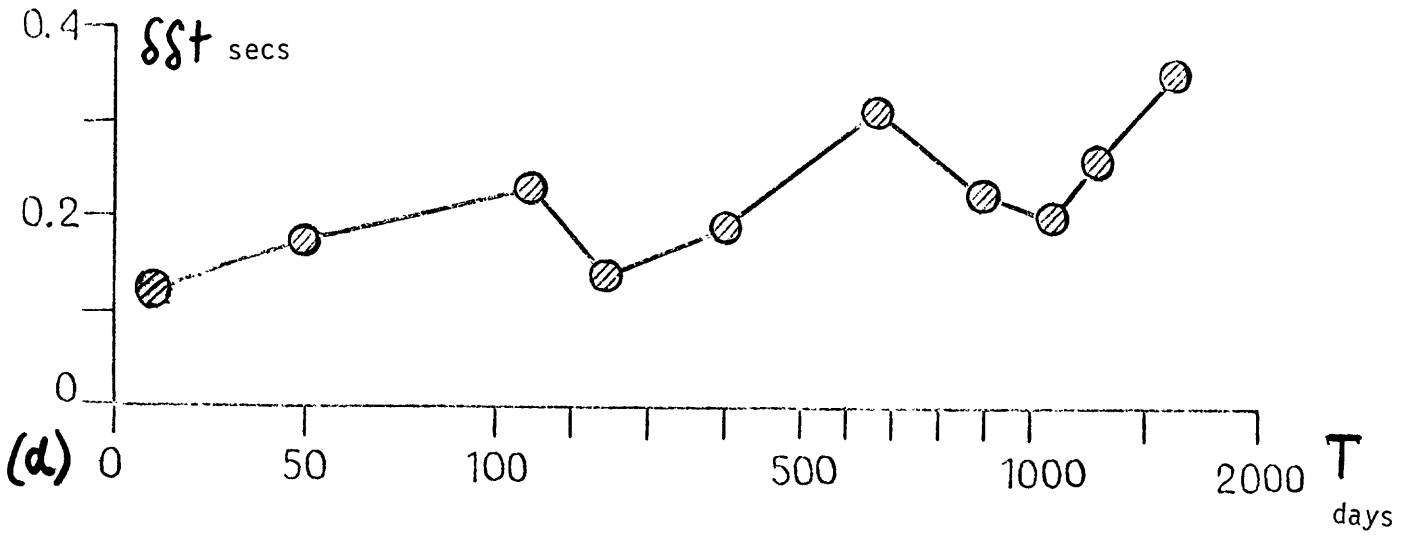
0.4
δδt secs
0.2
0
0
50
100
500
1000
2000
T
days
(d)

data set (figure 6a). The special feature of this group of points is the comparatively narrow range in variation over the interval of T up to 100 days, for which $|\delta\delta t| \approx 0 - 0.4$s. For T up to 500 days, the upper limit of $|\delta\delta t|$ rises to 0.8s, and then falls to 0.45s for T= 2000 days. Mean values are at about 0.2s., corresponding to σt level in northern California (figure 5). The increase after T = 500-1000 days, the subsequent decay and increase can be correspondingly identified in Figure 5, although here they are shifted to the left. Comparatively low values of $\delta\delta t$ =0.14s. with explosion time intervals of up to 15 days should be noted.

Figure 6b corresponds to the station pair IHC-EMM, and contains a comparatively small number of points. The mean value increases from 0.19 to 0.28 when T changes from 0-500 to 500-2000 days. For small values of T (0-15 days), values of $\delta\delta t$ are not large: the mean of the four available values is 0.13s and this is in good agreement with the pairs of IHC-SHG station data.

The same characteristics are noted for the station pair EMM-SHG (figure 6c). There are low values of $\delta\delta t$ for T=0 - 15 days (the mean is 0.12s.), followed by an insignificant increase in the range Δ =100-500 days, and a sharp growth of the $\delta\delta t$ values for T > 500 days.

The graph in figure 6d summarizes the features mentioned above. The $\delta\delta t$ anomalies have minimum values of 0.12s. for T=0-15 days and for the most part increase with increase of T. Characteristic features of this growth are a maximum to T=500-750 days, a decay to T=1000 days, and then a subsequent rise.

A variation in the absolute values of the second derivative of the time anomalies generally has the same format as the change in the root mean square value of the differences in travel time to the individual stations in California: nevertheless the characteristic elements in the graph of Figure 6d are displaced with respect to the corresponding elements of Figure 5.

As in the previous case $\langle|\delta\delta t|\rangle$ is assumed to be 0.12s for the interval T=0-15 days, and corresponds to the noise level. The contrast of this short period variation is found to be $(0.18^2-0.12^2)^{1/2}=0.13$s. Temporal variation in the fluctuations $(0.30^2-0.18^2)^{1/2}=0.24$s., corresponds to $\langle|\delta\delta t|\rangle=0.30$s, which is shown on the graph for T $\approx$ 1000-2000 days. This value significantly exceeds that observed for stations in central and northern California, that is, σt =0.15s despite the fact that the second derivative variations from a small base of records should be less than those of the root mean square: in practice they do not depend on the location of the focus and the accuracy in measuring time of occurrence. Centering the $\delta\delta t$ values eliminates the station residuals which are associated with the upper part of the profile. Thus time variations of the second derivative at the three stations chosen proved to be of more contrast than the first derivative variations at a large number of central and northern California stations, despite the fact that on the average, σt should apparently be greater than $\langle|\delta\delta t|\rangle$. This is due partly to the fact that data on the first derivatives (figure 5) are the product of data averaging from a group of stations, some of which do not reveal noticeable time anomalies in the δt behavior. Individual values of δt at the three stations chosen proved to be very variable: this might be due to the comparatively high seismic activity in the Bear Valley region, and by the three earthquakes that occurred there in February 1972.

Temporal variations of $\delta\delta t$ in the Oroville region

For the period 1970-1976, Bolt (4) investigated the behavior of P-wave travel for

explosions in Nevada to seismic stations at Oroville (ORV) and at Jamestown (JAS) in connection with the earthquake sequence in the Oroville region (the main event, M_L =5.7 occurred on 1 August, 1975). Bolt's list of events and those used in this study (Table 1) are very similar. According to the corrected travel times at ORV and JAS given in (4), we have calculated the second derivative for the i-th and j-th earthquake pairs

$$\delta\delta t_{ij} = \delta t_i - \delta t_j , \qquad \delta t = t_{ORV} - t_{JAS}$$

Values of $|\delta\delta t|$ for the time interval between pairs of blasts are shown in figure 7. Individual values are averaged according to several intervals, and mean values are shown by the large circles. The change in these values with time follows a characteristic pattern. The minimum value of $\langle|\delta\delta t|\rangle$ is 0.55s. with $0<T<15$ days; there is then a smooth rise to the 200-300 day interval, after which there is a decay and approaches an asymptotic value beginning with T = 500-750 days.

Assuming, as before, that the $\langle|\delta\delta t|\rangle$ =0.55s. value corresponds to noise and the level of experimental error, we find that the 15 day temporal variation contrast is about

$$(0.068^2 - 0.055^2)^{1/2} = 0.039s \approx 0.04s$$

The maximum temporal variation contrast in the second derivative is

$$(0.11^2 - 0.55^2)^{1/2} = 0.095s \approx 0.1s$$

The standard deviation of $\langle|\delta\delta t|\rangle$ is not identical in the different ranges of T, and is about $\pm 0.01s$ which is considerably less than the variation range of these mean values. The monotonic nature of the variation of $\langle|\delta\delta t|\rangle$ as T increases also supports the validity of the derived pattern. The results obtained proved to be much larger than the estimation of the δt anomaly prior to the earthquake of August 1, 1975. The results refer to the background process and show that the method we used in systematizing the initial data permit us to uncover patterns which were not evident.

Temporal variations of σt in central and northern California

It is interesting to compare our results with those of Robinson and Iyer (9), who studied temporal changes in the P-wave travel time from eight distant events during the period 1969-1975. After analyzing the records from more than 100 stations in northern California these authors concluded that there were no noticeable temporal variations exceeding the recording time error of ± 0.1s.

In discussing these data we first calculate the P-wave arrival-time anomalies for each station, and average their squares for each pair of events, that is, determine the σt value. The results are given in Table 2.

Table 2

Values of σt (in sec) for California seismic stations according to distant event data (9)

Event date	2	3	4	5
1. 14 Oct 1970	0.024	0.053	0.037	0.052
2. 27 Apr 1971		0.047	0.038	0.053
3. 28 Aug 1972			0.046	0.040
4. 12 Sep 1973				0.051
5. 29 Aug 1974				

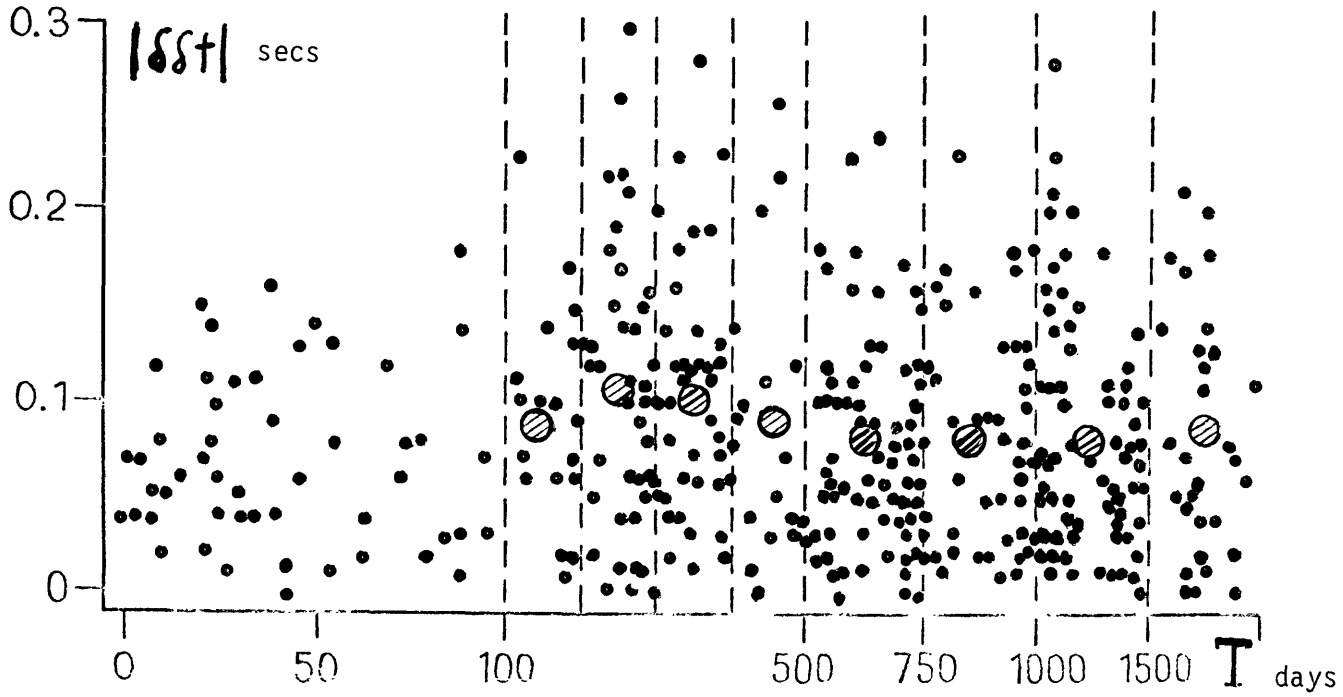

Figure 7 Relation of second derivative to the time interval between blasts for the Oroville region.

Those values of σt below a vaule of 0.45s and those above (underlined) are arranged in the table as if the medium were inhomogeneous and the travel time anomalies in 1972 and 1974 were of one type while those in 1970, 1971 and 1973 belong to another category. Values of σt corresponding to explosion pairs from only one of these two groups do not exceed 0.45s., whereas for combined pairs, for example, 1972-1973, the values exceed 0.45s. Thus the medium seemed to be in one state in 1970 and 1971, another state in 1972, returning to the first state in 1973, and then reverting to the second state again in 1974. The mean value of σt corresponding to explosions that occurred during the first and second states of the medium equals 0.035s and for the first and second states is 0.05s. Here we find that the temporal variations in the spatial travel time anomalies is $(0.05^2-0.035^2)^{1/2}=0.035$s. The correlation interval of the time fluctuations is about a year, with a periodicity of two years: this is in quantitative agreement with the data on nuclear explosions from Nevada (σt is a minimum in 350-500 day interval of figure 5). The 0.035s. amplitude of the anomaly is significantly less than that according to data from the Nevada explosions. This may be due to differences in the seismic ray paths: for distant sources, these pass through the earth's curst and upper mantle at angles close to the vertical, while rays from near-field sources in Nevada reach comparatively shallow depths $\sim$ 100 km., and approach the surface at shallow angles. Temporal variations seem to take place mainly in the upper medium; therefore waves from distant sources undergo less change than those from near sources.

Discussion

The question of temporal variations in seismic wave velocities was first put forward by the Japanese seismologist Imamura: he studied the apparent velocities of seismic waves at four seismic stations near Tokyo from eight local earthquakes that occurred from 1895 to 1898. The apparent velocity differences were explained by him as the result of both differences in epicenter position (the epicenters were separated by from 60 to 450 Km over an azimuth sector 50° to 315°), and velocity changes in the Tokyo region before the earthquakes occurred on August 10, 1898. Imamura termed this method ("seismic triangulation"), and he first used the term "seismic epoch," the field or hodograph conditions at a definite moment in time. In Imamura's data it is difficult to see any of the supposed effects, that were later interpreted by Kovesligethy (11) in terms of seismic hysteresis.

Later studies using different methods in different regions showed the existence of temporal velocity variations, but the data listed were not always clear and to a large extent were contradictory.

Table 3 summarizes the temporal variations in travel time (standard variations in σt, mean of the absolute value of the second derivatives of $\langle|\delta\delta t|\rangle, \delta t$ time residuals) determined by different authors from data on earthquakes and explosions both in small, individual regions, and in the whole of southern and central California. The duration of the temporal anomaly and the depth interval for a corresponding velocity anomaly, in particular, were determined very approximately. A considerable part of determining anomalies in travel time and rates of occurrence belongs to the period of time preceding a strong earthquake (Oroville, San Fernando, Parkfield and others). Therefore the appropriate measurements are concentrated at a small number of stations registering waves that pass through the focal region. Time anomalies identified by such investigations ought to show the most contrast.

Data from Table 3 on the temporal anomalies of δt, σt and $\langle|\delta\delta t|\rangle$ are shown in figure 8 as a function of the depth interval over which the anomaly occurs. These

Table 3 Data on the time anomalies in travel time of volumes waves

Location	Type of source	Frequency (Hz)	Parameter	Anomaly magnitude	Depth interval	Typical dimension (km)	Duration (days)	Remarks
Northern California Oroville								
Bolt. Ref 4	Nevada Test Site (NTS)		δt	<0.05	crust	<180		Anomaly prior to M=5.7 Aug. 1, 1975
Cramer Ref 13	Distant earthquake	1	δt	<0.05				
	Distant nuclear blast	1	$\delta\delta t$	0.1	crust	>10	365	Anomaly prior to M=5.7 Aug. 1, 1975
	NTS	3	δt	0.1	crust	10		Residual anomaly after eq.
Present study and Ref. 4	NTS		$\delta\delta t$ $\delta\delta t$	0.055 0.10	crust crust	180	15 100	Background process
Central California								
Present study	NTS	3-5	σt	0.20 0.15	crust crust	20-200 20-200	15 500-700	Background process
Robinson Ref 9	Distant nuclear blast	1	σt	± 0.05	crust	20-30	400-1500	Background process
Present study	NTS	1	σt	0.035	crust	20-200	730	Background process
Aki. Ref 2	Distant earthquake	1	σt	0.02	crust	20-30	365-730	Background process

Location	Type of source	Frequency (Hz)	Parameter	Anomaly magnitude	Depth interval	Typical dimension (km)	Duration (days)	Remarks
Parkfield								
Boore. Ref 20	Distant earthquake	1	δt	2	crust	20		Background process
	Local earthquake	5	δt	0.2	0-10	20		Before M=5.5 eq. 28 June 1966
		5	δt	0.25	crust	20		Before M=5.5 eq. 28 June 1966
	Quarry blasts	5	δt	0.15	0-10	20		Before M=5.5 eq. 28 June 1966
Stone Canyon								
Clymer Ref 17	Vibroseis	10-20	σt	10^{-3}	0-3	3	Hours	Background process
			σt	$1\text{-}3\times10^{-3}$	0-3	3	Days	
			σt	10^{-3}	0-3	3	Months	
			δt	10^{-3}	crust		Years	
			δt	$2\text{-}3\times10^{-4}$	crust		12 Hours	
Bear Valley								
Robinson Ref 21	Local earthquake	5-10	δt	0.3	0-5	>5	60	Anomaly prior to M=5.0 eq. Feb. 24, 1972
Cramer Ref 22	Distant earthquake	1	$\delta\delta t$	0.15	0-10	5-10	30	Bear Valley
This study	NTS	3-5	$\delta\delta t$	0.15	crust	20-30	15	Background process
	NTS	3-5		0.24	crust	20-30	1000	

Location	Type of source	Frequency (Hz)	Parameter	Anomaly magnitude	Depth interval	Typical dimension (km)	Duration (days)	Remarks
San Juan Batista								
Robinson Ref 21	Local earthquake	10	$\delta\delta t$	0.3	0-10	>5	120	Anomaly prior to M=4.9 eq. 4 Oct, 1972
McEvilly Ref 12	Quarry blasts	5	δt δt_s	0.1 0.3	0-5 0-5	>10		Background process
Cramer Ref 22	Distant earthquake	1	δt	1	crust	>20		Background process
Ellsworth Ref 18	Quarry blast	10	δt	0.05	0-5	>10	90	Background process
Southern California								
Whitcomb Ref 23	Local earthquake	5	$\delta (t_p/t_s)$	0.15	0-10	>10	1300	Anomaly before San Fernando eq. 9 Feb. 1971
			δV_p	(-0.19)÷(+0.08)	0-10		1300	
			δV_s	(-0.1)÷(+0.5)	0-10		1300	
Stewart Ref 24	Distant earthquake	1	δV_p	± 0.5	crust	>5	180	Prior to M=6.9 Point Mugu eq. 21 Feb. 1973
	Local earthquake	5	δt	-0.3	0-10	~ 10	500	Prior to M=6.9 Point Mugu eq. 21 Feb. 1973

Location	Type of source	Frequency (Hz)	Parameter	Anomaly magnitude	Depth interval	Typical dimension (km)	Duration (days)	Remarks
Kanamori Ref. 25	Tunnel blasts	5-10	$\delta\delta t$	0.2	0-5	>10	Several months	Background process
Kanamori Ref.27	Tunnel blasts		$\delta\delta t_s$	0.3			60-150	Background process
Kanamori Ref. 26	Tunnel blasts		$\delta\delta t$	0.1-0.2		30	365	Background process
Nevskiy (this volume)	Quarry blasts	5-10	$\delta\delta t$		0-10	>10	365	Background process

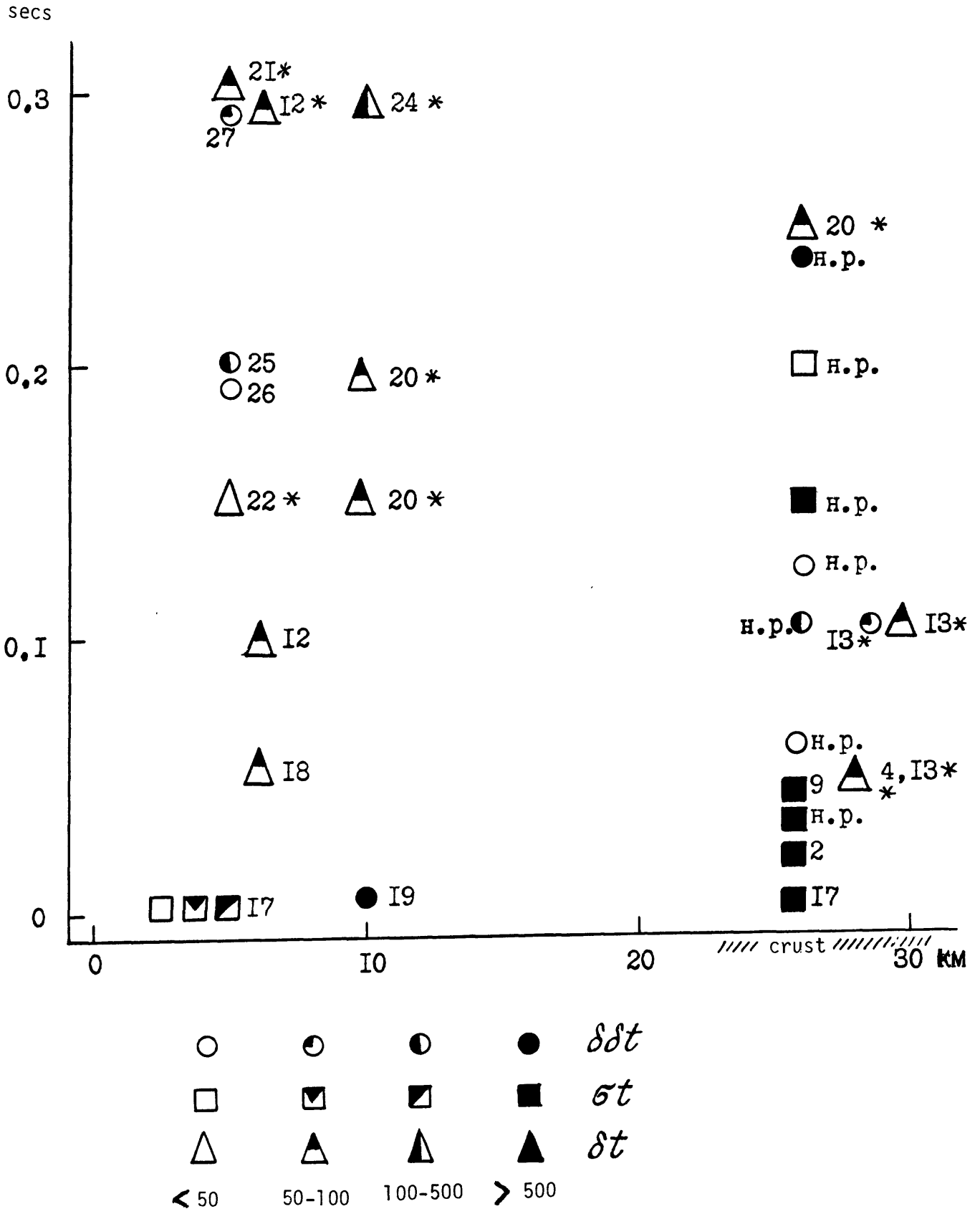

Figure 8 Values of the time anomalies $\delta\delta t$, σt and δt as a function of layer thickness. Numbers on the symbols indicate the references from which data were taken. Hp = present study. * = data from studies associated with earthquake prediction. Duration of anomaly in days also shown.

characteristics change in the time range 0 to 0.3s., values being concentrated near the higher end of the range: thus the value 0.3s. may be considered to indicate the upper limit of the time variations.

Anomalies which are forerunners of strong earthquakes show more contrast than those from background earthquakes. This can be explained by the uneven spatial distribution of the time anomaly contrast and by differences according to the way in which the initial data is chosen. These explanations also apply to differences within the two major groups of observations - for individual anomalies and for the background process. Large temporal anomalies in the travel time from distant earthquakes of up to 0.5s. have been identified by A. G. Prosorov from observations at many seismic stations in the Soviet Union, and in the WWSSN, LASA and NORSAR arrays (15).

These results are not supported by the observational data on travel times from earthquakes and nuclear explosions obtained in this or other studies (2, 3, 10, 13). One reason is apparently that the seismic sources were not divided into individual regions, and thus the grouping of foci reflects both the temporal effect and the ratio of the travel-time anomalies from the epicentral region.

The character of the time anomalies of P-wave velocities, their size, spatial dimensions and distributions, can be estimated in only a preliminary fashion. The predominant horizontal dimension corresponds approximately to the horizontal dimension of the time anomalies given in Table 2. To determine the velocity anomaly, the vertical dimension, that is, the depth of the anomaly layer, must be considered. The data in Table 3 are based on very rough estimations. The designation "crust" means that the anomaly is simply located in the crust and not necessarily spread throughout its entire thickness. Temporal variations are most probably concentrated in the upper 10 to 15 km layer characterized by high seismicity. In this case, time velocity anomalies of $\delta V \approx 0.5$ km/s., that is, about 10-15%, will correspond to maximum values of $\delta t \approx 0.3$s. The possibility that velocity anomalies ranging from a few tenths of a percent to one percent might arise, is confirmed by direct observations of t_p/t_s in California (23) and in other regions by measurements of velocity anomalies of volume waves before strong earthquakes (5, 6, 7, 8, 23, 24).

On the other hand, there is evidence in the data that the thickness of the layer involved in temporal variations is considerably greater, including the whole of the crust and perhaps the upper part of the mantle. The estimates of the time anomaly contrast from the second derivatives obtained from a large number of central and northern California stations using our data and that of Robinson and Iyer data show differences of 0.035s and 0.24s. If the corresponding velocity anomalies were located in the upper 10-15 Km layer of the crust, the σt value corresponding to the Nevada explosions would be less, of the order of 0.035s; in both cases, seismic waves pass through the upper part of the crust at steep angles and should therefore be exposed to similar variations.

The waves from the Nevada region travel in a 100 km thick section of the crust and upper mantle for the main part of their path. At the same time, teleseismic P-waves travel through this section at comparatively shallow angles, their path being approximately three times as short as for near earthquakes. These are the main differences in the seismic wave propagation paths. The other fact that influences whether temporal effects are revealed at the surface, is the degree of inhomogeneity in the spatial distribution. In California, it is likely that faults will control temporal inhomogeneity. Although there is no definite information on the depth of the San Andreas fault system, its influence is considered to extend to a great depth, and is expressed as anisotropic velocity anomalies, whose vertical dimensions are greater than

their horizontal (29). Thus on path intervals of equal distance, seismic waves propagated in the upper 100 km layer from Nevada to California encounter a larger number of inhomogeneity contrasts than do teleseimic waves. This feature, time variations in a relatively thick layer as much as 100 km thick, appears to be a characteristic feature of the background process, and not of the individual space-time anomalies associated with impending strong earthquakes. Indirect confirmation of this can be seen in the common character of the time variation in the travel-time anomalies throughout central and northern California. Thus the horizontal dimension of this homogeneous feature must be similar to its vertical extent.

It appears that rhythmic changes in the time anomaly contrast are significantly weaker in California than in the northern Tien-Shan and in the Garm region. Moreover the tendency towards a decreasing anomaly contrast for one, and two to five year intervals, is observed in both regions. The 15-day anomaly correlation interval that we have observed, perhaps occurs in other regions too: as yet it has not been identified because other studies have used earthquakes separated by too large a time interval. The data of Clymer and McEvilly (17) on the time scale of velocity changes are in quantitative agreement with our data. Moreover one should also not expect a more complete conformity of the intensity values of the time variation, since the results from these authors' VIBROSEIS method relate either to the uppermost part (0-3km) of the profile or to the entire earth's crust and describe a very small segment of the order of 10 km.

From a methods point of view, an important result of Clymer and McEvilly's work is the possibility for precise control of seismic wave velocities in time and space by means of a weak, transient source. As calculated from earthquake and explosion studies, temporal variations in a medium are a complex process where two components can be distinguished. This can be achieved by studying the travel-times of P and S waves from a large number of local and distant transient seismic sources. Nevertheless there is great promise for such active experiments that are carried out to study the time inhomogeneity.

References

1. I. L. Nersesov, A. V. Nikolayev. Time variation in the structure of the teleseismic P-wave at the Garm prediction polygon. Doklady AN SSR, v. 232.

2. K. Aki, I. L. Nersesov, Ye N. Sedova, D. D. Shaymer. Time variations in the amplitude fluctuations and travel times of the teleseismic P-wave at the Garm, California, LASA and NORSAR arrays. Collection of Soviet-American studies in earthquake prediction. vol 1, Book 1, "Donish," Dushanbe, 1976.

3. N. I. Kim, A. V. Nikolayev. Character of time changes in the fluctuations of teleseismic P waves in Northern Tien-Shan. Doklady AN SSSR, 1978.

4. B. A. Bolt. Constancy of P travel times from Nevada explosions to Oroville Dam station, Bull. Seismol. Soc. Amer., v. 67, no. 1, 1977.

5. I. L. Nersesov, A. N. Semenov, I. G. Simbineva. Space-time distribution of the ratios of travel times of longitudinal and transverse waves in the Garm region. In: "Eksperimental'naya Seysmologiya," Moscow, Nauka, 1971.

6. N. A. Dolbilkina, V. I. Myachkin. Variations in travel times of longitudinal seismic waves in the focal zone near the shores of Kamchatka. In: "Seismic studies in focal zones," Moscow, Nauka, 1976.

7. Y. P. Aggarval, L. R. Sykes, D. W. Simpson, P. G. Richards. Spatial and temporal variations in t_s/t_p and in P wave residuals of Blue Mountain Lake, New York: application to earthquake prediction. Journ. Geophys. Res., v. 80, no. 5. 1975.

8. M. Wyss. Precursors to the Garm Earthquake of March 1969. Journ. Geophys. Res., v. 80, no. 20. 1975.

9. R. Robinson, H. M. Iyer. Temporal and spatial variations of travel-time residuals in Central California for Novaya Zemlya events. Bull. Seismol. Soc. Amer., v. 66, no. 5, 1976.

10. L. V. Antonova and others. Experimental seismic investigations of the Earth's interior. Moscow. Nauka, 1978.

11. R. Kovesligethy. Sur l'hystersis seismique. Math. and Naturwiss. Berichte aus Ungarn. B.26, H.3, Leipzig, 1908.

12. T. V. McEvilly, L. R. Johnson. Stability of P and S velocities from Central California quarry blasts. Bull. Seismol. Soc. Amer., v. 64, no. 2 1974.

13. C. H. Cramer, C. G. Bufe, P. W. Morrison. P-wave travel-time variations before the August 1, 1975, Oroville, California earthquake. Bull. Seismol. Soc. Amer., v. 67, no. 1, 1977.

14. M. V. Kulagima, A. V. Nikolayev. Study of time variation in the Nurek region. In: "Physical processes in the source region." Nauka, in press.

15. A. G. Prosorov. Systematic variations of mean travel-time residuals in space and time. Pure and Appl. Geophys. Vol. 115, 1977.

16. W. L. Ellsworth. Bear Valley, California, earthquake sequence of February-March 1972. Bull. Seismol. Amer., v. 65, no. 2, 1975.

17. R. Clymer, T. V. McEvilly. Measured changes in crustal P-wave travel times. Earthquakes Notes, v. 49, no. 1. 1978.

18. W. L. Ellsworth. Variations of elastic wave velocity near earthquakes: theory and observations. In press.

19. M. V. Nevskiy, I. L. Nersesov, A. G. Lindh and S. Ashmoll. Analysis of the temporal variations of the residual of Pg waves from quarry blast data in central California. 1981. This volume.

20. D. M. Boore, A. G. Lindh, T. V. McEvilly, W. W. Tomashoff. A search for travel-time changes associated with the Parkfield, California earthquakes of 1966. Bull. Seismolog. Soc. Amer., v. 65, no. 6, 1975.

21. R. Robinson, R. L. Wesson, W. L. Ellsworth. Variations of P-wave velocity before the Bear Valley, California earthquake of 24 February 1972. Science, v. 184, no. 4143, 1974.

22. C. H. Cramer, R. L. Kovach. Time variations of teleseismic residuals prior to the magnitude 5.1. Bear Valley earthquakes of Febrary 24, 1972. Pure Appl. Geophys., v. 113, 1975.

23. J. H. Whitcomb, J. D. Garmany, D. L. Anderson. Earthquake prediction: variation of seismic velocities before the San Fernando earthquake. Science v. 180, 1973.

24. G. S. Stewart. Prediction of the Pt. Mugu earthquake by two methods. Proceed. Conf. Tectonic Prob. San Andreas Fault System., Stanford Univ., Calif., 1973.

25. H. Kanamori, W. J. Chung. Temporal changes in P-wave velocity in Southern California. Tectonophysics, v. 23, no. 1/2, 1974.

26. H. Kanamori, G. Fuis. Variations of P-wave velocity before and after the Galway Lake earthquake (M=5.2), California, June 1, 1975. Trans. Amer. Geophys. Union, v. 56, no. 12, 1975.

27. H. Kanamori, D. Hadley. Crustal structure and temporal velocity change in Southern California. Pure Appl. Geophys., v. 113, 1975.

28. K. Aki. Three dimensional seismic velocity anomalies in the lithosphere: Method and summary of results., Journ. of Geophys. Res. v. 43, no 1/2, 1977.

(page 167 follows)

ANALYSIS OF THE TEMPORAL VARIATIONS OF THE RESIDUALS OF Pg WAVES FROM QUARRY BLAST DATA IN CENTRAL CALIFORNIA

by

M. V. Nevskiy, I. L. Nersesov, A. G. Lindh and S. Ashmoll

During recent years temporal variations of the characteristics of wave fields have been studied intensively in investigations of the problem of earthquake prediction. The main goal of these studies is the discrimination of the precursors of strong earthquakes both on the basis of current observations, for the purposes of practical forecasting, and in a retrospective plan for the purpose of developing physical concepts and methodological aspects of the problem (1-9).

This paper is devoted to study of the temporal variations of fluctuations of the travel time of the first longitudinal waves in one of the seismically active regions in Central California. Emphasis is on investigation of relatively long-period temporal variations of travel time fluctuations reflecting manifestations of processes of a background character relative to earthquake precursors in the observation region. In this case the term "long-period variations" means variations with a characteristic time scale of about a year or more. The possible reasons for such variations of wave field characteristics may be relatively weak and slow variations of the velocities of elastic waves in the studied medium caused by a temporal change in the stress state as a result of appearances of geodynamic processes.

The investigation of long-period variations is of particular interest in a study of the characteristics of geodynamic processes in the crust and upper mantle. At the same time these investigations are important in a prognostic sense because specifically against a background of long-period variations it is necessary to discriminate the precursors of earthquakes in studies for their prediction.

At the present time there are many data on the precursors of earthquakes based on the characteristics of seismic waves (2, 4). However, ideas concerning the intensity of appearance and properties of background processes leading to long-period variations of the characteristics of wave fields have been developed relatively weakly and in a number of cases are to a considerable degree contradictory. This situation is particularly characteristic for the regions of Central and Southern

California where many authors with the use of different sources of oscillations (quarry and remote blasts, local and remote earthquakes, nonexplosive sources) have obtained estimates of the temporal variations of travel time of longitudinal waves varying from 0.005 to 0.5 second per year [10-17]. It is important that reference is to virtually one and the same regions of observation and the difference in the estimates of approximately two orders of magnitude in all probability is related to limitations in these methods for making observations and analysis of data.

In this study our objective is the evaluation and diagnosis of temporal variations of fluctuations of the travel time of the first longitudinal waves (Pg) propagating within the limits of focal zones in Central California. For the used range of epicentral distances (15-50 km) the maximum depths of penetration of rays for these waves do not exceed $\sim$5 km. As the source of elastic waves use has been made of industrial blasts in local quarries registered by a group of highly sensitive seismic stations included in the seismic network of the United States Geological Survey in Central California. The use of quarry blasts was dictated by the necessity for excluding uncertainties in estimates of travel time and their fluctuations caused by the migration of epicenters and the errors in determining coordinates, depth and origin time of the source. It is evident that in this respect quarry blasts have considerable advantages in comparison with such sources as remote and local earthquakes.

An important characteristic of this work is the use in the analysis of the fluctuations or residuals of travel time caused by the presence of local velocity inhomogeneities of a relatively small scale (5-10 km) in the upper part of the crust in the observation region, not the mean travel times [18, 19]. There is basis for assuming that the characteristics of such local inhomogeneities are more sensitive to weak changes in stressed state with time as a result of geodynamic processes [20].

1. Selection and Primary Processing of Experimental Data

In the study use was made of seismograms of industrial blasts in the "Natividad" quarry registered by a group of 22 seismic stations forming part of the United States Geological Survey in Central California. Figure 1 is a diagram of the location of the quarry and stations and also the principal seismically active dislocations in the observation region -- the San Andreas, Calaveras and Sargent faults.

The observation region is characterized by a high seismicity, whose appearance is for the most part associated with the zones of the mentioned faults, and also intensive recent movements accompanied by creep effects in fault zones. All these characteristics, together with the presence of a dense network of seismic stations, determine the choice of this region for carrying out work for the study of the temporal variations of the characteristics of the wave field as a result of geodynamic processes.

A group of six stations (DIL, SJG, FRP, SRS, MON, PNC) was used for location the blast points in the "Natividad" quarry and determination of the origin times of the blasts. The remaining 16 stations, situated at epicentral distances of approximately 15 to 50 km, were used in evaluating the temporal variations of the residuals.

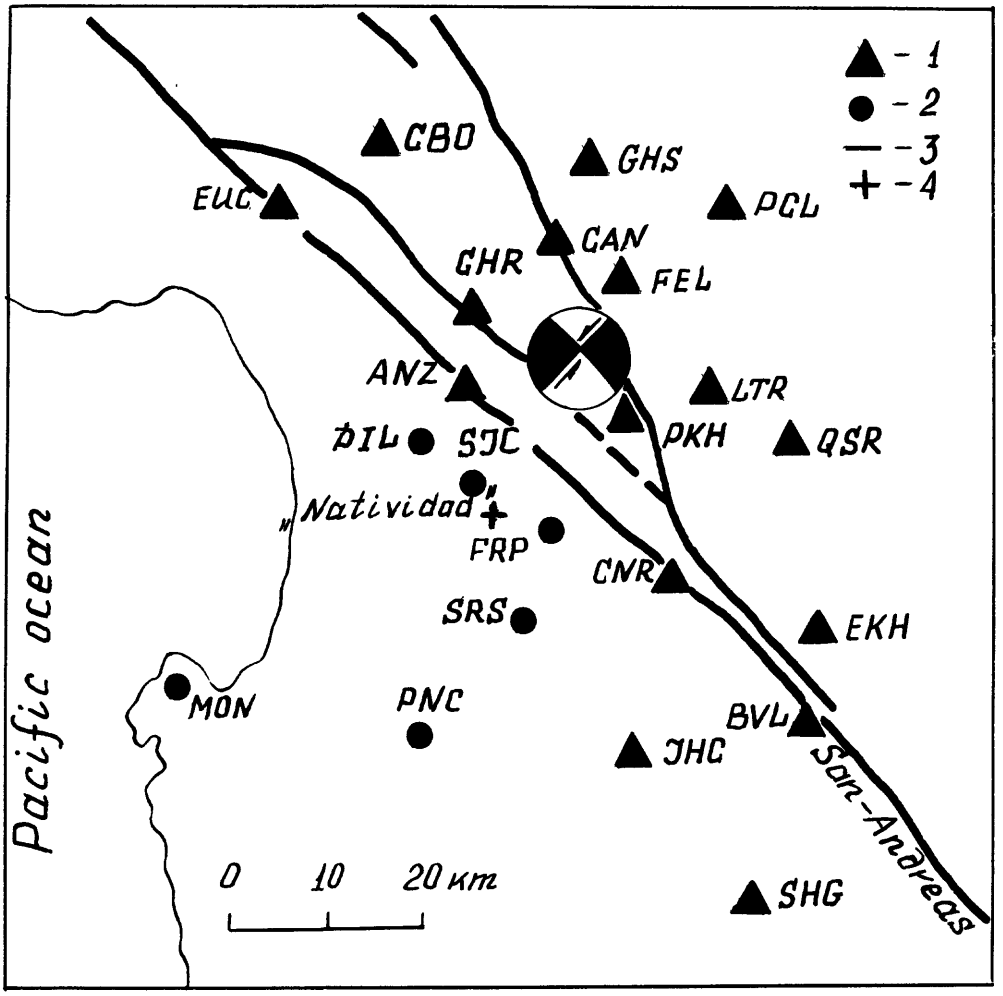

Fig. 1. Diagram of location of seismic stations and "Natividad" quarry. 1) stations of main group; 2) stations of locating group; 3) strikes of principal dislocations; 4) location of quarry. The position of the epicenter and the focal mechanism of the earthquake of 28 November 1974 in the vicinity of Hollister are indicated.

The results of the first reading were used in forming the matrix of residuals $[\delta t_{ki}]$ measuring 16 x 24, that is, for 16 stations and 24 events; the results of the repeated reading were used in forming a matrix measuring 14 x 15. Below we will refer to the matrix $[\delta t_{ki}]$ obtained using the first reading as the "primary" matrix, whereas the matrix of residuals formed using data from the repeated reading will be called the "edited" matrix.

In order to obtain a rough evaluation of the accuracy in determining the residuals, their values at some stations were compared for independent readings. The results of this comparison show that the root mean square error in determining the individual values of the residuals in the experiment does not exceed 0.05-0.06 sec. Figure 2 shows examples of a comparison of the values of the residuals obtained in the independent calculations for the three stations of the used group. More precise evaluations of the errors in determining individual values of the residuals will be given in an analysis of their temporal variations.

2. Method for the Analysis of Long-Period Variations

The model described below is used in an analysis of temporal variations of the residuals. Assume that the travel time residual at the k-th station in the group at the time T_i, corresponding to the time of the i-th blast, is the sum of the three components:

$$\delta t_{ki} = \eta_k + \xi_{ki} + \delta_{ki}. \qquad (1)$$

In (1) the component η_k represents the constant component: the component $\xi_{ki} = \xi_k(T_i)$ describes the temporal variations of the residuals and is regarded as some realization of a random process; the component δ_{ki} characterizes the random errors in determining the residuals.

We will assume that the errors δ_{ki} caused by random errors in determining the travel times (primarily reading errors) are uncorrelated from station to station and from event to event. The component $\xi_k(T_i)$, characterizing the long-period temporal variations of residuals has a quite prolonged time correlation interval which is at least $\sim$ 4 months. This component is also spatially correlated, that is, from station to station of the used group. We will also assume that the components ξ_{ki} and δ_{ki} are uncorrelated with one another.

For the adopted model the problems involved in the discrimination of the long-period variations of residuals and the study of their statistical characteristics can be solved with spatial-temporal averaging of the initial data for the purpose of suppressing random noise δ_{ki}. It should be emphasized that the possible short-period variations of residuals with a time scale $\sim$ 2 months or less in such an approach will be related to observation errors and suppressed or substantially weakened in processing the data. The loss of such information is inevitable because it is exceedingly difficult to differentiate short-period variations from observation errors.

The temporal variations of the residuals related to manifestations of geodynamic processes, in principle can have different signs at different stations in the used group. The reason for such an effect may be temporal variations of

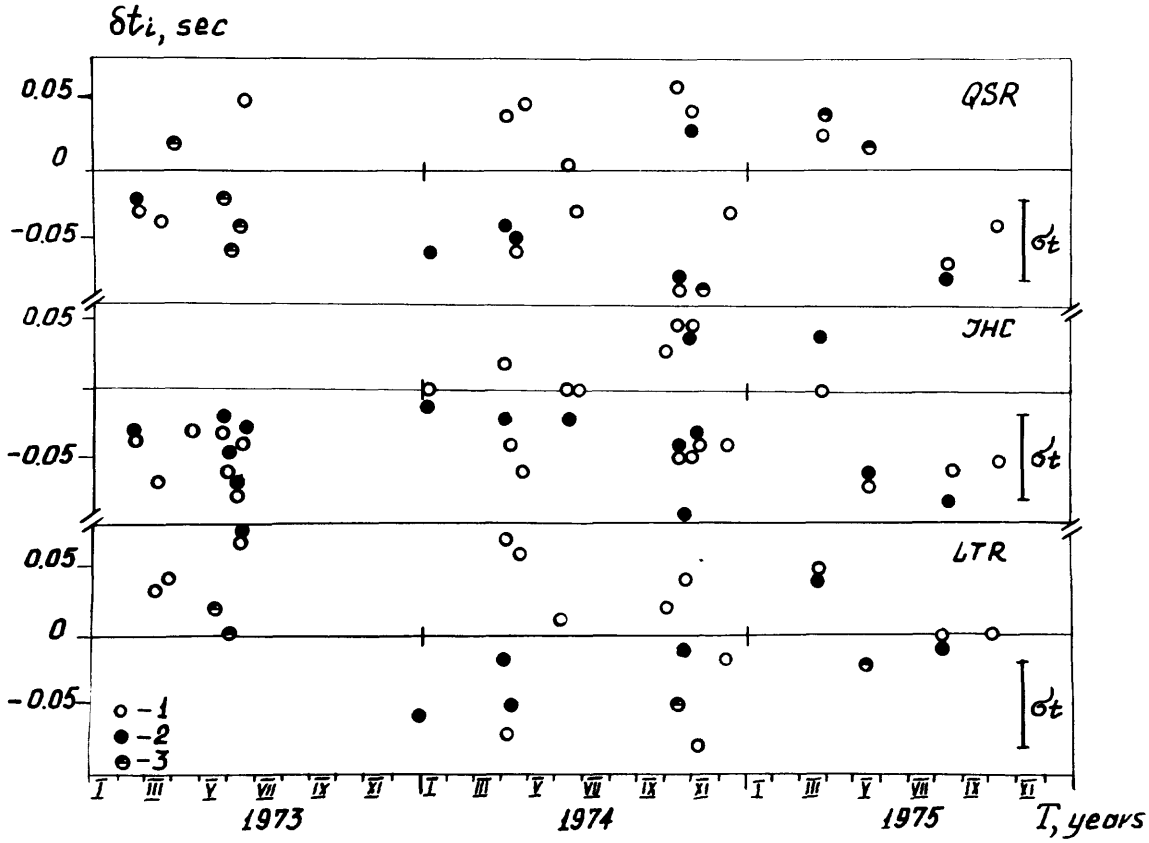

Fig. 2. Examples of temporal change of residuals δt_i for stations QSR, JHC, LTR. 1) data from primary reading; 2) data from repeated reading; 3) coinciding results of readings; σ_t standard deviation of evaluation of the residuals.

In the processing we selected seismograms of relatively powerful blasts with a total weight of the charge of about 8-10 tons during the observation interval February 1973-October 1975. The magnitudes of the selected events, determined in the routine processing of seismograms by the personnel of the Geological Survey by the method described in [21], involved a rather narrow interval of values:

$$M_L \approx 2.0\text{-}2.5.$$

During the period of observations from February 1973 through October 1975 we selected 24 events with an interval between blasts from approximately two days to six months. For the overwhelming majority of stations used the records of the first longitudinal waves (Pg) for the selected blasts have a typical pulse shape and are characterized by rather clear and sharp first arrivals. At the same time, due to malfunctions in the operation of several stations and the influence of microseismic noise not all of the selected events were reliably registered at all 22 stations of the group used.

The arrival times of the first longitudinal waves were read from microfilms of the seismograms on a viewer with a $20^{\times}$ magnification. Using data from the locating group (DIL, SJG, FRP, SRS, MON, PNC), in accordance with the program for determining the coordinates of the foci of local earthquakes, used in the practice of the epicentral service in Central California [22], it was possible to find the coordinates of the epicenters and the origin times of the selected events. The program involved use of a stratified-block model of the medium satisfactorily approximating the complex velocity structure of the observation region. Using this same program, with known coordinates of the epicenters and times of the blasts it was possible to compute the residuals or fluctuations of the travel time of the first longitudinal waves at the other 16 stations in the group.

The residuals were determined as the difference between the observed travel times and the travel times computed for a particular position of the epicenter using a stratified-block model of the medium. The parameters of this model were selected constant for the entire observation period. All the information collected in the processing was represented in the form of matrices of residuals $[\delta t_{ki}]$. Each column of the matrix of residuals corresponds to one event and all stations of the group and each row corresponds to one station and all the selected events in their chronological sequence.

In order to evaluate the stability of the results of analysis of temporal variations of the residuals the arrival times for the entire set of seismograms were read twice, independently by two specialists. In the first reading use was made of the seismograms for all 24 selected events. For some of them the positions of the epicenters and the times of the blasts were found not from the records of all six stations in the locating group, but five or even four stations. The second reading was made solely on the basis of the seismograms of the blasts, whose epicenters and times were determined from the records of six stations. Naturally, such a choice of events increases the reliability of evaluations of the residuals In addition, in the repeated reading the stations EKH and PKH were excluded from consideration due to the relatively low quality of the data.

different sign of the characteristics of local velocity inhomogeneities causing the appearance of fluctuations or residuals of travel time. In such situations it is desirable to carry out spatial-temporal averaging of the squares of the residuals or, in order to exclude the constant component, the squares of the differences of the residuals from blast to blast. In this case weak temporal variations of residuals of different sign will be accumulated simultaneously with the suppression of random noise.

A convenient tool for analysis of temporal variations of residuals is the structural functions approach, used for the first time for the processing of observations in seismic groups in [23, 24]. The method for computing the structural functions of temporal variations of residuals is essentially as follows.

For each pair of columns of the matrix $[\delta t_{ki}]$ corresponding to the i-th and j-th events the mean square of the difference of residuals is computed for the corresponding stations

$$\langle(\delta\delta t_{kij})^2\rangle = \langle(\delta t_{kj} - \delta t_{ki})^2\rangle. \tag{2}$$

The symbols "$\langle\ \rangle$" in (2) denote the operation of statistical averaging for all the stations in the group, that is

$$\langle\theta_{ki}\rangle = \frac{1}{n-1}\sum_{k=1}^{n}\theta_{ki},$$

where n is the number of stations in the used group. The mean square difference of the residuals determined from (2), corresponds to the time interval τ_{ij} between the i-th and the j-th events:

$$\tau_{ij} = T_j - T_i, \tag{3}$$

where $T_j > T_i$.

The entire set of pairs of values τ_{ij} and $C_{tij} = \langle(\delta\delta t_{kij})^2\rangle$ can be represented in the form of two matrices $[C_{tij}]$ and $[\tau_{ij}]$, or in the form of a plot of the values C_{tij} as a function of the values τ_{ij}. The structural function of the temporal variations of residuals $C_t(\tau)$ is determined as a result of averaging of the values C_{tij} in a moving time "window."

The analytical expression for the structural function $C_t(\tau)$, obtained using the described procedure, for a residual model of the type (1) can be represented in the form:

$$C_t(\tau) = \langle[\xi_k(T+\tau) - \xi_k(T)]^2\rangle + 2\sigma_t^2, \tag{4}$$

where τ is the time interval between events and the "$\langle\ \rangle$" symbols denote statistical averaging for the entire set of stations and the entire set of pairs of events with a time interval equal to τ. The first term on the right-hand side of (4), in accordance with (1), describes the structural function of temporal variations of residuals; the second term describes the doubled mean square of errors in determining the residuals δ_{ki}.

It follows from (4) that

$$C_t(0) = 2\sigma_t^2.$$

Thus, the level of values of the structural function is determined by double the value of the mean square of the errors in determining the residuals. In particular, the evaluation of the root mean square error in determining the residuals in the experiment can be found from the initial point of the structural function:

$$\sigma_t \approx \frac{1}{\sqrt{2}} C_t^{1/2}(\tau), \tag{5}$$

with $\tau \to 0$.

The growth and variations of the values $C_t(\tau)$ with an increase in the time interval τ will be evidence of the presence of temporal variations of the residuals. If the process of temporal variations of the residuals has a stationary character and is statistically homogeneous in space, the $C_t(\tau)$ values with an increase in τ should tend to saturation. The corresponding τ value in this will characterize the temporal scale of the variations and the C_t values themselves will characterize the intensity of their appearance.

Figure 3 shows the structural functions, obtained by the described method, computed from the primary and edited matrices $[\delta t_{ki}]$. Both curves virtually coincide in shape, but differ substantially with respect to the level of their values. The identity of the shape of the $C_t(\tau)$ curves obtained as a result of the independent readings of the arrival times can be regarded as a factor confirming the stability and reliability of the analysis made of the temporal variations of residuals.

The difference in the levels of the $C_t(\tau)$ curves for the two $[\delta t_{ki}]$ matrices is associated with the different accuracy in determining the residuals in the independent readings. Thus, for the primary matrix of residuals from the initial point of the $C_t(\tau)$ curve and formula (5) we obtain an evaluation of the root mean square error in determining the residuals $\sigma_t \leqslant 0.06$ sec. For the edited matrix $[\delta t_{ki}]$, obtained from reading the arrival times only for events with reliably determined epicentral coordinates, $\sigma_t \leqslant 0.04$ sec.

These results make it possible, with further analysis of the long-period variations of residuals to use a shortened list of events, and accordingly, an edited matrix $[\delta t_{ki}]$.

3. Variations of Residuals on the Basis of Observational Data

The zones of active dislocations in the observation region -- the San Andreas, Calaveras and Sargent faults -- are of the greatest interest for study of the temporal variations of the velocity characteristics of the medium as a result of manifestations of geodynamic processes. Such variations should be manifested in temporal changes in the residuals of the first longitudinal waves passing through the fault zones. For the used system of observations these waves are registered by a subgroup of stations located to the east of the strike line of the San Andreas fault (Fig. 1). A study of the temporal variations of residuals precisely at these stations makes it possible to localize the regions and medium subject to

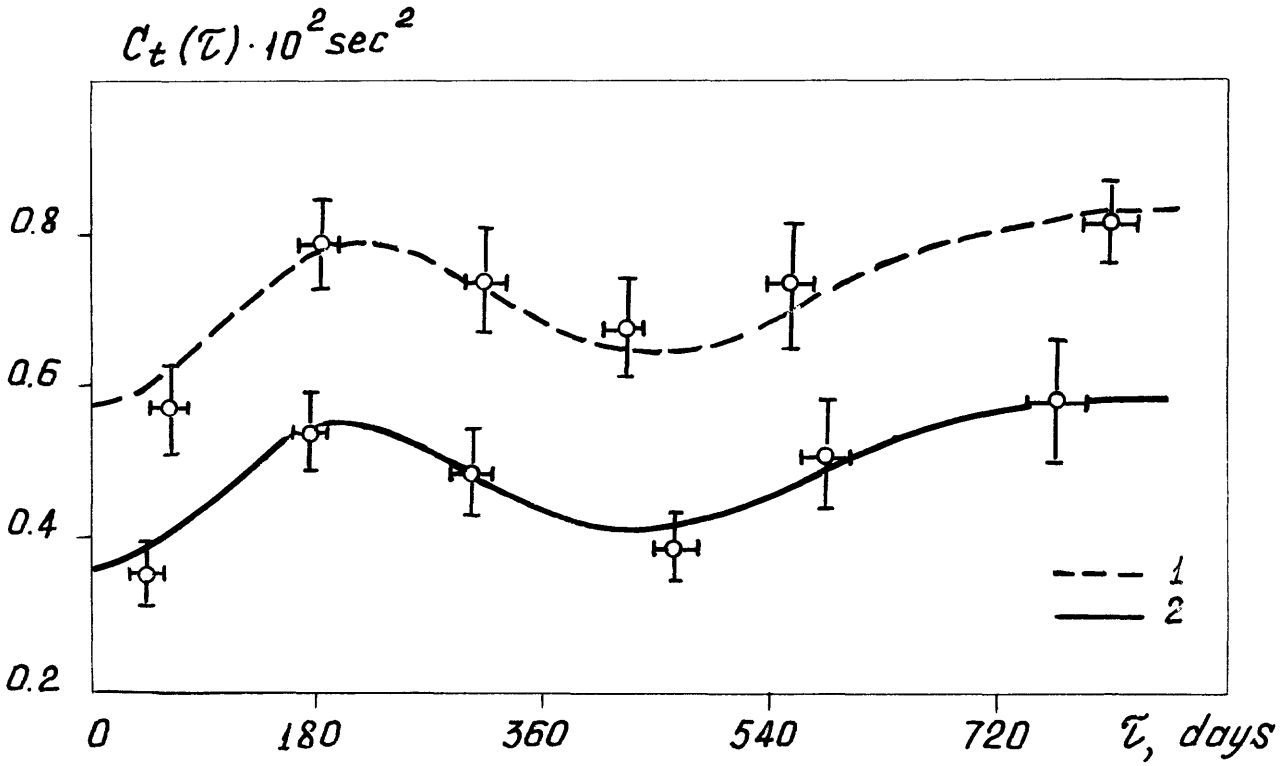

Fig. 3. Structural functions of temporal variations of residuals for used group of stations. 1) using data from primary reading; 2) using data from repeated reading. Here and below the standard deviation in determining the corresponding parameters is shown by vertical and horizontal lines.

temporal changes in the velocities of elastic waves.

In connection with what has been said, processing of experimental data was carried out separately for the entire group of 14 stations and a subgroup of 8 stations (QSR, CAN, CHR, LTR, PCL, CBD, FEL, GHS), situated to the east of the San Andreas fault.

Figure 4 gives the results of computation of the structural function of variations of residuals for the entire used group of 14 stations. It also shows individual values $\langle(\delta\delta t_{kij})^2\rangle$, as well as their averaged values describing the behavior of the structural function of the temporal variations of the residuals $C_t(\tau)$. The intervals of averaging of the $\langle(\delta\delta t_{kij})^2\rangle$ values are 4-8 months in time and are shown by vertical lines in the upper part of the figure.

Despite the observed substantial scatter of points, the minimum $\langle(\delta\delta t_{kij})^2\rangle$ values increase appreciably with an increase in the τ_{ij} values. For the maximum $\langle(\delta\delta t_{kij})^2\rangle$ values this tendency is traced to a considerably lesser degree, which is evidently associated with the influence of random errors in determining the residuals.

With an increase in the time interval the $C_t(\tau)$ values experience changes of a periodic nature with a period of about a year. However, periodic changes are observed against a background of a smooth increase in the values of the structural function. Thus, with $\tau \sim 40$ days $C_t = (0.35 \pm 0.04) \cdot 10^{-2}$ sec, but with $\tau \sim 760$ days $C_t = (0.59 \pm 0.08) \cdot 10^{-2}$ sec. The difference in the indicated values exceeds by a factor of 3 the maximum root mean square error in evaluating the structural function.

All the cited facts are evidence of entirely substantial and significant temporal variations of the residuals for a group of 14 stations.

Figure 5 shows similar data for the eastern subgroup of stations. Variations of a periodic character on the $C_t(\tau)$ curve in this case were expressed considerably more weakly, but the increase in C_t values with time is manifested more clearly than for all the used group of stations.

Thus, in both cases, as a result of analysis of the structural functions, it is possible to ascertain considerable temporal variations of residuals of a long-period character.

4. Diagnosis of Long-Period Variations of Residuals

The systematic temporal changes in residuals in principle can be caused not only by velocity variations in the studied medium, but also by the effects of a change in the conditions for the excitation of oscillations from event to event, in particular, the effects of migration of the epicenters and variations of the magnitudes of events [10, 14]. In connection with what has been said, for study of variations of the residuals associated with manifestations of geodynamic processes it is necessary to be able to diagnose the nature of the observed variations. A point of fundamental importance is the diagnosis of the influence of such factors as the migration of epicenters of blasts and variations of their magnitudes.

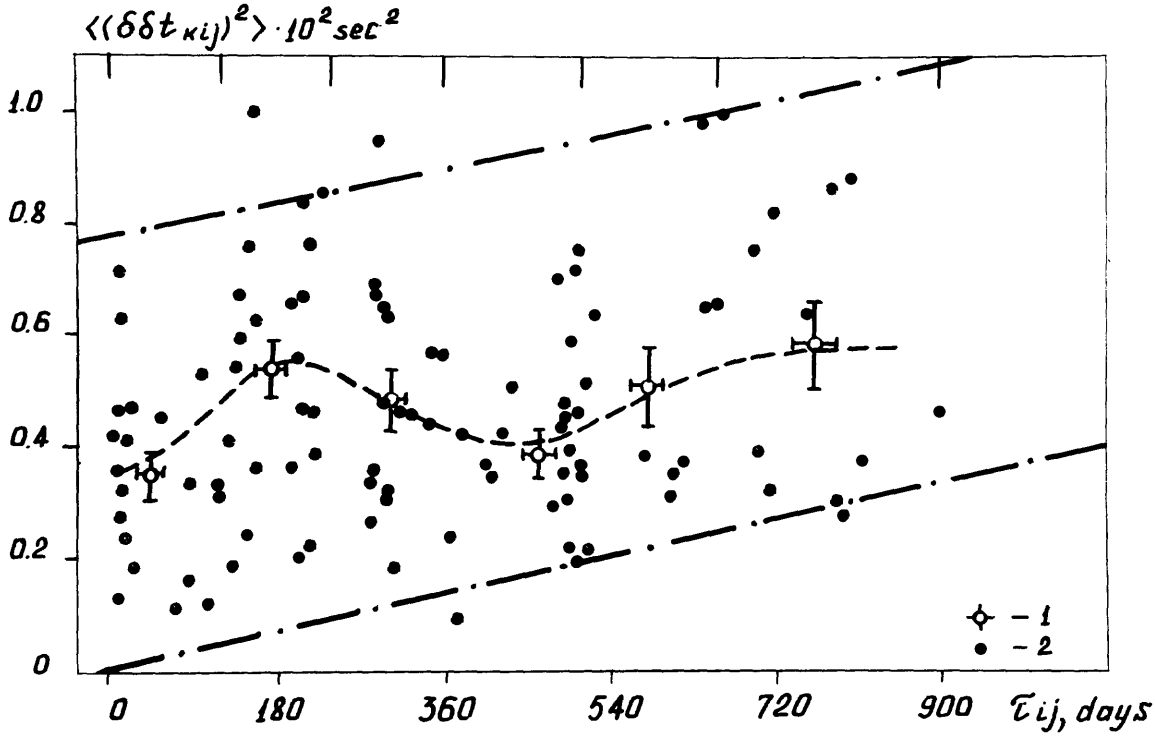

Fig. 4. Examples of construction of structural function of temporal variations of residuals $C_t(\tau)$ for the group of stations. 1) $C_t(\tau)$ values; 2) values of mean squares of difference of residuals $\langle(\delta\delta\ t_{kij})^2\rangle$ for corresponding time intervals τ_{ij}. The vertical lines in the upper part of the figure correspond to the intervals of averaging of the $\langle(\delta\delta\ t_{kij})^2\rangle$ values in time.

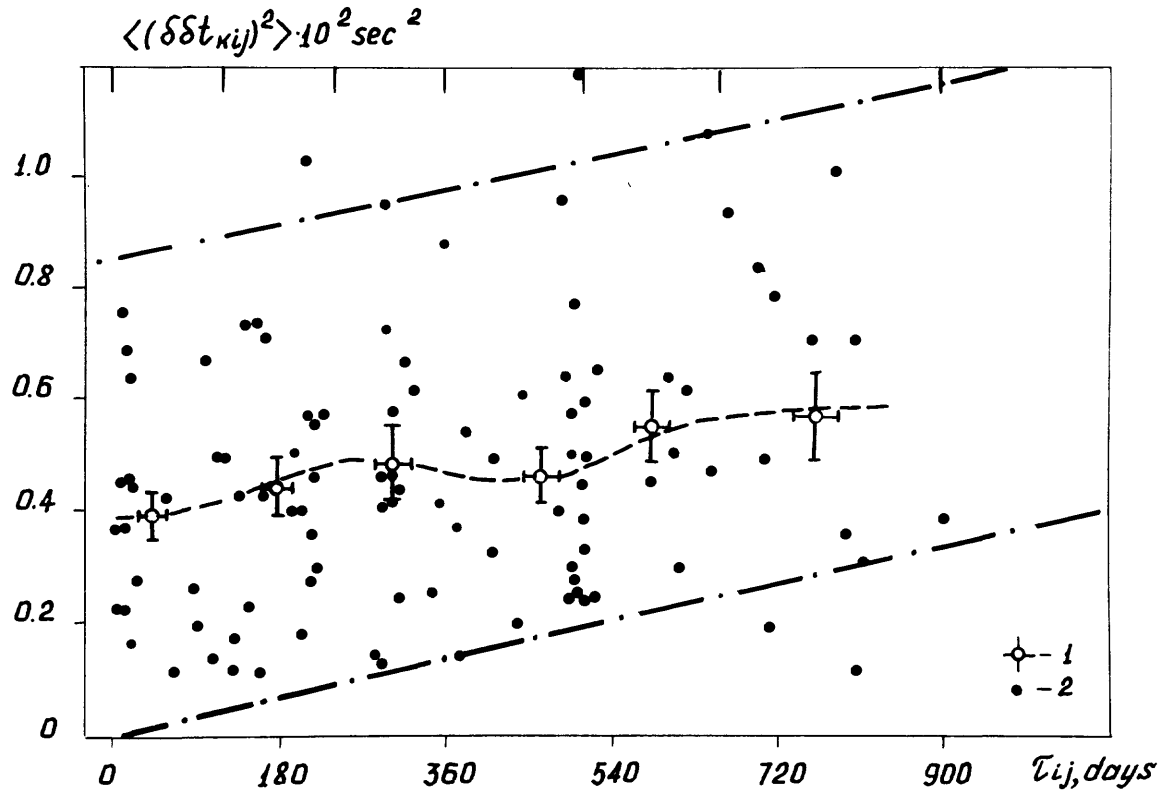

Fig. 5. Examples of construction of structural function $C_t(\tau)$ for eastern subgroup of stations. Notations same as in Fig. 4.

4.1. Migration of epicenters of events. The displacement of the epicenters of events from blast to blast for a medium with three-dimensional velocity inhomogeneity causes changes in travel time at each of the stations in the group associated with a change in the epicentral distance and a spatial change in velocities in the epicentral regions. The first effect is compensated when computing the residuals in travel time, taking into account the actual position of the epicenter. In order to ascertain the second effect it is necessary to use special analytical methods. One of the possible methods for solving such a problem was proposed in [14]. In this study the following relationship was found between the structural function of the variations of residuals $C_t(\tau)$ and the structural function of the process of migration of epicenters $C_\Delta(\tau)$:

$$C_t(\tau) \approx C_\Delta(\tau) \langle |\operatorname{grad} \delta t_k|^2 \cos^2 \alpha_k \rangle, \qquad (6)$$

where the symbol "<>" denotes statistical averaging for all stations in the group. The vector

$$\operatorname{grad} \delta t_k \tilde{=} \partial t_k / \partial v_0 \operatorname{grad} v_0$$

determines the magnitude and direction of spatial changes in velocity v_0 in the epicentral region, and α_k is the angle between the vector grad δt_k and the vector $\delta \vec{\Delta}(\tau)$, describing the effect of migration of the epicenters of events.

In a case when there are no temporal variations of velocities in the studied medium, in accordance with (6), between the $C_t(\tau)$ and $C_\Delta(\tau)$ values there should be a linear dependence in the form

$$C_t(\tau) \approx \beta C_\Delta(\tau),$$

an indicator of which is the close correlation between the corresponding values C_t and C_Δ. On the other hand, the absence of correlation between C_t and C_Δ is evidence of a decisive influence on the $C_t(\tau)$ values from effects unrelated to the migration of epicenters.

As indicated in [14], even an exceedingly weak migration of the epicenters of events can virtually completely govern the dependence $C_t(\tau)$. Accordingly, the evaluation of the influence of the effects of migration of epicenters on the $C_t(\tau)$ values must be made using the method described above and for the considered experimental data.

The method for constructing the structural function $C_\Delta(\tau)$ to all intents and purposes is similar to that described above for constructing the dependence $C_t(\tau)$. In this case the initial data will be the squares of the distances between the epicenters of the blasts or the squares of the moduli of the vectors $\delta \vec{\Delta}(\tau_{ij})$.

Figure 6 is a map of the epicenters of blasts in the "Natividad" quarry used in constructing the edited matrix of residuals. Figure 7 shows the structural function of the process of migration of epicenters in this quarry. The $C_\Delta(\tau)$ values experience considerable periodic variations with time, which requires checking of the nature of the correlation between C_t and C_Δ values. However, before carrying out such an analysis we will examine a second important effect capable of causing temporal variations of the residuals.

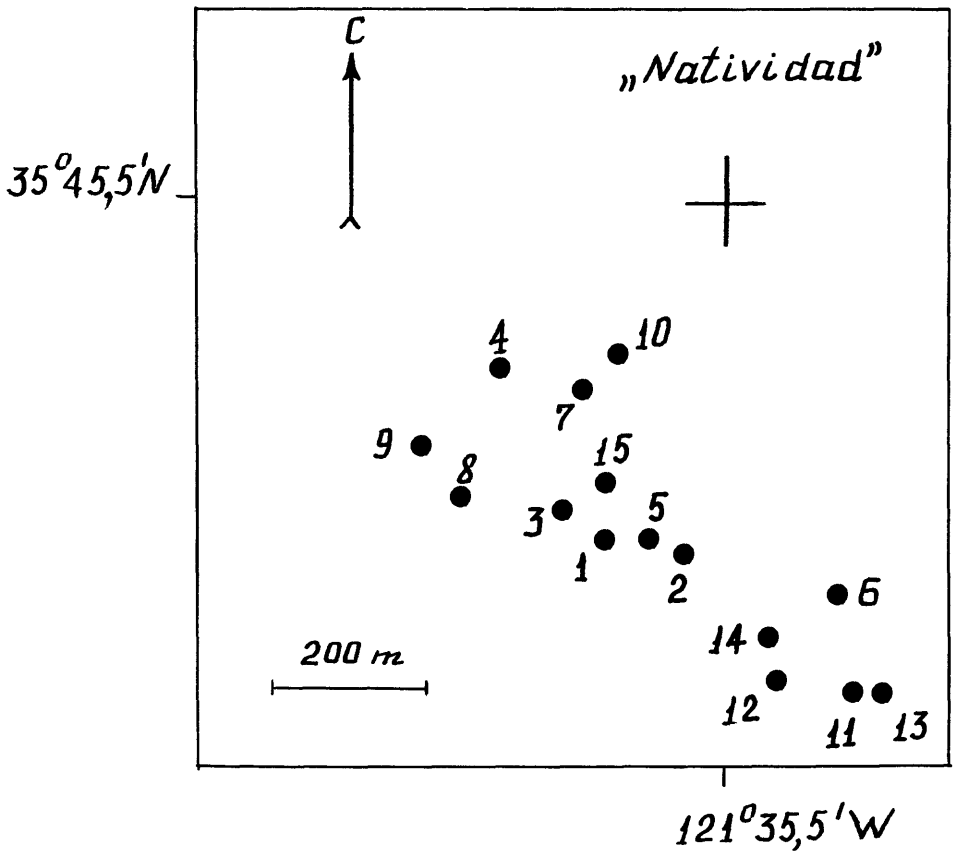

Fig. 6. Diagram of positions of epicenters of blasts in "Natividad" quarry. The numbers correspond to the sequence of events in time.

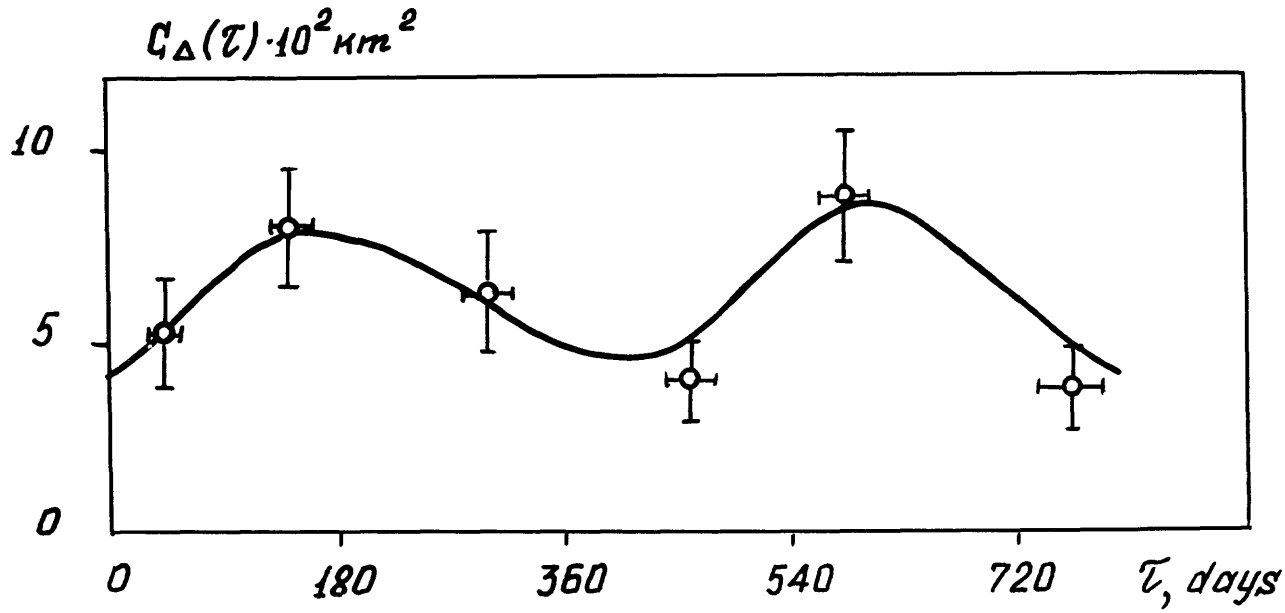

Fig. 7. Structural function $C_\Delta(\tau)$ of process of migration of epicenters of blasts in "Natividad" quarry.

4.2. Variations in magnitudes of events. Despite the fact that the range of magnitudes of the selected events is $M_L \approx 2.0$-2.5, for a whole series of stations there is a close negative correlation between the values of the δt_{ki} residuals and the magnitudes of the blasts M_{Li}. A similar effect of a dependence of the residuals and magnitudes of weak earthquakes in Central California was also noted earlier in [10]. The reason for this effect in our case becomes entirely obvious if it is taken into account that in reading the arrival times against a background of high-frequency microseismic noise it is possible to determine not the true arrival time, but the approximate time for which the current amplitude of the signal exceeds the mean level of the microseisms. In the case of greater magnitudes of blasts the determined times of the apparent arrivals will be closer to the true arrival times than in the case of lesser magnitudes.

Figure 8 shows examples of the dependences of δt_{ki} on M_{Li} for some stations in the group. We note that by no means is there a close correlation of the δt_{ki} and M_{Li} values for all stations. However, the presence of such a dependence for at least some stations in the used group requires investigations of the influence of variations of the magnitudes of the events on changes in the residuals with time.

Now we will evaluate the influence of variations of the magnitudes of events on the values of the structural function of variations of the residuals $C_t(\tau)$. Assuming a close correlation between the δt_{ki} and M_{Li} values, for some k-th station in the group we can write:

$$\delta t_{ki} \approx -k_k (M_{Li} - M_{ok}). \tag{7}$$

In (7) the $k_k > 0$ value determines the slope of the line of regression of the values of the residuals to the values of the magnitudes for the k-th station and M_{ok} is the intercept. The variation of the residual from the i-th event to the j-th event, in accordance with (7), is determined as

$$\delta\delta t_{kij} = \delta t_{kj} - \delta t_{ki} \approx -k_k \delta M_{Lij}, \tag{8}$$

where $\delta M_{Lij} = M_{Lj} - M_{Li}$ is the variation of the magnitude for the corresponding pair of events.

Squaring both sides of equation (8) and statistically averaging for all stations of the group, we find:

$$\langle (\delta\delta t_{kij})^2 \rangle \approx \langle k_k^2 \rangle (\delta M_{Lij})^2. \tag{9}$$

Averaging the values $\langle (\delta\delta t_{kij})^2 \rangle$ and $(\delta M_{Lij})^2$ in a moving time "window" gives the structural functions of variations of the residuals $C_t(\tau)$ and variations of the magnitudes $C_M(\tau)$. Thus, when there is a correlation between δt_{ki} and M_{Li} the structural functions $C_t(\tau)$ and $C_M(\tau)$, in accordance with (9), are related to one another by the linear expression:

$$C_t(\tau) \approx \beta C_M(\tau). \tag{10}$$

It follows from (10) that when there are considerable variations of the magnitudes of the events the temporal variations of the C_t values can be completely governed exclusively by this effect. In this case a close correlation should exist between the corresponding C_t and C_M values.

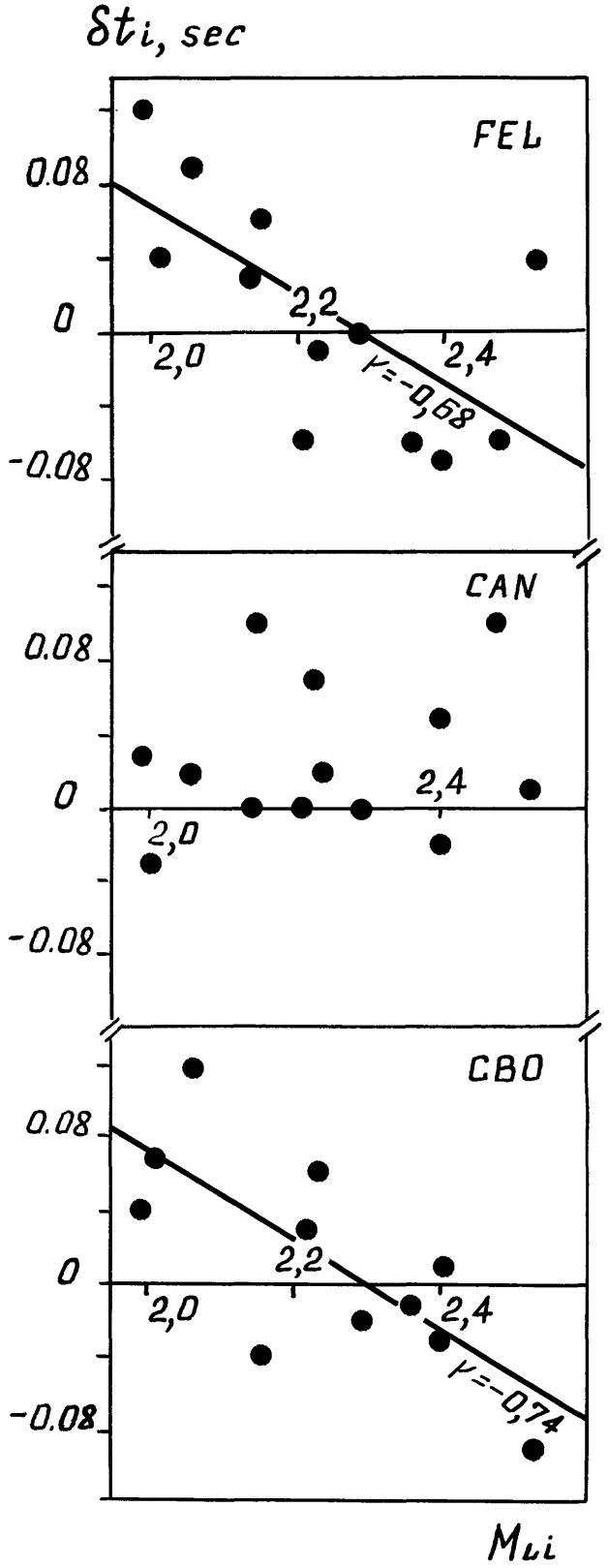

Fig. 8. Correlation diagrams of values of residuals δt_i and magnitudes of events M_{Li} for stations FEL, CAN, CBO.

Thus, a diagnosis of the influence of the effects of migration of epicenters and variations of magnitudes can be made when evaluating the nature of the correlation of the values C_t and C_M, C_Δ. The structural functions $C_t(\tau)$ and $C_\Delta(\tau)$, constructed using experimental data, were cited above. The structural function of variations of the magnitudes of blasts in the "Natividad" quarry during the observation period is shown in Fig. 9.

4.3. Differential variations of residuals. It is desirable that the joint influence of two factors -- migration of epicenters and variations of the magnitudes of events -- on the temporal changes of the structural function $C_t(\tau)$ be evaluated from the presence of a linear correlation in the form:

$$C_t = \beta_0 + \beta_1 C_\Delta + \beta_2 C_M, \tag{11}$$

where β_0, β_1, β_2 are constants. We will make an evaluation separately using data for the entire used group of stations and for the eastern subgroup.

The correlation coefficient between the C_t and C_Δ values, denoted r_{12}, for data for the entire group is ~ 0.25, whereas for data for the eastern subgroup it is -0.09. Accordingly, the epicenter drift effect exerts virtually no influence on the temporal changes in residuals both for the entire used group and for the eastern subgroup. The correlation coefficient r_{13} between the C_t and C_M values for the data for the entire group attains 0.60, and for the eastern subgroup ~ 0.44. Thus, the influence of the variations of magnitudes is more significant. There is no correlation between the C_Δ and C_M values ($r_{23} \approx 0.006$).

The composite correlation coefficient R_{123}, evaluating the presence of a correlation of the type (11) between C_t and C_Δ, C_M, with $r_{23} \approx 0$ can be found from the expression [25]:

$$R_{123} \approx [r_{12}^2 + r_{13}^2]^{1/2}.$$

The R_{123} value is 0.65 for the data for the entire group of stations and 0.44 for data for the eastern subgroup. With such values of the R_{123} coefficient it is desirable to exclude the influence of changes in the C_Δ and C_M values on the structural function of temporal variations of residuals. For this purpose, using the least squares method, it is necessary to find the numerical values of the coefficients β_0, β_1, β_2 in (11).

The difference values $\tilde{C}_t$, determined with known values β_0, β_1, β_2 from the expression

$$\tilde{C}_t \approx C_t - \beta_0 - \beta_1 C_\Delta - \beta_2 C_M, \tag{12}$$

will characterize the variations of the structural function of the residuals to a considerable degree free of the influence of the effects of migration of the epicenters and variations of their magnitudes. The $\tilde{C}_t(\tau)$ values, obtained from (12), are indeterminate with respect to their mean level. In order to exclude this indeterminancy the function $\tilde{C}_t(\tau)$ can be constructed in the following way

$$\tilde{C}_t(\tau) = C_t(\tau) - \beta_1[C_\Delta(\tau) - C_\Delta(0)] - \beta_2[C_M(\tau) - C_M(0)], \tag{13}$$

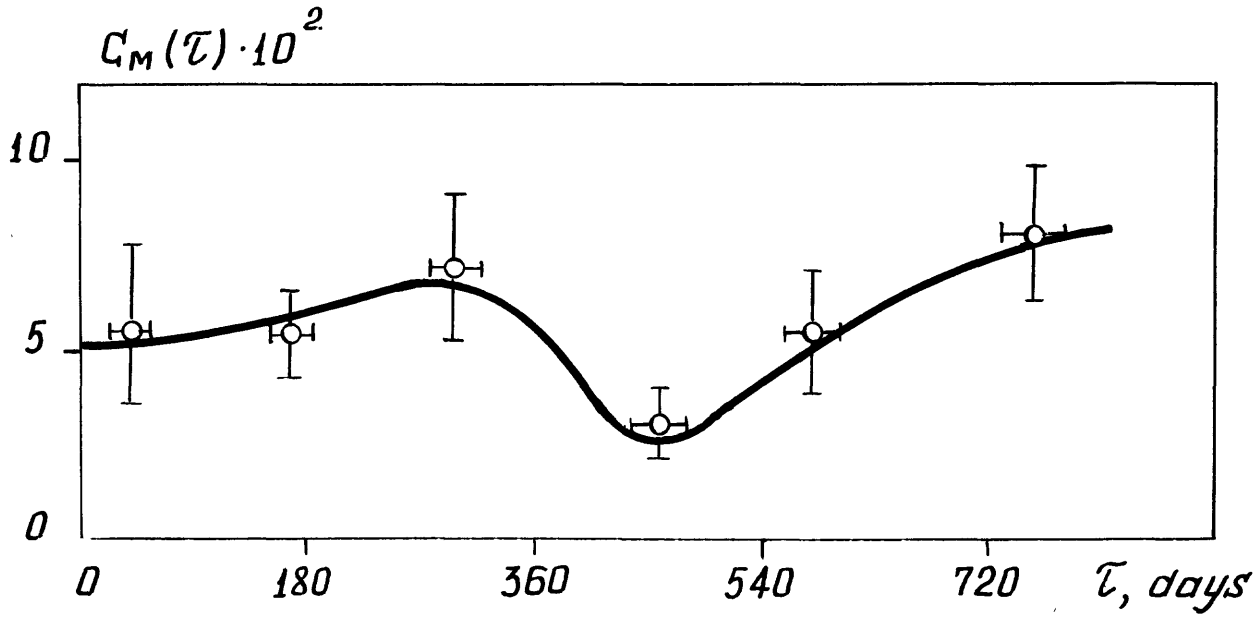

Fig. 9. Curve of structural function of variations of magnitudes of events $C_M(\tau)$.

which gives $\widetilde{C}_t(0) = C_t(0)$. For practical purposes as $C_t(0)$, $C_\Delta(0)$ and $C_M(0)$ it is possible to take the initial points of the corresponding curves, obtained from experimental data with $\tau \sim 40$ days.

The function $\widetilde{C}_t(\tau)$, constructed by the described method, characterizes the "differential" variations of the residuals with time, unrelated to the effects of migration of epicenters and variations in the magnitudes of events. The structural functions $\widetilde{C}_t(\tau)$, obtained on the basis of experimental data for the entire group of stations and stations in the eastern subgroup, are shown in Fig. 10.

The exclusion of the influence of the effects of variations of magnitudes and the migration of the epicenters of events substantially changed the form of the structural functions in comparison with the $C_t(\tau)$ curves shown in Figures 4, 5.

Variations of a periodic nature, observed on the $C_t(\tau)$ curves, for all practical purposes are completely excluded with correction of the structural functions for the effects of migration of the epicenters and variations of the magnitudes of the blasts. The $\widetilde{C}_t(\tau)$ values in Fig. 10 increase relatively smoothly with an increase in the time interval between the events. A systematic increase in the values of the structural functions $\widetilde{C}_t$ with an increase in the time interval τ confirms the fact of existence of "differential" temporal variations of residuals for the observation region.

It is important to note that the increment of the $\widetilde{C}_t$ values for a time interval ~ 2 years in the statistical sense is established relatively reliably. For example, for the eastern subgroup of stations the initial value $\widetilde{C}_t$ with $\tau \sim 40$ days is $(0.39 \pm 0.04) \cdot 10^{-2} \text{sec}^2$, and with $\tau \sim 76.0$ days $\widetilde{C}_t = 0.54 \pm 0.08) \cdot 10^{-2} \text{sec}^2$. Thus, the difference in the initial and final values $\widetilde{C}_t(\tau)$ in both cases exceeds the combined evaluation of the root mean square error of the mean values, being $\sim 0.09 \cdot 10^{-2} \text{sec}$. If it is assumed that the errors in evaluation of the mean $\widetilde{C}_t(\tau)$ values have a normal distribution, the indicated differences in the initial and final values of the structural function will be statistically significant with an approximately 15% significance level.

5. Statistical Characteristics of Long-Period Variations of Residuals

Now we will evaluate the principal statistical characteristics of the "differential" temporal variations of the residuals. The curves in Fig. 10 show that the values of the structural functions are virtually stabilized, that is, attain "saturations" with $\tau \sim 700$ days. This tendency is manifested especially graphically for the eastern subgroup of stations and to a lesser degree for the entire used group. Accordingly, as an evaluation of the characteristic time scale of the established variations of the residuals it is possible to use a time interval with a duration of about two years.

We will use the final and initial values of the structural function $\widetilde{C}_t(\tau)$ in evaluating the root mean square value of the temporal variations of residuals for a two-year period. This value can be adopted as a characteristic of the intensity of manifestation of the temporal variations. An evaluation of the root mean square value of the temporal variations of residuals $\langle (\delta\delta t)^2 \rangle^{1/2}$ is obtained using the formula:

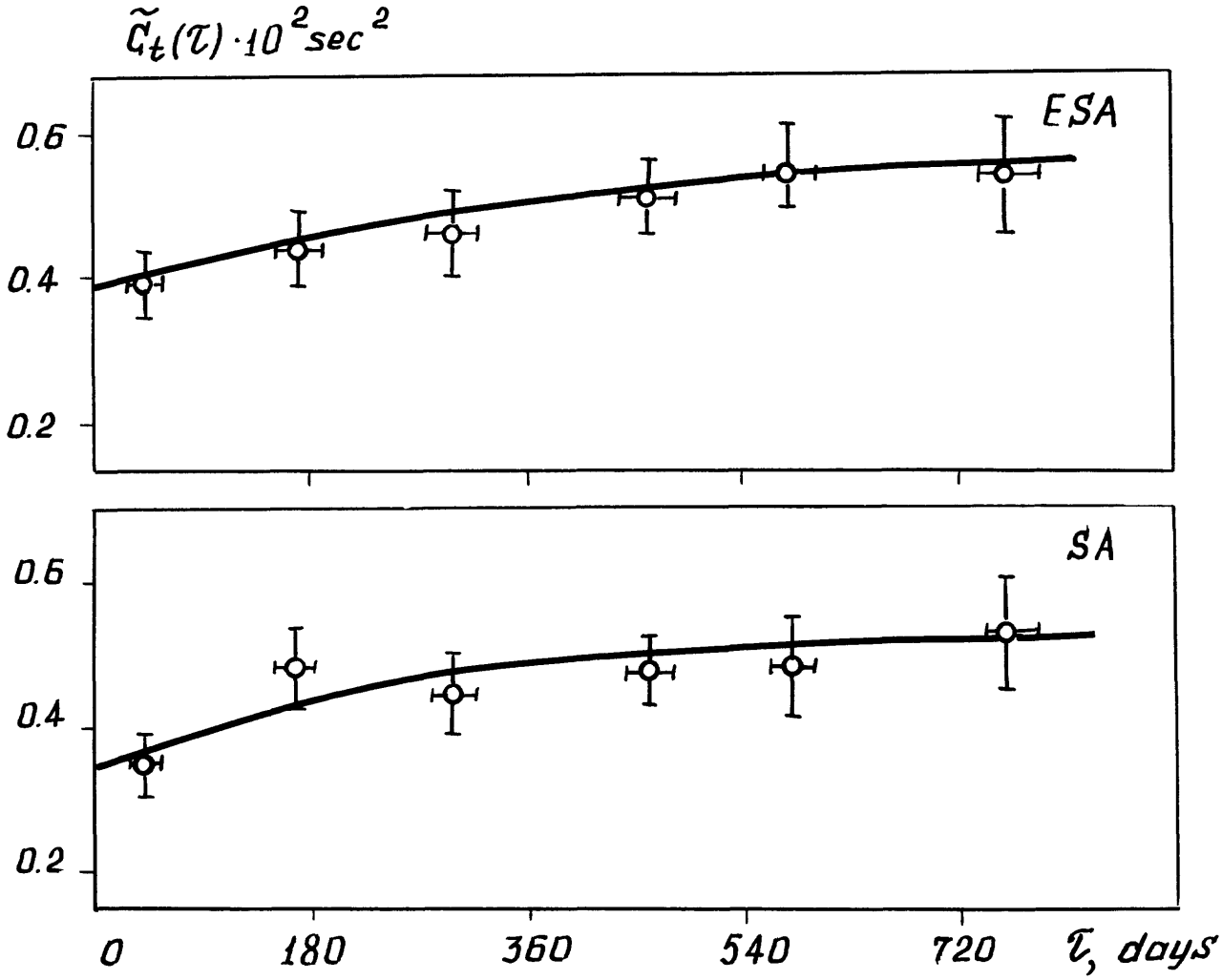

Fig. 10. Structural functions of temporal variations of residuals after exclusion of effects of migration of epicenters of events and variations of their magnitudes for eastern subgroup (ESA) and entire used group of stations (SA).

$$<(\delta\delta t)^2>^{1/2} \approx \frac{1}{\sqrt{2}} [\tilde{C}_t(\tau) - \tilde{C}_t(0)]^{1/2}.$$

In the latter expression as $\tilde{C}_t(0)$ it is possible to select the initial value of the structural function ($\tau \sim 40$ days), and as $\tilde{C}_t(\tau)$ its value with τ = 760 days.

The determined $<(\delta\delta t)^2>^{1/2}$ values are virtually equal both for the eastern subgroup and for the entire group of stations and are 0.03 sec. Thus, the increment of the root mean square value of the temporal variations of the residuals during a year in both cases does not exceed 0.015 sec.

In the analysis of the temporal variations of residuals associated with manifestations of modern geodynamic processes we attempted to exclude effects caused by imperfection of the observation method. At the same time, the established "differential" variations of the residuals cannot be related to manifestations of geodynamic processes without necessary proof. In actuality, the reason for the long-period variations may also be different exogenous processes, such as changes in the ground water level due to seasonal changes in the quantity of falling precipitation. The following factors can be regarded as proof of the correlation between the established "differential" variations and manifestations of geodynamic processes.

The coincidence of the $<(\delta\delta t)^2>^{1/2}$ evaluations for the eastern subgroup and the entire group of stations and also the virtual identity of the shape of the $\tilde{C}_t(\tau)$ curves for both groups make possible an approximate spatial localization of the regions and medium subject to temporal changes in velocity. A comparison of the $\tilde{C}_t(\tau)$ curves in Fig. 10 shows that the established temporal variations of the residuals for the most part are manifested at stations of the eastern subgroup, situated beyond the system of active faults in the region (Fig. 1) relative to the source of oscillations. The trajectories of the seismic rays for these stations, in contrast to the stations situated to the west of the San Andreas fault, intersect the zones of active faults in the observation region. In this connection it can be assumed that the processes of temporal changes in velocities are manifested most intensively in zones of active faults (San Andreas, Calaveras, Sargent) or, at least, within the limits of a block bounded by the San Andreas and Calaveras faults (Fig. 1). The range of depths in which are manifested the temporal changes in velocities causing the determined temporal variations of residuals is determined by the maximum depths of penetration of the rays of the first longitudinal waves and probably does not exceed 4-5 km.

In support of the assumption of a correlation between the established variations of residuals and manifestations of geodynamic processes there are also the results of geodetic measurements of deformations carried out during 1971-1978 in a network of 24 triangulation stations situated directly in the region of seismic observations [26]. Figure 11, constructed using data from [26], shows curves of the temporal change in "volume" deformation:

$$\Theta = \varepsilon_{11} + \varepsilon_{22}$$

for the entire area of the observation region and for a block situated between the San Andreas and Calaveras faults. The ε_{11} value in the latter expression determines the deformation in a west-east direction and ε_{22} determines the deformation in a north-south direction.

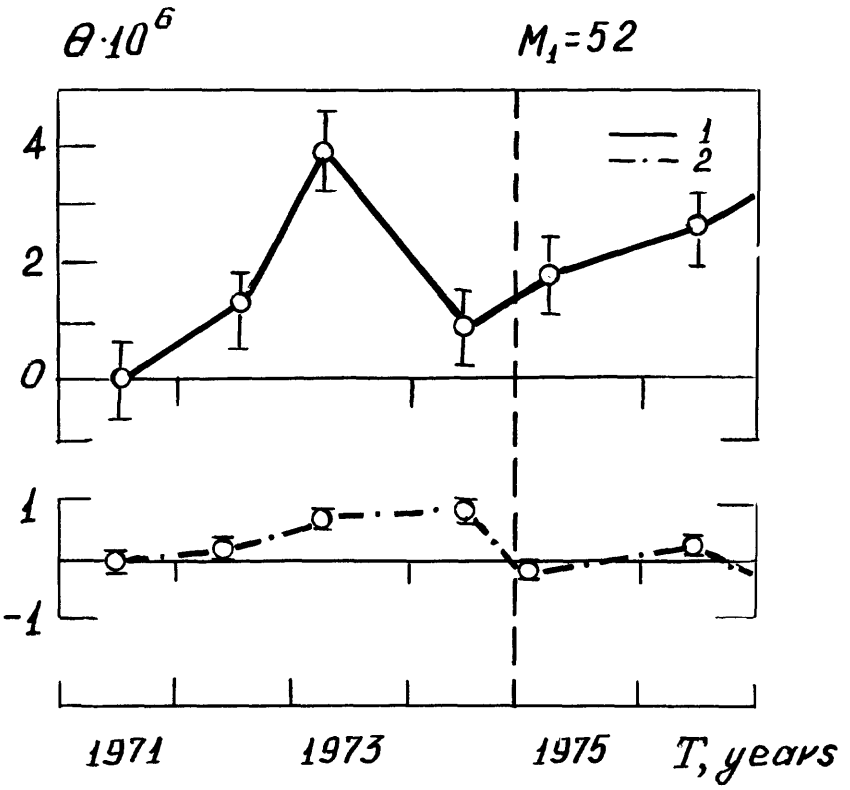

Fig. 11. Temporal change of "volume" deformation $\theta = \varepsilon_{11} + \varepsilon_{22}$ on basis of data from geodetic measurements (J. Savage, W. H. Prescott, M. Lisowski, N. King (26)). 1) for block of medium bounded by the San Andreas and Calaveras faults; 2) for entire observation region.

Temporal variations of θ can be regarded as a manifestation of temporal changes in deformations of the volume of the studied medium. In accordance with [26] these changes occur primarily due to dilatation of the studied volume of the medium in a west-east direction.

The temporal variations of the θ value of necessity may cause changes in the crack volume in the studied medium and accordingly also changes in the velocity of elastic waves. It is interesting to note that significant differences of the θ from zero values were observed approximately from mid-1972 to mid-1974, that is, the anomaly of θ values has an approximately two-year time interval of existence. In addition, the anomalous behavior of the θ values with time is manifested with the greatest contrast for a block of the medium bounded by the San Andreas and Calaveras faults. Similar conclusions with respect to the characteristic time scale of variations of residuals and the regions of their spatial manifestation were drawn above in an analysis of seismic data.

Thus, the results of geodetic measurements of deformations are in rather good agreement with the results of seismic observations. This circumstance makes possible a far more reliable interpretation of the determined temporal variation of residuals as a result of the manifestation of modern geodynamic processes leading to a change in the deformed state, and as a result, to a change in the velocities of elastic waves in the studied medium.

However, the obtaining of evaluations of the temporal variations directly of the velocities of elastic waves is a far more complex problem, requiring for its solution an adequately reliable localization of the volume of the medium to the greatest degree subject to temporal changes in the stressed-strained state. The experimental data employed do not make it possible to carry out such determinations. For this reason we will limit ourselves to the evaluations of the root mean square values of the temporal variations of residuals obtained above.

We will compare the estimates of the intensity of manifestation of the temporal variations which were made with the results of similar determinations by other authors for a number of regions in California. Source [13] gives a detailed summary of data on the temporal variations of the kinematic characteristics of wave fields measured during observations in California. The results of this article and [14] show that the effects of migration of the epicenters of events and variations of their magnitudes can lead to considerable changes in residuals with time and to a significant exaggeration of the estimates of intensity of manifestation of temporal variations associated with manifestations of geodynamic processes. In this connection, in a comparison of our results with the results of other authors we will limit ourselves to studies made with the use of artificial sources of oscillations.

The most precise and reliable results in the evaluation of temporal changes in the travel time of crustal longitudinal waves (Pg) in Central California were obtained using seismic vibrators as the sources of oscillations [17, 27]. The experiments of T. V. Mc Evilly and R. S. Clymer, carried out in the neighborhood of station BVL (Fig. 1), made it possible to obtain estimates of temporal variations of $\sim$0.005-0.010 sec per year with an accuracy in determining the travel time of $\sim 10^{-4}$ sec. These estimates agree well with our results in determining the root mean square

variation of residuals for Pg waves of $\sim$0.015 sec per year. A similar order of magnitude of variations of residuals for Pg waves ($\sim$0.01 sec per year) was obtained in Southern California for the region of the Mohave Desert [14]. In all the considered cases the investigations covered the upper part of the section to depths not greater than 10 km.

Variations of the residuals of the first longitudinal waves approximately an order of magnitude greater were obtained in Central California with the use of powerful blasts at epicentral distances 400-600 km [13]. The reasons for such significant differences in the estimates of temporal variations in this article and in [13] may be attributable in part to appreciable variations in the magnitudes and depths of the foci of events used in [13]. In addition, our investigations and the investigations in [13] cover substantially different ranges of depths and regions of the medium. Whereas in our case these were the upper 5-10 km of the crust, in [13] it was the crust and upper mantle to depths of 60-80 km. The authors of [13] also postulate more contrasting manifestations of temporal variations in the upper mantle, but a discussion of these matters is beyond the scope of this study.

The agreement of our estimates of the temporal variations of residuals for Pg waves with the results of the most precise measurements of variations in the travel time of crustal longitudinal waves carried out with the use of seismic vibrators [17, 27] can be regarded as a factor confirming the reliability of the analysis made in this article.

6. Variations of Residuals and Local Earthquakes in Observation Region

Above we obtained estimates of the characteristics of long-period variations of residuals or a background process caused by relatively slow changes in the stressed-strained state of the medium in the upper part of the section (to depths $\sim$5 km) in the observation region. At the same time, for the purpose of predicting earthquakes the short-period variations of residuals with a time scale of not more than 1-2 months are also of interest. Variations of such duration were suppressed when averaging the initial data for evaluating the characteristics of long-period variations. Using these same primary data, we will analyze short-period variations of residuals accompanying local earthquakes in the observation region.

During the observation period 1973-1975 the strongest earthquake was that of 28 November 1974 in the neighborhood of Hollister. The magnitude of this earthquake was M_L = 5.2 and the focal depth was 6 km. The position of the epicenter and the focal mechanism are shown in Fig. 1 on the basis of data in [10].

In order to analyze the short-period variations it is necessary to ensure, insofar as possible, a higher "frequency of interrogation" of the values of the residuals in time. For this purpose we will employ the primary matrix $[\delta t_{ki}]$, excluding from it individual elements for stations and events giving substantial (more than 0.07 sec) deviations from the corresponding elements of the edited matrix of residuals. In order to suppress the random errors in determining the residuals we will average the δt_{ki} values for each moment in time T_i at all stations in the group. The mean values of the residuals $\langle \delta t_i \rangle$ obtained in this way are shown in

Fig. 12. This same figure shows curves of the temporal changes in the magnitudes of the blasts and the distances $\delta\Delta$ between the epicenters of the first and subsequent blasts. In Fig. 12 the arrow pointing downward indicates the time of the earthquake of 28 November 1978 in the vicinity of Hollister.

In Fig. 12 the dependence of $\langle\delta t_i\rangle$ on time has a complex character. This is associated with the influence of random errors, as well as the effects of migration of the epicenters of blasts and their magnitudes. In particular, the $\langle\delta t_i\rangle$ variations in 1973 in antiphase duplicate the changes in the magnitudes of the corresponding blasts and evidently were caused precisely by this factor. At the same time, a distinguishing characteristic of the $\langle\delta t_i\rangle$ curve is a considerable and significant difference in the mean temporal values $\langle\delta t_i\rangle$ during the period preceding an earthquake (1973 - June 1974) and after it (December 1974 - October 1975). The first period is characterized by positive values of the residuals whereas the second period is characterized by negative values. Judging from the curves of change in M_L and $\delta\Delta$ in Fig. 12, it is impossible to attribute this peculiarity to the effects of migration of epicenters and variations of magnitudes of the blasts. Thus, the mentioned changes in the mean $\langle\delta t_i\rangle$ values are to a considerable degree a result of the appearance of long-period variations of residuals.

The mentioned peculiarity of behavior of $\langle\delta t_i\rangle$ values with time agrees rather well with the curve of change in the "volume" deformation θ for the entire observation region (Fig. 11). In actuality, positive θ up to the time of the earthquake of 28 November 1974 are indicative of a dilatation of the studied volume of the medium, which should cause a decrease in the velocities of longitudinal waves and an increase in the residuals. A decrease in θ approximately to zero in 1975 is accordingly accompanied by a decrease in the $\langle\delta t_i\rangle$ values, that is, an increase in the velocity of P waves.

The second interesting peculiarity of the $\langle\delta t_i\rangle$ curve is an exceedingly rapid, with a period of about two or three weeks, and strong change in the $\langle\delta t_i\rangle$ values of an oscillating (unstable) character approximately 1-2 months prior to the moment of an earthquake. A change in the $\langle\delta t_i\rangle$ values from approximately -0.03 sec to 0.08 sec exceeds the error in determining the $\langle\delta t_i\rangle$ value by a factor of approximately four, that is, is known to be significant. At the same time, changes in residuals of an unstable character, with respect to long-period variations, cannot be completely related to changes in the magnitudes of events and migration of their epicenters (Fig. 12).

The established characteristics of behavior of the observed values of the residuals $\langle\delta t_i\rangle$, averaged in area, are manifested in greater contrast if the averaging is not carried out for all stations but only for stations situated relatively close to the epicentral region of the considered earthquake. For example, for the stations CAN, FEL, GHS, LTR, CHR, PCL (Fig. 1) the seismic waves must travel either directly through the focal zone or close to it in comparison with the other used stations. The $\langle\delta t_i\rangle$ curve for the indicated subgroup of stations, shown in Fig. 12, illustrates the established peculiarities of manifestations of the spatial-temporal variations of the residuals.

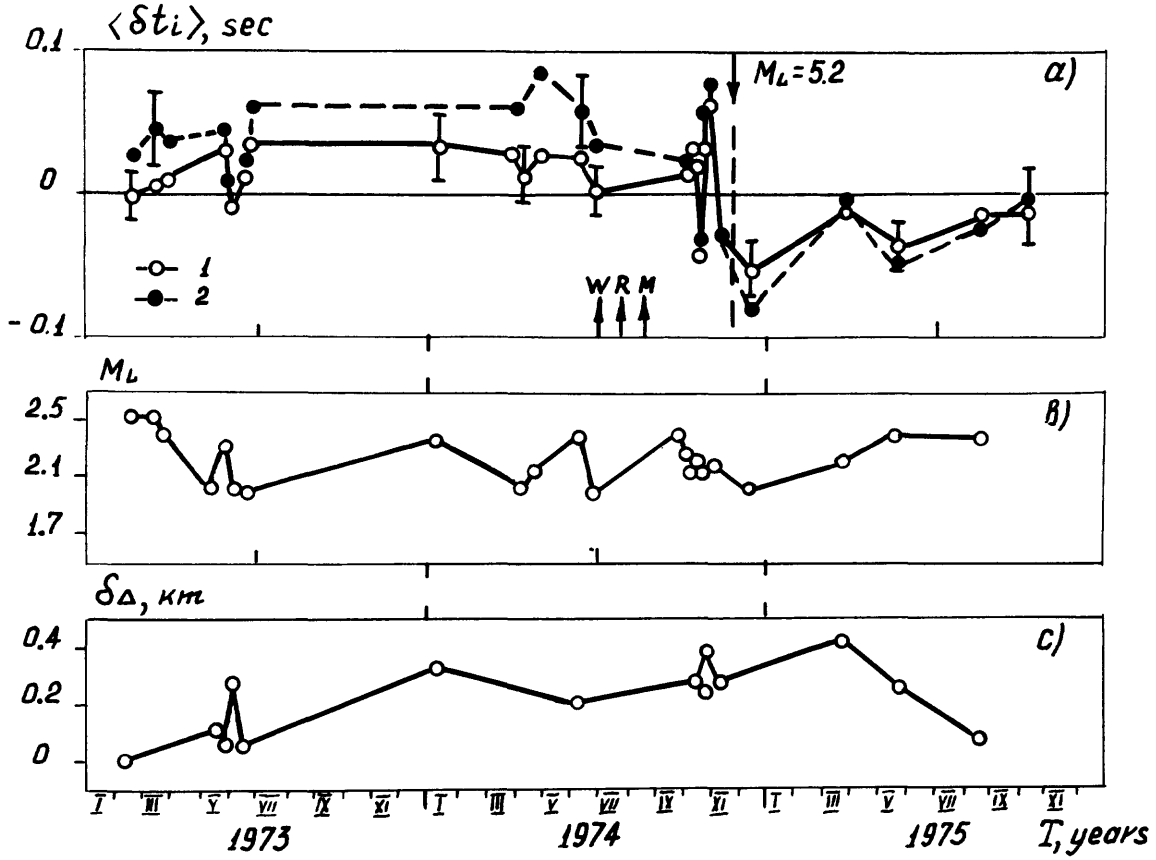

Fig. 12 Temporal change in mean values of residuals $\langle \delta t_i \rangle$ (a), magnitudes of blasts M_L (b) and distances between epicenters of first and subsequent blasts $\delta\Delta$ (c). 1) averaging of residuals for entire group of stations; 2) averaging for stations of eastern subgroup: CAN, FEL, GHS, LTR, CHR, PCL.

Conclusion

On the basis of the analysis which has been made the process of temporal variations of the residuals for the investigated region can be represented schematically in the following way. Against the background of relatively weak long-period variations of residuals evidently associated with manifestations of geodynamic processes in zones of seismically active faults, there are intensive and rapid changes in residuals of an oscillating (unstable) character preceding a local earthquake which was the strongest (M_L = 5.2) during the observation period. The long-period variations have a characteristic time scale $\sim$2 years and an intensity of appearance $\sim$ 0.03 sec (0.015 sec per year). The processes leading to such variations affect approximately the upper 5 km of the section. The long-period variations are manifested in a difference in the mean (in area and time) values of the residuals up to the time of the earthquake of 28 November 1974 and after it.

During a period of weak variations of a long-period character they are separated by a rather short (with a duration of about 2 months) period of unstable behavior of residuals characterized by intensive ($\sim$0.10 sec) short-period variations with a characteristic time scale of$\sim$2 weeks. We had to realize that statistical significance of these short-period variations are considerably lesser than the long-period ones.

On the basis of existing theoretical concepts on the processes of preparation for and possible precursors of earthquakes [3], the unstable behavior of the residuals 1-2 months prior to the time of the earthquake of 28 November 1974 could be regarded hypothetically as a precursor of this earthquake. If it is assumed that the established effect is a precursor, its nature is substantially different than the nature of the relatively well-known precursors of a baylike character [2, 4, and others]. In particular, the time of its appearance differs substantially from the time of appearance of baylike precursors. The latter comment is illustrated by Fig. 12, where the arrows indicate the times of appearance of baylike precursors, computed for an earthquake with M_L = 5.2 on the basis of the empirical expressions derived by T. Rikitake (R), J. Whitcomb (W), V. I. Myachkin and S. I. Zubkov (M) [2, 4, 16].

At the same time, on the basis of a single fact it is naturally impossible to regard with certainty the established effect of an unstable temporal behavior of residuals as a real earthquake precursor. Reliable results along these lines can be obtained only after the accumulation of a representative volume of data on the characteristics of the temporal variations of residuals of different spatial and time scales.

As indicated in this article, the problems involved in the method for the analysis of residuals or fluctuations of travel time play an exceedingly important role in obtaining reliable evaluations of the characteristics of temporal variations. In particular, a diagnosis of the variations associated with the migration of epicenters and changes in source intensity with time must become a necessary element of such an analysis when using blasts and especially earthquakes as the sources. The methods developed in this article can be used as specific procedures in the diagnosis of temporal variations.

BIBLIOGRAPHY

1. Nersesov, I. L., Semenov, A. N., Simbareva, I. G., "Spatial-Temporal Distribution of Ratios of Travel Times of Longitudinal and Transverse Waves in the Garm Region," EKSPERIMENTAL'NAYA SEYSMOLOGIYA (Experimental Seismology), Moscow, "Nauka," 1971.

2. Rikitake, T., "Earthquake Precursors," BULL. SEISM. SOC. AM., Vol 65, pp 1133-1162, 1975.

3. Sadovskiy, M.A., Nersesov, I. L., "Problems in Earthquake Prediction," IZV. AN SSSR, FIZIKA ZEMLI (News of the USSR Academy of Sciences, Physics of the Earth), No 9, 1978.

4. Myachkin, V. I., PROTSESSY PODGOTOVKI ZEMLETRYASENIY (Processes of Preparation for Earthquakes), Moscow, "Nauka," 1978.

5. Boore, D. M., Lindh, A. G., McEvilly, T. V., Tolmachoff, W. W., "A Search for Travel-Time Changes Associated With the Parkfield, California Earthquake of 1966," BULL. SEISM. SOC. AM., Vol 65, pp 1407-1418, 1975.

6. Cramer, C. H., Kovach, R. L., "Time Variations in Teleseismic Residuals Prior to the Magnitude 5.1 Bear Valley Earthquake of February 24, 1972," PURE APPL. GEOPHYS., Vol 113, pp 281-292, 1975.

7. Wesson, R. L., Robinson, R., Bufe, C. G., Ellsworth, W. L., Pfluke, J. H., Steppe, J. A., Seekings, L. C., "Search for Seismic Forerunners to Earthquakes in Central California," TECTONOPHYSICS, Vol 42, pp 111-126, 1977.

8. Cramer, C. H., "Teleseismic Residuals Prior to the November 28, 1974 Thanksgiving Day Earthquake Near Hollister, California," BULL. SEISM. SOC. AM., Vol 66, pp 1233-1248, 1976.

9. Cramer, C. H., Bufe, C. G., Morrison, P. W., "P-Wave Travel-Time Variations Before the August 1, 1975, Oroville, California Earthquake," BULL. SEISM. SOC. AM., Vol 67, pp 9-26, 1977.

10. Lindh, A. G., Lockner, D. A., Lee, W. H. K., "Velocity Anomalies: an Alternative Explanation," BULL. SEISM. SOC. AM., Vol 68, pp 721-734, 1978.

11. Aki, K., Nersesov, I. L., Nikolayev, A. V., Sedova, Ye. N., Shaymer, D. D., "Temporal Changes in Fluctuations of Amplitudes and Travel Times of the Teleseismic P Wave in the Garm, California, LASA, NORSAR Groups," SB. SOVETSKO-AMERIKANSKIKH RABOT PO PROGNOZU ZEMLETRYASENIY (Collection of Soviet-American Papers on Earthquake Prediction), Vol 1, Dushanbe-Moscow, "Donish," 1976.

12. Bolt, B. A., "Constancy of P Travel Times from Nevada Explosions to Oroville Dam Station 1970-1976," BULL SEISM. SOC. AM., Vol 67, pp 27-32, 1977.

13. Wesson, R. L., Nersesov, I. L., Nikolayev, A. V., Sedova, Ye. N., "Investigation of Temporal Changes in the Velocity of Longitudinal Waves in Northern California," SB. SOVETSKO-AMERIKANSKIKH RABOT PO PROGNOZU ZEMLETRYASENIY, Vol 2, Book 1, Dushanbe-Moscow, "Donish," 1979.

14. Kanamori, H., Fuis, G., Nevskiy, M. V., "Temporal Variations of Residuals of the Travel Times of Pg Waves at Stations in Southern California Using Data from Quarry Blasts," SB. SOVETSKO-AMERIKANSKIKH RABOT PO PROGNOZU ZEMLETRYASENIY, Vol 2, Book 1, Dushanbe-Moscow, "Donish," 1979.

15. Kanamori, H., Fuis, G., "Variations of P-Wave Velocity Before and After Galway Lake Earthquake (M_L = 5.2) and Goat Mountain Earthquakes (M_L = 4.7) 1975 in the Mohave Desert, California," BULL. SEISM. SOC. AM., Vol 66, pp 2017-2037, 1976.

16. Raikes, S. A., "The Temporal Variation of the Teleseismic P-Residuals for Stations in Southern California," BULL. SEISM. SOC. AM., Vol 68, pp 711-720, 1978.

17. Clymer, R., McEvilly, T. V., "Measured Changes in Crustal P-Wave Travel Times," EARTHQUAKE NOTES, EASTERN SECTION SSA, Vol 49, No 1, p 60, 1978.

18. Eaton J. P., Nevskiy, M. V., Nikolayev, A. V., "Fine Spatial Structure of Fluctuations of the Travel Time of Teleseismic P Waves in Central California," SB. SOVETSKO-AMERIKANSKIKH RABOT PO PROGNOZU ZEMLETRYASENIY, Vol 2, Book 1, Dushanbe-Moscow, "Donish," 1979.

19. Aki, K., Lee, W. H. K., "Determination of Three-Dimensional Velocity Anomalies Under a Seismic Array Using First P-Arrival Times from Local Earthquakes," JGR, Vol 81, No 23, 1976.

20. McNally, K. C., McEvilly, T. V., "Velocity Contrast Across the San Andreas Fault in Central California: Small-Scale Variations from P-Wave Nodal Plane Distortion," BULL. SEISM. SOC. AM., Vol 67, pp 1565-1576, 1977.

21. Lee, W. H. K., Bennet, R. E., Meagher, K. L., "A Method of Estimating Magnitude of Local Earthquakes from Signal Durations," USGS, Open-File Rept., 1972.

22. Lee, W. H. K., Lahr, J. C., "HYPO 71 (Revised): A Computer Program for Determining Hypocenter, Magnitude and First Motion Pattern of Local Earthquakes," USGS, Open-file Rept., 75-311, 1975.

23. Nersesov, I. L., Nikolayev, A. V., "Temporal Change in the Structure of Fluctuations of the Amplitudes of Teleseismic P Waves in the Garm Prognostic Polygon," DAN SSSR (Reports of the USSR Academy of Sciences), Vol 232, No 4, 1977.

24. Kim, I. A., Nikolayev, A. V., "Nature of Temporal Changes in Fluctuations of Teleseismic P Waves in the Northern Tien Shan," DAN SSSR (Reports of the USSR Academy of Sciences), Vol 239, No 3, 1978.

25. Korn, G., Korn, T., SPRAVOCHNIK PO MATEMATIKE (Handbook of Mathematics), Moscow, "Nauka," 1968.

26. Savage, J. C., Prescott, W. H., Lisowski, M., King, N., "Geodolite Measurements of Deformation Near Hollister, California, 1971-1978," USGS, Open-file Rept., 1979.

27. McEvilly, T. V., Clymer, R., "Monitoring Seismic Wave Velocities in situ," USGS EARTHQUAKE INF. BULL., Vol 11, No 6, 1979.

SEISMIC ZONATION IN THE PAMIR AND TIEN-SHAN REGIONS OF SOVIET CENTRAL ASIA

by

V. N. Krestnikov, I. L. Nersesov and D. V. Stange

Abstract

A new method of approach to seismic zoning is outlined. It is based on an analysis of Quaternary tectonics, surface relief of the Moho, paleodislocations and present day seismicity. A new version of the Pamir and Tien-Shan seismic zonation map is given.

Introduction

In the Soviet Union, investigations connected with seismic zonation have been carried out for some time. Using the techniques available at present, it has been possible to assess the seismic risk and to define seismic zones according to the probability of violent earthquakes (References 1, 2 and 3). Nevertheless, the present demands of assessing seismic hazards require continuing redefinition of the parameters involved (References 4, 5, 6 and 7). These are related to the quantitative characteristics of the seismic vibrations namely, amplitude, period and frequency as well as dependence on epicentral distance. There is also a need to be able to predict the expected strong ground motion. This calls for more detailed and reliable data on the sites of violent earthquakes than on general small-scale microzonation. In addition, one should have a reliable estimate of the possible maximum intensity of expected earthquakes, their recurrence intervals, and the geological characteristics of the earthquake source area. Formerly, one of the drawbacks in determining the seismic hazard of an area was that often no data were available on its tectonic development during the Quaternary epoch.

For the Pamir and Tien-Shan territories, such investigations have been carried out for the first time by a group of workers of the Academy of Sciences of the U.S.S.R., Institute of Earth Physics. Isolines of the tectonic movement of this region during the Pleistocene and Holocene have been determined (Reference 8). As a result, it has become possible to estimate the velocity of vertical movement and its lateral gradient; to pick out areas where changes in the tectonic regime occurred during the Pleistocene and Holocene; and to follow the activity of seismic zones in time and space. Thus, data on Quaternary tectonics from an extensive region can be used for seismic zonation. Present day tectonic activity, as it is reflected in seismic activity, has been estimated from movement on earthquake faults, as well as from paleoseismicity and present-day seismicity. For the first time in estimating seismic hazards, data from deep-seated structures have been used in investigating the earthquake source. This body of new and published geologic and seismic information has made it possible to approach the problem of the seismic hazard in the Pamir and Tien-Shan areas in a new way.

Brief history of tectonic movements

The area of investigation involves a complex, fold-block, mountain structure that has been developing for a long time. It covers parts of two different extensive geotectonic areas: the Epi-paleozoic platform and the Alpine geosyncline. During the formation of the platform, which began at the end of the Oligocene and coincided with the final stage of closure of the Alpine geosyncline, the Pamir and Tien-Shan mountains were produced: their present-day outlines originated during the Quaternary. Orogeny continued irregularly both in time and space: a quiet interval occurred during the Pliocene and early Pleistocene. Activity has continued to the present where it is shown by intense deformation and high seismicity.

To describe the geological data which have made it possible to identify the zones of greatest tectonic activity and violent earthquakes within the Pamir and Tien-Shan area, it is necessary first to outline the regional geologic history. Obviously, more is known about the most recent history.

As a result of intense tectonic movements in the Oligocene, the platform regime of the Mesozoic and Paleogene in the Tien-Shan was disturbed while the Pamir geosyncline continued to exist (References 9, 10, 11). Toward the end of the Cretaceous and the beginning of the Paleogene, a dying out of tectonic movements has been noted, whose new impulse was seen at the beginning of the endogenous Tien-Shan Epi-paleozoic platform activity. The tectonic activity heralded a new stage in the geologic history of this part of Asia. The area as a whole was characterised by differential movements, largely uplifts, that continued until the end of the Neogene. Great depressions and uplifts developed that were inherited from previous times (Reference 12). But at the same time that new structural elements were forming, old ones were becoming more complex or dying out. At all times, deep-seated faults played an important role. As well as defining large blocks of the crust, they also controlled the largest structural elements, often being their natural boundaries. It should be noted that with the beginning of tectonic activity, there were already differences between the central and northern Tien-Shan and the remaining part, separated by the Talasso-Ferghana fault (Reference 13). These differences had existed even at the platform stage of development during the Mesozoic, when the western part of the Tien-Shan to some extent was tectonically more mobile: the differences increased with the beginning of tectonic activity. At the time the scope and differentiation of the northern and central Tien-Shan remained much less than in the western Tien-Shan. At the same time in the Pamir, there was a sharply defined difference between the western and eastern parts, separated by the Pamir-Himalayan fault zone (Reference 14). Uplift of the eastern block lagged significantly behind that of the western block: this lag increased with time. This fault zone as well as differences between the western and eastern blocks of the Pamir existed since the Jurassic: their presence determined the tectonic regime during the Cenozoic. At the same time the ancient structural arch played practically no part, except for the northern and north-western areas connected with the Darvaz-Karakul fault. In the Pamir and Tien-Shan sections west of the Talasso-Ferghana fault, the intense differential uplift movements continued to the end of the Neogene. In the central and northern Tien-Shan during the Pliocene, these movements decreased significantly and vast areas became involved in downfolding which resulted in the formation of the lake regime. At the end of the Pliocene, the intensity of movements fell sharply and a period of tectonic quiescence occurred. During the Eo-Pleistocene intensive uplifts began once more in the central and northern Tien-Shan and have continued to the present. In the remainder of the Tien-Shan and Pamir, the period of tectonic quiescence began somewhat later during the Upper Pleistocene and ended in the middle of the Lower Pleistocene. Only in the Tadjic depression was it delayed to some extent, terminating at the end of the Upper Pleistocene. Here, as in the central and northern Tien-Shan, the end of the period of tectonic calm was marked by a new impulse of tectonic uplift.

During the Quaternary, development of the Pamir and Tien-Shan proceeded according to the regime inherited from the Eo-Pleistocene. The character of these movements during this period is shown in Figure 1 (Reference 8). Under the conditions of intense, differential uplift, the difference between the northern and central Tien-Shan and its remaining parts, and the western and eastern Pamir continued to increase. During the Quaternary, the maximum amount of movement over this area was 2000-3000 meters. This was greatest in the Pamir where the total movement was 2000-2500 meters. Uplift in the eastern Pamir was 700 meters less than that in the western Pamir, of which 50-150 meters can be ascribed to the Holocene. In the Tien-Shan, the most intensive uplift during the Quaternary occurred in the eastern part of the Turkestan ridge: here about 2500 meters occurred, including 120-160 meters in the Holocene. In

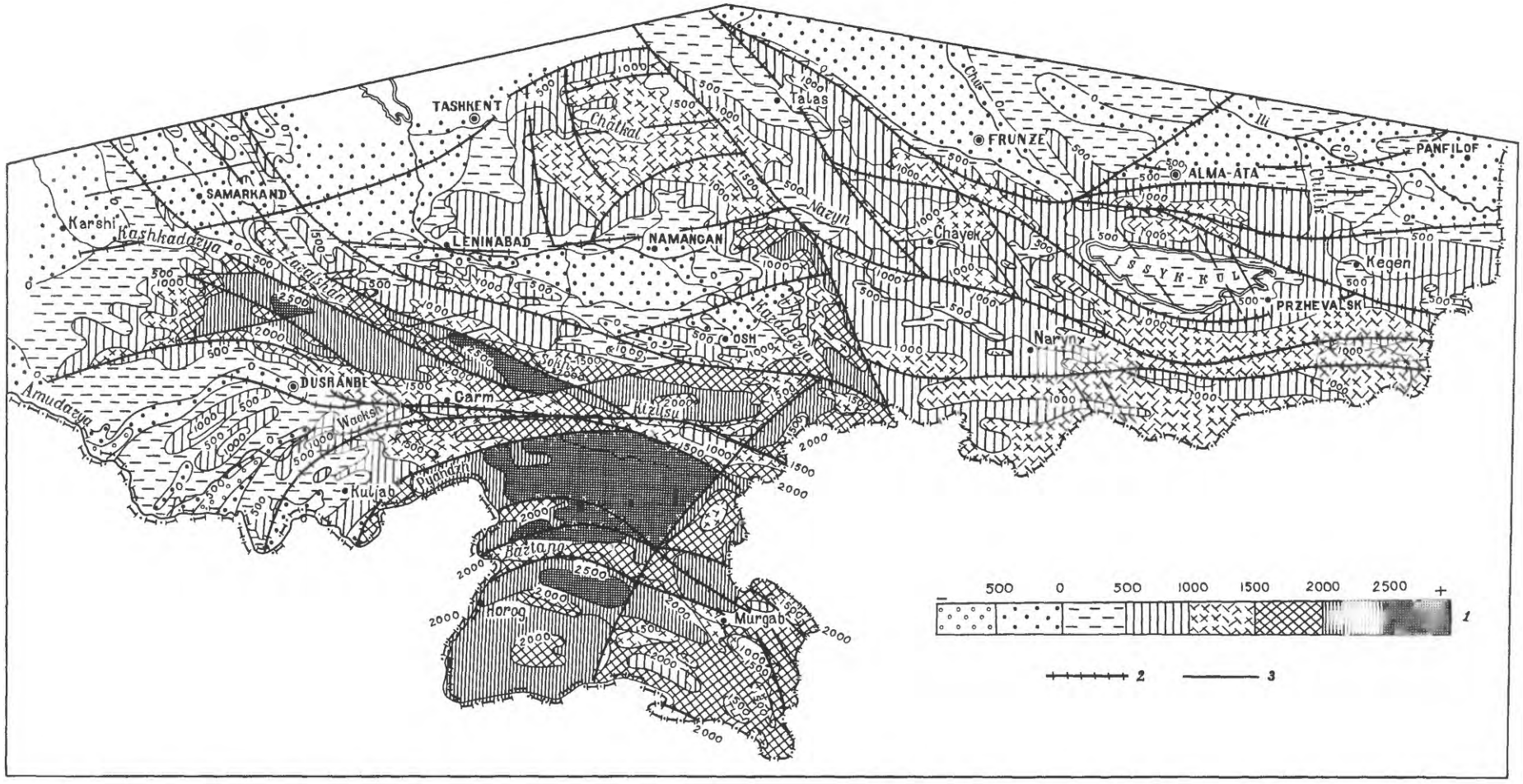

Figure 1. Schematic map summarizing vertical tectonic movements during the Quaternary period.

1. Amplitude of vertical tectonic movements in meters
2. Fault zones
3. Regional faults with an anti-Tien Shan strike

the central and northern Tien-Shan, the maximum amount of uplift was lower: it was about 1500 meters, the Holocene value being more than 120 meters. During the Pleistocene, absolute downwarps can be noted in the Tadjic depression, the central Ferghana area, and the Chui, Ilii and possibly Issyk-Kul depressions.

A general decrease in the amount of the downwarped area has been identified during the process of the area's tectonic development, both on an absolute scale and a relative scale, that is, within a broad region of uplift. By the end of the Holocene, only isolated, local areas within the large depressions were characterized by absolute downwarping. In the Ferghana depression during the Holocene, the sense of motion changed in an absolute sense. Throughout the Quaternary period, differences in the tectonic regime continued to increase between the central and northern Tien-Shan, and its western part, separated by the Talasso-Ferghana fault. The western Tien-Shan was characterised by significant differential movements connected with the shift of individual blocks of the Earth's crust along fault zones. These reached significant amplitudes in the Gissar-Alai in particular. In contrast, the central and northern Tien-Shan behaved as a single megablock. Its boundaries coincided in the north with faults separating the active part of the Tien-Shan Epi-paleozoic platform from the inactive part, and to the south with the Epi-proterozoic Tarim massif. To the west, the boundary was the Talasso-Ferghana fault. During the Quaternary period, the central and northern Tien-Shan block would rise with north-south distortion in the north-south direction. The greatest uplift has been documented in its southern part, while the least uplift occurred in the northern part. From the earliest epochs of the Pleistocene through the Holocene, the difference in the amplitude of uplift between the northern and southern parts of the block decreased: nevertheless, this can be seen clearly in a summary of Quaternary movements.

In order to correlate the characteristics of the tectonic regimes in individual areas of the Pamir and Tien-Shan, weighted-average tectonic rates have been calculated for the Quaternary according to the formula:

$$\frac{V_1S_1+V_2S_2+\ldots VnSn}{S_1+S_2+\ldots Sn}$$

where Vn = tectonic rate in individual areas
Sn = area for which tectonic rate has been determined

Graphs have been compiled for the Pamir, western Tien-Shan and its remaining territory which outline the tectonic rate during the Quaternary (figure 2). They show that the average tectonic rate increases from the early Pleistocene through the Holocene. Against this background of an overall increase, the highest rates are noted for the Pamir and lowest in the northern and central Tien-Shan.

It is quite probable that the increase in tectonic rate in the Holocene is not a local phenomenon but more widespread: as has been known, it is characteristic of the Quaternary as a whole (Reference 15). During the Pleistocene and Holocene, development of the Tien-Shan was influenced by ancient structures of Paleozoic age. All the principal structural elements, whether uplifts or depressions, were oriented east-west in the Tien-Shan and formed southward curving arcs. At the same time, opposing trends formed in northeast and northwest directions. One of the important differences in the Tien-Shan and Pamir tectonic regime is that the main part is linked with the Pamir-Himalayan transverse fault zone, and not to the more ancient east-west trend.

During the Quaternary, fault blocks played a premier role: they dissect the Earth's crust into individual blocks, whose boundaries influence the tectonic development of the area. Generally the boundary faults are high angle, with the dip exceeding 70°.

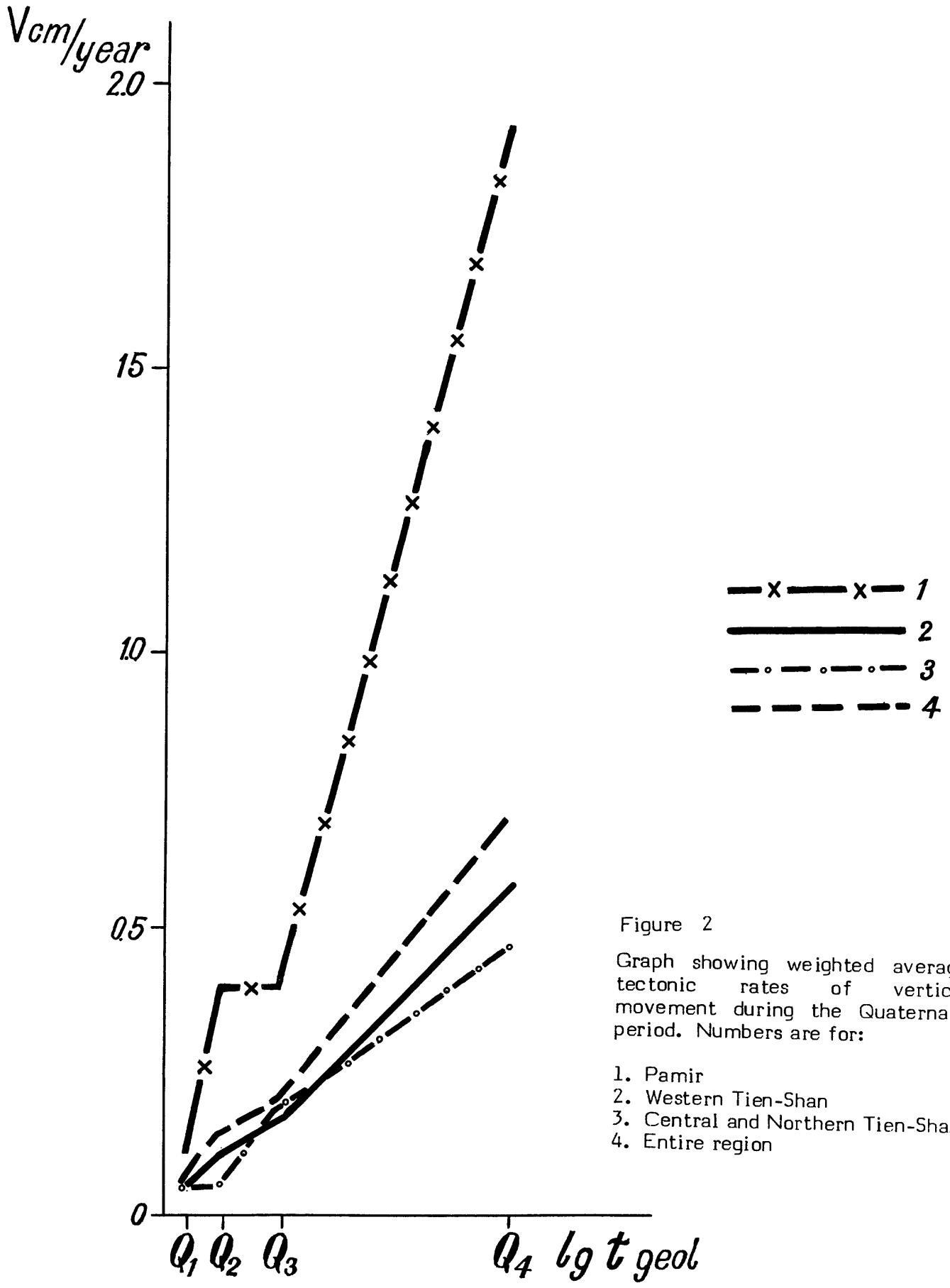

Figure 2

Graph showing weighted average tectonic rates of vertical movement during the Quaternary period. Numbers are for:

1. Pamir
2. Western Tien-Shan
3. Central and Northern Tien-Shan
4. Entire region

The amount of displacement along the fault varies in time and space. Nearly all the fault zones are of Paleozoic age; some of them are possibly of earlier age. The Pamir-Himalayan zone is an exception; displacements began only in the Mesozoic. Orientation of the Pamir and Tien-Shan fault zones is according to the general trend in the area; however, some of the fault zones are transverse to the general trend.

During the Quaternary, an increase in the differential uplift was reflected in the activity of the various fault zones. Using compilations of these movements, it has been possible to follow changes in individual faults from the early Pleistocene through the Holocene. In order to correlate the intensity of fault development over the entire territory throughout the Quaternary, an index of relative activity (a) has been used that relates activity in time and space (figure 3). It is the ratio of the amplitude of the displacement along a segment of the fault for a given time interval of the Quaternary (AQ_n) to the mean displacement amplitude over all the Pamir and Tien-Shan faults for the same period of time (A_mQ_n) where

$$a = \frac{AQ_n}{A_mQ_n}$$

In figure 3, the activity index is shown for the ranges <0.5; 0.5-1.5; >1.5 As can be seen, the activity of the fault zones differed significantly in time and space. The most intensive displacements occurred along the Darvaz-Karakul and Talasso-Ferghana zones: here the amplitudes reached over 2000m during the Quaternary and more than 120m during the Holocene. The least displacements occurred along the central Tien-Shan, Chatkalo-Kuramin Krai, and eastern Pamir faults. Somewhat more active were the Gissar-Alai, Pamir-Alai and the western Pamir fault zones. It should be noted that activity along the strike of the fault changed within rather broad limits. During the Quaternary history of the Pamir and Tien-Shan, regional faults were of great importance. In general, they may be classified in three main systems: a Tien-Shan system with a strike parallel to the general structural plan, and two "anti" Tien-Shan systems with northwest and northeast strikes. The Tien-Shan system persisted throughout the whole period of activity. Of greater interest are the "anti" Tien-Shan system of faults which showed their existence only from the Pleistocene. The system with northeast strikes parallel to the western Tien-Shan fault is characteristic of the western Tien-Shan; that with northwest strikes is characteristic of the cental Tien-Shan and is parallel to the Talasso-Ferghana fault zone. Most of these systems can be identified with geological data, while some can be defined only by means of geophysical methods. (References 16, 17). In general, they are characterised by significant activity, confinement to long narrow zones, as well as a supposed connection with Precambrian structural control. They are perhaps the surficial expression of ancient fault zones which were reactivated during the Quaternary. However, they could also be new structures associated with the process of reconstruction of the crust that will be shown to be taking place now.

Horizontal as well as vertical movements occurred on a number of the faults. The displacements are of overthrust, strike-slip and normal with strike-slip type. In some cases, these movements have been reliably established, in others movement is inferred on the strength of the complexity of displacement and the Cenozoic stratigraphy. Information on the nature of slips and upthrows is not considered reliable, especially when evaluating upthrow amplitudes in the Tadjic depression and slip along the Darvaz-Karakul fault (References 18, 19). The existence of great slip along the Talasso-Ferghana fault zone during the Quaternary time is doubtful and has not been confirmed (References 13, 20). The most widespread movements, as well as the most reliably documented, seem to be displacements in the horizontal component occurring at the

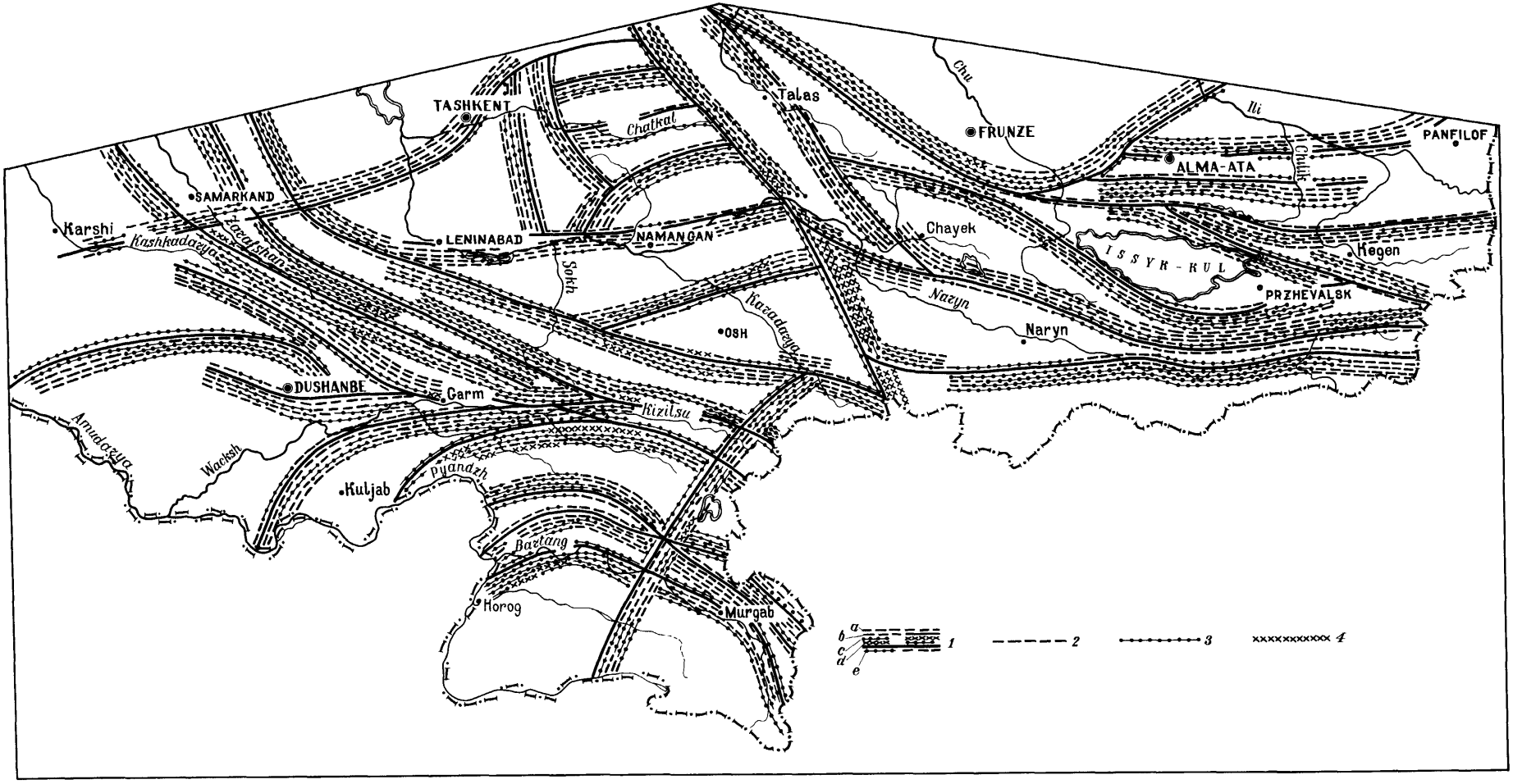

Figure 3. Fault activity in time and space. Numbers denote:

1. Fault zone activity during
   a. Holocene
   b. Late Pleistocene
   c. Middle Pleistocene
   d. Early Pleistocene
   e. Entire Quaternary
2. Activity index less than 0.5
3. Activity index from 0.5 to 1.5
4. Activity index greater than 1.5

same time as upthrow movements, the latter being typical of faults in this region. When the fault plane dips at 80°, the horizontal component of the upthrow reaches 170-180m for a vertical amplitude of 1 km. Thus, Quaternary horizontal movements in the Pamir and Tien-Shan are generally slight, and cases where they reach more than a kilometer are rare and not confirmed. Vertical displacements exceed 2-3 km: they are observed everywhere and were dominant in fashioning the structure of this part of Asia. Horizontal movements were caused mainly by horizontal compression whose existence has been reported by many investigators of Pamir and Tien-Shan structural geology. The axis of this horizontal strain is oriented in a northwest direction across the general strike of the main structural elements. Geological evidence for this is (1) linear elongation of the main structural elements in one direction, (2) upthrows predominant in the various fault zones, and (3) the presence of thrust structures. Horizontal compression is active even today. Because of this, fissure-type deformations are absent, in contrast to the Baikal rift zone. Throughout the long geological history of this part of Asia, the directions of horizontal strain do not seem to have changed except for the central and northern Tien-Shan. Before tectonic movements began here, compression had possibly been replaced by spreading. At the end of the Cretaceous-Paleocene in the central Tien-Shan there occurred insignificant but widespread extrusions of basaltic lava that are peculiar to areas of horizontal spreading, for example, the Baikal rift zone. But these strains were of short duration and were later replaced by compression. In the Quaternary, especially the Holocene, the character of strain seems to have changed somewhat: as a result rupture zones began to develop along "anti" Tien-Shan directions.

Association of modern structures with the Moho.

Comparison of the modern structural plan of the various regions with the surface relief of the Moho makes it possible to distinguish the independent segments of the Earth's crust that are in some cases bounded by seismogenic faults. New data have made it possible to refine more precisely the surface morphology of the Moho for the Pamir and Tien-Shan region. As well as seismic data on the Earth's crust, published information has also been used (References 21, 22, 23, 24). The method used so far has been described elsewhere (Refrence 25).

In the new scheme within the Tien Shan area (figure 4), two "bands" of the Earth's crust can clearly be seen that show a thickening in excess of 50 km and are separated by an area of shallow surface deposits. The northern band coincides with uplift of the Kirghiz, Zaalai Alatau and Kungei Alatau ridges: the southern one coincides with the Gissar-Alai system of uplifts. Besides these bands with a Tien-Shan strike, numerous transverse structural elements have been noted. For instance in the Issyk-Kul lake area, a north-south elongated area of crust has been traced that is thickened southwards. Such "anti" Tien-Shan structural elements connected with crustal thickening and thinning have been identified in other areas of the Tien-Shan: the transverse north-south character is generally typical of the western Pamir. It should be noted that most of the transverse structural elements derived from the surface relief of the Moho are poorly related to surface structure in the region. On the whole, however, those crustal areas that are of minimal thickness coincide with extensive Tien-Shan depressions that had been developing for a long time such as those at Chuii, Ilii, Naryn and Tadjic. At the same time, the Issyk-Kul and Ferghana depressions are characterised by crustal thickening. In most cases, the definite structural elements identified on the Earth's surface have no clearly related expression on the Moho surface, with the exception of the Kirghiz, Kungei-Alatau and Terskei Alatau ridge systems on the one hand, and the Gissar-Alai on the other. As a rule, fault zones seen on the surface are fully or partially expressed even on the surface relief of the Moho. This is particularly so of faults that separate large structural areas. They embrace the Alma-Atiu, Zaalai, Severno-Tienshan, West-Tienshan and Darvas-Karakul zones. Other zones are less well expressed in the surface relief of the Moho. It should be noted that in the transverse surficial and deep-seated structures,

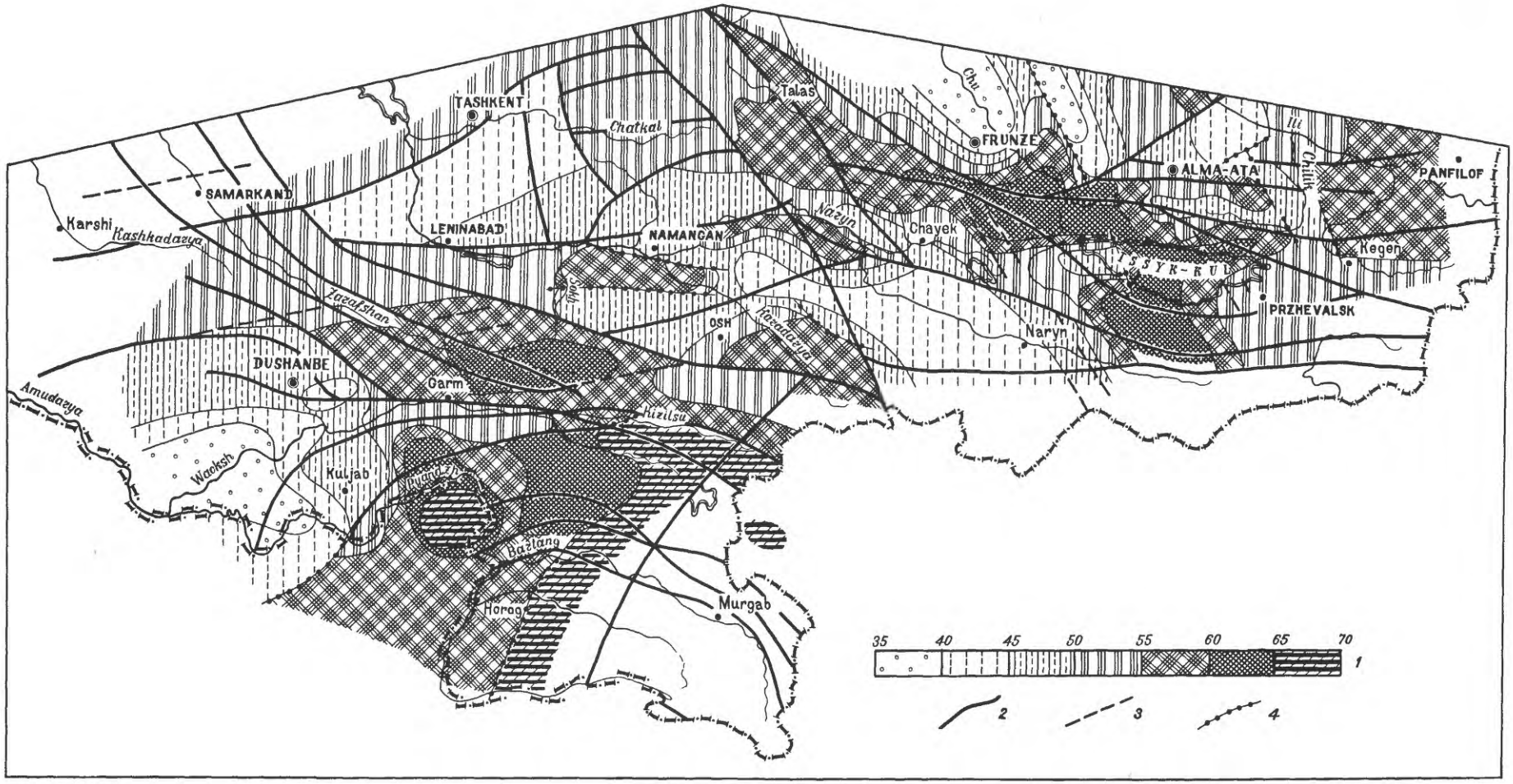

Figure 4 Moho surface relief. Numbers are:

1. Thickness of Earth's crust (kms)
2. Fault zones
3. Regional breaks with an anti-Tien Shan strike
4. Latent fault zones

"anti" Tien-Shan ruptures are expressed differently. It is found that the weaker the "anti" Tien-Shan disturbances are expressed in Pamir and Tien-Shan Quaternary movements, the clearer they are expressed in surface relief on the Moho. Thus, transverse disturbances that can be identified only by using geophysical methods, for example, in the Issyk-Kul Lake area, often show significant Moho displacement. In addition, we have identified a number of latent rupture zones that are clearly expressed in a deep-seated structure but not on the earth's surface. On the other hand, such an extensive fault zone as the Talasso-Ferghana, whose great activity during the Quaternary is unquestioned, has not been traced in the Moho surface relief.

On the whole, this scheme reflects the structure of the Tien-Shan and Pamir block of crust rather well. When it is combined with the scheme of Quaterary movements, we can identify a series of extensive blocks bounded by active faults and assess their activity. The present-day configuration of the Pamir and Tien-Shan when compared with Moho surface relief allows us to draw the following conclusion. Many structural elements that have been developing for a very long time because of their importance in building up a region, will also play a role in developing deep crustal layers. Nevertheless this does not always occur, as for example in the case of the Talasso-Ferghana fault and a number of other structural features. It is quite probable that as a result of new deformation, the more ancient surface of the Moho is reworked. Probably this process is very recent, possibly even as young as Holocene--a fact substantiated indirectly by the clearly expressed increase in Holocene tectonic activity. This interpretation is supported by the presence of developing, latent structural elements. Surface tectonic activities, therefore, lags behind deep-seated tectonic-activity being a relict. Undoubtedly it produces strain concentrations conditioned by the counteraction of surface and deep-seated deformation. A common analysis of Quaternary tectonics and relief on the Moho surface in this part of Asia allows us to project zones where these strains will most probably emerge.

Seismicity characteristics

Present-day tectonic activity in the Pamir and Tien-Shan cannot as yet be characterized by purely geological methods. Unbiased quantitative data reflecting deformation of the Earth's surface can be obtained by geodetic surveying. These are complex and laborious techniques that are not conducted over wide areas. It is possible to identify the most active tectonic areas by investigating seismic phenomena. To do this, earthquake-produced dislocations and geomorphologic forms that can be related to present and past dislocations have been studied. In the Pamir and Tien-Shan, three main features due to these deformation can be identified: rockfalls, mudflows and landslides, and rejuvenated areas. We have not differentiated such features as scarps and troughs, which are derivatives of the three main features. Features caused by open fissures, grabens and characteristics of tension have not been considered, as the area is under conditions of general horizontal compression (References 26, 27 28). The features resulting from deformation vary within wide limits depending on geologic conditions, surface relief and the size of the earthquake. Landslides and rock falls can involve hundreds of millions of cubic meters of material. The largest of these failures can block and partition river valleys so that lakes are formed, for example, Sarez in the Pamir, Iskanderkul, Sarychelck and lake systems such as the "Seven Beauties" and Karasu in the Tien-Shan.

Rejuvenated areas along which movements occurred as a result of violent earthquakes are of a different scope. They can vary from hundreds of meters to tens of kilometers, as for example in the Chan-Aksu river valley in the Kungei-Alatan ridge area. It should be noted that all the Pamir and Tien-Shan paleoseismodislocations are of Holocene age except for some late Pleistocene slips in the western Pamir. The overwhelming majority occurred during the last 5000 years judging from great landslides falling into flood plains. The size of the feature produced by the deformation depends

not only on the earthquake force but on geological and geomorphological characteristics too. It is often the case that earthquakes of the same size cause dislocations of quite different extent, and vice versa. Moreover, dislocations can be formed irrespective of seismic phenomena. An example is the Zarafshan river near the settlement of Aini: here collapse of the bedrock occurred along the fault plane in 1964 resulting in river ponding and the formation of a lake. Hence a careful approach must be taken in accounting for the many factors that cause deformation features.

To determine the conditions under which deformation structures are produced by a given stress regime, and their possible link with structural elements currently active throughout the Pamir and Tien-Shan region, the density of seismic and paleoseismic dislocations has been plotted in figure 5. The density was calculated for squares with 20 km side dimensions, and the figure shows deformation in zones. In most cases these coincide with the major known structural elements, that is, fault zones and transverse ruptures. The density contours are oriented parallel to the strike of the structural elements in the Pamir and Tien-Shan, that is, in east-west, north-east and north-west directions. The greatest concentration is clearly connected with faults that were very active during the Quaternary, for example, the Pamir-Himalayan, Talasso-Ferghana and others, as well as those to the west of Gissar-Alai with an "anti" Tien-Shan, northeast strike. The existence of paleodislocation features that are not connected with known earthquakes, has made it possible to interpret epicenters from violent earthquakes of magnitude $M \geqslant 6.5$ that are not recorded in historical documents. It should be remembered that the real epicenter may differ from the estimated epicenter, and that where one earthquake is postulated there may in fact have been several. This is related to the fact the area of maximum destruction does not always coincide with the epicenter, and that the relationship of a dislocation feature with a unique event is far from certain.

The results of seismological observations make it possible to estimate activity in the Pamir and Tien-Shan over the past tens and hundreds of years. The data are from Soviet seismological bulletins and other publications containing descriptions of macro effects from earthquakes (References 28 to 50). In addition data banks on earthquake investigations are available at the Institute of Physics of the Earth, U.S.S.R. Academy of Sciences, Moscow.

In order to obtain more reliable data about the classification of earthquake energy, class (K) 11 to 13 earthquakes (on the Soviet scale) have been re-evaluated for the period 1954 to 1970 from seismic stations in Tien-Shan and at Garm. Information on energy class 10 earthquakes has been obtained from the archives on earthquakes in the U.S.S.R. for the period 1962 to 1974. Earthquakes of $K \geq 14$, $M \geq 5.7$ are considered to be violent. Epicenters of all these earthquakes are shown in figure 6, as well as isoseismals for larger earthquakes. Data on weaker events in the range K=10 to 13 are useful in considerations of recurrence interval, and are necessary in evaluating the general seismic characteristics and completeness of the catalogs. The problem is that the data available to us, even on violent earthquakes in central Asia, are reliable only for the last 100 years, are less reliable for the past 250 years and are only episodic for historic time. Moreover, the data are not completely representative over the entire area. From 1960, earthquakes of K=10 on the Soviet scale have been uniformly recorded by seismic stations in central Asia. The catalog is complete for more violent earthquakes (K=11) beginning in 1954, while for K=14, M=5.7, it is complete for the last 50 years. The most violent earthquakes of K=15, M=6.5 seem to be represented rather well for the last 100 years and possibly 250 years.

Taking this coverage into consideration, an earthquake recurrence plot for central Asia as a whole, standardized for a period of 1 year is shown in figure 6. The data for earthquakes up to K=14 are reliable. We have taken the slope of the graph for earthquakes between the range K=10 to 14 as an average for the whole region in question (γ =0.48). For more violent earthquakes the slope proved to be steeper (γ=0.60). This

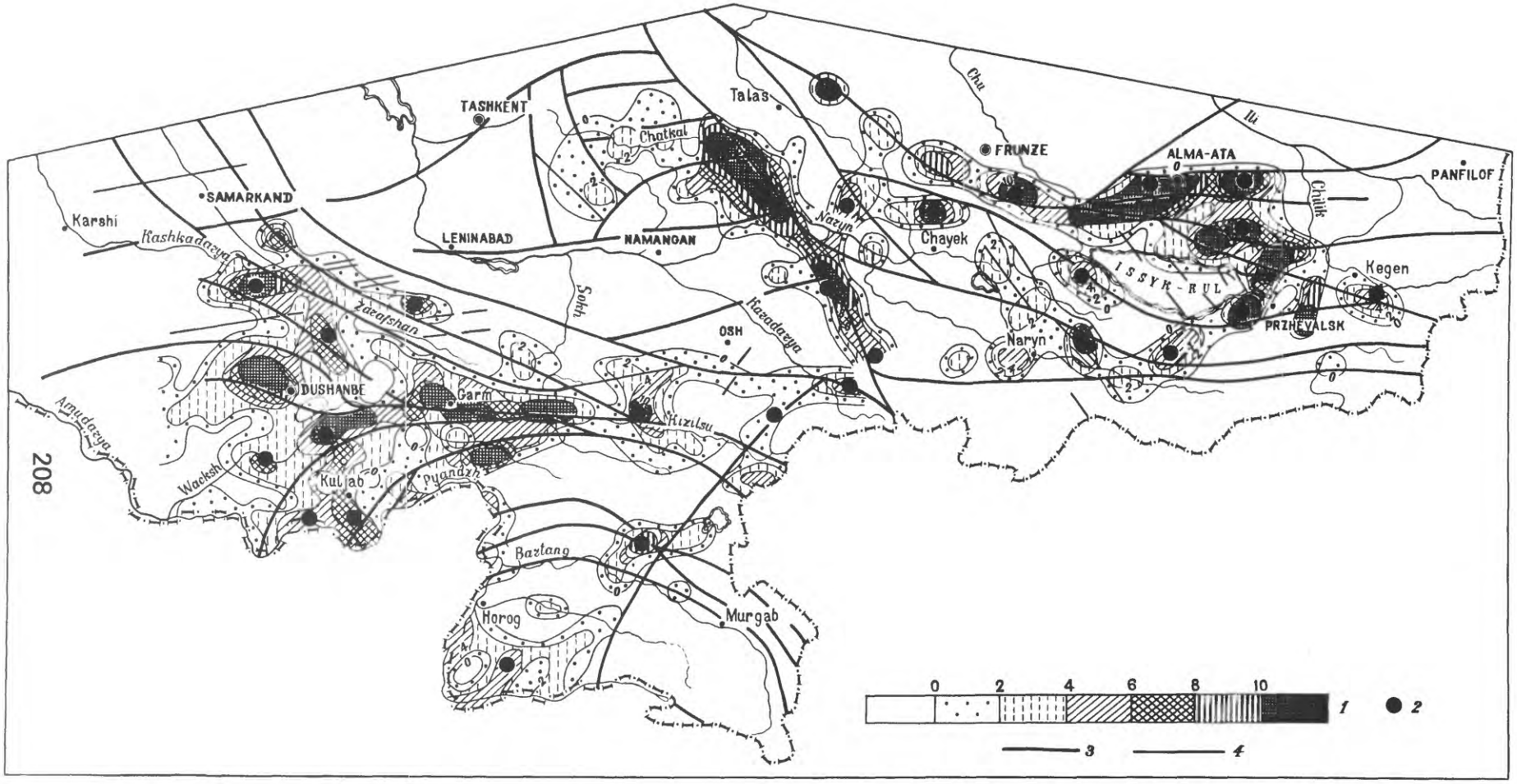

Figure 5. Densities of remanent deformation. Numbers are:

1. Scale of deformation densities
2. Earthquake epicenters of M 6.5 obtained from paleoseismic data
3. Fault zones
4. Regional faults with an anti-Tien Shan strike

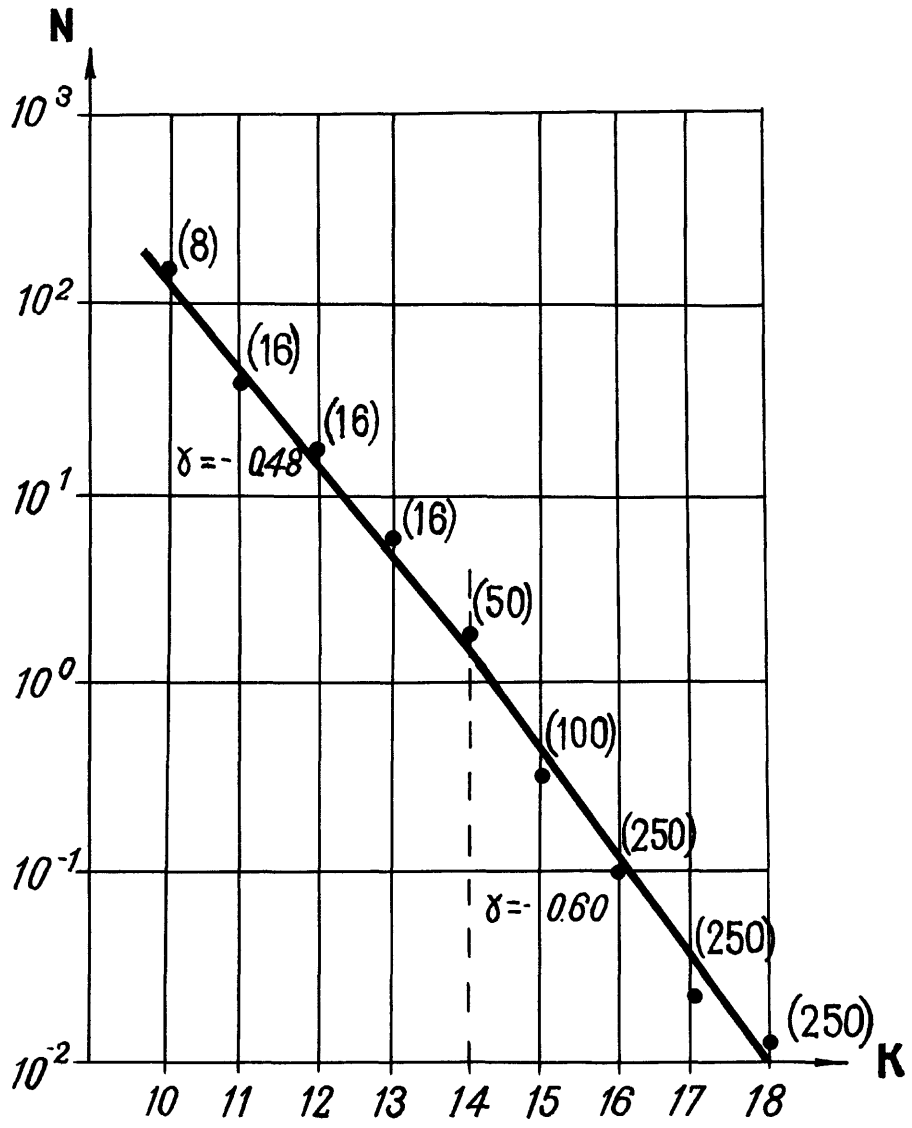

Figure 6. Graph of magnitude and earthquake recurrence for all Central Asia, normalized to one year. Time intervals for each normalized interval are also shown.

could indicate that the graph as a whole may be nonlinear or that 250 years is too long an interval to consider.

We can note a definite regularity in figure 7 in the distribution of earthquakes where K≥14 (M≥5.7). The most violent earthquakes are known from the northern Tien-Shan where they form a band that includes the northern side of the Kirghiz ridge uplift as well as a system of uplifts in the Zaalai Alatau and Kungei Alatau ridges. Here occurred such violent events as at Belovod (1885, M=6.9), Vernen (1887, M=7.3), Chilik (1889, M=8.3), Kebin (1911, M=8.2), Kebin-Chui (1938, M=6.9). The central Tien-Shan is characterized by earthquakes of lesser intensity, with the exception of the town of Przevalsk, where in 1970, there occurred an earthquake of M=6.8. The western Tien-Shan is characterized by higher seismic activity, but earthquakes of magnitude similar to those in the Northern Tien-Shan are not known here. Catastrophic events occurred at Karatag (1907) and at Khait (1949), and they were of 7.4 magnitude; at Chatkal (1946) the magnitude was 7.5. All of these sites are connected by fault zones which separate great structural elements that were active in the Quaternary. Within the Tien-Shan region it is possible to define several areas where there are epicenter concentrations for events of K≥14 (M≥5.7).

Along the eastern edge of the Ferghana depression between the towns of Uzgen and Namangan there is a band of epicenters that represent earthquakes whose greatest magnitude is M=6.5. Along the southern edge of the Ferghana, the epicenters are not as numerous, while along the western margin near Leninabad, a band of epicenters has a northeastern strike. To the north of the Ferghana depression, individual epicenters occur: they do not form a pattern, but the geological explanation of each is generally clear.

Against the general background of Pamir and Tien-Shan seismicity, there has been clearly demonstrated an area of concentrated epicenters. This is confined within the USSR to the zone where two geotectonic areas join, and follows eastwards along the massive junction of the Tarim and Tien-Shan zones. This band stretches for more than 1000 km. The greatest seismic activity occurs in the China segment where an earthquake of magnitude M=8.4 is known. Within the boundaries of this zone in the USSR, the greatest concentration of epicenters is found in the Garm region. It is only here in the last century that many earthquakes occurred with a magnitude exceeding 5.0. The strongest was the Khait event of 1949 (M= 7.4). The band of concentrated epicenters can be followed westward along the Gissar ridge uplift: here occurred also a number of violent earthquakes of M up to 6.5, with two of M=7.3 and M=7.4 at Karatag in 1907.

In the Pamir, the earthquake epicenters follow a band along the boundary between the eastern and western parts. Within this band a number of earthquakes of M up to 6.5 have occurred, with the catastrophic Sarez event of 1911 approaching magnitude 8. Over the remaining teritory of the Pamir, individual weak earthquakes are noted.

Comparison of modern and paleo seismicity shows that they coincide: that is, we should consider the stability of a particular seismic regime within an individual area in terms of the last 5000 years, and possibly even longer for the Holocene as a whole.

As for seismic zonation, a joint analysis of modern and paleoseismic data by established geological methods is of extreme importance. Seismological and geological methods that complement each other broaden our knowledge about the past and thereby increase the reliability of the final results. There is of course no guarantee that deformation features taken into account can be correlated with seismic processes: thus some earthquakes may be omitted.

An example is in the lower reaches of the Naryn River where detailed seismic observations have been carried out for some time. Since it is in the middle of central Asia and is well surrounded by regional stations, information on earthquakes in this region is complete for the last 50 years. The area is particularly suitable because of the presence of clear deformation features that, judging by their scale, may be connected

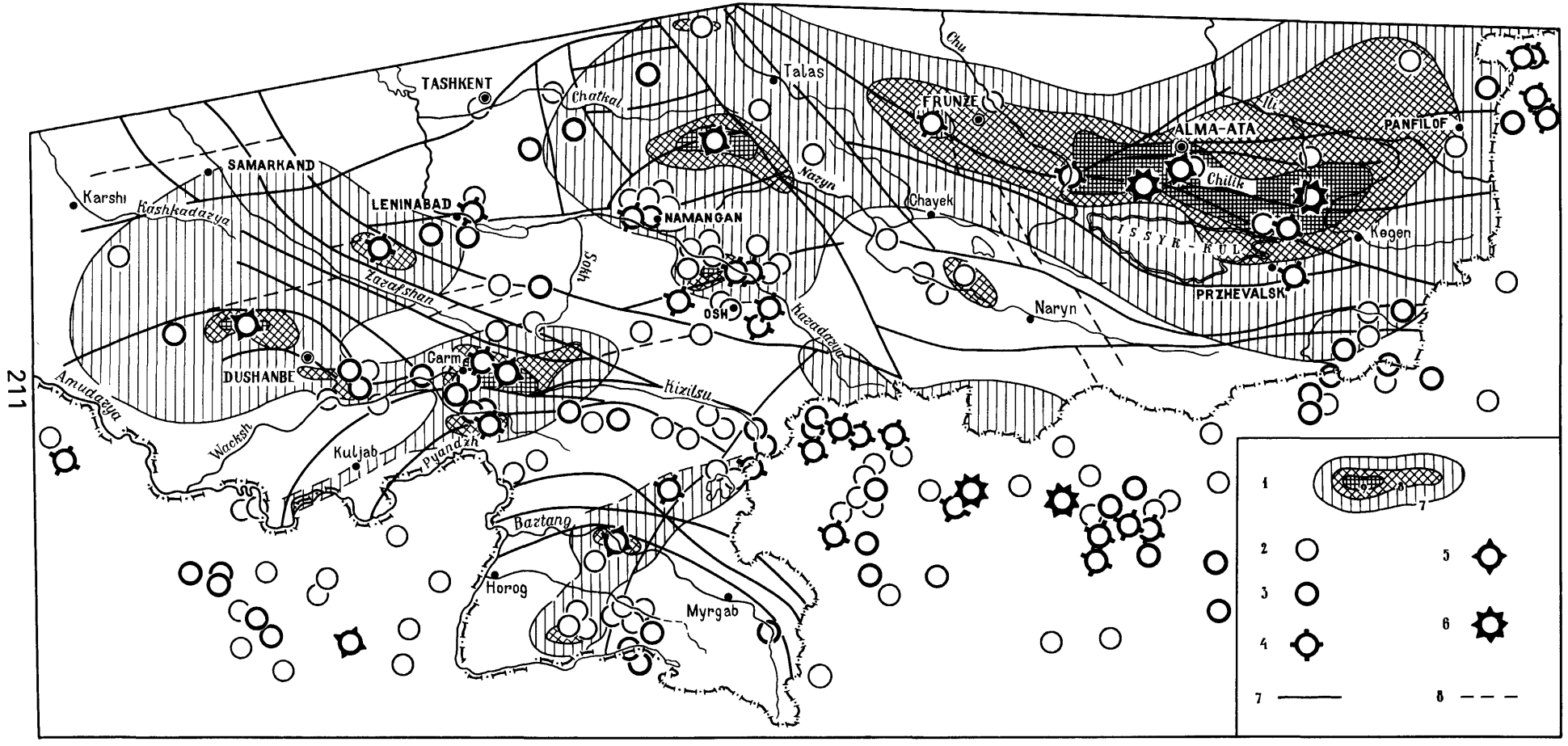

Figure 7. Epicenters of strong crustal earthquakes. Numbers are:

1. General isoseismals
2. M = 5.7
3. M = 6.5
4. M = 7.1
5. M = 7.7
6. M = 8.5
7. Fault zones
8. Regional faults with an anti-Tien Shan strike

with violent earthquakes that have occurred over the past 10,000 years. The features are related to the last half of the Holocene, but not the entire period.

In this region, two sets of features are clearly seen in the river of the eastern Karasu valley, two in the Sarychelek lake region, and one at the settlement of Karakul. In addition, collapse phenomena can be identified in the rivers of the Naryn and Karakulja valleys. From the scale of the deformation features observed, they are likely to be connected with earthquakes of magnitude close to 7.5 (K=17). By normalising data on these features that represent the last 5000 years (second half of the Holocene), and taking into account present-day observations, we obtain the recurrence intervals shown in figure 8. In the range K=11 to 12, the graph shows a clear-cut break with two slopes of value γ = -0.44 and γ =-0.60.

For strong earthquakes, the slope was analagous to the first graph (figure 6). Normalising the data to a 10,000-year interval changes the character of the graph only slightly.

The fact that both figures 6 and 8 are approximately similar allows us to suppose that the relationship between numbers of earthquakes and energy for violent earthquakes in central Asia differs from that for weak events. This is important because it means that for calculating recurrence intervals of violent earthquakes a simple extrapolation of the recurrence data from weak earthquakes to those for strong earthquakes would be wrong. An extrapolation of the line for small earthquakes would have overestimated the number of large earthquakes by a factor of two.

Our information on the repeat times of historical earthquakes in central Asia is extremely scanty: it is hardly possible to make definite judgements on violent earthquakes over central Asia as a whole using only the fragmentary information so far available. Once more it emphasises the importance of obtaining geological data on possible past earthquakes.

The joint use of seismological and paleoseismological data help to broaden our knowledge of the tectonic development of the Pamir and Tien-Shan over the last 10,000 years. They make it possible to define zones where present-day movements are the most intense and, therefore, pose the greatest danger. Thus, the areas where deformation features are concentrated and where earthquake epicenters adjoin fault zones in the northern Tien-Shan, Gissar-Alai, and Pamir-Alai as well as the Talasso-Ferghana and Pamir-Himalaya transverse faults, all indicate present-day, high tectonic activity. All these breaks, mainly of ancient origin, have been developing intensively throughout the Cenozoic--in particular, the Quaternary: their present-day activity is, therefore inherited. Moreover, the orientation of epicenters and zones of tectonic activity themeselves suggest the existence of other structural elements. Some can be established by geological methods: others must be surmised because as yet they have no surface expression; nevertheless their directions can be clearly followed. At present one of the most active areas is to the southwest of the Tien-Shan, and confined to the western parts of the Darvaz-Karakul, Gissar-Kokshaalsky, Northern-Gissar, Turkestan, Zarafshan and Southern Ferghana fault zones. In addition there are a number of transverse north-east directions. The combination of variously oriented structural elements make this an area of high tectonic activity.

In the central Tien-Shan, the absence of major paleoseismodislocations and violent earthquakes leads to the conclusion that there is little tectonic activity: this may be connected to the region's development as a single block. The most active modern and paleo-seismicity is connected with the deep-seated fault zones in the northern Tien-Shan, which during the Quaternary were characterized by only slight activity. It is possible that the intensity of present-day movements is connected with continued leveling of the central and northern Tien-Shan megablock. Significant activity has been noted also along the western boundary of the block, in the Talasso-Ferghana fault-zone. Intensive movements occurred along this fault zone throughout its existence, especially during the Quaternary. A very high density of deformation features has been noted along the fault

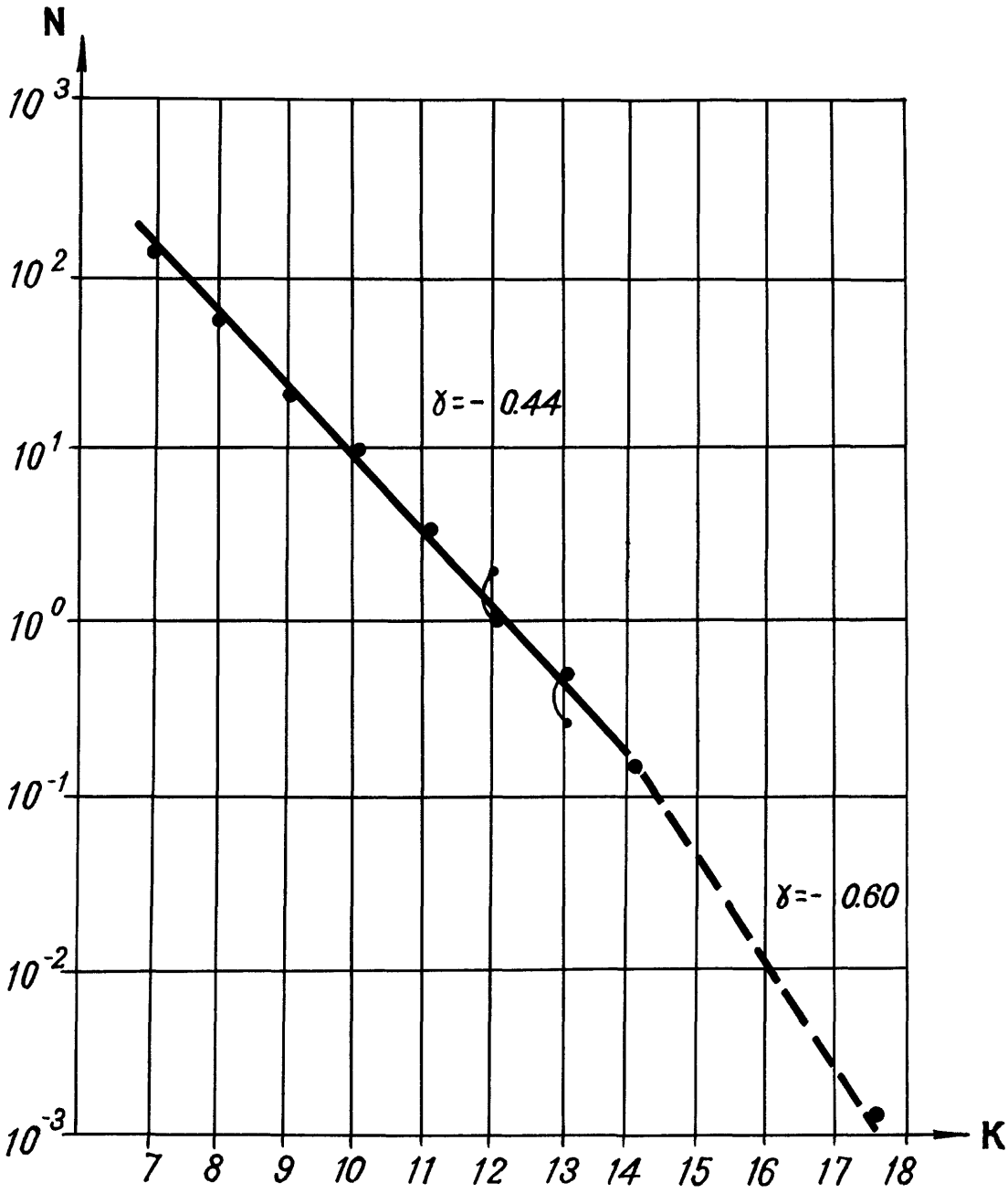

Figure 8. Graph of magnitude and earthquake recurrence interval for the lower reaches of the Naryn River, normalized to one year. Area (S) = 32,000 km^2.

zone: it shows that even at present this is one of the most active zones in the Tien-Shan region. The southern boundary of the Tien-Shan, connecting it with the eastern continuation of the Gissar-Kokshaal deep-seated fault, and separating it from epi-proterozoic platform of the Tarim massif is also tectonically active, on the basis of seismological data. This part of the Gissar-Kokshaal zone is outside the USSR and we have no data concerning its Quaternary history and deformation features, although seismodislocations can be expected here. Thus, seismic and paleoseismic data show that numerous structural elements that developed throughout the Quaternary are still active now, while areas of intensive activity began in the Holocene which in the past were rather weak. Once again this confirms the assumptions about the structural development of the Pamir and Tien-Shan crust that is taking place at present. Paleoseismological data confirm that this began at the Pleistocene-Holocene boundary: earthquake features older than Holocene are practically unknown.

An idea of the character of the strain pattern during the latest stage in the development of the region can be obtained by studying the earthquake focal mechanisms. For major earthquakes, the axes of compressive strain are mainly horizontal and oriented across the strike of the main structural elements (Reference 51). The axes of tensile strain are oriented parallel to the general structural trend. Study of focal mechanisms of minor earthquakes with shallow focal depths shows that as well as horizontal compression, there is horizontal extension too (Reference 52). It is known that interpretation of such strain data leads to ambiguous results: two equally probable rupture planes can be obtained. The selection of one depends not only on geological and geophysical data but also on the investigator's subjective judgement about the region's tectonic regime. However on the whole, along the planes deduced from major earthquakes, overthrusts and upthrusts predominate, with components of strike-slip also being present. Such strike-slip movements, noted in the focal data, can also be seen as surface movements in earthquakes such as San Francisco (1906), Gobi-Altai (1957), Charasan (1968) and others. Study of the focal mechanisms of minor earthquakes in the Garm and Naryn regions reveals the following point. In the upthrown areas, the axes of compressive stress are, as in the cases of violent earthquakes, subhorizontal and oriented predominantly across the strike of the principal structural elements. In downwarped areas, the tension axes are subhorizontal, but there is no systematic pattern to the displacement character at the focus.

At present, study of earthquake focal mechanisms has been carried out irregularly throughout the Pamir and Tien-Shan region. The greatest number of calculations on major earthquakes have been made for the Pamir, and for the Garm and Naryn regions for minor earthquakes. Thus, to draw conclusions about a general pattern throughout the area would be rather premature. Nevertheless, the investigation of strain and displacements from focal mechanism data is, we believe, one of the most promising means of studying present-day tectonic movements that are not yet reflected in surface phenomena.

Seismic zoning map

Study of this region's geological history, particularly the Quaternary, shows a record of differentiated movements, mainly uplift, under a regime of horizontal north-south compression. It is important to note that an abrupt increase in tectonic activity began comparatively late--during the Holocene. Analysis of the character of Quaternary movements has made it possible to identify the most actively developing structural elements, that is, great blocks of the Earth's crust bounded by fault zones. As a result of studying the development of the region during the Quaternary and its epochs, it has become possible to estimate the intensity and direction of movements along these zones in time and in space. When correlating the present-day structure of the Pamir and Tien-Shan with the surface relief of the Moho, we have succeeded in defining the boundaries of the block more precisely.

Having apparently begun in the Holocene, this structural regime persists even now. Naturally this process causes interaction between existing and developing structural elements of the Earth's crust. We have suceeded in identifying a number of areas where the greatest strain concentrations could occur. Analysis of both present-day seismicity and paleoseismicity has confirmed the increase in tectonic and seismic activity during the Holocene. It has also revealed where present-day movements are the most active.

In some cases, these areas with an anti-Tien-Shan strike proved to be ones connected with contemporaneous remobilization and phenomena accompanying it.

The new developing directions of tectonic remobilization are distinguished by the seismic regime as well. The characteristic of recent fault zones is their long interval of seismicity, and the stable, but regularly recurring, number of strong earthquakes. New trends are characterized by a background of low level microseismicity, against which violent earthquakes occur. Typical in this respect are the northern Tien-Shan and, apparently, southwest of Central Asia, where violent earthquakes are common in the band southeast of Leninabad in the direction of the Gissar range. It is characteristic that even microearthquakes in these zones tend to be at greater depth when compared with areas of inherited movements where micro seismicity is, as a rule, connected with shallow depths of the order of the first ten kilometres. No less important is the fact that it is on these newly forming structural trends that the maximum earthquake force tends to be greater when compared with that in other regions.

Thus, joint analysis of geological and seismological data has shown the principal patterns in the development of the Pamir and Tien-Shan crust: it has made it possible to identify the most tectonically active zones and evaluate their main parameters also. It has allowed a map to be constructed of the most likely earthquake foci, which can be classified them according to the expected intensity (figure 9). As outlined in reference (1) for the first time it was suggested that zones should be defined where possible earthquakes of a given magnitude could occur. In this paper, a more reliable scheme is presented by using a large number of present-day geological and seismological data.

The zones of possible earthquake occurrence have been the basis for constructing a new variation of the Pamir and Tien-Shan seismic zoning map (figure 10). It is different from other seismic zoning maps in that isoseismals outline the areas of expected shaking, expressed not by intensities but by velocity values. It has taken into consideration that 40 cm/s corresponds to intensity 9 on the Soviet scale , 20 cm/s to intensity 8 and 10cm/s to intensity 7 (Reference 53). The plotted isoseismals take into account velocity values decreasing to zero out of the zones of possible earthquake occurrence. Such a map differs considerably from a smoothed map. The areas of maximum shaking are better expressed than in a smoothed map: they coincide with the foci of major earthquakes and cover practically all of the areas where paleoseismic dislocations are concentrated.

We are aware that the approach presented here is only a first attempt to quantify the seismic hazard. Nevertheless it allows a fuller use of present day data on geology, seismology and the deep-seated structure of the crust. It also induces further investigations. More detailed geophysical studies allow the finer detail of the Earth's crust and upper mantle to be understood, and this will undoubtedly lead to an understanding of the entire tectonic development of a region. These investigations will significantly increase the quantity and reliability of the data base on seismic hazards in this territory. It will make it possible to understand both the patterns and the cause of earthquakes. The new variation of the Pamir and Tien-Shan seismic zoning map impartially reflects the seismic danger and helps to meet the demands for predictive documents of this kind.

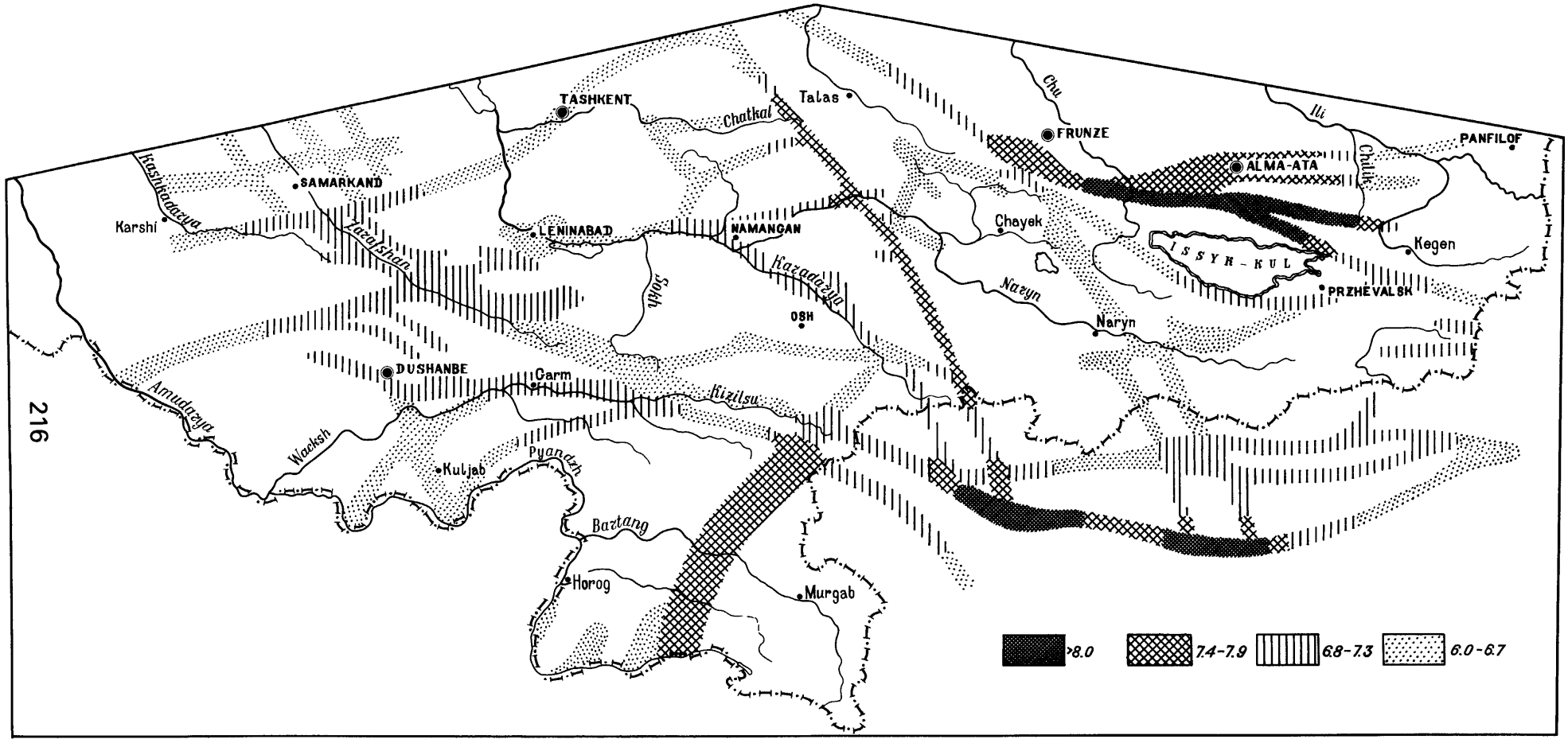

Figure 9. Most probable fault zones of violent crustal earthquakes. The scale of the expected earthquake intensity is shown in magnitude units.

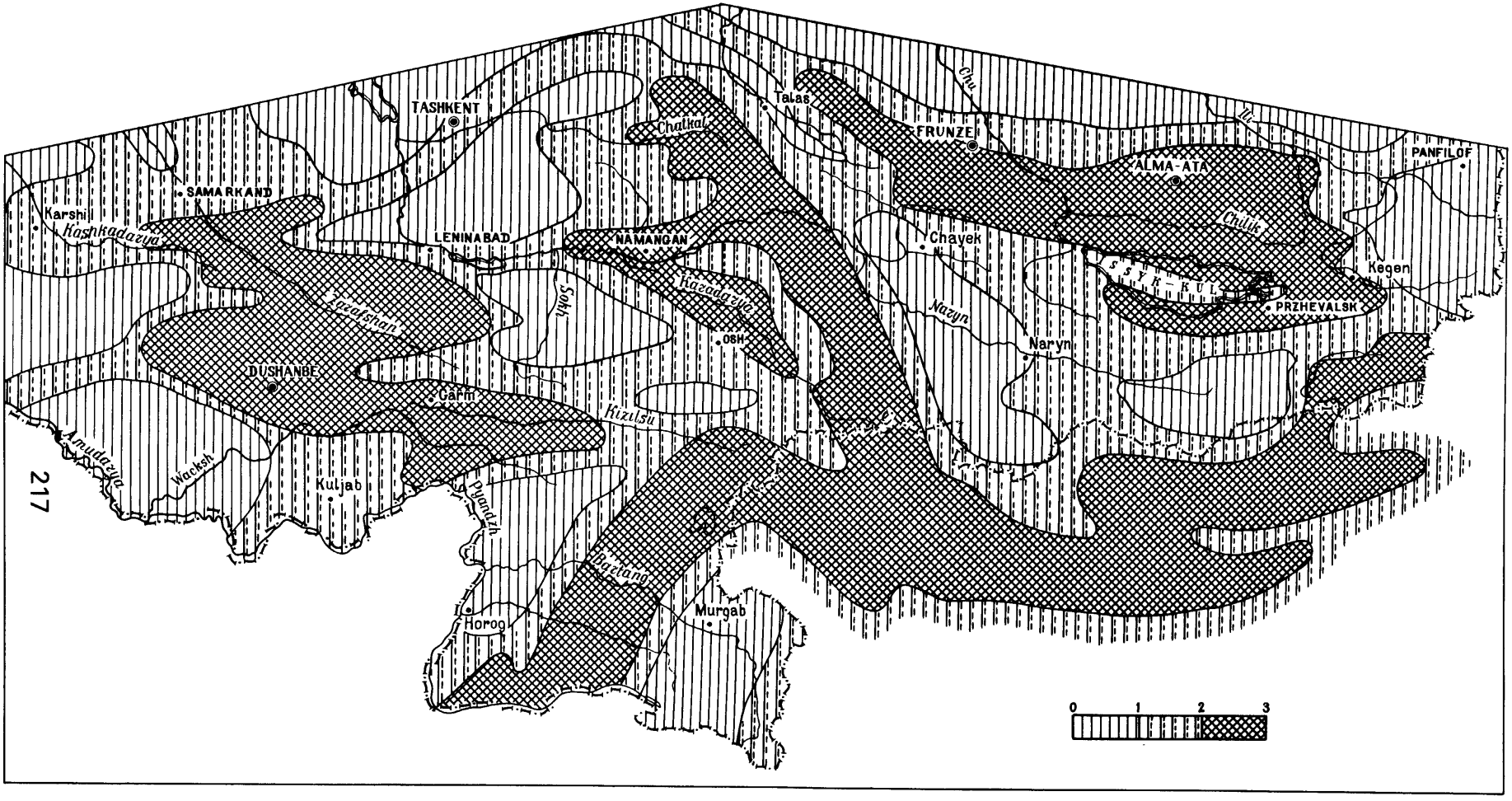

Figure 10. Seismic zoning of the Pamir and Tien Shan. The scale of the maximum expected velocities is given by:

1. 10 cm/sec
2. 20 cm/sec
3. 40 cm/sec.

References cited

1. M. V. Gzovsky, V. N., Krestnikov, I. L. Nersesov, G. I. Reisner. New principles of seismic zoning the Tien-Shan with the central part as an example. Izvestiya of the Academy of Sciences of the USSR, Geophysical Section, 1960, #2, 3.

2. Seismic zoning of the USSR. M., Nauka, 1968.

3. Methods and recommendations on seismic zoning of the USSR territory. M., 1974.

4. Ju. V. Riznichenko. Seismic activity and earthquake potential. In the book: "Seismic zoning of the USSR", "Nauka", M, 1968.

5. Ju. V. Riznichenko, E. A. Dgibladze. The assessment of maximum possible earthquakes using complex data for the Caucasus. M, Izvestia of the Academy of Sciences of the USSR, Earth Physics, 1975, #5.

6. Ju. V. Riznichenko, S. S. Seiduzova. Spectral seismic potential. M, Izvestia of the Academy of Sciences of the USSR, Earth Physics, 1975, #9.

7. Ju. V. Riznichenco. New seismozoning in the USSR and quantitative methods used for estimating seismic risk. In the book: "The problems of seismic risk and its quantitative estimate." Nauka, M, 1975.

8. V. N. Krestnikov, T. P. Byelousov, V. I. Ermilin, N. V. Chigarev, D. V. Stange. The Pamir and Tien-Shan Quaternary tectonics. M., Nauka, M, 1979.

9. V. N. Krestnikov. The history of geologic development of the Pamir and parts of Asia ajoining it during Mesozoic-Cenozoic time. Soviet Geology 1961, #4 and 7.

10. V. N. Krestnikov. History of oscillatory movements in the Pamirs and adjacent regions of Asia. Acad. Nauk USSR, 1962. Engl. transl. in Israel. Program for Scientific Translations 4. Oldbourne Press, London, 250 pp.

11. V. N. Krestnikov, G. I. Reisner. The Alpine tectonics of the central Tien-Shan. Soviet Geology, 1969, #12.

12. V. N. Krestnikov. On the influence of Paleozoic structure on development of uplift in the northern Tien-Shan during the Neogene and Quaternary periods. Bullet. MOIP, Geol. Section, 1955, Vol. XXX(6).

13. V. N. Krestnikov, D. V. Stange. On the Quaternary history of the Talasso-Ferghana fault zones. M., Izvestiya of the Academy of Sciences of the USSR, Earth Physics, 1977, 7.

14. V. N. Krestnikov, D. V. Stange. On the Pamir-Himalayan fault zone. Izvestiya of the Academy of Sciences of the USSR Earth physics, 1977, 7.

15. V. N. Krestnikov. The quantitative estimation of changes in vertical tectonic movements. Geotectonics, 1969, 3.

16. V. I. Knauf. On the character of the Tien-Shan deep-seated block structure. Transactions of Department of Geology and the Earth's Interior, at the Council of Ministers of the Kirghiz SSR, 2. M., Gosgeologtechizdat, 1962.

17. D. P. Rezvoi. Anti-Tien-Shan structural direction in Middle Asia tectonics. Geological collection of the L'vov Geological Society, #9, M., Nedra, 1965.

18. S. A. Zakharov. On peculiarities of neotectonics of the Tadjic depression "Takjikistan neotectonics and seismotectonics". Dushanbe "Donish", 1969.

19. V. P. Kondur, R. N. Kukushkin. On the age problem of the underthrust thickness in the Northern Babatag. The Tajic SSR Academy of Sciences, issue 43, #1, 1972.

20. V. S. Burtman. Modern horizontal displacements along the Tien-Shan Talasso-Ferghana fault. Collection. The earth crust modern movements, #2, 1965.

21. N. Ya. Kunin, V. I. Shatsilov. Deep seated structure of South Kazakhstan using the results of deep seismic sounding. Bull. MOIP, Geol. Section., M., 1970, #6.

22. N. Ya. Kunin, A. P. Ivanov, V. I. Shatsilov. Deep seated structure of the Earth's crust. In the book-Geology of the USSR. v. 40, M., Nedra, 1971.

23. I. K. Pushkarev, A. P. Ivanov, V. I. Shatsilov. Deep-seated seismic investigations along Arys-Balkhash profile. In the book "Geophysical investigations in Kazakhstan". A-A. Kazakhstan, 1968.

24. Collective Works under the editorship of I. X. Chairabeav. The Middle Asia earth crust and upper mantle. M., Nauka, 1977.

25. V. N. Krestnikov, I. L. Nersesov. The Pamir and Tien-Shan tectonic structure and its connection with surface relief of the Moho. Soviet Geology, 1962, #11.

26. V. P. Solonenko. Eastern Siberia seismic zoning. Irkutsk, the Academy of Sciences of the USSR, Siberian section. The Earth Crust Institute. 1963.

27. V. S. Chromovskich. Catastrophic earthquake traces in the Southern Baikal area. Geology and Geophysics. 1963, #3.

28. V. S. Chromovskich, V. P. Solonenko, V. M. Zhilin, S. D. Chilko, P. Ya. Zelenkov, R. M. Semenov. Western Caucasus seismogenic structures. Inform. Bullet., 1972, #4. Irkutsk, the Academy of Sciences of the USSR, Siberian section. The Earth Crust Institute.

29. Atlas of earthquakes in the USSR. The Academy of Sciences of the USSR, 1962.

30. Earthquakes in the USSR. The Academy of Sciences of the USSR, 1961.

31. The Problems of Engineering Seismology. Tr. IFZ issue 2, 3, 4, 7, 8, 9. Institute of Earth Physics. The Academy of Sciences of the USSR Press, 1959-1964.

32. Earthquakes in the USSR (annual) 1961-1974.

33. Seismic zoning of the USSR. Publishing house "Nauka", 1968.

34. Operative seismological bulletin. 1968-1972. Moscow.

35. Seismological Bulletins of the U.S. Coast and Geodetic Survey. 1964-1972.

36. Bulletin of the International Seismological Centre 1964-1968. Edinburgh, Scotland.

37. B. Gutenberg and C. F. Richter. Seismicity of the Earth. Foreign Literature Publishing House, 1954.

38. C. F. Richter. Elementary Seismology. Foreign Literature Publishing House, 1963.

39. N. V. Golubeva. Catalogue of the world's violent earthquakes for 1953-1967. Unpub. data, 1973.

40. A. A. Semenov. List of earthquakes in Middle Asia and countries adjoining it from ancient times up to 1830. The Academy of Sciences of the Tadjic SSR, vol. 94, 1958.

41. V. I. Bune, V. K. Kulagin, O. V. Soboleva. Vakhsh region seismic regime. Dushanbe, 1965.

42. Tadjikistan violent earthquakes, Dushanbe, 1970.

43. Violent earthquakes of Middle Asia and Kazakhstan, annual, #1, Tadjic Institute, Donish Publishing House, Dushanbe, 1970.

44. P. G. Semenov, V. A. Semenova. Catalogue of earthquakes felt over the Tadjic territory for 1865-1940 and 1941-1952 periods. Tr. the Academy of Sciences of the Tadjic SSR, vol. 36, issue 3, 1958.

45. Seismic regime symposium 12-17 December 1966. Dushanbe, 1969.

46. I. L. Nersesov, V. P. Green, K. Djanuzakov. On the seismic zoning of the Naryn river basin. The Academy of Sciences of the Takjic SSR. 1969, Publishing House, 1960.

47. Uzbekistan seismicity, Issue 1, 1961, Issue 2, 1964.

48. Earthquakes in the Turkestan region for 1865-1910. Tashkent, 1949.

49. The Tashkent earthquake 26/IV 1966. Publishing House FAN, Uzbek SSR, Tashkent, 1971.

50. G. P. Gorshkov. The problems of seismotectonics and seismic zoning to the People's Republic of China. The Council of Seismicity Bulletin, #7, 1960.

51. E. I. Shirokova. Detailed study of stresses and faults from Middle Asia earthquake foci. Earth Physics, 1974, #11.

52. V. N. Krestnikov, I. G. Simbireva. The relationship of tectonic structure and pecularities in the distribution parameters of earthquake foci. In the collection "The earth's crust in seismically dangerous zones", #10, M., "Nauka", 1973.

53. The seismic scale and methods of measuring seismic intensity. M., "Nauka", 1975.

An Earthquake Catalog and Velocity Model For the USGS Peter the First Range Seismic Array, Tadjikistan, USSR

by

Jack Pelton
and
Fred Fischer
345 Middlefield Road
Menlo Park, CA 94025

Open-File Report
80-840

INTRODUCTION

The U.S. Geological Survey has operated a ten station three-component radio-telemetered seismic array in the Peter the First Range near Garm, Tadjikistan, in the Soviet Union, since early August 1975. The array was established to pursue research goals as defined by the cooperative US-USSR program in earthquake prediction (Area IX of the US-USSR Joint Agreement on Cooperation in the Field of Environmental Protection of May 1972). The Peter the First Range area was chosen for the USGS array because Soviet seismicity catalogs indicated that small to moderate-sized earthquakes occurred there relatively frequently, thereby offering excellent opportunities to investigate the seismic source mechanism using the spectra of radiated seismic waves.

Analyses of data collected from the USGS Peter the First Range array have been discussed in both the Russian and English languages. The reports in English are primarily concerned with source mechanism parameters determined from seismic shear wave spectra (Fischer et al., 1980), and the design of experiments to determine corrections to seismic wave spectra for topography, Q-attenuation, and scattering effects (Levander and Monfort, 1980). This report has two objectives: (i) present a catalog of local earthquakes recorded by the USGS Peter the First Range array during the initial phase of its deployment (August 1, 1975 to December 31, 1977) and (ii) develop P-wave and S-wave velocity models for the upper crust beneath the Peter the First Range using least squares inversion of P and S arrival times from local earthquakes. These objectives were deemed necessary for future source mechanism studies for several reasons. First, a basic catalog of earthquakes was needed so

that the selection of waveforms for spectral analysis could be performed according to various criteria such as magnitude or focal depth. Second, an improved velocity model for the crust below the Peter the First Range was needed because hypocenter locations and takeoff angle calculations are dependent on the velocity model used. Third, inversion for velocity model parameters was expected to provide an existence test for the upper crustal low velocity zone proposed for the Garm region by Nersesov and Chepkunas (1971).

INSTRUMENTATION

The instrumentation history of the USGS Peter the First Range array may be divided into two time periods separated by a seventeen-month rebuilding program:

Period I - August 1, 1975 to December 31, 1977
Interim Rebuilding Program
Period II - June 1, 1979 to present

Instrumentation during Period I has been described in detail by Fischer et al., (1980). Briefly speaking, the seismic signals were detected by 1 second period seismometers, amplified, converted to frequency modulated tones, and relayed by FM VHF radio to a central recording point near Garm. The rebuilding program resulted in the modification of Period I instrumentation to accommodate two-level amplification and Russian-made short-period seismometers (F. G. Fischer, U.S. Geological Survey, Menlo Park, unpublished records).

ARRAY GEOMETRY

The USGS Peter the First Range array is centered on the crest of the Peter the First Range between the Surkhob River and the Obikhingou River (Figure 1). The average elevation of the array is 3400 meters above sea

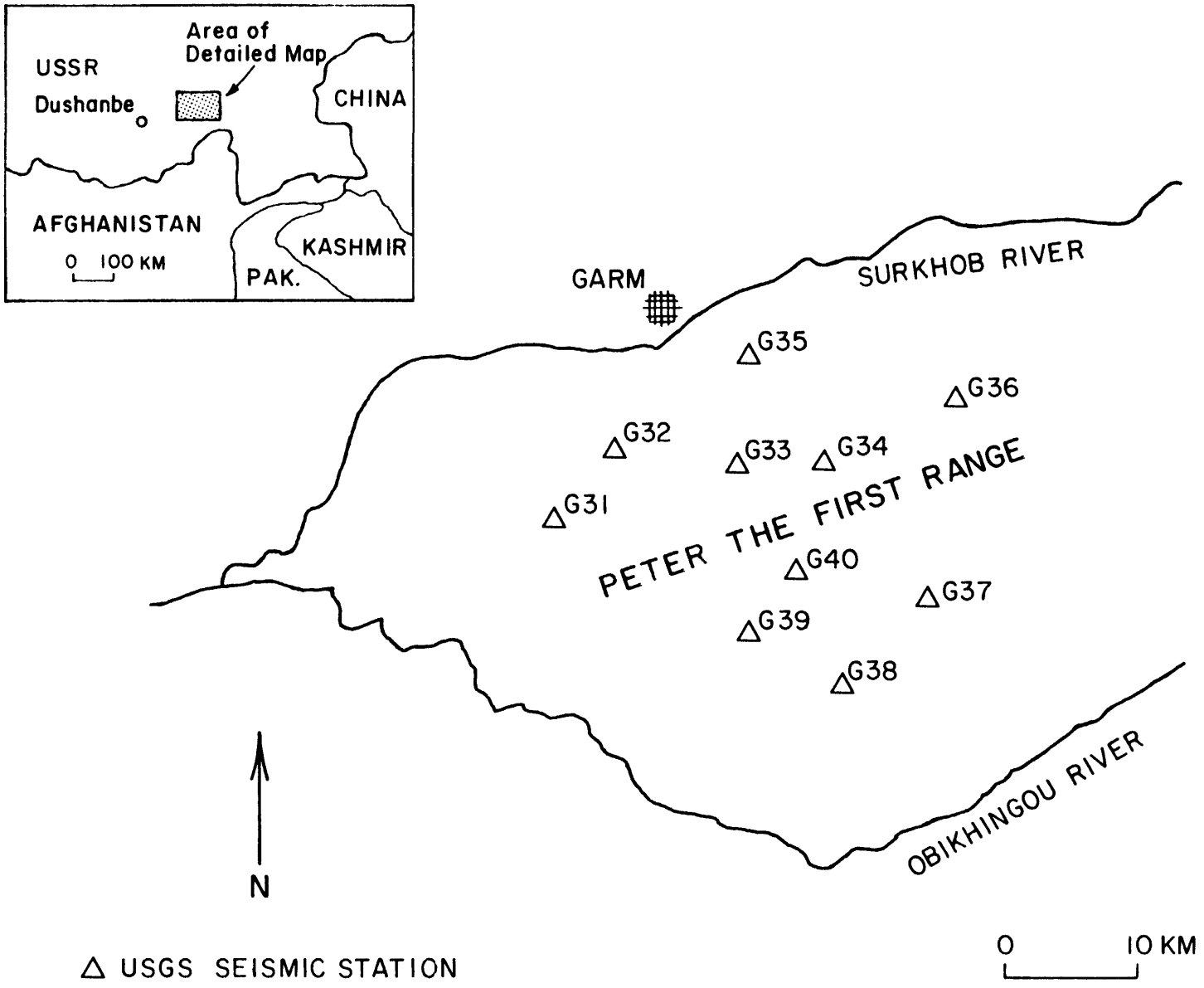

Figure 1. Map of the USGS Peter the First Range seismic array.

level, with a maximum relief between stations of 1640 meters. The original array involved ten stations (G31, G32, G33,..., G40) with an average spacing of 10 km. In June 1976 the field equipment at stations G35 and G40 was removed and used to establish the new stations G41 and G43 (not shown in Figure 1) at distances of about 60-70 km from the original array center. Stations G41 and G43 began operation in August 1976. This modification was undertaken to supplement the USSR Complex Seismological Expedition's network in the Garm area. Unfortunately, the move also resulted in a somewhat weakened geometry for the USGS array which was effectively reduced to eight stations for the recording of small local earthquakes. Station G42 (not shown in Figure 1) was simply a relay point at which a vertical seismometer was operated occasionally. During the rebuilding program, station G39 was relocated at the new station N39 (not shown in Figure 1) which began operation in late May 1979. Data from stations N39, G41, G42, and G43 were not used in the complilaton of the earthquake catalog or the inversion results presented in this report. Table 1 lists the geographic locations, elevations, and dates of operation for the USGS Peter the First Range seismic stations.

DATA REDUCTION

A basic catalog of 144 local earthquakes was generated for Period I by examining USGS Develocorder records for events listed in the Complex Seismological Expedition earthquake catalog for the Garm region. Only those events located by the Soviets within or near the boundaries of the USGS Peter the First Range array and of energy class $K \geq 6$ ($M_L \geq 1.2$)

Table 1

USGS Peter the First Range seismic stations

Station	Lat (N)		Long (E)		Elevation	Dates of Operation
	Deg	Min	Deg	Min	meters	
G31	38	53.83	70	16.75	3760	0875 to present
G32	38	56.60	70	19.51	3010	0875 to present
G33	38	55.74	70	25.00	3510	0875 to present
G34	38	56.18	70	29.17	3860	0875 to present
G35	38	59.70	70	25.30	2360	0875 to 0676
G36	38	58.25	70	35.40	3610	0875 to present
G37	38	50.84	70	34.40	4000	0875 to present
G38	38	47.85	70	29.75	3860	0875 to present
G39	38	49.80	70	25.50	3760	0875 to 0578
G40	38	51.95	70	27.50	2360	0875 to 0676
G41	39	03.76	71	05.00	3660	0876 to present
G43	38	24.20	70	20.50	3300	0876 to present
N39	38	50.40	70	27.10	3000	0579 to present

NOTE: Geographic coordinates for station G42 not available.

were considered (K is determined from measurements of maximum amplitude on seismograms; the original definition of K is given by Rautian (1964); for the Garm region, M_L = 0.56K-2.2, Rautian et al. (1978)). The basic catalog of 144 earthquakes cannot be considered a complete record of K $\geq$ 6 seismicity for the Peter the First Range during Period I because many USGS stations were disabled for long periods during winter months, thereby causing large temporal gaps in the records. Seismicity records for the Peter the First Range which are presumed complete at some level are maintained by the Complex Seismological Expedition at Garm.

A single 16 mm Develocorder with top and bottom time traces was used to record vertical and/or horizontal components of all stations of the USGS Peter the First Range array during Period I. The events of the basic catalog were timed from the projection of the Develocorder film onto the viewscreen of a 3M Model "400" Reader-Printer equipped with a 3M 12.05X lens and the optional large viewscreen (a few events were timed from Siemans Oscillomink records if Develocorder films were not available or of poor quality). Both P and S arrivals were timed to the nearest 0.05 sec with a Gerber scale (except for the few Oscillomink records which were timed to the nearest 0.01 second). This timing precision was chosen because the predominance of emergent arrivals on the Develocorder films led to uncertainties in picking accuracy of at least $\pm$ 0.10 second in many cases.

Both P and S arrivals were classified as either emergent or impulsive, but only P arrivals were assigned a polarity. Coda length was measured from Develocorder film records according to the following definition: coda length is the time in seconds between the first

P-arrival on the vertical component and that point where the peak-to-peak amplitude of the seismic waveform becomes permanently equal to or less than 5 mm on the viewscreen of a 3M Model "400" Reader-Printer equipped with a 3M 12.05X lens and the optional large viewscreen. Maximum amplitudes could not be routinely measured from Develocorder film records because of crowding of the traces.

Hypocenters, origin times, and coda magnitudes (FMAG) for the basic Peter the First Range catalog were determined using HYPOINVERSE (Klein, 1978; BASIC version of HYPOINVERSE by Fischer, unpublished computer program, 1979) and are presented in Table 2. Selected HYPOINVERSE program variables which were used for this study are listed in Table 3. The velocity model and Vp/Vs ratio were taken from inversion results which are described in the next section. Station corrections were not used because average station residuals from preliminary runs were not significant. The FMAG constants were arbitrarily chosen to be the same as those developed for the USGS Alaskan network (Klein, 1978, p. 33). Thus the FMAG values in Table 2 should be regarded as a relative ranking by size for the earthquakes of the basic catalog of this report only. All HYPOINVERSE computations were accomplished using a Hewlett-Packard System 45 desktop computer and the BASIC version of HYPOINVERSE.

Figure 2 is an epicenter map for the basic Peter the First Range catalog which also indicates depth distribution. The seismicity pattern is diffuse, but a concentration of events is noted near station G36 at the northeastern side of the array. Most events of the catalog lie in the focal depth range of 0 to 10 km. Relatively few events were located

HFINAL Peter the First Range Earthquake Catalog

EVENT No	DATE YrMoDa	ORIGIN HrMn	Sec	LAT Deg	Min	LON Deg	Min	DEPTH Km	RMS Sec	ERH Km	ERZ Km	GAP Deg	FMAG	DMIN Km	NWR
*1	750806	2306	9.71	38	51.82	70	24.17	25.01	.10	1.25	1.51	137	1.0	4.2	16
*2	750810	745	50.55	38	56.51	70	24.15	3.73	.06	1.09	2.35	103	1.2	1.9	8
3	750813	1024	14.60	38	56.51	70	32.55	3.81	.08	2.24	3.46	226	3.2	4.9	9
4	750813	1026	18.54	38	56.79	70	33.09	3.70	.05	4.27	3.33	263		5.8	6
5	750813	1048	59.14	38	57.93	70	33.46	5.17	.07	1.45	2.43	283	.9	7.0	10
6	750813	1505	48.31	38	57.50	70	33.89	4.96	.07	1.16	2.50	248	1.0	7.2	12
7	750830	1226	20.71	38	49.74	70	34.08	7.59	.07	1.42	.92	228	1.2	2.1	10
*8	750901	122	9.73	38	52.87	70	24.91	16.98	.07	1.53	3.63	107	1.5	4.1	10
9	750901	1245	36.02	38	52.56	70	18.59	10.26	.11	1.37	2.99	194	1.6	3.5	11
*10	750907	2049	13.65	38	50.74	70	29.68	9.46	.05	1.15	1.45	165	1.0	3.9	10
11	750910	1306	29.78	38	57.82	70	31.62	5.22	.09	.78	2.48	180	1.0	4.7	11
*12	750912	642	18.53	38	53.93	70	22.60	7.39	.07	1.16	3.79	116	1.9	4.8	8
*13	750912	815	27.67	38	53.85	70	22.55	7.66	.07	.88	2.68	118	1.0	5.0	10
14	750916	1539	22.91	38	52.37	70	16.42	6.78	.08	2.40	1.46	256	2.8	2.8	9
*15	750918	1914	7.89	38	53.38	70	26.25	7.75	.12	1.10	1.93	85	1.0	3.2	10
*16	750922	441	55.27	38	55.26	70	24.58	3.76	.10	.62	1.78	83	1.2	1.1	12
17	750922	1440	3.28	38	56.96	70	28.04	2.99	.10	.70	1.97	114	1.2	2.2	12
18	750927	1411	.07	38	58.10	70	26.52	.50	.11	1.08	16.05	118	.7	3.4	6
*19	751016	1041	56.76	38	58.25	70	30.31	21.20	.12	1.52	1.88	193	.9	7.3	10
*20	751020	517	20.24	38	57.47	70	29.72	4.02	.06	.66	1.41	110	.6	2.5	10
21	751205	730	22.14	38	55.08	70	28.14	1.90	.08	.67	2.15	113		2.5	10
*22	760120	1054	31.79	38	57.45	70	29.99	3.78	.10	.66	1.71	137		2.7	12
23	760121	1058	45.38	38	51.44	70	23.33	26.39	.14	2.15	1.42	162		4.4	12
*24	760815	1143	11.34	38	53.84	70	27.81	8.70	.06	.86	1.68	102	1.1	5.3	10
25	760903	402	4.89	38	57.21	70	35.31	5.34	.06	7.59	11.68	183	3.3	1.9	7
26	760903	2152	44.11	38	57.86	70	36.04	7.08	.05	2.19	1.26	243	4.2	1.2	8
*27	760908	2305	58.05	38	54.20	70	25.86	9.60	.08	.75	1.39	113	.5	3.1	9
28	760912	1541	36.78	38	57.39	70	35.45	3.14	.09	5.29	8.43	190	1.3	1.6	8
29	760913	830	2.24	38	58.03	70	31.16	5.32	.09	1.48	4.11	186	.9	4.5	6
30	760913	925	55.09	38	57.47	70	35.13	7.10	.04	1.53	1.32	189	1.3	1.5	8
31	760913	1849	36.37	38	58.28	70	35.23	5.64	.06	1.49	2.68	219	1.3	.2	8
32	760913	1935	34.12	38	58.10	70	35.78	5.27	.11	1.40	1.70	270	1.1	.6	9
33	760914	927	17.72	38	58.83	70	35.76	6.07	.05	1.42	2.43	304	.9	1.2	7
34	760915	1906	52.76	38	57.69	70	34.60	4.82	.08	2.75	4.66	144	1.9	1.5	8
35	760915	1920	47.90	38	58.37	70	35.53	4.22	.07	9.40	9.77	285	2.1	.3	7
36	760915	1934	8.97	38	58.26	70	35.04	7.03	.06	2.06	1.77	195	2.0	.5	7
37	760916	1025	18.14	38	58.01	70	35.23	5.80	.09	1.94	2.90	156	1.0	.5	9
38	760917	316	33.81	38	58.67	70	36.69	5.14	.06	1.04	1.41	291	1.0	2.0	10
*39	760919	1751	58.86	38	56.91	70	34.30	8.04	.06	1.20	2.32	169	2.0	2.9	9
40	760926	1049	33.99	38	58.40	70	34.89	6.92	.01	9.45	12.41	213	.9	.8	5
41	760927	1203	24.55	38	59.02	70	34.36	7.34	.07	2.09	3.03	135	.8	2.1	6
42	760928	402	9.21	38	58.73	70	35.73	6.49	.08	10.27	10.60	287	1.1	1.1	7
43	761010	434	5.04	38	57.80	70	20.55	.03	.11	1.27	99.00	231	1.0	2.7	6
*44	761217	1828	20.23	38	56.97	70	34.22	7.47	.08	1.03	1.94	144	0.0	2.9	9
*45	761218	615	31.44	38	55.82	70	29.76	6.20	.05	1.01	2.64	84	2.0	1.1	8
46	761219	1914	35.61	38	57.89	70	25.84	.27	.07	1.32	28.00	192	3.5	4.2	8
47	761225	101	11.03	38	47.75	70	28.73	13.21	.07	1.72	1.40	222	1.5	1.5	9
48	761225	1803	1.67	38	50.64	70	22.90	10.99	.06	.92	2.10	186	1.3	9.9	9
49	761226	1400	13.44	38	57.30	70	32.60	5.83	.07	1.00	2.40	160	.4	4.4	10
50	761227	1122	.04	38	58.84	70	36.94	5.87	.08	1.53	1.60	293	.9	2.5	9
51	770103	6	44.56	38	56.11	70	35.95	8.48	.08	1.78	2.40	204	.4	4.0	9
52	770113	44	52.82	38	57.32	70	34.68	6.22	.03	2.81	4.30	151	.7	2.0	5
*53	770115	111	46.36	38	52.87	70	27.57	10.68	.07	.79	1.54	82	.6	6.4	12
*54	770115	1232	16.22	38	54.89	70	28.63	8.35	.06	.62	1.77	130	.6	5.4	11
55	770122	947	16.39	38	54.85	70	44.42	5.03	.06	2.49	1.51	302	1.4	14.4	7
*56	770129	1826	33.24	38	48.29	70	29.37	13.60	.05	1.18	1.36	149	1.3	1.0	10
57	770211	1618	6.66	38	57.63	70	35.23	6.48	.06	2.11	3.04	174	1.7	1.1	8
58	770306	2123	22.51	38	58.88	70	37.46	6.39	.06	1.55	1.55	296	1.5	3.2	9
59	770306	2333	53.32	38	56.35	70	24.86	.09	.12	1.09	20.59	163	1.5	1.2	7
*60	770308	125	29.87	38	56.32	70	28.05	6.12	.05	1.09	2.42	158	1.7	1.6	8
*61	770721	1121	16.45	38	54.14	70	23.50	8.56	.06	.96	1.41	166	.9	3.7	10
*62	770721	1745	25.05	38	50.67	70	27.86	21.86	.04	3.07	10.79	138	.6	5.9	6

63	770722	824	26.50	38	58.26	70	35.98	4.72	.06	2.63	3.07	284	1.4	.9	6
64	770723	1551	37.33	39	6.59	70	30.68	11.07	.09	4.42	6.77	297	1.4	16.9	7
65	770724	1839	59.56	38	58.95	70	16.99	17.14	.06	8.79	5.96	272	.3	5.7	5
66	770729	828	11.33	38	56.14	70	24.02	4.35	.00	3.36	2.19	158	2.4	1.6	4
67	770806	1029	57.90	38	51.11	70	18.52	7.05	.03	5.26	8.73	276	1.3	10.3	5
68	770806	1102	22.60	38	55.90	70	20.69	6.58	.01	3.91	2.37	192	1.1	2.1	5
69	770806	1114	36.53	38	53.32	70	18.53	11.85	.07	5.82	4.73	271	.9	6.2	6
70	770806	1226	16.76	38	52.83	70	19.38	9.09	.02	4.01	2.97	261	1.7	7.0	6
71	770806	1257	18.11	38	50.00	70	16.50	4.87	.08	3.44	9.42	293	1.0	13.0	6
72	770806	1512	7.59	38	51.83	70	16.35	2.45	.04	5.93	24.67	293	1.6	9.9	5
73	770806	1521	20.65	38	53.82	70	19.46	7.96	.10	17.39	7.38	256	.8	5.1	5
74	770806	1719	22.50	38	52.89	70	18.11	14.45	.09	13.60	7.56	276	1.5	7.2	4
75	770809	1124	25.59	38	59.30	70	36.99	2.49	.08	14.68	3.21	295	1.7	3.0	5
76	770812	541	59.54	38	51.53	70	19.27	8.95	.04	3.36	7.21	205	1.8	5.6	6
*77	770815	1211	37.05	38	50.49	70	30.32	11.73	.05	1.33	1.97	162	1.7	5.0	8
78	770821	1049	34.54	38	49.52	70	29.56	12.12	.07	2.85	6.00	118	3.2	3.1	7
79	770823	2138	56.04	38	56.67	70	27.76	3.93	.07	.99	3.11	166	1.1	4.3	7
80	770827	308	25.76	38	56.44	70	27.88	4.10	.05	1.18	2.14	160	2.2	1.9	6
81	770831	2013	27.53	38	56.13	70	41.10	5.18	.06	2.02	4.35	290	1.3	9.1	6
82	770831	2052	12.56	38	56.65	70	38.95	7.15	.01	1.52	1.18	279	1.4	5.9	6
*83	770906	831	34.56	38	56.44	70	32.48	5.90	.05	.88	1.33	142	1.4	4.8	9
84	770907	1019	1.44	38	56.57	70	42.15	6.69	.06	2.45	.99	299	1.4	10.2	6
85	770907	2227	18.76	38	54.30	70	19.52	7.89	.10	2.18	1.82	127	1.5	4.1	6
86	770910	2307	51.93	38	52.95	70	15.27	7.84	.07	4.67	1.98	287	1.9	2.7	5
87	770911	938	1.43	38	57.64	70	25.54	.15	.08	.78	36.90	188	.9	3.6	8
88	770914	1115	43.97	38	55.42	70	34.88	8.61	.11	1.03	1.90	200	1.2	5.3	9
89	770915	100	16.40	38	57.65	70	28.72	.23	.18	1.13	78.77	182		6.4	6
90	770918	1448	40.49	38	56.23	70	32.78	4.07	.13	1.05	3.89	150	1.0	5.2	8
91	770921	1035	53.24	38	56.94	70	37.62	10.00	.12	3.89	3.95	267	1.4	4.0	5
92	770926	1653	39.89	38	57.33	70	33.86	7.80	.12	1.51	1.23	146	1.1	2.8	7
93	771004	202	9.00	38	40.39	70	31.42	6.89	.01	2.59	1.00	311	1.7	14.0	7
94	771004	1859	2.13	38	48.71	70	23.89	7.82	.20	3.51	1.69	212	2.2	8.6	6
95	771005	257	40.61	38	47.31	70	21.77	8.83	.02	4.83	8.45	246	2.1	11.5	6
96	771006	343	18.22	38	47.11	70	26.39	11.32	.05	1.70	1.90	238	1.1	5.0	8
97	771008	1158	50.98	38	55.55	70	33.67	2.32	.06	1.45	9.02	175	1.5	5.5	6
98	771010	1224	1.24	38	56.15	70	33.40	.51	.15	1.62	35.18	162	1.1	4.8	6
99	771014	3	42.24	38	48.69	70	13.38	3.54	.13	18.23	26.50	293	1.7	10.7	6
100	771106	2223	20.14	38	53.78	70	23.20	8.14	.04	2.26	7.37	131	1.2	7.4	7
101	771110	50	38.24	39	4.58	70	30.90	9.15	.05	8.65	8.22	285	1.7	13.4	6
*102	771110	1546	14.33	38	48.53	70	29.49	13.92	.04	1.10	1.65	134	1.1	1.3	9
103	771116	1029	15.75	38	45.46	70	25.44	7.84	.08	2.09	.88	268	.8	7.6	8
104	771117	1233	54.85	38	47.59	70	26.74	12.38	.07	1.23	1.17	226	.9	4.3	10
105	771119	20	30.18	38	56.18	70	24.54	3.49	.10	4.08	3.43	281		1.1	5
106	771124	903	27.37	38	36.43	70	30.05	6.90	.05	25.94	3.00	317	2.9	21.2	6
107	771128	457	29.99	38	47.70	70	20.01	14.23	.07	1.93	3.48	250	1.8	12.3	8
108	771128	534	17.36	38	47.15	70	19.66	6.74	.14	1.71	1.26	258	1.4	13.1	8
109	771128	538	4.57	38	47.10	70	19.38	6.99	.17	1.88	.97	260	1.4	13.0	9
110	771128	713	36.18	38	50.61	70	19.63	6.06	.21	2.52	10.43	216	1.3	7.3	7
111	771128	743	57.22	38	50.35	70	19.79	12.67	.10	6.07	5.32	239	1.1	7.8	5
112	771202	426	7.96	38	49.66	70	26.12	15.15	.06	1.60	1.46	177		6.2	6
113	771204	1502	36.54	38	58.29	70	35.64	5.57	.06	2.07	2.91	285	1.5	.4	7
114	771206	2059	29.14	38	47.41	70	21.97	11.12	.05	2.79	2.02	243	1.5	11.2	8
115	771207	203	26.37	38	40.61	70	35.18	6.74	.03	18.64	1.56	313	3.6	15.6	7
116	771214	231	39.37	38	56.42	70	38.05	4.92	.05	13.34	16.30	255	1.4	5.1	6
117	771214	2342	56.35	38	47.75	70	21.76	8.29	.02	4.43	8.62	239	1.2	11.5	6
118	771217	2208	35.33	38	57.79	70	30.20	5.24	.06	.95	4.55	182	1.6	7.5	7
*119	771220	417	35.20	38	56.48	70	31.19	5.68	.06	.70	3.47	150	1.0	6.9	9
120	771220	1010	56.55	38	49.89	70	24.79	8.81	.03	1.47	4.41	185	1.7	8.1	7
121	771225	1738	30.73	38	57.97	70	36.76	3.85	.11	10.74	9.06	270	3.6	2.0	7
122	771226	600	26.33	38	57.33	70	36.23	5.35	.06	6.86	9.25	227	1.6	2.1	5
123	771226	842	11.80	38	58.89	70	38.11	6.64	.09	2.90	1.12	299	1.6	4.1	7
124	771226	916	56.52	38	58.12	70	37.50	5.10	.06	2.72	2.69	284	1.6	3.0	6
125	771226	1206	46.88	38	59.47	70	40.28	6.24	.07	3.57	1.40	308	1.6	7.4	7
126	771226	1356	13.68	38	57.50	70	36.25	4.62	.08	9.03	10.62	234	2.2	1.8	6
127	771227	821	48.59	38	58.98	70	36.98	5.76	.05	14.11	10.28	302	2.0	2.7	6

Table 2 (continued)

128	771227	853	19.06	38	58.78	70	37.79	5.18	.06	19.95	11.65	297	1.2	3.6	5
129	771227	1821	49.95	38	57.17	70	35.70	4.69	.08	10.56	15.76	201	1.8	2.0	6
130	771228	1243	39.95	38	58.95	70	37.10	5.09	.06	2.59	2.15	294	2.0	2.8	8
131	771228	1649	47.95	38	58.45	70	38.17	4.27	.10	15.64	9.05	297	2.0	4.0	7
132	771229	307	18.54	38	57.62	70	37.28	3.17	.08	12.12	11.12	265	3.4	2.9	7
133	771229	756	34.82	38	58.66	70	38.19	4.72	.07	22.17	12.27	299	1.9	4.1	6
134	771229	845	42.44	38	58.11	70	37.34	3.98	.07	19.06	13.82	282	2.0	2.8	6
135	771229	850	5.77	38	58.31	70	38.73	6.30	.08	1.92	1.13	296	1.6	4.8	7
136	771229	922	26.83	38	58.48	70	38.27	6.19	.07	1.56	1.76	298	1.5	4.2	7
137	771229	1112	9.93	38	58.95	70	38.94	6.39	.08	3.38	1.29	302	1.7	5.3	7
138	771229	1900	47.70	38	57.89	70	37.73	5.07	.05	1.31	2.22	279	1.4	3.4	7
139	771229	2139	4.10	38	57.53	70	37.15	2.51	.05	1.35	2.90	259	1.3	2.9	7
140	771229	2347	59.04	38	54.79	70	42.39	5.89	.07	2.24	1.54	291	1.5	11.9	6
141	771230	150	54.27	38	57.65	70	36.85	2.39	.13	3.63	3.44	258	1.5	2.4	6
142	771230	446	16.32	38	57.56	70	37.33	3.85	.05	2.37	3.26	264	1.2	3.0	7
143	771230	1437	27.65	38	57.19	70	36.41	6.34	.09	10.84	14.07	230	1.4	2.4	5
144	771230	2321	12.87	38	54.59	70	38.29	2.74	.20	2.34	11.54	255	1.6	7.9	6

Definitions:

DEPTH - Focal depth in km below the seismograph array.

RMS - The root mean square of the weighted traveltime residuals r_i with weights w_i:

$$RMS^2 = \sum(w_i r_i)^2 / \sum w_i^2$$

ERH - Horizontal error in km, defined as the greatest length of the horizontal projections of the three principal axes of the error ellipsoid.

ERZ - Vertical error in km, defined as the greatest length of the vertical projections of the three principal axes of the error ellipsoid.

GAP - The largest azimuthal gap between azimuthally adjacent stations.

FMAG - Coda magnitude; see Klein (1978, p.33) for formula.

DMIN - Distance to nearest station reporting an arrival with weight larger than 0.1.

NWR - Number of arrival times (P and S) with weight greater than 0.1.

* - Indicates an earthquake used in the inversion experiments of this report.

Table 3
HYPOINVERSE Program Variables

CRUST

MODEL:	1			2			3		
LAYER	VEL	DEPTH	THICK	VEL	DEPTH	THICK	VEL	DEPTH	THICK
1	5.30	0.00	8.00	0.00	0.00	0.00	0.00	0.00	0.00
2	6.10	8.00	8.00	0.00	0.00	0.00	0.00	0.00	0.00
3	7.70	16.00	999.00	0.00	0.00	0.00	0.00	0.00	0.00

TEST PARAMETERS

-ITERATION AND CONVERGENCE-		-WEIGHTING, ERROR, TRIAL DEPTH-	
20=Itrlim	.9000=Damp	50.0000=Discut	.1600=Rmscut
.0400=Dquit	.0010=Drqt	1.0000=Diswl	1.5000=Rmswl
7.0000=Dxfix	.0120=Eigtol	3.0000=Disw2	3.0000=Rmsw2
12.0000=Dzmax	.0200=Rback	1.0000=Swt	.2500=Rderr
.5000=Dzair	.6000=Bacfac	7.0000=Ztr	1.0000=Ercof

-DURATION MAG CONSTANTS-

-1.1600=Fma1	2.0100=Fmb1	.0070=Fmz1	.0035=Fmd1	9000.0000=Fmbrk
0.0000=Fma2	0.0000=Fmb2	0.0000=Fmz2	0.0000=Fmd2	1.7700=Pos

NOTE: See Klein (1978) for definition of HYPOINVERSE program variables.

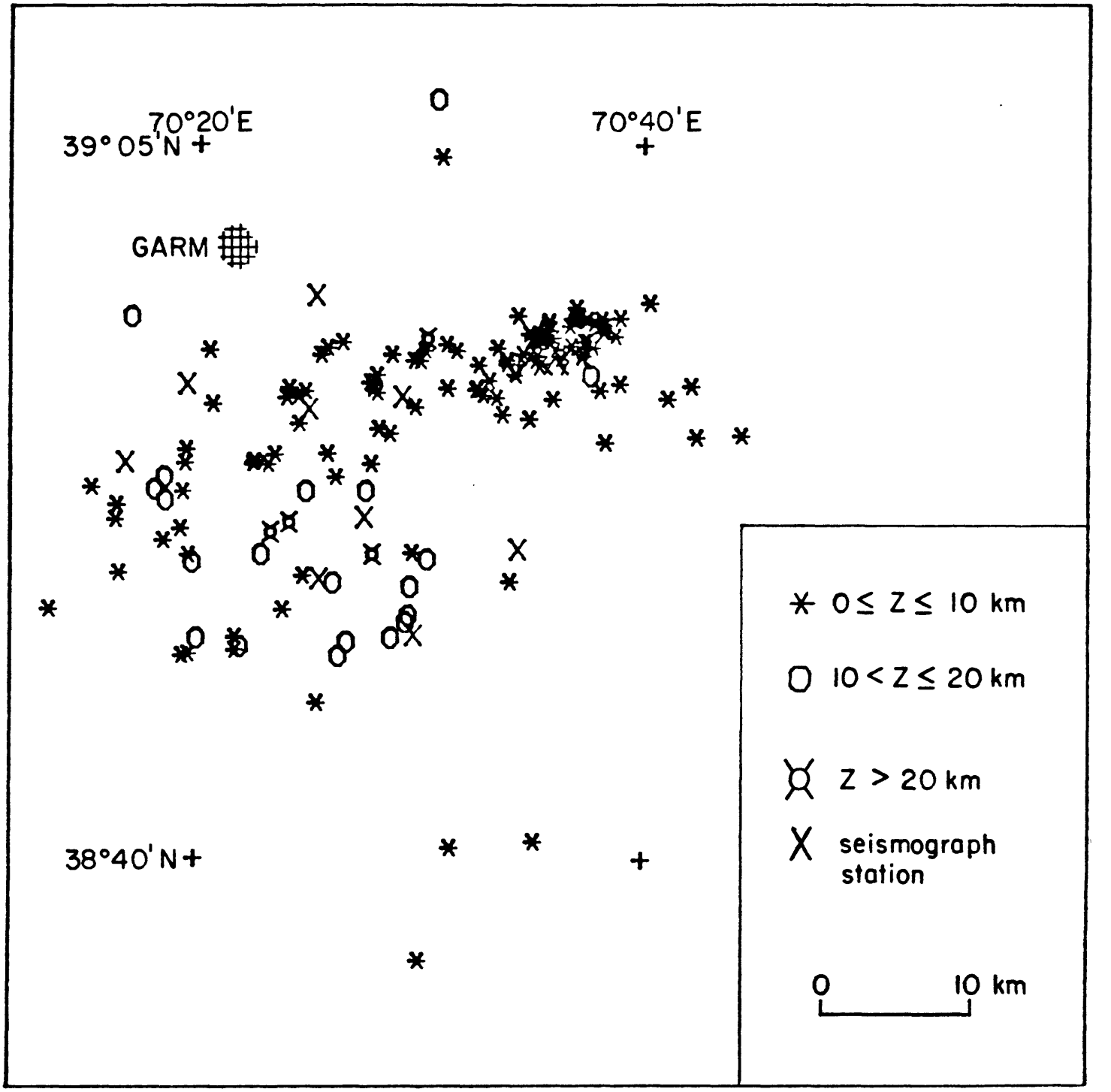

Figure 2. Epicenter map of basic catalog of 144 earthquakes listed in Table 2.

between 10 and 20 km focal depth, and only four events have focal depths greater than 20 km. Most of the earthquakes located at depths greater than 10 km have epicenters in the southern half of the array.

INVERSION

Arrival times of P and S phases from local earthquakes recorded on a dense array of seismographs jointly contain information on origin times, hypocenter locations, and the local velocity structure. One way to extract this information involves the assumption of a particular velocity model which may be completely described by N adjustable parameters, where N plus the number of elements in the set of earthquake origin times and hypocenter coordinates is less than the number of arrival time observations (i.e., the over-constrained inversion problem). The adoption of a particular velocity model automatically specifies a theoretical arrival-time function for a given phase at a given station, where the independent variables of the arrival-time function are the origin time, the hypocenter coordinates, and the velocity model parameters. Simultaneous adjustment of these independent variables in some logical manner is presumed to eventually lead to values which give a unique "best fit" of the set of theoretical arrival times to the set of observed arrival times. In this way, the "best" estimates of both hypocenter coordinates and velocity model parameters are obtained.

Crosson (1976) formulated the adjustment of the independent variables for the over-constrained inversion problem in terms of an iterative damped least squares technique. This formulation was adopted by W. L. Ellsworth and R. L. Nowack (U.S. Geological Survey, Menlo Park, personal

communication, 1980) for their inversion program VELEST2, which is based on a velocity model composed of horizontal layers. Each layer is assumed to have a uniform and fixed thickness, with a uniform but adjustable seismic velocity. VELEST2 accepts both P and S arrival times from a set of local earthquakes and provides simultaneous estimates of: (i) P and S velocities for each layer, (ii) origin times, (iii) hypocenter coordinates, and (iv) resolution and covariance information. Inclusion of station corrections in the parameter list is optional.

It is not known whether or not the seismic velocity structure beneath the Peter the First Range can be adequately parameterized by flat-lying layers (each layer having uniform thickness and uniform velocity), but this type of parameterization is a logical first step. An inversion using VELEST2 was designed and carried out for a crustal velocity model consisting of two 8-km thick layers over a half-space. Input data involved P and S arrival times for 26 local earthquakes from the basic catalog with preliminary hypocenters in the 0-27 km depth range (241 total observations for 110 total parameters). Figure 3 is an epicenter map showing the distribution of earthquakes used in the inversion (the earthquake locations used to construct Figure 3 were taken from Table 2). The 8 km layer thicknesses were chosen by trial and error to give satisfactory resolution for the velocities in the upper 16 km of the crust, where most earthquakes occur. The initial velocities increased with depth (the alternative is an initial model with a low velocity layer, which will be discussed next). The ratio of total iterations to the number of iterations which included adjustment of velocity parameters

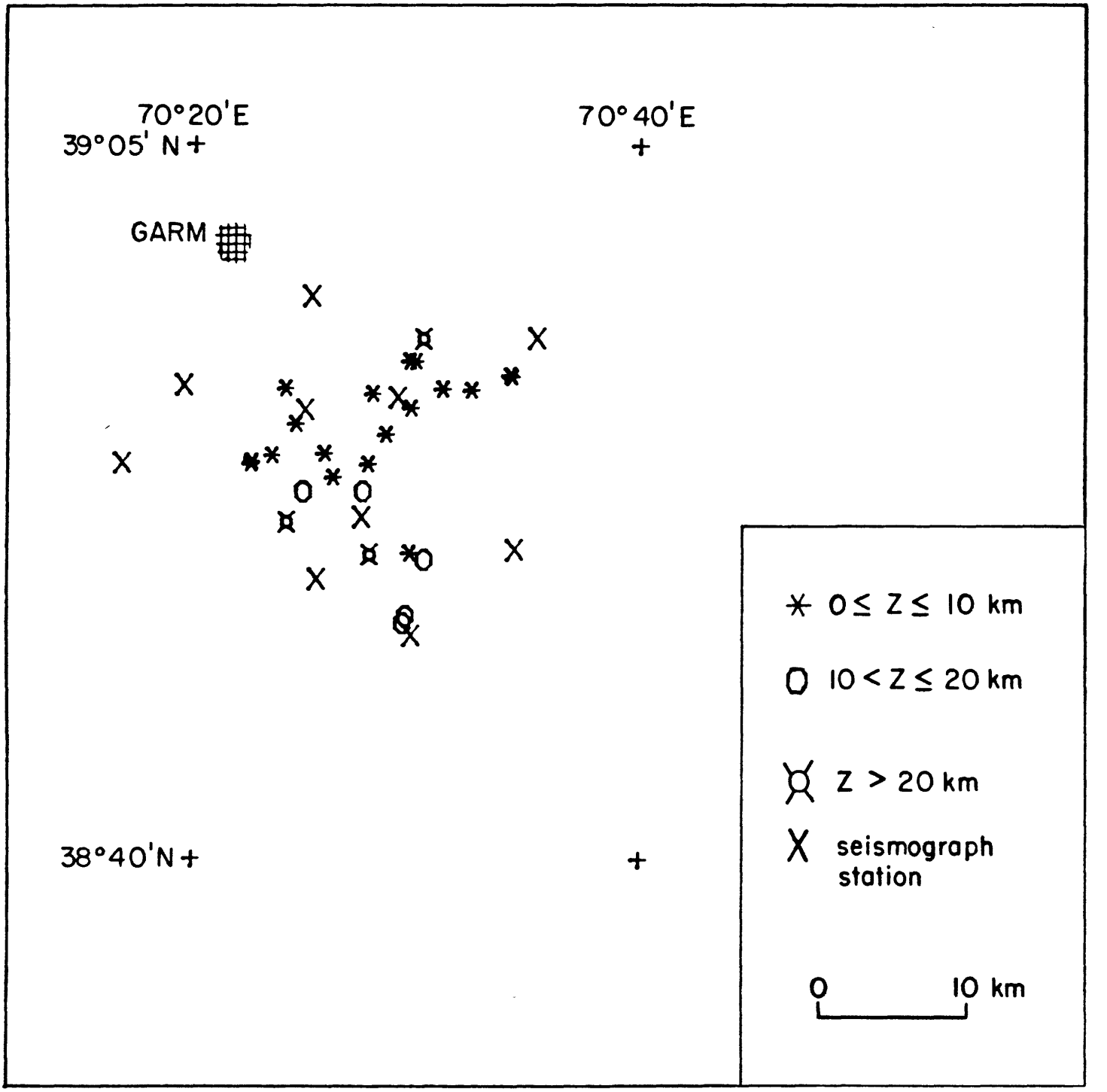

Figure 3. Epicenter map showing distribution of earthquakes used in the least squares inversions for velocity and hypocenter parameters. Earthquake locations taken from Table 2.

was five, with forty total iterations necessary to make the magnitude of each velocity adjustment less than the estimated standard deviation of the corresponding velocity parameter. The damping factor was small (see Table 4) so that the inversion approximated classical least squares theory. Station corrections were not included in the parameter list. Selected VELEST2 program variables used in this report are summarized in Table 4.

The initial and final velocity models are shown in Figure 4 and indicate that although a general increase in velocity within each layer and within the half-space was favored by the inversion, the trend of increasing velocity with depth was preserved. The value on the diagonal of the appropriate row of the resolution matrix suggests that resolution of the velocities was satisfactory except for the half-space P velocity. (Ideally, the diagonal value should be close to unity and all other row values close to zero). However, any interpretation of the inversion results in terms of "true" velocity parameters implicitly assumes that the two layer over a half-space model is an adequate parameterization of the actual velocity structure. At this time there is no study which unambiguously indicates the correct parameterization for the crustal velocity structure beneath the Peter the First Range. Therefore, if we assume that convergence proceeded to the global minimum in parameter space, the strongest conclusion that we can make from the inversion is the following: the final P and S layer velocities together with the final set of origin times and hypocenter coordinates provide the best least squares fit of the theoretical and observed arrival times under the

Table 4

VELEST2 Program Variables

Total number of iterations = 40

Ratio of total number of iterations to number of iterations including velocity adjustments = 5

Velocity damping factor = 0.01

Epicenter damping factor = 0.01

Origin time damping factor = 0.01

Focal depth damping factor = 0.01

Number of P and S arrival time observations = 241

Total number of parameters = 110

Shear wave weighting factor = 0.75

Station corrections not included in parameter list.

constraint of the assumed parameterization of layer thicknesses. The final P velocity model of Figure 4 was used in the final HYPOINVERSE run to produce the catalog given in Table 2. A Vp/Vs ratio of 1.77 $\pm$ .04 was estimated by averaging the ratios for the two layers above the half-space and assuming independent random error.

The final velocity models of Figure 4 show increasing P and S velocities with depth. This result must be compared with the results of a study by Nersesov and Chepkunas (1971) who suggested a low velocity zone beneath the Garm region with a top at about 12 km depth and a bottom at about 25 km depth. Their conclusion is based on trial and error modeling of travel-time curves (deduced from local earthquakes) to obtain "optimum" continuous P and S velocity functions of depth, and is supported by observations of body wave attenuation (Chepkunas, 1971). The continuous velocity functions of Nersesov and Chepkunas (1971) are easily parameterized in terms of horizontal velocity layers as follows: first layer, 12 km thick, Vp = 6.0 km/sec, Vs = 3.4 km/sec; second layer, 13 km thick, Vp = 5.6 km/sec, Vs = 3.2 km/sec; half-space, Vp = 6.8 km/sec, Vs = 3.9 km/sec.

As a test, the parameterized velocity models of Nersesov and Chepkunas (1971) and the P and S arrival times for the 26 earthquakes of the inversion data set (see Figure 3 and Table 2) were input to VELEST2. Program variables were the same as those listed in Table 4. The initial and final velocity models are shown in Figure 5, along with the appropriate values on the diagonal of the resolution matrix. The velocity decrease at the interface between the first and second layers was clearly not favored by the inversion. The resolution values are satisfactory for the upper two layers, but the final half-space

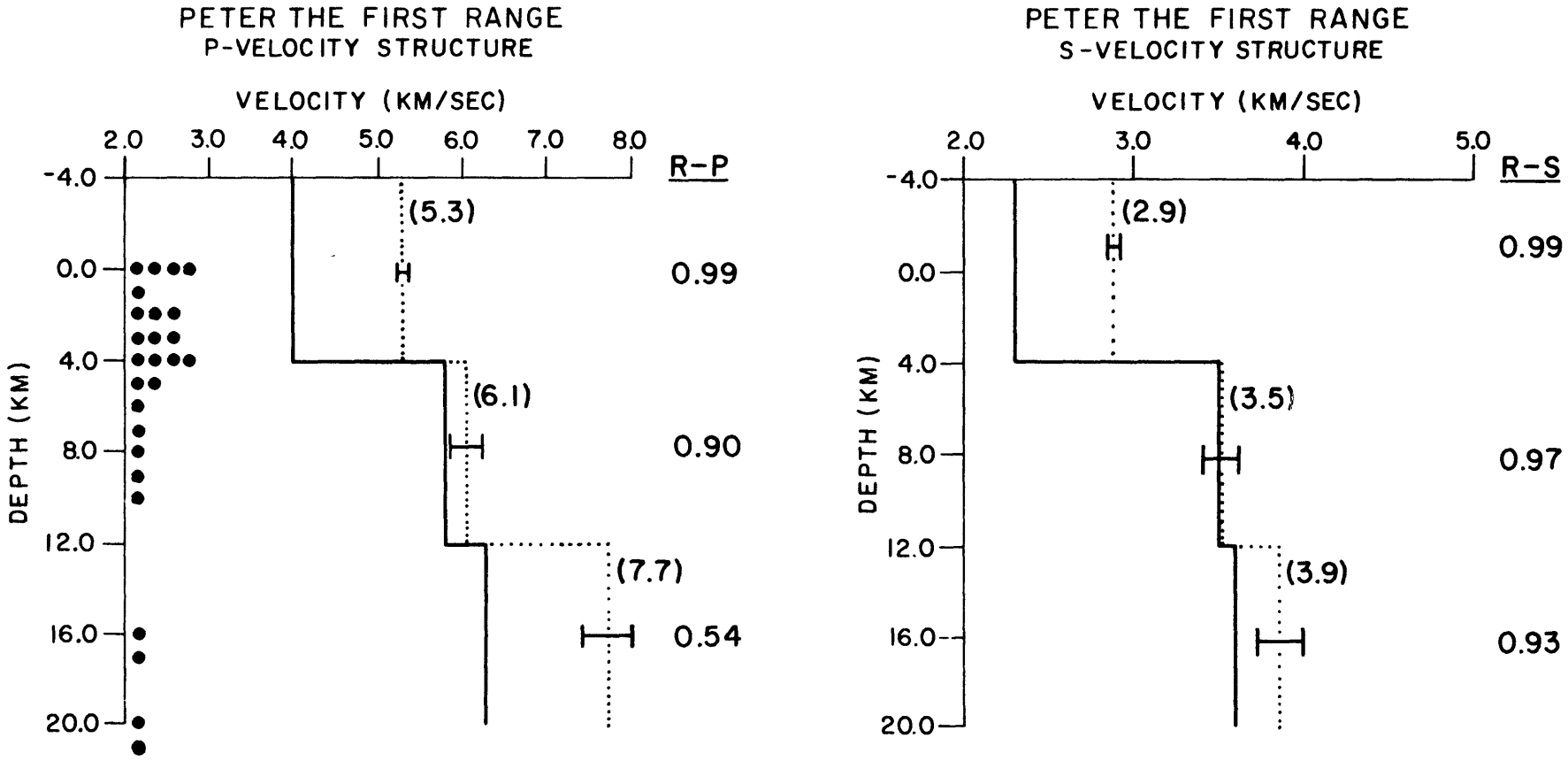

Fig. 4. Inversion results for initial model in which P and S velocities increase with depth. Solid line--initial model; dotted line--final model. Length of error bar is two standard deviations. Final layer velocities given in parentheses. Valen on diagonal of resolution matrix given under R-P column for P velocities, and under R-S column for S velocities. Black dots show final depth distribution of earthquakes used in the inversion (plotted to nearest km). Sea level is at depth 0.0 km.

FIGURE 4

velocities were very poorly resolved and are therefore not shown. This is a result of the fact that only one earthquake had a final location within the half-space, which resulted in very few direct travel paths in that part of the model (all USGS stations apparently were also within the cross-over distance for head waves from the half-space interface). However, this deficiency in the data for the detection of deeper velocity structure should not prevent the detection of the velocity decrease at the interface between the first and second layers if it actually exists. For example, Crosson (1976) conducted a test on synthetic data in which the true velocity structure was similar to the parameterization considered here: two horizontal layers over a half-space, with the second layer being a low velocity layer (LVL). Crosson generated synthetic travel times from earthquakes placed only in the LVL above the half-space, and these data were input to the inversion routine. For an initial model with layer boundaries positioned correctly, Crosson found that the true velocity model was estimated accurately (including the LVL and the half-space velocity). The only fundamental difference between the station distribution in the test by Crosson (1976) and the station distribution in this study is that Crosson theoretically had stations beyond the cross-over distance for head waves from the half-space, so that the half-space velocity was adequately sampled.

The principal conclusion to be drawn from the inversion results illustrated in Figure 5 and the test results of Crosson (1976) is that the upper crustal low velocity zone suggested by Nersesov and Chepkunas (1971) for the Garm region probably does not exist beneath the USGS Peter

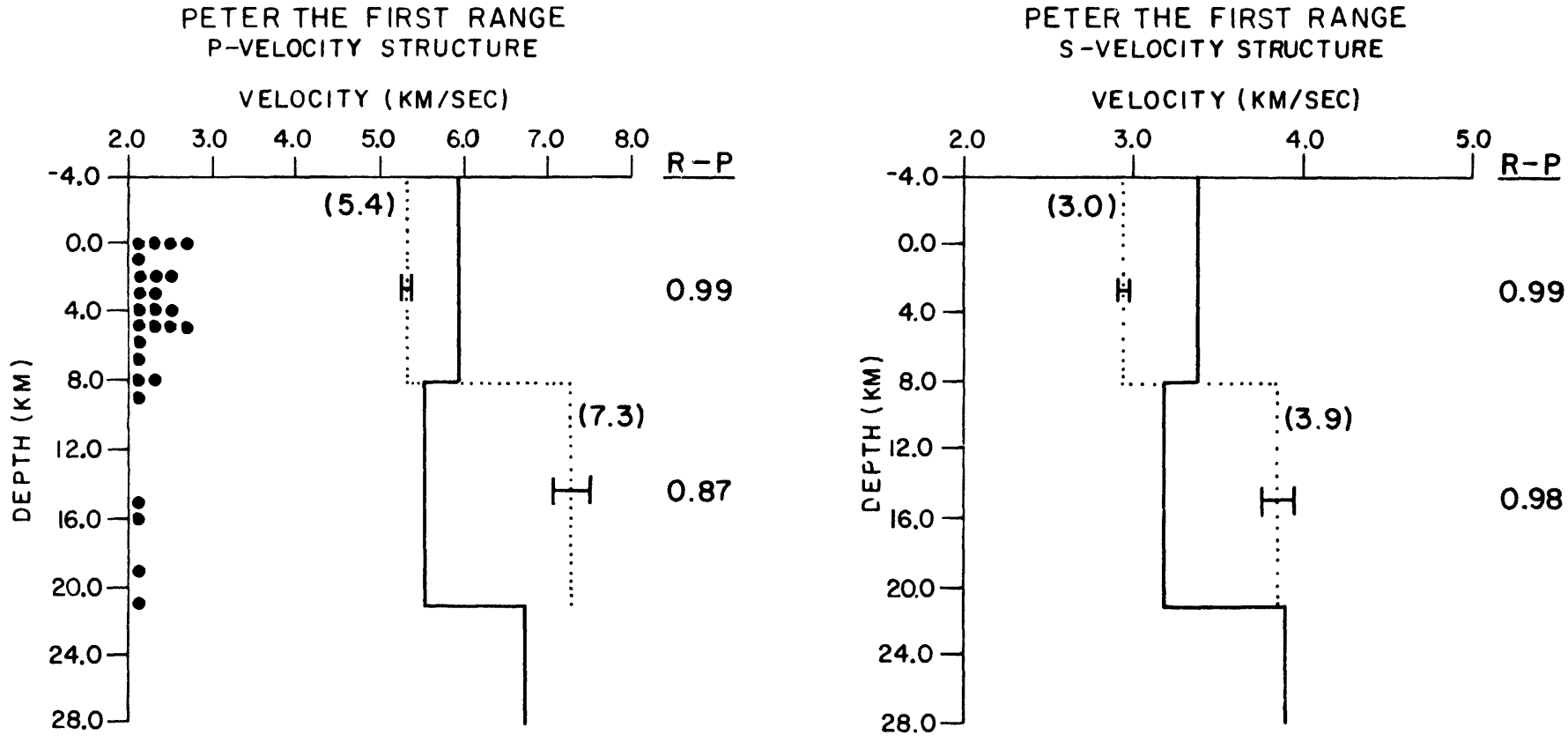

Fig. 5. Inversion results for initial model containing a low velocity layer. Solid line-initial model; dotted line-final model. Length of error bar is two standard deviations. Final layer velocities given in parentheses. Value on diagonal of resolution matrix given under R-P column for P velocities, and under R-S column for S velocities. Black dots show final depth distribution of earthquakes used in the inversion (plotted to nearest km). Sea level is at depth 0.0 km.

FIGURE 5

the First Range array. This conclusion is based on the fact that a reasonable parameterization of the hypothesized low velocity structure is converted by the inversion process to a velocity structure in which P and S velocities increase in a normal manner with depth. Indeed, the final P and S velocity models of Figure 5 compare nicely (within 4%) with a weighted average (over depth) of the final P and S velocity models of Figure 4. Such excellent agreement is notable because the final models of Figure 4 represent an entirely different parameterization of layer thicknesses, and they were deduced from entirely different initial layer velocities. Furthermore, the final depth distribution of earthquakes from both inversions is virtually the same (compare Figures 4 and 5). Thus we have internally consistent results from the inversion experiments which strongly suggest increasing P and S velocities with depth in the upper crust beneath the USGS Peter the First Range array. To strengthen this conclusion, additional deep earthquakes (greater than 20 km focal depth) should be included in the inversion data set, inversion tests on LVL models should be run with synthetic arrival time data generated for a station distribution identical to that of the USGS Peter the First Range array, and data from the Complex Seismological Expedition's regional network should be incorporated in the inversion if possible.

SUMMARY

A basic catalog of 144 local earthquakes recorded by the USGS Peter the First Range seismic array for the time period August 1, 1975 to December 31, 1977 has been compiled. A level of completeness (i.e., a

statement guaranteeing the inclusion in the catalog of all earthquakes which are above a certain magnitude or energy class and which occur within the array) cannot be established for this catalog because much of the array was disabled during winter months, but all 144 earthquakes have been assigned an energy class $K \geq 6$ by the USSR Complex Seismological Expedition.

The seismicity pattern defined by the earthquakes of the catalog is diffuse, but some concentration of seismicity is noted near station G36 at the northeastern corner of the array. Focal depths range from 0 to 26 km, with most earthquakes located between 0 and 10 km depth. A major portion of the deeper earthquakes have epicenters in the southern half of the array.

Least squares inversion of P and S arrival times from local earthquakes was used to estimate P and S velocities in an assumed velocity structure consisting of two layers over a half-space. Two different initial models were considered: (i) a model in which velocities increased with depth in a "normal" manner, and (ii) a model in which the second layer was a low velocity layer (i.e., a parameterized version of the continuous velocity functions of Nersesov and Chepkunas (1971) for the Garm region). The inversion procedure converged in both cases to final P and S velocity models which indicate increasing velocities with depth, thereby suggesting that the low velocity zone of Nersesov and Chepkunas (1971) may not extend beneath the Peter the First Range. To strengthen this conclusion, three recommendations are made: (i) additional deep earthquakes (greater than 20 km focal depth) should

be included in the inversion data set,(ii) inversion tests on LVL models should be run with synthetic arrival time data generated for a station distribution identical to that of the USGS Peter the First Range array, and (iii) data from the Complex Seismological Expedition's regional network should be incorporated in the inversion if possible.

ACKNOWLEDGEMENTS

Nikolai Tarasov and Nadia Krevenok assisted in the compilation of the basic earthquake data set for the USGS Peter the First Range seismic array during Period I. Bill Ellsworth suggested that the velocity inversion of the arrival times be carried out with VELEST2. Bob Nowack provided advice and encouragement throughout the inversion experiments, and his suggestions led to much improvement in the interpretation of the final results.

REFERENCES

Chepkunas, L. S., Detection of a low-velocity layer in the Earth's crust in the Garm area from the attenuation of body waves from local earthquakes, in Experimental Seismology, edited by M.A. Sadovski, USSR Academy of Sciences, Institute for Physics of the Earth, pp. 203-310, 1971.

Crosson, R. S., Crustal structure modeling of earthquake data 1. Simultaneous least squares estimation of hypocenter and velocity parameters, Journal of Geophysical Research, (81), 3036-3046, 1976.

Fischer, F. G., Macksimov, A. B., Nersesov, I. L., and Wesson, R. L., Spectral studies of local earthquakes, Garm, USSR, in preparation, U.S. Geological Survey Open-file Report, Menlo Park, California, 1980.

Klein, F. W., Hypocenter location program HYPOINVERSE, Part 1: User's guide to versions 1, 2, 3, and 4, U.S. Geological Survey Open-file Report 78-694, Menlo Park, California, 1978.

Levander, A., and Monfort, M.E., Examination of recording site effects, wave propagation characteristics and microearthquake radiation patterns in the Garm region, U.S.S.R., Final Technical Report for U.S. Geological Survey Contract No. 14-08-0001-16855, 1980.

Nersesov, I. L., and Chepkunas, L. S., The low-velocity layer in the Earth's crust in the Garm area, in Experimental Seismology, edited by M. A. Sadovski, USSR Academy of Sciences, Institute for Physics of the Earth, 191-203, 1971.

Rautian, T. G., About the determination of energy of earthquakes at distances up to 3,000 km, Trudy Inst. Earth Phys., (199), 88-93, in Russian, 1964.

Rautian, T. G., Khalturin, V. I., Martynov, V. G., and Molnar, P., Preliminary analysis of the spectral content of P and S waves from local earthquakes in the Garm, Tadjikistan region, Bulletin of the Seismological Society of America, (68), 949-971, 1978.

Reprinted by permission
JOURNAL OF GEOPHYSICAL RESEARCH, VOL. 86, NO. B2, PAGES 1070-1080, FEBRUARY 10, 1981

Surface Deformation, Crack Formation, and Acoustic Velocity Changes in Pyrophyllite Under Polyaxial Loading

HARTMUT A. SPETZLER,[1] GENNADY A. SOBOLEV,[2] CARL H. SONDERGELD,[3] BORIS G. SALOV,[2] IVAN C. GETTING,[3] AND ANOTOLI KOLTSOV[2]

Jacketed cubes of pyrophyllite (31.6 mm on an edge) with variable water content were stressed monotonically to failure under polyaxial compression ($\sigma_1 > \sigma_2 = 2\sigma_3$). The maximum and minimum principal stresses, σ_1 and σ_3, were applied with pistons, and the intermediate stress σ_2 with a transparent fluid. An optical window in the pressure vessel allowed in situ measurements of the σ_2 face deformation by optical holography. In addition, the more conventional techniques of stress, strain, and elastic wave velocity measurements as well as optical and electron microscopy were used to study the formation and propagation of fractures. The strength $(\sigma_1 - \sigma_3)_f$ of the samples increased by about 50% as σ_2 was increased from 5 MPa to 100 MPa. Air dry samples were stronger than water-soaked samples by about ~20%. Increasing the strain rate from 2×10^{-8} to 10^{-6} s^{-1} at $\sigma_2 = 5$ MPa and 30 MPa increased the strength by about 10%. At $\sigma_2 = 100$ MPa this trend was reversed, and samples that were deformed at the low strain rate were stronger by approximately 5%. The crack morphology of recovered samples was studied by optical and scanning electron microscopy. Subparallel sets of fractures and en échelon fracture patterns ahead of the macrofracture were easily visible with the unaided eye when σ_2 was 5 MPa or 30 MPa. However, at $\sigma_2 =$ 100 MPa these fracture patterns were only visible under the microscope, and the cracks appeared much thinner. The holographic observations of the σ_2 face revealed the following: as σ_1 was increased, broad bulges formed in a crosslike pattern along the lines of the maximum shear stress. Macrofracture initiation, which occurred in a corner, was preceded by concentrated surface deformation. As the macrofracture propagated across the sample, it deviated from the direction of the maximum shear stress. Ahead of the tip of the macrofracture and migrating with it was a pronounced bulge. In response to monotonically increasing σ_1, the displacement in the σ_2 direction of a point adjacent to the eventual crack plane went through a local maximum that was followed by a local minimum as the crack passed. The results of elastic wave velocity measurements in the σ_2 direction were very sensitive to the spatial relationship of the macrofracture and the elastic wave travel path. However, in general, above ~50% of $(\sigma_1 - \sigma_3)_f$ the velocities decreased. As the migrating bulge approached an elastic wave travel path, the velocity decrease became more pronounced. The velocity increased again as the bulge passed.

INTRODUCTION

Modern attempts to predict earthquakes are often based on observations of temporal changes of different properties of large rock masses in seismically active areas. Many precursory changes in physical properties have been reported in the literature [e.g., *Sadovsky and Nersesov*, 1974; *Kisslinger and Suzuki*, 1978; *Rikitake*, 1976]. Differences in the magnitudes and durations of precursors may be related to the different tectonic provinces within which they occur. Since the physical mechanisms of the precursors in nature are poorly understood, it is important to gain a better understanding through the study of these phenomena in the laboratory under controlled conditions. To understand the spatial variation of precursors, it is necessary to measure physical properties both near and far from the macrofracture of a laboratory specimen. In most previous experiments, seismic velocities and strains were reported as average values over the sample. The limited sample size in most high-pressure experiments prevents the application of many strain gauges and transducers. Notable exceptions, albeit without confining pressure (two-dimensional loading), are the experiments on meter-sized specimens by *Pratt et al.* [1974] and *Dieterich* [1979*a*, *b*].

The principal aim of the present work is to measure in detail the local distribution of strain together with compressional and shear wave velocities under polyaxial loading and to relate these measurements to the crack morphology as observed in recovered samples. Optical and scanning electron microscopy were employed to determine the crack morphology.

In a previous paper, *Sobolev et al.* [1978] reported on precursory phenomena in pyrophyllite when it was deformed under biaxial loading ($\sigma_1 > \sigma_2 > \sigma_3 = 0$). The major results of this work were as follows:

1. The formation of a preferential zone of deformation was identified on the surface where the intermediate principal stress σ_2 was applied. It was first recognized as a broad zone at approximately 50% of the ultimate maximum principal stress σ_1 at failure. At higher values of σ_1 the zone became more concentrated. Nearly randomly oriented microcracks and then en échelon cracks formed within this concentrated zone. The coalescence of the en échelon cracks into a macrofracture led to the ultimate failure of the sample.
2. Both compressional and shear elastic wave velocities decreased initially during the stage of development of the deformation zone. As the zone concentrated before failure, the velocities increased.
3. Velocity recoveries were convincingly observed only at the lowest experimental strain rate of $\approx 10^{-8}$ s^{-1} on wet samples.

One of the purposes of the present work is to check the above observations under a polyaxial stress state when σ_3, the least principal stress, is not zero ($\sigma_1 > \sigma_2 = 2\sigma_3 > 0$). In previous experiments, the study of the surface deformation associated with the intense deformation zone required unloading

[1] Cooperative Institute for Research in Environmental Sciences and Department of Geological Sciences, University of Colorado/NOAA, Boulder, Colorado 80309.
[2] Institute of the Physics of the Earth, Academy of Sciences of the U.S.S.R., Moscow.
[3] Cooperative Institute for Research in Environmental Sciences, University of Colorado/NOAA, Boulder, Colorado 80309.

Paper number 80B1067.
0148-0227/81/080B-1067$01.00

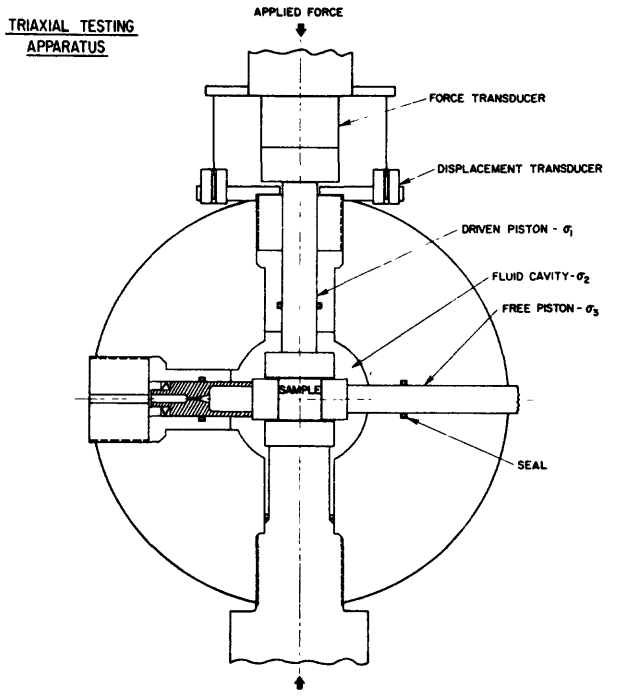

Fig. 1. Schematic experimental arrangement. The intermediate principal stress σ_2 is applied by the confining fluid. The minimum principal stress σ_3 is also applied by the confining fluid; its magnitude is reduced by the effect of free pistons, which are sealed to the sample and exposed to atmospheric pressure outside the pressure chamber. The maximum principal stress is applied conventionally by a 1-MN ram in a hydraulic press.

of the sample, removal of the σ_2 pistons, and reloading under uniaxial stress ($\sigma_1 > \sigma_2 = \sigma_3 = 0$). The present results were obtained within a pressure vessel in which the intermediate principal stress was applied with a transparent fluid and the maximum and minimum principal stresses were applied with pistons (Figure 1). An optical window in the pressure vessel allowed viewing of the σ_2 face, which is the surface intercepted by the major fractures.

Sample Description and Preparation

All experiments were performed on 31.6-mm cubes of pyrophyllite. Experiments TR-7 through TR-19 were performed on samples cut from one block, while samples for TR-20 through TR-27 were cut from a second block. Both blocks were obtained through American Lava Corporation of Chattanooga, Tennessee. The orientation of the samples was chosen such that the visible layering in the pyrophyllite was always perpendicular to σ_1. The intermediate and least principal stresses were applied to the other sets of faces, always maintaining the same orientation.

The samples are characterized as dry, wet, and saturated. Dry samples were stored in laboratory air at approximately 30% relative humidity. Wet samples were immersed in water for a period of at least 2 hr. Complete penetration was achieved in less than 20 min, as determined by breaking and visually examining a sample after that time. Saturated samples were evacuated for about 3 hr and then immersed in water under vacuum for about 12 hr. The densities of dry, wet, and saturated samples were 2.75, 2.80, and 2.81 $\times$ 10^3 kg/m^3, respectively.

All samples were jacketed in 0.13-mm soft copper foil; σ_3 spacers were soldered to the copper and formed part of the jacket. Jackets were partially assembled on a dumby block. Before the last solder joint on a σ_3 spacer was made, the sample was removed from its dry, wet, or saturated environment and placed into the partially completed jacket. An extra 0.13-mm sheet of copper was placed on each σ_1 face to avoid jacket rupture during loading. Use of a large heat sink prevented heating of the sample above an estimated 40°C during the completion of the last solder joint.

The jacket was seated against the sample by placing the sample in the pressure vessel, emplacing the σ_3 pistons, and raising the fluid pressure to the value of σ_2 to be used during the experiment. The values of σ_1 and σ_2 were then equal and twice that of σ_3. Any jacket failure resulted in the σ_3 pistons being pushed outward against their stops by the fluid pressure within the vessel. The present design of the sample and pressure vessel configuration does not lend itself to pore pressure measurements.

One-megahertz piezoelectric shear transducers 6.4-mm in diameter were epoxied in pairs to the σ_2 faces of the jacket. Their locations S_1, S_2, and S_3 are shown in Figure 2. Particle motion is the σ_3 direction. Small P wave arrivals yielded compressional velocities in addition to the shear velocities. P wave transducers in the σ_1 pistons yielded compressional velocity measurements in the direction of maximum principal stress. Therefore, when everything worked correctly, seven velocities were measured during each experiment, namely, V_p in the σ_1 direction and V_{p1}, V_{p2}, V_{p3}, V_{S1}, V_{S2}, and V_{S3} in the σ_2 direction.

Data Collection and Reduction

1. The maximum principal stress σ_1 was determined by use of a force gauge outside the pressure vessel. Corrections for the fluid pressure and seal friction were made.

2. The intermediate and least principal stresses, σ_2 and σ_3, were kept constant during each experiment. In these experiments, $\sigma_2 = 2\sigma_3$ = fluid pressure, which was measured by a Heise gauge to within $\pm$0.5 MPa (5 bar).

3. The strain of the sample in the σ_1 direction, ϵ_1, was determined by displacement measurements outside the pressure vessel. These measurements were corrected for apparatus distortion. For high strain rate experiments ($\sim 10^{-6}$ s^{-1}) the rate of stress increase was kept constant.

For the low strain rate experiments ($\sim 2 \times 10^{-8}$ s^{-1}) the rate of stress increase was initially the same as for the high strain rate experiments, but it was gradually reduced by 2 orders of magnitude until a strain rate of approximately 2×10^{-8} s^{-1} was achieved at about half of the strain at failure ($\epsilon_1 = 1/2\epsilon_{1f}$). The rate of stress increase was then kept nearly constant until failure. The strain rate in high and low strain rate experiments started to accelerate after $\sim\epsilon_1/\epsilon_{1f} = 0.8$.

4. The seven elastic wave travel times mentioned in the previous section are time of flight measurements. Both the first arrival and the first peak were recorded. The scatter in the first arrival measurements was greater than in the peak measurements, so the latter were used in calculating the changes in velocities.

To convert the P wave travel time data in the σ_1 direction into velocity data, the time delay within the pistons and the strain ϵ_1 of the sample are considered. Since no direct measurement of ϵ_2 is made, it is necessary to estimate the length change in that direction. At failure, ϵ_1 was approximately 10^{-2}. Assuming a Poisson ratio of 0.3, we estimated ϵ_2 to be about 3×10^{-3} near failure. Since velocity changes are several

percent, this correction is small, and errors in the correction are probably smaller than our scatter. The travel time measurements were reproducible to ±20 ns.

5. The surface deformation of the copper jacket in the σ_2 direction was observed by optical holography [*Heflinger et al.*, 1973; *Spetzler et al.*, 1974; *Meyer and Spetzler*, 1976] through a window in the pressure vessel. Each doubly exposed hologram yields a topographic map of the surface deformation that accumulates between the two exposures. To obtain the complete surface deformation of one σ_2 face during an entire experiment, between 20 and 30 holograms were taken at ϵ_1 intervals of approximately 4×10^{-4}. The copper jackets usually remained intact even during the propagation of the major fracture, allowing holographic observation during unloading. Real time holography during the final stages of one experiment enabled the experimenter to observe the real time evolution of the surface deformation via a TV monitor, thus avoiding the otherwise apparent ambiguity of the formation of ridges and valleys. A growing ridge has fringes emanating from the area of fastest growth, while a depression that is forming has fringes moving toward the point that is most rapidly descending.

During an experiment, several hundred data points each for σ_1 and ϵ_1 and the seven travel times were recorded. The force and displacement gauges were automatically read by a data acquisition system. The appropriate corrections were made, and $(\sigma_1 - \sigma_3)$ versus ϵ_1 was plotted in real time on an X-Y plotter. Travel time data were directly entered into the data acquisition system by reading, upon command, the potential across a delayed-sweep potentiometer on an oscilloscope. The beginning of the intensified delayed sweep was placed at the first desired arrival or peak. The character and distribution of cracks was studied in recovered samples under a scanning electron microscope (SEM) and an optical microscope.

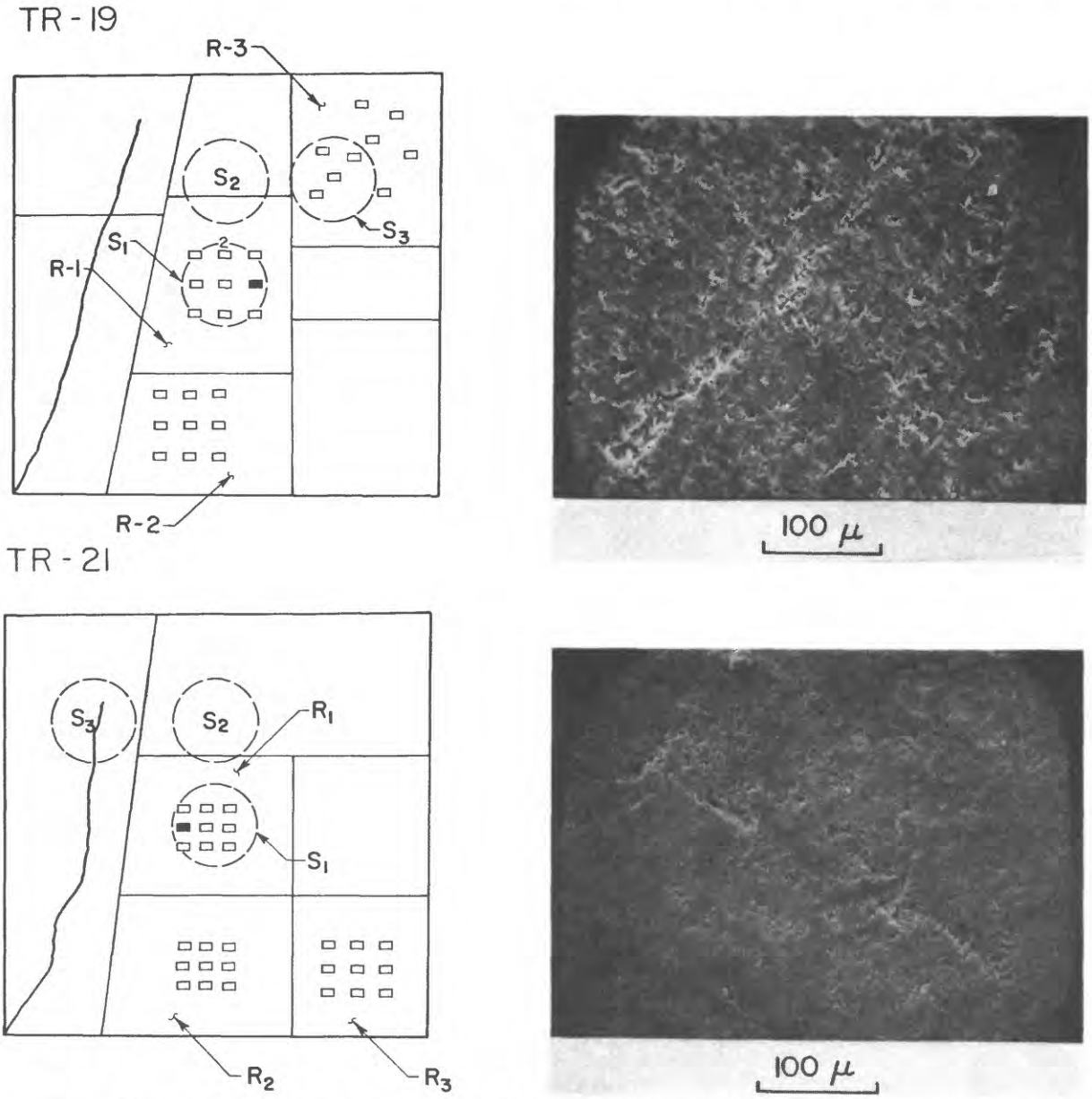

Fig. 2. Crack distributions for samples TR-19 ($\sigma_2 = 30$ MPa, $\dot{\epsilon} \sim 10^{-8}$ s^{-1}) and TR-21 ($\sigma_2 = 5$ MPa, $\dot{\epsilon} \sim 10^{-8}$ s^{-1}) were studied in the areas indicated by R_1, R_2, and R_3. The crack traces show the extent of the macrofracture when the experiments were stopped. The piezoelectric transducer locations are also indicated S_1, S_2, S_3. The SEM photomicrographs are from within the R_1 region, as indicated by the black rectangle.

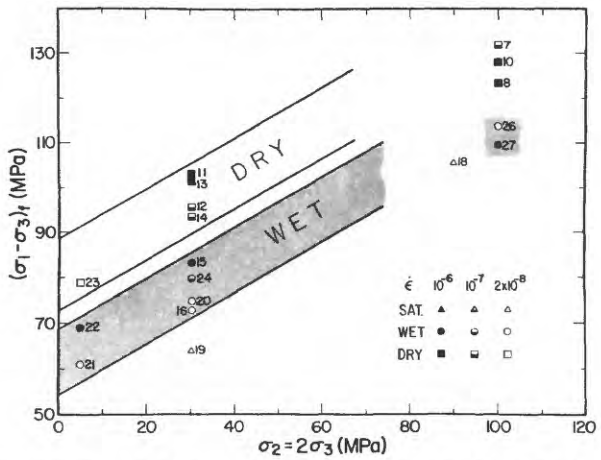

Fig. 3. (Opposite) The stress, $\sigma_1 - \sigma_3$, at failure is shown for 18 experiments. The variables are strain rate $\dot{\epsilon}$, moisture content, and σ_2.

Results

Strength. Figure 3 summarizes the experimental conditions and results of 18 experiments. The value of $(\sigma_1 - \sigma_3)_f$ refers to the peak value of the differential stress at failure, which usually occurred when the first macrofracture extended from a corner to past the middle of the sample. The value given for the strain rate $\dot{\epsilon}_1$ refers to the value during the linear part of the stress (σ_1) strain (ϵ_1) graph when ϵ_1 is greater than half of ϵ_{1f}.

The strength $(\sigma_1 - \sigma_3)_f$ of pyrophyllite is a function of $\sigma_2 = 2\sigma_3$, moisture content, and strain rate (Figure 3). At constant moisture content and strain rate, an increase of σ_2 from 5 MPa to 100 MPa increases the strength of the samples by up to 80% (for example, TR-21, TR-20, and TR-26). At constant σ_2 and strain rate, a decrease in moisture content also increases the strength of samples, for example, by 30% from wet to dry at 5 MPa and $\dot{\epsilon}_1 \approx 2 \times 10^{-8}$ s^{-1} (TR-21 and TR-23). At constant

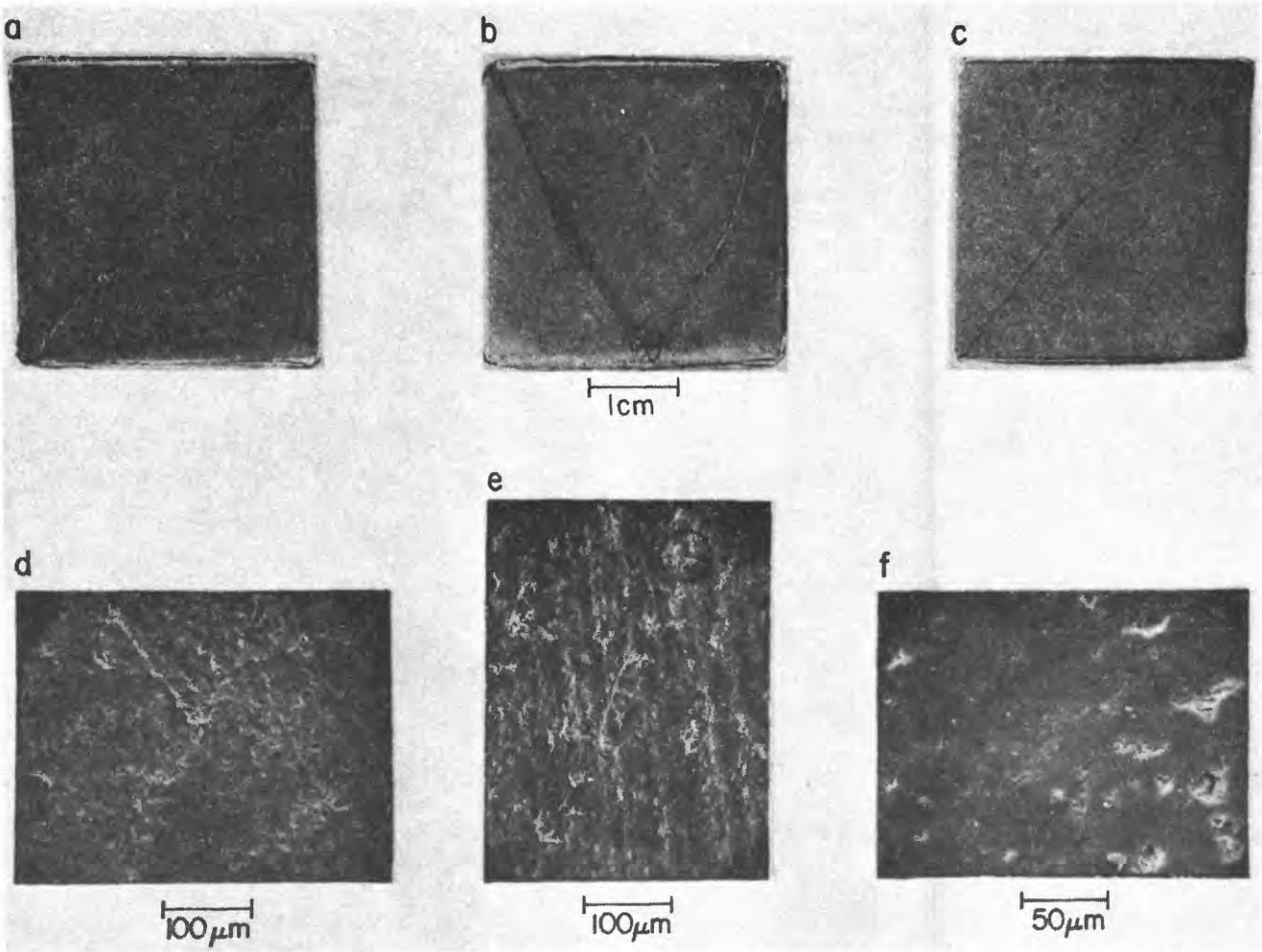

Fig. 4. Characteristic fracture patterns viewed in the σ_2 direction; σ_1 is always vertical. (*a*) Unconnected subparallel fractures form a zone following the direction of one of the two maximum resolved shear stresses (σ_2 = 30 MPa, $\dot{\epsilon} \sim 10^{-6}$ s^{-1}, wet sample TR-15). Note that macrofractures start at corners. (*b*) A typical fracture pattern for most experiments at $\sigma_2 \leqq 30$ MPa. Fracture systems with complementary cracks appear first (σ_2 = 30 MPa, $\dot{\epsilon} = 10^{-8}$ s^{-1}, saturated sample TR-17). Complementary fractures on this scale were not seen in any experiments wherein σ_2 was ≧90 MPa. (*c*) A partial development of macrofracturing is seen; being able to stop an experiment at this stage makes it possible to study microcracks in the vicinity of the macrofracture (σ_2 = 30 MPa, $\dot{\epsilon} \sim 10^{-7}$ s^{-1}, wet sample TR-24). (*d*) This SEM picture of a macrocrack illustrates the discontinuous nature of cracking and branching (σ_2 = 30 MPa, $\dot{\epsilon} \sim 10^{-8}$ s^{-1}, saturated sample TR-19). The macrocrack is similar to that shown in *c*. (*e*) The discontinuous nature of a near vertical macrocrack and its relation to some precursory near horizontal cracks (sample TR-18). Note the unconnected set of near horizontal cracks in the left upper portion of the picture. Branching of the precursory cracks is frequently observed and easily visible in the circle. (*f*) Precursory en échelon cracks appearing ahead of the macrocrack (sample TR-26).

moisture content, increasing the strain rate by 1 order of magnitude at $\sigma_2 = 5$ MPa or $\sigma_2 = 30$ MPa increases the strength by approximately 7% (for example, TR-21, TR-22; TR-12, TR-14, and TR-11, TR-13). At $\sigma_2 = 100$ MPa, our data show this trend to be reversed; the strength increases as the strain rate decreases (for example, TR-26 and TR-27). In several cases, we repeated experiments under identical conditions of pressure, moisture content, and strain rate. The reproducibility in strength is 5%.

Crack development. Macrofractures visible to the unaided eye always initiated at a corner. At $\sigma_2 = 5$ MPa and $\sigma_2 = 30$ MPa, the formation of the first macrofracture was often preceded or accompanied by an extensive set of complementary fractures. Figures 4*a–c* show examples of macrofracture patterns. Complementary fractures on this scale were never observed when $\sigma_2 \approx 100$ MPa. The macrofracture looks like that shown in Figure 4*c*. However, on a smaller scale, as shown in the SEM pictures 4*d* and 4*e*, complementary fractures are seen to exist near or are connected with the macrofracture. In Figure 4*d* the macrocrack extends from bottom left to top right and makes a larger angle with the vertical (σ_1) direction than the macrocrack in Figure 4*e*. Note the set of subparallel unconnected cracks on the left middle of Figure 4*e*. Close examination of the marked complementary crack and of others shows branching into two cracks that are parallel to the macrofracture. The complementary cracks in samples deformed at $\sigma_2 \approx 100$ MPa are shorter and appear much thinner than those in samples deformed at $\sigma_2 = 30$ MPa or $\sigma_2 = 5$ MPa.

En échelon fracture patterns, as shown in Figure 4*f*, are observed preceding and trending parallel to the macrofracture. The individual cracks are not connected. The angle between these cracks and σ_1 is greater than the angle between the macrofracture and σ_1. The observed macrofractures often are not continuous throughout their extent. They are interrupted by regions of unbroken material, as seen in Figures 4*d* and 4*e*. The discontinuous nature of the cracks is not unique to pyrophyllite. *Brace et al.* [1972] and *Brace and Bombolakis* [1963] have made similar observations on Westerly granite and glass, respectively.

The statistical distribution of microcracks in a plane perpendicular to σ_2 was studied in samples TR-19 and TR-21. For this purpose, the surfaces were polished and subdivided

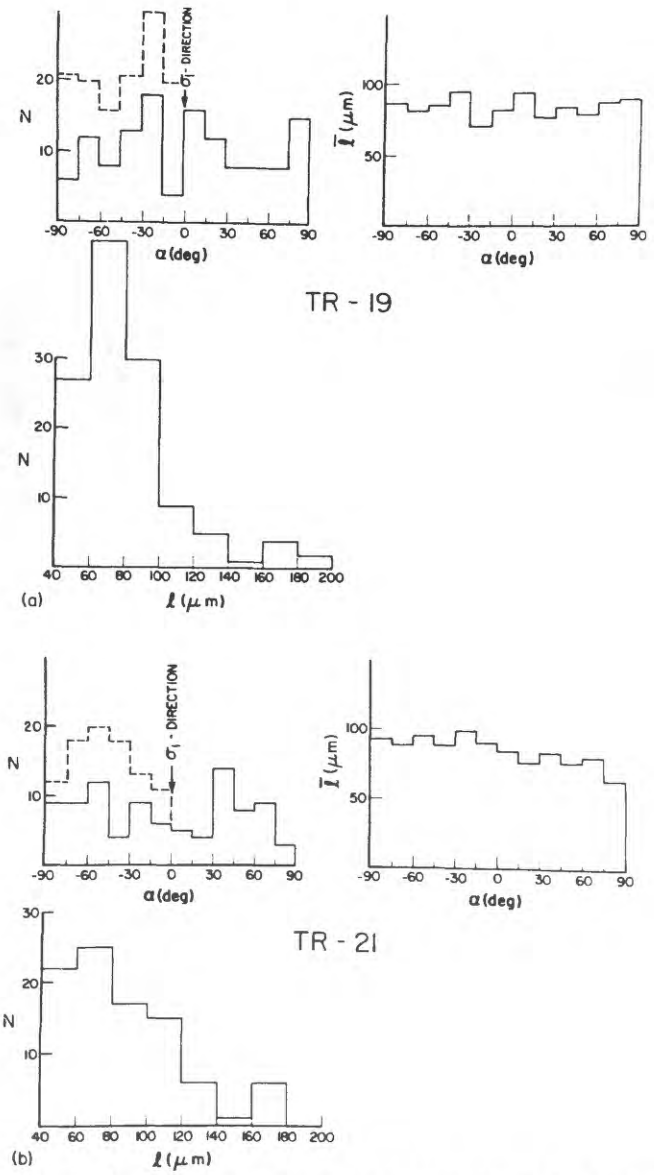

Fig. 5. Histograms for all cracks longer than 50 μm that were found in regions R_1, R_2, and R_3. See Figure 2 for the locations of R_1, R_2, and R_3 in samples TR-19 and TR-21. N is the number of cracks; α is the angle between the trace of the cracks on the photomicrograph and the direction of σ_1, the maximum applied stress; $\bar{l}$ denotes the average length of crack traces for an interval in α; and l is the length of crack traces. The dashed lines represent the number of cracks found for positive and negative values of α.

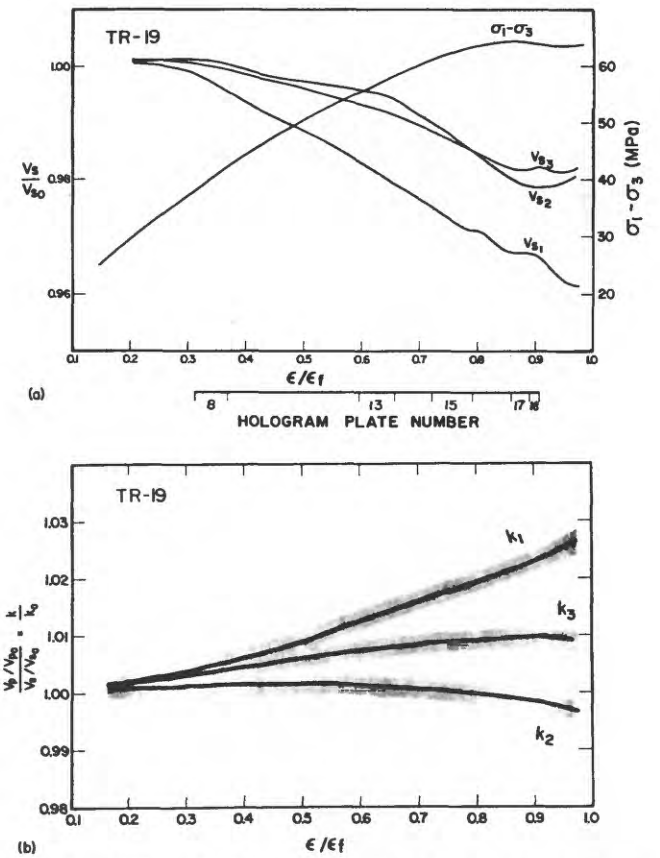

Fig. 6. (*a*) Normalized shear velocities for three paths and $\sigma_1 - \sigma_3$ versus normalized ϵ_1; ϵ_f is ϵ_1 at failure. For transducer locations, see Figure 2. (*b*) Normalized V_p/V_s ratios show no discernible reversal within the scatter (shaded areas) of the data.

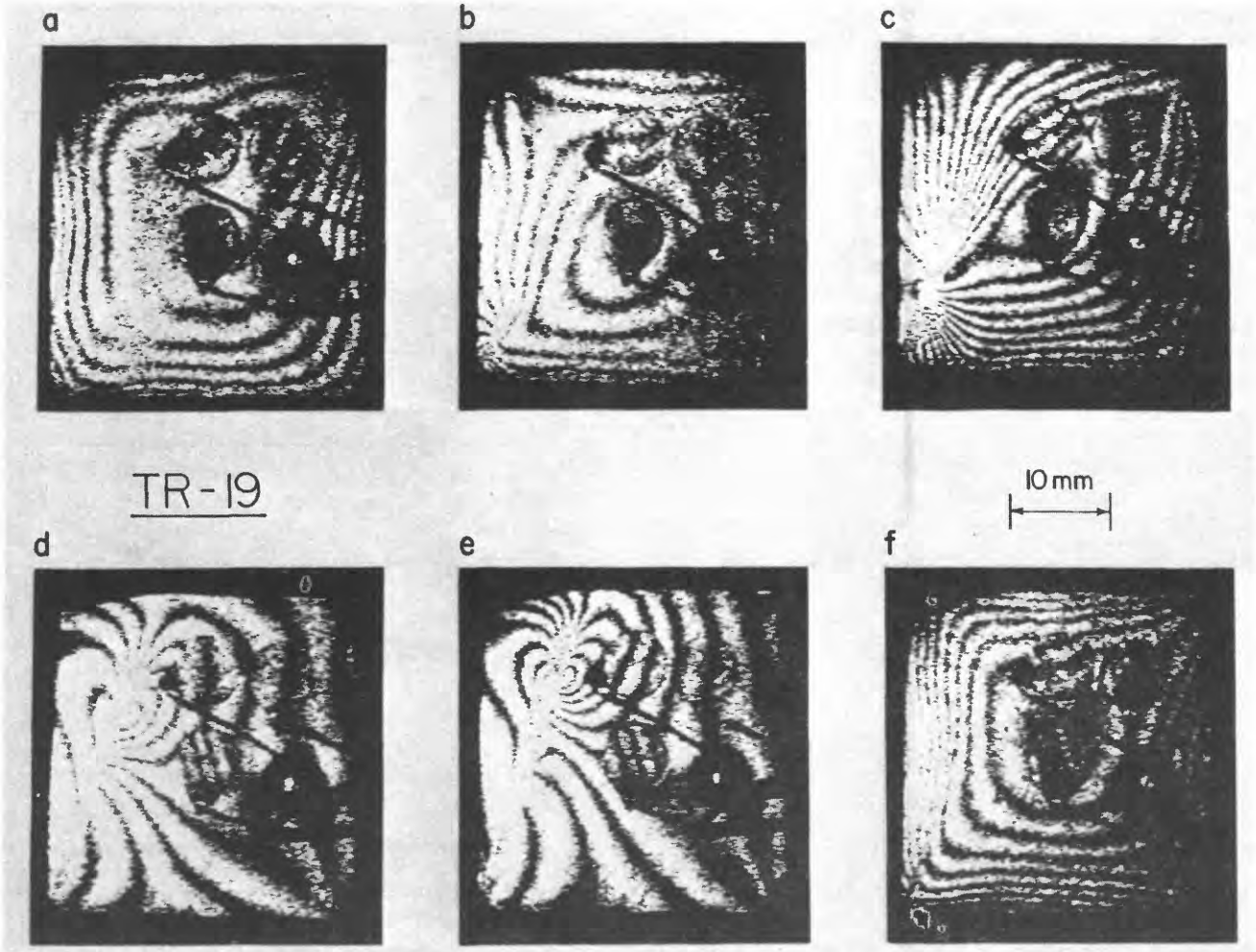

Fig. 7. Selected photographs of doubly exposed holograms show the surface deformation (topographic maps) for sample TR-19 in the direction of σ_2. Photographs *a*, *b*, *c*, *d*, and *e* correspond to intervals 8, 13, 15, 17, and 18, respectively, in Figures 6*a* and 8*a*. During increasing stress σ_1, the strain and stress intervals were 3.5×10^{-4}, 3.8 MPa; 4.6×10^{-4}, 3 MPa; 3.7×10^{-4}, 2 MPa; 2.1×10^{-4}, 0.2 MPa; and 1.7×10^{-4}, 0.3 MPa, respectively. During unloading, i.e., decreasing σ_1, the corresponding strain and stress intervals for *f* were 5×10^{-4} and 22.5 MPa. Note that there is no discontinuity (strain concentrations) associated with the macrofracture in the surface deformation in the direction of σ_2 during unloading. Three transducers (see Figure 2*a*) and a ground connection are visible on the photographs.

into the following several regions, not including the macrofracture (Figure 2): central R_1 region, where ϵ_2 is the greatest, corner R_3 region, where the stress concentration is the greatest, and an intermediate region, R_2. Spot checks on parallel planes at various depths revealed no noticeable difference in the character or distribution of cracks. Neither polishing nor ion cleaning changed the crack statistics. To learn to identify cracks induced during deformation, two reference samples were investigated. The first of these, a virgin sample, contained pores and cracks smaller than 40 μm. The second was jacketed and subjected to the jacket seating procedure, i.e., $\sigma_1 = \sigma_2 = 2\sigma_3 = 30$ MPa. Again the pores and cracks were generally smaller than 40 μm, although in this sample there seemed to be fewer pores. For the statistical analysis of TR-19 and TR-21, only cracks whose maximum dimensions exceeded 50 μm and whose length to width ratio exceeded 10 were counted. In a similar study of crack densities performed by *Hadley* [1976] on Westerly granite, it was noted that the unstressed granite samples also possessed a preponderance of small cracks (i.e., length < 50 μm). The crack statistics of the combined regions R_1, R_2, and R_3 for the two samples are given in the histograms of Figure 5. The total number of cracks counted in each sample exceeds 100. The differences between the three regions within each rock are barely discernible. On the basis of the total number of cracks in both samples, the corner regions have fewer vertical (σ_1 direction) cracks than the central region, and the crack density in the center is slightly higher ($\approx 20 \pm 12\%$) than in the corner regions.

There does not appear to be a preferred orientation of microcracks in the σ_1 direction in the pyrophyllite samples (see Figure 5). This is different from observations made under uniaxial or very low confining pressure conditions, where axial cracking clearly dominates [*Friedman et al.*, 1970; *Hallbauer et al.*, 1973; *Kranz*, 1979]. Maxima are observed, however, for cracks making angles between 15° and 30° with σ_1 for sample TR-19 and for angles between 45° and 60° for sample TR-21.

Velocity changes and surface deformation. Elastic wave velocities were determined over four different paths. Three of these were in the σ_2 direction, allowing us to measure velocity changes in close proximity to the fault and distant from it. Only the *P* wave velocity was measured in the σ_1 direction.

In Figure 6, shear velocities and the normalized V_p/V_s are shown for sample TR-19. This sample was saturated with water and deformed at $\dot{\epsilon}_1 = 2 \times 10^{-8}$ s^{-1} and $\sigma_2 = 30$ MPa. The

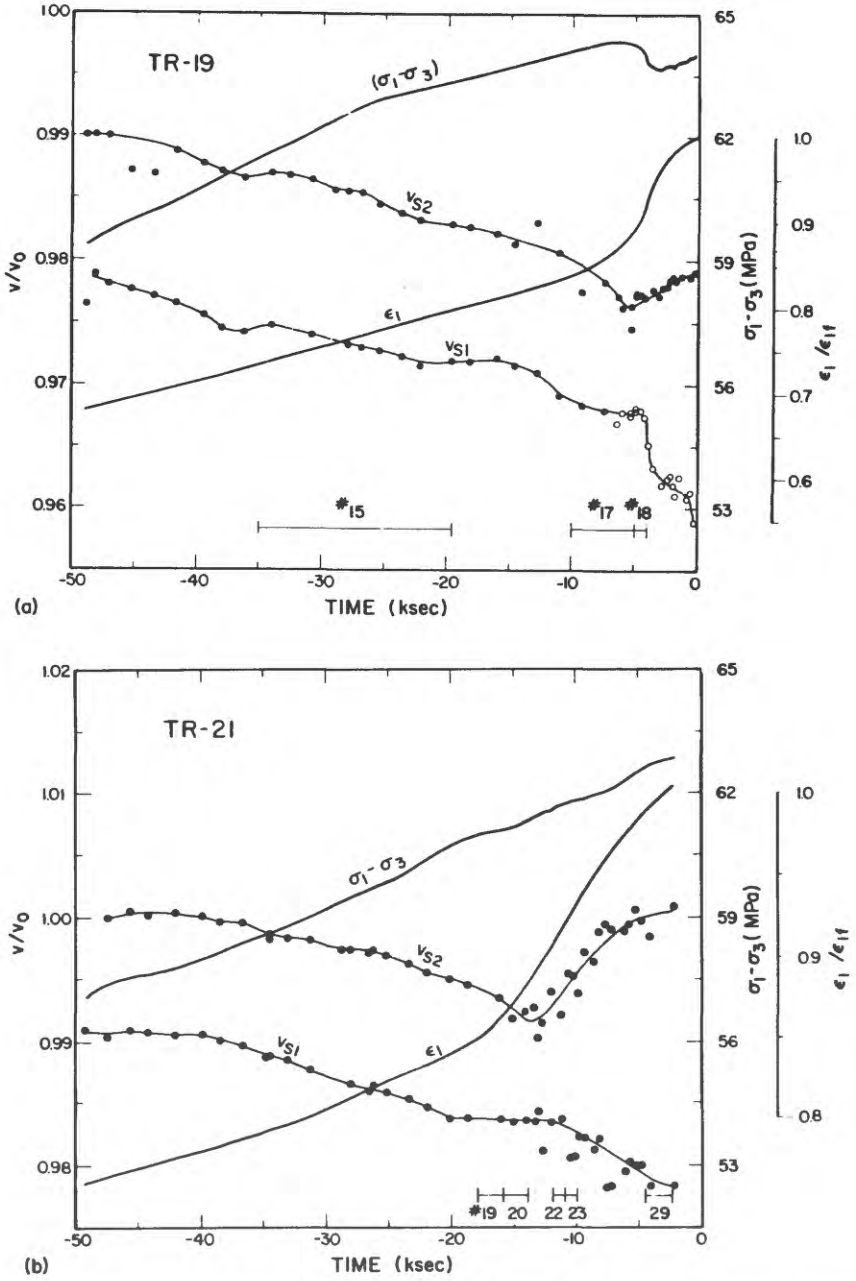

Fig. 8. Detailed velocity, stress, and strain data for samples TR-19 and TR-21 during the stage of macrocrack formation before failure and during partial unloading. For transducer locations and crack position, see Figure 2. For corresponding holograms, see Figures 7 and 10. The open circles for V_{s1} in sample TR-19 indicated velocity measurements that were taken after the bond of transducer S_1 became partially broken. Photographs *d* and *e* in Figure 7 clearly show that the tilt of S_1 does not conform to the surface deformation in its vicinity. It is important to note that especially for experiment TR-21, if only stress $(\sigma_1 - \sigma_3)$, strain (ϵ_1), and velocity measurements had been available, the sample would have been judged to have failed after the velocity reversal. Only through the use of holography do we know about the slowly propagating macrocrack (Figure 10) and its relationship to the velocity reversal.

locations of the transducers are shown in Figure 2. All velocities in the σ_2 direction increased slightly upon increasing σ_1 above the value of σ_2. Later they decreased. This decrease was largest for the path measured by the centrally located transducer S_1. The velocities V_{s2}, V_{p2}, V_{s3}, and V_{p3} showed smaller decreases and smaller partial recoveries shortly before failure. The velocities V_{s2} and V_{p2}, measured nearest the eventual macrofacture, showed a definite reversal. The normalized velocity ratios $k_1 = (V_{p1}/V_{s1})/(V_{p1}/V_{s1})_0$ did not reflect this reversal; k_2 was nearly constant, while k_1 and k_3 increased monotonically by ~2.5% and 1%, respectively. These increases resulted from small decreases in *P* wave velocities but larger decreases in *S* wave velocities.

The *P* wave velocity in the σ_1 direction increased monotonically for all experiments, as discussed by *Sondergeld et al.* [1980]. This differs from our earlier results [*Sobolev et al.*, 1978], where we observed a velocity reversal in the σ_1 direction. The addition of confining pressure in the present experiments may inhibit the opening of small cracks to such an extent that the overall compression in the σ_1 direction dominates the velocity.

The observation of the σ_2 face by holography made it pos-

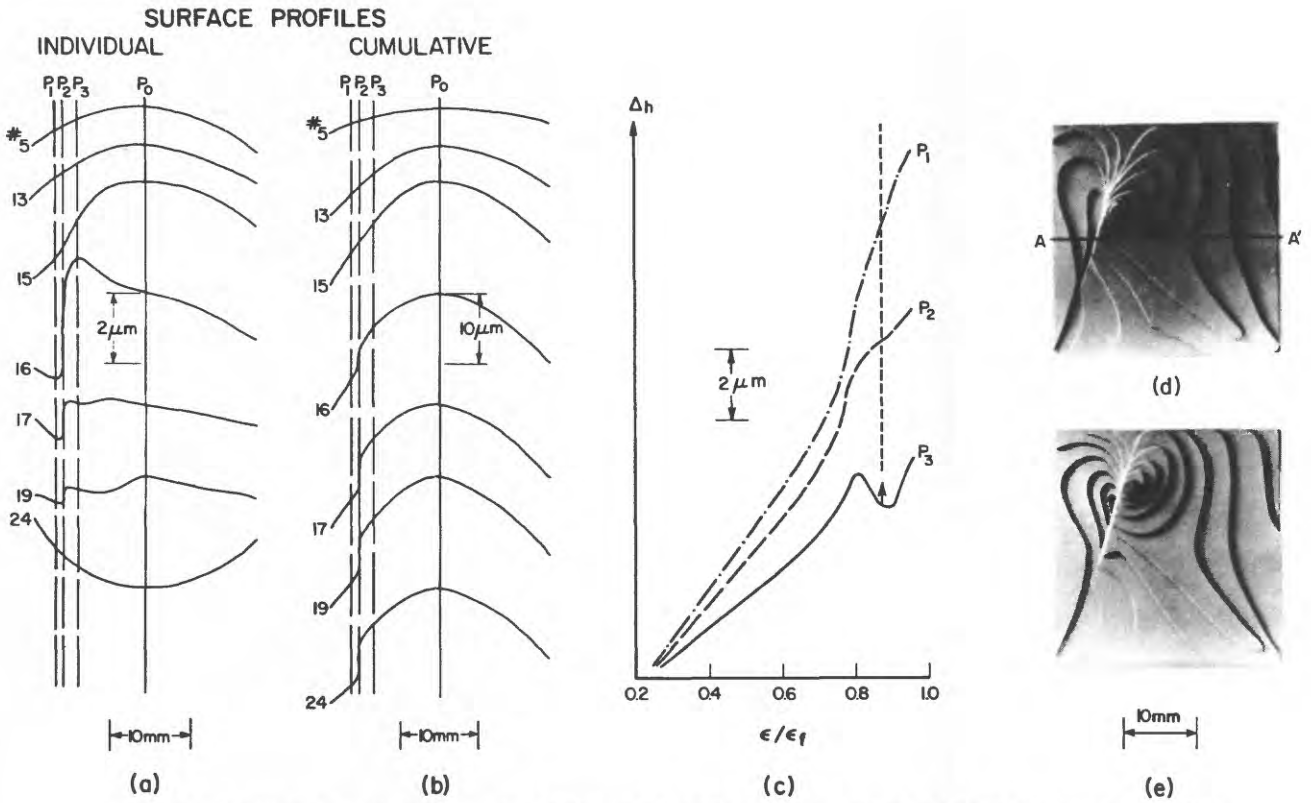

Fig. 9. Progression of surface deformation for TR-19 in the direction of σ_2. Individual (*a*) and cumulative (*b*) surface profiles at selected stages of development for cross section A-A′ (*d*). The uplift of point P_0 relative to the points P_1, P_2, and P_3 is shown in (*c*) as a function of normalized strain in the σ direction, ϵ/ϵ_f. Point P_0 is approximately at the center of the line A-A′ in (*d*). Points P_1, P_2, and P_3 lie on the line A-A′, respectively, just to the left of, on, and just to the right of the fault. Figures *d* and *e* are photographs of models that were constructed from photographs *d* and *e* in Figure 7 (intervals 17 and 18).

sible to correlate the velocity changes, shown in Figures 6 and 8, with the surface deformation. Representative examples of the doubly exposed holograms, or deformation maps, for TR-19 are shown in Figure 7; the intervals over which they were made during loading are indicated in Figure 6*a*. A general bulging and a diagonal ridge system appear on the deformation map during interval 8 (Figure 7*a*).

During interval 13 (Figure 7*b*), a macrocrack formed at the bottom left corner. The surface deformation is most concentrated there, but S_2 and S_3 also experience considerable tilting. Further development of the macrocrack is shown in Figures 7*c–e*, corresponding to hologram intervals 15, 17, and 18, respectively. During and following interval 13 (Figure 7*b*), the velocities V_{s2} and V_{s3} decreased more rapidly, while the changes in both V_s and uplift at location S_1 remained the same. As the macrocrack propagated across the sample, a pronounced bulge formed near its tip. During intervals 17 (Figure 7*d*) and 18 (Figure 7*e*), the rate of differential stress increase decreased, becoming slightly negative (see Figures 6 and 8), and the velocities V_{s2} and V_{s3}, as well as the corresponding longitudinal wave velocities, increased slightly. After interval 15 (Figure 7*c*) the velocity V_{s1} reversed its decreasing trend on more than one occasion and then leveled out. The development of an intense zone of deformation extending from the location of transducer S_1 (see Figure 2 for identification of transducers) to the bottom right seemed to counteract an increase in velocity, hence the general decrease was maintained. The sudden drop in the V_{s1} velocity was coincident with the appearance of a large number of interference fringes on S_1 during intervals 17 (Figure 7*d*) and 18 (Figure 7*e*). These fringes document a tilt of S_1 that was larger and different in direction from the surface tilt, indicating that the transducer had become at least partially unbonded.

The stress σ_1 was reduced after the macrocrack had extended a little beyond S_2 (see Figure 2*a*). The deformation map of interval 24, shown in Figure 7*f*, was obtained during unloading. This map looks very similar to 7*a*; however, in contrast to Figure 7*a*, the surface in Figure 7*f* is now going down. Note that there is no indication of the existing fracture, i.e., the surface deformation in the direction of σ_2 shows very little or no distortion of the strain field in the vicinity of the macrocrack.

To illustrate the surface deformation of the sample TR-19, several models of single-interval deformation maps were constructed, and a sequence of surface profiles were calculated. Photographs of the models for intervals 17 (Figure 7*d*) and 19 (not included in Figure 7) are shown in Figure 9. The line A-A′ in Figure 9*d*, drawn through the photograph of the model for interval 17 (Figure 7*d*); shows where the cross sections were taken. Figure 9*a* shows representative cross sections for selected hologram intervals. The uplift during interval 5 was nearly symmetric about the middle but became asymmetric during interval 13 (Figure 7*b*), showing a greater concentration of uplift on the left side. The point of inflection in cross section 15 (Figure 7*c*) indicates where the most rapid change in strain took place. During interval 16, the fault crossed the section A-A′. The concentrated bulge, which migrated with the fault tip, is clearly evident to the right of the fault. Sub-

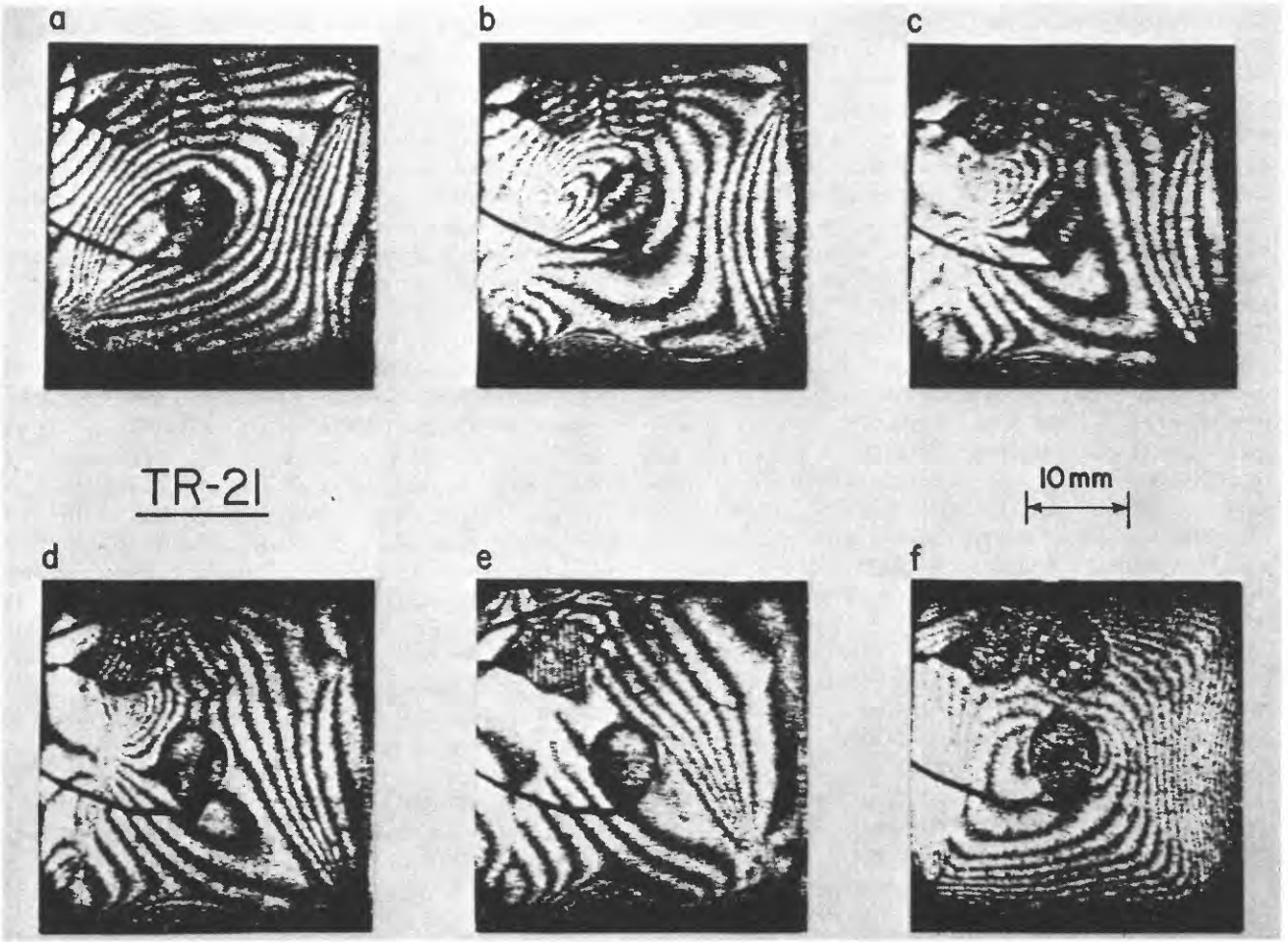

Fig. 10. Photographs of doubly exposed holograms from TR-21 during macrocrack formation and partial unloading. For corresponding stress and strain intervals, see Figure 8*b*. Photographs *a*, *b*, *c*, *d*, and *e* correspond to intervals 19, 20, 22, 23, and 29 in Figure 8*b*, respectively. Photograph *f* was taken during unloading. Again, no discontinuity in the strain pattern appears where the fault exists.

sidence on the left is seen in cross sections 16, 17 (Figure 7*d*), and 19. Cross section 24, calculated from a hologram taken during unloading, shows no preferential deformation in the vicinity of the fault, but nearly symmetrical subsidence across the entire sample.

Cumulative cross sections at various stages of fault development are shown in Figure 9*b*. The decreases in length in the σ_1 direction for intervals 5, 13, 15, and 16 were about 11 μm, while for intervals 17 and 19 they were 2.6 μm. The accumulated differential uplift across the visible σ_2 side at the end of interval 19 is approximately 20 μm. This compares with an accumulated change of $\approx$200 μm in the σ_1 direction.

Points P_0, P_1, P_2, and P_3 lie on the line A-A′. P_0 is an arbitrary reference point located approximately in the center of the transducer S_2, P_2 is directly on the macrocrack, while P_1 lies to the left and P_3 to the right of the macrocrack. The difference in heights between P_0 and P_1, P_2, and P_3 are shown in Figure 9*c* as a function of ϵ_1/ϵ_{1f}. An arrow indicates approximately where the visible macrocrack crosses the line A-A′. The height of P_2 is difficult to determine, since it lies directly on the cliff between the areas of bulging and subsidence. For consistency, the center of the cliff was always chosen. Point P_3 shows the effect of the concentrated bulge moving across the profile (see photographs of models for intervals 17 and 19; Figures 9*d* and 9*e*). It is important to emphasize that the individual photographs of the doubly exposed holograms show only the deformation that has accumulated between the two exposures. The migrating bulge leaves a ridge in its wake. The deformation and related uplift associated with the advance of the macrocrack are so intense, however, that there is a partial subsidence when the bulge passes. A well-developed bulge associated with the tip of the propagating macrocrack was also observed during experiment TR-21. Velocities, differential stress ($\sigma_1 - \sigma_3$), and strain ϵ_1 during the 14 hr (50 ks) before failure are given for this experiment in Figure 8*b*. Representative deformation maps for hologram intervals 19, 20, 22, 23, and 29 are shown in Figures 10*a*–*e*. The deformation map in Figure 10*f* was taken during unloading. Again there is no pronounced discontinuity in subsidence in the vicinity of the fault.

INTERPRETATION OF RESULTS

When subjected to triaxial stress, pyrophyllite fails predominantly by the interaction of microcracks. A long period of time ($\dot{\epsilon}_1 \approx 2 \times 10^{-8}$ s^{-1}) and an abundance of moisture in the pores provide an environment where microcracks can grow and interact, leading to the formation of a fault on a time scale that is amenable to laboratory studies. Low confining pressures ($\sigma_2 \leqq 30$ MPa), long time (low $\dot{\epsilon}_1$), and high

moisture content reduce the failure strength $(\sigma_1 - \sigma_3)_f$. We interpret this to be due to stress corrosion [*Wiederhorn,* 1968; *Martin,* 1972; *Scholz,* 1972]. The mechanical effect of the pore pressure is masked by the effect of stress corrosion. For example (see Figure 3), for the difference in strength between the dry (TR-21) and wet (TR-23) samples at $\sigma_2 = 5$ MPa to be due to the mechanical effect of the pore pressure, the effective pressure (i.e., confining pressure minus pore pressure) would have to be negative. At high confining pressure ($\sigma_2 \geqq 90$ MPa) the roles of high moisture content and long time seem to be reversed (see Figure 3, TR-26 and TR-27; TR-7, TR-8, and TR-10). The reason for this reversal is not yet understood.

Both on a macroscopic and a microscopic scale (Figures 2 and 4) we find the cracks that develop under high confining pressure ($\sigma_2 \geqq 90$ MPa) to be considerably narrower (smaller thickness to length ratio) than those for low confining pressure ($\sigma_2 \leqq 30$ MPa). Smaller velocity decreases before failure, by a factor of two or more, and a much less pronounced bulging associated with the advancing fault observed in experiments with high confining pressure ($\sigma_2 > 30$ MPa) lead us to suspect that the roles of dilatancy and stress corrosion are diminishing as σ_2 is raised.

While the stress concentrations on the boundaries of the sample control the origin of the macrocrack, its propagation through the sample is controlled by the local stress field. As the maximum principal stress σ_1 increases, microcracks of near random distribution are formed (see Figure 5). Uplift in the σ_2 direction due to opening of microcracks is most pronounced along directions of the maximum shear stress, diagonally across the visible σ_2 face of the sample. The initiation of the macrofracture is preceded by a concentrated uplift near its point of origin (Figures 7*b* and 10*a*). This concentrated uplift in plan view appears as an elliptical bulge. This bulge moves with the tip of the macrofracture (fault) as it propagates across the sample (Figures 7, 9, and 10). Stress concentrations associated with the propagating fault cause existing microcracks to open and produce new fractures. These new fractures form a precursory system of en échelon or subparallel cracks (see Figure 4 and *Sobolev et al.* [1978]) ahead of the fault tip. The long axis of these precursory cracks lies nearer to the direction of maximum shear than does the direction of the eventual fault. The normal stress across the precursory cracks is too great to allow them to propagate very far and to become major fractures. The fault advances by the coalescence and/or linking of the precursory cracks. As the migrating bulge approaches the observation point P_3 near the eventual fault (Figure 9), the point rises rapidly, then experiences some subsidence as the fault tip passes. A general topographic high or ridge is associated with the fault and remains a permanent feature even during the decrease of σ_1. We believe that increased porosity due to debris-filled microcracks and asperity mismatch are responsible for the persistence of the ridge. Contributions due to plastic deformation cannot be excluded.

McGarr [1971] presented a photograph of en échelon fractures in quartzite which, except for the scale, appear identical to those observed in pyrophyllite (see Figure 4). However, in contrast to the evolution proposed by *McGarr* [1971], we find that the complementary or shear fractures (equivalent to McGarr's type 1 fracture) appear first and are not a product of the macrofracture. Further support for this temporal relationship can be found in the observations of *Brace* [1964] and *Brady* [1976]. Very few shear cracks were observed by *Tapponnier and Brace* [1978] in deformed samples of Westerly granite. However, their samples were deformed at rates of 2 to 3 orders of magnitude faster than ours.

Brady et al. [1973] and *Brady* [1974, 1976] used a fluorescent dye and optical microscopy to examine the cracks developed in rocks deformed in a stiff loading machine. They identified a region ahead of a propagating fault (macrocrack) that is composed of many smaller and often differently oriented cracks. The region was observed to be very localized, a finding that is in agreement with our holographic observations on Westerly Granite [*Spetzler and Martin,* 1974; *Spetzler et al.,* 1977] and the slit diffraction observations of *Liu and Livanos* [1976], also on Westerly Granite. In addition, the detailed crack studies of *Hallbauer et al.* [1973] also indicate that crack development and hence dilatancy are very localized.

Results from elastic wave velocity measurements depend very strongly upon transducer locations and support the above interpretation [*Sondergeld et al.,* 1980]. In general, the velocities show the most pronounced decrease wherever the uplift is the greatest. Velocity recovery (Figures 6 and 8) is related to the local modification of the stress field associated with the migrating bulge. The recovery is greatest for the transducers located nearest the fault and is observed for both *P* waves and *S* waves over the same path, such that no recovery is noted in a normalized V_p/V_s ratio (Figure 6).

Pronounced migrating bulge development and velocity recovery were only observed during experiments when the rock was either wet or saturated and the strain rate low ($\dot{\epsilon}_1 = 2 \times 10^{-8}$ s^{-1}). We conclude, especially from the absence of a V_p/V_s anomaly, that the major role of water in the samples was to influence the time-dependent behavior of cracks.

SUMMARY

The simultaneous measurements of the evolution of the surface topography, the spatial and temporal variation of elastic wave velocities, the observation of the macrocrack development during the experiments, and the optical and scanning electron microscope studies after the experiments lead us to the following conclusions:

1. Changes in elastic wave velocities and in surface topography are strongly dependent upon the proximity of the observation point to the macrofracture.

2. Changes in the elastic wave velocities depend upon confining pressure, moisture content, and strain rate. Velocity reversals were found only when the velocities were measured near the macrocracks and when the moisture content in the samples was high and the strain rate low.

3. In most cases, the macrocrack forms by the coalescence of precursory cracks. The length and width of the precursory cracks decrease markedly with increasing confining pressure. The orientation of the precursory cracks differs from that of the macrocrack.

Often the applicability of the results of laboratory experiments to the earth is questioned. Recently, we have been finding greater similarities between field and laboratory observations. *Sadovsky et al.* [1972] and *Sadovsky and Nersesov* [1974] report principal stress axes rotations as interpreted from focal mechanisms prior to larger earthquakes in the Garm district of the USSR. Similarly, *Engdahl and Kisslinger* [1977] recorded foreshocks to an Adak Island earthquake with resolved principal stress axes different from those for the main event. On a laboratory scale we observe precursory cracks that have major axis orientations different from that of the main fault. In addition, *Brady* [1976] presents similar observations

on an oil shale. In these cases, the precursory events are more closely aligned with the maximum shear stress.

The localized uplift and subsequent subsidence of P_3 (Figure 9) as the rupture advances are reminiscent of the recent activity in the Palmdale area [*Castle et al.*, 1976; *Castle*, 1978]. A maximum vertical uplift of 35 mm occurred between 1959 and 1974. Subsidence of 170 mm was observed between mid-1974 and mid-1976 and was accompanied by migration of the buldge to the southeast. This was followed by an increase in the number of small earthquakes. The focal mechanisms of these events were also found to rotate with time [*McNally et al.*, 1978].

Acknowledgments. Part of this work was carried out under the auspices of the Soviet-American Earthquake Prediction program through U.S. Geological Survey contract DOI-P32701 and in part by U.S. Geological Survey contract DI-14-08-0001-15256. One of us (C. H. S.) was supported as a visiting fellow in CIRES under a cooperative program between the University of Colorado and the National Oceanographic and Atmospheric Administration under contract DOC-03-7-022-35191. Constructive critiques by two anonymous reviewers are greatly appreciated and contributed to the improvement of this paper.

REFERENCES

Brace, W. F., Brittle fracture of rocks, in *State of Stress in the Earth's Crust*, edited by W. R. Judd, pp. 110–178, Elsevier, New York, 1964.

Brace, W. F., and E. G. Bombolakis, A note on brittle crack growth in compression, *J. Geophys. Res., 68*, 3709–3713, 1963.

Brace, W. F., E. Silver, K. Hadley, and C. Goetze, Cracks and pores: A closer look, *Science, 178*, 162–164, 1972.

Brady, B. T., Theory of earthquakes, I, A scale independent theory of rock failure, *Pure Appl. Geophys., 112*, 701–725, 1974.

Brady, B. T., Theory of earthquakes, IV, General implications for earthquake prediction, *Pure Appl. Geophys., 114*, 1031–1032, 1976.

Brady, B. T., W. I. Duvall, and F. G. Horino, An experimental determination of the true uniaxial stress-strain behavior of brittle rock, *Rock Mech., 5*, 107–120, 1973.

Castle, R. O., Leveling surveys and the southern California uplift, *Earthquake Inform. Bull. 10*(3), pp. 88–92, U. S. Geol. Surv., Reston, Va., 1978.

Castle, R. O., J. P. Church, and M. R. Elliott, Aseismic uplift in Southern California, *Science, 192*, 251–253, 1976.

Dieterich, J. H., Modeling of rock friction, I, Experimental results and constitutive equations, *J. Geophys. Res., 84*, 2161–2168, 1979*a*.

Dieterich, J. H., Modeling of rock friction, 2, Simulation of preseismic slip, *J. Geophys. Res., 84*, 2169–2174, 1979*b*.

Engdahl, E. R., and C. Kisslinger, Seismological precursors to a magnitude 5 earthquake in the central Aleutian Islands, *J. Phys. Earth, 25*, S243–250, 1977.

Friedman, M., R. D. Perkins, and S. J. Green, Observations of brittle-deformation features at the maximum stress of Westerly granite and Solenhofen limestone, *Int. J. Rock Mech. Min. Sci., 7*, 297–306, 1970.

Hadley, K., Comparison of calculated and observed crack densities and seismic velocities in Westerly granite, *J. Geophys. Res., 81*, 3484–3494, 1976.

Hallbauer, D. K., H. Wagner, and N. G. W. Cook, Some observations concerning the microscopic and mechanical behavior of quartzite specimens in stiff, triaxial compression tests, *Int. J. Rock Mech. Min. Sci. Geomech. Abstr., 10*, 713–726, 1973.

Heflinger, L. O., R. F. Wuerker, and H. Spetzler, Thermal expansion coefficient measurement of diffusely reflecting samples by holographic interferometry, *Rev. Sci. Instrum., 44*(5), 629–633, 1973.

Kranz, R. L., Crack growth and development during creep of Barre granite, *Int. J. Rock Mech. Min. Sci. Geomech., Abstr., 16*, 23–35, 1979.

Kisslinger, C., and Z. Suzuki (Eds.), Earthquake Precursors, Proceedings of the U.S.-Japan Seminar on Theoretical and Experimental Investigations of Earthquake Precursors, *J. Phys. Earth, Suppl., 25*, 1978.

Liu, H. P., and A. C. R. Livanos, Dilatancy and precursory bulging along incipient fracture zone in uniaxially compressed Westerly granite, *J. Geophys. Res., 81*, 3495–3510, 1976.

Martin, R. J. III, Time-dependent crack growth in quartz and its application to creep of rocks, *J. Geophys. Res., 77*, 1406–1419, 1972.

McGarr, A., violent deformation of rock near deep-level tabular excavations—seismic events, *Bull. Seismol. Soc. Am., 61*, 1453–1466, 1971.

McNally, K. H., H. Kanamori, J. C. Pechmann, and G. Fuis, Earthquake swarm along the San Andreas fault near Palmdale, southern California, 1976 to 1977, *Science, 201*, 814–817, 1978.

Meyer, M. D., and H. A. Spetzler, Materials properties using holographic interferometry, *Exp. Mech., 16*, 434–438, 1976.

Pratt, H. R., A. D. Black, and W. F. Brace, Friction and deformation of jointed quartz diorite, in *Proceedings of the Third International Congress on Rock Mechanics*, vol II, part A, pp. 306–310, National Academy of Sciences, Washington, D. C., 1974.

Rikitake, T., *Earthquake Prediction*, Elsevier, New York, 1976.

Sadovsky, M. A., and I. L. Nersesov, Forecasts of earthquakes on the basis of complex geophysical features, *Tectonophysics, 23*, 247–255, 1974.

Sadovsky, M. A., I. L. Nersesov, S. K. Nigmatullaev, L. A. Latynina, A. A. Likk, A. N. Semenov, I. G. Simbireva, and V. I. Ulomov, The processes preceding strong earthquakes in some regions of middle Asia, *Tectonophysics, 14*, 295–307, 1972.

Scholz, C. H., Static fatigue of quartz, *J. Geophys. Res., 77*, 2104–2114, 1972.

Sobolev, G., H. Spetzler, and B. Salov, Precursors to failure in rocks while undergoing anelastic deformations, *J. Geophys. Res., 83*, 1775–1784, 1978.

Sondergeld, C. H., I. C. Getting, H. A. Spetzler, and G. A. Sobolev, Velocity changes associated with generalized triaxial deformation of pyrophyllite, *Pure Appl. Geophys., 118*, in press, 1980.

Spetzler, H. A., and R. J. Martin III, Correlation of strain and velocity during dilatancy, *Nature, 252*, 30–31, 1974.

Spetzler, H., C. H. Scholz, and T. Lu Chi-Ping, Strain and creep measurements on rocks by holographic interferometry, *Pure Appl. Geophys., 112/3*, 571–581, 1974.

Spetzler, H. A., N. Soga, H. Mizutani, and R. J. Martin III, Strain fields associated with fracture under high pressure, viewed with holographic interferometry, in *High-Pressure Research, Applications in Geophysics*, edited by M. H. Manghnani and S. J. Akimoto, pp. 625–635, Academic, New York, 1977.

Tapponnier, P., and W. F. Brace, Development of stress-induced microcracks in Westerly granite, *Int. J. Rock Mech. Min. Sci. Geomech. Abstr., 13*, 103–112, 1976.

Wiederhorn, S. M., Moisture assisted crack growth in ceramics, *Int. J. Fract. Mech., 4*, 171–177, 1968.

(Received April 27, 1979;
revised February 25, 1980;
accepted March 14, 1980.)

Pageoph, Vol. 118 (1980), Birkhäuser Verlag, Basel

Velocity Changes Associated with Generalized Triaxial Deformation of Pyrophyllite

By C. H. SONDERGELD[1]), I. C. GETTING[1]), H. A. SPETZLER[2]) and G. A. SOBOLEV[3])

Abstract – Compressional and shear-wave velocities (V_p and V_s) were measured during the generalized triaxial deformation (i.e. $\sigma_1 \neq \sigma_2 = 2\sigma_3$) of pyrophyllite. Observed velocity changes could be ascribed to crack development during dilatancy. Velocity changes were very localized with respect to the ultimate failure plane. The orientation and development of the failure plane was continuously observed with laser holography. Velocity reversals, i.e. changes from a decreasing trend to an increasing trend, were documented in a wet sample in both V_p and V_s. These changes in both V_p and V_s are inconsistent with dilatancy-diffusion models. The reversals were interpreted as a reflection of local stress reorientation caused by a slowly propagating fault.

Key words: Rock mechanics; Dilatancy-diffusion, Velocity changes.

Introduction

In recent years much experimental effort has been made to study the mechanics of deformation of simulated fault gouge under various stress fields and boundary conditions, see for example the recent rock mechanics summary of BRACE (1978) or BYERLEE (1978). The question of what constitutes real fault gouge is very difficult to answer specifically. However, efforts have been made to investigate properties of crushed granite, possibly a very fresh gouge material (ZOBACK and BYERLEE, 1976; BYERLEE and SUMMERS, 1976) and clays, a weathering product (WU, 1978; WU *et al.*, 1975). Clays display extreme variability in structure and chemistry and hence an extreme in response to superposed stress fields. We have in this paper included the study of pyrophyllite to this list of candidate gouge materials.

Pyrophyllite and talc are most notable for their softness. They are structurally very similar to micas and clays. In fact, PAULING (1972) considers pyrophyllite and talc clay minerals. Pyrophyllite differs from common clays (e.g. montmorillonite) and micas in that it is composed entirely of electrically neutral layers held together solely by very weak van der Walls forces. (Montmorillonite is used for comparison here because of its chemical similarity to pyrophyllite.) There are no additional electrostatic forces holding the sheets together as in micas or montmorrilonite, for

[1]) All at the Cooperative Institute for Research in Environmental Sciences, University of Colorado/NOAA, Boulder, Colorado 80309, USA.

[2]) At the Cooperative Institute for Research in Environmental Sciences, and the Department of Geological Sciences, University of Colorado, Boulder, Colorado, 80309, USA.

[3]) Institute of the Physics of the Earth, Academy of Sciences of the U.S.S.R., Moscow.

example. Common clays also exhibit varying degrees of swelling upon absorption of water. The addition of water dramatically changes clay rheology. In contrast, the pyrophyllite structure does not allow water absorption; hence, the intrinsic rheology changes little in the presence of water. Furthermore, as with all sheet silicates, the mineral, pyrophyllite (monoclinic symmetry) exhibits marked elastic anisotropy. Our samples are aggregates of this mineral and display a much reduced anisotropy due to the dominance of the overprint of a slight metamorphic fabric. Pyrophyllite occurs largely through the hydrothermal alteration of feldspars and is often found in regions of low grade metamorphism in association with dolomitic limestones and ultrabasic rocks. Its ubiquity along fault zones remains to be investigated; however, if found it will most likely occur at shallow depths unless exposed through uplift.

The early work of BRIDGMAN (1949) on the uniaxial compression of soapstone, a rock composed predominantly of talc, indicated to BRACE *et al.* (1966) that even materials such as talc can behave in a brittle manner and display dilatancy. RALEIGH and PATERSON (1965) studied the mechanical behavior of serpentinite during triaxial experiments and also showed that rocks composed almost entirely of sheet silicates exhibit dilatancy.

Pyrophyllite represents a viable material analog of fault gouge if not a constituent. Furthermore, it is a rock which possesses very small elastic moduli (SACHSE and RUOFF, 1975), behaves 'elastically', exhibits dilatancy, and fails audibly over a limited range of stress and strain rate.

Experimental techniques

The pressure vessel and loading system have been adequately described (GETTING, 1979). The specimens were machined into cubes with an edge dimension of 31.6 mm. Copper jackets (0.013 mm thick) were used to seal the sample from directly contacting the confining fluid. One set of faces was sealed by *o*-rings to spring loaded pistons terminated to the atmosphere. Fluid pressure acted over one entire set of faces and over the area of the faces not sealed by the *o*-rings. The ratio of areas was made such that the fluid pressure (σ_2) was equal to twice the pressure on the sealed faces (σ_3). A uniaxial stress (σ_1) was applied to the remaining faces. This configuration resulted in a generalized triaxial stress field where ($\sigma_1 > \sigma_2 = 2\sigma_3$). Uniaxial stress was calculated from a force gauge output and could be determined to within ± 10 bars. Fluid pressure was read from a Heise gauge to within ± 5 bars. Displacements used to calculate the strain in the σ_1 direction were measured with a pair of linear displacement transformers and allowed strain resolution to $\pm 0.05\%$. Corrections for apparatus distortion (GETTING, 1979) were computed during data acquisition.

Acoustic velocities were measured with the simple time of flight technique. Both the initial input pulse and the transmitted waveform were displayed on an oscilloscope. After calibration, the voltage across the delayed sweep potentiometer of the oscilloscope, proportional to the time delay through the sample, was routed into the data

acquisition system and used to determine the velocities of both *P*- and *S*-waves through the sample. One megahertz shear mode (PZT) transducers (6.4 mm diameter) were used to measure the change in both the *P* and *S* velocities. Changes in acoustic velocities as small as $\pm 0.1\%$ could easily be resolved. Shear waves propagated in the direction of σ_2 with particle motion in the σ_3 direction.

Laser holography was used to monitor the surface displacements in the σ_2 direction. The spatial relation of the transducers to surface deformation and their proximity to the failure crack could be observed. In addition, the incremental tilt of individual transducers was clearly resolved. Surface displacements on the order of ~ 20 nm were measurable.

Samples were deformed at strain rates of 10^{-6} sec^{-1} and 2×10^{-8} sec^{-1} at a fluid pressure of (σ_2) 0.05 kb, and nominally laboratory dry (30% relative humidity) or wet. The term fluid pressure is used in describing these generalized triaxial experiments and is different from the term confining pressure used to describe degenerate triaxial experiments. (Fluid pressure in our experiments is equal to $\sigma_2 = 2\sigma_3$.)

Observations

Of the sixteen generalized triaxial experiments performed (SPETZLER *et al.*, 1979) we choose only three (TR-21, TR-22, TR-23) for discussion in this paper. $\sigma_2 = 0.05$ kb and $\sigma_3 = 0.025$ kb in these three experiments. TR-21 was wet and strained at a rate of 2×10^{-8} sec^{-1}. TR-22 was also wet but strained at a rate of 10^{-6} sec^{-1}. TR-23 was dry and strained at a rate of 2×10^{-8} sec^{-1}. The main reason for choosing only these three experiments is that dilatancy (BRACE *et al.*, 1966) occurs in pyrophyllite

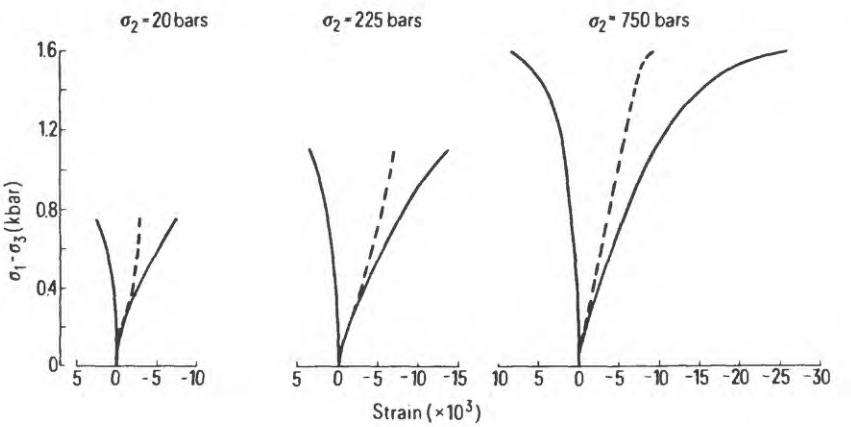

Figure 1

The results of three degenerate triaxial experiments ($\sigma_1 > \sigma_2 = \sigma_2$) at different confining pressures and at the same strain rate of 10^{-6} sec^{-1} are plotted. Dashed lines indicate the volumetric strain change for each experiment. Solid curve to the right and left represent the axial and transverse strain respectively. Maximum dilatancy is observed when $\sigma_2 = 0.02$ kb.

at low confining pressures in degenerate triaxial (i.e. $\sigma_1 \neq \sigma_2 = \sigma_3$) tests conducted by us. It can be seen from Fig. 1 that dilatancy does occur in pyrophyllite but only at low confining pressure. At a confining pressure of 1 kb, the confining pressure is almost equal to the strength of pyrophyllite and it behaves plastically. Therefore, to relate observed velocity changes to crack development we must deal with the experiments performed at low fluid pressures, i.e. below approximately 300 bars.

Measurements of V_p in the direction of σ_1 during the deformation of pyrophyllite at $\sigma_2 = 0.05$ kb showed a 22% increase over a range of differential stress of 0.8 kb. The same measurement at $\sigma_2 = 1$ kb showed only a 5% increase over a range of $(\sigma_1 - \sigma_3) = 0.6$ kb. The smaller increase in V_p noted for the greater fluid pressure experiment attests to the closing of pores by the action of fluid pressure alone.

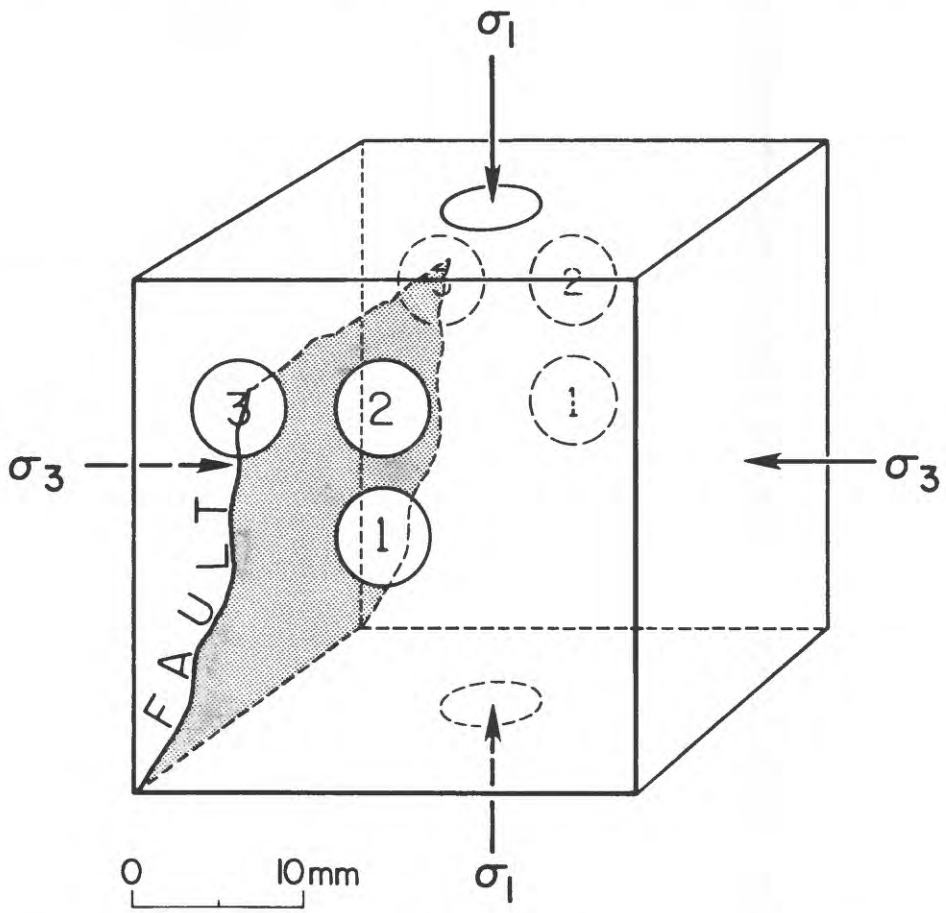

Figure 2

Scaled drawing of the sample as seen from the σ_2 direction with transducers located at 1, 2 and 3. Principal stress directions are indicated. Relative crack location for TR-21 is also shown. Transducer configuration is identical for TR-21 through TR-23.

The measured changes in both P and S wave velocities in the σ_2 direction are shown in Figs. 3 through 5 for experiments TR-21, TR-22, and TR-23, respectively. The changes associated with TR-21 are perhaps the most interesting in that they show a distinct velocity reversal, i.e. a change from decreasing to increasing prior to failure (see Fig. 3). A similar velocity reversal was observed in another wet experiment performed at higher fluid pressure but it will not be discussed here. There are significant gaps in the data for TR-21 at the very beginning necessitating normalization to a velocity appropriate to $(\sigma_1 - \sigma_3) = 0.325$ kb. This experiment was carried out at $\dot{\epsilon} = 2 \times 10^{-8}\,\text{sec}^{-1}$, $\sigma_2 = 0.05$ kb, and wet. The first dip in all six curves can be attributed to sample movement relative to the platens. This was observed directly by laser holography. The interval beyond $(\sigma_1 - \sigma_3) = 0.4$ kb shows that velocity changes are not uniform on the σ_2 face but depend upon the exact location of sending and receiving transducers relative to zones of deformation. We note about a 1% difference

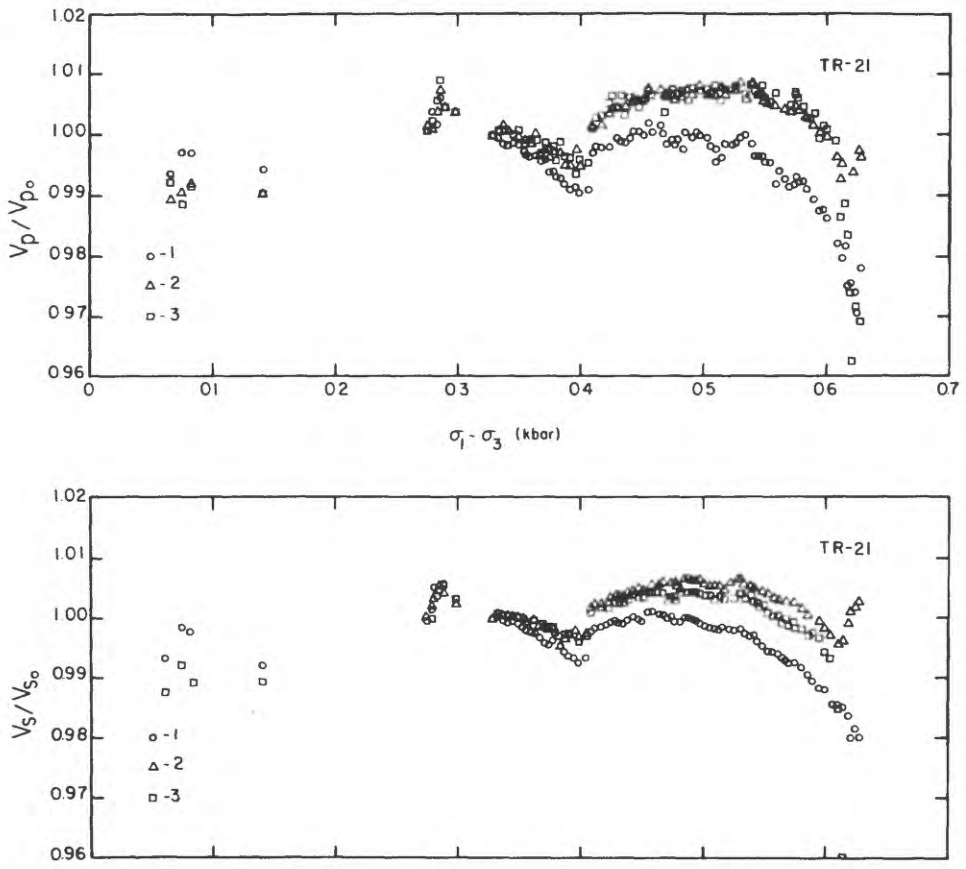

Figure 3

Normalized V_p and V_s changes observed during experiment TR-21 ($\dot{\epsilon} = 2 \times 10^{-8}\,\text{sec}^{-1}$, $\sigma_2 = 0.05$ kb, and wet) at locations 1, 2 and 3. A true velocity reversal is observed at location 2 for both V_p and V_s just prior to failure.

between the P-wave velocities measured at location 1 and those measured at locations 2 or 3 (See Fig. 2 for the relative transducer locations.) This difference is also reflected in the shear wave velocities. Both the P- and S-wave velocities at location 2 possess a reversal with a minimum centered about $(\sigma_1 - \sigma_3) = 0.61$ kb. The S-wave decreases 1.1% and then recovers to within 0.7% of its maximum value while the P-wave decreases 1.5% and recovers to within 0.6% of its previous maximum value. The recovery of both V_p and V_s is not predicted by dilatancy-diffusion models. Since both V_p and V_s change sympathetically no dramatic change is observed in the ratio V_p/V_s.

The smooth and continuous decrease in both V_p and V_s throughout experiment TR-22 is indicated in Fig. 4. Again note the sensitivity of the velocity changes to transducer location. TR-22 represents an experiment at $\dot{\varepsilon} = 10^{-6}$ sec^{-1}, $\sigma_2 = 0.05$ kb, and wet. The magnitude of the velocity decreases are about 3% and 4% for V_p and V_s, respectively.

Experiment TR-23 was performed at conditions of $\dot{\varepsilon} = 2 \times 10^{-8}$ sec^{-1}, $\sigma_2 = 0.05$ kb, and laboratory dryness. The associated velocity changes are given in Fig. 5. Both V_p and V_s initially increase to as much as 2% above their initial values. The

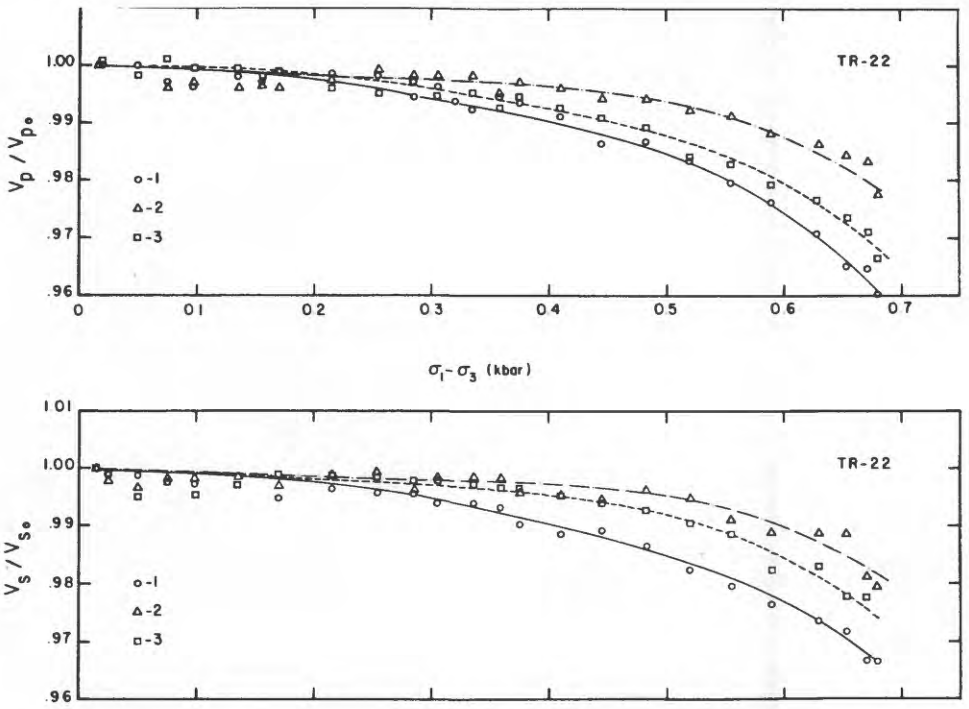

Figure 4

Normalized V_p and V_s changes observed during experiment TR-22 ($\dot{\varepsilon} = 10^{-6}$ sec^{-1}, $\sigma_2 = 0.05$ kb, and wet) at locations 1, 2 and 3. Note that both the magnitude and timing of velocity changes depend sensitively upon relative transducer locations.

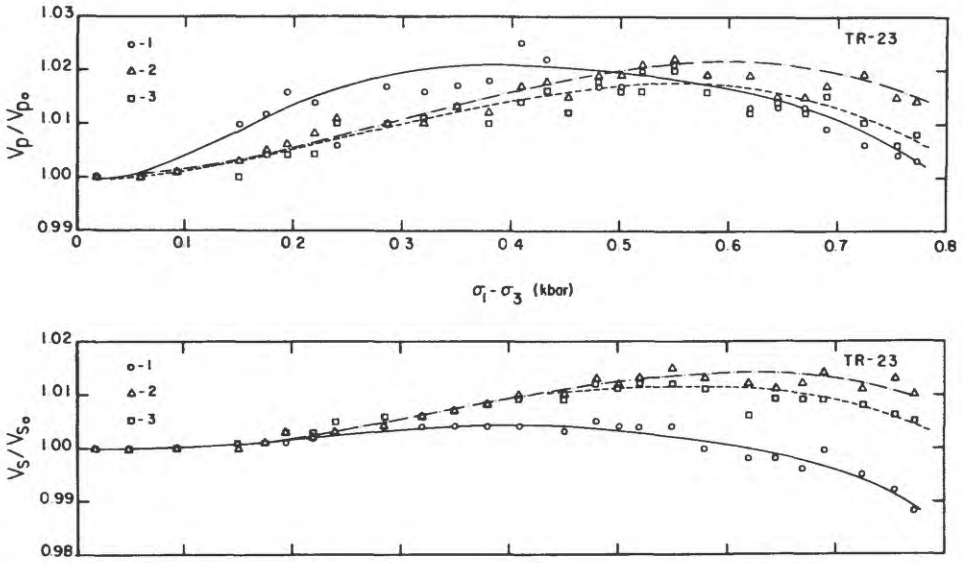

Figure 5

Normalized V_p and V_s changes observed during experiment TR-23 ($\dot{\epsilon} = 2 \times 10^{-8}$ sec^{-1}, $\sigma_2 =$ 0.05 kb, and dry) at locations 1, 2 and 3. The rather anomalous velocity changes are associated with the failure mode of the specimen.

maximum is then followed by a decrease in velocities to levels near or below the starting values. The location sensitivity is again extremely evident in this data set.

For experiment TR-21 the elevation, h, and the incremental tilt (arrows) of each of the three transducers are plotted in Fig. 6 against strain in the σ_1 direction (i.e. ε_1). The elevation is the relative change in height at the location of each transducer measured in the σ_2 direction as the sample is deformed by application of σ_1. In general, the elevations increase with increasing σ_1 indicating that crack volume is continuously contributing to this displacement throughout the experiment. It would therefore be expected that both V_p and V_s should decrease continuously at each location. Referring to Fig. 2, the transducer at location 1 is further away from the failure plane than either of the transducers at 2 or 3; in fact, 3 appears to be centered on the failure plane. The failure crack as viewed in the σ_2 direction moves from the bottom left to the middle of the top in Fig. 2. It is therefore anticipated that in time location 1 should sense the influence of the crack before either 2 or 3 but that the magnitude of the effect should be the greatest at 3. The observed velocity change at 3 is about 4% while the transducer at 2 shows a reversal and observations at 1 indicate changes of less than 2%. We note that there exists an accelerated change in the observed velocities at location 3 when the value of ε_1 approached 1.1%. This change correlates well with the observed change in incremental tilt represented by the direction and length (magnitude of incremental tilt) of the arrows superposed on the elevation curves of Fig. 6. The velocity reversal indicated in Fig. 6(2) has a minimum centered about

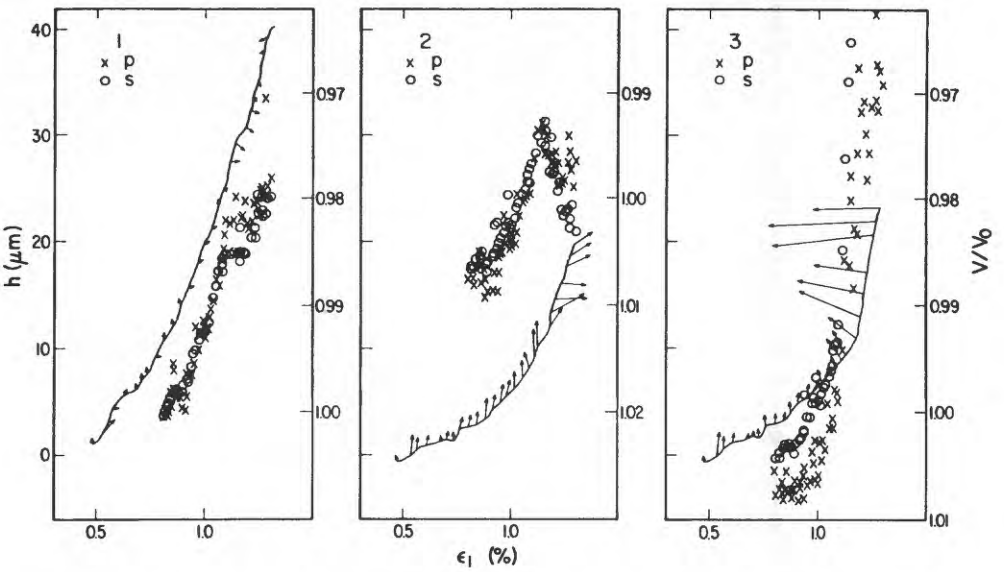

Figure 6

Plots of the cumulative change in elevation, h, for the transducers located at 1, 2 and 3 (see Fig. 2) relative to the edge of the specimen as a function of strain in the direction (ε_1, solid curve). The left ordinate scales are identical. The arrows superposed on the solid curves represent the direction and magnitude (arrow length) of incremental transducer tilt. Normalized values of V_p and V_s, crosses and open circles respectively, are plotted decreasing away from the abscissa. Note the correlation of both V_p and V_s reversals with the apparent change in incremental tilt direction at location 2.

$\varepsilon_1 = 1.15\%$. The change in the direction of incremental tilt indicated on the elevation curve also occurs at $\varepsilon_1 = 1.15\%$. Note that there is no suggestion of an elevation decrease before or after the strain value of 1.15%. Furthermore, the velocity recovery is observed in both the *P*- and *S*-waves.

The elevation change at location 1 is of a larger magnitude than that observed at the other locations; however, the greatest decrease in velocity is associated with location 3. This suggests that while the amount of local dilatation does influence the measured velocities, the orientation of such cracks plays the dominant role.

Discussion

Some field evidence exists in which seismic velocity changes prior to a major earthquake were observed (e.g. SEMENOV, 1969; AGGARWAL *et al.*, 1973; AGGARWAL *et al.*, 1975; WYSS and JOHNSTON, 1974; and JOHNSTON, 1978). Noteworthy also are the negative results of MCEVILLY and JOHNSON (1973) and BAKUN *et al.* (1973). Major velocity changes have also been observed in the laboratory during the failure of rock and gouge (e.g. MATSUSHIMA, 1960; NUR and SIMMONS, 1969; NUR *et al.*, 1973; GUPTA, 1973a, b; SOGA *et al.*, 1978; HADLEY, 1975; WANG *et al.*, 1975; PESELNICK *et al.*, 1976; and LOCKNER *et al.*, 1977). In fact, the marriage of field and laboratory

observations led to the dilatancy-diffusion model for earthquake prediction (SCHOLZ *et al.*, 1973; WHITCOMB *et al.*, 1973). However, while theoretically predicted and plausible, no velocity reversal has been observed in the laboratory prior to the failure of a brittle rock sample. We have, in contrast, observed velocity reversals prior to the ultimate failure of pyrophyllite. These reversals occur over periods of hours and are therefore not consistent with precursory times (msec) required by the inclusion model (Brady 1974, 1975). Reversals have been reported during the deformation of plexiglass (SOBOLEV, 1975) and of other pyrophyllite samples (SOBOLEV *et al.*, 1978). Furthermore, we find velocity changes to be very localized.

Typical catastrophic failure of brittle rock involves to a larger extent than often desired the energy stored in the loading system. Because pyrophyllite has such low elastic moduli this stored energy is very much reduced, enabling a slower progression to failure to prevail. This permits us to track velocity changes and to detect such fine features as velocity reversals.

The velocity changes noted in this study may be compared with the field observations of AGGARWAL *et al.* (1975). Their results indicate that the dilatancy-diffusion model is not totally acceptable for thrust-type earthquakes. In a most recent analysis of the Blue Mountain Lake, New York, data AGGARWAL (personal communication, 1978) found that the *S*-wave velocities show a partial recovery. This finding is in accord with our laboratory observations. However, the stress system in our laboratory experiments corresponds to that responsible for normal faulting. JOHNSTON (1978), studied temporal changes in teleseismic *P*-wave residuals at Hawaii and found that 3.5 years prior to a $M_s = 7.2$ normal faulting earthquake there existed a delay in the arrival times of *P*-waves. In addition, he found this delay to be very localized. His findings are in agreement with our laboratory observations which were made under a stress system appropriate to normal faulting.

On a laboratory scale the fault locks on asperities (SCHOLZ and ENGELDER, 1976 and ENGELDER and SCHOLZ, 1976) many times smaller than the overall fault dimensions. The region of intense dilatancy would then be confined locally in each of the regions surrounding the locked asperities and most probably would not be observed even by seismic waves passing directly through these small anomalous zones.

Had the present experiments been carried out without holography we would not have observed a slowly propagating fault but would have relied upon a stress-drop to indicate failure. We would therefore have concluded that the observed velocity reversals occurred prior to failure. Considering the sample as analogous to an asperity on a fault and the loading system analogous to the surrounding medium in which the elastic energy is stored, the slow failure of the asperity is then the real precursor to the final stress drop, i.e. the earthquake.

Conclusions

During the progressive deformation of pyrophyllite the velocities of both *P*- and *S*-waves were observed to decrease and then increase. This reversal was observed to

be very localized and unique to a low rate of deformation and complete saturation with water. The magnitude of velocity change depends upon the location of the sensing transducers relative to the ultimate fault plane. The correlation of velocity changes with observed tilt suggests that crack response alone and not dilatancy-diffusion could be responsible for the velocity changes. The exact scaling of these observations to the field requires much more work. Conceptually, the sample in the loading system is analogous to an asperity in a fault system. Phenomena associated with the slow failure of asperities are then precursory to stress drops associated with earthquakes.

Appendix A

Local crack response

Let us now examine the implications of the velocity observations of Fig. 6(2) in terms of the local crack response using the analysis of ANDERSON *et al.*, (1974) as reformulated by SOGA *et al.*, (1978). The *P*-wave in the σ_2 direction, V_{22}, and the shear wave, V_{32}, have been measured at location 2 and can be determined from:

$$\nu_p = (V_p/V_{p0})^2 = 1 - (a_1\varepsilon_2 + a_2\varepsilon_3 + a_2\varepsilon_1) \tag{1}$$

$$\nu_s = (V_s/V_{s0})^2 = 1 - (b_1\varepsilon_2 + b_1\varepsilon_3 + b_2\varepsilon_1). \tag{2}$$

Here ε_i is the crack density parameter appropriate to the i direction and $a_1 = 1.45$, $a_2 = 0.192$ and $b_1 = 0.601$ (SOGA *et al.*, 1978). One can argue that the velocity measurements in the σ_1 direction reflect the sensitivity of the low elastic moduli of pyrophyllite (SACHSE and RUOFF, 1975). There is good reason to neglect ε_1 since most cracks in that direction should be closed at the level of stress at which the reversal is observed. We can simplify equations (1) and (2) and express the time rate of change as:

$$\dot{\nu}_p = -a_1\dot{\varepsilon}_2 - a_2\dot{\varepsilon}_3 \tag{3}$$

$$\dot{\nu}_s = -b_1\dot{\varepsilon}_2 - b_1\dot{\varepsilon}_3. \tag{4}$$

Figure 6(2) suggest that $\dot{\nu}_p = \dot{\nu}_s = \dot{\nu}$ both before and after the velocity minimum. Combining (3) and (4) by eliminating $\dot{\nu}$ we obtain

$$\dot{\varepsilon}_3 = 2.08\dot{\varepsilon}_2. \tag{5}$$

The increase in the time rate of change of the crack density parameter is the greatest in the σ_3 direction, the direction of least principal stress. The velocity observations require both crack density parameters to decrease (see Fig. 7a) after the velocity minimum (see Fig. 6(2)). Holography of the σ_2 face indicates that the elevation, h, increases monotonically at all three transducer locations. The continuous elevation increase implies an increase in the number and/or thickness of the type 2 cracks. We define type i penny shaped cracks as those with normals in the ith direction.

SOGA *et al.* (1978) modified the isotropic definition of the volumetric crack density

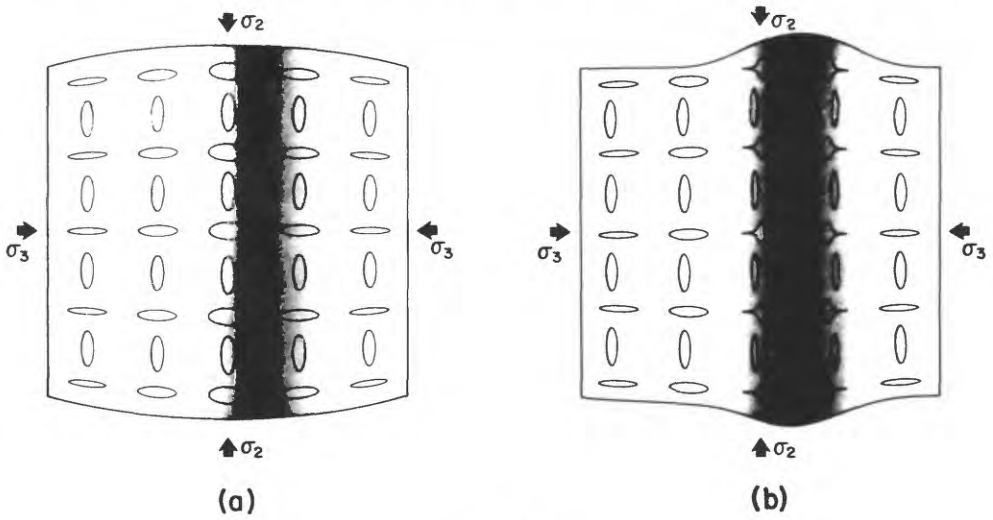

Figure 7

The local response of penny-shaped cracks as required by our velocity observations to a propagating fault is portrayed schematically in (a) and (b). Cracks are nearly uniformly distributed throughout the sample during the early stages of deformation. In the neighborhood of the fault (stippled region) we envisage the aspect ratio of type 2 cracks to become larger. As the fault intercepts our plane of section (b), it changes the aspect ratio; cracks with normals in the σ_3 direction become skinnier and shorter and those with normals in σ_2 direction change their effective lengths and become fatter.

parameter (O'CONNELL and BUDIANSKY, 1974) to obtain an approximate linear crack density parameter:

$$\varepsilon_i = \frac{\phi_i}{\alpha_i} = \frac{\phi_i a_i}{c_i} = N_i \langle a_i \rangle^3 \tag{6}$$

where N_i is the number of cracks per unit length; a_i is the length of the cracks, c_i is the thickness of the cracks, and the subscript i gives the appropriate direction. We note from (6) that continuously increasing N_i cannot cause ε_i to change $\langle$sense$\rangle$ as required by the velocity observations at location 2. Consider now that the cracks can change shape in response to local stress changes. The change in porosity ϕ_i must be directly proportional to changes in the observed elevation, h_i. Therefore, to change the sense of ε_i the sense of α_i, the aspect ratio, must change. This requires that (1) the thickness of type 2 cracks must increase and (2) that their length decrease. Since the velocity increase requires that ε_2 must decrease, the shortening must dominate over thickening. Information concerning type 3 cracks is severely lacking; we can only say that the velocity observations at location 2 require $|\dot{\varepsilon}_3| > |\dot{\varepsilon}_2|$ (see equation 5). Within the weakened zone near the failure crack, type 3 cracks are expected to partially collapse decreasing both in thickness and effective length (see Fig. 7b). The amount of collapse is a function of distance from the failure crack and is manifested as the observed incremental tilt changes shown in Fig. 6.

Similar analysis could be made for transducer locations one and three. However, not enough data exist to describe these crack populations. The change in crack patterns as we perceive them are shown schematically in Fig. 7. As the sample becomes dilatant type 1 cracks are closed and type 2 and 3 cracks open. Because of the rigid boundary condition provided by the σ_3-pistons, type 3 cracks are uniformly distributed throughout the sample. They also have a constant aspect ratio at this stage. Type 2 cracks have a total crack volume which is about one-half that of the type 3 cracks. The gentle central bulging observed in the σ_2 direction is a result of the boundary conditions and causes a variation of aspect ratios of type 2 cracks across the sample. Type 2 cracks are fatter (i.e. they have larger aspect ratios) the further they are from the σ_1 and σ_3 pistons. The fault depicted in Fig. 7 forms by the coalescence of small cracks and has associated with it a stress concentration which results in a pronounced bulge in the σ_2 direction near the fault tip. The formation of the fault involves considerable deformation in a zone surrounding the incipient fault. This zone considerably weakens the sample which accelerates the strain in the σ_1 direction, causes uplift in the σ_2 direction (Fig. 6).

While cracks of type 2 and 3 must generally be opening to accommodate the accelerating strain in the σ_1 direction, type 3 cracks within the intense deformation zone are being closed such that their aspect ratios decrease. Type 2 cracks in this region are being squeezed such that they are partially closing along their long direction but are becoming fatter; thus, an increasing aspect ratio, decreasing length and increasing thickness.

The location of the transducers relative to the intense deformation zone critically determines if a velocity reversal is measured. At location 1 in experiment TR-21 (Fig. 2) the closing of cracks within the intense deformation zone was not sufficient to overcome the general trend of opening of cracks throughout the sample. Instead of a velocity reversal (Fig. 6(1)) we find a period during which the velocities did not change. At location 2 the transducer is closer to the loading platen where friction between the sample and platen retard the opening of cracks; here the partial closing of cracks predominates resulting in a velocity reversal. The velocity data at location 3 are marred by the transducer coming loose. The tilt of this transducer is incompatible with the change in surface topography as determined by holography. However, the possibility that the very local intense cracking associated with the advancing fault may be in part responsible for the observed effect cannot be excluded.

Summary

The following summarizes observations consistent with our velocity and holographic measurements:

(1) Velocity observations appear to be very dependent upon their spacial location relative to the ultimate failure plane.

(2) A velocity reversal was observed in both *P*- and *S*-waves in pyrophyllite being triaxially deformed at a strain rate of 2×10^{-8} sec^{-1}, fluid pressure of 50 bars and wet.

(3) The reversals in *P*- and *S*-waves correlate with changes in the local incremental tilt.

(4) Changes in local crack geometry were invoked to explain observations of tilt, elevation, and velocity changes.

(5) Our velocity observations cannot be explained either by the dilatancy-diffusion model (SCHOLZ *et al.*, 1973 and WHITCOMB *et al.*, 1973), or by the inclusion model (BRADY 1974, 1975).

Acknowledgements

The authors would like to thank B. Salov and A. Koltsov for technical assistance in the laboratory and L. Granryd for her help in data reduction. Part of this work was carried out under the auspices of the Soviet–American Earthquake Prediction program through U.S. Geological Survey contract DOI-PO #32701 and in part by U.S. Geological Survey contract DI-14-08-0001-15256. One of us (C.H.S.) was supported as a Visiting Fellow of CIRES under a cooperative program between the University of Colorado and the National Oceanographic and Atmospheric Administration under contract #DOC-03-7-022-35191.

REFERENCES

AGGARWAL, Y. P., SYKES, L. R., ARMBRUSTER, J. and SBAR, M. L. (1973), *Premonitory changes in seismic velocities and prediction of earthquakes*, Nature *241*, 101–104.

AGGARWAL, Y. P., SYKES, L. R., SIMPSON, D. W. and RICHARDS, P. G. (1975), *Spatial and temporal variations in t_s/t_p and in P wave residuals at Blue Mountain Lake, New York: Application to earthquake prediction*, J. Geophys. Res. *80*, 718–732.

ANDERSON, D. L., MINSTER, B. and COLE, D. (1974), *The effect of oriented cracks on seismic velocities*, J. Geophys. Res. *79*, 4011–4015.

BAKUN, W. H., STEWART, R. M. and TOCHER, D., *Variations in V_p/V_s in Bear Valley in 1972*, in *Proceedings of the Conference on Tectonic Problems of the San Andreas Fault System*, ed. by R. L. Kovach and A. Nur (Stanford University Press, 453–462, 1973).

BRACE, W. F., *Recent laboratory studies of earthquake mechanics and prediction*, in *Earthquake Precursors*, ed. by C. Kisslinger and Z. Suzuki (Japan Scientific Societies Press, Tokyo, Japan, 185–202, 1978).

BRACE, W. F., PAULDING, B. W., Jr. and SCHOLZ, C. (1966), *Dilatancy in the fracture of crystalline rocks*, J. Geophys. Res. *71*, 3939–3953.

BRADY, B. T. (1974), *Theory of earthquakes I. A scale independent theory of rock failure*, Pageoph *112*, 701–725.

BRADY, B. T. (1975), *Theory of earthquakes II. Inclusion theory of crustal earthquakes*, Pageoph *113*, 149–168.

BRIDGMAN, P. W. (1949), *Volume changes in the plastic stages of simple compression*, J. Appl. Phys. *20*, 1241–2151.

BYERLEE, J. D. (1978), *A review of rock mechanics studies in the United States pertinent to earthquake prediction*, Pageoph *116*, 586–602.

BYERLEE, J. D., and SUMMERS, R. (1976), *A note on the effect of fault gouge thickness on fault stability*, Int. J. Rock Mech. Min. Sci. and Geomech. Abstr. *13*, 35–36.

CRAMER, C. H. and KOVACH, R. L. (1975), *Time variations in teleseismic residuals prior to the magnitude 5.1 Bear Valley earthquake of February 24, 1972*, Pageoph *113*, 281–292.

ENGELDER, J. T. and SCHOLZ, C. H. (1976), *The role of asperity indentation and ploughing in rock friction-II; Influence of relative hardness and normal load*, Int. J. Rock Mech. Min. Sci. and Geomech. Abstr. *13*, 155–163.

GETTING, I. C. (1979), *A new 3 kilobar pressure vessel with an optical window for rock mechanics studies*, in preparation.

GUPTA, I. N. (1973a), *Dilatancy and premonitory variation of P and S travel times*, Bull. Seismol. Soc. Amer. *63*, 1157–1161.

GUPTA, I. N. (1973b), *Seismic velocities in rock subjected to axial loading up to shear failure*, J. Geophys. Res. *78*, 6936–6942.

HADLEY, K. (1975), *V_p/V_s anomalies in dilatant rock samples*, Pageoph *113*, 1–23.

JOHNSTON A. C. (1978), *Localized compressional velocity decrease precursory to the Kalapana Hawaii, Earthquake*, Science *199*, 882–885.

LOCKNER, D., WALSH, J. B. and BYERLEE, J. D. (1977), *Changes in seismic velocity and attenuation during deformation of granite*, J. Geophys. Res. *82*, 5374–5378.

MCEVILLY, T. V. and JOHNSON, L. R. (1973), *Earthquakes of strikeslip type in central California: Evidence on the question of dilatancy*, Science *182*, 581–584.

MATSUSHIMA, S. (1960), *Variation of the elastic wave velocities of rocks in the process of deformation and fracture under high pressure*, Disaster Prev. Res. Inst. Kyoto Univ. Bull. *32*, 2–8.

NUR, A. (1971), *Effect of stress on velocity anisotropy in rocks with cracks*, J. Geophys. Res. *76*, 2022–2034.

NUR, A. and SIMMONS G. (1969), *Stress-induced velocity anisotropy in rock: An experimental study*, J. Geophys. Res. *74*, 6667–6674.

NUR, A., BELL, M. L. and TALWANI, P., *Fluid flow and faulting, 1: A detailed study of the dilatancy mechanism and premonitory velocity changes*, in *Proceedings of the Conference on Tectonic Problems of the San Andreas Fault System*, ed. by R. L. Kovach and A. Nur (Stanford University Press, Stanford, California, 391–404, 1973).

O'CONNELL, R. J., and BUDIANSKY, B. (1974), *Seismic velocities in dry and saturated cracked solids*, J. Geophys. Res. *79*, 5412–5426.

PAULING, L., *The Nature of the Chemical Bond* (Cornell University Press Ithaca, New York, 1972), 644 pp.

PESELNICK, L., DIETERICH, J. H., V. I. MJACHKIN and SOBOLEV, G. A. (1976), *Variation of compressional velocities in simulated fault gouge under normal and direct shear stress*, Geophys. Res. Letters *3*, 369–372.

RALEIGH, C. B. and PATERSON, M. S. (1965), *Experimental deformation of serpentinite and its tectonic implications*, J. Geophys. Res. *70*, 3965–3985.

SACHSE, W. and RUOFF, A. L. (1975), *Elastic moduli of precompressed pyrophyllite used in ultra high-pressure research*, J. Appl. Phys. *46*, 3725–3730.

SCHOLZ, C. H. and ENGELDER, J. T. (1976), *The role of asperity indentation and ploughing in rock friction—I; Asperity creep and stick-slip*, Int. J. Rock Mech. Min. Sci. and Geomech. Abstr. *13*, 149–154.

SCHOLZ, C. H., SYKES, L. R. and AGGARWAL, Y. P. (1973), *Earthquake prediction; A physical basis*, Science *181*, 803–810.

SEMENOV, A. M. (1969), *Variations in travel-time of transverse and longitudinal waves before violent earthquakes*, Bull Acad. Sci. USSR, Phys. Solid Earth *3*, 245–248.

SOBOLEV, G. A. (1975), *The study of precursors of failure under biaxial compression*, Pageoph *113*, 45–49.

SOBOLEV, G., SPETZLER, H. and SALOV, B. (1978), *Precursors to failure in rocks while undergoing anelastic deformations*, J. Geophys. Res. *83*, 1775–1784.

SOGA, N., MIZUTANI, H., SPETZLER, H. and MARTIN, R. J., III (1978), *The effect of dilatancy on velocity anisotropy in Westerly granite*, J. Geophys. Res. *83*, 4451–4458.

SPETZLER, H. A., SOBOLEV, G. A., SALOV, B., SONDERGELD, C. H., GETTING, I. C. and KOLTSOV, A., *Failure of a weak rock under generalized triazial loading*, submitted 1979.

WANG, C. Y., GOODMAN, R. E. and SUNDARAM, P. N. (1975), *Variations of V_p and V_s in granite premonitory to shear rupture and strike-slip sliding: Application to earthquake prediction*, Geophys. Res. Letters *2*, 309–311.

WHITCOMB, J. H., GARMANY, J. D. and ANDERSON, D. L. (1973), *Earthquake prediction: Variation of seismic velocities before the San Fernando earthquake*, Science *180*, 632–635.

WU, F. T. (1978), *Mineralogy and physical nature of clay gouge*, Pageoph *116*, 655–689.

WU, F. T., BATTER, L. and ROBERSON, H. (1975), *Clay gouges in the San Andreas fault system and their possible implications*, Pageoph *113*, 87–95.

WYSS, M. and JOHNSTON, A. C. (1974), *A search for teleseismic P residual changes before large earthquakes in New Zealand*, J. Geophys. Res. *79*, 3283–3290.

ZOBACK, M. D. and BYERLEE, J. D. (1976), *A note on the deformational behavior and permeability of crushed granite*, Int. J. Rock Mech. Min. Sci. and Geomech. Abstr. *13*, 291–294.

(Received 10th April 1979)

(page 275 follows)

ULTRASONIC FRACTURE RADIATION IN A ROCK SPECIMEN UNDER COMPRESSION

by

G. Sobolev*
H. Spetzler**
A. Koltsov*
C. Sondergeld***

*Institute of the Physics of the Earth,
Academy of Sciences of the U.S.S.R., Moscow

**Cooperative Institute for Research in Environmental Sciences
and Dept. of Geological Sciences,
University of Colorado/NOAA, Boulder, CO 80309

***University of Colorado/NOAA, Boulder, CO 80309

ABSTRACT

The dynamic characteristics of ultrasonic radiation due to propagation of shear fractures have been studied in pyrophyllite samples. Holographic interferometry and scanning electron microscopy were used to investigate strain distribution and fracture structure. Two sources of ultrasonic radiation are related to the fractures and may represent the subdivision of the fracture into smaller elements of two principal sizes. The amplitudes of the high frequency components of the ultrasonic pulses gradually increase, while the low frequency components maintain a constant value during the shear fracture formation. These observations are attributed to the breaking of progressively stronger elements. A comparison of our result with field data is made.

Attention has recently been focused on the discovery of regular changes in the frequency spectrums in seismograms prior to strong earthquakes in the Garm region (Rulev, 1971, 1975; Rautian, et al. 1978). These frequency changes can be interpreted as changes in the source (Brune, 1970; Hanks and Wyss, 1972; Kostzov, 1975) or temporal variations in the Q structure. Successful modeling of seismic waves due to rock fracture in the laboratory, where the properties of both the material and the fracture itself are known, would aid in the interpretation of field data. Experimental difficulties exist, unfortunately in recording the ultrasonic wave forms as they range from hundreds to thousands of kHz throughout the course of an experiment of several hours duration.

Some interesting results have been obtained in studies of artificial faults in glass and plastic. (Wu et al., 1972; Schamina et al., 1976; Vinogradov, 1978). In these experiments the rupture velocity was measured and its effect on the frequency of radiated signals estimated. The biggest differences in waveforms have been noticed for the patterns originating from fault surfaces with homogeneous and heterogeneous friction distribution. The dynamic characteristics of stick-slip events, including stress drop value, have been measured recently in granite samples (Blacic and Malone, 1977).

The main goal of our study was to study the radiation characteristics of "natural" shear fractures which are thought to accompany the final stages of rock deformation.

Method and Techniques

This study was carried out on samples of pyrophyllite whose mechanical properties have been described previously (Sobolev et al., 1978; Sondergeld et al., 1980; Spetzler et al, 1980). The longitudinal wave velocity in air dry specimens is 3.5 m/s and increases up to 4.0-4.3 km/s in the direction of maximum load under niaxial or biaxial compression. Some characteristic features of

pyrophyllite are its homogeneity and fine grain size. Its strength is about 80 MPa in uniaxial compression at a relatively high strain rate ($\dot{\varepsilon} \approx 10^{-5} s^{-1}$).

Samples were rectangular prisms of three sizes, (A) 32 x 32 x 16mm (B), 32 x 38 x 15mm (C) and 63 x 63 x 31.5mm. Uniaxial compressive stress was always applied perpendicular to the smallest faces of the sample.

In most experiments two holes were drilled through each sample prior to loading to initiate internal fracture development (Figure 1). The diameters of the holes were 2mm for samples with geometries A and B and 3mm for those with geometry C. The distance between the holes was an independent variable. The angle between the line joining the centers and the direction of maximum compression varied from 35–45°. In some experiments small notches were made in the circumference of the drilled holes to increase the stress concentrations there. This was done to guarantee that a fracture would be initiated at these notches, and propagate between the holes.

Photographs of the large faces of samples taken subsequent to experiments are shown in Figure 1. The direction of uniaxial stress in all figures is vertical. In Figure 1a one can see the initiation of a macrofracture between the holes. (This will be referred to as a "type 1" fracture.) Under continued loading the macrofracture extended into the two areas external to the holes ("type 2" fractures) as shown in Figure 1b. The geometry of a complete macrocrack is shown in Figure 1c.

The uniaxial force, F_1, and the corresponding change in sample length, ΔL_1, were measured during each experiment by means of a force gauge and a linear variable differential transformers (LVDT). The data were read as voltages automatically by a data acquisition system which had been programmed to calculated stress (σ_1) and strain (ε_1) from these inputs. These two parameters were printed and plotted on an X-Y plotter in real time.

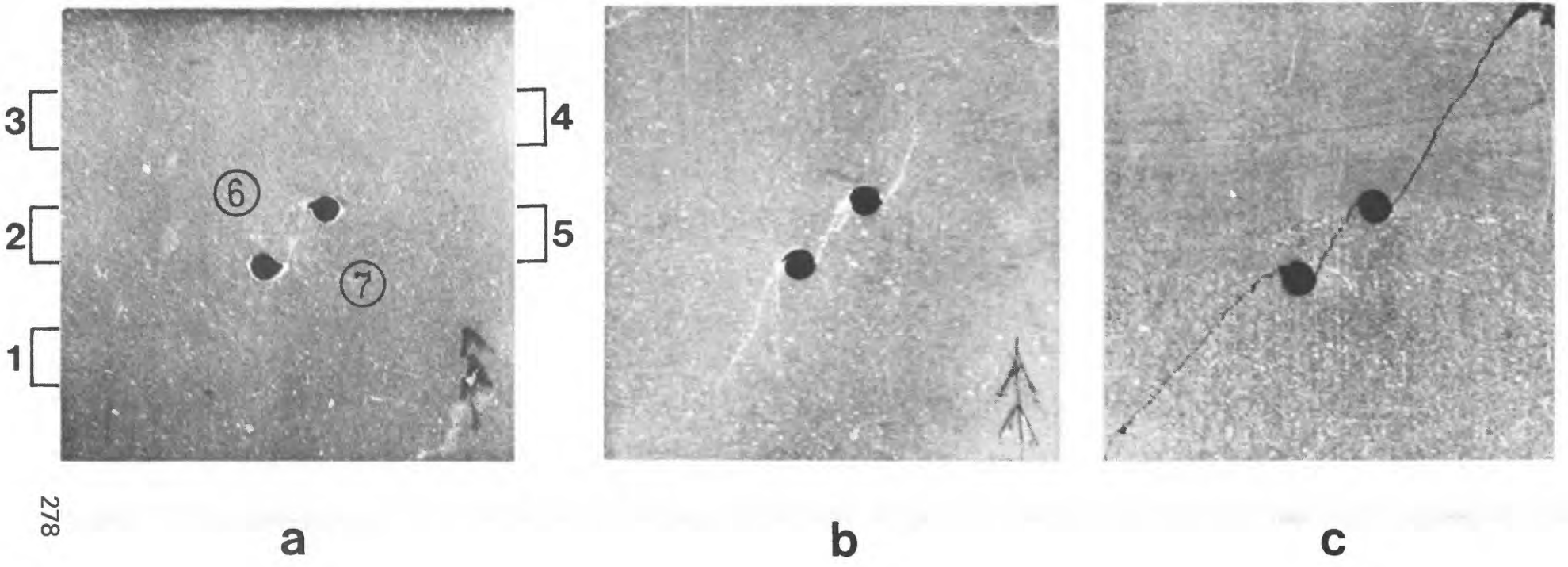

Figure 1. The photographs of sample faces after loading to failure: (a) with type 1 fracture between the drilled holes; (b) with type 1 and 2 fractures; (c) complete failure. Positions of the ultrasonic transducers are identified in (a).

The cylindrical P-wave PZT transducers (1MHz) were glued to the sample as shown in Figure 1a. Only two transducers were used simultaneously. In most experiments these occupied positions 1 and 3 (see Figure. 1a) however other combinations were sometimes used. The polarity response of the transducers was determined and kept constant in all experiments. Acoustic signals from the fractures passed through amplifiers with flat frequency responses up to 1 MHz and were recorded on Nicolet digital oscilloscopes. The oscilloscopes could simultaneously record two ultrasonic signals and and store them on a floppy disk. Each signal is composed of 1024 points with 50 nsec between consecutive points. At the highest frequencies ($\sim 1MHz$) this digitization rate yielded a 20 points per cycle resolution. The use of two transducers allowed us to outline the source region and discriminate against the signals emanating from contact areas between the pistons and sample.

Stress was incremented slowly in discrete steps of 0.5 MPa. The resulting strain in the σ_1 direction (ε_1) was approximately (0.005 - 0.01)% per step. The active stage of each loading step required about 10 seconds and an interval of 20-30 seconds was allowed between steps. The loading stages were sometimes interrupted prior to completion where strong ultrasonic signals were recorded. During one experiment about 100 loading increments were made prior to sample failure.

The failure stress for samples with holes was about 50 MPa and 67 MPa for water saturated and air dried respectively. The ultimate strain ε_1 was less than 1%. In some experiments, where samples were not loaded to failure, unloading was performed gradually over a period of minutes. Forty-four experiments were conducted and about 20 waveforms recorded during each.

Holographic interferometry was used in four experiments in addition to stress, strain, and ultrasonic emission measurements, to determine the strain

distribution during fracture initiation and growth. We have used this technique previously during investigation of the precursors to failure in polymethylmethacrillate (plexiglass) and pyrophyllite (Spetzler et al., 1976, 1980; Sobolev et al., 1978).

Holograms of one sample face were made periodically. The wavelength (λ) of laser light used was 0.6328 μm. A single exposure results in a hologram of the sample surface due to interference of the reference and reflected beams. Double exposure produces a system of fringes (Figure. 2) which represent changes in displacement in the viewing direction produced between two successive exposures. Adjacent fringes correspond to a differential normal surface displacement of $\lambda/2$.

Examination of the holograms shows that at low differential stress the sample deforms uniformly and the artificial holes do not act as measureable strain (stress) concentrators. When the stress (σ_1) reaches one half of the failure stress, σ_f , the zones of high strain concentration (bulges and valleys) appear near the holes, as seen in Figure 2. Bulges form adjacent to each hole, towards the outer edge of the samples, marking intense zones of compression.

The effect of a round hole of radius a on a uniform uniaxial stress field is well known for plane elastic deformation (e.g. Timoshenko and Goodier, 1970). The stress field is distorted such that given a horizontal axis through the center of the hole, at the point r= a (on the circumference of the hole), the uniaxial stress in the vertical direction is larger than the applied stress by a factor of 3. In our case this stress is compressive. On a vertical axis passing through the center of the hole, at the point r= a horizontally oriented tensile stresses exist and are two times larger than the applied stress. To a first approximation, distortion of the stress field decreases as $(a/r)^2$. In our experiments the deformation was neither plane nor elastic so this simple theory can be used only as a

a b c

Figure 2. A sequence of photographs of doubly exposed holograms is shown. (a) As stress was raised from 0.69 σ_f to 0.73 σ_f (b) The stress interval 0.97 σ_f to 0.98 σ_f occurs just before type 1 fracture propagation; (c) type 1 fracture propagation is complete and the initial stage of type 2 fractures formation has begun. The hologram was made over the interval $\sigma_1 = \sigma_f$ to $\sigma_1 = 0.97\ \sigma_f$.

qualitative guide. Additionally one can see an interaction of the stress fields from both holes leading to the formation of a ridge between the holes (Figure. 2a, b). As σ_1 is increased the height of the bulge near each hole and that of the ridge between them increase. As shown in Figures 2a and c, these patterns remain distinct after σ_1 exceeds 0.7 σ_f. At $\sigma_1=0.7\sigma_f$ a visible en echelon crack system or thin fracture first appears between the holes. The hologram of Figure 2a shows the deformation which occurred as stress was raised from 0.69 σ_f to 0.73 σ_f. The corresponding change in strain (shortening, $\Delta\varepsilon_1$) was 9×10^{-3}%. The hologram of Figure 2b was made over the stress interval $0.97\sigma_f$ and $0.98\sigma_f$. The corresponding change in strain was $\Delta\varepsilon_1 = 0.003$%. Despite the strain change in the second hologram (Figure 2b) being less than that in the first (Figure 2a), by a factor of three, the local relief and distortion is much larger on the hologram of Figure 2b. The hologram of Figure 2c was made as a fracture of type 1 (see Figure 1a) developed between the holes. This was followed by a stress decrease from $\sigma_1 = \sigma_f$ to $\sigma_1 = 0.97\sigma_f$ ($i.e.\ \Delta\sigma_1 = -0.181 MPa$). The strain increment ($\Delta\varepsilon_1$) was within the range of our accuracy, approximately 1×10^{-3}%. Comparison of Figures 2b and 2c shows that a dramatic change in strain distribution resulted from the appearance of a type 1 fracture. The zone between the holes was unloaded and the strain (stress) concentrations which resulted may now be observed external to the holes (Figure 2c). If loading of the sample were to be continued, the stress concentrations would propagate outwards, simultaneous with the tips of the type 2 factors (see Figure 1b).

The Fracture Structure

Of the samples tested not all contained artificial holes, and the locations of the holes were varied among those that did. In those samples which did not contain holes macrofracture formation was usually initiated in corner regions or in the areas of sample-piston contact. Holes were first connected by a type 1

macrofracture. If the distance between the two holes was greater than 1/6 of the diagonal length of the sample, then the fracture (type 1) propagated unstably through the entire sample. If this distance was less than 1/6 of the diagonal length (as in Figure 1a) then the type 1 fracture was stopped at the holes and an increase in σ_1 was required to produce additional fractures (type 2). All macrofractures developed episodically, during loading increments. A type 1 fracture initially appeared as an en echelon crack system and joined gradually, as described previously (Sobolev et al., 1978). As soon as one type 2 fracture (Figure 1b) exceeded 1/2 of the distance to the specimen's edge it would propagate unstably followed by complete failure of the sample (Figure 1c).

An optical and scanning electron microscope (SEM) study of previously loaded specimens was carried out. In the light colored zones (see Figure 3a) along type 1 and 2 fractures the regions of high porosity (microcrack concentrations) are displayed. The locations of these regions in space coincide with zones of intense relief changes (Figure 2b). This affirms that the ridge between the holes was formed at least in part by a dilatant rock. It is interesting to note that near the ends of type 2 fractures (Figure 3a), which elongated relatively quickly, areas of high porosity are hardly visible.

The detailed structure of a type 1 fracture is shown in Figure 3b which was constructed from analysis of tens of SEM photomicrographs. One can definitely see that the whole macrofracture is composed of segments or elements of length $\tilde{l}_2$, of about 0.5 - 1mm. Each element $\tilde{l}_2$ consists in turn of relatively straight elements 0.1 - 0.2 mm in length. These smaller elements are distinctly visible on the photomicrographs. The development of such elements in pyrophyllite samples under biaxial compressive stress has been noticed previously (Sobolev et al., 1978). In Figure 3b one can also see two elements ($\tilde{l}_1$) greater than 2mm in length which emanate from the borders of the holes. The bridge

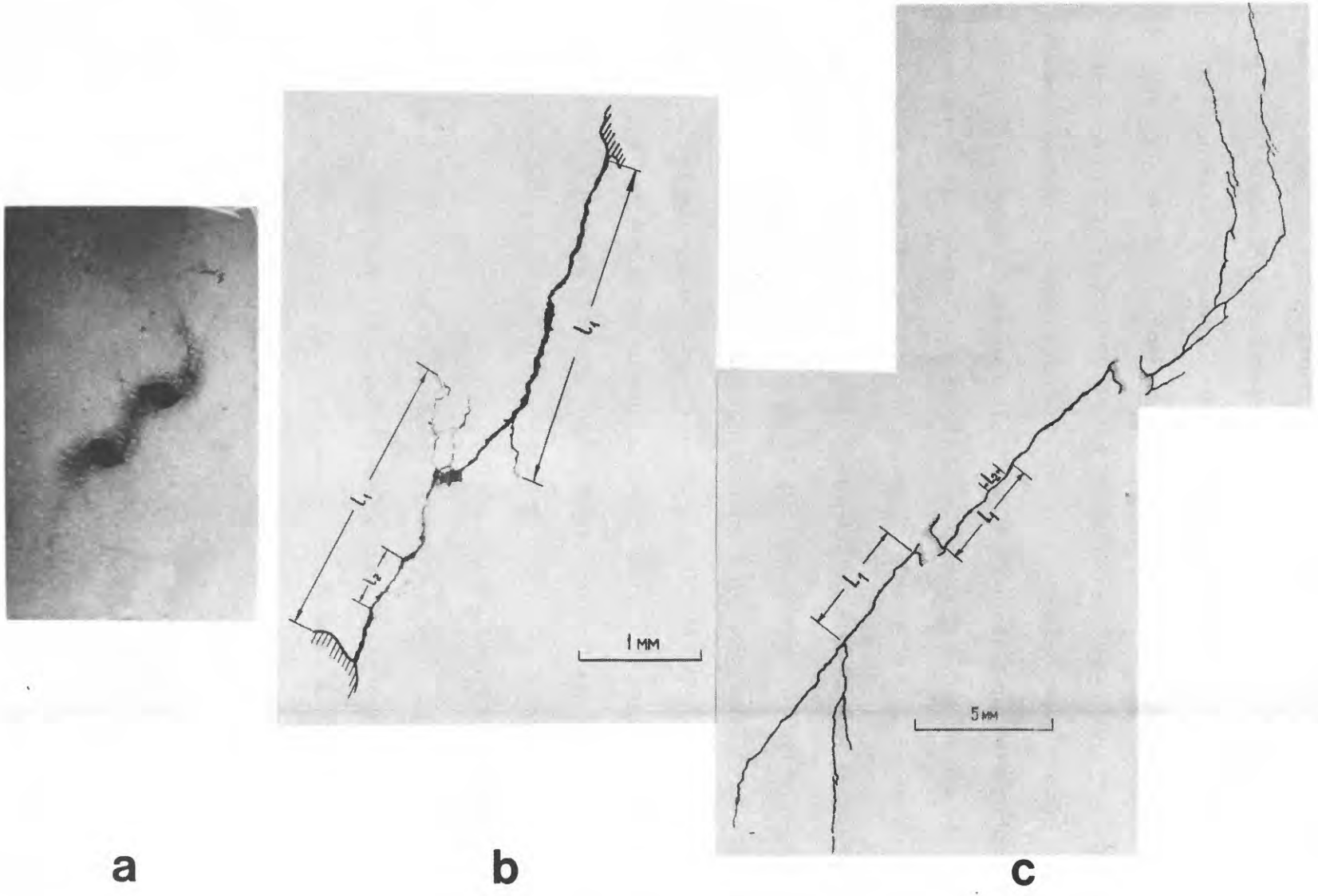

Figure 3. The results of SEM study of fractures: (a) dense microcrack concentrations areas along type 1 and 2 fractures; (b) the structure of a type 1 fracture; (c) the pattern of the fracture system.

between these elements is broken by an intermediate fracture about 1mm in length. Photomicrographs at low magnification are compiled in Figure 3c. The fractures in Figure 3c reveal an ordered structure with the lengths of main elements being 0.5-0.7mm and 3.5-5mm. Analysis of photomicrographs again show (as in the case of Figure 3b) the presence of elements 0.1-0.2mm in length.

From SEM studies of the fracture patterns associated with variable specimens sizes (A, B and C as defined previously) and with variable spacings between the holes one can draw the following conclusion: fractures of types 1 and 2 which occurred during deformation of pyrophyllite samples represent shear faults consisting of first order elements (average length $\tilde{l}_1$ = 3.7mm), second order elements ($\tilde{l}_2$ = 0.75mm), and 3rd order elements ($\tilde{l}_3$ = 0.15mm). From a previous SEM analysis (Sobolev and Koltsov, 1980), we conclude that this hierarchy of fracture elements is continuous to element of higher (4, 5, 6) order with average element lengths of 30 μm, 5 μm and about 1 μm, respectively. The lengths of a 5th order element is that of the grain size and microcracks of 6th order are more equidimensional in shape. (i.e., they are pore-like defects rather than flat cracks.) The ratio of consecutive order element lengths is approximately 5. For the samples we have tested (the largest sample being 63 x 63 x 31.5 mm) the lengths of 1st, 2nd and 3rd order elements seem to be uneffected by sample size.

Ultrasonic radiation of fractures.

We focused our attention most closely on the elastic radiations which we observed during formation of type 1 fractures. To do this, a transducer was placed in either position 1 or 2 (Figure 1a) and another in position 3, 4 or 5, such that we could estimate the source region from the difference in P-wave arrival times. Additional information concerning source location was inferred from the distortion of the strain field as observed with holography (Figure 2). The growth of type 1 fractures was also visually observed in a number of experiments. The

planes of types 1 and 2 fractures were usually parallel to the axes of the holes.

During the initial stage of loading most acoustic emission (AE) events emanated from sample-piston contact areas. These signals had a smooth form (Figure 4, waveforms 1,2) and started with a negative phase.

In each experiment 10-20 events were counted which were from the contact areas. The rate of occurrence of these events decreased exponentially as the load was increased and ceased at $\sigma_1 \approx 0.3\sigma_f$. These AE pulses probably resulted from the breaking of asperities on the specimen surface. In the range $\sigma_1 = (0.3-0.5)\sigma_f$ acoustic quiescence was observed in all experiments. After σ_1 reached values above $0.5\sigma_f$, pulses from the zone between the holes were detected; 2 to 5 such pulses were usually recorded during type 1 fracture formation. A sequence of events from experiment 28 is shown in Figure 4 (waveforms 3, 4, 5, 6). Waveforms 3 and 4 were recorded at $\sigma_1 = 0.53\sigma_f$ and $\sigma_1 = 0.68\sigma_f$, respectively. Waveform 5 was recorded at maximum stress (*i.e.*, $\sigma_1 = \sigma_f$), and waveform 6, some seconds later while σ_1 decreased by $\Delta\sigma_1 =$ 0.9 MPa or 1.7% of σ_f. After waveform 6 was recorded the sample was unloaded gradually. Only one acoustic emission occurred during unloading, when the stress reached $0.1\ \sigma_f$. (Waveform 7 of Figure 4). Only a type 1 fracture developed during experiment 28 as is shown in Figure 1a. Waveform 3-6 of Figure 4 reflect the following basic features of ultrasonic events peculiar to type 1 fracture formation.

1. The spectra as shown in Figure 5 are dominated by two main frequency ranges $F_l = 100-200kHz$ and high $f_h = 200-600$ kHz. The amplitude of the low frequency components remains constant during formation of a type 1 fracture while the amplitude of the high frequency components gradually increases.

2. For transducers located in positions 1 or 2 (Figure 1a) the polarity of the first arrival of low frequency ultrasonic signals remains the same, i.e., positive. The high frequency wave polarity was usually positive, with approximately 10% of

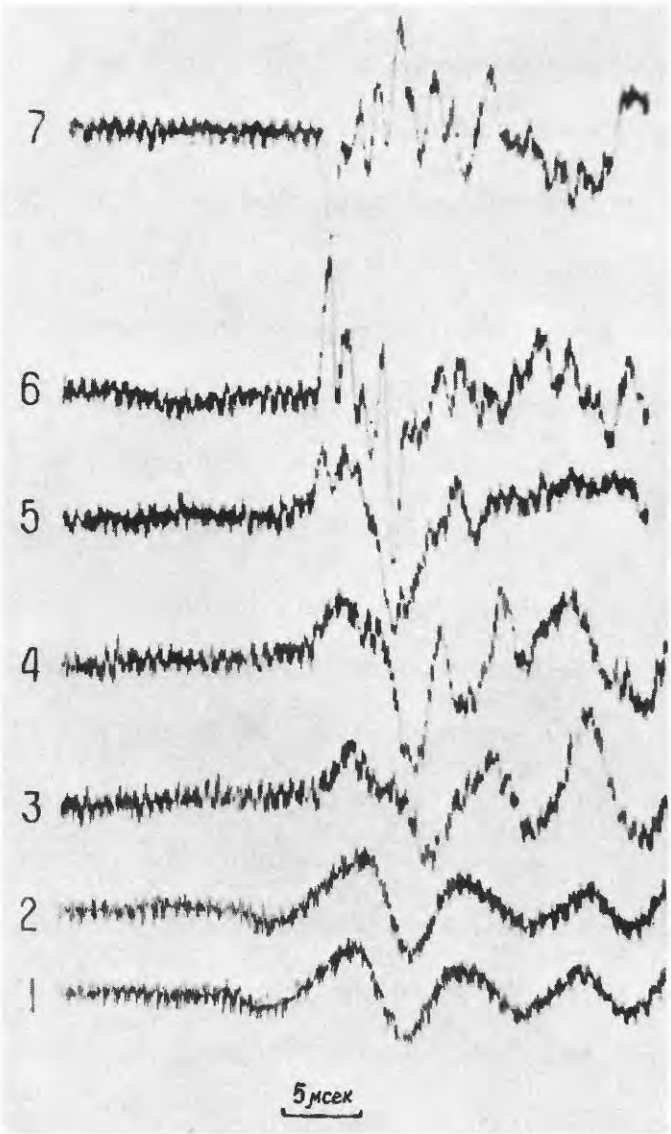

Figure 4. Typical AE waveforms. Source region for 1 and 2 is the contact area between the sample-piston; for 3, 4, 5, and 6 - from the zone of type I fracture formation during gradual loading. Waveform 7 occurred during unloading. The transducer was located at position 1 (see Figure 1a).

the events showing a negative polarity. For transducers occupying position 3 this regularity was not observed. The number of observations obtained from other positions were not sufficient for conclusions to be made.

3. The shape and main frequencies of the signals do not change substantially for different sample size or distances between holes.

4. Some of the "unloading" waveforms resembled mirror images (reversed polarity) of previous waveforms recorded during sample loading. Other "unloading" waveforms have a more visible low frequency component.

The observations described above (1 and 3) are primarily applicable to the initial phases of the waveforms (P-waves), up to 4-5 μsec after the first arrival. The latter part of the waveform was usually distorted by reflected P and S waves.

We now consider separately the low and high frequency components of signals emitted by type 1 fractures (waveforms of Figure 4). Amplitude spectra for the initial parts of the waveform were computed. Filters of high or low frequencies have been used to eliminate either all frequencies above 300 kHz (Figure 5a) or those below 300 kHz and above 1 MHz (Figure 5b). The waveforms with the same numbers as Figures 4 and 5 correspond to the same event. One can see from Figure 5 that the amplitude of the low frequency component measured between the first large peak and following trough changes little during the formation of the type 1 fracture (waveforms 3, 4, 5, 6) or during uploading (waveforms 7). These amplitudes compare as 1, 1.5, 1.5, 1.3, 0.9 (i.e. the amplitudes remain approximately constant). Note that the polarity of the "unloading" waveform (7) is reversed, and that its shape coincides with that of the last "loading" waveform (6).

The amplitude of the high frequency component increases during formation of type 1 fracture. Amplitudes from waveforms 3,4, 5 and 6 compare as 1, 1.4, 2.1, 5.2 respectively The record of the "unloading" (waveform 7) is characterized

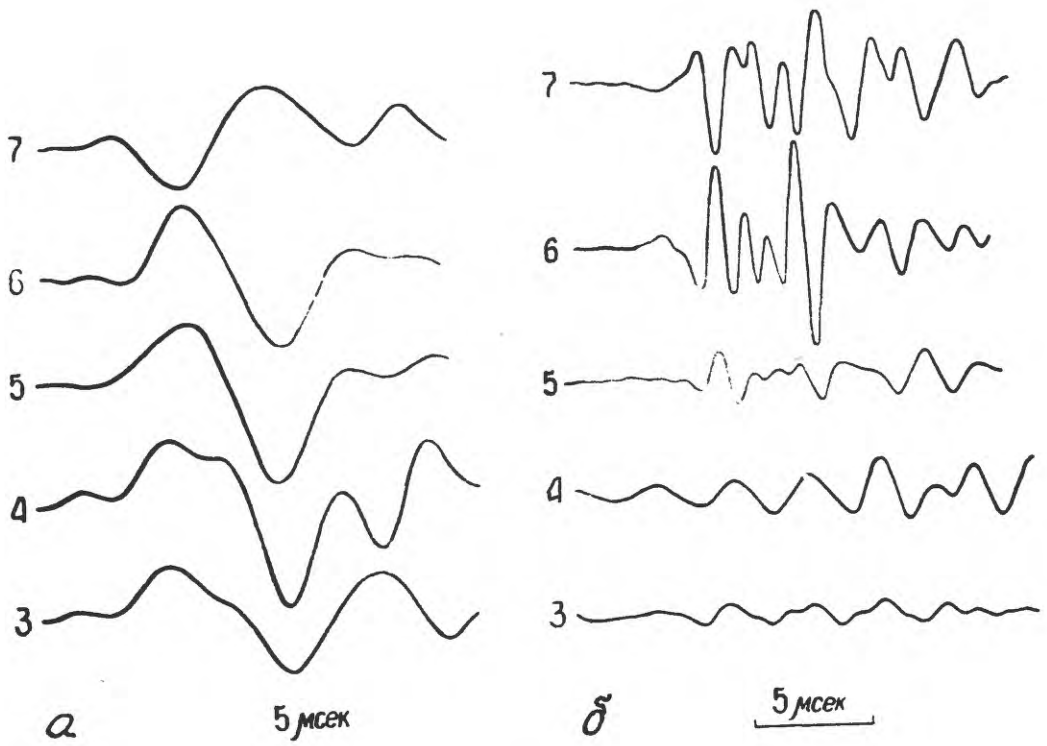

Figure 5. Recalculated filtered waveforms 3, 4, 5, 6 and 7 of Figure 4: (a) filtered through a low pass filter with a cutoff fe = 300 kHz. (b) bandpass filtered Δf =300kHz-1 MHz.

by a reversed polarity and a slightly smaller amplitude (-4.3) when compared with waveform 6.

The qualities of waveforms from type 1 fractures described above are also typical of the recorded events radiated by type 2 fractures (those which propagated from the external borders of holes to the sample edges). Additionally, the waveform shape and frequency content does not strongly depend upon the distance between the holes, sample size or transducer position. This is demonstrated in Figure 6 where a series of waveforms are shown. Waveform 1 is the same as 6 in Figure 4. It was emitted by a type 1 fracture during the final stage of its formation (experiment 28, size b). The transducer was in position 2 (Figure 1a).

Waveform 2 of Figure 6 was recorded during experiment 31, nominally identical to experiment 28 except that the distance between the holes was increased from 4.5mm to 10.5mm. Waveform 3 of Figure 6 was recorded during experiment 37 (size c), during the lengthening of a type 2 fracture. The transducer was in position -1. The distance between the holes was 7.7mm. The last waveform (4) of Figure 6 emanated from a type 1 fracture, also on a large sample (size c) during experiment 39. The distance to the epicenter from the transducer (located in position 6, (Figure 1a) was equal to 6mm. Comparison of the waveforms in Figure 6 shows that within the initial parts of each of the signals (first 5 μsec), the relative amplitudes of low and higher frequency components does not change.

Conclusion

The study of waveforms of AE events from fractures combined with SEM analysis of fracture structure and holographic investigation of the strain field during loading of pyrophyllite led us to several conclusions. The presence of two principal frequency ranges in the spectra can be explained by the presence of two failure elements of different size in each macrofracture. For large shear

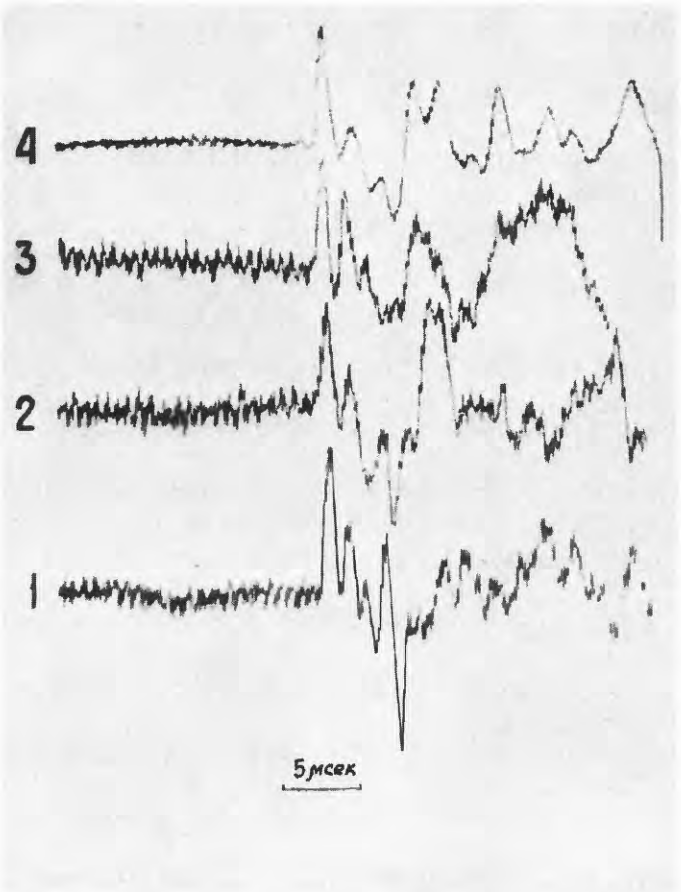

Figure 6. Waveforms recorded under different experimental conditions, i.e. with the various size samples and recorded at different transducer locations.

ruptures, both type 1 and 2 fractures contain length segments of first order with an average length $\tilde{l}_1$ = 2.5 - 5.0 mm and second order with $\tilde{l}_2$ = 0.5 - 1mm. The element lengths appear to be independent of sample size in the range investigated. It is reasonable to assume that the low and high frequency components of waveforms, f_l = 100 - 200 kHz and f_h = 200 - 600 kHz respectively, are radiated due to rupture of these elements. Emissions that may be due to rupture of smaller elements, (order 3 to 6) present in the fracture structure, were not recorded.

In these experiments as failure was approached we observed an increase in the ratio of high to low frequency amplitudes A_h/A_l as is in agreement with field observations (Rulev 1971, 1975).

The explanation proposed for field results, namely that the average normal stress across the fault is increasing (Rulev, 1975) is not sufficient to explain our results. We measured both the average stress (σ_1) and the local strain distribution and noticed that increasing A_h/A_l occurred even as σ_l decreased during the final stage of shear fracture formation. The increase in this ratio occurs due to changes in the value of the A_h.A_l remains constant. This phenomenon may be explained by the gradual breaking of progressively stronger or smaller rock bridges by en echelon like fractures or by stick slip movements along second order elements (length ~ 0.75mm). Naturally, these AE events occurred as local strains near the corresponding elements increased, as was seen with holography. The average stress along first order fracture elements however, was seen to either remain constant or even to decrease.

Acknowledgement

This work was carried out under the auspices of the Soviet-American Earthquake prediction program through U.S. Geological Survey contract DOIP32701. We wish to thank B. Salov, I.C. Getting and N. Brodsky for useful technical help and discussions.

REFERENCES

Blacic, J. D. and S. D. Malone, Preliminary analysis of micro acoustic signals associated with rock fracture, Geophys. Res. Lett. 4, 447-480, 1977.

Brune, J. N., Tectonic stress and the spectra of seismic shear waves from earthquakes, J. Geophys. Res. 75, 4997-5009, 1970.

Hanks, T. C. and M. Wyss, The use of body-wave spectra in the determination of seismic-source parameters, Bull. Seism. Soc. Amer., 62, 561-589, 1972.

Kostrov, B. V., On the crack propagation with variable velocity, Int. J. Fract. Mech., 11, 47-56, 1975.

Rautian, T. G., V. I. Khalturin, V. G. Martynov and P. Molnar, Preliminary analysis of the spectral content of P and S waves from local earthquakes in the Garm, Tadjikistan region, Bull. Seism. Soc. Amer. 68, 949-971, 1978.

Rulev, B. G., 1971. Earthquake and explosion as a double source of seismic waves. Experimental Seismology, Moscow, Nauka, (in Russian).

Rulev, B. G., 1975. The forecasting aspect of double frequencies of seismic wave radiation. Reports of Academy of Science USSR, 221, No. 6, (in Russian).

Shamina, O. G., Pavlov, A. A., and Strizkov, S. A., 1976. A modeling of shear displacement along a preexisting fault with friction. The study of Earthquake Physics, Moscow, Nauka, (in Russian).

Sobolev, G. A. and Koltzov, A. V., 1980. The study of microcracking in soft rock specimens. Physical Process in Earthquake Sources, Moscow, Nauka, (in Russian).

Sobolev, G. A., H. Spetzler and B. Salov, Precursors to failure in rocks while undergoing anelastic deformations, J. Geophys. Res., 83, 1775-1784, 1978.

Sondergeld, C. H., I. C.Getting, H. A. Spetzler and G. A. Sobolev, Velocity changes associated with generalized triaxial deformation of pyrophyllite, PAGEOPH, 118, 975-989, 1980.

Spetzler, H. A., G. A. Sobolev, N. Soga and H. Mizutani, About the mechanism of deformation and failure of PMMA samples under biaxial compression. Results of Soviet-American Collaboration on Earthquake Prediction, National Academy of Sciences of the USSR, Dushanbe, USSR, 1976, (in Russian).

Spetzler, H. A., G. A. Sobolev, C. H. Sondergeld, B. Salov, I. C. Getting and A. Koltsov, Surface deformation, crack formation and acoustic velocity changes in pyrophyllite under polyaxial loading, J. Geophys. Res., in press, 1980.

Wu, F. T., Thomson, K. C., and Kuenzler, H., 1972. Stick-slip propagation velocity and seismic source mechanism, Bull. Seism. Soc. Amer., 62, No. 6.

Vinogradov, S. D., 1978. The effect of heterogeneity of fault on the elastic wave radiation. Izvestia Academy of Science of USSR, Physics of the Earth, No. 1, (in Russian).

(page 295 follows)

Idealized Models of Fault Behavior Prior to Dynamic Rupture

by

B. V. KOSTROV

Institute of Physics of the Earth,

Academy of Sciences, Moscow, USSR

and

SHAMITA DAS

Lamont-Doherty Geological Observatory

of Columbia University

Palisades, New York 10964

Submitted to Bulletin of Seismological Society of America

ABSTRACT

We present a theoretical model, based on fracture mechanics concepts, of the behavior of an earthquake source prior to the occurrence of the earthquake, to understand under what conditions precursory slip may occur on a fault. We consider a two-dimensional fault consisting of in-plane periodic shear cracks and unbroken zones in an infinite, homogeneous elastic medium. Between the cracks of length 2a and the unbroken zones are 'intermediate' zones in which the stress drop occurs when a 'critical shear displacement' (CSD) is reached (Panasyuk-Dugdale model) at the crack-tip. The unbroken zones can also be interpreted in terms of friction as regions where the stress is lower than the static frictional stress, so that our model can be interpreted from the point of view of fracture or friction. Let the period of this system be 2d. As the load at infinity is slowly increased, the intermediate zones grow quasi-statically. It is found that when the cracks are very small or very large or the CSD is large, the intermediate zones will coalesce before the CSD is reached, i.e., the entire fault is ruptured and additional pre-seismic slip occurs. The initial conditions for dynamic rupture occurring at a later time on the fault is then a stress condition. Thus for the initial stages of the dynamic problem (not studied here) one need not solve a mixed boundary value problem but only the much simpler stress boundary problem. The rupture velocity of the dynamic rupture on such a fault which is entirely broken, may have any value up to the P-wave velocity, in principle. The average slip on the fault at the point of coalescence increases with crack size from zero at zero crack length up to $a/d \lesssim 0.67$ and then decreases to

zero at a/d = 1. The displacement distribution on the crack and the shear stress distribution around the crack as a function of increasing load and increasing crack size a/d are studied. It is shown that strain accumulation occurs not only at the ends of a Griffith crack but also in broad regions off the crack in the normal direction. This may be a possible explanation for occasionally observed aftershock clusters which lie off the fault. Corresponding to the unbroken zone, there is a similar zone but of strain release off the crack. This zone becomes more and more pronounced for large cracks and high loads. For very long cracks, the increase in shear stress off the crack becomes very very small but the decrease off the initially unbroken zone becomes very pronounced. Interaction between cracks is correctly accounted for in our method.

INTRODUCTION

In this paper, we develop a model to understand the physics of fault behavior prior to the occurrence of an earthquake. We do not claim to study a model which corresponds to a physically realistic fault, but only to study an oversimplified mechanical model of faulting, which has some of the characteristics of the real physical system, to gain insight into the effects of these characteristics on a real fault. Our model of faulting will allow different physical interpretations, depending on the scale we are looking at. Our model is scale independent but the interpretation of the results will be scale-dependent. The problem can be studied on any scale from the crystal to the geologic, so a term like 'real area of contact' is a relative concept, depending on the wavelength we are interested in. Thus, that which is called 'friction of rock' on one scale can be looked at, on a much smaller scale, as the 'fracturing of asperities' [Kragelskii, 1965; Barton, 1976; Teufel and Logan, 1978]. We shall first describe our model and then discuss its various physical interpretations.

Let the fault consist of a set of two-dimensional in-plane shear cracks with friction at equal distances apart in an infinite, homogeneous medium, which is linearly elastic everywhere off the crack plane (Figure 1). In between the cracks let there be unbroken regions shown by the shaded zones. Between the unbroken zones and the cracks are some 'intermediate' zones. These zones may be interpreted as zones of plastic deformation as in the Dugdale [1960] fracture model or as a zone of weakened connections or partially broken zones as in the Leonov-Panasyuk fracture model described by Kostrov and Nikitin [1970]. Two criteria are

required to determine the two edges of these intermediate zones - the two edges being the edge adjacent to the crack and the edge adjacent to the barrier - to see where the rupture process starts and ends. The first condition is that the stress at the crack-tip is finite, i.e., the stress-intensity factor is zero there. The second condition is that at the edge adjacent to the crack when the relative slip has reached some critical value, say $[u_o]$, the cohesive forces disappear, stress is allowed to drop and the crack allowed to grow. We shall call $[u_o]$ the 'critical-shear displacement' (CSD) (Figure 1) in analogy with the term 'crack-opening displacement' (COD) used for tension cracks. Figure 2 shows the shear stress at a point that is initially in the intermediate zone as a function of slip, for such a model. At first, the point slips quasi-statically at the stress level σ_y, say, until it reaches the CSD. It then drops to some value σ_f, say, which may be taken as the kinetic friction on the crack. Once σ_f is reached, dynamic rupture may occur but we do not consider that stage of the process in this paper, i.e. we confine our analysis to the stages when the shear displacement in the intermediate zone is less than the CSD. $[u_o]$ is thus the CSD required for the stress to drop. The stress level σ_y is interpreted as the 'yield point' for the Dugdale model and as the 'theoretical shear strength' for the Leonov-Panasyuk model. This CSD is the same as the D_o defined by Ida [1972] in his "cohesive-force diagram" for dynamic ruptures, and our Figure 2 is exactly the same as Ida's Model 1 but for the quasi-static problem. Palmer and Rice [1973] used a similar concept in their discussion of the "slip-weakening" model. These are the two possible interpretations of our model from the point of view of fracture.

We could now reinterpret the same model from the point of view of friction. Then we would take the unbroken zones on the fault to be zones where the two sides of the fault are actually physically separate but are stuck together due to the fact that the shear stress there is less than the static friction limit. Physically these would correspond to some 'asperities' [Bowden and Tabor, 1973] on the fault. $[u_o]$ would now be interpreted as the 'critical premonitory displacement' and σ_y would be the static frictional limit. In this case, in reality, the value of σ_y may not be constant for all slip less than $[u_o]$ and may actually be of the form shown by the dotted line in Figure 2. The stress at a point increases from the initial prestress level σ_o, say, to some higher level at which slip is initiated. The stress may continue to increase as slip occurs (strain-hardening) until it reaches σ_y and then drop to σ_f along the dotted line [Rummel et al., 1978; Rice, 1980; Dieterich, 1980; Wong, 1980]. However, we shall take it as constant in our calculations. The static friction on the fault may consist of two parts, that part which is proportional to the normal stress and that part which is called adhesion, and is independent of the normal stress.

We shall consider the fault system described above as the tectonic stress at infinity is slowly (quasi-statically) increased, and study the behavior of the cracks. Our condition is that as the stress is increased, the crack remains fixed in size until the CSD is reached. Only then can the crack extend. We shall determine when and under what conditions the intermediate zones of two adjacent cracks will coalesce before the CSD is reached. At coalescence additional pre-seismic slip occurs on the fault under constant stress, because it is not possible to increase the stress on the fault any further. Indeed, the shear stress is σ_f on the cracks, and

is σ_y between them so that the average stress is constant, which implies that the two sides of the fault may only slip as rigid bodies. Our results will also provide realistic initial conditions for the study of dynamic crack propagation problems, in which, up to now, the crack propagation has been initiated rather artificially.

Our model is a very idealized model and has, in particular, the following limitations. The geometry of crack distribution is two-dimensional and periodic and the loading is homogeneous. We take the stress to drop immediately from the value of σ_y to the kinetic frictional limit. For the solution of our problem, we need to take σ_y and σ_f as constant but the CSD may be taken as variable over the fault plane. We do not consider the rate dependence of fracture, friction, or of any other material property of the medium. (The rate dependence of fracture has been discussed, among others, by Kostrov and Nikitin [1970] and by Das and Scholz [1980]. The rate dependence of friction has been demonstrated by Scholz et al. [1972] and Dieterich [1978, 1979a, 1980].) This means that we allow the slip across the crack before coalescence of the intermediate zones to increase only when the load is increased whereas for rate-dependent fracture or friction, the shear displacement would increase with time, even for a constant load. In fact, for three-dimensional models where the unbroken zones are finite in the third dimension as well as when the rate dependence of fracture or friction is taken into account, the growth of the intermediate zones and hence the coalescence of the cracks would occur faster than in our present model. We have considered two-dimensional in-plane shear (Mode II) cracks but our solution <u>on</u> the crack plane is also valid for tension (Mode I) and anti-plane shear (Mode III) cracks, with the appropriate value of κ [Rice, 1968], where κ is defined in the glossary

below. We have considered an elastic medium but we expect the main features of our model to be observed even for visco-elastic media, although we do not study this case here. If the CSD is reached before coalescence, the crack extends but we shall not consider the problem of how it extends; i.e., does the fault now start extending dynamically or does it extend quasi-statically. In other words, is the process of growth and coalescence of these intermediate zones itself stable? To investigate this formally, we would need to study the energy balance of the whole system and this is clearly beyond the scope of this paper. All we say is that when the CSD is reached at a point, the stress there drops from σ_y to σ_f; this may or may not lead to dynamic rupture. Our results in this paper are thus valid only up to the time at which the CSD is reached or the intermediate zones have coalesced.

GLOSSARY OF SYMBOLS

a = crack (broken zone) half-length

b = length of intermediate zone + crack half-length

d = half-period of total system of broken, intermediate and unbroken zone

G = modulus of rigidity

p_o = cohesive force in unbroken zone, across crack plane, in the absence of normal compressive stresses

p, q = constants

S = value of shear stress on crack in terms of incremental stresses in broken zones

S_1 = value of shear stress on crack in terms of incremental stresses in intermediate zone

$[u_o]$ = critical shear displacement (CSD) required for stress-drop

$[u]^{NOR}_{COALESCENCE}$ = normalized shear displacement at crack tip at the point of coalescence of the intermediate zone

$[u]^{NOR}_{AV}$ = normalized shear displacement averaged over the fault plane

$[u]_{\xi_1}$ = value of displacement discontinuity in displacement component u_1 across crack plane, at $\xi = \xi_1$

u_1, u_2 = displacements

u_1', u_2' = derivatives of u_1, u_2, w.r.t., x_1, respectively

x_1 x_2 = coordinates

z = complex quantity $x_1 + ix_2$

$\bar{z}$ = complex conjugate of z

[any quantity] = jump of quantity across crack plane

{any quantity} = quantity$_+$ $(x_1 + i0)$ + quantity$_-$ $(x_1 - i0)$

$\alpha = \tan \frac{\pi a}{2d}$

$\beta = \tan \frac{\pi b}{2d}$

ζ = complex quantity $\xi + i\eta$

η = imaginary axis in ζ -plane

κ = $3 - 4\nu$ for mode I and II cracks
= 3 for mode III cracks

λ = Lamé parameter

μ = coefficient of kinetic friction on crack

μ_1 = coefficient of static or internal friction depending on interpretation of our model

ν = Poisson's ratio

ξ = real axis in ζ-plane

σ_{ij} = stress components

σ_{ij}^{∞} = stress applied at infinity

σ_{12}^{NOR} = value of σ_{12} normalized by stress drop $(S_1 - S)$

σ_f = frictional stress on crack region

σ_y = yield point for Dugdale model

= theoretical strength for Panasyuk model

= static frictional limit for friction model

τ_{ij} = incremental stress components

τ_{12}^{NOR} = value of τ_{12} normalized by stress drop $(S_1 - S)$

ϕ, ψ = analytic functions (of Mushkehilishvili)

Φ, Ψ = $\frac{d\phi}{dz}$, $\frac{d\psi}{dz}$, respectively

$\overline{\Phi}$ = complex conjugate of Φ

Φ' = $\frac{d\Phi}{dt}$

Φ_1 = analytic functions of z

Φ_* = analytic function of ζ

FORMULATION OF THE PROBLEM

Let us consider an infinite periodic set of in-plane shear (Mode II) cracks of length 2a distributed along the x_1-axis as shown in Figure 1. The x_1-coordinate of the intermediate zones at the ends of the crack extends to $\pm$ b for the crack closest to the origin and these zones are shown by the hatched regions. The regions between the cracks are taken as unbroken, indicated by the solid shading. These unbroken regions may be regions where the two sides of the fault are actually physically unbroken or they may be regions where the two sides of the fault are actually physically separate but the two sides are held together by friction. The same mathematical model which we develop here will permit these different interpretations. The intermediate zones will be taken to have the properties discussed in the introduction, of the Dugdale-Panasyuk fracture model. The period of the whole system of crack, intermediate zone and unbroken zone is taken as 2d. Let the whole system be under a homogeneous stress field σ^{∞}_{ij}, applied at infinity. Let u_1 and u_2 denote the displacement on the crack plane in the x_1 and x_2 directions and let $[u_i]$ denote the displacement discontinuity of u_i across the plane $x_2 = 0$. We will use [ ] from here on to denote the discontinuity of quantities across the $x_2 = 0$ plane. The friction acting on the cracked or broken portions of the crack plane will be given by

$$\sigma_{12} = -\mu\sigma_{22} \tag{1}$$

where μ is the coefficient of kinetic friction on the broken portions of the crack plane. The normal stress σ_{22} does not change on the crack plane due to the presence of the crack or due to the extension of the crack. Equation (1) is simply Coulomb's law without static limit. If $[u_o]$ is the CSD, then the broken parts of the crack plane are defined by the relation $[u_1] \geq [u_o]$. For the unbroken parts of the crack plane, i.e., where $[u_1] = 0$, we have the condition that the tangential stress is less than the limiting static frictional yield stress. This gives for these regions, the condition

$$\sigma_{12} + (\mu_1 \sigma_{22} - p_o) \leq 0, \tag{2}$$

where p_o is the cohesive force acting across the crack plane in this region in the absence of normal compressive stresses and μ_1 is the coefficient of static friction in these regions. (For regions that are actually unbroken, μ_1 has to be interpreted as the 'coefficient of internal friction'.) For the intermediate zones, the tangential stress is just equal to the limiting frictional stress and sliding is permitted but is always less than the CSD $[u_o]$. Such regions are thus defined by the relation $0 \leq [u_1] \leq [u_o]$ and the stress condition here is

$$\sigma_{12} + \mu_1 \sigma_{22} - p_o = 0 \tag{3}$$

Figure 3 shows one set of these cracks with these conditions marked on it. We have two further conditions. Firstly, $[u_2] = 0$ all over the crack (i.e., the crack is closed) and secondly, σ_{i2} is continuous across the crack plane $x_2 = 0$; i.e.,

$$[\sigma_{i2}] = 0.$$

Rewriting all the above conditions in terms of the incremental stress τ_{ij} where $\tau_{ij} = \sigma_{ij} - \sigma^{\infty}_{ij}$, we finally get the boundary conditions for our problem as follows.

$$[u_2] = 0, \quad -\infty < x_1 < \infty, x_2 = 0 \tag{4}$$

$$[\tau_{i2}] = 0, \quad -\infty < x_1 < \infty, \ x_2 = 0 \tag{5}$$

On the unbroken parts, i.e., $a + b \leq \left|x_1 - nd\right| \leq d$, where $n = -\infty, \ldots -1, 0, 1, \ldots \infty$, we have

$$[u_1] = 0, \quad \tau_{12} + \mu_1 \tau_{22} \leqq p_0 - \sigma^{\infty}_{12} - \mu_1 \sigma^{\infty}_{22} = S_1, \text{(say)} \tag{6}$$

For the intermediate zones, i.e., $a \leq \left|x_1 - nd\right| \leq a + b$, we have

$$[u_1] \leqq [u_0], \ \tau_{12} + \mu_1 \tau_{22} = S_1 \tag{7}$$

On the broken parts, i.e., $\left|x_1 - nd\right| \leq a$, we have

$$[u_1] \geqq [u_0], \ \tau_{12} + \mu \tau_{22} = -\sigma^{\infty}_{12} - \mu \sigma^{\infty}_{22} = S, \text{ (say)} \tag{8}$$

Equations (4) through (8) give the complete set of boundary conditions for the problem.

The governing equations for the system are the equations of equilibrium

$$\tau_{ij,j} = 0 \text{ where } \tau_{ij} = \lambda \delta_{ij} u_{k,k} + C \left(u_{i,j} + u_{j,i}\right)$$

G is the modulus of rigidity, and λ is Lamé's parameter.

We also have the condition that the incremental stress τ_{ij} and the displacement components u_i vanish at infinity.

SOLUTION OF THE PROBLEM

The solution to this problem is generally known. Bilby, Cottrell, Smith and Swinden [1963], Bilby and Swinden [1965], and Smith [1966] have determined the solution for the length of the plastic zone and the crack-opening displacement at the crack-tip, for a periodic crack system. (COD and CSD are exactly the same, respectively, for Mode I and II as discussed earlier.) We shall need several relationships in our study which were not determined by these authors so we redo the solution. Then we can write the stresses and displacements in rectangular coordinates as

$$\tau_{22} + \tau_{11} = 2(\Phi + \overline{\Phi}) = 4 \operatorname{Re} \Phi \tag{9}$$

$$\tau_{22} - \tau_{11} + 2i\tau_{12} = 2(\overline{z}\Phi' + \Psi) \tag{10}$$

$$2G(u_1 + iu_2) = \kappa\varphi(z) - z\overline{\Phi} - \overline{\psi(z)} \tag{11}$$

where $\kappa = (3-4\nu)$ for plane strain problems and ν is Poisson's ratio and $\Phi = d\phi/dz$ and $\Psi = d\psi/dz$. ϕ, ψ, Φ and Ψ are analytic over the whole z-plane, except some parts of the x_1-axis where the displacement discontinuity occurs. Also since τ_{ij} and u_1, u_2 vanish at ∞, Φ and $\Psi \to 0$, as $z \to \infty$ along any path parallel to the real axis. Taking the derivative of (11) with respect to x_1, we get

$$2G(u_1' + iu_2') = \kappa\Phi - \overline{\Phi} - z\Phi' - \overline{\Psi} \tag{12}$$

Taking the complex conjugate of (12) and adding it to the sum of (9) and (10) we get

$$\tau_{22} + i\tau_{12} + 2G(u_1' - iu_2') = (\kappa + 1)\overline{\Phi} \tag{13}$$

Taking the imaginary part of (13) and remembering that [ ] denotes discontinuities of quantities across the $x_2 = 0$ plane, we get

$$[\tau_{12}] - 2C[u_2'] = (\kappa + 1)Im[\Phi]$$

which gives $Im[\Phi] = 0$ using (4) and (5)

$$i.e., \quad [\Phi - \overline{\Phi}] = 0 \tag{14}$$

Denoting $\overline{\Phi(\overline{z})} = \Phi_1(z)$, to indicate that it is an analytical function of z, we finally get $[\Phi + \Phi_1] = 0$ over the $x_2 = 0$ plane. Now $\Phi + \Phi_1$ is analytic over the whole z-plane and vanishes at ∞. Hence, by Liouville's theorem,

$$\Phi + \Phi_1 = 0 \quad \text{everywhere on the z-plane.} \tag{15}$$

Adding (9) and (10) and considering the discontinuity of this relation across $x_2 = 0$ and using (5), we get

$$[\Phi - \Phi_1 + z\Phi' + \Psi] = 0 \qquad \text{and again by Liouville's theorem,}$$

$$\Psi = \Phi_1 - \Phi - z\Phi' = -2\Phi - z\Phi' \tag{16}$$

Hence we have reduced the problem to finding only one analytic function and we can now write the required stresses and displacements in terms of it, as

$$\begin{aligned} \tau_{22} + i\tau_{12} &= \overline{\Phi} + \Phi_1 + (\overline{z} - z)\Phi' \\ &= \overline{\Phi} - \Phi + (\overline{z} - z)\Phi' \end{aligned} \tag{17}$$

and $$\tau_{22} - \tau_{11} + 2i\tau_{12} = 2(\bar{z}\Phi' + \Psi)$$

and $$2G(u_1' - iu_2') = (\kappa + 1)\bar{\Phi} - (\tau_{22} + i\tau_{12}) \tag{18}$$

On the crack plane $x_2 = 0$, these reduce to

$$\tau_{22} + i\tau_{12} = \bar{\Phi} + \Phi_1 \tag{19}$$

and $$2G(u_1' - iu_2') = (\kappa + 1)\Phi \tag{20}$$

The boundary conditions (6) through (8) then can be reduced, using the properties of Φ determined above, to

$$[\Phi] = 0 \qquad \text{on the unbroken parts of the } x_2 = 0 \text{ plane} \tag{21}$$

$$\{\Phi\} = -iS_1 \qquad \text{on the intermediate zones} \tag{22}$$

$$\{\Phi\} = -iS \qquad \text{on the broken zones,} \tag{23}$$

where $\{\Phi\} = \Phi^+(x_1 + i0) + \Phi^-(x_1 - i0)$ and the + and - mean that the value of Φ is determined on the $x_2 = 0$ plane by approaching it along the positive and negative portions of the x_2-axis.

Due to the periodicity of the geometry of our problem, we may guess that the solution would also be periodical. Assuming this, we consider the conformal transformation

$$\zeta = \tan\frac{\pi z}{2d} = i\frac{1 - \exp(\frac{i\pi z}{d})}{1 + \exp(\frac{i\pi z}{d})} \tag{24}$$

where $\zeta = \xi + i\eta$

Then $\alpha = \tan\frac{\pi a}{2d}$

$\beta = \tan\frac{\pi b}{2d}$

and $\zeta \to \infty$ at $z = d$.

The ζ-plane is shown in Figure 4. Each set of the cracks maps onto the same portions of the ξ-axis.

Let us consider a solution of Φ of the form

$$\Phi = -i\frac{S_1}{2} + \Phi_*$$

where $\Phi_* = \frac{F}{\sqrt{\zeta^2 - \beta^2}}$

Then, $\Phi_*^+ + \Phi_*^- = \frac{F^+}{i\sqrt{\beta^2 - \xi^2}} - \frac{F^-}{i\sqrt{\beta^2 - \xi^2}} \quad . \quad |\xi| < \beta$

$$= \frac{[F]}{i\sqrt{\beta^2 - \xi^2}}$$

$$[F] = i\sqrt{\beta^2 - \xi^2}\,\{\Phi_*\}, \quad |\xi| < \beta \tag{25}$$

The boundary conditions (21) through (23) can be rewritten in terms of F as

$$[F] = \begin{cases} \sqrt{\beta^2 - \xi^2}\,(S - S_1) & \text{if } |\xi| < \alpha \\ 0 & \text{if } |\xi| > \alpha \end{cases} \tag{26}$$

The solution of F can be written in terms of Schwartz's integral as

$$F = \frac{1}{2\pi i}\int_{-\alpha}^{\alpha} \frac{[F]\,d\xi}{\xi - \zeta} + (p + q\zeta)i$$

where p and q are real constants and then finally, we obtain the solution of Φ as

$$\Phi = \frac{S_1}{2i} - \frac{(S - S_1)}{2\pi} \ln \left(\frac{\dfrac{i\xi}{\sqrt{\xi^2 - \beta^2}} - \dfrac{\alpha}{\sqrt{\beta^2 - \alpha^2}}}{\dfrac{i\xi}{\sqrt{\xi^2 - \beta^2}} + \dfrac{\alpha}{\sqrt{\beta^2 - \alpha^2}}} \right) \tag{27}$$

The terms of the form $(p + q\zeta)i$ vanish due to the condition that the stresses are finite at the crack tip $\xi = \beta$. Using the condition that $\Phi = 0$ as $z \to \infty$ along any path parallel to the real axis x_1, which in the complex plane ζ is the condition that $\Phi = 0$ at $\zeta = \pm i$, we get the relation to determine β in terms of α and the loading parameters S and S_1 as

$$\frac{\alpha\sqrt{1 + \beta^2}}{\sqrt{\beta^2 - \alpha^2}} = \tan\frac{\pi S_1}{2(S_1 - S)} \tag{28}$$

Equation (28) can easily be reduced to equation (227) of Rice [1968] using appropriate notation. Substituting the value of Φ into (20) and integrating, we find the displacement discontinuity $[u_1]$ at any point, say ξ_1, $(0 < \xi_1 < \beta)$ is given by

$$\frac{\pi^2 G[u]_{\xi_1}}{2(\kappa+1)(S_1-S)d} = \int_{\beta}^{\xi_1} \ln \left| \frac{\dfrac{\xi}{\sqrt{\beta^2-\xi^2}} - \dfrac{\alpha}{\sqrt{\beta^2-\alpha^2}}}{\dfrac{\xi}{\sqrt{\beta^2-\xi^2}} + \dfrac{\alpha}{\sqrt{\beta^2-\alpha^2}}} \right| \frac{d\xi}{1+\xi^2} \qquad (29)$$

We define the left-hand side of the above equation to be $[u]^{NOR}$. The condition for the cracks to coalesce <u>before</u> reaching some critical value of shearing displacement, CSD, is given by

$$\frac{\pi^2 G\ CSD}{2(\kappa+1)(S_1-S)d} \geq \int_{-\alpha}^{\alpha} \ln \left| \frac{\xi-\alpha}{\xi+\alpha} \right| \frac{d\xi}{1+\xi^2} \qquad (30)$$

The left-hand side of the above inequality is defined by us as $[u]^{NOR}_{COALESCENCE}$. The right side can be reduced to equation (228) of Rice [1968], with appropriate notation. The CSD is a material constant but can be variable as a function of position on the fault. The average value of the displacement over the whole zone of length d at coalescence is given by

$$\frac{\pi^2 G[u]_{AV}}{2(\kappa+1)(S_1-S)d} = -\alpha \int_0^1 \ln \left| \frac{\eta-1}{\eta+1} \right| \left(\frac{\text{atan } \alpha/\eta}{\alpha^2+\eta^2} + \frac{\text{atan } \alpha\eta}{1+\alpha^2\eta^2} \right) d\eta \qquad (31)$$

The left-hand side of the above equation is defined by us as $[u]^{NOR}_{AV}$.

The stress component τ_{12} around the crack is obtained, using (17) and (27) as

$$\tau_{12} = S_1 - (S_1-S)\,\text{Im} \left(\frac{1}{\pi} \ln \frac{\dfrac{\xi}{\sqrt{\beta^2-\xi^2}} - \dfrac{\alpha}{\sqrt{\beta^2-\alpha^2}}}{\dfrac{\xi}{\sqrt{\beta^2-\xi^2}} + \dfrac{\alpha}{\sqrt{\beta^2-\alpha^2}}} - \frac{(1+\xi^2)\alpha x_2 \sqrt{\beta^2-\alpha^2}}{d(\xi^2-\alpha^2)\sqrt{\xi^2-\beta^2}} \right) \qquad (32)$$

Writing

$$\sigma_{12}^{NOR} = \frac{-S}{S_1 - S}$$

and

$$\tau_{12}^{NOR} = \frac{\tau_{12}}{S_1 - S}$$

and using (6) and (8), we get, finally,

$$\tau_{12}^{NOR} = (1 - \sigma_{12}^{NOR}) - \mathrm{Im}\left(\frac{1}{\pi} \ln \frac{\frac{\xi}{\sqrt{\beta^2-\xi^2}} - \frac{\alpha}{\sqrt{\beta^2-\alpha^2}}}{\frac{\xi}{\sqrt{\beta^2-\xi^2}} + \frac{\alpha}{\sqrt{\beta^2-\alpha^2}}} - \frac{(1+\xi^2)\alpha x_2 \sqrt{\beta^2-\alpha^2}}{d(\xi^2-\alpha^2)\sqrt{\xi^2-\beta^2}} \right) \quad (33)$$

as the expression for the dimensionless shear stress component around the crack. The normalization factor (S_1 - S) is the stress drop at the crack tip when the CSD is reached.

In the next section, we show the results obtained using the equations developed in this section. The integrations in (29) and (30) are done numerically using Simpson's quadrature formula, with variable spacing to account for integration at points where the integrand has (integrable) singularities.

RESULTS

Condition for coalescence of intermediate zones prior to CSD being reached

This condition is given by equation (30). The solid line in Figure 5 shows the right-hand side of equation (30) against the normalized crack length a/d. The abscissa also shows the values of the real area of contact (for the two-dimensional problem, one should really say 'real length of contact') corresponding to the values of a/d. For any a/d and CSD (which is a material property) above this line, coalescence will occur before the CSD is reached. For all materials, we see that for very small and very large cracks this condition is satisfied. It may at first seem surprising that the condition is satisfied for very small cracks, but it makes sense when we realize that for a given CSD, the length of the intermediate zone is very large for very small cracks. For materials for which the normalized CSD is always above $\sim$1.01 (the maximum value of $[u]^{NOR}_{COALESCENCE}$ in Figure 5) will always occur prior to the CSD being reached. Let us study the normalization factor for the $[u]^{NOR}_{COALESCENCE}$ to see if we can determine when this may occur in realistic situations. Table 1 shows the values of the factor $\pi^2 G/[2(\kappa+1)(S_1-S)]$ for the three physical interpretations of our model, the meanings of S_1 and d for the models, and the approximate minimum values (order of magnitude estimates) of the quantity CSD/d for coalescence to occur for all crack sizes a/d. The quantity (S_1-S) CSD is the same as the usual definition of the 'fracture energy' in fracture mechanics [see, e.g., Palmer and Rice, 1973]. We see that for the three models if the CSD is larger than 1%, 0.1%

TABLE 1. $\nu = 0.25$, $\kappa = 2$, $\frac{\pi^2}{2(\kappa+1)} = 1.65$

Model Interpretation	Physical Interpretation of S_1	Physical Interpretation of d	Physical Interpretation of CSD	Order of Magnitude Estimate of (S_1-S)	$\frac{\pi^2}{2(\kappa+1)} \frac{G}{S_1-S}$	Minimum Value of CSD/d for Coalescence (order of magnitude)
Panasyuk	Theoretical strength (in shear)	Wavelength of inhomogeneities or distance between microcracks	Critical shear displacement	G/10	16.5	0.01
Dugdale	Yield stress (in shear)			G/100	165	0.001
Friction	Static limiting friction	Wavelength of roughness	Critical premonitory displacement	G/1000	1650	0.0001

magnitude estimates only) of the wavelength of heterogeneities or roughness, the condition for coalescence will always be met. If the condition for coalescence prior to the CSD being reached is met, then additional preseismic slip equal to the difference between the CSD and $[u]_{x_1=a}$ will occur on the fault since the stress on the fault cannot then be increased any further, so that the two sides of the fault will now slip as rigid bodies until the CSD is reached at extremity.

Since preseismic slip is observed to occur before stick-slip in laboratory friction experiments [Scholz et al., 1972; Dieterich, 1979a], this may mean that the required condition is met in these experiments. The quantity d_c measured by Dieterich [1979a] in friction experiments in the laboratory is twice our 'critical premonitory displacement' [Rice, 1980], but his definition of surface roughness is clearly different from our 'wavelength of roughness' d. Using Dieterich's [1979a] values for CSD which are of the order of 1-10 μm, we would need a d $\lesssim$ of the order of 1-10 cm from the last column of Table 1 for coalescence to occur prior to the CSD being reached. Rummel et al. [1978], on the other hand, find values of the order of 0.2 to 0.5 mm, for friction as well as fracture experiments, and Wong [1980] finds similar values from fracture experiments. This would mean that d $\lesssim$ of the of 5 m for friction experiments and d $\lesssim$ of the order of 0.5 m for fracture experiments for coalescence (Dieterich's [1979a] experiments were conducted under a compressive stress of 6 MPa whereas those of Rummel et al. [1978] were done under a compressive stress of 500 MPa (5 kbar) [Rice, 1980].)

To predict from our model whether coalescence should occur prior to the CSD being reached in the earth, clearly depends on good estimates of CSD and d. We also face the usual problem of scaling of laboratory results

to natural faults, as has been discussed by, e.g., Rice [1980]. Rice [1980] suggests that as the fault area increases, the CSD may increase. On the other hand, Sayles and Thomas [1978] have suggested from observations of different size surfaces, that the wavelength of roughness of topography is also a function of the sample size. Such concepts are certainly not well understood at this time, but our work indicates the need for further study of these properties and reliable estimates of CSD and d.

Average slip on fault at time of coalescence of intermediate zones

$[u]_{AV}$ determined in equation (31) is just the part of preseismic slip occurring before the coalescence of the intermediate zones. The normalized value of $[u]_{AV}$ as a function of a/d are shown by the dotted line in Figure 5. It can be seen from this figure that $[u]^{AV}$ reaches its maximum value at $a/d \simeq 0.67$, is less than the CSD for small a/d and greater than the CSD for large a/d. In other words, $[u]_{AV}$ may be much larger than the slip at the crack edge for small values of the real area of contact. As a result, the critical premonitory slip observed as average over the fault is not directly connected with the CSD which is a local characteristic of the strength of the material. It may be possible to use the comparison between $[u]_{AV}$ and CSD in Figure 5 to determine the CSD. For example, if we know d, the wavelength of roughness or inhomogeneities and we conduct a fracture or friction experiment on a rock to determine $[u]_{AV}$, the pre-slip, then using Figure 5 we can obtain an order of magnitude estimate of the CSD. The values of the CSD thus obtained will be of interest in understanding behavior of materials during fracture and in problems of determining the energy absorption at the crack-tip.

Compliance of fault at coalescence

Let us now consider the quantity $[u]_{AV}/(\sigma_{AV}-\sigma_f)$, where σ_{AV} is the average stress on the fault at coalescence, so that the denominator is the average stress drop on the fault at coalescence. This quantity has the same units as the term 'compliance of an asperity' [c.f., e.g., Walsh and Grozenbaugh, 1979] used in studies of contact of two rough surfaces in compression. In analogy with this, we shall call $[u]_{AV}/(\sigma_{AV}-\sigma_f)$ the 'average compliance in shear' of the fault and its reciprocal the 'average stiffness of the fault'. To explain this definition further, we plot qualitatively, the form of $[u]_{AV}$ as a function of σ_{AV} in the inset at the top left-hand corner of Figure 6. The dotted line indicates the value of σ_{AV} at coalescence and the dashed line shows the expected form of $[u]_{AV}$ against σ_{AV} for the purely elastic problem. Then, $[u]_{AV}/(\sigma_{AV}-\sigma_f)$ is the average or secant compliance at coalescence. The local (or tangent) compliance at coalescence is obviously infinite because the slip $[u]_{AV}$ will now increase without any increase of σ_{AV} (rigid body motion). The deviation of $[u]_{AV}$ from the elastic line is due to the increase in the lengths of the intermediate zone. The dependence of the maximum (at coalescence) dimensionless compliance on the length of the initial crack (or real area of contact) is shown in Figure 6. This quantity is found to increase with a/d until $a/d \lesssim 0.96$, after which it decreases sharply and is undefined at $a/d = 1$. Hence the average compliance of the fault depends on the lengths of the initial cracks in the medium. The fault is more compliant when the initial cracks in the medium are larger but when the initial cracks are very long so that the fault is effectively pinned at small asperities, the fault becomes stiffer, according to our model.

Displacement distribution on the fault

Figure 7 shows the normalized displacement distribution $[u]^{NOR}$ as a function of normalized position x_1/d along the crack [equation (29)], for one period d. For a given crack length a/d, the maximum possible values of the normalized stress σ_{12}^{NOR}, i.e., the value at which coalescence occurs, is found, from condition (28), to be (1-a/d). We plot $[u]^{NOR}$ at different stress levels for different crack sizes. For short cracks and low loads, the intermediate zone is extremely short and the interaction between cracks is negligible so that the displacement distribution is almost the same as expected for a single Mode II Griffith crack. The expected value at the center for the Griffith crack, using our normalization factor, is 0.12 and our value with the small intermediate zone present is 0.10.

The topmost line in each figure is the displacement at the maximum possible value of σ_{12}^{NOR}, i.e., just at the time of coalescence of the intermediate zones. For a given a/d, as the stress is increased, the growth of the intermediate zone is very well illustrated in our figure. As the crack length a/d is increased, the final displacement at the point of coalescence increases until a/d reaches 0.5 and then starts decreasing. This is due to the fact that the stress level at coalescence for larger a/d is lower.

Shear stress distribution around the fault

Figure 8 shows the normalized incremental stress component τ_{12}^{NOR} (equation (32)) as a function of $(x_1/d, x_2/d)$ for $\sigma_{12}^{NOR} = 0.01$ and $a/d = 0.01$, i.e., a very short crack and a very low load. We plot τ_{12}^{NOR} in a region three times the crack length in the x_1 and x_2 directions. We expect the stresses to be very similar to a single Griffith in-plane shear crack, and the intermediate zones are very small. The expected stress concentration at the crack tip can be seen. Along the x_2-direction it is found that the stress does not monotonically approach the zero value of τ_{12}^{NOR} at infinity, but actually changes sign and decreases to zero from a positive value. Figure 9 shows τ_{12}^{NOR} as a function of x_2/d for the same case. The change in sign of τ_{12}^{NOR} occurs at exactly half the crack length away along x_2. For our parameters, this increase is about 10% of σ_{12}^{NOR}. An increase of about this size from theoretical calculations (Kostrov and Friedman, unpub. data) was reported in Osokina and Tsvetkova [1979a] and by Niewiadomski [1975], and found in laboratory experiments by Gzovsky et al. [1974], for a single Griffith in-plane shear crack. Segall and Pollard [1980] calculated the shear stress field around a single crack and our contour plot of Figure 8 agrees with their corresponding figure, but they do not show the small increase of shear stress along x_2 or discuss its implications. This is a test for our calculations. Two-dimensional constant slip dislocation models [Chinnery, 1963; Smith and Van de Lindt, 1969] also show an increase in τ_{12} off the fault plane. Thus, regions of strain accumulation occur not only at the ends of faults but also in broader regions in directions normal to the fault surface. Superposition

of these broad regions in areas with many parallel faults leads to discovery of broad high stress zones parallel to the faults. A detailed discussion of this effect and resulting patterns of strain accumulation in California is given by Smith and Van de Lindt [1969] for California and by Osokina et al. [1979a,b,c] for California and Central Asia. Clusters of aftershocks can sometimes be seen off the fault in these regions of strain increase, e.g., the 1968 Borrego Mountain earthquake [Hamilton, 1972], the 1979 Homestead Valley earthquake [Hutton et al., 1980] in California, as discussed by Das and Scholz [1981], the 1972 Managua, Nicaragua earthquake [Ward et al., 1974].

Figures 10a-d show the distribution of τ_{12}^{NOR} in a region three times the crack size, for a/d = 0.01, for σ_{12}^{NOR} = 0.5, 0.8, 0.95, 0.985 (almost at coalescence). One quadrant of the x_1-x_2 plane is shown. The other quadrants are simply mirror reflections of this quadrant about the x_1 and x_2 axes. The maximum value of σ_{12}^{NOR}, i.e., at coalescence, can be determined from equation (28) as (1-a/d). Figure 10e shows τ_{12}^{NOR} for a/d = 0.01 and σ_{12}^{NOR} = 0.985 but now the total half-period d is shown. As σ_{12}^{NOR} increases, the length of the intermediate zone grows larger, the stress concentration at the crack tip becomes stronger and the level and distance from the crack of the increase in τ_{12}^{NOR} in the x_2 direction increases. At the same time a minimum in τ_{12}^{NOR} at $x_1/d = 1$ in the x_2 direction develops and decreases and occurs at slightly higher x_2/d until at σ_{12}^{NOR} = 0.985 it occurs at $x_2/d = 0.84$. From our calculations for the case shown in Figure 10e, the maximum extent of the increase along x_2 at $x_1/d = 0$ is of the order of the half-period d of the roughness or inhomogeneities.

Figures 11a-c show τ_{12}^{NOR} for $a/d = 0.5$ for $\sigma_{12}^{NOR} = 0.01,\ 0.4,\ 0.499$. The size of the region shown is one half-period d in both the x_1 and x_2 directions. As the crack length a/d increases, comparing Figures 8 and 11a we see that the maximum along x_2 decreases for the same σ_{12}^{NOR}. The development of the negative along the x_2 at $x_1/d = 1$ is starting to be seen and in Figures 11b and 11c is very clearly seen. The classic lobes seen for the Griffith crack are distorted in Figure 11a and completely disappear in Figure 11c. Figure 11c is particularly interesting. The crack length is exactly half the period, so that at coalescence exactly half the period d is the broken zone and the other half is the intermediate zone. τ_{12}^{NOR} is found to be anti-symmetric about $x_1/d = 0.5$. Thus, corresponding to the increase in τ_{12}^{NOR} along $x_1/d = 0$, there is a decrease in τ_{12}^{NOR} along $x_1/d = 1$.

Figure 12 shows τ_{12}^{NOR} for $a/d = 0.9$ and $\sigma_{12}^{NOR} = 0.1$. There is still a 'bump' in τ_{12}^{NOR} along the x_2 axis at $x_1/d = 0$, i.e., τ_{12}^{NOR} does not go monotonically to zero at infinity. The negative 'bump' in τ_{12}^{NOR} along x_2 at $x_1/d = 1.0$ is very clear. Note that the lobes at the end of the crack which usually point away from the crack now point towards the crack, i.e., one can seen the effect of the interaction between adjacent cracks.

All our results in this paper are for the elastic medium. For a viscoelastic medium, it can be shown that the stress component τ_{12} will be the same as for the elastic body so our results for τ_{12} (and only for τ_{12}) are also true for the viscoelastic medium.

CONCLUSIONS

We have developed a simple idealized mathematical model to gain insight into the processes that may occur on a fault prior to the occurrence of an earthquake. The fault plane consists of broken and unbroken zones with intermediate zones in between. For stress drop to occur at any point of the intermediate zone, the slip there has to reach some critical value, which we called the CSD (critical shear displacement) and then the broken zone will extend. We increase the load at infinity and study the condition under which coalescence of the intermediate zones may occur prior to the CSD being reached. We show that the necessary conditon is satisfied for very small and very large cracks or if the CSD is large. Experimental values of CSD are not available. We have shown by using order of magnitude estimates of the other parameters in the problem that if the CSD is larger than the order of 1%, 0.1%, or 0.01% of the wavelength of roughness (or inhomogeneity, as the case may be) for the Panasyuk, Dugdale, and frictional models. respectively, the condition for coalescence prior to the CSD being reached will be satisfied. Once this condition is met, seismic pre-slip will occur on the fault since any further increase of load will cause the two sides of the faults to slip as rigid bodies. In reality since the CSD along the fault will be variable, the pre-slip will be confined to certain portions of the fault. The limitation in our model due to the assumption of periodicity of crack distribution prevents us from getting any idea of the size and distribution of such zones of pre-slip on real faults. The coalescence of the intermediate zones prior to the CSD being reached physically means that the fault plane is completely ruptured. The initial conditions for any ensuing dynamic rupture on such

regions of the fault is then a stress condition. Thus for the initial stages of the dynamic problem (not studied here) we need only solve a problem with stress boundary conditions rather than the more complex mixed boundary value problem. The rupture velocity of the dynamic rupture on such a fault which is entirely broken may have any value up to the P-wave velocity, in principle. We did not solve the dynamic problem in this paper but only indicate that the results of our work have these implications for the dynamic rupture problem.

We also study the slip on the crack and stress distribution around the crack, as the load is slowly increased until coalescence occurs. For very small cracks and very low loads which is a good approximation to a single Griffith crack, our results agree with those for a single Griffith crack. The increase in shear stress off the fault in the normal direction for such cracks is used to explain the occurrence of two clusters of aftershocks of the 1968 Borrego Mountain earthquake and the 1979 Homestead Valley earthquake, which lie off the fault in the normal direction from the fault. Since the increase in the stress off the fault is found to be very low, this may imply that the pre-stress in the region around this fault is close to the stress required for rupture. For cracks with intermediate zones comparable to the crack size, there are alternating regions of strain accumulation and strain release on the two sides of the fault about half a crack length away in the normal direction. For very long cracks, the increase in the shear stress off the crack becomes very small but the decrease off the initially unbroken zone becomes very pronounced. The interaction between cracks occupying the larger part of the period between the cracks can be seen in our figures. All results <u>on</u> the crack plane such as size of plastic zone and slip on the crack are valid for all modes of

crack propagation, with a minor change in constants for the anti-plane shear mode. The shear stress field τ_{12} is also valid for a viscoelastic medium.

ACKNOWLEDGMENTS

This work is part of a joint program in earthquake prediction under Area IX of the US-USSR Agreement in the Field of Environmental Protection. Most of this work was done while S. Das was at the Institute of Physics of the Earth, Moscow and she would like to thank the USSR Government and the IPE, Moscow for support and use of facilities. Chris Scholz pointed out that some of the Borrego Mountain aftershocks may be explained by our model. Chris Scholz and Paul Richards reviewed the manuscript. The American part of the work is supported by the National Science Foundation under Grant Number EAR 80-07426.

REFERENCES

Barton, N., The shear strength of rock and rock joints, Int. J. Rock Mech. Min. Sci., 13, 255-279, 1976.

Bilby, B. A., and K. H. Swinden, Representation of plasticity at notches by linear dislocation arrays, Proc. Roy. Soc. (London), Ser. A, 285, 23-33, 1965.

Bilby, B. A., A. H. Cottrell, E. Smith, and K. H. Swinden, Proc. Roy. Soc. (London), Ser. A, 272, 304-314, 1963.

Bowden, F. P., and D. Tabor, Friction: An Introduction to Tribology, 178 pp., Anchor, Garden City, New York, 1973.

Chinnery, M. A., The stress changes that accompany strike-slip faulting, Bull. Seismol. Soc. Am., 53, 921-932, 1963.

Das, S., and C. H. Scholz, Theory of time-dependent rupture in the earth, J. Geophys. Res., in press, 1981.

Das, S., and C. H. Scholz, Examples and a possible explanation for occasionally observed clusters of off-fault aftershocks, submitted to Bull. Seismol. Soc. Am., Letter to the Editor, 1981.

Dieterich, J. H., Time-dependent friction and the mechanics of stick-slip, Pure Appl. Geophys., 116, 790-806, 1978.

Dieterich, J. H., Modeling of rock friction, 2. Simulation of preseismic slip, J. Geophys. Res., 84, 2169-2175, 1979a.

Dieterich, J. H., Modeling of rock friction, 1. Experimental results and constitutive equations, J. Geophys. Res., 84, 2161-2168, 1979b.

Dieterich, J. H., Experimental and model study of fault constitutive properties, Solid Earth Geophys. Geotech., AMD, ASME, edited by S. Nemat-Nasser, 21-29, 1980.

Dugdale, D. S., Yielding of steel sheets containing slits, J. Mech. Phys. Solids, 8, 100-110, 1960.

Gzovsky, M. B., D. N. Osokina, A. A. Lomakin, and B. B. Kudreshova, Stresses, ruptures and earthquake foci (modelling results), in Regional Study of Seismic Regime, 113-124, Stiinitza, Kishinev, 1974 (in Russian).

Hamilton, R. B., Aftershocks of the Borrego Mountain earthquake from April 12 to June 12, 1968, in The Borrego Mountain Earthquake of April 9, 1968, U. S. Geol. Surv. Prof. Paper 787, 31-54, U. S. Govt. Printing Office, 1972.

Hutton, L. K., C. E. Johnson, J. C. Pechmann, J. E. Ebel, J. W. Gwen, D. M. Cole, and P. T. German, Epicentral locations for the Homestead Valley earthquake sequence, March 15, 1979, California Geology, May 1980, 110-114, 1980.

Ida, Y., Cohesive force across the tip of a longitudinal-shear crack and Griffith's specific surface energy, J. Geophys. Res., 77, 3796-3805, 1972.

Koiter, W. T., Solution of some elasticity problems by asymptotic methods, in Applications of the Theory of Functions in Continuum Mechanics, 15-31, Nauka, Moskow, 1965.

Kostrov, B. V., and L. V. Nikitin, Some general problems of mechanics of brittle fracture, Archiwum Mechaniki Stosowanej, 22, 1970.

Kragelskii, I. V., Friction and Wear, 346 pp., Butterworths, Washington, 1965.

Leonov, M. Y., and V. V. Panasyuk, Development of the smallest cracks in a solid, PM, vyp. 4, 1959 (in Russian).

Muskhelishvili, N. I., Some Basic Problems of Mathematical Theory of Elasticity, Noordhoff, Groningen, Holland, 1953.

Niewiadomski, J., Analysis of crack stresses and its application to problems of orogen mechanics, Publ. Inst. Geophys. Pol. Acad. Sci., 85, 3-79, 1975.

Osokina, D. N., and H. U. Tsvetkova, Method of modelling the local stress field near a tectonic fault and at earthquake foci, in Stress and Deformation Fields in the Lithosphere, 139-162, Nauka, Moscow, 1979 (in Russian).

Osokina, D. N., I. O. Gushinko, V. I. Lukov, and H. U. Tsvetkova, Modelling of local field of tectonic stress for deep faults (based on two examples from Central Asia), in Stress and Deformation Fields in the Lithosphere, 185-203, Nauka, Moscow, 1979 (in Russian).

Osokina, D. N., A. A. Nikonov, and H. U. Tsvetkova, Modelling of the local stress field around the San Andreas fault system, in Stress and Deformation Fields in the Lithosphere, 204-226, Nauka, Moscow, 1979 (in Russian).

Palmer, A. C., and J. R. Rice, The growth of slip surfaces in the progressive failure of over-consolidated clay, Proc. Roy. Soc. (London), Ser. A, 332, 527-548, 1973.

Rice, J. R., Mathematical analysis in the mechanics of fracture, Fracture, An Advanced Treatise, edited by H. Liebowitz, 2, 191-311, 1980.

Rice, J. R., The mechanics of earthquake rupture, Phys. Earth Interior, Soc. Italiana di Fisica, Bologna, Italy, LXXVIII, Corso, 555-649, 1980.

Rummel, F., H. J. Alheid, and C. Frohn, Dilatancy and fracture induced velocity changes in rock and their relation to frictional sliding, Pure Appl. Geophys., 116, 743-764, 1978.

Sayles, R., and T. Thomas, Surface topography as a nonstationary random process, Nature, 271, 431-434, 1978.

Scholz, C. H., P. M. Molnar, and T. Johnson, Detailed studies of frictional sliding of granite and implications for the earthquake mechanism, J. Geophys. Res., 77, 6392-6406. 1972.

Segall, P., and D. D. Pollard, Mechanics of discontinuous faults, J. Geophys. Res., 85, 4337-4350, 1980.

Smith, E., Fracture at stress concentrations, Proc. 1st Intl. Conf. Fracture, Edited by T. Yokobori, T. Kawasaki, and J. L. Swedlow, Jap. Soc. Strength and Fracture of Materials, Tokyo, I, 133-152, Sendai, 1966.

Smith, S. W., and W. Van de Lindt, Strain adjustments associated with earthquakes in southern California, Bull. Seismol. Soc. Amer., 59, 1569-1589, 1969.

Teufel, L. W., and J. M. Logan, Effect of shortening rate on the real area of contact and temperature generated during frictional sliding, Pure Appl. Geophys., 116, 840-865, 1978.

Ward, P. L., J. Gibbs, D. Harlow, and A. Aburto Q., Aftershocks of the Managua, Nicaragua earthquake and the tectonic significance of the Tiscapa fault, Bull. Seismol. Soc. Am., 64, 1017-1029, 1974.

Wong, T. F., Post-failure behavior of Westerly granite at elevated temperatures, Ph.D. thesis, Massachusetts Inst. Tech., 1980.

FIGURE CAPTIONS

Figure 1. Schematic diagram showing two-dimensional infinite periodic system consisting of in-plane shear crack, intermediate zone and broken zone and the coordinate axes. Inset shows a schematic diagram of the CSD.

Figure 2. Shear stress at a point which is initially in the intermediate zone, as a function of the slip on the fault (cohesive-force diagram [Ida, 1972]). $[u_o]$ is the 'critical shear displacement' (CSD).

Figure 3. Stress conditions on the different regions of the fault plane.

Figure 4. The complex ζ-plane and conditions satisfied by Φ and F on the different parts of the ξ-axis.

Figure 5. The solid line shows the condition for coalescence of intermediate zones prior to CSD being attained. For points above this line, coalescence will occur. The dotted lines show $[u]_{AV}^{NOR}$ against a/d.

Figure 6. Dimensionless average compliance as a function of normalized crack length at coalescence. Inset shows qualitative form of $[u]_{AV}$ against $(\sigma_{AV}-\sigma_f)$.

Figure 7. Normalized displacement $[u]^{NOR}$ as a function of normalized position x_1/d along the crack. The crack length a/d and the stress σ_{12}^{NOR} are shown below each figure. For the lowest figure on the left-hand side, the five sets of $[u]^{NOR}$ are for σ_{12}^{NOR} = 0.2, 0.4, 0.6, 0.8, 0.9. Similarly for the other cases. The highest value of σ_{12}^{NOR} for each case is the value at coalescence.

Figure 8. τ_{12}^{NOR} as a function of x_1/d and x_2/d for a/d = 0.01, σ_{12}^{NOR} = 0.01. The map size is 3a/d. The stippled areas indicate regions where τ_{12}^{NOR} increases due to the presence of the crack.

Figure 9. τ_{12}^{NOR} as a function of x_2/d for the same case as in Figure 8. Arrows indicate the position of the maximum values of τ_{12}^{NOR}.

Figure 10a-e. τ_{12}^{NOR} against $(x_1/d, x_2/d)$ for different σ_{12}^{NOR} for a/d = 0.01. One quadrant is plotted, the other three being mirror reflections of this about x_1 and x_2.

Figure 11a-c. Same as Figure 10 for a/d = 0.5.

Figure 12. Same as Figure 10 for a/d = 0.9.

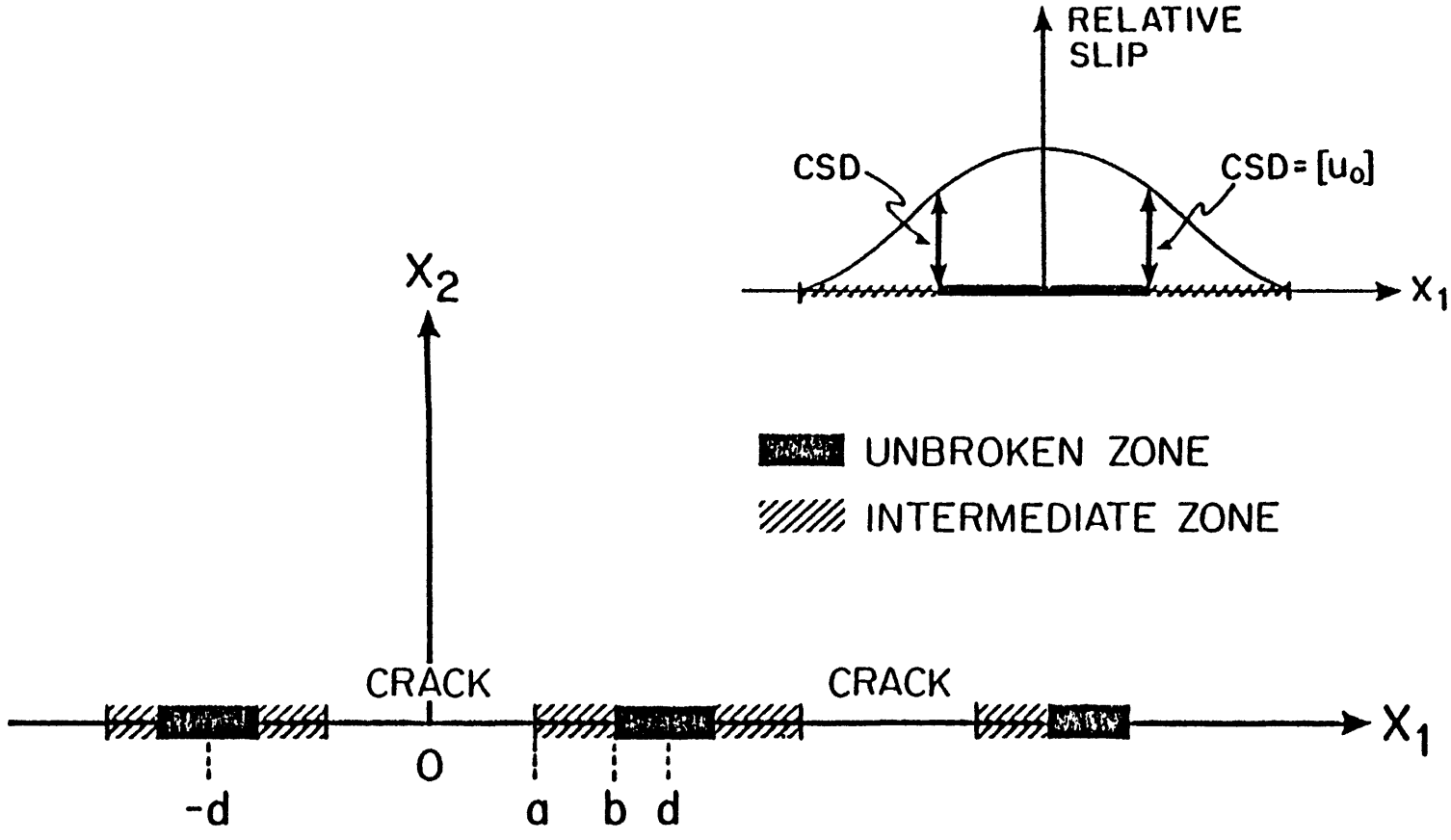
RELATIVE
SLIP
CSD
CSD= [u0]
X1
X2
UNBROKEN ZONE
INTERMEDIATE ZONE
CRACK
CRACK
X1
-d
0
a
b
d

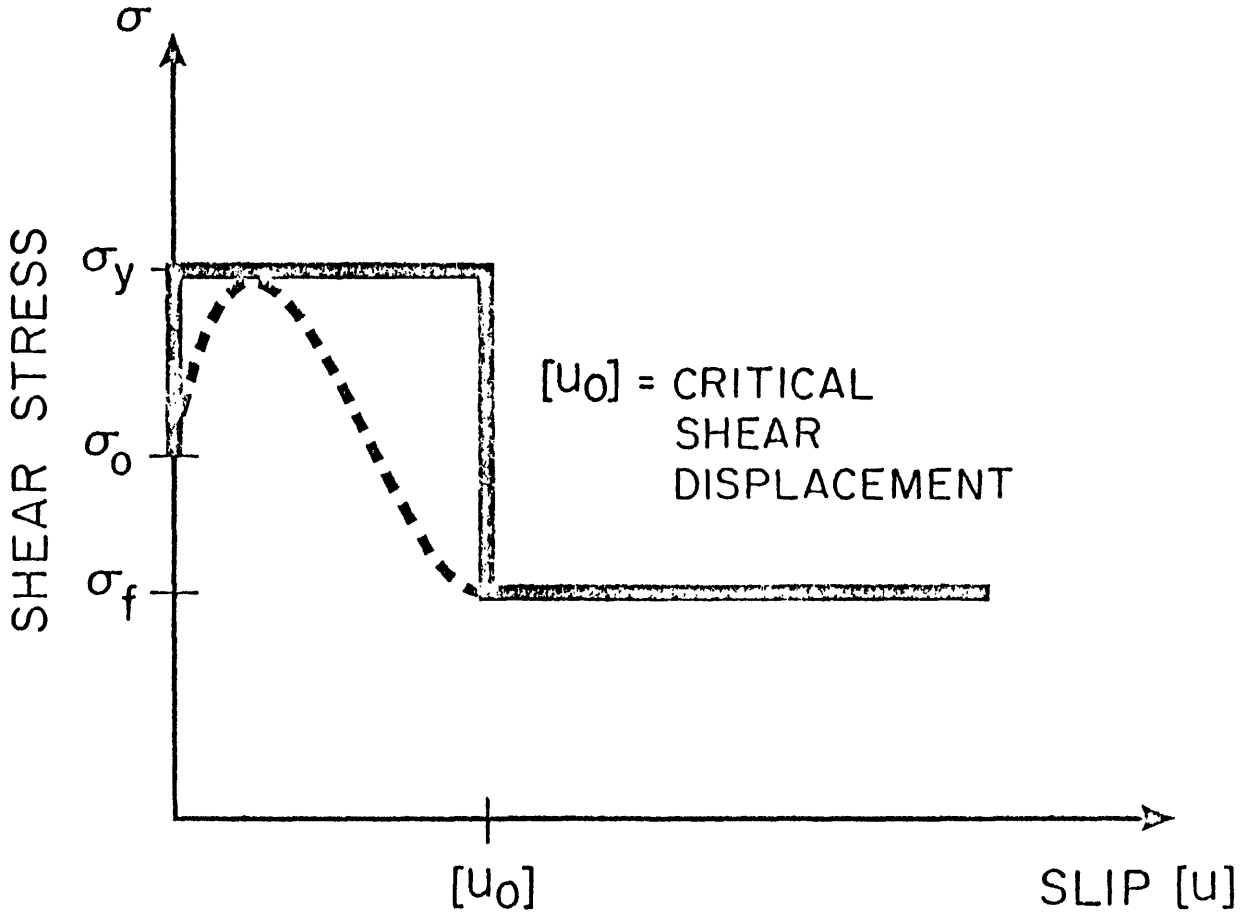
σ
SHEAR STRESS
σy
σo
σf
[uo] = CRITICAL
SHEAR
DISPLACEMENT
[uo]
SLIP [u]

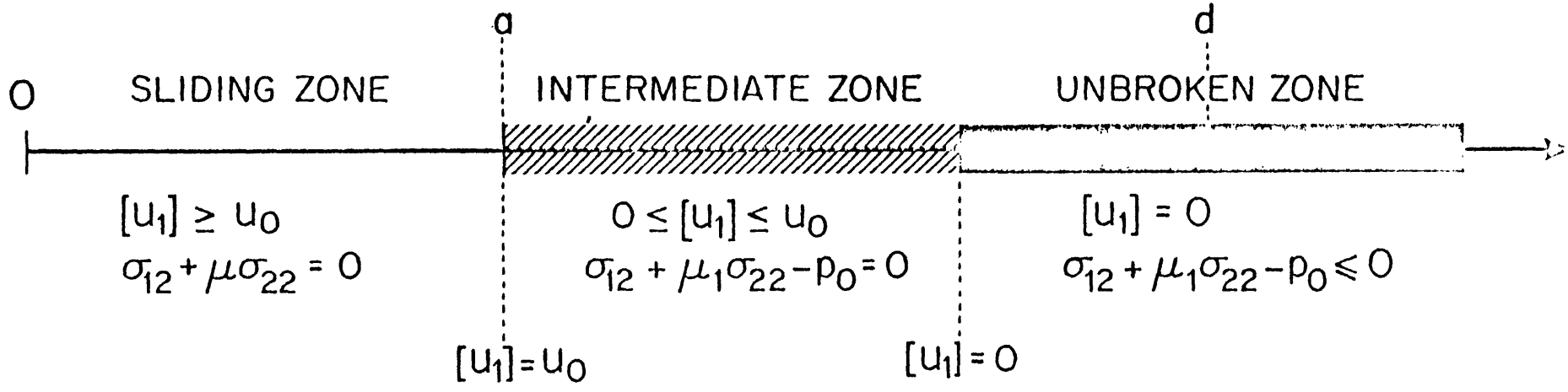
a
d
0
SLIDING ZONE
INTERMEDIATE ZONE
UNBROKEN ZONE
$[u_1] \geq u_0$
$\sigma_{12} + \mu\sigma_{22} = 0$
$0 \leq [u_1] \leq u_0$
$\sigma_{12} + \mu_1\sigma_{22} - p_0 = 0$
$[u_1] = 0$
$\sigma_{12} + \mu_1\sigma_{22} - p_0 \leq 0$
$[u_1] = u_0$
$[u_1] = 0$

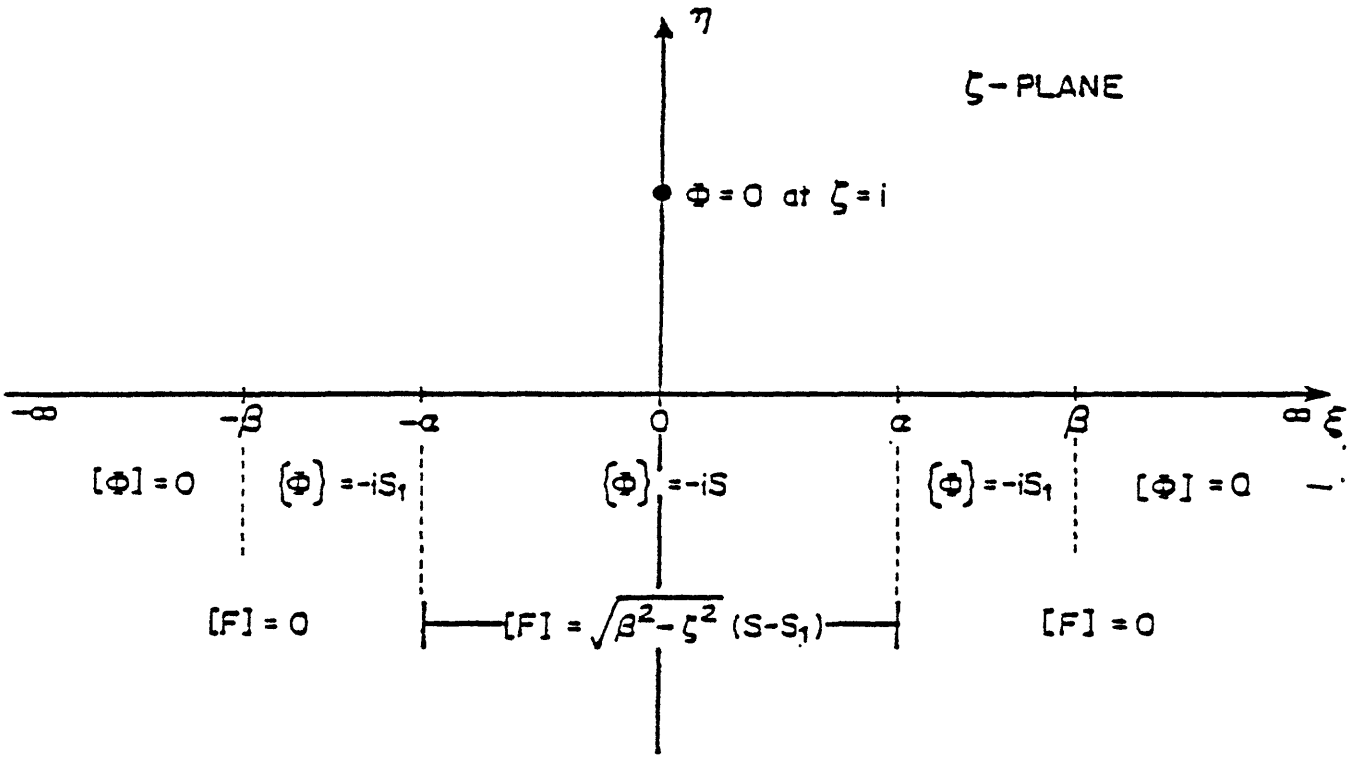
η
ζ-PLANE
Φ = 0 at ζ = i
-∞
-β
-α
0
α
β
∞
ξ
[Φ] = 0
{Φ} = -iS₁
{Φ} = -iS
{Φ} = -iS₁
[Φ] = 0
[F] = 0
[F] = √(β²-ζ²) (S-S₁)
[F] = 0

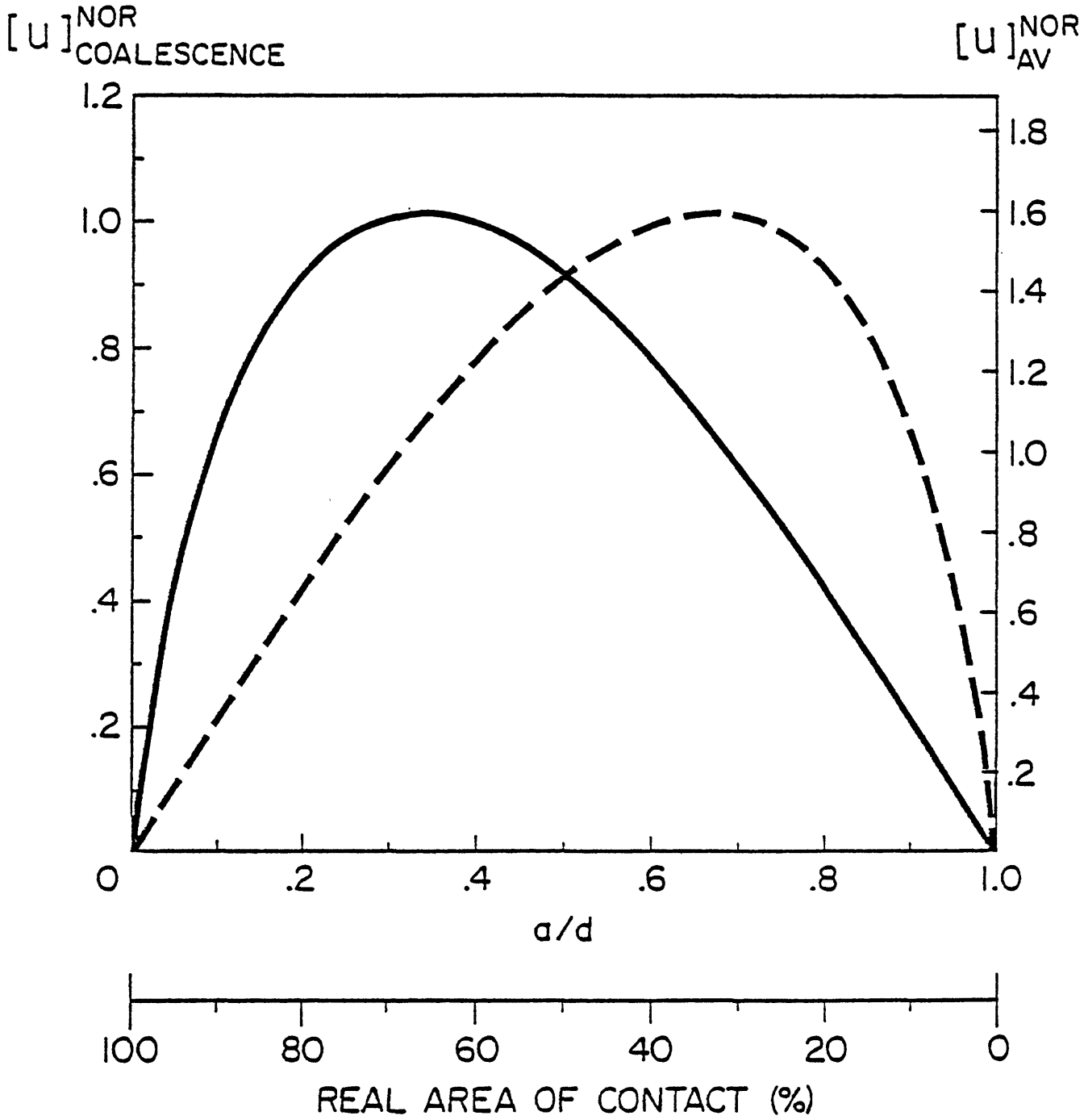
[u]NOR COALESCENCE
[u]NOR AV
1.2
1.0
.8
.6
.4
.2
0
1.8
1.6
1.4
1.2
1.0
.8
.6
.4
.2
0
.2
.4
.6
.8
1.0
a/d
100
80
60
40
20
0
REAL AREA OF CONTACT (%)

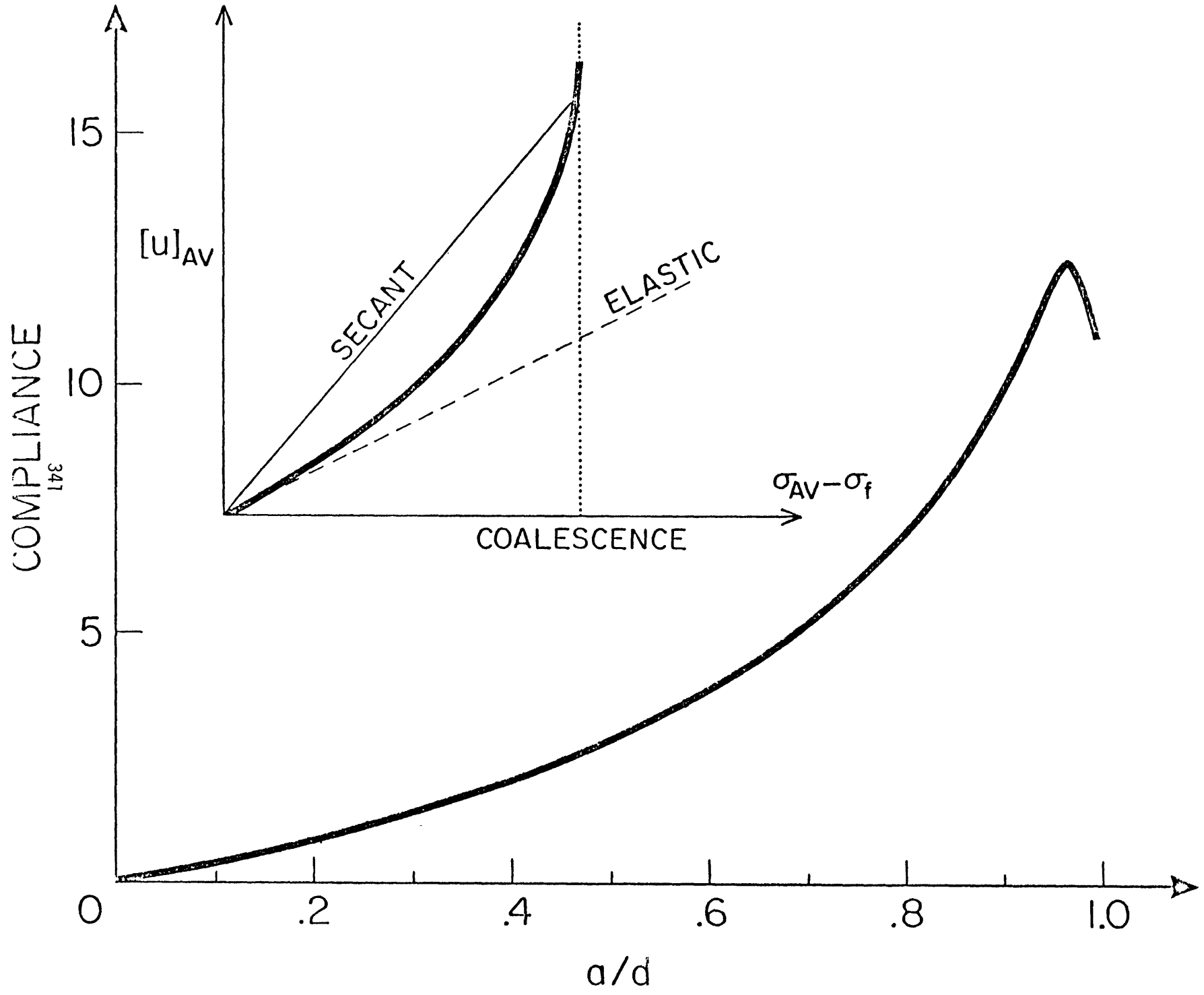
COMPLIANCE
15
10
5
0
.2
.4
.6
.8
1.0
a/d
[u]AV
SECANT
ELASTIC
σAV−σf
COALESCENCE

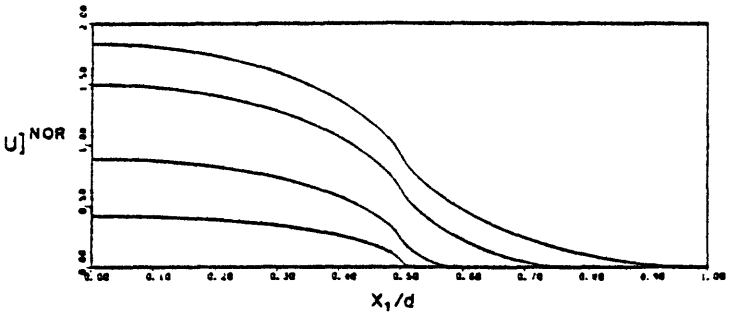

NORMALIZED STRESS FROM 0.15 TO 0.50
NORMALIZED CRACK LENGTH IS 0.50

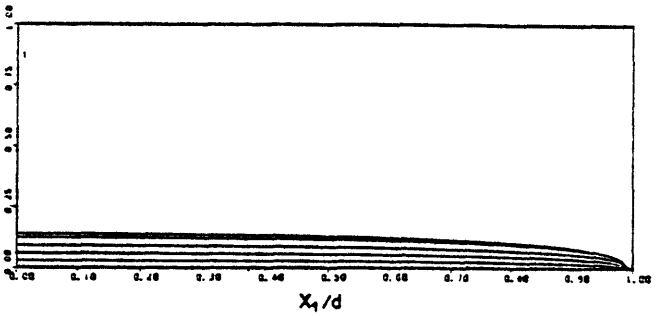

NORMALIZED STRESS FROM 0.002 TO 0.01
NORMALIZED CRACK LENGTH IS 0.99

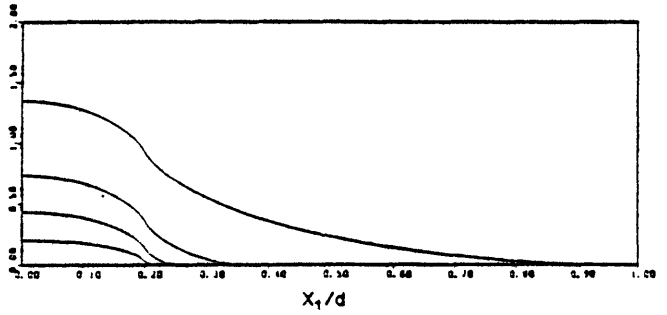

NORMALIZED STRESS FROM 0.20 TO 0.80
NORMALIZED CRACK LENGTH IS 0.20

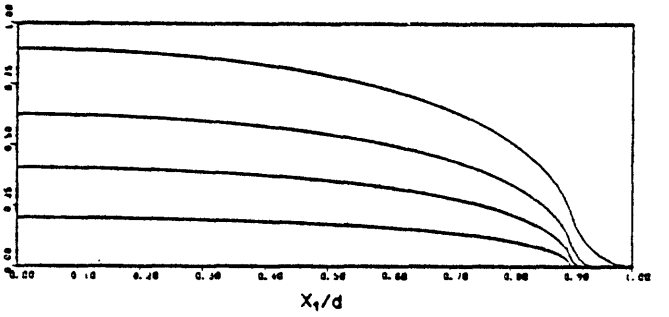

NORMALIZED STRESS FROM 0.025 TO 0.10
NORMALIZED CRACK LENGTH IS 0.90

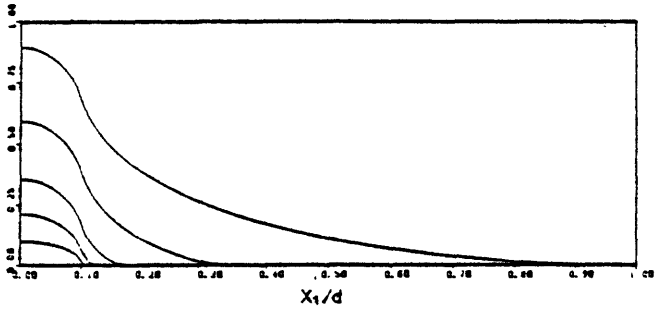

NORMALIZED STRESS FROM 0.20 TO 0.90
NORMALIZED CRACK LENGTH IS 0.10

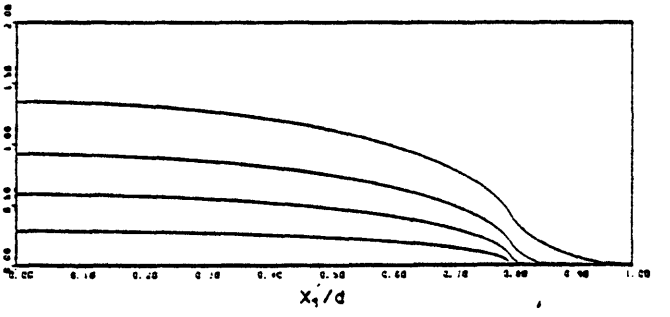

NORMALIZED STRESS FROM 0.05 TO 0.20
NORMALIZED CRACK LENGTH IS 0.80

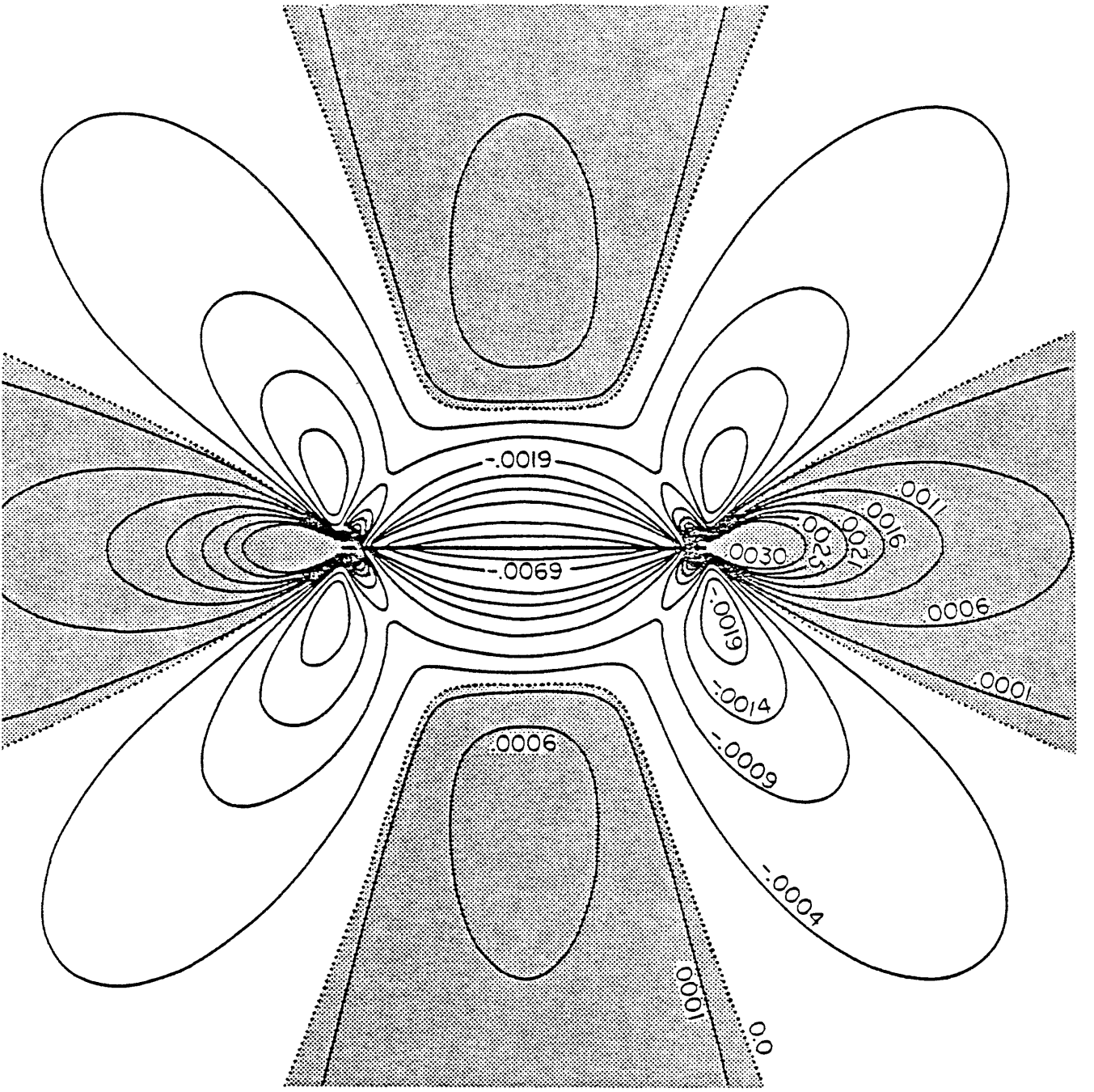

$a/d = .01, \quad \sigma_{12}^{NOR} = .01$

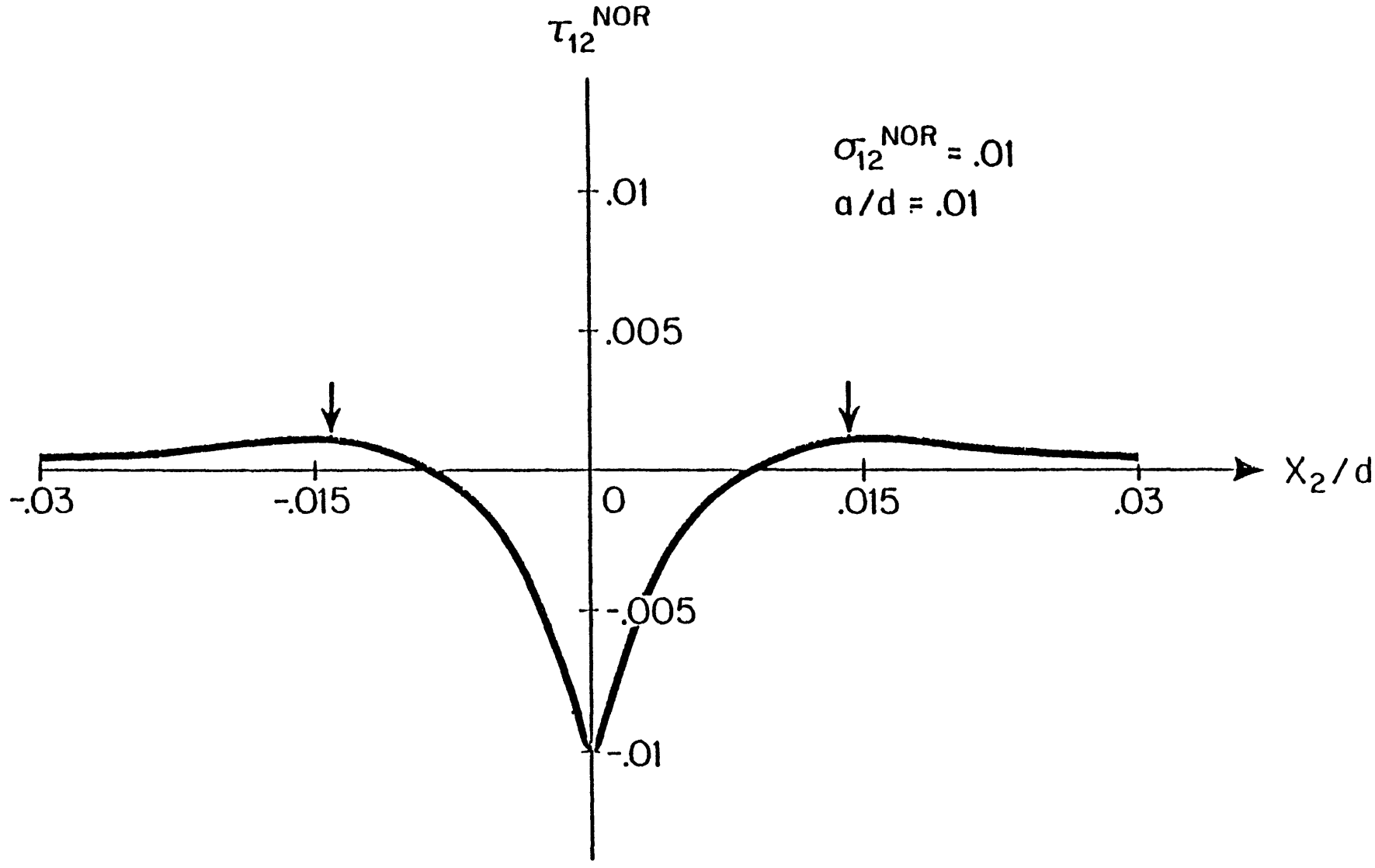
τ_{12}^{NOR}
$\sigma_{12}^{NOR} = .01$
a/d = .01
.01
.005
-.005
-.01
-.03
-.015
0
.015
.03
X_2/d

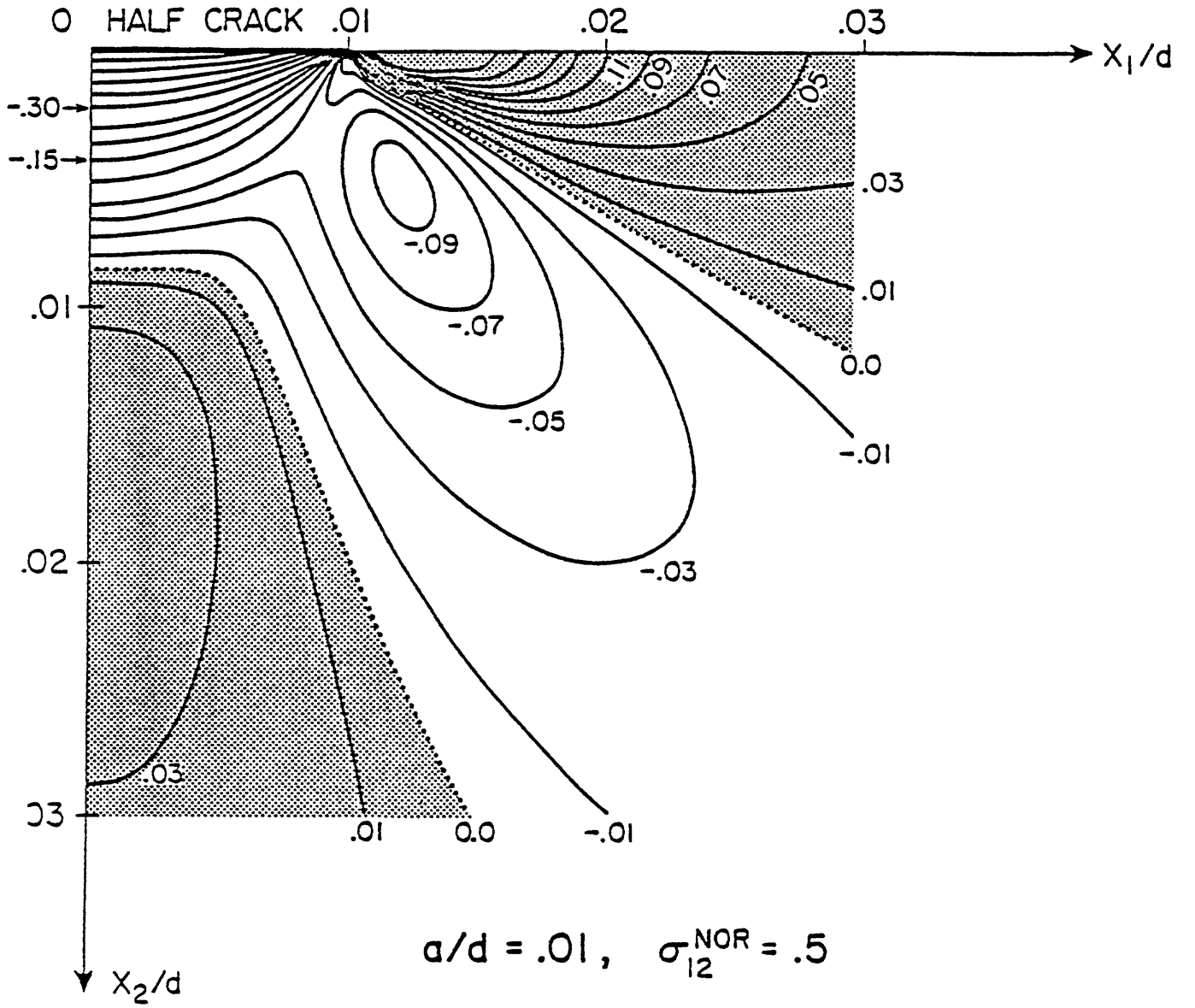

$a/d = .01, \quad \sigma_{12}^{NOR} = .5$

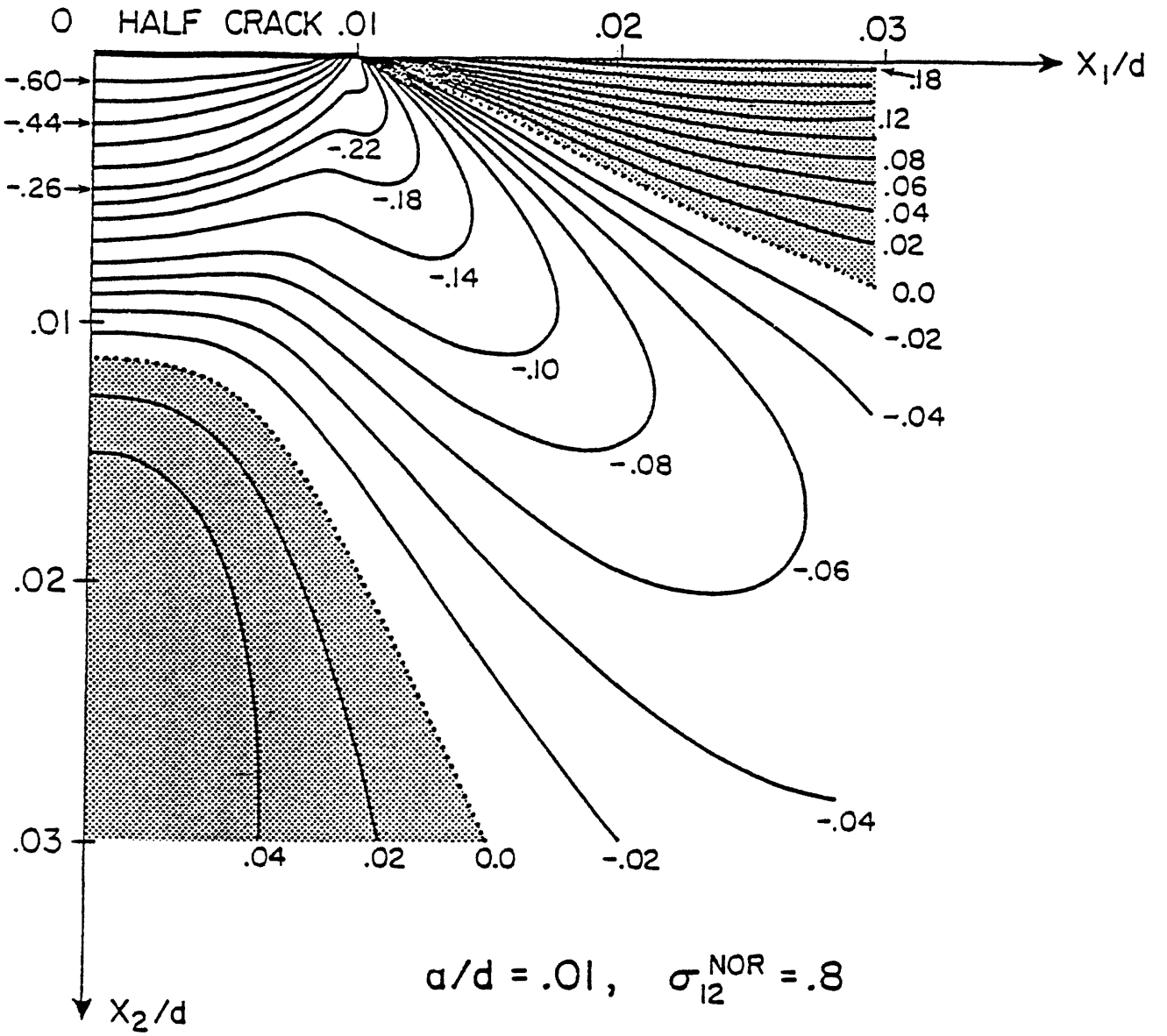

$a/d = .01, \quad \sigma_{12}^{NOR} = .8$

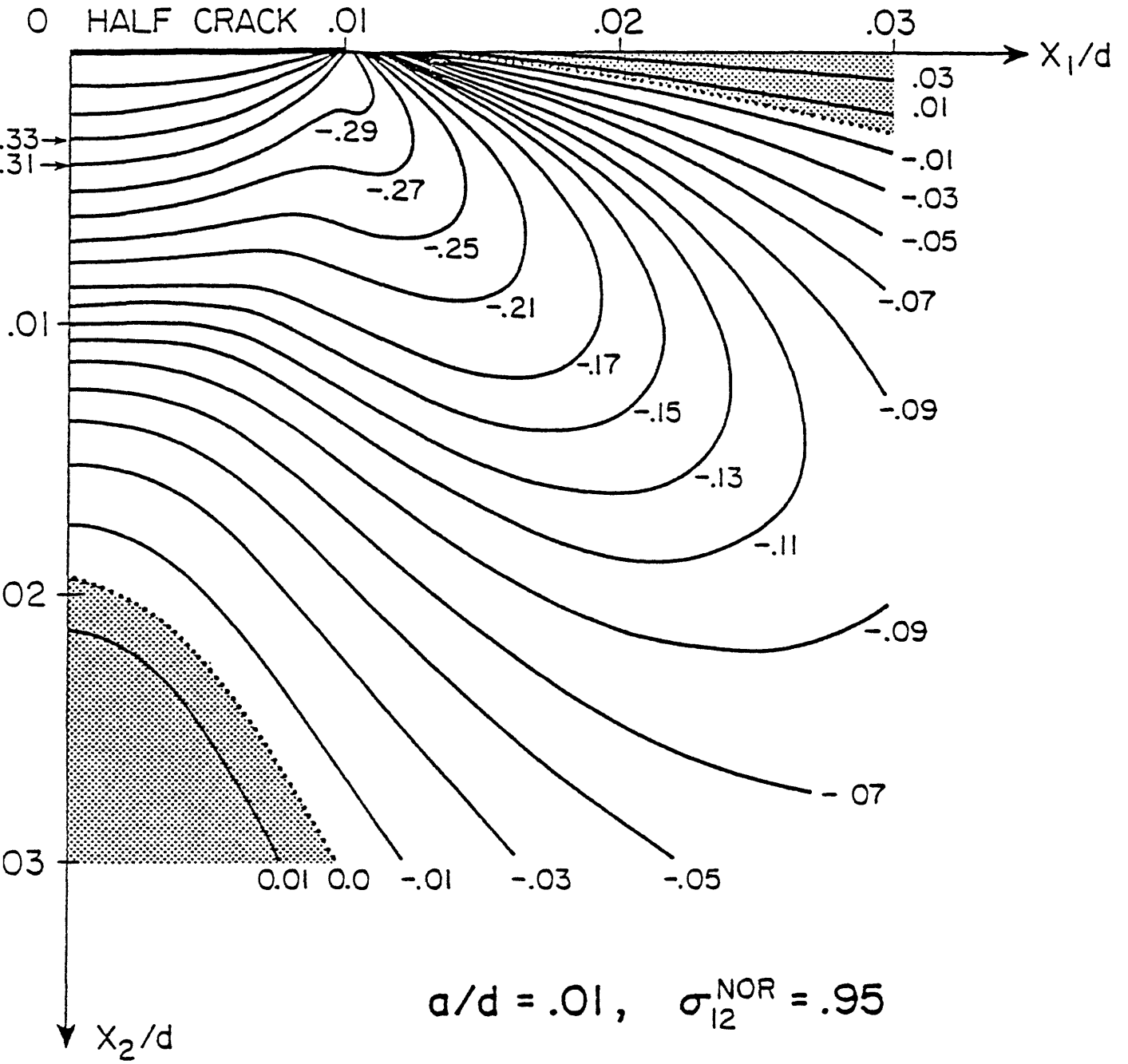

$a/d = .01, \quad \sigma_{12}^{NOR} = .95$

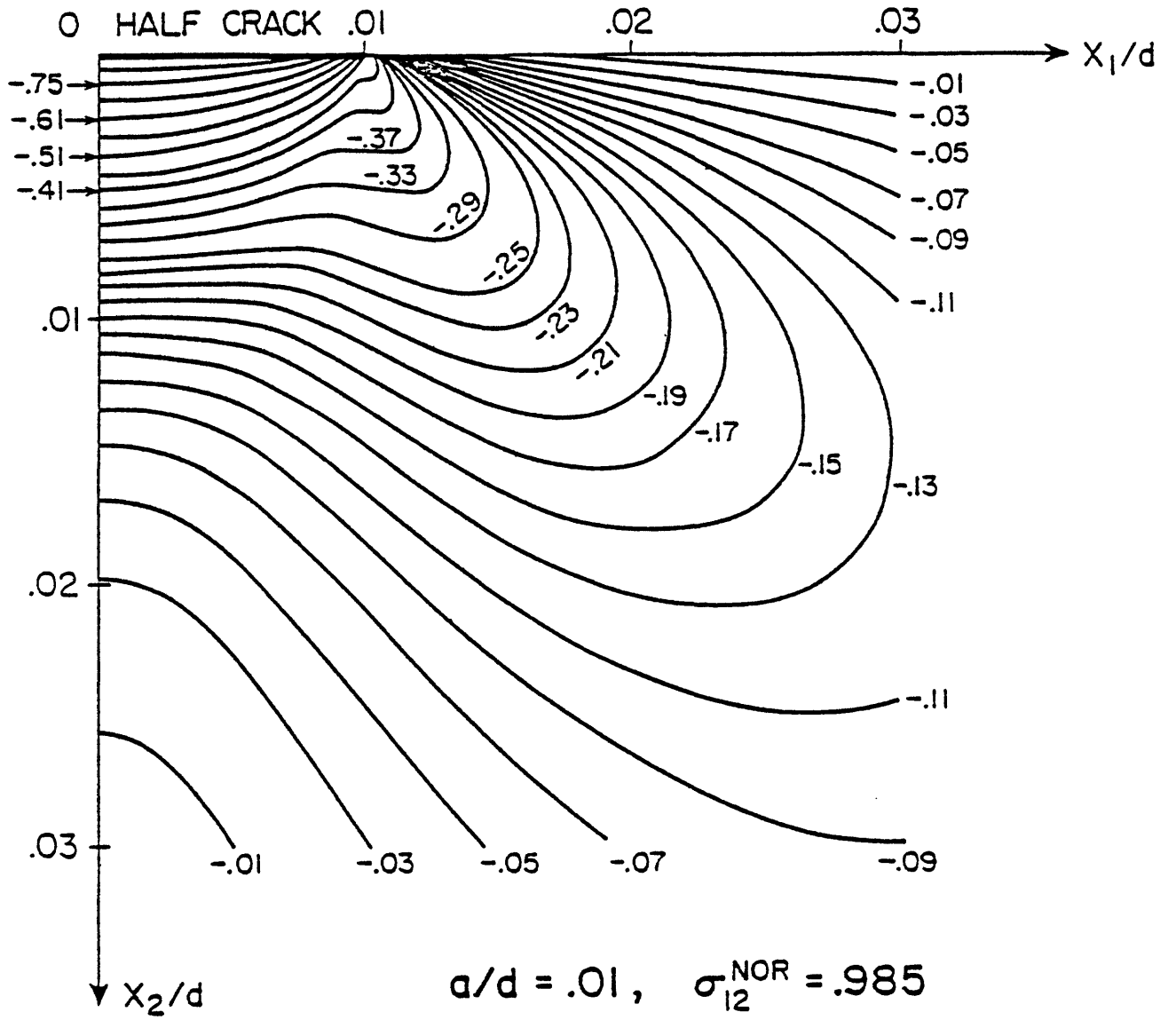
0 HALF CRACK .01
.02
.03
X_1/d
-.75
-.61
-.51
-.41
-.37
-.33
-.29
-.25
-.23
-.21
-.19
-.17
-.15
-.13
-.11
-.09
-.07
-.05
-.03
-.01
.01
.02
.03
-.01
-.03
-.05
-.07
-.09
-.11
X_2/d
$a/d = .01, \quad \sigma_{12}^{NOR} = .985$

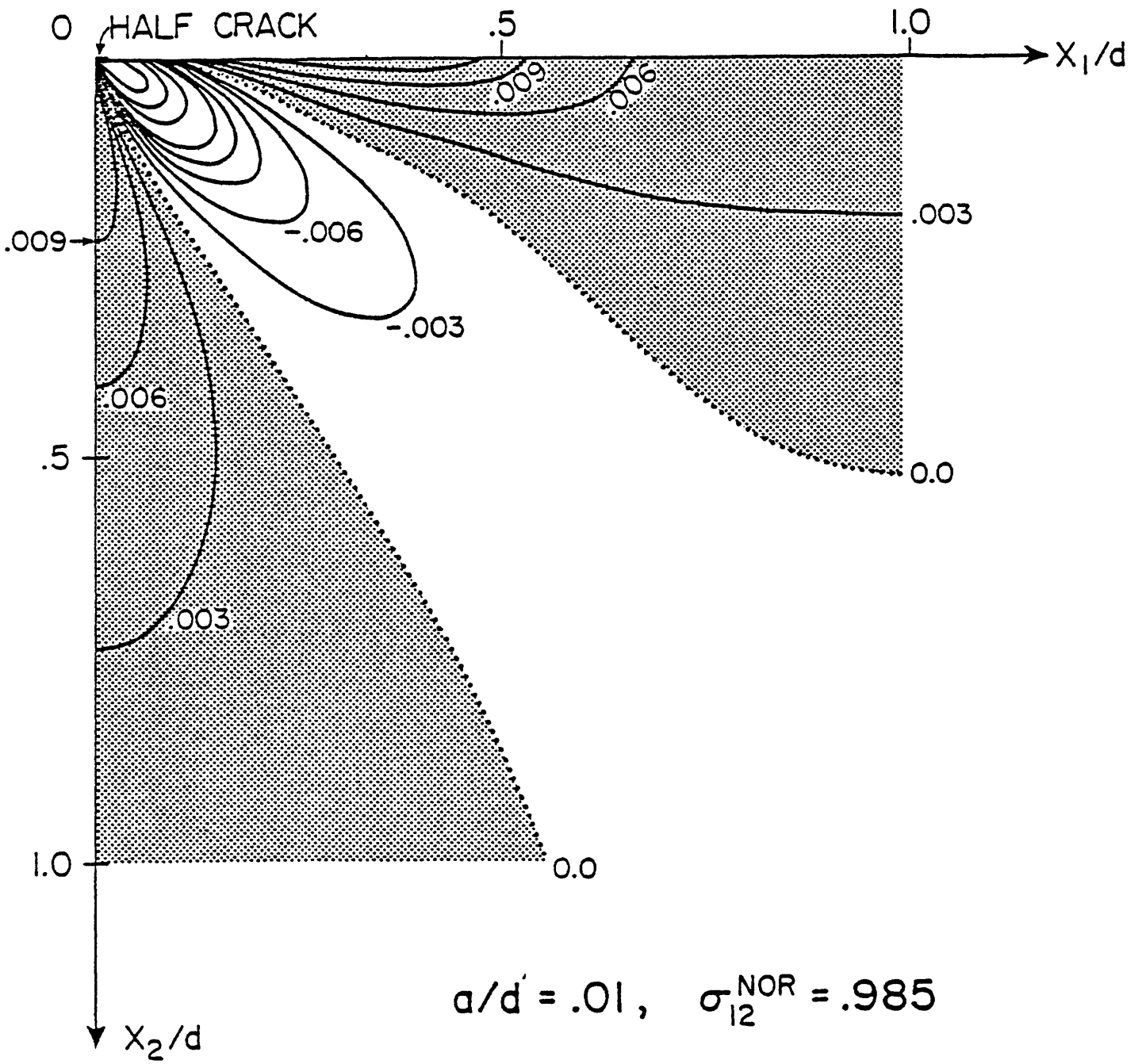
0
HALF CRACK
.5
1.0
X_1/d
.009
.006
.003
-.006
-.003
.009
.006
.003
0.0
.5
1.0
0.0
X_2/d
$a/d = .01, \quad \sigma_{12}^{NOR} = .985$

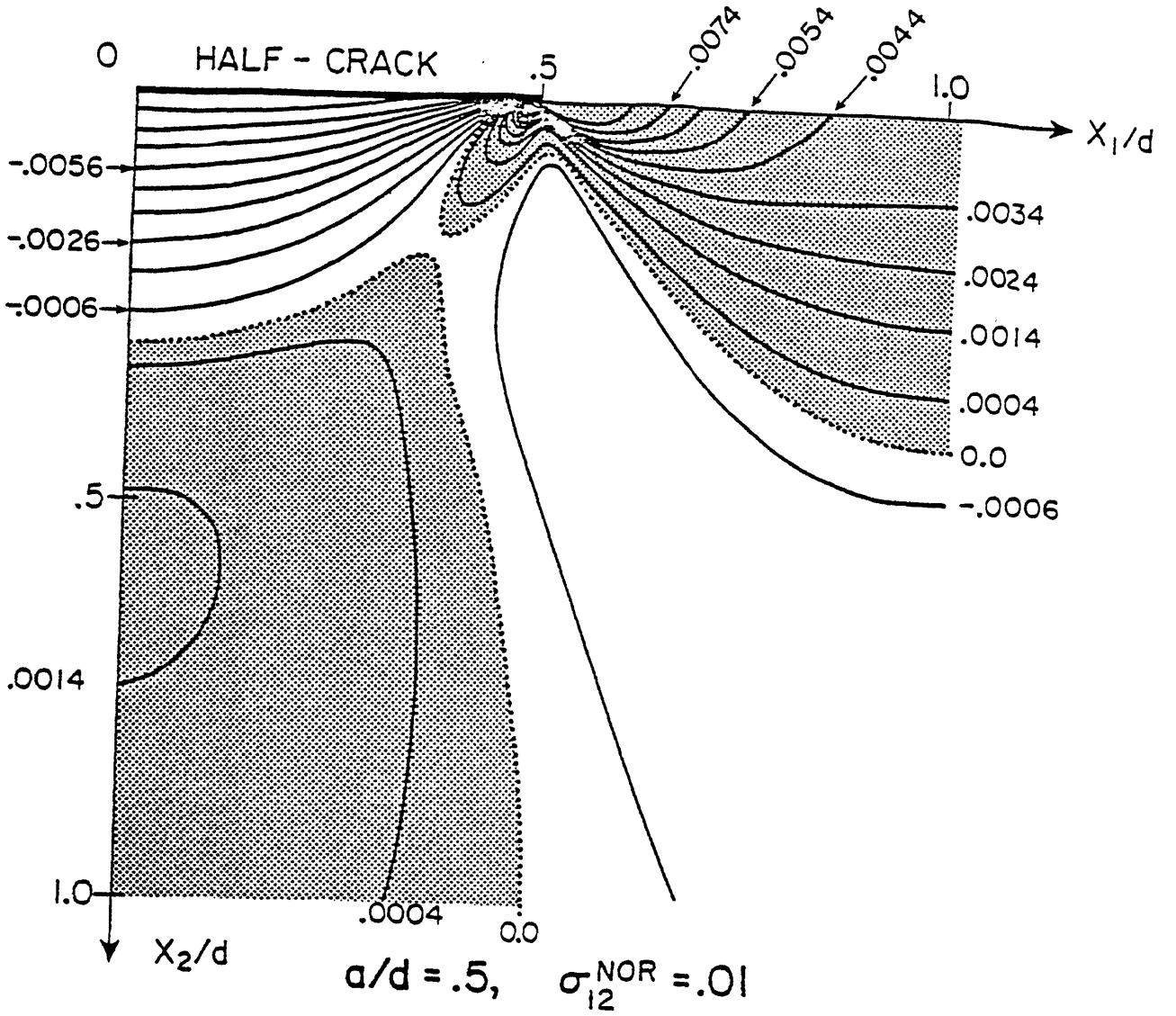
0
HALF - CRACK
.5
1.0
.0074
.0054
.0044
X_1/d
-.0056
-.0026
-.0006
.0034
.0024
.0014
.0004
0.0
-.0006
.5
.0014
1.0
.0004
0.0
X_2/d
$a/d = .5, \quad \sigma_{12}^{NOR} = .01$

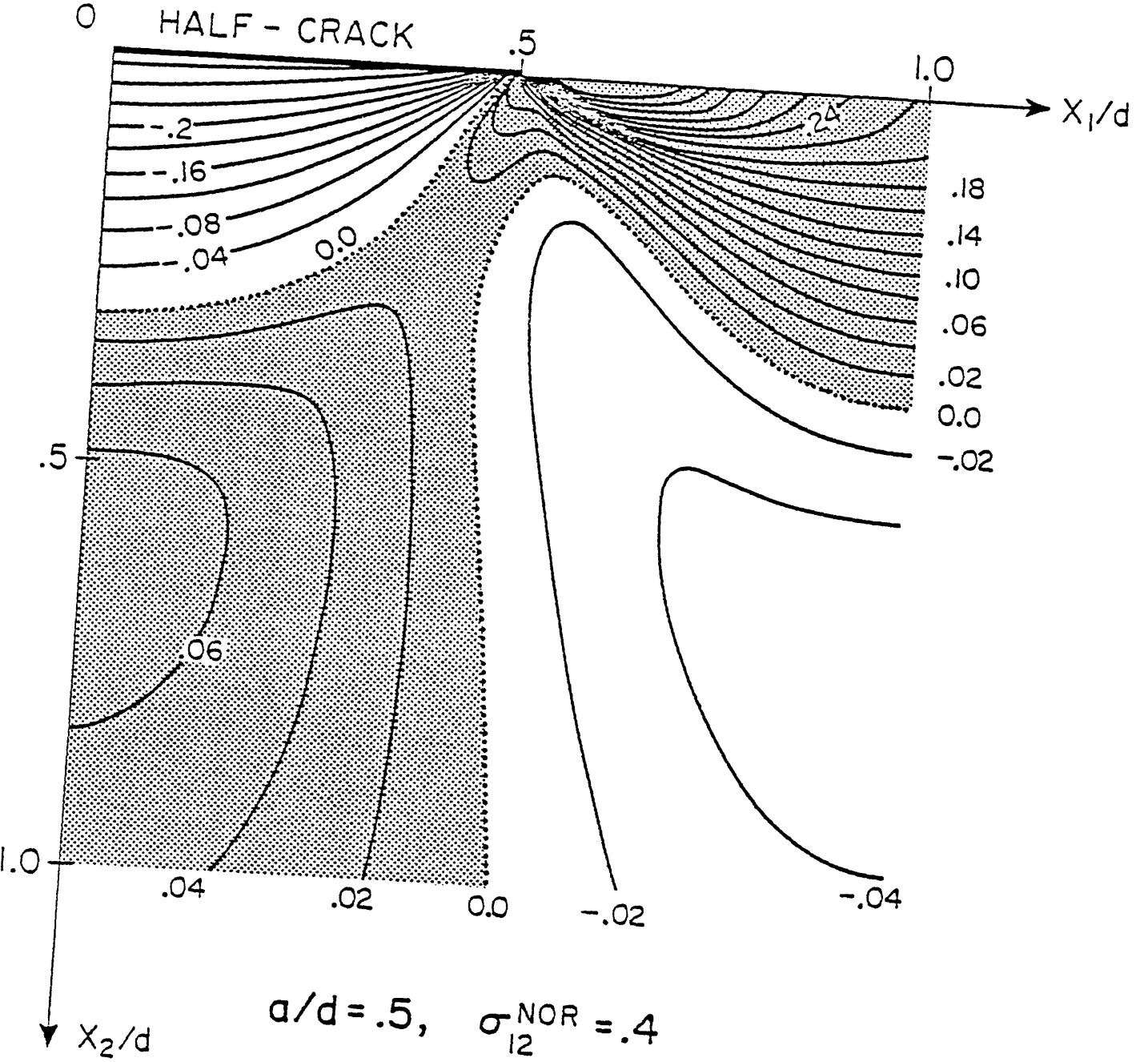
0
HALF - CRACK
.5
1.0
X_1/d
-.2
-.16
-.08
-.04
0.0
.24
.18
.14
.10
.06
.02
0.0
-.02
.5
.06
1.0
.04
.02
0.0
-.02
-.04
X_2/d
$a/d = .5, \quad \sigma_{12}^{NOR} = .4$

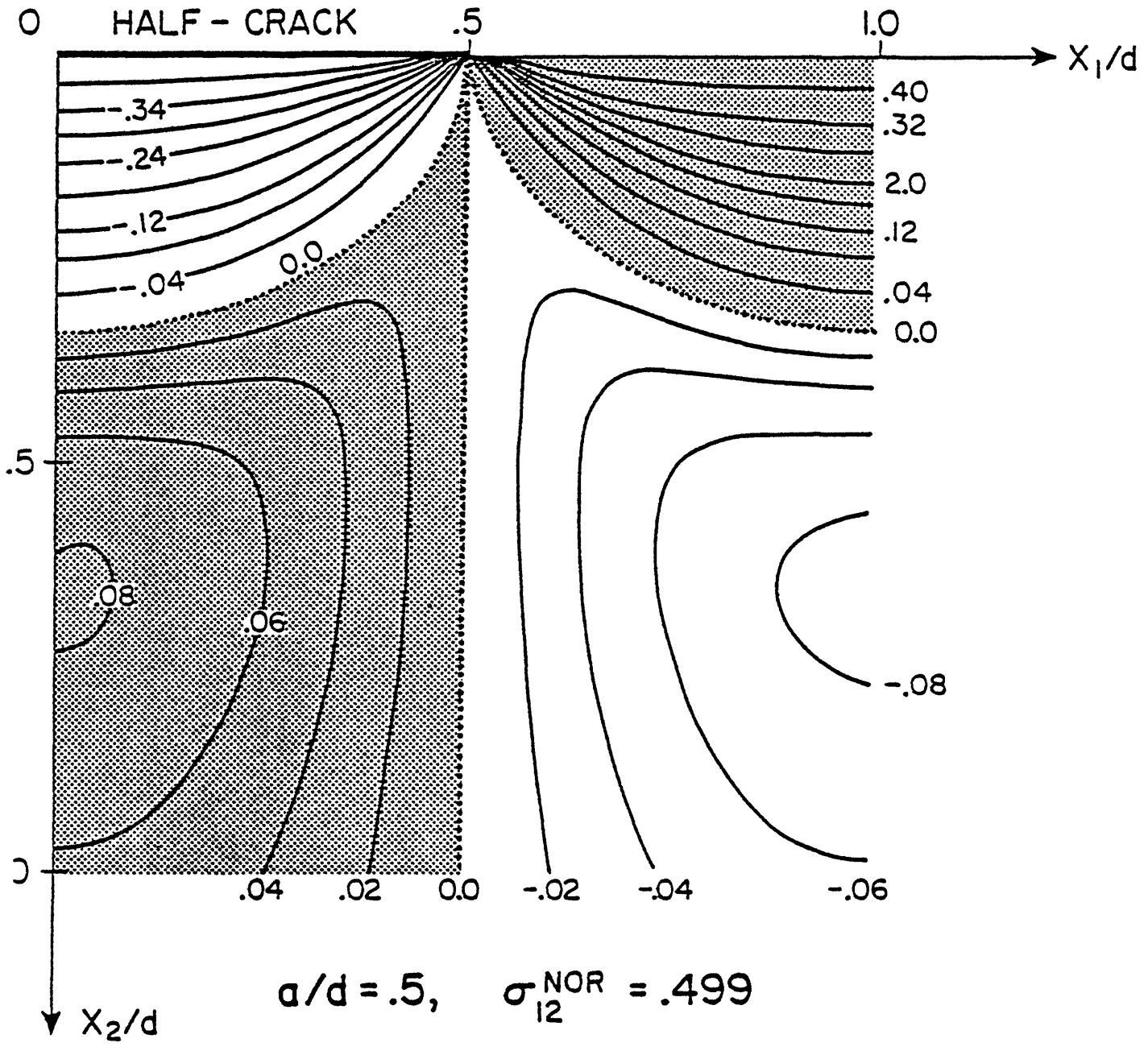
0
HALF - CRACK
.5
1.0
X_1/d
-.34
-.24
-.12
-.04
0.0
.40
.32
2.0
.12
.04
0.0
.5
.08
.06
-.08
0
.04
.02
0.0
-.02
-.04
-.06
X_2/d
$a/d = .5, \quad \sigma_{12}^{NOR} = .499$

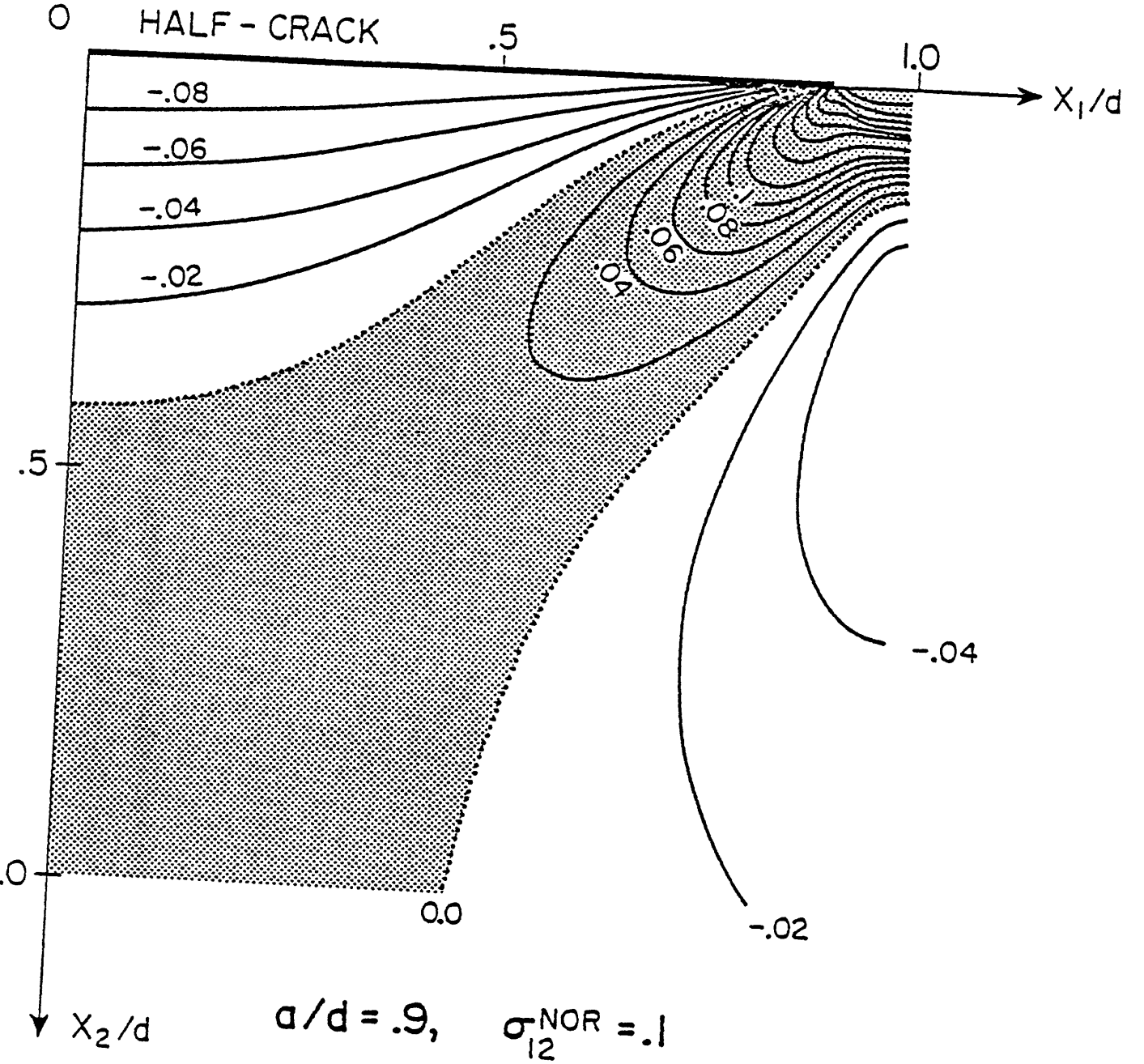

(page 355 follows)

Reprinted from Nature, Vol. 283, No. 5744, pp. 259-263, January 17 1980

Bursts of aftershocks, long-term precursors of strong earthquakes

V. I. Keilis-Borok*, L. Knopoff† & I. M. Rotvain*

* Institute of the Physics of the Earth, Academy of Sciences, Moscow, USSR
† Institute of Geophysics and Planetary Physics, University of California, Los Angeles, California 90024

Earthquakes that are followed within a short time by abnormally large numbers of aftershocks are hypothesised to be long-term precursors of stronger earthquakes. In a test of the hypothesis, 18 out of 23 strong earthquakes, in five regions worldwide, were predicted retrospectively. In comparison with a random model the precursory pattern occurs at a satisfactorily high confidence level.

THE hope that patterns of seismicity exist that are premonitory to strong earthquakes relies on the fact that the occurrence of earthquakes is controlled by the distribution of stresses and strengths within the Earth and that each earthquake in turn changes these fields. At present we cannot anticipate what such patterns should be, because the theoretical basis is inadequate. One reason for this is the absence of firmly established empirical regularities in seismicity which would provide a factual basis for theoretical studies of earthquake occurrence.

Searches for premonitory patterns of seismicity have attracted much attention, as these may possibly be established by the analysis of earthquake catalogues which are the longest record of the relevant observations. With regard to precursors of large earthquakes, there have been many purported descriptions of premonitory patterns of seismicity. These patterns are of three basic types—quiescence, activation and migration of epicentres. Although the results from some of these studies support the hope that premonitory patterns of seismicity exist, nevertheless, with a few exceptions, their definition is not specific enough to estimate the reliability of the pattern. To obtain such estimates one should be able to detect the pattern by a formal algorithm and to count how often it is successful as a precursor. Without such estimates of reliability, any premonitory pattern would be uncertain.

We present here an attempt to derive a formal definition of some premonitory seismicity patterns from the analysis of an earthquake catalogue, which yields a reasonable success-to-failure ratio in retrospective long-term earthquake prediction. The definition also provides constraints on the theory of earthquake occurrence.

One reason why the search for premonitory patterns of seismicity has not been successful is that aftershocks are usually disregarded as being highly predictable phenomena. The results we describe below show that, while aftershocks are indeed highly predictable, some specific traits of aftershock sequences are highly informative. These traits may represent important, descriptive aspects of the distribution and redistribution of stresses and strengths within the Earth.

Definitions

Let t be the origin time of an earthquake, λ, ϕ the longitude and latitude of its epicentre (west and south are negative), h its focal depth, and M its magnitude. The subscript j will indicate the sequence number of an earthquake in the catalogue, $t_j < t_{j+1}$.

We seek precursors of earthquakes with magnitudes $M \geq M_0$. These are called strong earthquakes. Our patterns will be constructed from earthquakes in the magnitude range $M_2 \equiv M_0 - \mu_2 \leq M \leq M_0 - \mu_1 \equiv M_1$ and in a time interval of duration s; the values of μ_1, μ_2 and s may be different for each of the three patterns that we will discuss.

Aftershocks are defined as follows. Consider two earthquakes with sequence numbers i and j, $j > i$. The second earthquake is

Table 1 Score of patterns B

Regions	1 Southern California	2 N. California–Nevada (excluding Mendocino area)	3 Southern Japan	4 Northern Japan	5 New Zealand	Totals
Catalogue ref.	4, 11, 12	9	10, 14	10, 14	13	
Span of catalogue (yr)	1932–78	1945–76.5	1926–76.5	1940–76.5	1945–77	201.5
M_0	6.5	6.2	8	7.6	6.6	
C	11–13	6–12	4–10	4–6	9–14	
Strong earthquakes						
total	6	4	2	4	7	23
'predicted'	5	3	2	4	4	18
Relative time of alarms	0.46	0.27	0.18	0.36	0.27	0.31
N_m	36	39	9	45	65	194
N_A/N_B	9/14	3/6	2/4	7/13	7/8	28/45
T_τ/T	0.37	0.28	0.10	0.27	0.53	0.30
P	96%	79%	95%	96%	95%	

N_m, total number of main shocks; N_B, number of main shocks which generate pattern B $h_i \geq C$, for upper value of C; N_A, number of occurrences of pattern B which are followed by strong earthquakes within τ yr; T_τ, sum of times τ before each strong earthquake, counting overlapping parts only once; T, span of the catalogue (yr); C, threshold for identification of pattern B. A variation of C within the limits indicated in the table will introduce either zero or one additional error; P, confidence level for upper value of C.

an aftershock of the first if the following conditions are satisfied: the distance between their epicentres is less than $R(M_i)$; $t_j - t_i \leq T(M_i)$; $h_j - h_i \leq H(M_i)$; $M_j \leq M_i$. Here $T(M)$, $R(M)$ and $H(M)$ are empirical functions. If we apply this definition to an earthquake catalogue, starting with the first earthquake, we can separate the catalogue into main shocks and their aftershocks. The first earthquake of the catalogue is identified as a main shock. Each succeeding main shock can be identified after the deletion of aftershocks of the preceding main shocks. Formulas of this type have been developed[1-3] for both the worldwide and the southern California[4] catalogues for use in other aspects of the study of aftershocks and sequences or chains of interdependent earthquakes.

Pattern B (burst of aftershocks). Let $b_i(e)$ be the number of aftershocks following the ith main shock within time interval e. We consider only those main shocks with magnitudes between M_2 and M_1 and only aftershocks with magnitudes at or above some threshold $m \equiv M_0 - \mu_3$. We invoke the thresholds M_2 and m for practical reasons as all catalogues are incomplete and inhomogeneous for small magnitudes. However, these thresholds may be of some value in explaining physical relationships, as the details of premonitory patterns may be different in different magnitude ranges.

Pattern B consists of a main shock and its aftershocks for which $b_i \geq C$. A more flexible definition of a threshold for b_i can be given[5], but it is not required for the present purposes.

An alarm is declared for a period of τ years after pattern B is diagnosed. A strong earthquake is expected during this period, having been predicted by pattern B. The alarm is terminated either at the time a strong earthquake takes place or at the end of this period, whichever comes first.

Pattern S ('swarms') was introduced elsewhere and its parameters were adjusted to the Italian earthquake catalogue[6]. We count the number of earthquakes in a time-window from $(t-s)$ to t, in the same magnitude range as above and in a restricted depth range. Let $N(t)$ be the total number of such earthquakes in the region. A reduced number of earthquakes $n(t)$ is obtained from $N(t)$ by the elimination of aftershocks of strong earthquakes. We then consider the map of the epicentres that are counted to determine $n(t)$. From this map we determine a third function $r(t)$ which is the maximum number of epicentres that can be surrounded by a small rectangular cell of dimensions $\Delta\phi$ in latitude and $\Delta\lambda$ in longitude.

Pattern S consists of a group of earthquakes such that $n(t) > \max\{C_1, C_2\bar{N}(t)\}$ and $r(t) > C_3 n(t)$. $\bar{N}(t)$ is the average of $N(t)$ over the interval t_0 to t or from $(t-ks)$ to t. The threshold M_1 plays no part in the identification of this pattern.

Pattern Σ has been introduced elsewhere[7] and its parameters were adjusted to some of the strongest earthquakes of the world. It is represented by a peak of the function $\Sigma(t) = \sum_i G(M_i)$ where the summation takes place over the same band of time and magnitude intervals as above. Aftershocks of strong earthquakes are eliminated from the summation. $G(M)$ is specified[7] to be $G(M) = 10^{d(M-f)}$ where d and f are numerical parameters. Pattern Σ consists of earthquakes satisfying the condition $\Sigma(t) \geq \bar{\Sigma}$. The values $\bar{\Sigma} = cG(M_0)$, $c = 0.5$, $d = 0.91$ have been assumed elsewhere[7].

Alarms after patterns S and Σ are declared in the same manner as indicated after pattern B.

Data processing

We have tested pattern B in a retrospective 'prediction' of strong earthquakes in the five regions indicated in Table 1. Arbitrary decisions have had to be made regarding the definition of the geographical boundaries of these regions as well as the values of all parameters. No *a priori* theoretical limits can be imposed on these decisions and we have to obtain them by data fitting. This creates a danger of self-deception as the number of these decisions is rather large. To decrease this danger we have tried to make these decisions simple, uniform and, if possible, *a priori*. Also we have accepted, when possible, the arbitrary choices of parameters or thresholds made in previous studies, and we have

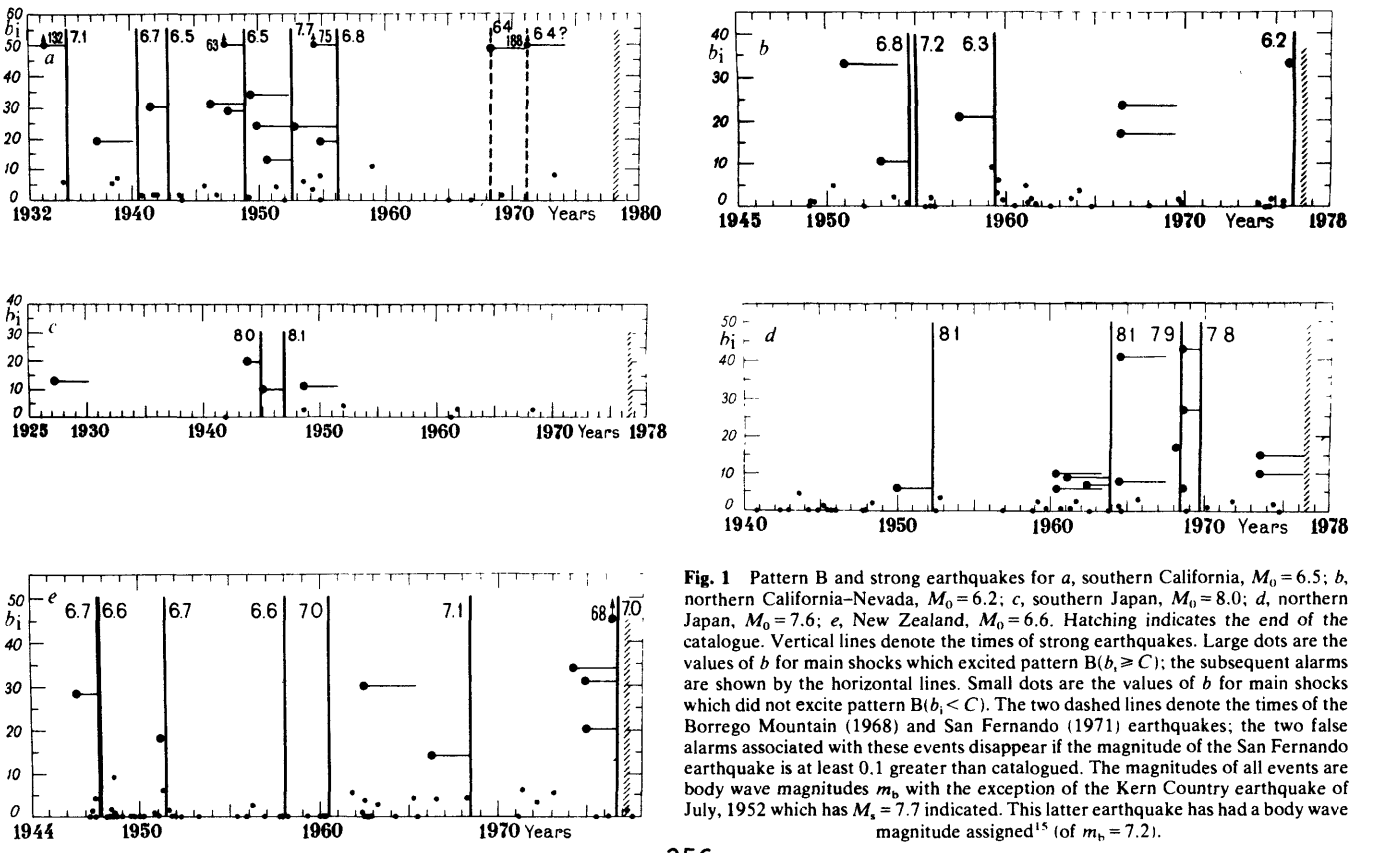

Fig. 1 Pattern B and strong earthquakes for *a*, southern California, $M_0 = 6.5$; *b*, northern California–Nevada, $M_0 = 6.2$; *c*, southern Japan, $M_0 = 8.0$; *d*, northern Japan, $M_0 = 7.6$; *e*, New Zealand, $M_0 = 6.6$. Hatching indicates the end of the catalogue. Vertical lines denote the times of strong earthquakes. Large dots are the values of b for main shocks which excited pattern B($b_i \geq C$); the subsequent alarms are shown by the horizontal lines. Small dots are the values of b for main shocks which did not excite pattern B($b_i < C$). The two dashed lines denote the times of the Borrego Mountain (1968) and San Fernando (1971) earthquakes; the two false alarms associated with these events disappear if the magnitude of the San Fernando earthquake is at least 0.1 greater than catalogued. The magnitudes of all events are body wave magnitudes m_b with the exception of the Kern Country earthquake of July, 1952 which has $M_s = 7.7$ indicated. This latter earthquake has had a body wave magnitude assigned[15] (of $m_b = 7.2$).

Table 2 Pattern B and strong earthquakes

Month-day-year	epicentre ϕ	λ	M	b_i $R = 50(100)$ km $e = 2$ d	$e = 7$ d	δT (yr)	n_m
Southern Japan							
Polygon: (30; 130), (33; 139), (39; 136), (33; 127.5)							
3- 7-27	35.6	135.1	7.5	13	18	7.8	
9-10-43	35.5	134.2	7.4	20	25	1.24	
12- 7-44	33.7	136.2	8.0	3	3		3
1-13-45	34.7	137.0	7.1	10	17	1.94	
12-21-46	33.0	135.6	8.1	2	3		1
6-28-48	36.1	136.2	7.3	11	11	≥30	
Northern Japan							
Polygon: (33; 139), (37; 145), (40; 146), (45; 154), (49; 150), (45; 140), (39; 136)							
12-26-49	36.7	139.7	6.7	6	7	2.19	
3- 4-52	42.2	143.9	8.1	6(21)	9(28)		14
3-21-60	39.8	143.5	7.5	10(13)	19(30)	3.56	
3-23-60	39.3	143.8	6.7	6	6	3.56	*
1-16-61	36.0	142.3	6.8	9(13)	9(13)	2.74	
4-12-62	38.0	142.8	6.8	7(8)	10(12)	1.50	
10-13-63	43.8	150.0	8.1	4(8)	9(16)		15
5- 7-64	40.3	139.0	6.9	8	10	4.03	
6-16-64	38.4	139.2	7.5	41(42)	48(52)	3.92	
1-29-68	43.2	147.0	6.9	17(21)	23(33)	0.30	
5-16-68	40.7	143.6	7.9	12(45)	17(65)		6
5-16-68	41.4	142.8	7.5	27	50	1.24	*
5-17-68	39.8	143.5	6.7	6	7	1.24	
6-12-68	39.4	143.1	7.2	43(45)	51(55)	1.17	
8-12-69	42.7	147.6	7.8	7(37)	18(66)		4
6-17-73	43.0	146.0	7.4	15(30)	18(45)	>4	
6-24-73	43.0	146.8	7.1	10(30)	16(45)	>4	*

Values of b_i for $R = 100$ km are indicated only if they are not the same as for $R = 50$ km; δT, time from the given pattern B until the next strong earthquake; n_m, the number of all main shocks between the given and preceding strong earthquakes, or since the beginning of the catalogue in the case of the first strong earthquake; * denotes a main shock, that would have been identified as an aftershock with $R = 100$ km.

tested the stability of our results with regard to variations in each of these choices. We have considered only those earthquakes with $h \leq 100$ km.

We have assigned the following values: $\tau = 3$ yr; $e = 2$ days; $\mu_1 = 0.1$; $\mu_2 = 1$; $\mu_3 = 3.5$. These values were obtained by data fitting for southern California[5]. To define aftershocks we took $R = 50$ km; $T(M) = 0.5$ years for $5.0 \leq M \leq 5.4$, $T(M) = 1$ yr for $5.5 \leq M \leq 6.4$ and $T(M) = 2$ yr for $M \geq 6.5$. The values of $R(M)$, $T(M)$ given elsewhere[3] for the southern California catalogue give better results, but these fine gradations are hardly warranted in view of the accuracy of some of the other catalogues used in this study. The values of $R(M)$ and $T(M)$ assumed here have the advantage that they can be used for a fast diagnosis of pattern B even before the epicentres of aftershocks are determined precisely.

The values of M_0 and C listed in Table 1, have been chosen separately for each region due to lack of experience and a satisfactory theory. The fact that these two parameters have been chosen *a posteriori* contributes the single largest difficulty in the evaluation of the significance of our results.

We have chosen the other parameters to be the same for all regions, even if they are unreasonably simple. This suffices for our present purpose which is to test the existence and stability of pattern B. For actual predictions, the parameters could probably be better adjusted to match the specific geophysical characteristics of the region as well as its own earthquake catalogue. More detailed studies of pattern B in some specific regions will be published elsewhere[8].

The boundaries of the southern California as well as the northern California–Nevada regions are defined elsewhere[4,9]. We straightened these boundaries slightly from the original definitions, and have deleted the area around Cape Mendocino from the northern California study as it has a distinctly isolated cluster of epicentres. The boundaries of the other regions are based on large-scale neotectonics and on the densities of epicentres.

Results

The results are summarised in Table 1. Examples of the details are documented in Table 2 and displayed in Fig. 1. The total span of all five catalogues is 202 yr. Twenty-three strong earthquakes occurred in the five regions during these time intervals. Eighteen of these earthquakes were retrospectively predicted, that is, they took place during the intervals of alarms sounded after each instance of pattern B. The total duration of these alarms is 60 yr or 30% of the total span of the catalogues. If we exclude the results for southern California, which were highly involved in the data fitting, that is, in the adjustment of parameters, we have 13 out of 17 strong earthquakes predicted for the remaining four regions; the total duration of alarms is 39 out of 155 yr or 25% of the total time.

Although these numerical values illustrate the practical efficiency of pattern B as a tool in prediction, they cannot be used in statistical tests of the existence of pattern B as, by the definition above, an alarm is terminated by the occurrence of a strong earthquake. To perform this statistical test (of the exis-

tence of pattern B), the values of the three parameters, N_A, N_B, and T_τ/T were tabulated and listed in Table 1.

The probability that a random binomial process could do as well or better than pattern B in anticipating strong earthquakes is given by the quantity $(1-P)$. This is the probability that N_A events or more will occur out of N_B tries in the fraction T_τ/T of the total catalogue time T according to a random binomial process. The values of P strongly support the hypothesis that B is a premonitory pattern, although these values of probability should only be used in a qualitative sense rather than literally. The fact that some thresholds were chosen *a posteriori* leads to an overestimation of P. On the other hand, the fact that some thresholds are chosen to be the same for all regions, leads to an underestimation of P. For example, the earthquake in southern Japan of 28 June 1948 could be deleted as a cause of a false alarm (Table 2) either by (1) changing e from 2 to 7 days, and/or (2) changing m to 5.0 from 4.5. Both of these changes are not unreasonable: in the first instance because $M_0 = 8$ is especially large and in the second because the catalogue[10] is more reliable for magnitudes greater than 5 than it is for magnitudes between 4.5 and 5. The last two false alarms for the southern California catalogue (Fig. 1) disappear if we assume that the magnitude of the San Fernando earthquake of 9 February 1971 is 6.5 instead of 6.4; this question is discussed elsewhere[5]. Similarly, the values of P could be increased by adjusting some of the parameters to take into account specific traits of the observed seismicity for each region separately. However, these adjustments would be non-unique; for the purpose of testing the existence of pattern B as a precursor, it is better to keep the criteria for all regions as uniform as possible, and that we make them, insofar as possible, *a priori*, and hence avoid tampering with the results by intuitive 'improvements' after inspection of the tabulations.

In the case of the northern California–Nevada catalogue we took $m = 3$, instead of $m = 2.7$ which would have been obtained from a literal application of our uniform definition $\mu_3 = 3.5$; this catalogue is especially inhomogeneous for $m < 3$. The errors in prediction with $m = 2.7$ and $m = 3$ are the same.

Table 2 lists the strong shocks as well as the main shocks that trigger pattern B; the strong shocks are underlined. Thus it is possible to see whether or not a strong shock was preceded by pattern B within 3 yr. Table 2 shows that our results remain essentially unaltered when the value of R is changed to 100 km and/or e to 7 d. Similar results have been obtained for the other catalogues.

We have indicated in Table 2 those events that would have been identified as aftershocks of the event immediately preceding had we used $R = 100$ km; deletion of these events from our listing would have improved our success rate as these invariably result in a reduction in N_B without a corresponding decrease in N_A. There are two examples of entries of this type in the southern California catalogue and none in the northern California and New Zealand catalogues.

A more detailed analysis of the stability of pattern B as well as the choice of the optimum parameters for the diagnosis of pattern B requires a separate study for each region. We have tried here to emphasise that pattern B can score quite satisfactory success-to-failure ratios, even with parameters that are uniform for all regions, despite the fact that each region has widely different tectonics, seismicity and quality of earthquake catalogue from the others.

A speculation on generalisation

The same catalogues were processed to detect the presence of patterns S and Σ (Fig. 2). The value of M_0 is assumed to be the same as for pattern B. As in the papers where these patterns were introduced[6,7], the parameters were taken to be as follows: $C_1 = 0$, $C_2 = 1$, $C_3 = 0.5$, $\mu_2 = 2$, $\mu_1 = 0.5$ for Σ (absent for S), $d = 0.91$, $f = 4.5$, $s = 1$ yr for S. For Σ we varied $\bar{\Sigma}$ and s for each of the regions (Fig. 2). The absence of a pattern signifies that it could not be detected for the given region. We added data for Alaska in view of the striking success of pattern Σ.

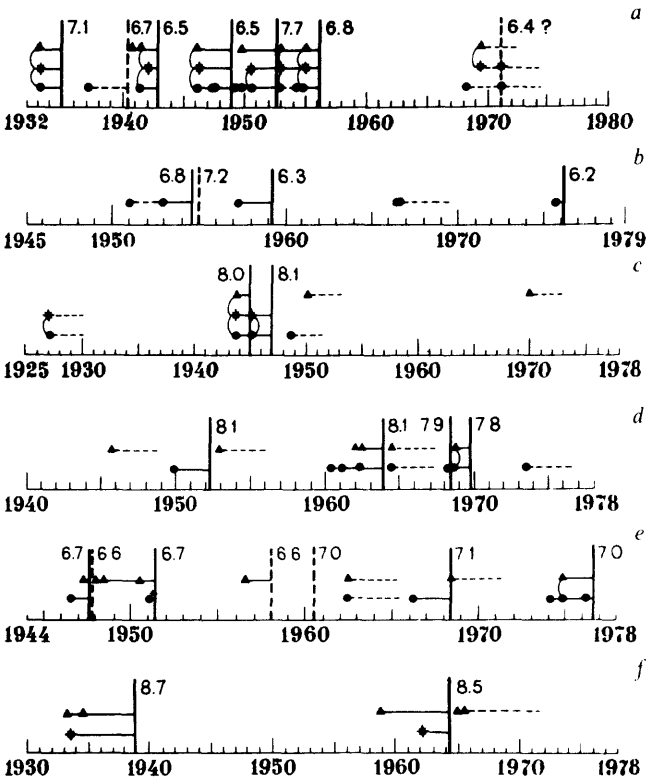

Fig. 2 Occurrence of patterns B (●), S (+) and Σ (▲).

	$\bar{\Sigma}$	s (yr)	$\Delta\phi$	$\Delta\lambda$
a, Southern California	60	1	0.4°	0.6°
b, Northern California–Nevada				
c, Southern Japan	900	3	0.4	0.6
d, Northern Japan	700	1	1.0	1.4
e, New Zealand	95	0.5	0.4	0.6
f, Alaska	770	2	0.5	1.0

Solid horizontal line is period of alarm; dashed is false alarm. Solid vertical line is time of strong earthquake; dashed is strong earthquake not predicted by pattern B. Brackets denote different patterns generated by the same main shock and the appropriate parts of its aftershock series.

In several cases the same main shock and its aftershocks will give rise to several different patterns from among Σ, S, B. This result is not unreasonable as by definition, a main shock and its aftershocks will generate:

(1) pattern B if the number of aftershocks during the first e days is large enough;

(2) pattern S if the number of aftershocks during the time interval s, or during any part of it, is large enough; we usually take $s = 1$ yr;

(3) pattern Σ if a sufficiently large number of events have magnitudes close to the upper limit M_1.

In most cases in southern California the same main event plus its aftershocks generate two or even all three patterns. Moreover, the coincidence of a combination of two or three of the patterns eliminates false alarms without adding any failures-to-predict[5].

Patterns Σ and S also appear in conjunction before extremely strong earthquakes in the Tibet–Himalaya region[8]; in this region pattern B cannot be diagnosed, as the catalogues that are available do not include aftershocks.

We find that prediction by pattern B is successful when two conditions are satisfied: not only is a large number of aftershocks b_1 required but also the main shock producing it must have a large enough magnitude; if the magnitude of a main shock is too

low, but is still followed by an exceedingly large b_1, a false alarm will be generated. We have therefore introduced the threshold M_2. On the other hand we find both the numbers of false alarms and failures-to-predict increase significantly if we ignore the number of aftershocks produced by a main shock and merely consider the occurrence of a main shock itself as a possible precursor: for example, these numbers increased when we considered as a premonitor any earthquake with magnitude up to M_0, that is, by removing the gap between M_2 and M_0, by increasing M_1 and ignoring the threshold C.

We can imagine that a hypothetical generalised premonitory pattern exists which is an abnormal clustering of earthquakes in a space–time–energy domain. We call this hypothetical pattern a 'burst of seismicity'. Our three particular patterns may represent different projections of this generalised pattern. The definitions of the three are neither unique nor optimised; the use of discrete magnitude thresholds, especially in regard to large uncertainties in magnitudes of earthquakes in the catalogues, is an inadequate and troublesome aspect of the work so far. Our results indicate, however, that these patterns exist and deserve attention.

We have refrained from providing additional refinements, such as geological regionalisations or to assign probabilities to the forecasts as functions of time to the forthcoming event and its magnitude. The results of the present exploration indicate that such refinements are necessary and we hope that they would improve our success ratios, which are surprisingly high despite the simplicity of the criteria we have used.

This research was performed as part of Project III of the US–USSR cooperative programme in earthquake prediction. V.I. K.-B. was a Fairchild Scholar at the Seismological Laboratory, California Institute of Technology, and visiting professor at the Institute of Geophysics and Planetary Physics, University of California, Los Angeles. The following members of the Seismological Laboratory supported this research: C. Allen, D. Anderson, D. Harkrider, H. Kanamori, K. McNally, B. Minster. We also thank D. Eckelmann, T. Hearn, C. Johnson, J. Gardner, Y. Kagan, B. Bolt, J. Evernden, W. Lee, and R. Lamoreaux for comments and assistance. Financial support of the Office of Earthquake Studies, US Geological Survey is also acknowledged. This is publication no. 1882 of the Institute of Geophysics and Planetary Physics, University of California, Los Angeles and contribution no. 3261 of the Division of Geological and Planetary Sciences, California Institute of Technology, Pasadena.

Received 15 December 1978, accepted 8 November 1979

1. Keilis-Borok, V. I., Podgayetskaya, V. M. & Prozorov, A. G. *Comput. Seis.* **5**, 55–79 (1971).
2. Knopoff, L. & Gardner, J. K. *Geophys. J. R. astr. Soc.* **28**, 311–313 (1972).
3. Gardner, J. K. & Knopoff, L. *Bull. seis. Soc. Am.* **64**, 1363–1367 (1974).
4. Hileman, J. A., Allen, C. R. & Nordquist, J. M. *Seismicity of the Southern California Region, 1 January 1932 to 31 December 1972* (Seismological Laboratory, California Institute of Technology, 1973).
5. Keilis-Borok, V. I., Knopoff, L., Rotvain, I. M. & Sidorenko, T. M. *J. geophys. Res.* (in the press).
6. Caputo, M. *et al. Annali Geofis.* (in the press).
7. Keilis-Borok, V. & Malinovskaya, L. N. *J. geophys. Res.* **69**, 3019–3024 (1964).
8. Keilis-Borok, V., Knopoff, L. & Allen, C. R. *J. geophys. Res.* (in the press).
9. Bolt, B. & Miller, R. D. *Catalog of Earthquakes in Northern California and Adjoining Areas 1 January 1910–31 December 1972* (Seismological Stations of the University of California at Berkeley, 1975).
10. *Catalog of Major Earthquakes which occurred in and near Japan, 1926–52* (Japan Meteorological Agency).
11. Friedman, M. F., Whitcomb, J. H., Allen, C. R. & Hileman, J. A. *Seismicity of the Southern California Region, 1 January 1972 to 31 December 1974* (Seismological Laboratory, California Institute of Technology, 1976).
12. *Catalog of the Earthquakes of Southern California, 1974–77* (Seismological Laboratory, California Institute of Technology).
13. Smith, W. V. Z. *J. Geol. Geophys.* **19**, 393–4 (1976).
14. *U.S. Geological Survey, Earthquake Hypocenter Data File* (NOAA, 1977).
15. Bolt, B. A. *Bull. seis. Soc. Am.* **68**, 513–515 (1978).

(page 361 follows)

JOURNAL OF GEOPHYSICAL RESEARCH, VOL. 85, NO. B2, PAGES 803-811, FEBRUARY 10, 1980

Bursts of Seismicity as Long-Term Precursors of Strong Earthquakes

V. I. KEILIS-BOROK

Institute of Physics of the Earth, USSR Academy of Sciences, Moscow

L. KNOPOFF

Institute of Geophysics and Planetary Physics, University of California, Los Angeles, California 90024

I. M. ROTVAIN AND T. M. SIDORENKO

Institute of Physics of the Earth, USSR Academy of Sciences, Moscow

One or more earthquakes with abnormally large numbers of aftershocks at the beginning of their aftershock sequences are possible long-term precursors of a stronger earthquake. This precursor, named pattern B (bursts of aftershocks), was tested together with two other possible premonitory patterns, S and Σ, described previously. Pattern S (swarm) consists of the spatial clustering of earthquakes at a time when the seismicity of the region is above average. Pattern Σ consists of an increase in the sum of earthquake energies to the 2/3 (roughly) power, in a sliding time window. These three patterns were tested by retrospective long-term prediction of earthquakes of Southern California, 1932-1977, with magnitudes ≥6.5. The total duration of identified periods of elevated probability of occurrence is about 14 years. Five out of six earthquakes occurred during these intervals. However, the patterns do not indicate the exact location of future strong earthquakes within the region. All three patterns seem to represent different projections of the same general pattern, of 'bursts of seismicity,' i.e., an abnormal clustering of earthquakes in the time-space-energy domain. Pattern B also precedes strong earthquakes in New Zealand and Italy; Pattern Σ precedes strong earthquakes in New Zealand.

1. INTRODUCTION

The logic of a search for premonitory seismicity patterns to identify precursors of large earthquakes is based on certain simple assumptions which take the form of platitudes.

1. If causally related earthquakes are present in a catalog, then the statistics of the earthquakes in the catalog do not exhibit a Poissonian distribution.

2. The study of very large earthquakes in a given relatively homogeneous region usually leads us to a listing of such a small number of large events that we have a population that is too small to apply statistical methods.

The existence of precursors to earthquakes implies that causal relationships exist. In our model, such causal relationships can be taken to be either passive or active. If the precursors are passively related to a subsequent large shock, we may assume that both are the result of some third process such as increasing nonlinearity of the rocks surrounding a fault. If the precursors are actively related to the subsequent shock, they are triggering agents. We seek to identify patterns in earthquake sequences which are causally related to later larger earthquakes. (With regard to the first of the assumptions above, we remark that triggering relationships among earthquakes are all too abundant: aftershocks, in a conventional sense, are most obviously events that are triggered by other earthquakes.)

Let us suppose that aftershocks can be identified, even if by an arbitrary parameterization. If these aftershocks are removed from the catalog, the residual catalog is found to be Poissonian in character [*Gardner and Knopoff*, 1974]. This means that any identifiable causal relationship between relatively infrequent earthquakes, if it is present at all, is a small effect and is likely to be lost if it is imbedded in a large residual catalog from which aftershocks have been removed.

Kagan and Knopoff [1976] have devised one method of increasing the sensitivity of the search within a mostly Poissonian residual catalog to try to identify causally connected events preceding large earthquakes. Indeed, the method can be applied to complete catalogs and need not be applied solely to residual catalogs. Kagan and Knopoff have computed the second moment of the occurrence of earthquakes in a catalog in which the number of earthquakes occurring within a given magnitude interval, time interval, and distance interval of any event in the full catalog is tabulated. In their study, as could have been anticipated, the most obvious feature of the second moment of the catalog is that aftershocks are clustered at short distance intervals and short time intervals. One weak but statistically significant feature in their work shows considerable promise for our present task, which is evidence for a causal relationship between large earthquakes and other slightly smaller earthquakes at distances of the order of hundreds of km and times of the order of years. We remark that there is an implication that there is still a large enough catalog to test the statistical significance.

In this paper we present the results of an exploration of a hypothesis that causal relationships are prominent events at the level of large magnitudes and are not merely a small fluctuation on an otherwise Poissonian process. If our hypothesis is correct, then the effect of foreshock pair correlations for large earthquakes should be enhanced at a distance range of the order of hundreds of km and times of the order of years. Again, if our hypothesis is correct, the reason for the observation of only weak correlations in the earlier study may be due to the method of averaging across a number of different geographic regions to increase statistical populations or the choice of a simple space-time projection to display correlations; if smaller magnitude earthquakes are included in a catalog, they serve to increase the size of the population, but if pair correlations are negligible or absent in this magnitude

Paper number 9B1330.
0148-0227/80/009B-1330$01.00

TABLE 1. Window for Identification of Aftershocks

M	R, km	T, days
2.5	19.5	6.
3.0	22.5	11.5
3.5	26.	22.
4.0	30.	42.
4.5	35.	83.
5.0	40.	155.
5.5	47.	290.
6.0	54.	510.
6.5	61.	790.
7.0	70.	915.
7.5	81.	960.
8.0	94.	985.

range, this will lower the statistical significance of possible correlations for larger earthquakes. If the accentuated effect can be identified and is sufficiently strong, then this may become a useful precursor for the forecasting of strong earthquakes. Here we face the ominous barrier of the second assumption. If we reduce the geographic scope of our investigations to a small scale, we lose the advantages of testing our conjectures by statistical methods, since the number of strong earthquakes occurring in the time span of modern, well-documented catalogs is generally small for most regions of the world on the distance scale of a few hundreds of kilometers. Because of this, we can only construct our model as conjecture and display the results; but we cannot substantiate these results, if any, on statistical grounds. A similar situation has arisen in the case of prediction of locations of epicenters of large earthquakes [*Gelfand, et al.*, 1976].

2. Bursts of Aftershocks: Pattern B

We wish to study seismicity patterns premonitory to earthquakes with magnitude $M \geq M_0$. Such earthquakes will be called strong. In the first example we have used below, namely, that of earthquakes in Southern California, we have set $M_0 = 6.5$. There are five independent events with $M_0 \geq 6.5$ in the Southern California catalog 1932–1978. We study earthquakes with magnitudes less than M_0 as events that are possible candidates for causal connection with subsequent strong earthquakes. These are presumed to be relatively large

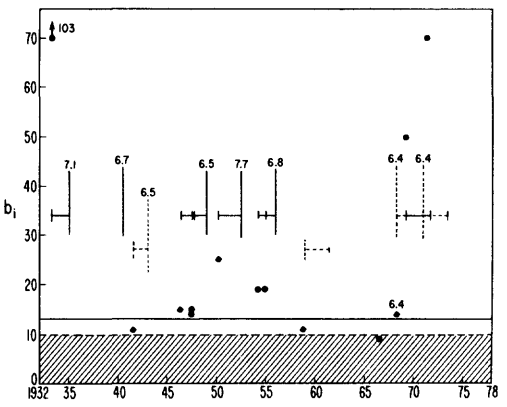

Fig. 1. Pattern B for Southern California. Aftershocks have been identified by the windows given in Table 1. Black dots are the numbers of aftershocks in the first 2 days following a main shock. Most of the main shocks have $b_i \leq 10$ and are not shown. Long vertical strokes indicate the dates of strong earthquakes with magnitudes indicated. Horizontal bars span the prediction windows. The heavy horizontal line is the threshold $\bar{b}$.

shocks in the next lower band of magnitudes. Earthquakes with $M_1 \leq M < M_0$ are called main shocks. In the Southern California example we restrict main shocks to be in the band $5.4 \leq M < 6.5$. We specifically exclude from the class of main shocks those shocks in this magnitude band that are aftershocks of strong earthquakes.

We seek to identify main shocks with an abnormally large number of aftershocks concentrated at the beginning of the aftershock sequence. We test whether such events are premonitory to strong earthquakes. The pattern of such premonitory events will be referred to as pattern B.

We now define aftershocks, which is necessary for two reasons. First, we shall count aftershocks in order to define those main events which have abnormally large numbers of aftershocks associated with them. Second, we wish to delete aftershocks of strong earthquakes from the class of main shocks, even though they are in the correct magnitude band.

To avoid bias in the counting process due to inhomogeneity in the catalog, we truncate the catalog at some lower magnitude threshold m, rejecting all shocks with magnitudes less than m. There are several possible inhomogeneities we wish to avoid including (1) inadequate coverage of small earthquakes, (2) a possibility that inadequate numbers of small and moderate sized earthquakes are tabulated immediately after a large event, (3) the catalog may include earthquake sequences which have been the subjects of special studies, including microearthquake studies. *Knopoff and Gardner* [1969] have given an empirical procedure for determining the lower magnitude threshold of homogeneity of the catalog. For Southern California it has been found that from 1934 to 1952, $m \approx 3.8$; from 1952–1967, $m \approx 2.8$. For the Southern California catalog 1932–1978 that we have processed, we take $m = 3.8$.

An aftershock is defined as an event occurring within a time interval $\Delta T(M)$ after a main shock and within the spatial distance $\Delta\phi(M)$, $\Delta\lambda(M)$ of the epicenter (ϕ_i, λ_i) of the ith main shock. For Southern California earthquakes we need not apply a depth interval. Examples of catalog-filtering windows of this type have been given by *Keilis-Borok et al.* [1971], *Knopoff and Gardner* [1972], and *Gardner and Knopoff* [1974].

As our measure of the propensity of the earthquake to cause aftershocks, we count the number of aftershocks occurring within a time e following a main shock. In the example of Southern California we have chosen $e = 2$ days. We let b_i be the number of aftershocks during the first e days following the ith main shock.

We introduce a threshold $\bar{b}(t)$. If $b_i > \bar{b}$, then we declare that a main shock has occurred associated with a burst of aftershocks. In this circumstance a period of enhanced probability of occurrence of a strong earthquake is declared. This period of enhanced probability is terminated after the first strong earthquake in the region or after τ years, whichever comes first. In the Southern California case we take $\tau = 2.5$ years. We would prefer to call these periods of enhanced probability of occurrence alarms as a procedural description, but the shorter phrase probably has stronger connotations than we wish to impart at this time. However, we will use the phrase false alarm in this paper for brevity, implying thereby a declared period of enhanced probability of occurrence during which no strong earthquake occurs.

There are several definitions of the threshold $\bar{b}$ that are adequate to our purpose. First, we define $b(t)$ to be the maximum value of b_i in a sliding time window of width s, i.e., $b(t)$ is the largest value of b_i in the interval from $t - s$ to t. Then we may

TABLE 2. Strong Earthquakes and Pattern B in Southern California

N	Date	Epicenter λ, °W	Epicenter φ, °N	M	b_i (2 days)
	3-11-33	118.0	33.6	6.3	103
1*	12-31-34	114.8	32.0	7.1	
2	5-19-40	115.5	32.7	6.7	
	7-1-41	119.6	34.4	5.9	11
3†	10-21-42	116.0	33.0	6.5	
	3-15-46	118.1	35.7	6.3	14
	4-10-47	116.6	35.0	6.2	14
	7-24-47	116.5	34.0	5.5	15
4	12-4-48	116.4	33.9	6.5	
	7-28-50	115.6	33.1	5.4	18‡
5	7-21-52	119.0	35.0	7.7	
	3-19-54	116.2	33.3	6.2	19
	11-12-54	116.0	31.5	6.3	19
6	2-9-56	115.9	31.8	6.8	
	12-1-58	115.8	32.3	5.8	11
7	4-9-68	116.1	33.2	6.4	13
	3-21-69	114.2	31.2	5.8	42§
8	2-9-71	118.4	34.4	6.4	69

*Preceded by strong foreshock: date, 12-30-34; λ = 115.5; φ = 32.3; M = 6.5.

†Aftershock of 2.

‡26 shocks in 2-day interval straddling this event including foreshock and M = 5.5 aftershock.

§49 shocks in 2-day interval straddling this event, including foreshocks.

take $\bar{b}(t)$ to be the average value of $b(t)$ over the interval from the start of the catalog to time t; or we may take $\bar{b}(t)$ to be the average of $b(t)$ in the interval from $t - D$ to t, $D > s$. Or we may take $\bar{b}$ to be a constant proportional or equal to the long-term average of $b(t)$. Other definitions are possible.

Another measure of the strength of a burst of aftershocks could be the parameter B_1 in the Omori Law of aftershock occurrence, $\dot{n}(t) = B_1/t$, where $\dot{n}(t)$ is the number rate of occurrence of aftershocks at a time t after the main shock. According to our hypothesis, if a value of B_1 occurs which exceeds a certain threshold, we assume that the event causing the aftershocks is a precursor of a strong earthquake. If the number of aftershocks after a main shock is large enough, this measure may be preferable to the preceding one. We have not used this measure in the present analysis.

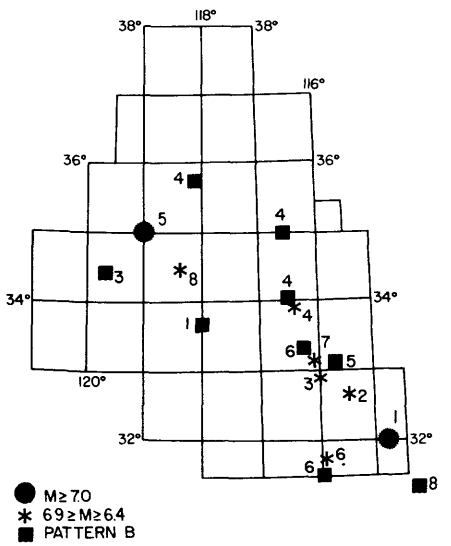

Fig. 2. Location of strong earthquakes and pattern B in Southern California.

3. Analysis of the Southern California Catalog

To test the hypothesis that bursts of aftershocks of main events are precursors of strong shocks, we first make some arbitrary decisions regarding the values of the thresholds and windows M_0, M_1, m, e, ΔT, $\Delta\lambda$, $\Delta\phi$, s, etc. There are so many adjustable parameters that we run the risk of self-deception by having a system with a large number of degrees of freedom. Hence it may be difficult to perform the job of data fitting honestly.

An updating of the Southern California catalog [*Hileman et al.*, 1973; *Friedman et al.*, 1976] to span the years 1932–1978 has provided the basis for the processing with the parameters M_0, M_1, m as above. We used the formula of *Gardner and Knopoff* [1974] to define aftershocks (Table 1). We also used other similar expressions to define aftershocks, to show that our results are not strongly sensitive to the details of the aftershock formula over a wide range of variation. We chose $e = 2$ days and $\tau = 2.5$ years, a posteriori. We have set the thresholds for identification of strong main shocks with large short-term bursts of aftershocks as $M_1 = 5.4$, $\bar{b} = 13$ aftershocks.

The results we have obtained are shown in Figure 1. We have plotted the numbers of aftershocks within 2 days, $b_i(2)$, following a precursory main event with $5.4 \le M \le 6.4$, as black dots in the figure. Most of the main shocks have values of $b_i(2)$ that are imbedded in the shaded region of Figure 1 and are not plotted in detail. In addition, we have not plotted the number of aftershocks of strong events. Strong events with $M \ge 6.5$ are identified by vertical lines occurring at the times of the events. The windows associated with the precursors are shown as horizontal bars. Of the five strong earthquakes ($M \ge 6.5$) in the Southern California geographic area, whose times are indicated in the figure, four were 'predicted' by pattern B. We failed to 'predict' one earthquake with $M = 6.7$ which occurred on May 19, 1940; that is to say, this earthquake was not preceded by any event up to 2.5 years before that had more than 13 aftershocks within 2 days and had a magnitude within the range $M_1 \le M < M_0$.

We discuss details of the interpretation. A false alarm would appear to be associated with the event of March 21, 1969 (M = 5.8). This event forecasts a strong earthquake within 2.5 years. In point of fact, we may identify the San Fernando earthquake (M = 6.4) as one which occurred within the specified time window. However, the magnitude of this event is 0.1 too small to fit the threshold of M_0. If we were prepared to lower the threshold of M_0 to 6.4, we would have been able to predict the San Fernando event, but in this case we must add the Borrego Mountain earthquake (April 9, 1968, M =

TABLE 3. Window for Identification of Aftershocks

M	R, km	T, days
$2.4 \ge M \ge 2.0$	20	1.43
$2.9 \ge M \ge 2.5$	20	2.85
$3.4 \ge M \ge 3.0$	20	5.70
$3.9 \ge M \ge 3.5$	40	11.41
$4.4 \ge M \ge 4.0$	40	22.81
$4.9 \ge M \ge 4.5$	40	45.63
$5.4 \ge M \ge 5.0$	40	91.25
$6.4 \ge M \ge 5.5$	40	182.5
$M \ge 6.5$	80	365.3

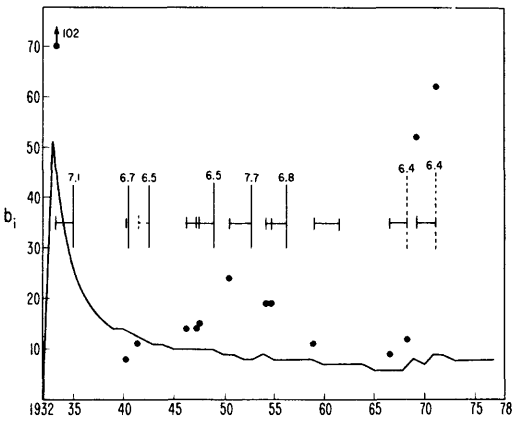

Fig. 3. Pattern B for Southern California. Aftershocks are identified by the windows in Table 3. The notation is the same as in Figure 1. The threshold $\bar{b}(t)$ is shown by the continuous curve.

6.4) to the list of strong earthquakes to be predicted. The Borrego Mountain event was not preceded by pattern B. Furthermore, if M_0 is not lowered, then the San Fernando earthquake also generated a false alarm, since it was not followed in the requisite 2.5 years by a strong earthquake. The Borrego Mountain earthquake is also an acceptable precursor under hypothesis B, but the window for this event is kept open by the succession of the two later events, each with magnitude acceptable in the range of M_1. Thus our score of success for the sequence of three earthquakes spanning the Borrego Mountain and San Fernando events is one failure to predict if $M_0 = 6.5$. If we lower the threshold for M_0 to 6.4, then our score for this triplet of events is one failure to predict and one success. If, however, the magnitude of the San Fernando earthquake were to have been underestimated by 0.1 magnitude or more, then our success score becomes one successful prediction. This discussion is given here to show how dependent our assessment is on the discretization of magnitudes, which of itself has large errors. This is one of the disadvantages of an algorithm which uses discrete thresholds and inaccurately measured magnitudes, themselves inappropriate to measure the size of an earthquake. One of the tasks of the future is to replace b_i by some smoothed functionals.

If we were to lower the threshold of $\bar{b}$ from 13 to 10, then two additional events become precursors. In the case $\bar{b} = 10$, we find that neither of the two new main events is followed by a strong succeeding earthquake within the time window. However, the precursor of July 1, 1941 ($M = 5.9$), actually was followed, within schedule, by an event with $M = 6.5$ (October 21, 1942). The latter event was identified by the windows in Table 1 as a late aftershock of the strong event with $M = 6.7$ (May 19, 1940), itself not predicted.

The second main shock that is introduced if we lower the threshold for $\bar{b}$ (December 1, 1968, $M = 5.8$) generates a false alarm.

The premonitory patterns B and corresponding strong earthquakes are summarized in Table 2. The locations of the events listed in the table are given in Figure 2. The distances between the premonitory pattern and the ensuing strong earthquakes are rather large on occasion.

Periods of enhanced probability occurred for 13.8 years or 30% of the 46-year period of the catalog if we assume that the interval begun by the Borrego Mountain earthquake is a false alarm. We say that since the algorithm predicted five events for which the windows were potentially open for 17.3 years, the probability of capturing four events and failing to capture a fifth, or capturing all five events, by a random binomial process would be

$$5\left(\frac{17.3}{46}\right)^4\left(\frac{28.7}{46}\right)+\left(\frac{17.3}{46}\right)^5 = 0.07$$

Therefore this method has a 7% chance of being a random predictor. We must be careful here, since we do not know how many degrees of freedom have been lost due to the introduction of a posteriori constraints. Only tests of pattern B on other regional catalogs, which use the same parametric values, can overcome this problem. Furthermore, we have not evaluated the effects of keeping windows open beyond the 2.5-year period due to a succession of precursors. As a predictor, our method has been successful at the 80% level, having successfully predicted four out of five events. If the magnitude of the San Fernando earthquake were 6.5 or greater, periods of enhanced probability occur for 24% of the time, the chance that pattern B is a random predictor is 3.5%, and all forecasts are followed by strong earthquakes.

We have made an alternative assessment of the same catalog using a different threshold, We have reduced m to zero, i.e., we have used all earthquakes as listed, without regard to homogeneity of the catalog. In this case, aftershocks were defined by the window specified in Table 3.

The results are shown in Figure 3. In this case, as before, we listed the number of aftershocks that occur in a 2-day interval following all main shocks $5.4 \leq M \leq 6.4$. The function $\bar{b}(t)$ was constructed using $s = 1$ year; the quantity $\bar{b}(t)$, shown as the solid curve in Figure 3, is the running average of $b(t)$ from the start of the catalog. The Long Beach earthquake of 1933 ($M = 6.3$) had 102 aftershocks in a 2-day interval, and this leads to the large spike in $\bar{b}(t)$ at the beginning of the time interval. After a long time, the curve of $\bar{b}(t)$ stabilizes near a value of about 8. Twelve events in the magnitude range $5.4 \leq M \leq 6.4$ had aftershocks that were above threshold $\bar{b}(t)$. The event of October 21, 1942 ($M = 6.5$), identified as a late large aftershock in our first study, now emerges as an independent strong event. Neither this event nor that of its parent in the first study (May 19, 1940, $M = 6.7$) are 'predicted' by this algorithm, in which a window is once again opened for 2.5 years following the precursor. The remaining four strong earthquakes are predicted, as before. There is one false alarm not introduced before.

With regard to the Borrego Mountain–San Fernando pair, there are four precursors, including these two events themselves. None of these 'precursors' was followed by a shock with $M \geq M_0 = 6.5$. Since these events occur in sufficiently close succession to keep the prediction window open, this sequence must be counted as generating one false alarm. If, however, we lower the threshold to $M_0 = 6.4$, both Borrego Mountain and San Fernando events are successfully pedicted. Our score for this sequence is therefore one false alarm if $M_0 = 6.5$, two successful predictions if $M_0 = 6.4$, one successful prediction if $M_0 = 6.5$ and the magnitude of the San Fernando event is 6.5 or greater. We have already mentioned above the disadvantages of the use of discrete thresholds.

We have noted that the Long Beach earthquake of 1933 keeps the threshold $\bar{b}$ considerably higher than its asymptote for about 20 years due to the method of using a running average from the start of the catalog. This is an initial transient; later strong events such as 1969 and 1971 did not produce such a strong effect. If we lower $\bar{b}$ to a value close to its

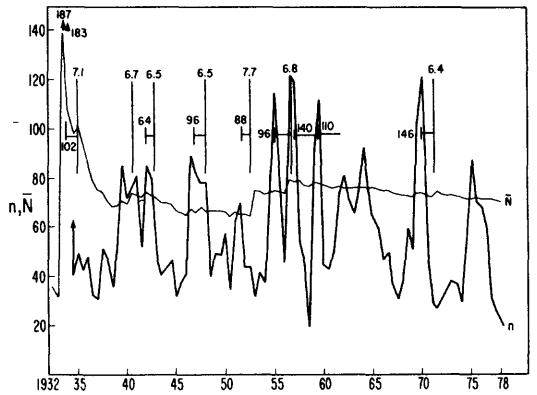

Fig. 4. Pattern S for Southern California. Alarms start at the date when pattern S ($n > \bar{N}$, $2r \geq n$) is diagnosed. The number at the beginning of the prediction window is the value of $2r$. Other notation as in Figure 1.

asymptotic value of 8, then one additional main shock (1941) emerges above threshold and becomes a predictor for the strong earthquake of October 21, 1942 ($M = 6.5$).

A curiosity is the main event with eight aftershocks which occurred on May 18, 1940. This number of aftershocks is at the asymptotic threshold. This event preceded the strong earthquake with $M = 6.7$ by only 23 hours; the two events are widely spaced at a distance of about 160 km. The threshold number of aftershocks was not attained within 23 hours. Whether this is to be counted as a precursor or not depends on (1) whether we use a literal interpretation of the threshold and (2) whether the model accommodates the maintenance of a regional interval of enhanced probability after a strong earthquake has occurred. By our definition this main event is not a precursor to the $M = 6.7$ event.

With a uniform threshold of $\bar{b} = 8$, with $M_0 = 6.4$ our score in this variation is seven successes, one failure to predict, and one false alarm.

4. Earthquake Swarms: Pattern S

A second premonitory pattern, S, can be considered as a variation of the first [*Caputo et al.*, 1978; *Keilis-Borok and Rotvain*, 1978; *Evison*, 1977]. A swarm is defined as a group of earthquakes concentrated in time and in space and occurring at a time when the seismicity of the region is not below average. In this case we analyze seismic activity over a longer time span than in the case of pattern B. In the case of Southern California we use a span of 1 year, as in the examples of the literature cited.

We make the following definitions:

1. Let $N(t)$ be the total number of earthquakes with $M \geq m$ occurring within the time interval from $t - s$ to t and within an entire region such as Southern California. The count includes aftershocks of strong earthquakes.

2. Let $\bar{N}(t)$ be the running average of $N(t)$ using a time window which either starts at the beginning of the catalog or uses a window extending from $t - D$ to t; $D > s$.

3. Let $n(t)$ be the number of earthquakes with $M \geq m$ occurring within the time interval extending from $t - s$ to t and within the entire region, but in this case, excluding aftershocks of strong earthquakes.

4. Let $r(t)$ be the maximum number of earthquakes with $M \geq m$ in the time interval from $t - s$ to t and occurring within a rectangle R of dimensions $\Delta\phi$ in latitude and $\Delta\lambda$ in longitude and arbitrarily located within the region.

We declare that pattern S, or a swarm, has occurred if

$$n(t) > C_1\bar{N}(t)$$

and

$$r(t) > C_2 n(t)$$

for at least one rectangle R, where C_1 and C_2 are constants. In this circumstance a period of enhanced probability of occurrence of a large earthquake is initiated. As before, the interval of higher probability is terminated after the first strong earthquake in the region, or after τ years, whichever comes first. This interval can be extended beyond τ years by recurrence of pattern S within an existing interval. Since $\bar{N}(t)$ may be too small to determine pattern S near the start of some catalogs, we add the condition $n(t) > C_3$.

The results for Southern California are shown in Figure 4. The cutoff magnitude has been chosen to be $M = 3.8$ as before. The curve of $n(t)$ is computed using a 1-year window; adjacent points are overlapping evaluations taken 6 months apart. The rectangles, as in the cases of Anatolia and Italy, were of dimensions 20 × 20 km; in practice we find we may use Tables 1 or 3 with equal ease. We have used the window of Table 1. The curve for $\bar{N}(t)$ is computed as a running average from the start of the catalog. As before, there is a huge spike associated with the Long Beach earthquake which occurs shortly after the start of the catalog. The much more irregular curve is the graph of $n(t)$, which shows periods of elevated seismicity in Southern California not associated with large earthquakes. Some of the elevated seismicity is of a broad regional character, and some of it is local. We have identified the locally intense regions from the calculation of $r(t)$. We choose $C_1 = 1$ and $C_2 = \frac{1}{2}$, as in the examples of Anatolia and Italy. The times for which $2r(t)$ exceeds $n(t)$ are shown by the short vertical strokes which indicate the start of a period of enhanced probability. The value of $2r$ is shown next to the short vertical stroke. The score for our analysis is the same as before: all earthquakes predicted by pattern B are predicted once again by pattern S. The Borrego Mountain sequence acts as a precursor for the San Fernando sequence. We continue to have one false alarm starting in 1959. We fail to predict the 1940 ($M = 6.7$) earthquake. The magnitude 6.5 aftershock of this event is predicted by a precursor which is near the threshold. Finally, the same events that serve as precursors by generating pattern S also serve as precursors by generating pattern B. This means that short-term aftershock activity, i.e., within 2 days of a main event, necessary for generating pattern B, is also associated with activity over an annual interval which generates pattern S.

5. Pattern Sigma

Some unease is certain to occur regarding the counting of numbers of earthquakes in the preceding patterns. The cessation of rupture in the dynamical earthquake process may depend on inhomogeneities in the rheological environment [*Knopoff*, 1972]. A given budget of stress-energy can be released by a wide variety of individual frequency-magnitude sequences, each presumably reflecting the local variations in strength of rocks. The question arises whether we should give more attention to a sequence of small earthquakes which may mirror the presence of a series of 'unbreakable objects' in the fault region with a relatively short spacing in comparison with a single large earthquake. For example, should two associated events of magnitude 5.0 count as the cardinal number two in a counting scheme and hence have twice as much weight as a

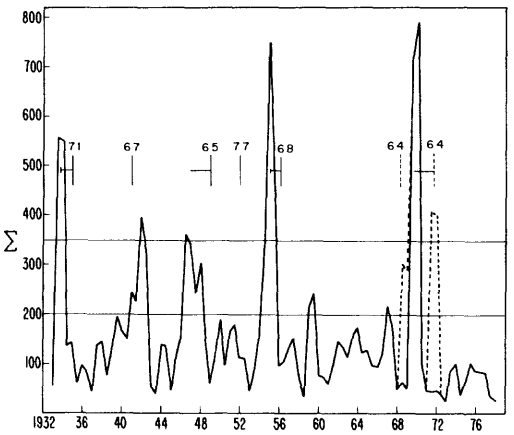

Fig. 5. Pattern Σ for Southern California. Prediction windows start when Σ is above the threshold value indicated by the horizontal line. Other notation as in Figure 1.

single event of magnitude 6.0, even though the latter releases more energy than the two smaller events combined? To sum the energies, instead of the number of earthquakes, is similarly unsatisfactory, since this sum is completely dominated by the largest earthquakes, and we may as well neglect the smaller events. Benioff summed the square roots of the energies, which he called 'strain;' this is a compromise between the two extremes. *Keilis-Borok and Malinovskaya* [1964] summed the energies raised to the $\frac{2}{3}$ power, which is roughly equivalent to the summation of the areas of the fracture surfaces in the sources.

The summation formulas are essentially of the form

$$\Sigma(t) = \sum C10^{kM_i}$$

In accord with the algorithm used by *Keilis-Borok and Malinovskaya* [1964] we construct a running sum of $\sum(t)$, taking all events occurring with $t - s < t_i < t$ for some window interval s; we restrict M_i to some band of magnitudes less than M_0 and eliminate all aftershocks of events with $M \geq M_0$ from the summation, even if the aftershock magnitudes fall within the permissible band of M_i. *Keilis-Borok and Malinovskaya* [1964] have shown that $\sum(t)$ has a sharp peak in excess of $\frac{1}{2}C10^{kM_0}$ before many strong earthquakes in the Gutenberg-Richter catalog. This value therefore is one half of the value of $\sum$ generated by a threshold earthquake that we are trying to predict. As in the case of pattern B, earthquakes with $M \geq M_0$ are not included in the summation. If $\sum(t) \geq \overline{\sum}$, where $\overline{\sum}$ is some threshold, we declare that a group of earthquakes has occurred which generated pattern $\sum$. In this circumstance, once again, a period of enhanced probability of occurrence of a large earthquake is initiated. The interval of higher probability is terminated after the first strong earthquake in the region, or after τ years, whichever comes first.

The results for Southern California are shown in Figure 5, with parameters $k = 0.91$, the window $s = 1$ year, and $4 \leq M_i \leq 6.5$. The solid curve is for the case $M_0 = 6.4$, and the dashed curve is the case $M_0 = 6.5$; the two curves differ only in our interpretation of the Borrego Mountain and San Fernando earthquakes, either as strong shocks or as main shocks, respectively.

Figure 5 shows that the success of the pattern $\sum$ as a predictor depends critically on the choice of the threshold. The a priori threshold above was too low, and we have had to determine it by a posteriori methods. If we arbitrarily choose the threshold $2C10^{kM_0}$, then the thresholds are $\sum = 287$ and 354 in the two cases $M = 6.4$ and 6.5. At these thresholds, we predict three earthquakes and fail to predict two others: the Kern County earthquake of 1952 ($M = 7.7$) is one of our failures. There is the usual uncertainty about the Borrego Mountain–San Fernando pair. If $M_0 = 6.5$ and the magnitude of the San Fernando event is greater than 6.4, we successfully predict one of these events, but we turn our success into one failure to predict if its magnitude is 6.4. If $M_0 = 6.4$, we have one success and one failure. If the threshold is lowered to 200, we predict five events with $M \geq 6.4$ and fail on the same two events as before, but now have added one false alarm to our tabulation. If the threshold is lowered still further to 180, we predict all seven events successfully with one false alarm. Further lowering of the thresholds introduces more and more false alarms until, ultimately, we have simply one continuous episode of enhanced probability for the entire duration of the catalog.

6. NEW ZEALAND

The premonitory patterns described above need to be tested in other seismic regions. Thus far we have tested them on New Zealand and Italy. The results are described below. We considered earthquakes within the region of New Zealand delineated in Figure 6 and having focal depths less than 100 km. We used the revised catalog of New Zealand earthquakes

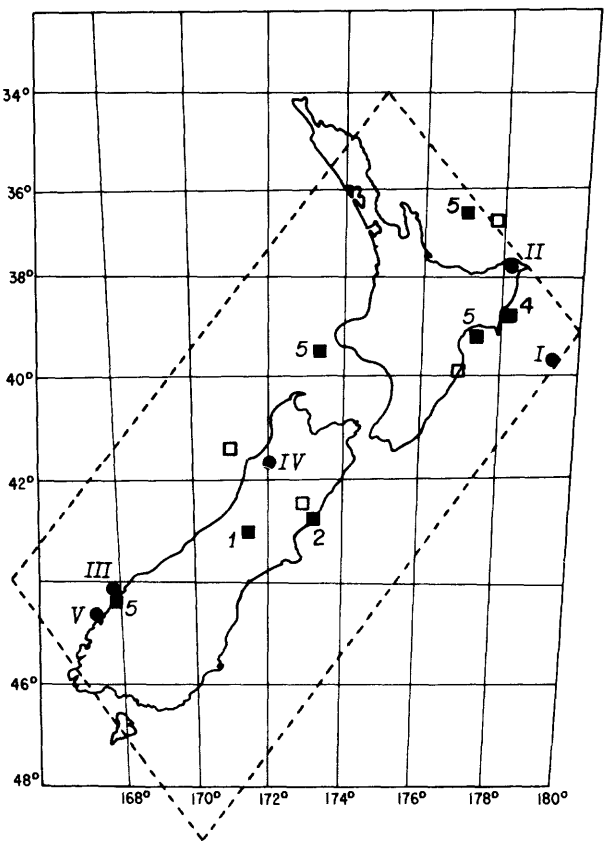

Fig. 6. Location of strong normal earthquakes and pattern B for New Zealand. Circles are epicenters of strong earthquakes. Roman numerals are the same as in Table 4. The solid squares are the epicenters of earthquakes which generated pattern B, i.e., an abnormal number of aftershocks in the first 7 days. Arabic numbers are the same as in Table 4. Open squares are locations of events triggering false alarms. The boundary of the region is shown as a dashed line.

TABLE 4. Strong Earthquakes and Pattern B in New Zealand

Date	ϕ, °S	λ, °E	h, km	M	B^* (7 days)	$B\dagger$ (7 days)	Number on Figure 6
6-24-42	40.9	175.9	12	7.0	3	28	
8-1-42‡	41.0	175.8	55	7.1	0	6	
2-17-43	45.2	167.9	95	6.9	1	4	
8-2-43§	46.1	167.0	33	6.7	2	3	
9-22-43	36.0	177.0	33	6.8	0	0	
6-26-46	43.2	171.5	30	6.2	4	33	1
8-27-47	39.7	179.2	33	6.7	6	6	I
5-22-48	42.5	172.9	25	6.2	6¶	13	
1-10-51	42.8	173.2	12	5.6	5	38	2
4-23-51	37.8	178.2	12	6.7	0	0	II
8-28-52	39.9	176.9	12	5.8	1	11	
3-14-56	36.7	177.7	12	5.5	4 ‖	9	
5-24-60	44.2	167.7	12	7.0	7	66	III
5-10-62	41.7	171.3	12	5.9	0	40	4
3-4-66	38.8	178.2	33	6.2	0	15	4
5-23-68	41.8	172.0	12	7.1	9	103	IV
2-28-74	36.6	177.0	12	5.6	6	68	5
9-20-74	44.4	168.0	12	5.9	1	34	5
11-5-74	39.5	173.5	12	6.1	2	26	5
3-20-76	39.3	177.5	12	5.6	3	75	5
5-4-76	44.7	167.5	12	7.0	1	62	V

*For window, see Table 1, $m = 5.0$.
†For window, see Table 3, $m = 2.0$.
‡Aftershock of preceding.
§Outside seismic region.
¶This earthquake is an aftershock of 2-10-51, $M = 6.4$ according to this window. The parent event had no aftershocks $M > M_1$ within 7 days.
‖ Including foreshocks, 6 events occurred within a 7-day interval straddling this event.

1940–1977 compiled by Warwick Smith. The choices of the region and depth were made a priori, largely on the basis of tectonic considerations. Most of the arbitrary parameters were taken to be the same as for Southern California. However, we raised the threshold M_0 to 6.7, the after shock window e to 7 days, and used thresholds for $\bar{b}$ as indicated below.

The catalog was processed separately with aftershocks defined by Tables 1 and 3. We assumed $m = 5.0$ and $M_1 = 5.5$. The results are summarized in Table 4 and Figure 7. The cluster of five strong earthquakes in 1942–1943 was not predicted.

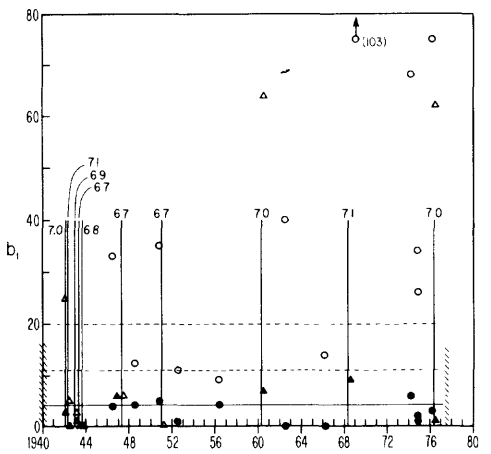

Fig. 7. Pattern B for New Zealand. Solid circles are the values of b_i for the windows in Table 1 and $m = 5.0$. Open circles are values for windows in Table 3 and $m = 2$. Closed and open triangles are values of b for strong earthquakes with $M \geq 6.7$ in the cases of aftershocks given by Tables 1 and 3. Hatched columns indicate the end of the catalog. Thresholds of $\bar{b} = 4, 11, 20$. Other notation as in Figure 1.

Of these five, the second is an aftershock of the first, and the fourth fell outside the region outlined in Figure 6. Both of these have been listed for completeness. A visual inspection of the catalog indicates that tabulation of shocks in the magnitude range of 5.0–6.0 is accountably weak in the early years, due to sparseness of the network. It is our belief that simply not enough aftershocks of main events were tabulated in these early years to establish pattern B.

We therefore focus our attention on the remaining five strong events. In these cases, we are dealing with values of b_i that are small due to the high cutoff threshold m. We place our threshold for prediction at $\bar{b} = 4$, admittedly a small number and therefore one which places the use of prediction pattern B on rather unstable ground. If $\tau = 2.5$ years, our score is three successes, two failures, and two false alarms as indicated in Table 5. Periods of enhanced probability occurred for 8.6 years, or 23% of the time, and were terminated by successful predictions as indicated above; if no strong earthquakes had occurred, the windows would have remained open for 11.9 years, or 32% of the time. The probability that any window open for 11.9 years will 'capture' three or more strong earthquakes and fail to capture two or less strong earthquakes occurring randomly is given by the binomial distribution and is 19%. The 'success rate' in this case is $\frac{3}{5}$, since three strong earthquakes followed the five periods of enhanced probability that were identified. Scores for other combinations of thresholds as well as for aftershocks defined by Table 3 are also found in Table 5. In the latter cases we have used virtually all the earthquakes in the catalog.

Table 5 illustrates some rather obvious consequences concerning the choice of thresholds:

1. As we increase the duration of the window of the period

TABLE 5. Forecasting Scores for New Zealand Catalog 1945–1977

Filter Window	Threshold $\bar{b}$	τ, years	Success	Failure	False Alarms	Actual Enhancement Window Duration	Potential Enhancement Window Duration	Random Prediction	Success Rate	m
Pattern B										
I	4	2.5	3	2	2	23%	32%	19%	3/5	5.0
I	4	3	3	2	1	23%	36%	25%	3/4	5.0
I	5	3	2	3	0	13%	23%	32%	2/2	5.0
III	11	2.5	4	1	3	36%	43%	11%	4/7	2.0
III	20	2.5	3	2	1	17%	27%	12%	3/4	2.0
Pattern Σ										
I	250	2.5	4	1	2	26%	60%	34%	67%	4.5

of enhanced probability, we increase our chances at successful prediction but also increase the probability that a random prediction will do about as well as our algorithm.

2. If we increase the threshold $\bar{b}$ for the number of aftershocks, we get more failures but also decrease the number of false alarms and hence improve our success rate, as well as reduce the amount of time spent in enhancement windows. Conversely, if we lower the threshold $\bar{b}$, we increase the amount of time spent in enhancement windows; ultimately with a sufficiently low value of $\bar{b}$, we have a continuously open window. We predict more and more events successfully but also increase the number of false alarms.

In the case of the pattern of $\sum$ for New Zealand (Figure 8), a choice of a threshold such as 250 generates four successes, one failure to predict, and two false alarms. As in the case for Southern California, patterns B and $\sum$ give substantially the same predictions.

7. ITALY

We considered the four subregions of Italy outlined in *Caputo, et al.*, [1979]; the regionalization was made on the basis of tectonics and geomorphology. From north to south these are (1) the Po Valley and the adjoining Alps, (2) Northern Apennines, (3) Central Apennines, and (4) Calabria and Eastern Sicily. Pattern S for these subregions was studied by Caputo et al. We used the catalog 1920–1972 with the same threshold $M_0 = 5.8$. The lower threshold M_1 for main shocks was taken to be 4.8. For several events in the catalog, no magnitudes are supplied; instead these are listed as having intensity VIII. Events with intensity VIII were assumed to be main shocks. No lower threshold m for aftershocks was taken, so that no eligible earthquakes were rejected; in other words, we disregarded the inhomogeneity of the catalog.

The results of the study of pattern B for the first three regions are shown in Figure 9 from north to south. The duration of the windows of enhanced probability of occurrence was taken to be $\tau = 4$ years, a posteriori. The results would be unchanged with the a priori value $\tau = 6$ years which was assumed in Caputo et al. for the pattern S in the same regions. There were six strong shocks of which five were predicted.

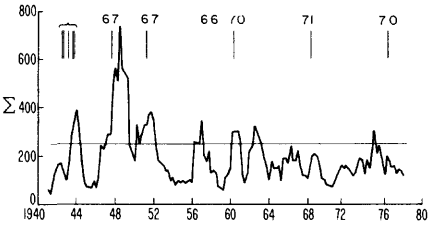

Fig. 8. Pattern Σ for New Zealand.

There was one false alarm. Although if taken literally, the sequence from January to June 1972 in Central Italy must be considered a false alarm, the largest event, with intensity VIII, occurred on June 14, 1972. Nevertheless it preceded the Friuli earthquake of the northernmost region ($M = 6.5$) by less than 4 years; this result may be a consequence of our discrete regionalization, or it may be a result of our arbitrary choice of the probability enhancement window τ. In any case, this example points out a difficulty combined with geographical edge effects that we have not yet considered closely.

Pattern S was considered in Caputo et al. and will not be further elaborated here. The test of pattern $\sum$ has not been made here mainly because of the difficulty of associating magnitudes with intensities. Pattern B was not detected for the fourth subregion, Calabria and Eastern Sicily; one distinction of this region is that many strong earthquakes have intermediate focal depths.

We consider these results to be a confirmation of the existence of the premonitory pattern B. But its actual use for prediction on the catalog at our disposition would be premature. Our principal hesitation here arises because of the incompleteness of the catalog.

8. CONCLUSIONS

Bursts of seismicity, i.e., anomalous clusterings of earthquakes in the time-space-energy domain may be regarded as

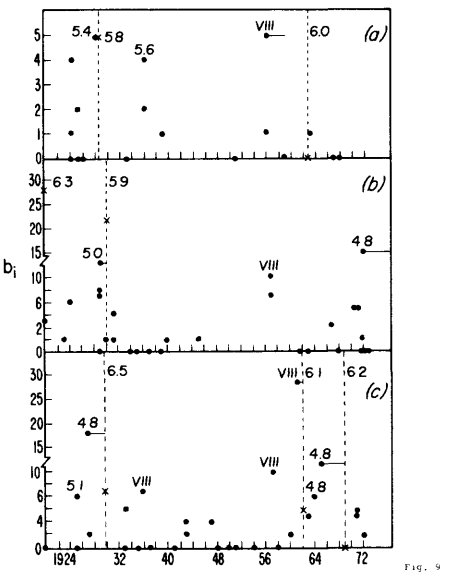

Fig. 9. Pattern B for three regions of Italy. Circles are the values of b for main shocks. Crosses are the values of b for strong earthquakes. (*a*) Po Valley, (*b*) Northern Apennines, (*c*) Central Apennines.

patterns of seismicity that are precursory to strong earthquakes. These bursts may be diagnosed by constructing certain projections of earthquake catalogs, three of which have been considered in this paper. In all likelihood, these projections are strongly overlapping. These projections are (1) pattern B (bursts of aftershocks): earthquakes of intermediate magnitude, having abnormally large numbers of aftershocks within a short time interval after their occurrence; (2) pattern S (swarms): high concentration of earthquakes in space at a time at which the background of seismicity is high; and (3) pattern $\sum$ (power law of energy): sharp increase in the sum $\sum_i E_i^n$, where E_i is the energy of an earthquake occurring within a limited magnitude range and within a moving time window; we have used the exponent n of about $\frac{2}{3}$. We have described a parameterization of these definitions. This parameterization is certainly nonunique and is probably not optimum as well. However, it provides a framework for the uniform analysis of earthquake catalogs.

An application of these patterns to the catalog of earthquakes of Southern California for the years 1932–1978 gave seven periods of enhanced probability with a total duration of about $13\frac{1}{2}$ years. At least five out of seven strong earthquakes of this region, with $M \geq 6.4$, occurred during these periods. The application of these methods to the catalogs of Italy and New Zealand showed that pattern B also preceded the strongest earthquakes of these regions. Our exploration of the applicability of these patterns to other regions will be reported separately.

These premonitory patterns take place in almost all cases at some distance from subsequent strong earthquakes. This leads us to form a conjecture that small but significant stress redistribution due to medium-sized earthquakes at moderate distances can act as a triggering agent; to account for the delays between the triggering and the triggered events, we must invoke a creep rheology for the rocks in the vicinity of the triggered event. Modeling of this process will be explored in a subsequent paper.

Acknowledgments. This research was carried out as part of Project III of the U.S.-U.S.S.R. cooperative program in earthquake prediction. During the course of this research, one of the authors (V. I. K.-B.) was a visiting scientist at the Institute of Geophysics and Planetary Physics of the University of California, Los Angeles, and at the Seismological Laboratory of the California Institute of Technology, where he was a Sherman Fairchild Distinguished Scholar. Support for this work, including computing and other expenses, was provided by the Office of Earthquake Studies, United States Geological Survey. Consultation and assistance of J. K. Gardner, Y. Y. Kagan, and D. Eckelmann is gratefully acknowledged. Comments of K. Aki and M. Caputo were especially helpful. Publication number 1961, Institute of Geophysics and Planetary Physics, University of California, Los Angeles. Contribution number 3327, Division of Geological and Planetary Sciences, California Institute of Technology, Pasadena.

REFERENCES

Caputo, M., P. Gasperini, V. Keilis-Borok, L. Marcelli, E. Ranzman and I. Rotwain, Earthquake swarms as precursors of strong earthquakes in Italy, *Ann. Geofis. Rome,* in press, 1979.

Evison, F. F., Fluctuations of seismicity before major earthquakes, *Nature, 266,* 710–712, 1977.

Friedman, M. E., J. H. Whitcomb, C. R. Allen, and J. A. Hileman, *Seismicity of the Southern California Region, 1 January 1972 to 31 December 1974,* Seismological Laboratory, California Institute of Technology, Pasadena, 1976.

Gardner, J. K., and L. Knopoff, Is the sequence of earthquakes in Southern California, with aftershocks removed, Poissonian?, *Bull. Seismol. Soc. Amer., 64,* 1363–1367, 1974.

Gelfand, I. M., Sh. A. Guberman, V. I. Keilis-Borok, L. Knopoff, F. Press, E. Ya. Ranzman, I. M. Rotwain, and A. M. Sadovsky, Pattern recognition applied to earthquake epicenters in California, *Phys. Earth Planet. Interiors, 11,* 227–283, 1976.

Hileman, J. A., C. R. Allen, and J. M. Nordquist, *Seismicity of the Southern California Region, 1 January 1932 to 31 December 1972,* Seismological Laboratory, California Institute of Technology, Pasadena, 1973.

Kagan, Y., and L. Knopoff, Statistical search for non-random features of the seismicity of strong earthquakes, *Phys. Earth Planet. Interiors, 12,* 291–318, 1976.

Keilis-Borok, V., and L. N. Malinovskaya, One regularity in the occurrence of strong earthquakes, *J. Geophys. Res., 69,* 3019–3024, 1964.

Keilis-Borok, V., and I. Rotvain, Two long-term precursors of strong earthquakes, *Comput. Seismol., 12,* in press, 1979.

Keilis-Borok, V. I., V. M. Podgayetskaya, and A. G. Prosorov, On the local statistics of catalogs of earthquakes (in Russian), *Comput. Seismol., 5,* 55–79, 1971.

Knopoff, L., Model for aftershock occurrence, in *Flow and Fracture of Rocks, Geophys. Monogr. Ser.,* vol. 16, edited by H. C. Heard, pp. 259–263, 1972.

Knopoff, L., and J. K. Gardner, Homogeneous catalogs of earthquakes, *Proc. Nat. Acad. Sci., 63,* 1051–1054, 1969.

Knopoff, L., and J. K. Gardner, Higher seismic activity during local night on the worldwide earthquake catalog, *Geophys. J. Roy. Astron. Soc., 28,* 311–313, 1972.

(Received November 2, 1978;
revised August 17, 1979;
accepted August 20, 1979.)

Physics of the Earth and Planetary Interiors, 11 (1976) 227–283

PATTERN RECOGNITION APPLIED TO EARTHQUAKE EPICENTERS IN CALIFORNIA

I.M. GELFAND [1], Sh.A. GUBERMAN [1], V.I. KEILIS-BOROK [2], L. KNOPOFF [3], F. PRESS [4], E.Ya. RANZMAN [5], I.M. ROTWAIN [6] and A.M. SADOVSKY [2]

[1] *Institute of Applied Mathematics, Academy of Sciences, Moscow (U.S.S.R.)*
[2] *Institute of Physics of the Earth, Academy of Sciences, Moscow (U.S.S.R.)*
[3] *Institute of Geophysics, University of California, Los Angeles, Calif. (U.S.A.)*
[4] *Department of Earth and Planetary Sciences, Massachusetts Institute of Technology, Cambridge, Mass. (U.S.A.)*
[5] *Institute of Geography, Academy of Sciences, Moscow (U.S.S.R.)*
[6] *Laboratory of Mathematical Methods in Biology, Moscow University, Moscow (U.S.S.R.)*

(Received October 3, 1975; accepted for publication November 21, 1975)

"This is the only way it clicks ...
It doesn't make sense otherwise ...
But this is just a theory, isn't it? ...
Call it any name you like. It's good enough for me."

Dashiel Hammett

Gelfand, I.M., Guberman, Sh.A., Keilis-Borok, V.I., Knopoff, L., Press, F., Ranzman, E.Ya., Rotwain, I.M. and Sadovsky, A.M., 1976. Pattern recognition applied to earthquake epicenters in California. Phys. Earth Planet. Inter., 11: 227–283.

A pattern recognition procedure is explained which uses geological data and the earthquake history of a region, in this case California, and learns how to separate earthquake epicenters from other places. Sites of future earthquake epicenters are predicted as well as places where epicenters will not occur. The problem is formulated in several ways and control experiments are devised and applied in order to test the stability of the procedures and engender confidence in the results. Some of the combinations of geological features which the computer recognized as significant discriminants are discussed.

1. Introduction

Pattern recognition is not a new subject but its application to geological and geophysical problems has been minimal. This is surprising because the methods of pattern recognition, though paradoxically simple, can extract more results from a body of data, by a more intensive analysis, than many alternative procedures.

Geology and geophysics are essentially experimental disciplines in which large amounts of data are accumulated and are in need of winnowing, codification, correlation, and interpretation. More so than in many other fields, hypotheses flow from data analysis, and prediction is important in a practical sense as well as a means of hypothesis testing. Pattern recognition offers a powerful tool for achieving these results. Yet care must be taken in its application, for pattern recognition itself is an unexplored field lying somewhere between logic and statistics. Its procedures are not yet formalized and the user must be on guard against self-deception.

In this paper we examine the possibility that geological patterns can be recognized which distinguish places where epicenters of large earthquakes have occurred in the past and can occur in the future, from other places which have not been and will not be the sites of epicenters. The primary data for recognition

come from California, though insights and procedures stem from earlier applications of these methods to central Asia and Anatolia. If we are successful we will have predicted the sites of future epicenters (but not the times) and we will have learned something about the geological environment of epicenters.

2. Method

2.1. The problem

We place the problem of recognition in the following form: a set of objects is given, with each object described by the answers to a questionnaire. Each object belongs to one and only one of several (usually two) classes. Our goal is to find which class each object belongs to. To solve this problem we first need to go through a "learning phase" using examples of objects of each class as "learning material".

Let us make this specific for our particular problem. Objects are points on a map, representative of a local geographic region. The problem is to find those objects where the epicenters of strong earthquakes may occur in the future. Note that we mean the epicenter or place where the earthquake is initiated and not the entire length of faulting. We shall call these objects D, "dangerous". The rest of the objects we shall call N, "non-dangerous". By strong we mean earthquakes with magnitude M not lower than some threshold M_0; in the text below, "earthquake" and "epicenter" refer to strong earthquakes unless indicated otherwise.

A specific difficulty arises because the learning material consisting of known epicenters is mixed. Because of errors in locating epicenters, objects called D in the learning phase may really be N and vice versa. Also some objects which are classified N in the learning phase are really D because they will be the sites of future epicenters. It is these objects we wish to identify by pattern recognition in order to predict future epicenters. This leads us to the following problem: the objects are divided a priori into classes I and II – correspondingly close to and far from known epicenters; the goal is to recognize objects D in each class.

2.2. The algorithm

The recognition algorithm consists of three stages: learning, voting and control experiments.

Learning: certain critical questions or combinations of questions, called the distinctive features of objects D and N, are determined by analyzing the learning material, as will be described in the next two sections.

Voting: the numbers n_D and n_N of distinctive features characteristic of D and N are determined for each object. Recognition is based on their difference $\Delta = n_D - n_N$. We recognize an object as D if $\Delta \geqslant \bar{\Delta}$, where $\bar{\Delta}$ is some threshold. Making $\bar{\Delta}$ smaller will reduce the number of D objects which will be misidentified as N. At the same time more "false alarms" will occur, i.e. more N will be misidentified as D.

Control experiment: the stability and reliability of recognition are tested by numerical (logical) experiments, in order to convince ourselves that the results are significant since recognition cannot be proven either mathematically or statistically. This is a decisive stage which takes up most of the effort, after the questionnaire is formulated and answered.

Learning is based on the algorithm CORA-3. This algorithm in slightly different form has been used in several other problems (Bongard et al., 1966). For our particular problem it can be formulated as follows. The objects, used in learning, are divided into classes I and II, correspondingly close to and far from known epicenters. As stated earlier, each class may contain objects D and N:

class I is $\{D_I, N_I\}$

class II is $\{D_{II}, N_{II}\}$

Here D_i and N_i are objects D and N, respectively, in the ith class; i = I and II. In other words, D_I and N_I are objects D and N, which lie close to at least one known epicenter. D_{II} and N_{II} are the objects D and N, which lie far from all known epicenters. Each object is described in binary code, which contains the answers to the questionnaire. All binary digits and the combinations of two and three digits are considered as traits of an object.

We repeat this definition more formally.
The object A is described in binary code:

$$A = A_1 A_2 \ldots A_L \tag{1}$$

where the component A_i is the answer to the ith question in the questionnaire, expressed as 1 for yes and 0 for no. *The trait* τ is an array of six integers:

$$\tau = p, q, r, P, Q, R \qquad (2)$$

Here $p = 1, 2, ..., L$; $q = p, p+1, ..., L$; $r = q, q+1, ..., L$; L is the same as in object (1); $P = 0$ or 1; $Q = 0$ or 1; $R = 0$ or 1. If $q = r$, then $Q = R$; if $p = q = r$, then $P = Q = R$; if $q = p$, then $Q = P$. An object (1) has the trait (2), if $A_p = P$; $A_q = Q$; $A_r = R$. Here A_p is the pth component in (1) etc. In the cases $p = q = r$ and $p \neq q$, $q = r$ the trait corresponds to one and two components of (1), respectively. The cases $p = q$, $q \neq r$ are redundant.

As an example, the object $A = 0110$ has traits as represented in Table I.

Thus the value of PQR in the trait with pqr equal to 222, for example, is the response to question $i = 2$ in A and has been identified in the pqr array by the value of P; the values of q and r are redundant and have been set equal to 2 to provide a complete syntactical statement. Similarly, the value of PQR in the trait with pqr equal to 233, for example, is the response to both questions $i = 2$ and 3 in A and is identified in pqr by the value of p and q; the value of r is redundant. The value of PQR in trait with pqr equal to 134 is the response to questions $i = 1, 3$ and 4 in A.

Thus, an object (1) has $L + C_{L2} + C_{L3}$ traits, where C_{LM} is the number of combinations of L things taken M at a time ($C_{L1} = L$). Eight different traits are possible for fixed p,q,r, if $p \neq q \neq r$: $(P,Q,R) = (0,0,1)$ or (0,1,0) etc. up to (1,1,1). If $p \neq q$, $q = r$, only four different traits are possible for fixed p,q: $(P,Q) = (0,0)$, (0,1), (1,0) or (1,1). If $p = q = r$, only two different traits are possible for fixed p: $P = 0$ or 1.

Therefore, the total number of different traits which are possible in objects of length L is:

$$2L + 4C_L^2 + 8C_L^3$$

The features of D and N are selected from among the traits. A *feature* of D is a trait which is present relatively frequently in class I and relatively infrequently in class II. A feature of N is defined analogously. The formal rule defining features is given in Table II.

Next we eliminate equivalent and weaker features, whose definitions follow. Consider two features of a class and the objects of this class only. Some set of these objects has the first feature, another has the second. If these sets coincide, the features are *equivalent.* If one set is part of another, the corresponding feature is *weaker* than the other. If $M_n/M_u \geqslant 1 - \epsilon$, these features are called "ϵ-equivalent". Here M_n is the number of objects which belong to both sets; M_u is the total number of objects which belong to both or to any one of the sets. Evidently, for equivalent features, $M_n = M_u$, i.e. $\epsilon = 0$. The definition of ϵ-equivalence is used later.

We eliminate all but one feature from each group of equivalent features, and all features which are weaker than some other one. The features remaining after this elimination are called distinctive features and are used in voting. As mentioned above voting consists of tallying the number of D and N distinctive features at each object of class I, II and III.

Class III consists of objects not used in learning.

TABLE I

Traits for the object $A = 0110$

p	q	r	P,Q,R
1	1	1	0
2	2	2	1
3	3	3	1
4	4	4	0
1	2	2	0,1
1	3	3	0,1
1	4	4	0,0
2	3	3	1,1
2	4	4	1,0
3	4	4	1,0
1	2	3	0,1,1
1	2	4	0,1,0
1	3	4	0,1,0
2	3	4	1,1,0

TABLE II

Definition of features* in learning by algorithm "CORA-3"

A feature of objects	Should be found in the class	
	I	II
D	in $\geqslant k_1$ objects	in $\leqslant \tilde{k}_1$ objects
N	in $\leqslant k_2$ objects	in $\geqslant k_2$ objects

* Each feature is a unit or a combination of two or three units in the binary code of the object.

We could divide all objects into classes I and II only, according to whether or not the point lies near an epicenter. However, we separate some objects into class III if we are uncertain about their assignment or if we use them for control experiments. Objects in class III are considered in voting, however.

The algorithm assumes that the number of epicenters is sufficient for the following two hypotheses to hold:

Hypothesis 1: most objects, which are far from known epicenters, are N.

Hypothesis 2: most objects near known epicenters are D.

The second hypothesis will be replaced by a weaker one, when we use another algorithm for learning called "CLUSTERS", which we describe next.

Algorithm "CLUSTERS" is fully described for the first time in this paper; a brief description was given in Gelfand et al. (1974a). The objects of class I are subdivided into clusters. Each cluster corresponds to a certain epicenter and includes those objects which are close to this epicenter. An object may be included in several clusters. Class II is specified as before. Thus:

Class I is $\{C[D_{\mathrm{I}}^{c}, N_{\mathrm{I}}^{c}]\}$

Class II is $\{D_{\mathrm{II}}, N_{\mathrm{II}}\}$

Here C is a cluster of objects near some epicenter; D_{I}^{c} and N_{I}^{c} are the objects D and N in the cluster C. The problem is to recognize D_{I} and D_{II}.

As in CORA-3 all traits of all objects in the learning materials are considered in the learning phase. We assume that a cluster has some trait if at least one object in the cluster has this trait. (In another version this condition is more flexible in that at least N/K objects in the cluster must have this trait. Here N is the number of the objects in the cluster, and K is some constant common for all clusters; naturally, if $N/K < 1$ it is replaced by 1.) With these definitions the features are selected by the rules specified in Table III.

As before equivalent and weaker features are then eliminated. Although they can be determined exactly as in CORA-3, we preferred to use the clusters rather than objects in testing for equivalent or weaker D features. After this elimination we are left with the distinctive features of D and N, which are used in voting. The voting is carried out separately for each object, whether or not it has been assigned to a cluster.

TABLE III

Definition of features* in learning by algorithm "CLUSTERS"

A feature of objects	Should be found in the		
	clusters C **	single objects in clusters (class I)	single objects outside the clusters (class II)
D	in $\geqslant k_1$ clusters	in $\geqslant k_3$ objects	$\leqslant \bar{k}_1$ objects
N	–	in $\leqslant \bar{k}_2$ objects	$\geqslant k_2$ objects

* Each feature is a unit or a combination of two or three units in the binary code of the object.

** A cluster has some trait if at least one object in the cluster has this trait.

This voting enables us to recognize the objects D near each known epicenter (D_{I}) and far from all of them (D_{II}). In particular we can divide each cluster into D_{I} and N_{I}. The essential advantage, compared to CORA-3 is that objects D_{I} need not dominate the clusters. They may even be in the minority in many clusters, or in every cluster if $k_3 = 0$.

Formally this algorithm differs from CORA-3 only by the introduction of an additional threshold (compare Tables II and III). It may seem therefore, that the algorithm constrains the learning materials more severely. In fact, the opposite occurs, since k_3 in Table III can be much smaller than k_1 in Table II. Frequently we even take $k_3 = 0$. In effect we have replaced hypothesis 2 by a much broader one:

Hypothesis 3: most of the known epicenters have at least one D object nearby.

Hypotheses 1 and 3 seem to be close to minimally necessary ones. Without them our problem is hopeless.

2.3. Control experiments

The main control experiment will now be described. Let us neglect the data on a specified part of the list of earthquakes. These earthquakes can be the most recent ones or can be selected otherwise. Objects which are near the epicenters of these and only these earthquakes will be reassigned in the learning stage to class II. We apply the same algorithms of learning and

voting and check whether these objects will be recognized as D_{II}. If the earthquakes we have neglected are the most recent ones we refer to this experiment as experiment EH ("earthquake history"), since it is equivalent to learning on the basis of an early part of an earthquake catalog and testing our ability to predict the subsequent seismic history, i.e. recognize the earthquakes in the later part of the catalog.

We must also take care that the number of objects identified as dangerous does not grow unduly large "in the future". To check this possible instability, we continue the EH experiment into the future, reassigning into group I all objects recognized as D_{II}. This is referred to as "experiment EF" ("earthquake future"). This procedure is evidently iterative and can be carried out on both experiments EH and EF.

As a further check we have compared our results against those obtained using variations of the data, the questionnaire and its answers, the criteria for the selection and classification of objects, the catalog of epicenters, and the values of numerical parameters, including k_i and $\tilde{k}_i$. We have also used tests involving random variation and even random generation of data, the use of different algorithms of recognition, and the application of the characteristic features identified in one region to recognition in another, but seismically similar region.

3. Strike-slip earthquakes of California

3.1. The problem

Here we consider strong ($M \geqslant 6.5$) strike-slip earthquakes in the region shown in Fig. 1a. The catalog of earthquakes is given in Table IV. We assume that the epicenters are associated with major strike-slip faults (referred to as faults in what follows). The system of faults is depicted in Fig. 1a. The *Tectonic Map of the United States* (USGS, 1962) is the prin-

TABLE IV

Epicenters of strike-slip earthquakes with $M \geqslant 6$

N	Year	Day, month	Latitude (°N)	Longitude (°W)	*M*	Closest point (see Fig. 1)
1	1836		37.5	121.9	>7	*3*
2	1836		37.7	122.1	>7	*4*
3	1836		37.8	122.3	>7	*5*
4	1857		34.7	118.8	>7	*11*
5	1906	18, IV	38.25	122.95	8.25	*2*
6	1911	1, VII	37.25	121.75	6.6	*6*
7	1918	21, IV	33.75	117	6.8	*13*
8	1922	10, III	35.75	120.25	6.5	*10*
9	1923	22, I	40.5	124.5	7.2	*23*
10	1923	23, VII	34	117.25	6.25	*12*
11	1926	22, X	36.75	122	6.1	*7*
12	1933	11, III	33.6	118	6.25	*22*
13	1934	8, VI	36	120.5	6.0	*9*
14	1934	30, XII	32.25	115.5	6.5	*20*
15	1934	31, XII	32	114.75	7.0	*21*
16	1937	25, III	33.5	116.5	6.0	*15*
17	1940	19, V	32.7	115.5	6.7	*19*
18	1942	21, X	33	116	6.5	*18*
19	1948	4, XII	33.9	116.4	6.5	*14*
20	1951	8, X	40.25	124.5	6.0	*1*
21	1952	22, XI	35.8	121.2	6.0	*8*
22	1954	19, III	33.28	116.18	6.2	*17*
23	1968	9, IV	33.4	116.2	6.9	*16*

cipal source of fault information, with a few additions on our part. The problem is to find where on these faults earthquake epicenters may fall.

3.2. *The objects*

Objects of recognition are points on faults. We consider points of the following three kinds:

(1) Projection of each epicenter onto the closest fault. Epicenters of all strike-slip earthquakes with $M \geqslant 6.0$ (Table IV) are used. We call these points centers. They have ordinal numbers from *1* to *23* in Fig. 1b.

(2) Points on faults at distances of 25 km from centers. They have ordinal numbers from *24* to *61* in Fig. 1b. To locate these points we drew circles of 25-km radius around each center. The intersections of the circles with the faults are these points of the second kind. We call these points associates of corresponding centers. For example, point *60* is an associate of point *22* in Fig. 1b. If it occurs that two centers lie on the same fault with distance in the range $25 < r \leqslant 50$ km from each other, then the two associates between them lie closer than 25 km. In this case the two associates are replaced by one point in the middle. Points *38* and *48* are examples of such points.

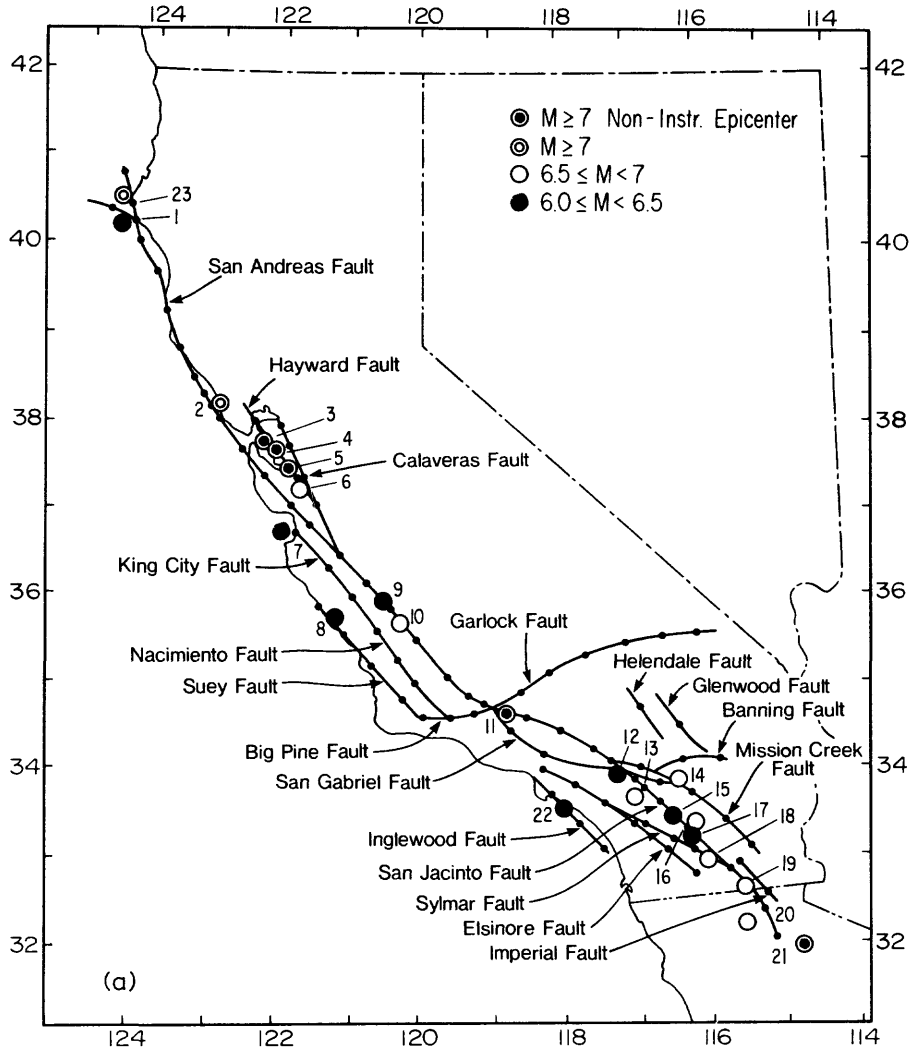

Fig. 1. (a) Major strike-slip faults of California.

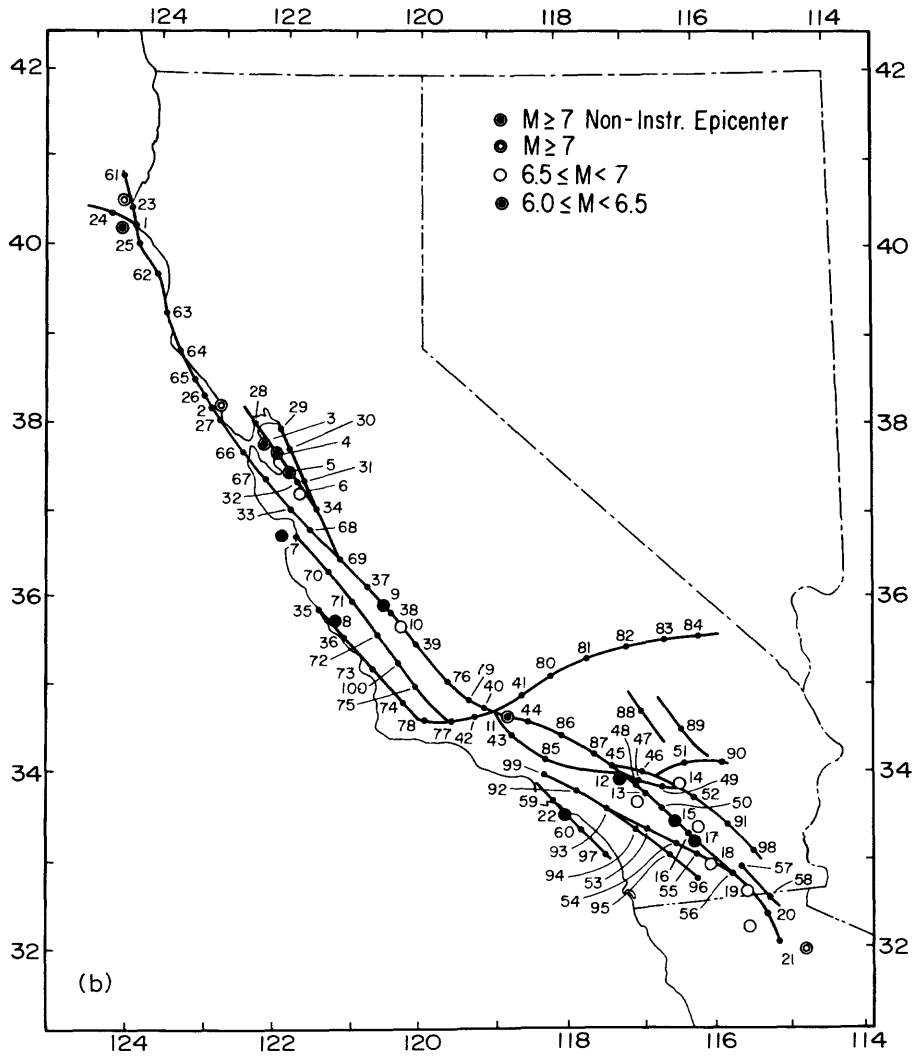

Fig. 1. (b) Identification numbers of objects of recognition (points).

If two centers lie on the same fault with distance $r \leqslant 25$ km, then we eliminate the associate of each center which lies in the direction of the other center on the same fault.

(3) We eliminate from consideration all parts of faults between each center and its associates, i.e. parts of the faults within the above mentioned circles of radius 25 km. On the remaining parts of each fault we place the points at intervals of 50 km, beginning with the northern end of the fault. These are points of the third kind.

If it occurs that a point of the third kind is at the distance $r \leqslant 100$ km from some associate point on the same fault, the next point of the third kind is placed at a distance $r/2$ km (instead of 50 km) from the preceding point. Examples are points *28* and *59*.

The class definitions for objects, in the learning stage, are as follows: Class I contains the centers and their associates (points of the first and second kind), corresponding to earthquakes with $M \geqslant 6.5$. Each of these centers together with its associates forms a cluster. Two clusters were eliminated in the learning stage because the corresponding epicenters occur too far from the nearest fault. Points *16* and *20* are the

centers of these clusters. The remaining 13 clusters were used for learning. Class II contains points of the third kind (which are at a distance $r > 25$ km from all centers).

With this classification of objects we proceed through a learning stage in which each cluster (formed of a center and two associate points on the same fault) is in class I and the remaining objects are in class II. We are uncertain about the classification of objects in clusters associated with earthquakes for which $6.0 \leqslant M < 6.5$, so we place them in class III. Some associates were recognized as D. These and only these associates were used with centers to form clusters in the final variant of learning, leading to the results described in later sections. Voting was carried out for all 100 points shown in Fig. 1b.

3.3. The data

We considered the parameters listed in Table V for use in characterizing the objects. Some comments on their choice are in order. The diversity of data that might be used is limited in this case by the small number of known epicenters. Increasing the assortment of data would lead to more distinctive features and in the subsequent voting the objects would divide more readily into two classes. However, this would also increase the probability that the division is random. Thus, we cannot include all data which might be relevant. Our choice depends strongly on physical and geological intuition and experience. Parameters 1–6 and 19–24 (Table V) are considered because they characterize the intensity and degree of contrast of neotectonic movements represented in topography. Parameters 8–11 and 18 are considered because they characterize fracturing of the crust. The rest of the parameters reflect various hypotheses on conditions favorable for the occurrence of strong earthquakes.

Each parameter will be assigned a threshold in the form of an inequality, and Table V becomes a questionnaire applied to each object. In coding the answers to the questionnaire which will be used to describe each object, "1" will signify that the corresponding inequality is satisfied, "0" indicates that it is not satisfied at the object.

Two questions now arise. Which of the parameters in Table V should be used for recognition and what discrete thresholds should we assign to them? Two extreme situations should be avoided. Too narrow a range for the parameters is barred by the limited learning material because too few objects will fall in each interval. On the other hand, with too few parameters and/or overly wide ranges, much needed information might be eliminated and recognition will fail because few if any distinctive features will be found.

The parameters and their assigned thresholds were selected in the following way: For each parameter we determined a one-dimensional distribution of its occurrence among the objects as a function of the value of the parameter. These are shown as histograms in Fig. 2. Dashed lines refer to objects of class I and solid lines to objects of class II; they are more likely D and N, respectively. Those parameters for which the distributions turned out to be sufficiently different were selected for further analysis. They are listed in Table VI, together with the thresholds assigned to discriminate between the two groups. Some comments on the choice of thresholds are in order. For some parameters, such as No. 12, we could have chosen the thresholds in such a way that classes I and II would separate better. Such parameters would then play a dominant role in recognition. However, the sharp division of histograms may be random, since the learning material is rather small. Experience tells us that in such cases many errors in recognition of D_{II} objects can occur. We have found that it is safer to choose the thresholds in such a way that objects of both groups are slightly mixed with no group forming too large a majority in any interval. Then more parameters will be used in distinctive features and recognition as a rule becomes more reliable.

3.4. Results

Distinctive D and N features found by algorithm CLUSTERS are given in Table VIIA. The table lists eight D features and eleven N features, each a combination of two or three parameters. Table VIIB lists distinctive D and N features for an EH experiment in which learning was based on a portion of the earthquake catalogs extending through the year 1922.

Results of voting are given in Table VIII and in Table IX under the column for 1948. We note that recognition is formally successful in two ways: many distinctive features of D and N are found and voting divides the objects into two rather distinctive groups,

TABLE V

Characterization of objects: List of parameters considered

N	Parameter name
1	maximal elevation, h_{max} (m)
2*	minimal elevation, h_{min} (m)
3*	elevation difference, $\Delta h = h_{max} - h_{min}$ (m)
4*	distance between points with minimum and maximum elevation, l_1
5*	"gradient", $\Delta h/l_1$
6*	relative area of soft sediments, q (%)
7*	type of rocks (igneous I, metamorphic M, sediments S)
8	distance to closest fault, r_1 (km)
9	distance to closest intersection of faults, R_1 (km)
10	distance to closest end of fault, R_2 (km)
11	distance to closest end or intersection of faults, r_2 (km)
12	distance to geothermal zone, r_3 (km)
13	distance to a region of large precipitation, R_3 (km)
14	distance to closest large water reservoir, r_6 (km)
15	distance to closest occurrence of Franciscan rocks along the fault, R_4 (km)
16	distance to the closest spreading center, r_4 (km) (40.5°N, 126.6°W or 33.2°N, 115.6°W)
17	distance to the reference point (intersection of San Andreas and Big Pine faults), r_5 (km)
18*	the number of unnamed faults on the *Tectonic Map of U.S.* (USGS, 1962), N_1
19*	the types of relief (surface morphology) featured across the fault
20*	the number of changes of the types of relief along the fault, n_2
21*	the types of relief featured along the fault
22**	maximal elevation, H_{max} (m)
23**	minimal elevation, H_{min} (m)
24**	elevation difference, $\Delta H = H_{max} - H_{min}$ (m)
25**	distance between points with minimum and maximum elevation, l_2
26**	"gradient", $\Delta H/l_2$
27**	the number of unnamed faults on the *Tectonic Map of U.S.* (USGS, 1962), n_1
28**	the types of relief (surface morphology), featured across the fault
29**	the types of relief featured along the fault
30**	the number of contacts between rocks of different age on the *Geological Map of North America* (USGS, 1965), n_3
31***	the number of parallel faults, n_4
32**	the number of faults, n_5
33***	the number of ends and intersections of faults, n_6
34***	the number of intersections, N_2
35	the angle between the fault and the dominant structural trend in the region

* Measured inside the circle $r = 12.5$ km.
** Measured inside the circle $r = 25$ km.
*** Measured inside the circle $r = 50$ km.

with only a small number of "neutral" results. The latter may be seen from the fact that out of 100 objects, 84 have the distinctive features of only D or only N, and only two points in all clusters have $\Delta < 0$. Experience with recognition based on real as well as random data (see below) indicates to us that these results are encouraging, though nothing more.

The threshold of recognition was chosen as follows:

$$\bar{\Delta} = \Delta^* - \tau, \qquad \Delta^* = \min_c [\max \Delta_c]$$

Here $\max \Delta_c$ is the maximal value of Δ for points in the cth cluster; $\min_c$ signifies the smallest value among all clusters. We subtract τ to decrease the probability of missing a D point; although this increases the probability of false alarms, this is preferable in our problem.

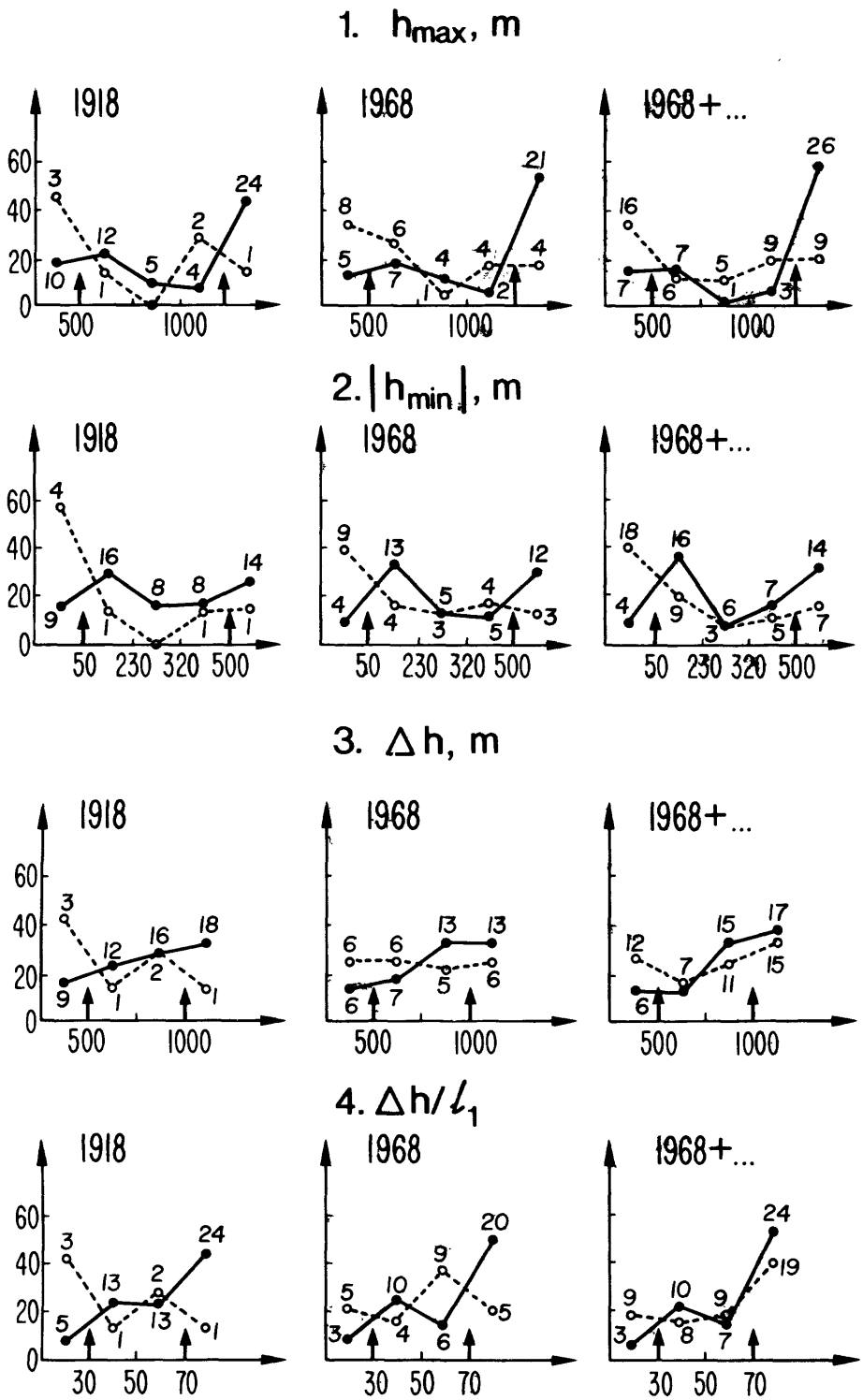

Fig. 2. For caption see p. 245.

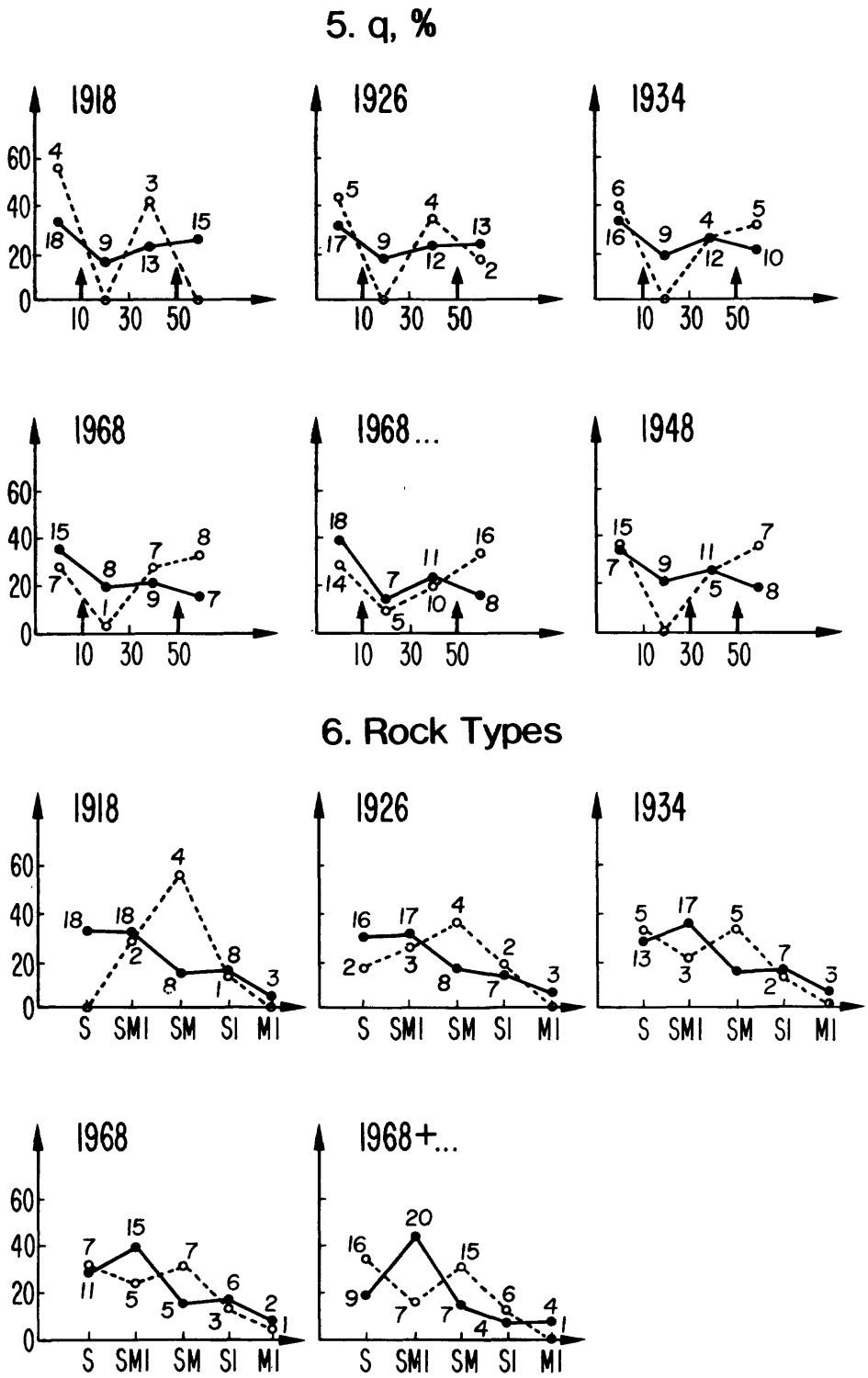

Fig. 2. For caption see p. 245.

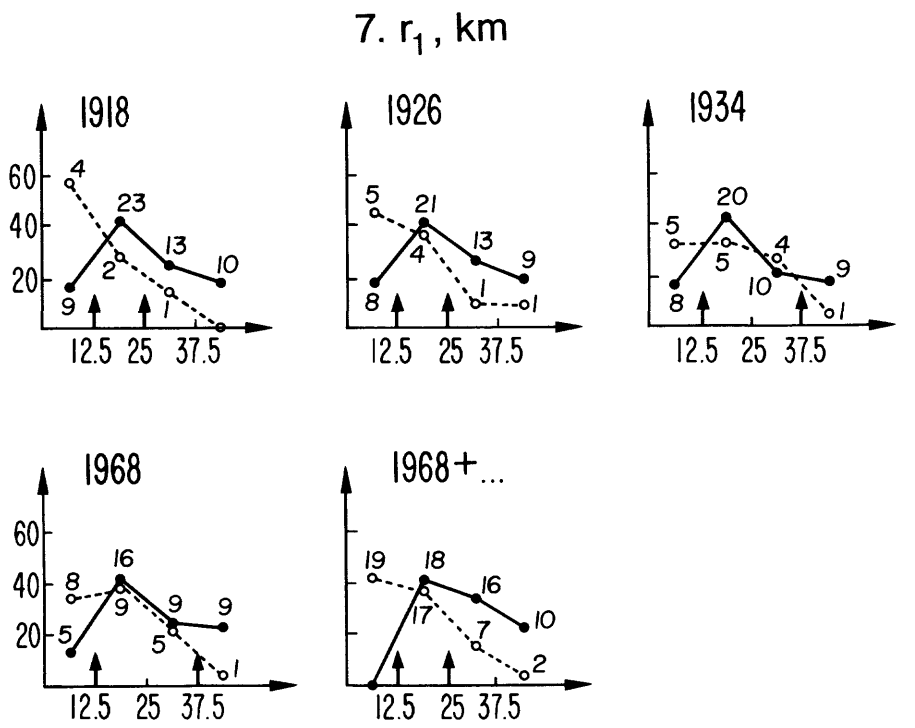

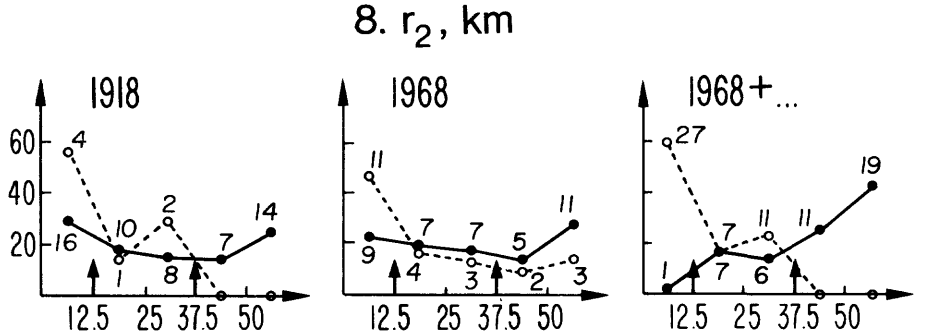

Fig. 2. For caption see p. 245.

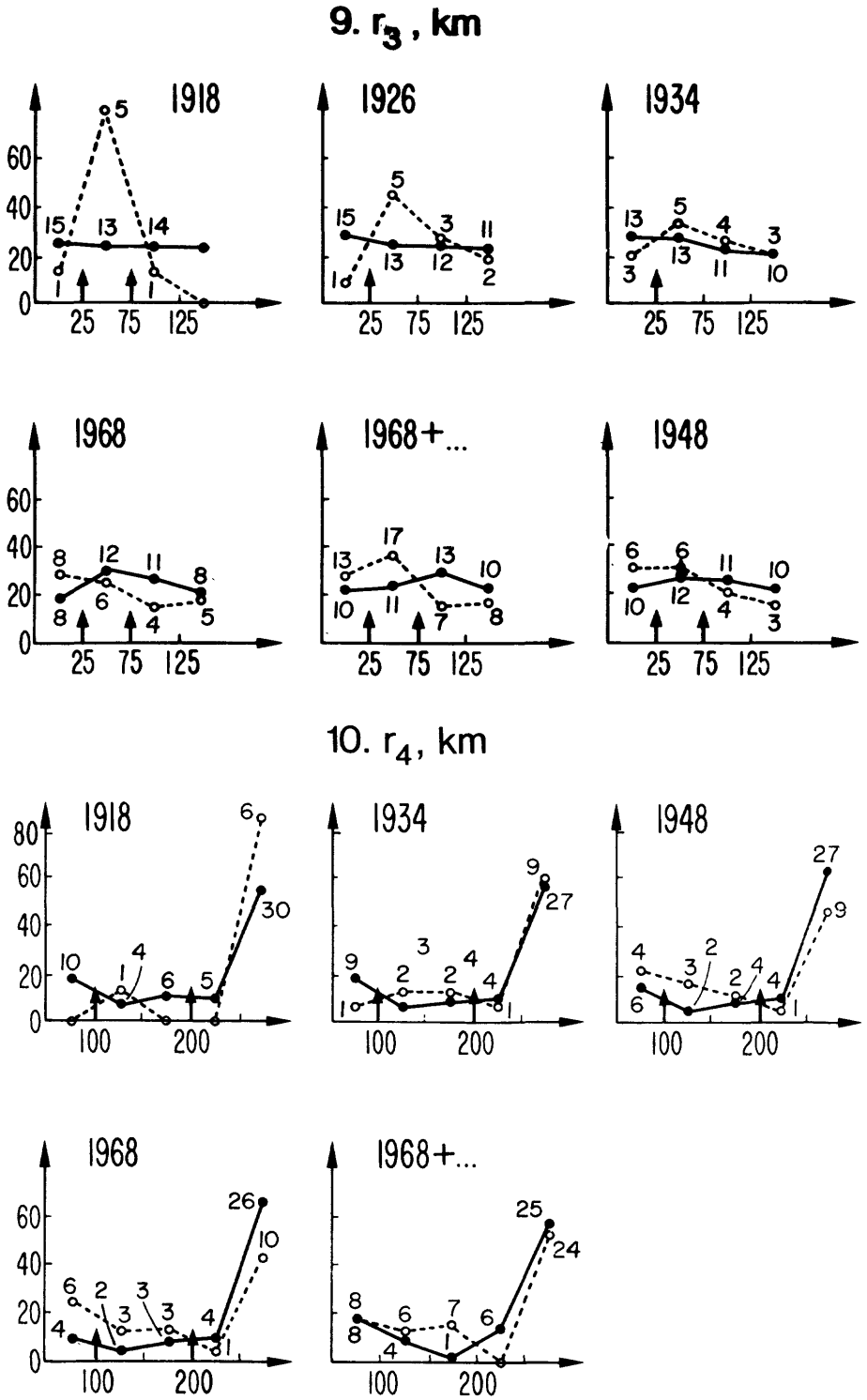

Fig. 2. For caption see p. 245.

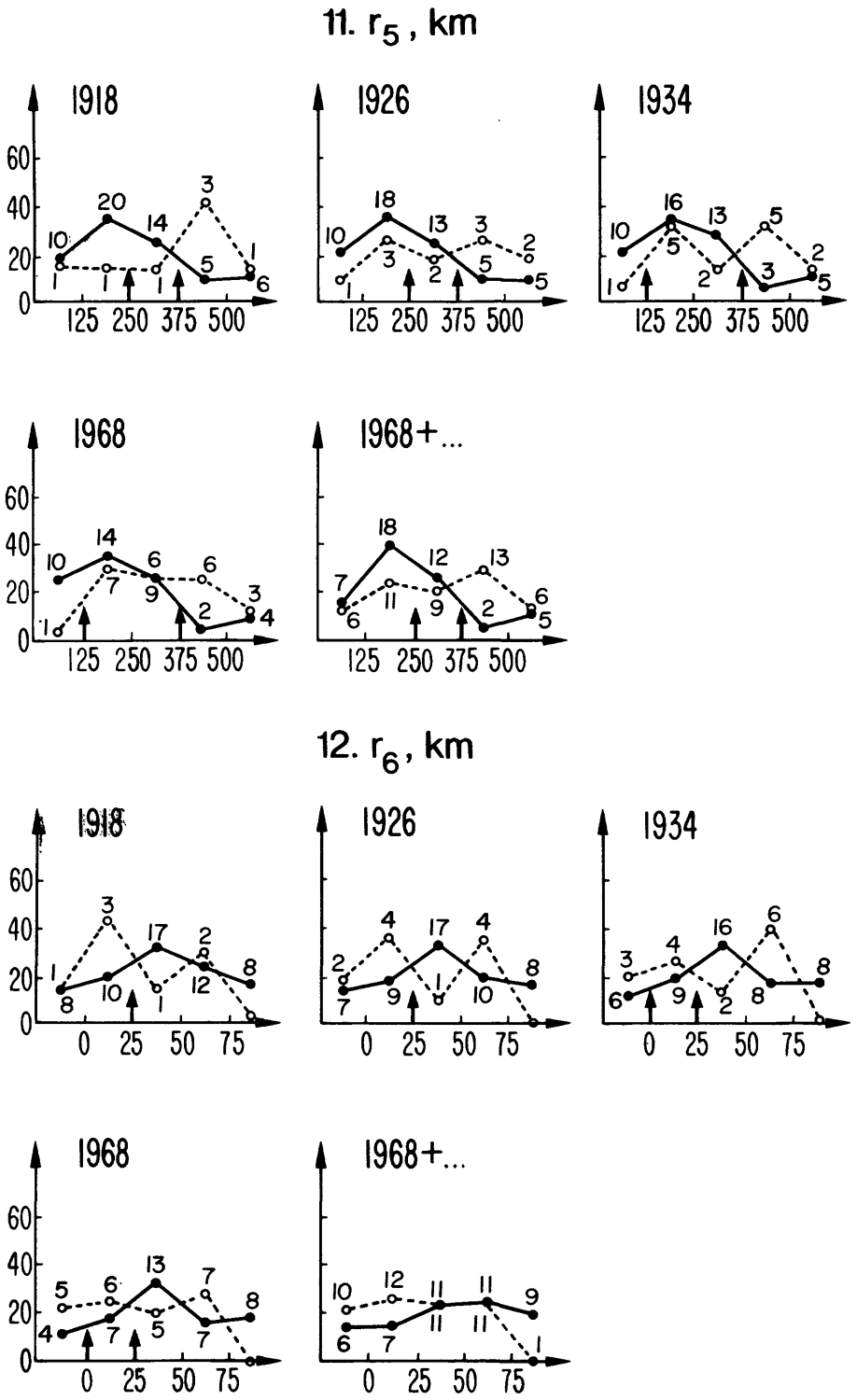

Fig. 2. For caption see p. 245.

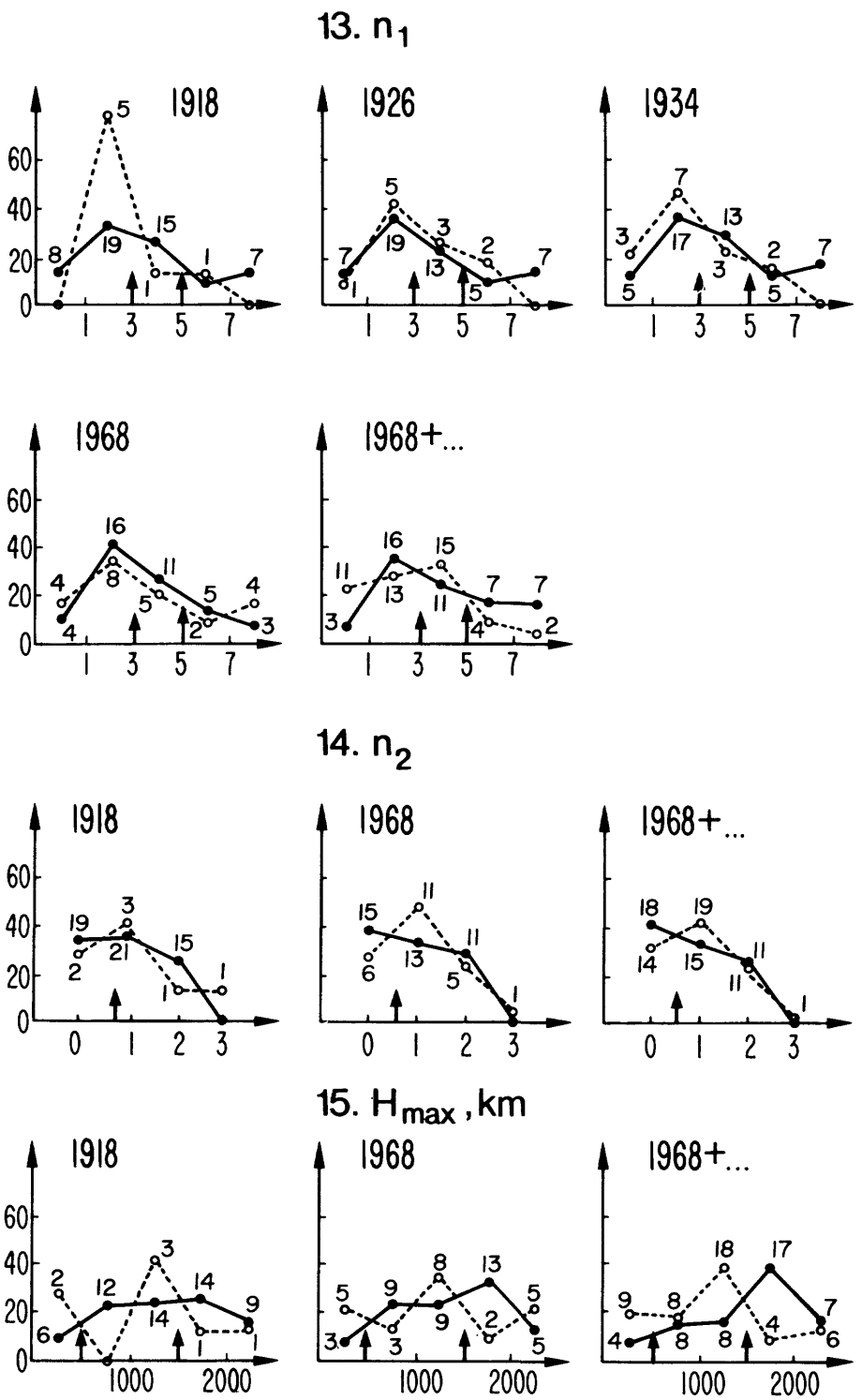

Fig. 2. For caption see p. 245.

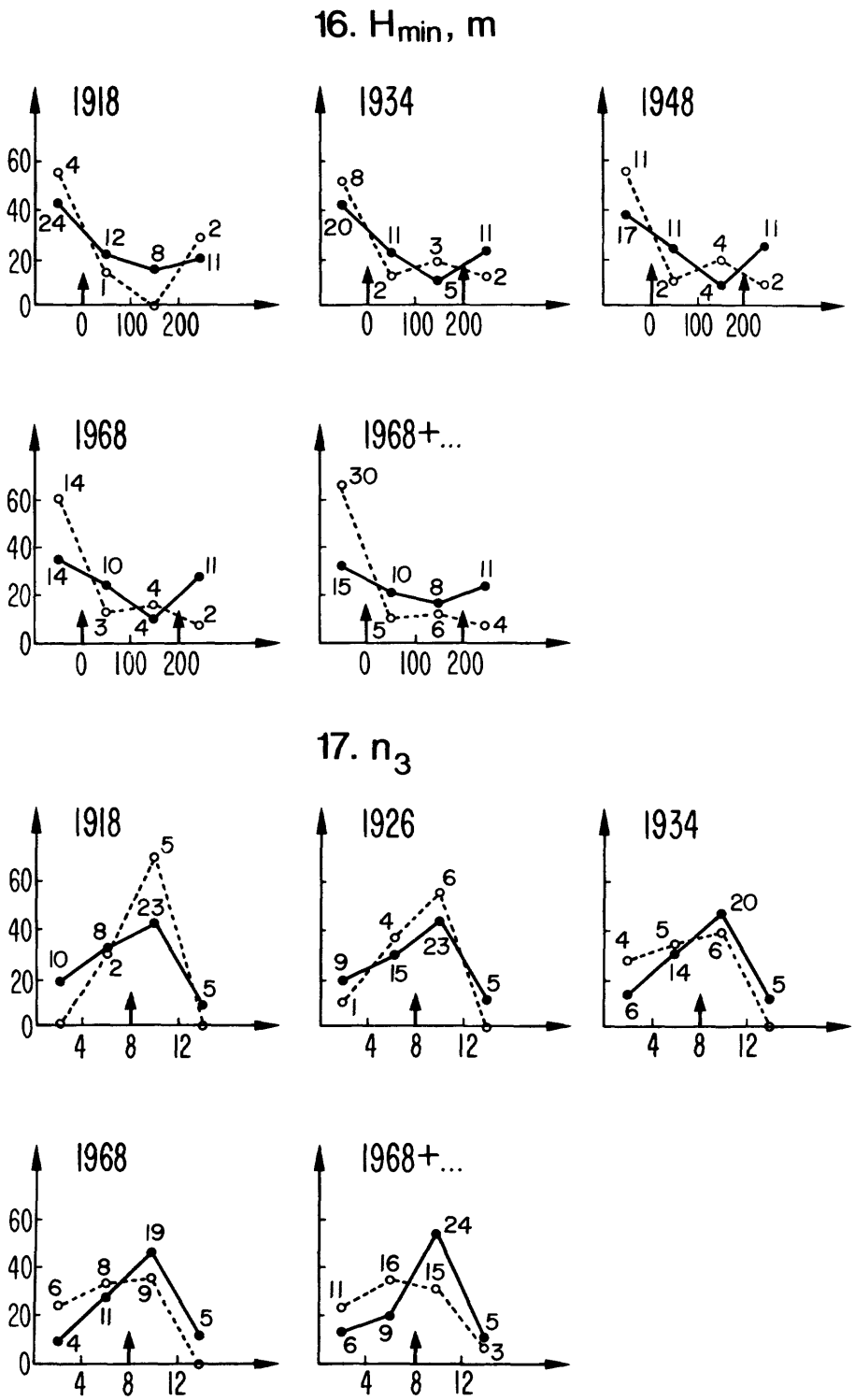

Fig. 2. For caption see p. 245.

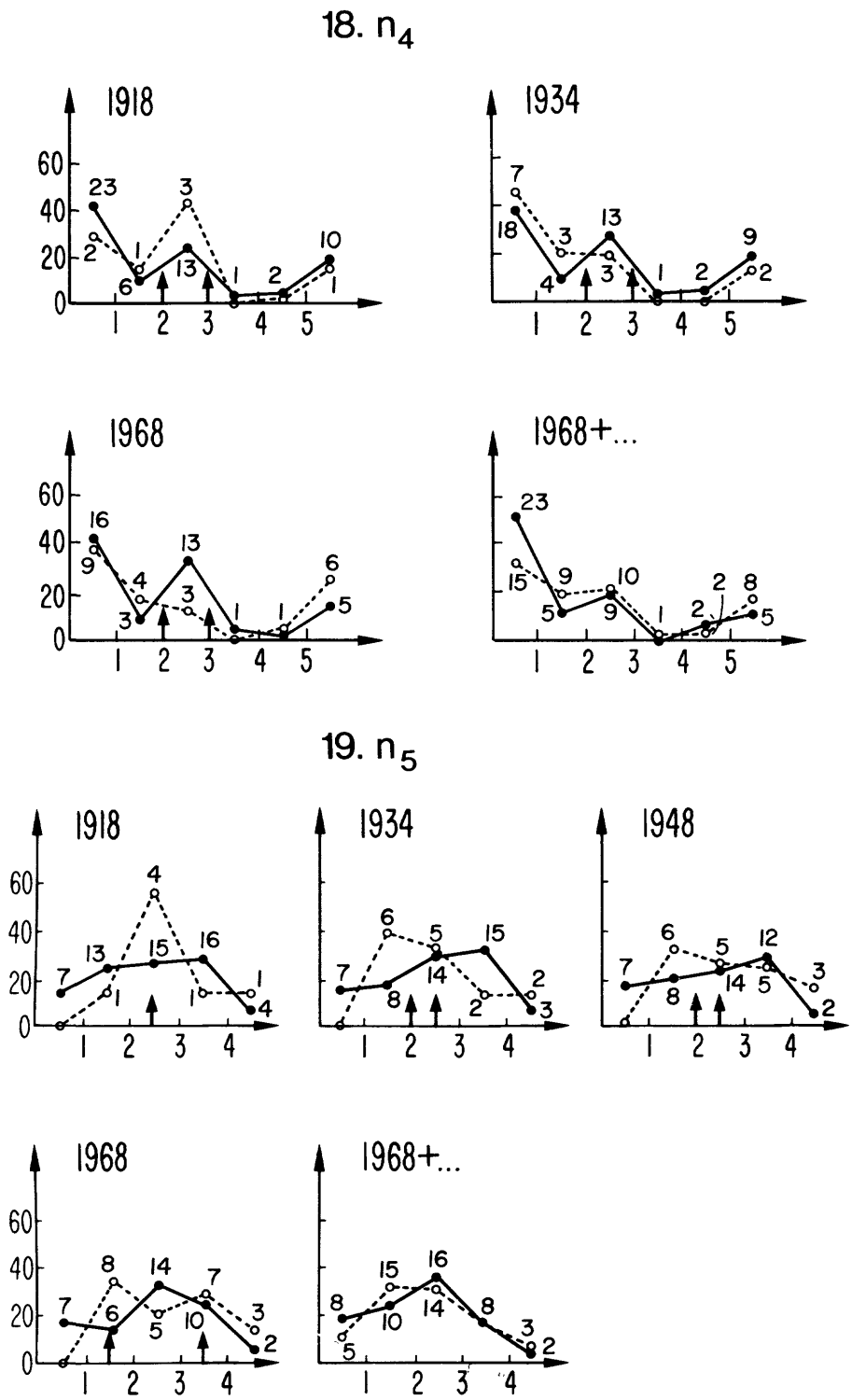

Fig. 2. For caption see p. 245.

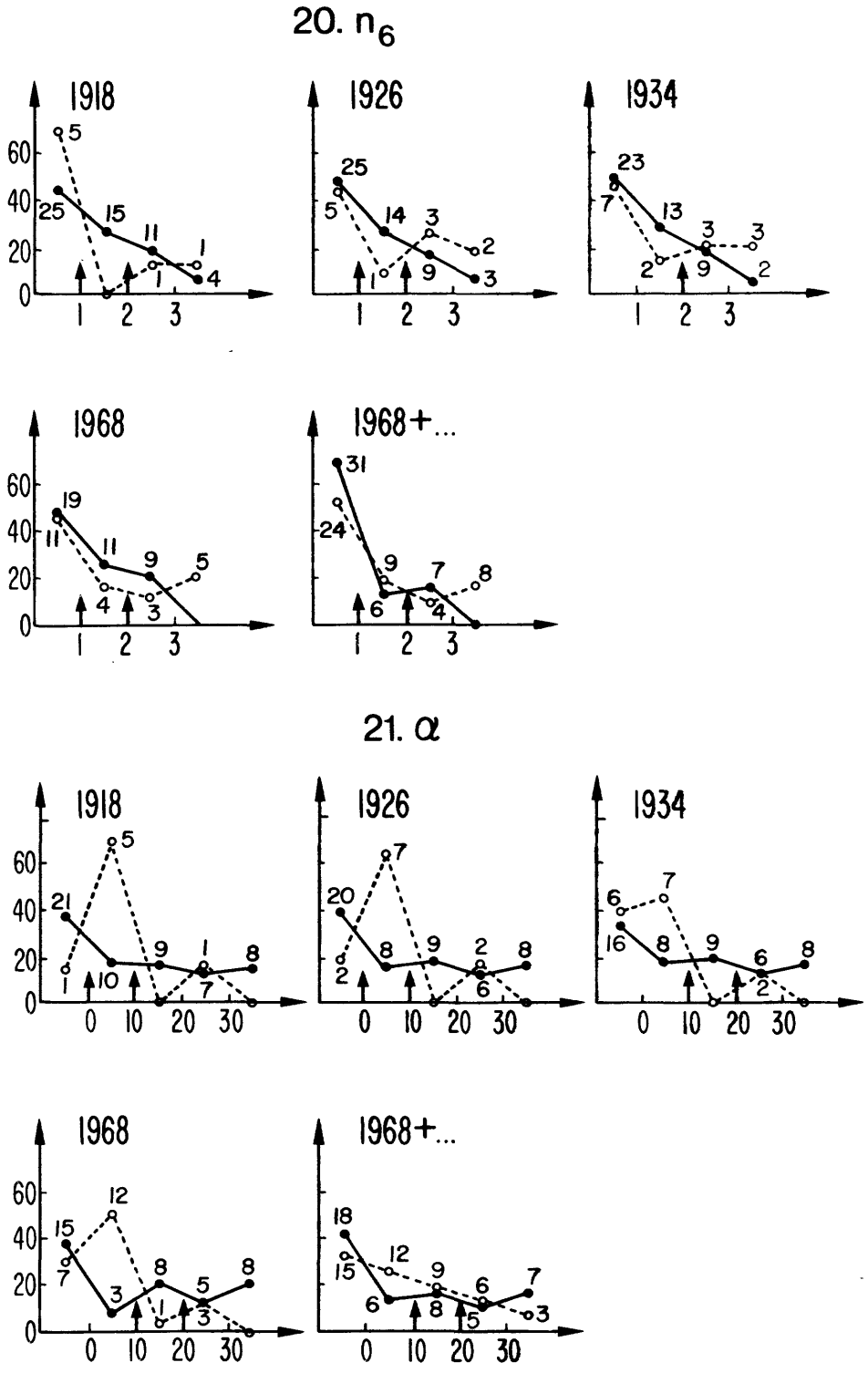

Fig. 2. For caption see p. 245.

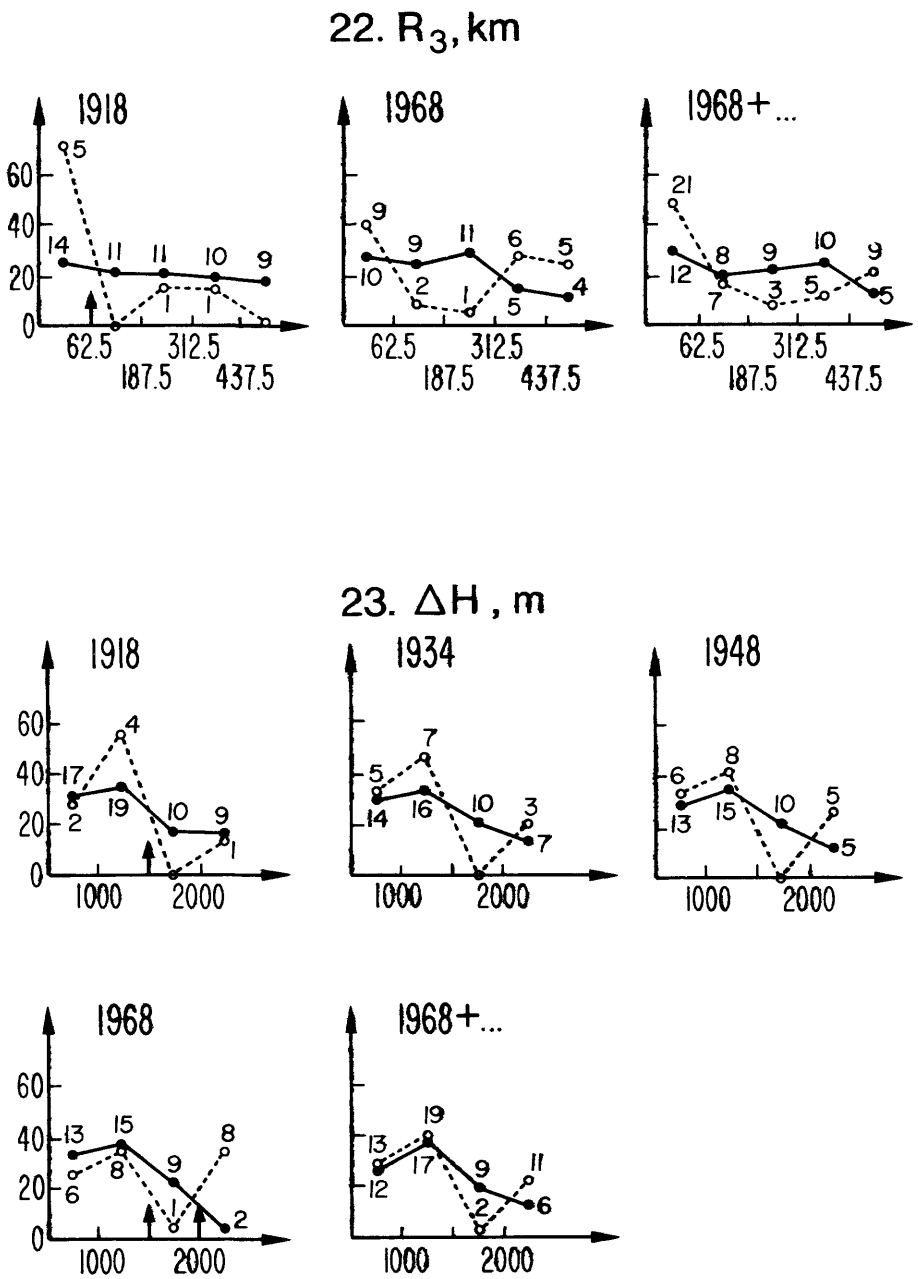

Fig. 2. One-dimensional distributions of parameters for points on major strike-slip faults of California shown in Fig. 1. 1968 = Last year in earthquake catalog; earthquakes up to this year inclusive are used in the separation of objects into classes; other dates are used to denote terminal years of EH experiment; 1968+... refers to the control experiment EF with objects recognized as D, after learning on full catalog, assigned to class I; $h_{\min}$, etc. are the ordinal number and symbol for parameter as used in Table VI. The values of parameters are indicated on the horizontal axis; the dashed line is the histogram for points of the first kind (near known epicenters); the solid line is the histogram for points of the third kind (far from known epicenters); the assigned thresholds are shown by arrows; the number next to each point refers to the number of objects for which the values of parameters fall into the given interval shown on the abscissa; the ordinate is the same number expressed as a percentage of the total number of objects in the corresponding class.

TABLE VI

Parameters used for recognition

N	Number in Table V	Name of parameter	Symbol	Assigned threshold
1	1	maximal elevation	h_{max}	$\leqslant$ 500
				$\leqslant$1,250
2	2	minimal elevation	h_{min}	$\leqslant$ 50
				$\leqslant$ 500
3	3	elevation difference	Δh	$\leqslant$ 500
				$\leqslant$1,000
4	5	"gradient"	$\Delta h/l_1$	$\leqslant$ 30
				$\leqslant$ 70
5	6	relative area of soft sediments	q	$\leqslant$ 10
				$\leqslant$ 50
6	7	type of rocks	–	presence of I
7	8	distance to closest fault	r_1	$\leqslant$ 12.5
				$\leqslant$ 37.5
8	11	distance to closest end or intersection of faults	r_2	$\leqslant$ 12.5
				$\leqslant$ 37.5
9	12	distance to geothermal zone	r_3	$\leqslant$ 25
				$\leqslant$ 75
10	15	distance to the closest zone of divergence	r_4	$\leqslant$ 100
				$\leqslant$ 200
11	17	distance to the reference point (intersection of San Andreas and Big Pine faults)	r_5	$\leqslant$ 125
				$\leqslant$ 375
12	14	distance to closest water reservoir	r_6	$\leqslant$ 0
				$\leqslant$ 25
13	27	the number of unnamed faults on *Tectonic Map of U.S.* (USGS, 1962)	n_1	$\leqslant$ 3
				$\leqslant$ 5
14	20	the number of changes in types of relief	n_2	= 0
15	22	maximal elevation	H_{max}	$\leqslant$ 500
				$\leqslant$1,500
16	23	minimal elevation	H_{min}	$\leqslant$ 0
				$\leqslant$ 200
17	30	the number of contacts between rocks of different age on *Geological Map of North America* (USGS, 1965)	n_3	$\leqslant$ 8
18	31	the number of parallel faults	n_4	$\leqslant$ 2
				$\leqslant$ 3
19	32	the number of faults	n_5	$\leqslant$ 1
				$\leqslant$ 3
20	33	the number of ends and intersections	n_6	$\leqslant$ 1
				$\leqslant$ 2
21	35	the angle between the fault and the dominant structural trend in the region (°)		$\leqslant$ 10
				$\leqslant$ 20
22*	13	distance to a region of large precipitation	R_3	$\leqslant$ 62.5
23*	24	elevation differences	ΔH	$\leqslant$1,500

The rule for coding the description of a point is the following: "1" means that the inequality in the last column is fulfilled.

* These parameters were used in control experiments only with learning based on earthquakes prior to 1934.

TABLE VII

Distinctive D and N features

(A) Based on entire earthquake catalog for points located on faults:

Feature number	Maximum elevation, h_{max} (meters)	Gradient $\Delta h/l_1$	Relative area of soft sediments, q %	Type of rocks	Distance to closest end or intersection of faults, r_2, km	Distance to nearest geothermal zone, r_3, km	Distance to nearest body of water, r_6, km	Minimum elevation, H_{min} (meters)	Number of contacts between rocks of different age on geologic map	Number of faults n_5	Angle between fault and dominant regional strike (deg.)
	1	4	5	6	8	9	12	16	17	19	21
					D						
1					≤37.5	≤75					≤10
2				no I	≤37.5						≤10
3				no I	≤37.5					≤3	
4			>10		≤12.5					>1	
5					≤37.5			≤200	≤8		
6			>10		≤37.5			≤0			
7				no I	≤37.5	>25					
8			≤50		≤12.5	>25					
					N						
1							>20		>8	≤3	
2					>37.5			≤0		≤3	
3				I		>25				≤3	
4	>500			I						≤3	
5					>12.5		>20		>8		
6					>12.5	>75			>8		
7				I		>75			>8		
8					>37.5	>25		≤200			
9			>10		>37.5			≤200			
10	>500				>37.5			≤200			
11	>500		>10		>12.5						

(B) Based on earthquake catalog extending through 1922:

Feature number	Maximum elevation, h_{max} (meters)	Minimum elevation, $\lvert h_{min} \rvert$ (meters)	Elevation difference, Δh, (meters)	Gradient, $\Delta h/l_1$	Type of rocks	Distance to nearest fault, r_1, km	Distance to closest end or intersection of faults, r_2, km	Number of contacts between rocks of different age on geologic map	Distance to the zone of large precitation, r_3, km	Elevation difference ΔH, (meters)
	1	2	3	4	6	7	8	17	22	23
					D					
1	≤1250				SM					≤1500
2			≤1000				>37.5	>8		
3			≤1000			>12.5		>8		
4	≤1250					≤12.5		>8		
5	≤1250			>30				>8		
					N					
1	>500							≤8	≤62.5	
2			>500					≤8		
3	>500				no SM			≤8		
4	>500				no SM		>37.5			
5	>1250					>12.5				

Parameter number corresponds to Table VI

The points recognized as D with this threshold and $\tau = 1$ are shown in Fig. 3a. It is encouraging that these points do not occur erratically, but form a limited number of compact segments. This might be expected however, because of the spatial continuity of some of the parameters. We see from Fig. 3a that significant parts of major faults are recognized as N. These should be segments where epicenters will not occur, though faulting could extend into these regions from epicenters on adjacent segments of the fault. Among the N segments the major branch of the San Andreas fault north of San Francisco, between the points *62* and *26*, seems especially surprising as does the Garlock fault. D segments concentrate at five areas from north to south between points *61–25* (lat. 41–40°N), *27–7* (38.5–37°N), *35–43* (36–34.5°N), *45–97* (34.2–33°N), and *18–21* (33–32.2°N). We shall discuss these areas later.

3.5. Control experiments

3.5.1. Experiment EH

In conducting this experiment the histograms of parameters are redetermined (see Fig. 2) because cataloged earthquakes after a specific year are not used in learning; their corresponding clusters are disbanded and their points are placed in class II. This may lead to the selection of new thresholds and even of other parameters. In practice, however, such changes will not occur at each step of the EH experiment, because the histograms are stable by definition and because the thresholds are chosen rather roughly. The histograms, corresponding to several steps, from 1918 to 1966 are compared in Fig. 2. The only changes that occur from histogram to histogram are the following: learning on the basis of earthquakes through 1918 we would assume different thresholds

TABLE VIII

Results of voting for points on major California faults – main variant

n_N \ n_D	0	1	2	3	4	5	≥6
≥7	~~70,74,80,83,~~ ~~89,90~~ 82,84,86,91						
6	~~69,88~~						
5	36,37,81						
4	~~65,66,73,94,~~ ~~95~~ 16,44, 52,54,76						
3	~~62,63,64,67,~~ ~~87~~ 17,22, 50,53,60						
2	⑨ ㉖ ~~71~~ ~~92,96~~ 15,38	~~85~~	~~72~~				
1	41	㊶ ~~68~~	~~75~~,7,33,45,46	㊺	⑥	⑳ 8,25	
0	~~77, 79~~	⑪ ⑬ ㊼ ~~93~~ 42	*2 27* 30 34 *40 43* ㊽ ㊾ ~~100~~	*12* ~~78~~	⑱ ③ ⑩ ㉓ ㉔ ㉘ ㊽ ⑥	*1 19* ~~98~~ *21* ㉛ ~~99~~ *39 56* 59 *57* 29	*4* ⑤ ⑭ *32* ~~97~~ 35

n_D

Circled number = number of a point in a cluster; italicized number = number of a point in a cluster which has largest value of $n_D - n_N$ in its cluster; ordinary number with tilde = number of a point not in a cluster used in learning stage; ordinary number without tilde = number of a point not in a cluster, not used in learning stage.
$k_1 = 7, k_2 = 9, \tilde{k}_1 = 4, \tilde{k}_2 = 1$ and $k_3 = 0$.

for seven parameters (No.'s 6, 7, 11, 12, 16, 19 and 21) and select for recognition two more parameters (22 and 23). The changes in the values of the thresholds are indicated in Table X.

The results of recognition in the EH control experiment are shown in Table IX and in Figs. 3b and c. They are successful since by and large the results based on a partial catalog agree with those based on the full catalog (Fig. 3a). At least one point in each cluster was recognized as D before the corresponding earthquake occurred. Moreover, at least one point in each cluster was recognized as D at all steps since 1911 with three exceptions: clusters corresponding to the earthquakes of 1923, 1940 and 1942 were not recognized with learning through 1918 and 1923.
However, at least one object in these clusters was recognized as D before the actual earthquake for all other steps in the EH experiment. The recognition of the objects in classes II and III also appears to be stable.

3.5.2. Experiment EF

The results shown in Table IX also illustrate the stability of our procedures. The identification of only seven points changed. Four D_{II} points are reclassified as N_{II} and three N_{II} points are reclassified as D_{II}. Thus, our D objects will neither wander nor proliferate over all of California, but strong earthquakes are predicted for the limited number of D_{II} points identified.

3.5.3. Inverse EH experiment

In this experiment we eliminated earthquakes from learning in the order of their occurrence, the first to occur, the first eliminated, beginning with 1836. In this and the following experiments we did not redetermine the histograms of parameters although we verified the stability of recognition by varying the learning materials.

The results of this experiment are shown in Table XI. Recognition remains successful until the 1906 earthquake. The points near its epicenter are not

TABLE IX

Recognition results for control experiments EH and EF

Number of point on Fig. 1	Year of earthquake which defines cluster	Learning based on earthquakes from 1836 through the year								
		1911	1918	1922	1923	1934	1940	1942	1948	1948+...
					Clusters $\{D_1 + N_1\}$:					
14	1948	+	+	+	+	+	+	+	+	+
49		+	+	+	+	o	o	o	+	+
51		o	+	+	o	+	o	o	+	+
18	1942	+	+	+	o	+	+	+	+	+
55		+	o	o	o	o	o	+	+	+
56		+	+	+	o	+	+	+	+	+
19	1940	+	+	+	o	+	+	+	+	+
56		+	+	+	o	+	+	+	+	+
57		+	+	+	o	+	+	+	+	+
58		+	+	+	o	+	+	+	+	+
21	1934	+	o	+	o	+	+	+	+	+
20		o	+	+	+	+	+	+	+	+
23	1923	o	o	+	+	+	+	+	+	+
1		+	o	+	+	+	+	+	+	+
24		o	o	+	+	+	+	+	+	+
61		o	o	+	+	+	+	+	+	+
10	1922	o	o	o	+	+	+	+	+	+
9		+	o	+	o	o	o	o	o	o
39		o	+	+	+	+	+	+	+	+
13	1918	o	+	+	+	+	+	+	+	+
12		+	+	+	+	+	+	+	+	+
47		+	+	+	+	+	+	+	+	+
6	1911	+	+	+	+	+	+	+	+	+
31		+	+	+	+	+	+	+	+	+
32		+	+	+	+	+	+	+	+	+
34		+	+	+	+	+	o	+	+	+
2	1906	+	+	+	+	+	+	+	+	+
26		+	+	+	o	+	o	o	o	o
27		+	o	+	+	+	+	+	+	+
11	1857	+	+	+	o	+	o	o	+	+
40		+	+	+	+	+	+	+	+	+
43		o	+	+	+	+	+	+	+	+
3	1836	+	+	+	+	+	+	+	+	+
28		+	+	+	+	+	+	+	+	+
4		+	+	+	+	+	+	+	+	+

TABLE IX (*continued*)

Number of point on Fig. 1	Year of earthquake which defines cluster	Learning based on earthquakes from 1836 through the year								
		1911	1918	1922	1923	1934	1940	1942	1948	1948+...
4	1836	+	+	+	+	+	+	+	+	+
3		+	+	+	+	+	+	+	+	+
5		+	+	+	+	+	+	+	+	+
30		+	+	+	+	+	+	+	+	+
5	1836	+	+	+	+	+	+	+	+	+
4		+	+	+	+	+	+	+	+	+
30		+	+	+	+	+	+	+	+	+
32		+	+	+	+	+	+	+	+	+
					Class II, $\{D_2 + N_2\}$:					
62		+	o	+	o	o	o	o	o	o
63		o	o	+	o	o	o	o	o	o
64		o	o	o	o	o	o	o	o	o
65		o	o	o	o	o	o	o	o	o
66		+	o	+	o	o	o	o	o	o
67		+	o	+	o	o	o	o	o	o
68		+	+	+	o	o	o	+	+	+
69		o	o	o	o	o	o	o	o	o
70		o	o	o	o	o	o	o	o	o
71		o	o	o	o	o	o	o	o	o
72		o	o	o	+	o	o	o	+	o
73		o	o	o	o	o	o	+	o	o
74		+	o	+	o	o	o	o	o	o
75		+	o	o	o	o	+	+	+	+
77		+	o	o	o	+	o	+	+	+
78		+	o	o	o	o	o	+	+	+
79		o	+	+	o	+	+	+	+	o
80		o	o	o	o	o	o	o	o	o
83		o	o	o	o	o	o	o	o	o
85		o	+	o	o	o	o	o	o	+
87		o	+	o	o	o	o	o	o	o
88		o	+	o	o	o	o	o	o	o
89		o	+	+	o	o	o	o	o	o
90		o	o	o	o	o	o	o	o	o
91		o	o	o	o	o	o	o	o	o
92		+	+	+	o	o	o	o	o	o
93		+	+	+	+	+	o	o	+	+
94		o	o	o	o	o	o	o	o	o
95		o	o	o	o	o	o	o	o	o
96		o	o	o	o	o	o	o	o	o
97		o	o	+	+	+	+	+	+	+
98		o	+	+	+	+	+	+	+	+
99		+	o	+	+	+	+	+	+	+
100		+	o	o	o	o	o	o	+	+

TABLE IX (continued)

Number of point on Fig. 1.	Year of earthquake which defines cluster	Learning based on earthquakes from 1836 through the year								
		1911	1918	1922	1923	1934	1940	1942	1948	1948+...
		Class III (objects for voting but not for learning):								
7		o	+	+	o	+	+	+	+	+
8		+	o	o	+	+	+	+	+	+
15		o	+	o	o	o	o	o	o	o
16		o	+	o	o	o	o	o	o	o
17		o	+	+	o	o	o	o	o	o
22		o	o	+	o	o	o	o	o	o
25		o	o	o	+	+	+	+	+	+
29		+	+	+	+	+	+	+	+	+
33		+	+	+	+	o	o	+	+	+
35		+	o	o	+	+	+	+	+	o
36		+	o	+	o	o	o	o	o	o
37		+	+	o	o	o	o	o	o	o
38		+	o	o	o	o	o	o	o	o
41		o	+	o	o	o	o	o	+	o
42		+	+	+	+	+	+	+	+	o
44		o	+	+	o	o	o	o	o	o
45		+	+	+	o	o	o	o	+	+
46		+	+	+	o	o	o	o	+	+
48		+	+	+	+	+	+	+	+	+
50		o	+	+	o	o	o	o	o	o
52		o	o	o	o	o	o	o	o	o
53		o	o	o	o	o	o	o	o	o
54		o	o	o	o	o	o	o	o	o
59		+	+	+	+	+	+	+	+	+
60		o	o	+	o	o	o	o	o	o
76		o	o	o	o	o	o	o	o	o
81		o	o	o	o	o	o	o	o	o
82		o	o	o	o	o	o	o	o	o
84		o	o	o	o	o	o	o	o	o
86		o	o	o	o	o	o	o	o	o

+ = object recognized as D; o = object recognized as N; year refers to the data through which earthquakes in the catalog were used for learning; last earthquake used was in 1948; last column (1948+...) refers to experiment EF; blank lines separate the clusters, each identified by the year of the earthquake associated with the cluster; vertical lines show the time when the cluster was included in learning; to the left of this line the points of this cluster were included in class II during the learning stage.

recognized as D_{II}, after we transfer them in the learning stage to class II. However, after we also eliminate the 1911 epicenter, a D point is again recognized in each cluster. Thus, on the basis of learning on seven earthquakes (1918–1948) we recognized as dangerous the sites of the earthquakes for the period 1836–1911, except for 1906.

3.5.4. Uniformity of the region

Several areas were selected in Table IX, each corresponding either to a group of epicenters or to a part of a group. The epicenters in these areas were assumed to be unknown and the corresponding clusters were eliminated from learning. The results, shown in Table XII, indicate that recognition is reasonably

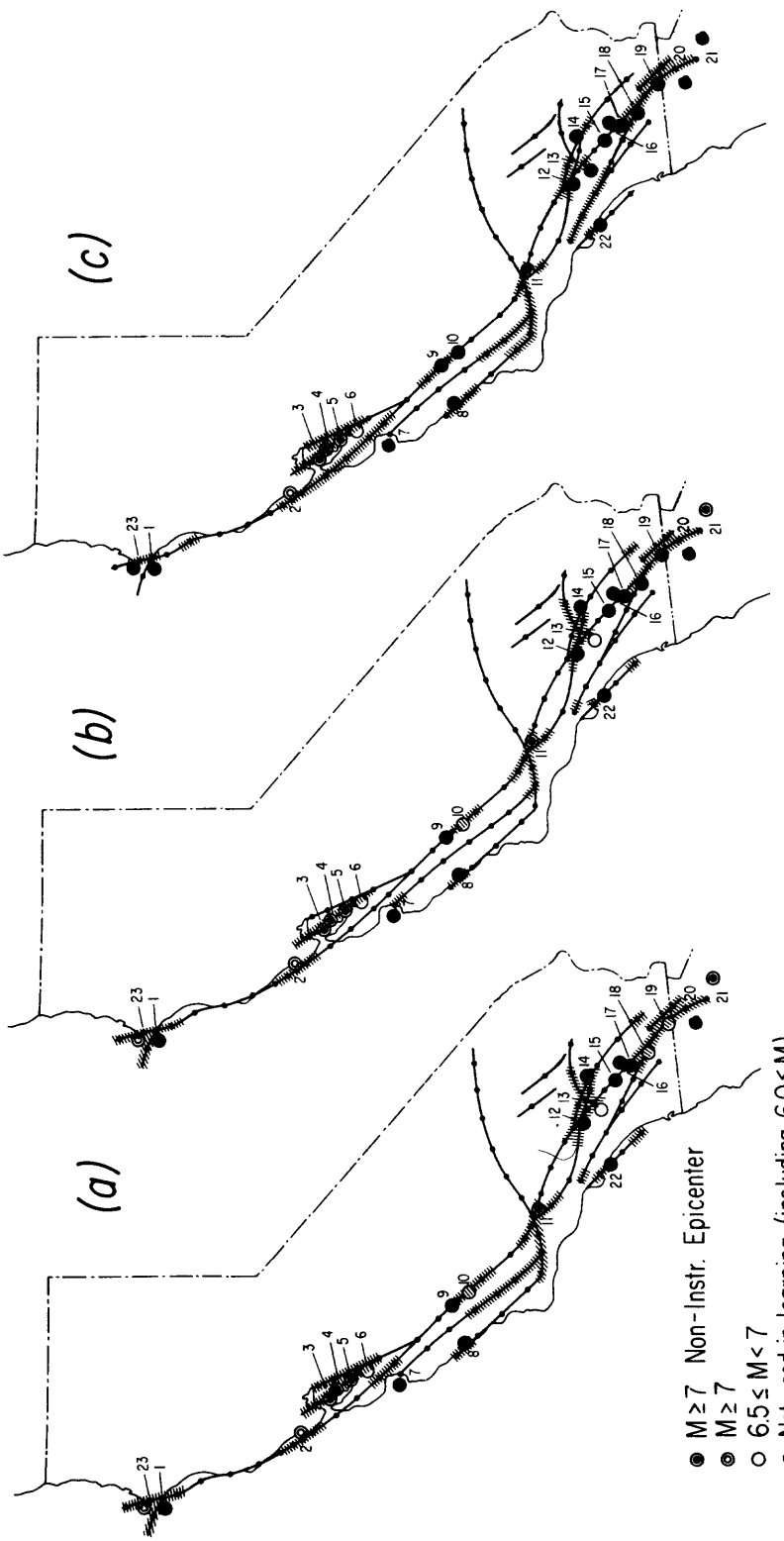

Fig. 3. Results of recognition for strike-slip earthquakes in California. Hachured regions of faults are recognized as dangerous. All earthquakes except those shown by solid circles were used in learning.
(a) All earthquakes $M \geq 6.5$ used in learning except those shown as solid.
(b) All earthquakes $M \geq 6.5$, prior to 1934 are used in learning.
(c) All earthquakes $M \geq 6.5$, prior to 1911 are used in learning.

TABLE X

Change in thresholds of discretization in experiment EH

Number in Table VI	The name of parameter	Thresholds for learning through the year	
		1968	1918
6	type of rocks	I	not SM
7	distance to closest fault, r_1 (km)	$\leqslant$ 12.5	$\leqslant$ 12.5
		$\leqslant$ 37.5	$\leqslant$ 25
11	distance to the reference point (intersection of San Andreas and Big Pine faults), r_5 (km)	$\leqslant$125	$\leqslant$ 250
		$\leqslant$375	$\leqslant$ 375
12	distance to closest water reservoir, r_6 (km)	= 0	
		$\leqslant$ 25	$\leqslant$ 25
16	minimal elevation, $H_{\min}$ (m)	$\leqslant$ 0	$\leqslant$ 0
		$\leqslant$200	
19	the number of faults	$\leqslant$ 1	$\leqslant$ 2
		$\leqslant$ 3	
21	the angle between fault and dominant strike in the region, α (°)	$\leqslant$ 10	= 0
		$\leqslant$ 20	$\leqslant$ 10
22*	distance to a region of large precipitation, R_3	–	$\leqslant$ 62.5
23*	elevation difference, ΔH (m)	–	$\leqslant$1,500

* Parameter used only in learning with earthquakes prior to 1934.

stable to variations in learning material. They also indicate how homogeneously known earthquakes should cover a D area for successful recognition. At least one point near each eliminated epicenter was recognized as D in variants 1, 5, 7 and 8. These variants correspond to elimination of earthquakes in the southern and northern parts of the regions under study, namely, the Mendocino fault (variant 1), the intersection of the Garlock and San Andreas faults (variant 5), the San Jacinto Mountains (variant 7), and the Salton Sea depression (variant 8). With the other variants, 2, 3, 4 and 6, where earthquakes in the central area between San Francisco and Parkfield were eliminated, the corresponding D objects were not recognized.

3.5.5. Variations of the set of parameters

In this control experiment we eliminated each parameter (one at a time) from the data set and repeated the learning and voting. The results are shown in Table XIII. The order, in which the parameters are listed, corresponds to their increasing role in recognition. We see that r_2, the distance to a fault end or an intersection of faults, is most important. The importance of r_2 is confirmed in other ways. For example, to get a decent number of distinctive features with r_2 eliminated, we had to relax k_2 to 7 and $\tilde{k}_2$ to 2. The objects separate poorly in the voting stage, and the results of recognition are unstable with respect to changes in the threshold $\bar{\Delta}$. The reason for the importance of this parameter is discussed in a later paragraph.

Recognition is stable with respect to the elimination of the other parameters, as Table XIII shows.

3.5.6. Variation of the algorithm

In this control experiment we use the algorithm CORA-3 instead of CLUSTERS. In this case class I is composed of the centers of the clusters; class II is unchanged. The results are very similar to those discussed before. This experiment confirms that a somewhat different algorithm for our recognition procedures leads to similar results. At the same time it confirms the advantage of the algorithm CLUSTERS for our particular case because the results obtained by CORA are much less stable to variations in the learning material, and especially to changes in the threshold $\bar{\Delta}$.

TABLE XI

Recognition results for inverse EH experiment (see Table IX for notation)

Number of point on Fig. 1	Year of earthquake which defines cluster	Year of first earthquake allowed for in learning						
		1836	1836	1836	1857	1906	1911	1918
14		+	+	+	+	+	+	+
49	1948	+	+	+	+	o	o	+
51		+	+	o	+	o	+	+
18		+	+	+	+	+	+	+
55	1942	+	+	+	o	+	+	+
56		+	+	+	+	+	+	+
19		+	+	+	+	+	+	+
56	1940	+	+	+	+	+	+	+
57		+	+	+	+	+	+	+
58		+	+	+	+	+	+	+
21	1934	+	+	+	+	+	+	+
20		+	+	+	+	+	+	+
23		+	+	+	+	+	+	+
1	1923	+	+	+	+	+	+	+
24		+	+	+	+	+	+	+
61		+	+	+	+	+	+	+
10		+	+	+	+	+	+	+
9	1922	o	o	o	o	+	+	+
39		+	+	+	+	+	+	+
13		+	+	+	+	+	o	+
12	1918	+	+	+	+	+	+	+
47		+	+	+	+	+	+	+
6		+	+	+	+	+	+	+
31	1911	+	+	+	+	+	+	+
32		+	+	+	+	+	+	+
34		+	+	+	+	+	+	+
2		+	+	+	+	+	o	o
26	1906	o	o	o	o	+	o	+
27		+	+	+	+	+	o	o
11		+	o	+	+	o	o	+
40	1857	+	+	+	+	+	+	+
43		+	+	+	+	+	+	+
3	1836	+	+	+	o	+	o	+
28		+	+	+	+	+	o	+
4		+	+	+	+	+	+	+
3		+	+	+	o	+	o	+
5	1836	+	+	+	+	+	+	+
30		+	+	o	o	o	o	+

TABLE XI (*continued*)

Number of point on Fig. 1	Year of earthquake which defines cluster	Year of first earthquake allowed for in learning						
		1836	1836	1836	1857	1906	1911	1918
5		+	+	+	+	+	+	+
4	1836	+	+	+	+	+	+	+
30		+	+	o	o	o	o	+
32		+	+	+	+	+	+	+
62		o	o	o	o	o	+	+
63		o	o	o	o	o	+	+
64		o	o	o	o	o	o	+
65		o	o	o	o	o	o	+
67		o	o	o	o	o	o	+
68		+	+	+	+	o	+	+
69		o	o	o	o	o	o	+
71		o	o	o	o	+	+	+
72		+	+	o	o	o	+	+
74		o	o	o	o	o	o	+
75		+	+	+	+	+	o	+
77		+	+	+	+	+	+	+
78		+	+	+	+	+	+	+
79		+	+	+	+	+	o	+
85		o	o	o	o	o	o	+
87		o	o	o	o	o	o	+
88		o	o	o	o	o	o	+
90		o	o	o	o	o	o	+
91		o	o	o	o	o	o	+
92		o	o	o	o	+	o	+
93		+	+	+	+	o	o	+
94		o	o	o	o	o	o	+
95		o	o	o	o	o	o	+
96		o	o	o	o	o	o	+
97		+	+	+	+	+	+	+
98		+	+	+	+	+	+	+
99		+	+	+	+	+	+	+
100		+	+	+	+	o	o	+
7		+	+	+	+	+	+	+
8		+	+	+	+	+	+	+
15		o	o	o	o	o	o	+
16		o	o	o	o	o	o	+
17		o	o	o	o	o	o	+
22		o	o	o	o	+	+	+
25		+	+	+	+	+	+	+
29		+	+	+	+	+	+	+
33		+	+	+	o	o	o	+
35		+	+	+	+	+	+	+
36		o	o	o	o	o	o	+
37		o	o	o	o	o	+	+
38		o	o	o	o	+	+	+
41		o	o	o	o	o	o	+
42		+	+	+	+	+	+	+

TABLE XI (*continued*)

Number of point on Fig. 1	Year of earthquake which defines cluster	Year of first earthquake allowed for in learning						
		1836	1836	1836	1857	1906	1911	1918
44		o	o	o	o	o	o	+
45		+	+	o	+	+	+	+
46		+	+	o	+	+	+	+
48		+	+	+	+	+	+	+
50		o	o	o	o	o	o	+
52		o	o	o	o	o	o	+
53		o	o	o	o	o	o	+
54		o	o	o	o	o	o	+
59		+	+	+	+	+	+	+
60		o	o	o	o	+	+	+
76		o	o	o	o	o	+	+
84		o	o	o	o	o	o	+

The earthquakes are eliminated cumulatively from learning in the order of their occurrence: first one, then two, etc. Year in top row refers to the first earthquake allowed for in learning. The rest of the notation is analogous to Table IX.

TABLE XII

Recognition in the control experiment "uniformity of the region" (elimination of groups of clusters from learning). Parentheses indicate the eliminated clusters. Otherwise the notation is the same as in Table IX

No. of point in Fig. 1	Number of variant							
	1	2	3	4	5	6	7	8
Clusters:								
14	+	+	+	+	+	+	(+)	(+)
49	+	+	+	o	+	+	(+)	(+)
51	+	o	o	o	o	+	(+)	(+)
18	+	+	+	+	+	+	+	(+)
55	o	o	o	+	+	+	+	(+)
56	+	+	+	+	+	+	+	(+)
19	+	+	+	+	+	+	+	(+)
56	+	+	+	+	+	+	+	(+)
57	+	+	+	+	+	+	+	(+)
58	+	+	+	+	+	+	+	(+)
21	+	+	+	+	+	+	+	(+)
20	+	+	+	+	+	+	+	(+)
23	(o)	+	+	+	+	+	+	+
1	(+)	+	+	+	+	+	+	+
24	(o)	+	+	+	+	+	+	+
61	(o)	+	+	+	+	+	+	+

No. of point in Fig. 1	Number of variant							
	1	2	3	4	5	6	7	8
10	+	+	+	+	+	(o)	+	+
9	o	o	o	+	o	(o)	o	+
39	+	+	+	+	+	(o)	+	+
13	+	o	o	+	o	+	(+)	+
12	+	+	+	+	+	+	(+)	+
47	+	+	+	+	+	+	(+)	+
6	+	+	+	(o)	+	o	+	+
31	+	+	+	(o)	+	+	+	+
32	+	+	+	(o)	+	+	+	+
34	+	+	+	(o)	+	+	+	+
2	(+)	(o)	(o)	(o)	+	+	+	+
26	(o)	(o)	(o)	(o)	o	o	+	+
27	(+)	(o)	(o)	(o)	+	+	+	+
11	+	+	+	+	(o)	+	+	+
40	+	+	+	+	(+)	+	+	+

TABLE XII (*continued*)

No. of point in Fig. 1	Number of variant 1	2	3	4	5	6	7	8
43	+	o	o	+	(+)	+	+	+
3	+	+	(o)	(o)	+	+	+	+
28	+	o	(o)	(o)	+	+	+	+
4	+	+	(+)	(+)	+	+	+	+
4	+	+	(+)	(+)	+	+	+	+
3	+	+	(o)	(o)	+	+	+	+
5	+	+	(+)	(o)	+	+	+	+
30	+	+	(o)	(o)	+	+	+	+
5	+	+	(+)	(o)	+	+	+	+
4	+	+	(+)	(+)	+	+	+	+
30	+	+	(o)	(o)	+	+	+	+
32	+	+	(+)	(o)	+	+	+	+
Group II:								
62	o	o	o	+	o	o	o	o
63	o	o	o	+	o	o	o	o
64	o	o	o	+	o	o	o	o
65	o	o	o	o	o	o	o	o
66	o	o	o	o	o	o	o	o
67	o	o	o	+	o	o	o	o
68	+	o	o	o	o	+	+	+
69	o	o	o	o	o	o	o	o
70	o	o	o	o	o	o	o	o
71	o	o	o	+	o	o	o	+
72	o	o	o	o	+	o	o	o
73	o	o	o	o	o	o	o	o
74	o	o	o	o	o	o	o	o
75	+	o	o	o	+	+	+	o
77	+	o	o	+	+	+	+	o
78	+	+	+	+	+	+	+	o
79	+	o	o	+	o	+	o	o
80	o	o	o	o	o	o	o	o
83	o	o	o	o	o	o	o	o
85	o	o	o	o	o	o	o	o
87	o	o	o	o	o	o	o	o
88	o	o	o	o	o	o	o	o
89	o	o	o	o	o	o	o	o
90	o	o	o	o	o	o	o	o
91	o	o	o	o	o	o	o	o

No. of point in Fig. 1	Number of variant 1	2	3	4	5	6	7	8
92	o	o	o	+	o	o	o	o
93	+	+	o	o	o	+	+	+
94	o	o	o	o	o	o	o	o
95	o	o	o	o	o	o	o	o
96	o	o	o	o	o	o	o	o
97	+	+	+	+	+	+	+	+
98	+	+	+	+	+	+	+	+
99	+	+	+	o	+	+	+	+
100	+	o	o	o	+	+	+	+
Group III:								
7	+	o	o	o	+	+	+	+
8	+	+	o	+	+	+	+	+
15	o	o	o	o	o	o	o	o
16	o	o	o	o	o	o	o	o
17	o	o	o	o	o	o	o	o
22	o	o	o	+	o	o	o	o
25	+	+	+	+	+	+	+	+
29	+	+	+	o	+	+	+	+
33	+	o	o	o	+	o	+	+
35	+	+	+	+	+	+	+	+
36	o	o	o	+	o	o	o	o
37	o	o	o	o	o	o	o	o
38	o	o	o	+	o	o	o	+
41	o	o	o	o	o	o	o	o
42	+	+	+	+	+	+	+	+
44	o	o	o	o	o	o	o	o
45	+	+	+	o	+	+	+	+
46	+	+	+	o	+	+	+	+
48	+	+	o	+	+	+	+	+
50	o	o	o	o	o	o	o	o
52	o	o	o	+	o	o	o	o
53	o	o	o	o	o	o	o	o
54	o	o	o	o	o	o	o	o
59	+	+	+	+	+	+	+	+
60	o	o	o	+	o	o	o	o
76	o	o	o	o	o	o	o	o
81	o	o	o	o	o	o	o	o
82	o	o	o	o	o	o	o	o
84	o	o	o	o	o	o	o	o
86	o	o	o	o	o	o	o	o

3.5.7. Recognition of randomly described objects

The binary codes, which describe points, are replaced by random binary numbers in this control experiment. Learning proceeds using the algorithm CLUSTERS. In a first step we use the same k_i and $\tilde{k}_i$, as with the real data described earlier. In this case 32 distinctive D features and no N features are found, an unsatisfactory result. This is not sufficient to

TABLE XIII

Control experiment: change of recognition due to the elimination of parameters

After elimination of the parameter	Recognition of the following points changed:		Class in learning
	D changed to N	N changed to D	
h_{max}, r_6, n_3, or n_5 (only one at a time)		*85* or *96*	II
α	*72*		II
		41	III
r_3		*87* and *96*	II
		41	III
type of rocks	*72*	*96*	II
	25 and *35*		III
q	*51*		I
	72	*85* and *92*	II
	45 and *46*		III
H_{min}	*51*	*26*	I
	72		II
		22 and *60*	III
r_2	*49* and *6*	*9* and *26*	I
	68, 77, 79 and *100*	*66, 67, 71, 87, 62, 63, 64, 65* and *92*	II
	45 and *46*	*17, 22, 36, 38, 41, 52, 60* and *76*	III

reject the possibility of recognition with random data, because the values of k_i and $\tilde{k}_i$ in the processing of real data are not predetermined; they are varied until sufficient and comparable numbers of distinctive D and N features are obtained. The only limitation is that k_i should be sufficiently large and $\tilde{k}_i$ not too large. Therefore, k_i and $\tilde{k}_i$ should be varied in this control experiment. With $k_1 = 12, k_2 = 9, \tilde{k}_1 = 5$, $\tilde{k}_2 = 2$ we find twelve distinctive features of D and fifteen of N. However, the separation of points by voting is rather vague, as is seen by comparing Tables VIII and XIV. Each feature occurs in fewer points; for example, each distinctive D feature is found at an average of fourteen points, whereas for real data the corresponding number is 21.

Also, the results are unstable, in that experiment EF results in twelve new D points in contrast to three points for real data. Furthermore the D segments of major faults are more scattered.

In this way the experiment with random data supports the results found with real data. We also learn that reliable results show up in a high degree of separation of the objects by voting.

3.6. Geological implications

To understand the geological implications of this work we pose the question: what makes a place D and not N? To answer this question, we review the parameters which make up the D and N features. We must review not only distinctive features, but also their equivalent and ϵ-equivalent features which were identified but not used in voting. Let us recall the definition of these features. Consider two features of some class F_1 and F_2. The sets of objects of the same class, which have F_1 or F_2, are called S_1 or S_2, respectively. F_1 and F_2 are equivalent, if S_1 and S_2 coincide. They are ϵ-equivalent, if only the ϵth fractions of the

TABLE XIV

Results of voting after learning on random data

n_N \ n_D	0	1	2	3	4	5	6	≥7
≥7	64, 75, 79 87, 95, 98 42							
6	15							
5	36	62, 76	88	7				
4	73, 91	69	67, 33, 35		(47)			
3	78, 85 92, 60	(39) 72 16, 29, 44	(26) 52	77, 90	84			
2	63, 66 68	71, 46 54	(43) 59 81	(57)	(9) 97	70, 8	(6)	
1	(40)	(19) 74 22, 38	(1) 83 100, 25, 37, 50	(55) (12) (27) 93, 94	(18) (61) (31) 45		(51) 99	
0		(58) (13) (3) (5) 48, 86 96, 89	(4) 80 82	(23) 53	(14) (21) 10 17, 41	32 34	56 20 24	49 2 11 28 30 65

$k_1 = 12$, $k_2 = 7$, $\tilde{k}_1 = 5$ and $\tilde{k}_2 = 2$ (k_i and $\tilde{k}_i$ are relaxed compared to main variant).

objects is S_1 and S_2 do not coincide (the fraction is relative to the total number of objects in S_1 and S_2; each object is counted once). Equivalent and ϵ-equivalent features, like distinctive features, carry significant information of geologic interest. They were not used in voting in order not to bias the vote by repeated contributions by some subsets of objects.

Although 21 parameters indicated in Table VI were considered in the learning stage, only eleven were selected for incorporation in distinctive features. Since we are examining features for their "geological content" we might as well broaden the number, using more parameters in the process. We do this by rerunning the algorithm, relaxing the k_i slightly. We also used objects recognized as D or N rather than points assigned to class I or II in this new learning stage aimed at finding more features. We will next discuss 177 distinctive, equivalent and ϵ-equivalent features, involving all 21 parameters of Table VI, found this way. Table XV summarizes these features.

First consider the left-hand side part. Parameters are indicated in the uppermost row, with notation the same as in Tables V and VI. The second row indicates the thresholds for the parameters. All parameters used in the original learning stage (Table VI) are considered; parameters, which were selected for recognition in this earlier stage (Table VIIA) are marked by an asterisk. The features are divided into groups, separated by thin horizontal lines. Each group consists of one distinctive feature (from Table VIIA) and its equivalent and ϵ-equivalent features. A distinctive feature is indicated by a heavy number at the top of the group. The digit "1" means that the parameter must satisfy the threshold condition in row 2; "0" means that it must not. The numbers to the left of the table indicate the ordinal number of the distinctive feature in Table

TABLE XV

Distinctive features, examined for geological content for points located on faults. Left-hand side displayed in tabular form, right-hand side as flow diagram. (See paragraph 3.6 for explanation.)

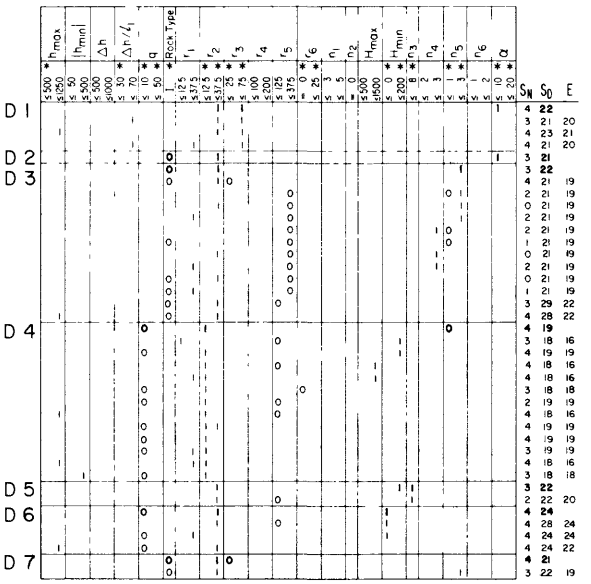

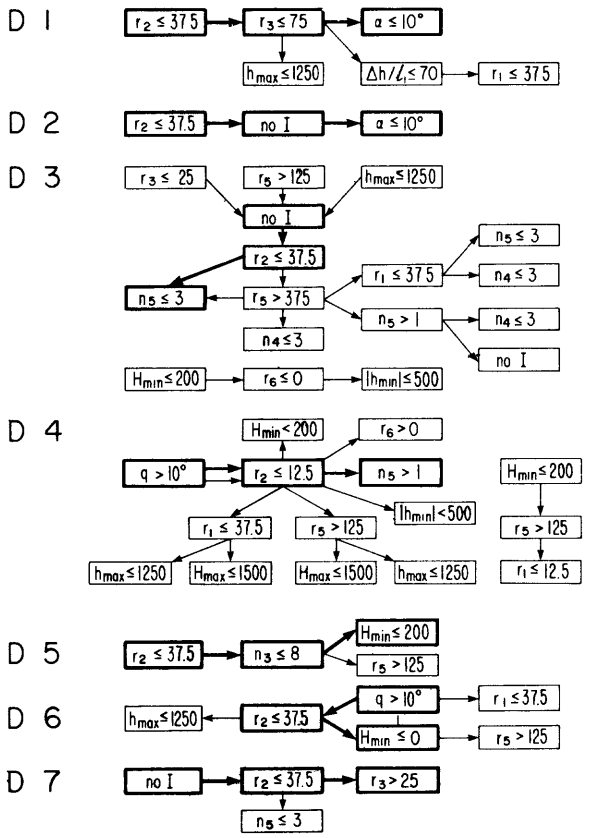

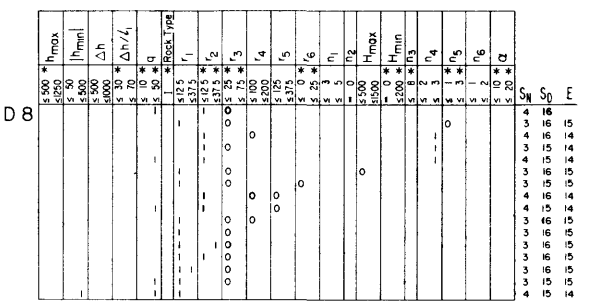

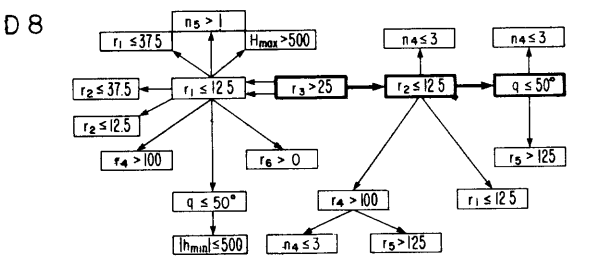

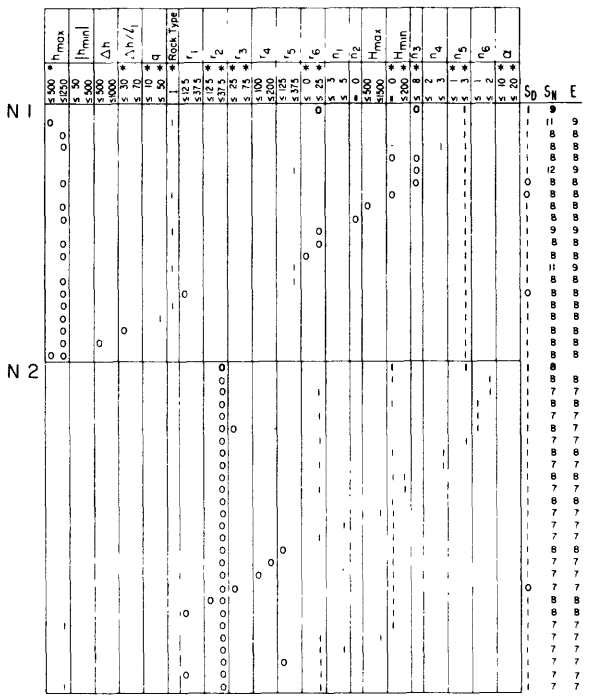
N 1
N 2
Rock Type
S_D
S_N
E

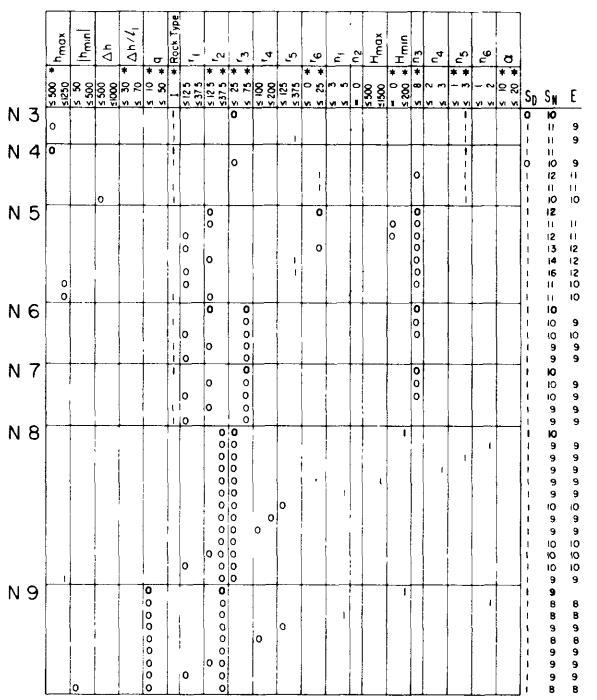
N 3
N 4
N 5
N 6
N 7
N 8
N 9
Rock Type
S_D
S_N
E

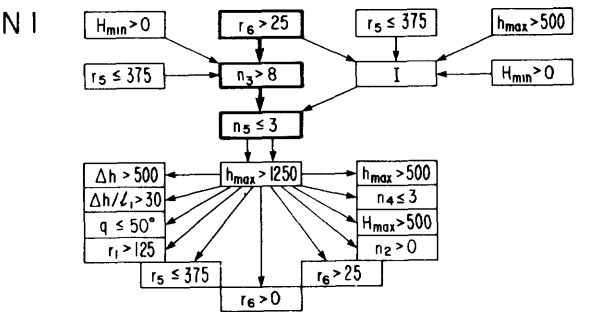
N 1
H_min > 0
r_6 > 25
r_5 ≤ 375
h_max > 500
r_5 ≤ 375
n_3 > 8
I
H_min > 0
n_5 ≤ 3
Δh > 500
Δh/l_1 > 30
q ≤ 50°
r_1 > 125
h_max > 1250
h_max > 500
n_4 ≤ 3
H_max > 500
n_2 > 0
r_5 ≤ 375
r_6 > 25
r_6 > 0

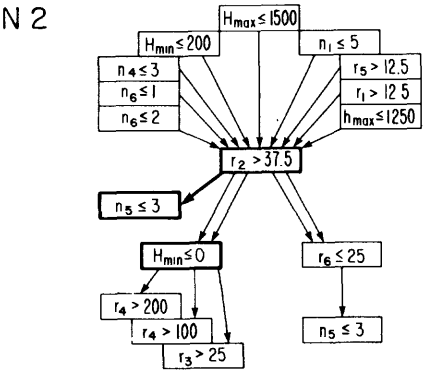
N 2
H_max ≤ 1500
H_min ≤ 200
n_1 ≤ 5
n_4 ≤ 3
n_6 ≤ 1
n_6 ≤ 2
r_5 > 12.5
r_1 > 12.5
h_max ≤ 1250
r_2 > 37.5
n_5 ≤ 3
H_min ≤ 0
r_6 ≤ 25
r_4 > 200
r_4 > 100
r_3 > 25
n_5 ≤ 3

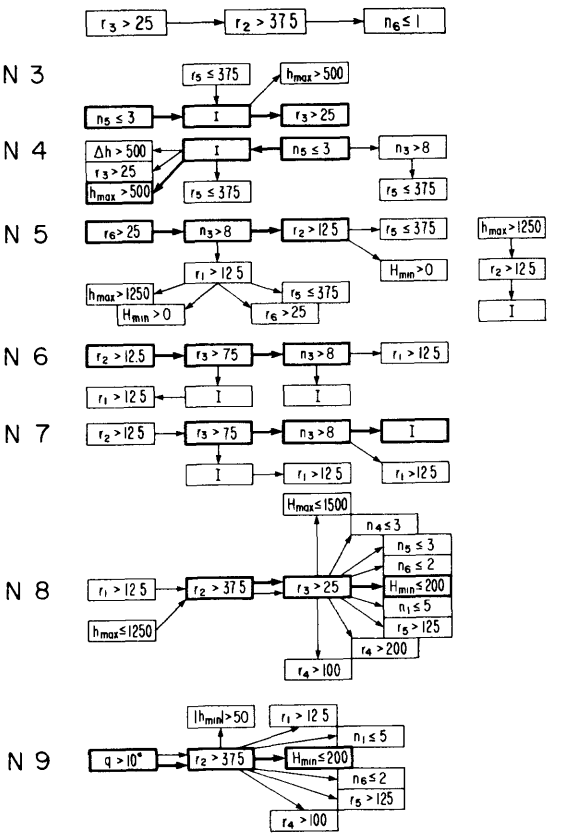
r_3 > 25
r_2 > 37.5
n_6 ≤ 1
N 3
r_5 ≤ 375
h_max > 500
n_5 ≤ 3
I
r_3 > 25
N 4
Δh > 500
r_3 > 25
h_max > 500
I
n_5 ≤ 3
n_3 > 8
r_5 ≤ 375
r_5 ≤ 375
N 5
r_6 > 25
n_3 > 8
r_2 > 12.5
r_5 ≤ 375
H_min > 0
r_1 > 12.5
h_max > 1250
H_min > 0
r_5 ≤ 375
r_6 > 25
h_max > 1250
r_2 > 12.5
I
N 6
r_2 > 12.5
r_3 > 75
n_3 > 8
r_1 > 12.5
r_1 > 12.5
I
I
N 7
r_2 > 12.5
r_3 > 75
n_3 > 8
I
I
r_1 > 12.5
r_1 > 12.5
N 8
H_max ≤ 1500
n_4 ≤ 3
n_5 ≤ 3
n_6 ≤ 2
H_min ≤ 200
n_1 ≤ 5
r_5 > 125
r_4 > 200
r_1 > 12.5
r_2 > 37.5
r_3 > 25
h_max ≤ 1250
r_4 > 100
N 9
|h_min| > 50
r_1 > 12.5
n_1 ≤ 5
q > 10°
r_2 > 37.5
H_min ≤ 200
n_6 ≤ 2
r_5 > 125
r_4 > 100

TABLE XV (*continued*)

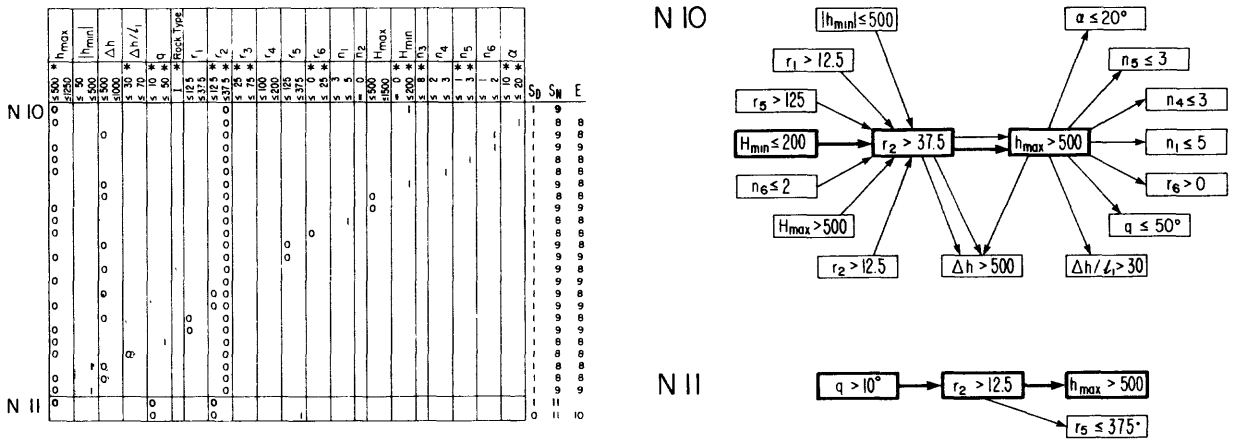

VIIA. D and N indicate which type of feature it is. S_D and S_N to the right of the table indicate how many objects of class I and II, respectively, have this feature. E is the number of objects which have both this feature and the distinctive feature associated with it.

Now consider the right-hand side of Table XV. It shows another representation of the same groups which we call "the structure of the group". This form of representation becomes clear after comparison with the left-hand side of Table XV. Any group of three consecutive rectangles which are adjacent to one another in the direction of the arrows corresponds to some feature made up of a triplet of statements, which occurs on the left-hand side of Table XV (the direction of arrows can be reversed of course, but only simultaneously for all arrows). Rectangles, connected by double arrows, correspond to a feature consisting of a doublet of statements; the second arrow should be ignored in determining the triplet features. Distinctive features are indicated by heavy lines for the two arrows and three rectangles involved. We can now proceed to the geological interpretation of the features summarized in Table XV.

The distance to the closest intersection of faults, or to the closest end of a fault (r_2) is a dominant parameter for the following reasons:

(1) In 6 out of 8 D-groups all features, except one, contain the condition that r_2 is smaller than the threshold; in the two remaining exceptions, D3 and D8, half of the features has this condition.

(2) In 8 out of 11 N-groups at least two features have the condition that r_2 is larger than the threshold.

(3) In the groups D3 and D8, the exceptions mentioned in (1), all features which do not have limitations on r_2 have instead either one or both of the conditions: The distance r_1 from the closest major fault is small or the number n_5 of major faults nearby is > 1. Both of these conditions indirectly indicate proximity to an intersection.

(4) r_2 plays a dominant role in the test for stability of recognition (Table XIII).

This result (that r_2 is small for D and large for N) supports the hypothesis (Gelfand et al., 1972, 1973a, b, 1974a, b) that epicenters of strong earthquakes tend to be situated near the intersections of major lineaments. Because of this support for the hypothesis we are encouraged to apply it to California in Section 4.

The distance r_2 from the end of a fault or an intersection of major faults, which we have just considered, though important, is not sufficient by itself in that not all ends and intersections are found in D areas. It may be seen, for example, from Fig. 2 that the situation $r_2 < 37.5$ km occurs not only for all D points, but also for 14 out of a total 44 N points (Fig. 2,

histogram No. 8, 1968+). This is why r_2 must be used only in combination with other parameters in forming features.

The statistics of some of the parameters of D and N features are summarized in Table XVI. The table does not consider r_2 and r_1, which have already been discussed in order to highlight other features. In Table XVI it is interesting to compare features of three types:

D: points which are always close to the end of or an intersection of faults
NC: N points which may be close to the end of or an intersection of faults (r_2 not specified or $\geqslant$12.5 km only)
NF: N points, which are far from the end of and an intersection of faults ($r_2 \geqslant 37.5$ km)

The difference between D and NC is the difference between points D which are certainly near intersections and such points N which may be close to intersections. The difference between D and NF is the difference between D points and points far from ends and intersections, which are always N. We note first of all that some measure of elevation is small for most D points and large for NC points. For NF points the features show both large and small elevations, signifying that no clear dependence on height is established far from intersections.

An examination of geological maps of the region suggests that most of the other characteristics of D features in Table XVI may also be interpreted as an indirect indication of low elevation. These include the absence of igneous rocks, proximity to a large area of recent sediments, and the small number of contacts (n_3) on a geological map. At first sight the last parameter behaves contrary to expectations in that large n should be associated with intensive fracturing of the crust, which is a characteristic for D

TABLE XVI

Summary of the role of different parameters (excluding r_2 and r_1) in D and N features

Parameter		In how many D		In how many NC				In how many NF	
				(with $r_2 > 12.5$ km)		no condition on r_2		(with $r_2 > 37.5$ km)	
		groups	features	groups	features	groups	features	groups	features
Elevation is (h_{max}, or h_{min}, or H_{max}, or H_{min})	small	6	17	–	–	–	–	5	30
	large	1	1	2	5	1	18	2	19
Igneous rocks (I) are	present	–	–	3	7	1	5	2	7
	absent	3	10	–	–	–	–	–	–
q is	small	1	5	–	–	1	1	1	1
	large	2	11	1	2	–	–	1	9
Large water reservoir (r) is	close	2	2	–	–	–	–	1	11
	far	–	–	1	2	1	4	1	1
α is	small	2	2	–	–	–	–	1	1
	large	–	–	–	–	–	–	–	–
Number of contacts (n_3) on geological map is	small	1	2	–	–	–	–	–	–
	large	–	–	3	13	1	4	1	1
Reference point (r_5) is	close	–	–	2	3	1	3	1	2
	far	5	18	–	–	–	–	4	6

(Gelfand et al., 1972, 1973a, b, 1974b). However, only neotectonic fracturing is characteristic of D according to Gelfand et al. (1972, 1973a, b, 1974a, b), whereas n_3 represents the integrated tectonic history. A survey of places with large and small n_3 indicates that small n_3 tend to go with subsidence and low elevations.

The small distance r_6 to a large water reservoir (parameter 12, Table VI) is another characteristic of D. This indirectly implies relatively low elevation, and recalls some modern ideas on the role of water in triggering earthquakes. However, for many points small r_6 indicates proximity to the ocean, so that these interpretations are by no means firm.

Small values of the angle α between the strike of the fault and the dominant strike of the San Andreas system is characteristic of D. This suggests the reasonable notion that the strike-slip earthquakes considered in this paper tend to occur away from bends in the San Andreas fault system. Earthquakes with dip-slip components might be more characteristic of bends in the fault.

Large distance from the reference point (defined by the intersection of the San Andreas and the Big Pine faults) is characteristic of D, perhaps for the reason that earthquakes with dip-slip tend to occur in the Transverse Ranges which are adjacent to a bend in the San Andreas fault.

Other parameters which play a role in D or N features occur. We defer offering possible explanations for them. Among these parameters are the distance r_3 to a geothermal zone, the number n_4 of parallel faults. Parameters which are present in the same way in both D and N features (for example $n_4 \leqslant 3$) are puzzling. Perhaps they were selected as features by chance, due to a random interplay of events, independent of their geological meaning. Perhaps they take on meaning only in combination with the other parameters they link up with, which are different for D and N features.

The qualitative conclusion which emerges is that D areas are characterized by proximity to the end or to an intersection of major faults in association with low relief and often with some kind of downward neotectonic movement, expressed in topography and geology. Apparently, we did not formulate an adequate single parameter for such movements, so that the indication shows indirectly through several different parameters.

Also the fact that minimal and maximal elevations are simultaneously small for many D points suggests that D points for these strike-slip earthquakes are often characterized by relative low relief or subsidence on a background of weak uplift. N points near the intersections or ends of major faults are characterized by higher elevations or uplift with less contrast in relief.

4. Intersections of major lineaments

4.1. The problem

The results of Section 3 (see paragraph 3.6) suggest the hypothesis that the epicenters of strong earthquakes in California are associated with intersections of major lineaments (Gelfand et al., 1972, 1973a, b, 1974a, b; Briggs and Press, in preparation). More specific formulation of this hypothesis as well as the definition of lineaments is given in the Appendix. The major lineaments of California and adjacent regions, based on a synthesis of published data (Atwood, 1940; Richter, 1958; USGS, no date, 1962, 1965; Wright and Frey, 1965; Cook, 1966; Hamilton and Myers, 1966; Hill, 1966; Thompson, 1966; Dickinson and Grantz, 1968; King, 1969; Hain, 1971), are shown in Fig. 4. Explanation and justification is provided in Ranzman (in preparation). The transverse lineaments in Fig. 4 may raise some doubts, since they are to a large extent based on geomorphic evidence. We believe that ERTS photographs of the region support these interpretations (Ranzman, in preparation).

The objects of recognition, according to the hypothesis, are now the intersections of the lineaments. The problem, formulated exactly as in paragraph 2.1, is to find such intersections (D_{I} and D_{II}) near which the epicenters of strong earthquakes may occur. However, new objects are defined. A larger area is considered, and dip-slip and strike-slip earthquakes are not distinguished. The last difference is not significant, since the area contains only two strong dip-slip earthquakes (1952, near intersection *165*; and 1971, near intersection *119*; the first epicenter is near that of a strong strike-slip earthquake). In the numerical experiments (paragraph 4.5) we eliminated these two earthquakes from learning. The distinctions between recognition of San Andreas and Basin–Range earthquake sources are considered in Briggs and Press (in preparation).

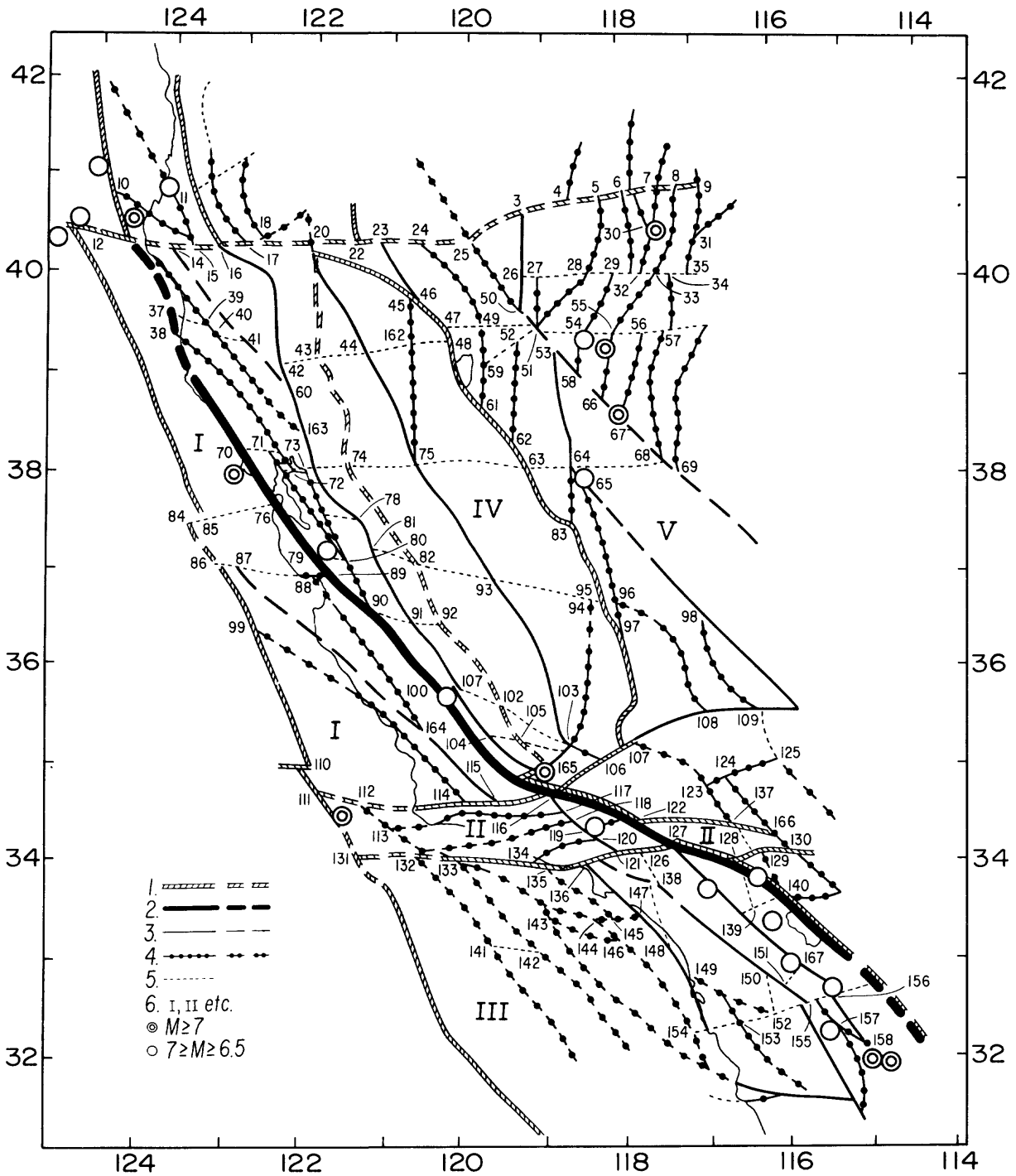

Fig. 4. Major lineaments of California (for definitions, see Appendix).
(1) Lineaments of first rank (boundaries of morphostructural countries).
(2) Major branch of San Andreas system; solid segments are reasonably certain, dashed segments are uncertain, underwater or buried under soft sediments.
(3) Lineaments of second rank (boundaries of morphostructural countries) megablocks.
(4) Lineaments of third rank (boundaries of morphostructural countries) blocks.
(5) Transverse lineament.
(6) The number of morphostructural country in the description of the scheme (second paragraph of Appendix); epicenters are shown as in legend.

TABLE XVII

Parameters of intersections

N	Parameter	Parameterization	
		learning for California	learning for Anatolia
1	absolute elevation, h_1 (m)	$\leqslant$ 200 $\leqslant$1,200	$\leqslant$ 200 $\leqslant$1,200
2*	maximal elevation, h_{max} (m)	–	
3*	maximal difference of elevations, Δh (m)	–	
4*	the distance between points with maximal elevations, l_1 (km)	–	
5*	$\Delta h/l_1$	–	$\leqslant$ 75 $\leqslant$ 125
6*	the number of lineaments, departing from intersection, n_1	–	$\leqslant$ 3
7*	morphology (most contrasting combinations in the forms of relief)	MM (mountain–mountain) MP (mountain–plain) and all the rest	
8*	types of tectonic structures	–	
9*	relative area of soft sediments, q (%)	–	
10	type of intersection	x or $\perp$	
11	how pronounced is the lineament	strong feeble	strong feeble
12	the distance to the closest lineament, r_1 (km)	= 0 $\leqslant$ 25	= 0
13	the distance to the second closest lineament, r_2 (km)	$\leqslant$ 25 $\leqslant$ 37.5	$\leqslant$ 25 $\leqslant$ 37.5
14	the distance to the closest lineament of the first rank, $R_{1.1}$ (km)	–	
15	the distance to the second closest lineament of the first rank, $R_{1.2}$ (km)	–	
16	the distance to the closest lineament of the second rank, $R_{2.1}$ (km)	–	
17	the distance to the second closest lineament of the second rank, $R_{2.2}$ (km)	$\leqslant$ 50 $\leqslant$ 100	$\leqslant$ 50 $\leqslant$ 100
18	the distance to the closest lineament of the third rank, $R_{3.1}$ (km)	–	
19	the distance to the second closest lineament of the third rank, $R_{3.2}$ (km)	–	
20	the distance to the second closest longitudinal lineament, r_3 (km)	–	= 0 < 25
21	the distance to the second closest transverse lineament, r_4 (km)	–	< 62.5 < 100
22	the length of longitudinal lineament, l_2 (km)	–	
23	the length of the transverse lineament, l_3 (km)	–	
24	the distance to the closest intersection, r_5 (km)	= 0 $\leqslant$ 37.5	= 0 $\leqslant$ 37.5
25	the distance to the second closest intersection, r_6 (km)	–	$\leqslant$ 37.5 $\leqslant$ 50
26	the distance to the closest intersection inside some cluster, r_7 (km)	–	
27	maximal elevation, H_{max} (m)	$\leqslant$1,500	$\leqslant$1,500 $\leqslant$3,000
28	minimal elevation, H_{min} (m)	$\leqslant$ 100	
29**	maximal difference of elevations, ΔH (m)	–	$\leqslant$2,000 $\leqslant$3,000
30**	the distance between points with maximal and minimal elevations, l_4 (km)	–	

TABLE XVII (continued)

N	Parameter	Parameterization	
		learning for California	learning for Anatolia
31**	$\Delta H/\varrho_4$	$\leqslant$ 40	
32**	relative area of soft sediments, Q_2 (%)	–	
33**	morphology	–	
34**	the number of intersections, n_2	$\leqslant$ 4	$\leqslant$ 4
		$\leqslant$ 7	$\leqslant$ 7
35***	the weighted rank of lineament, M	$\leqslant$ 15	$\leqslant$ 15
		$\leqslant$ 17	$\leqslant$ 17
36	the distance from San Andreas fault, l_5 (km)	–	–

Thresholds are indicated only for parameters used in learning.

* Parameter is determined in a circle of 12.5-km radius around intersection.

** Parameter is determined in a circle of 62.5-km radius around intersection.

*** $M = \sum_{j=1}^{n} (m_i/62.5)(62.5 - R_{ij})$ where i is the rank of the lineament; m_i is the weight of the rank ($m_1 = 5$, $m_2 = 4$, $m_3 = 3$); R_{ij} is the distance to the jth lineament of the rank i; n is the number of lineaments in the circle of 62.5-km radius around the intersection.

We apply recognition to the land part of California – the territory between the latitude of the Mendocino fault on the north, the Mexican border on the south and the axis of Great Valley on the east. In Fig. 4 this territory is bounded by lineaments *76–13–20–106–107–123–125* and the oceanic shore to the south of intersection *76*.

4.2. The data

4.2.1. Definitions

As in Section 3, we use for recognition only certain parameters which roughly characterize tectonic fracturing of the crust or the intensity and degree of contrast of neotectonic movements. This selection does not imply lack of significance to other factors, such as seismicity, geophysical anomalies, tectonic history, the structure of the crust, etc. The parameters used for recognition are listed in Table XVII. Parameters 6, 11, 21, 24–26, 34 and 35 characterize tectonic fracturing. Parameters 1–5, 7, 9 and 27–33 show the intensity and degree of contrast of the vertical neotectonic movements. Parameter 10 characterizes the presence of strike-slip faults. Some additional comments follow.

4.2.2. Conditions on lineaments

All lineaments are continuous and may change only at intersections; if the rank of a lineament changes at an intersection we consider it as two lineaments; if the strike of a lineament changes by more than ν degrees we consider it as two lineaments (in practice we took $\nu = 15°$).

4.2.3. Separate intersections

If the distance between intersections was less than δ we replaced them by one intersection at the midpoint (in practice we took $\delta = 12.5$ km or 5 mm on a map with scale 1:2,500,000; not more than three intersections were merged by this rule).

4.2.4. Vicinity of intersections

Parameter 1 is determined directly at the point of intersection. Parameters 2–11 are determined within the circle of radius $\epsilon_1 = 12.5$ km with a center at the intersection. Parameters 27–35 are determined in a larger circle of radius $\epsilon_2 = 62.5$ km.

4.2.5. Continuity of parameters

Since the lineaments are drawn approximately, all

parameters are defined in such a way that they are continuous with respect to displacement of lineaments. They should also be continuous in the arbitrary parameters ϵ_1 and ϵ_2. Parameters 12–19 and 24–34 may become discontinuous if an intersection is formed by three or more lineaments, since after the displacement of any lineament several new intersections will appear and the considered characteristics will change sharply. To preserve the continuity we specify the definition of these parameters in the following way. Let us imagine that we displace the axes of lineaments slightly in such a way that they will not be parallel, will intersect only in pairs and that a T-intersection will not become a crossing. Each parameter converges to some limit when this displacement decreases. This limit is taken as the value of the parameter. In practice it is equivalent to the following rules (Table XVII):

Parameter numbers $N = 12$, 13 and 24: $r_1 = r_2 = r_5 = 0$ if more than two lineaments depart from intersection.
$N = 34$: $n_2 = 1, 3$ and 6 if the number of intersecting lineaments is 2, 3 and 4, respectively.
$N = 25$: $r_6 = 0$ if more than four lineaments intersect.
$N = 14$, 16 and 18: $R_{i.1} = 0$ if a lineament of rank i goes through the intersection.
$N = 15$, 17 and 19: $R_{i.2} = 0$ if more than one lineament of rank i goes through the intersection.

For example intersection *116* has $r_1 = r_2 = 0, n_3 = 6$; intersection *143* has $r_1 = 0, r_2 \neq 0, n_3 = 2$.

4.2.6. The length of lineaments (parameters 22 and 23).

Suppose that all the longitudinal lineaments are placed in order of rank, with highest rank first. Lineaments of the same rank are placed in order according to their length, with greatest length first. After that ordering the first length will be l_2; l_3 is specified similarly.

4.2.7. One-dimensional distributions

The parameters specified in the preceding section can be determined from the scheme of lineaments (Fig. 4) and topographic and tectonic maps. Their one-dimensional distributions are shown in Fig. 5. Dashed lines correspond to the intersections closest to epicenters; solid lines correspond to all the remaining intersections. We see that the histograms for the

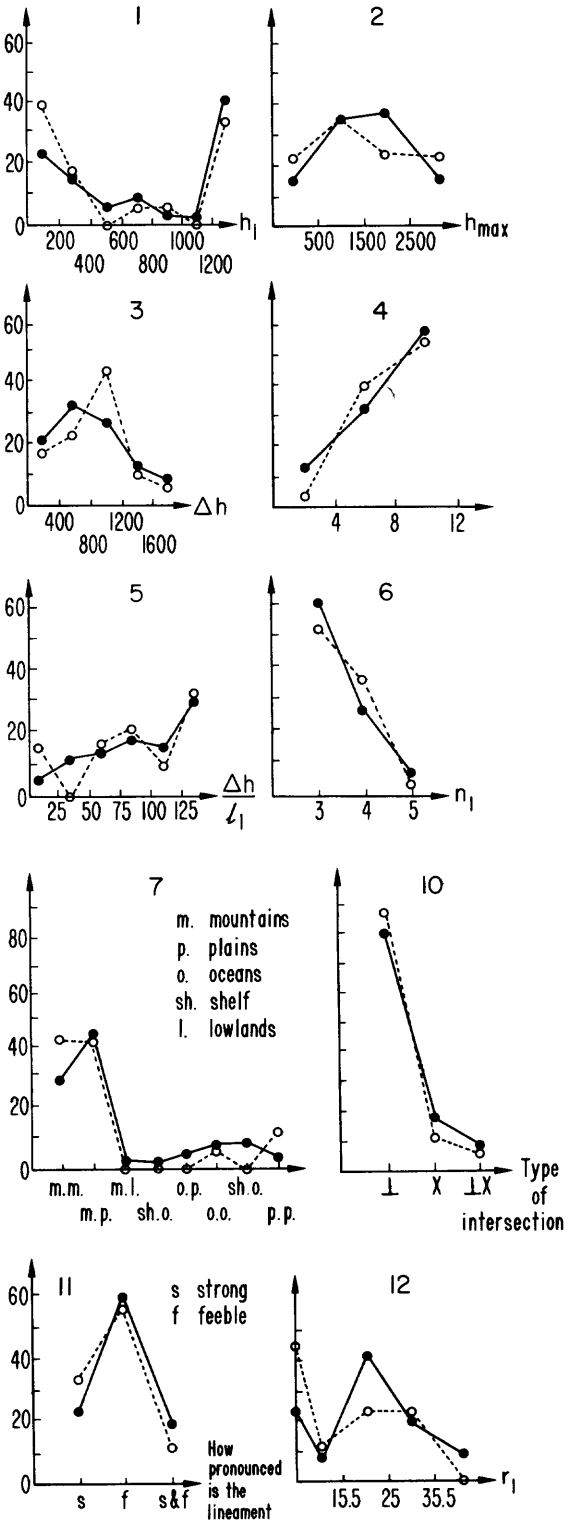

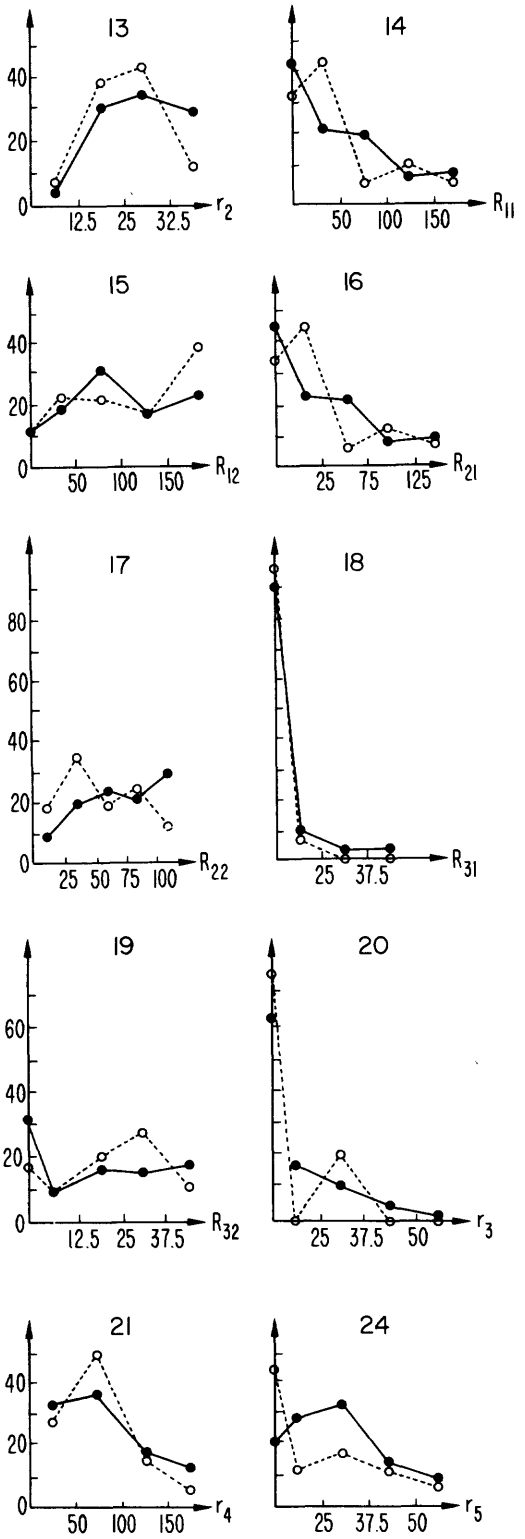

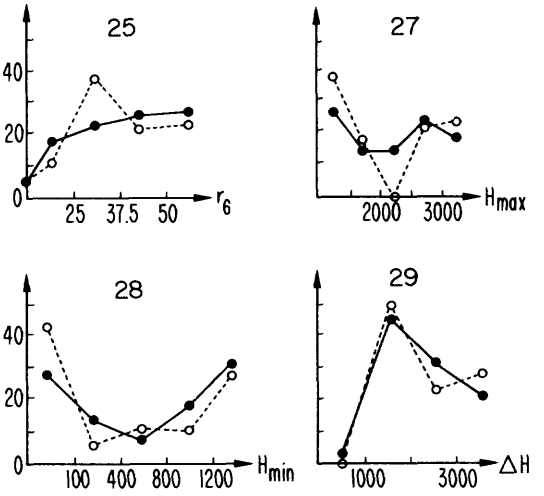

Fig. 5. Examples of one-dimensional distributions of parameters for intersections of lineaments shown in Fig. 4. The number and notation of parameters correspond to Table XVII. Otherwise, the notation is the same as in Fig. 2.

two groups are very similar for parameters 2–4, 7–9, 14–16, 18, 19, 22, 23, 28 and 30–33. These parameters were not used. The parameter l_5, distance from the San Andreas fault, was not selected for the opposite reason that it would dominate the characteristic features; the histograms separate too well. Since most known epicenters are close to this fault, the results of recognition would be trivial. Discrete values were assigned to the remaining parameters as shown in the third column of Table XVII.

Fig. 5 contains the histograms for the whole area shown in Fig. 4. Histograms based only on California data separate better, allowing thresholds such that the two groups have few or no common values of some parameters. This is undesirable for the reason indicated in paragraph 3.3; this is why we assumed thresholds corresponding to the data for the entire area in Fig. 4 although recognition was carried out for only a portion of the area.

4.3. Results

Algorithm CLUSTERS was used. Intersections within 50 km of an epicenter formed a cluster. The division of intersections between the clusters and classes II and III in learning is indicated in Table XIX.

TABLE XVIII

Distinctive D and N features for points located at intersections of lineaments

		1	7	12	13	17	24	27	28	31	34	35
		h_1	Morph-ology	r_1	r_2	$R_{2,2}$	r_5	H_{max}	H_{min}	$\Delta H / l_4$	n_2	M
D	1					>50						>17
	2	≤200										>17
	3		m,m						≤100			>15
	4		no m,m				≤12.5					>15
	5	>200					≤12.5					>15
	6		m,p		>25							>15
	7		m,m	≠0								>15
	8				>25				≤100		>4	
	9				>25				≤100	>40		
	10			≤25					≤100	>40		
	11		no m,m			≤50			≤100			
	12	≤200		≤25					≤100			
	13			≤25	>25			≤1500				
N	1							>1500				≤15
	2					>50					≤4	≤17
	3							>1500	>100			≤17
	4					>50		>1500				≤17
	5		no m,p				≤37.5					≤17
	6		no m,p			≤100						≤17
	7			≤25			≤37.5					≤15
	8	≤1200	no m,p									≤15
	9							>1500			≤4	
	10						≤37.5				≤4	
	11					≤100				≤40	≤4	
	12	≤1200	no m,m								≤4	

m - mountains p - plains

TABLE XIX

Results of voting for points at intersections of lineaments in California (see Table VIII for definitions of symbols)

n_N	0	1	2	3	4	5	6	≥7
≥10	$\tilde{40}, \tilde{123}, \tilde{124}, \tilde{134}, \tilde{145}, \tilde{148}, \tilde{149}$	$\tilde{92}$						
9								
8								
7		$\tilde{37}, \tilde{125}, \tilde{154}$						
6	$\tilde{91}$	$\tilde{38}, \tilde{114}$						
5	(10) $\tilde{41}$, $\tilde{42}$, $\tilde{43}$, $\tilde{82}$							
4	$\tilde{39}$, $\tilde{60}$, $\tilde{135}$, 144, $\tilde{153}$	143, 146	$\tilde{107}$					
3	141, $\tilde{147}$ (166)	$\tilde{132}$	$\tilde{102}$, $\tilde{104}$, $\tilde{115}$	(100)		*158*		
2	$\tilde{74}$ (150)	$\tilde{17}$, $\tilde{152}$ (164)						
1	142	(88) 133	$\tilde{90}$, $\tilde{130}$	137				
0	(70) $\tilde{76}$ (78) (79) $\tilde{106}$, $\tilde{121}$	$\tilde{15}$ (118) (119) (120)	(14) $\tilde{18}$, $\tilde{36}$, 138 $\tilde{127}$ (136) (89)	*13* $\tilde{72}$, $\tilde{126}$ (151) 163 (167)	$\tilde{16}$ 168 *80* (81) *101* (116) *117* *122* 77	$\tilde{20}$ *71* $\tilde{73}$ (103) (105) (128) (129) (139)	*155* *156* *140* *157* *165*	

n_D

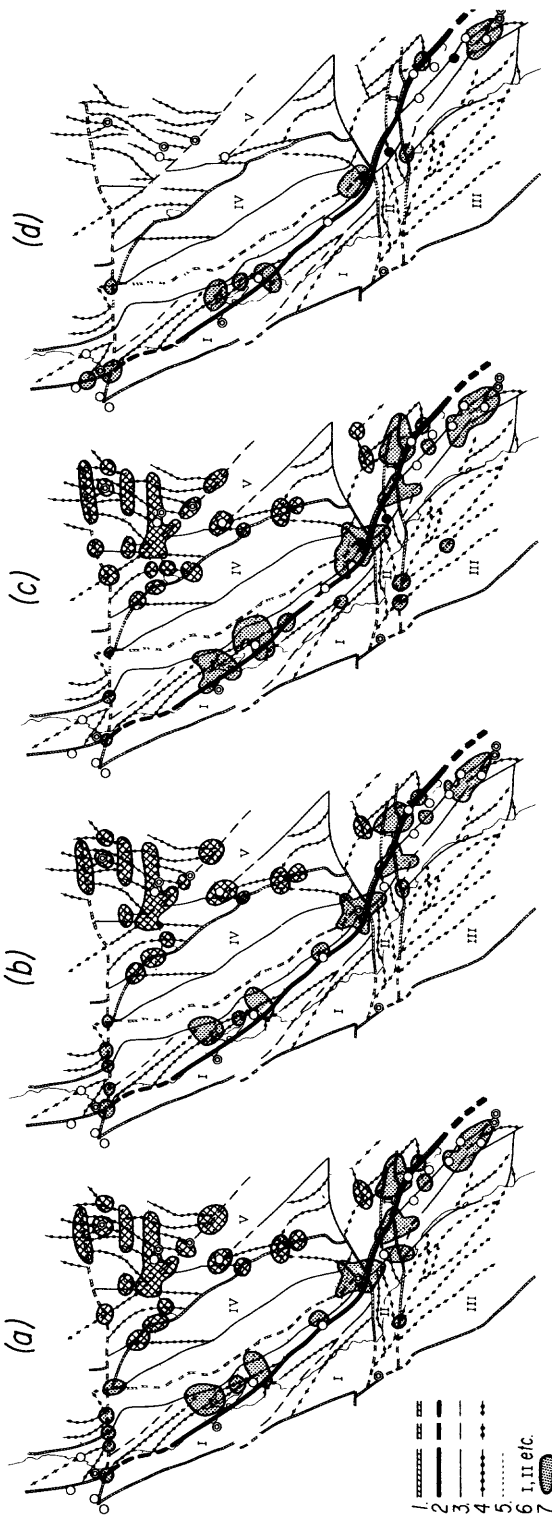

Fig. 6. Results of pattern recognition for intersections of major lineaments of California.
Dotted shading surrounds areas recognized as D for California. Crossed shading surrounds areas recognized as D for Sierra Nevada and adjacent parts of Basin and Range.
(a) Experiment EF.
(b) Main variant; all known earthquakes up to 1974 are used in learning.
(c) Experiment EH: all known earthquakes up to 1948 are used in learning.
(d) Experiment EH: all known earthquakes up to 1940 are used in learning.

TABLE XX

Recognition for control experiments EH and EF. The notation is the same as in Table IX. Uncertain ("neutral") voting: ± corresponds to $\Delta = \bar{\Delta}$; o corresponds to $\Delta = \bar{\Delta} - 1$

Number of intersection on Fig. 4	Year of earthquake which defines cluster	Learning based on earthquakes from 1836 through the year							
		1934	1940	1942	1948	1952	1968	1971	1973+...
					Clusters $\{D_1 + N_1\}$:				
119		o	o	o	o	o	o	o	o
120		o	o	o	o	o	o	o	+
118	1971	o	o	o	o	o	o	o	o
136		+	+	o	+	+	+	+	+
117		o	o	o	+	+	+	+	+
122		o	o	o	+	+	+	+	+
140	1968	o	+	+	+	+	+	+	+
139		o	o	o	+	+	+	+	+
165		o	+	+	+	+	+	+	+
116		o	o	o	±	+	+	+	+
103	1952	o	o	o	±	+	+	+	+
105		o	+	+	+	+	+	+	+
117		o	o	o	+	+	+	+	+
128		o	o	o	±	+	+	+	+
129		o	o	o	±	+	+	+	+
139	1948	o	o	o	+	+	+	+	+
140		o	+	+	+	+	+	+	+
166		o	o	o	o	o	o	o	o
167		o	o	+	+	+	+	+	+
151	1942	o	o	+	+	+	+	+	+
150		o	o	o	±	o	o	o	o
155		o	+	+	+	+	+	+	+
156		o	+	+	+	+	+	+	+
157	1940	o	+	+	+	+	+	+	+
155		o	+	+	+	+	+	+	+
158	1934	+	+	+	±	±	±	±	o
157		o	+	+	+	+	+	+	+
13		±	±	+	+	+	+	±	±
10	1923	±	±	o	o	o	o	o	o
14		o	o	o	o	±	±	±	o
101		o	o	±	+	+	+	+	+
164	1922	+	±	o	±	o	±	o	o
100		o	o	o	o	o	o	o	o
158	1915	+	+	+	±	±	±	±	o

TABLE XX (*continued*)

Number of intersection on Fig. 4	Year of earthquake which defines cluster	Learning based on earthquakes from 1836 through the year							
		1934	1940	1942	1948	1952	1968	1971	1973+...
80		±	±	+	+	+	+	+	+
79		⊙	⊙	○	±	⊙	±	○	○
89		±	±	+	+	+	+	±	+
88	1911	±	±	±	+	±	+	○	○
81		⊙	○	+	+	+	+	+	+
77		⊙	±	+	+	+	+	+	±
78		⊙	⊙	⊙	±	⊙	±	○	○
70	1906	⊙	⊙	⊙	±	⊙	±	○	○
71		+	+	+	+	+	+	+	+

Number of intersection on Fig. 4	Year of earthquake which defines cluster	Learning based on earthquakes from 1836 through the year						
		1940	1947	1948	1954	1954	1959	1973+...
		Class II $\{D_2 + N_2\}$:						
3		○	+	+	○	○	○	○
5		±	+	+	+	+	±	+
6		+	+	+	+	+	+	+
8		+	+	+	+	+	±	+
9		○	±	±	+	±	○	○
25		○	⊙	±	+	±	○	+
26		○	+	+	+	+	+	+
27		○	+	+	+	+	+	+
46		+	+	+	+	±	±	±
50		+	+	+	+	+	±	+
57		+	+	+	+	+	±	+
59		+	±	+	+	+	±	+
61		○	+	+	+	○	○	○
68		+	+	+	+	+	±	+
69		○	+	+	+	+	±	+
94		○	±	○	○	○	○	○
95		+	+	+	+	+	±	+

The remaining intersections were recognized only as N.

The characteristic features are shown in Table XVIII.

The results of voting are shown in Tables XIX and XX, and in Fig. 6b.

The threshold for recognition was chosen as follows: $\bar{\Delta} = \Delta^*$ with Δ^* having the same definition as in paragraph 3.4.

We note that the recognition is successful in that most of the intersections are divided by voting into two rather distinctive groups, with only a small number of intersections given a "neutral" vote. Each cluster has at least one D intersection (Table XX). The majority of D and N intersections belong to class I (clusters) and to class II, respectively. The results are also encouraging for the following reasons.

(1) Non-instrumental data for the 19th century

show four earthquakes in the area of interest with estimated magnitude 7 or more. Epicenters of all these earthquakes are close to intersections recognized as D.

(2) Among D are the intersections closest to epicenters, with only two exceptions. One of the exceptions is the San Francisco earthquake of 1906. Intersection *70* which is closest to the 1906 epicenter was recognized as N; however, intersection *71*, which is slightly farther away, was recognized as D. The second exception is the epicenter of the 1971 earthquake, which is of the dip-slip variety. The closest intersection *119* is recognized as N; intersection *136* is recognized as D in the same cluster.

4.4. Interchangeability of distinctive features from different regions

Let us apply to California the distinctive features obtained for Anatolia, and vice versa. In this way we check our ability to recognize intersections near which epicenters of strong earthquakes actually fall, using criteria developed elsewhere. This is an important control experiment, since the features in the two

TABLE XXI

Distinctive features for recognition in Anatolia (Gelfand et al., 1974a)

		1	5	6	10	11	12	13	17	20	21	24	25	27	29	34	35
		h_1	$\Delta h / l_1$	n_1	inter-section	lineament strength	r_1	r_2	$R_{2,2}$	r_3	r_4	r_5	r_6	H_{max}	ΔH	n_2	M
D	1											12.5-37.5					>9
	2			=3								>12.5					>9
	3					s or f										>2	
	4				⊥											>2	
	5								≤100				≤100			>2	
	6				⊥				≤100				≤100		≤3000		
	7									≤50					≤3000		
	8								≤100				≤100		>2000		
	9									>12.5			≤100	≤3000			
	10								≤100				≤100	>2000			
	11								≤100			>12.5	≤100				
	12		>150									>12.5	≤100				
	13					s or f				≤50		>12.5					
N	1			>3		s and f										≤4	
	2	>200								>50						≤2	
	3											>37.5			>3000		
	4							>25						>3000	>2000		
	5					f							>62.5	>3000			
	6						>25	>62.5						>2000			
	7					s and f							>62.5				
	8	>200								>50			>62.5				
	9	>200						>62.5					>62.5				
	10	>200											>62.5				
	11	>200								>50		>37.5					
	12	>1000	≤300			f						>37.5					
	13					f	>25		≤100								
		1000 ↓ 1200	150 300 ↓ ↓ 75 125				25 ↓ 12.5	62.5 ↓ 37.5					62.5 100 ↓ ↓ 37.5 50	2000 ↓ 1500		2 4 ↓ ↓ 4 7	9 ↓ 15

s=strong f=feeble

regions were obtained completely independently. Success would have important geological implications.

The characteristic features, obtained in Gelfand et al. (1974a, b) for Anatolia, are shown in Table XXI. They were applied to California with one natural exception: the parameter thresholds were reset to values appropriate for California.

The results of voting, shown in Fig. 7c, are quite good. We first note that the intersections in California receive many votes; the average $(n_D + n_N)$ is 8, despite the fact that the distinctive features were derived from Anatolian data. The intersections are distinctly divided by voting into two groups, so that recognition is stable with respect to the choice of $\bar{\Delta}$.

Second, with $\bar{\Delta} = 0$ (the same threshold used in Gelfand et al. (1974a, b), for Anatolia) we recognize as D all intersections closest to each epicenter, even number *70* near the 1906 epicenter.

Third, we recognize as D all the same intersections, as in paragraph 4.3 as well as a few additional ones.

We can reverse the procedure and apply to Anatolia the characteristic features found for California (Table XVIII). Again, we changed the thresholds assigned to the parameters. The results are analogous. The intersections have many votes and are distinctly divided by voting. With $\bar{\Delta} = 0$ we recognize the intersections near each known epicenter (Fig. 8) except one (near intersection *33*). D areas are in good agreement with those found in Gelfand et al. (1974a, b), where learning was based on Anatolian data.

The ability to transfer the criteria of high seismicity from Anatolia to California seems natural, since most of the Anatolian earthquakes are connected with strike-slip movements, as is the case in California. However, the complete recognition of intersections near all known epicenters and the good agreement with results based on Californian data is astonishing and implies some generality to the distinctive features which were found. This particular control experiment argues against the criticisms that the pattern recognition results were fortuitous, or simply a restatement of the idea that future epicenters occur near previous ones.

For the Sierra Nevada and Basin and Range (regions *IV* and *V* in Fig. 4) the Anatolian criteria give negative results in that no intersections are recognized as D in the vicinity of 2 out of 5 epicenters. This failure is expected since the eastern California–Nevada regions are dominated by dip-slip focal mechanisms. This result underlines the success for California.

4.5. Control experiments

Experiment EH (Figs. 6c, d and Table XX) shows quite satisfactory results. Learning from earthquakes through the year 1940, we would have recognized at least one dangerous intersection in the cluster around the epicenter of each subsequent strong earthquake. After the 1942 earthquake, we would miss only one cluster, namely that corresponding to the 1971 earthquake. This cluster would be recognized by learning on all shocks up to and including the 1948 earthquake. To save time we did not redetermine the histograms of parameters at each step as we did in paragraph 3.5. The parameters and their thresholds were the same for each step. Therefore the results of this experiment only illustrate the stability of recognition with respect to the learning material.

Experiment EF (Fig. 6a) also shows the stability of recognition in that only four more intersections were recognized as D (*120*, *15*, *130* and *133*); and two intersections were transferred to N (*14* and *158*).

To test the sensitivity of results to the particular algorithm used, CORA-3 was applied. Class I contained the intersections closest to an epicenter, class II included all the rest. The threshold $\bar{\Delta} = 0$ was chosen. The results of recognition are shown in Fig. 9b. They basically confirm the results of paragraph 4.3. Experiment EH was successful up to 1942.

In another test we assumed other thresholds for parameters, obtained from histograms based on California data only. The results of recognition by algorithm CLUSTERS are in satisfactory agreement with paragraph 4.3. The control experiment results were good, though somewhat degraded. Thus our results are stable to changes in the thresholds, but the thresholds assumed in paragraph 4.3 are preferable.

4.6. Clarifying experiments

4.6.1. Epicenters or total fault breaks?

Does the epicenter have some special meaning, or is it just a random point on a fault break, say the place where by chance the stress first reaches the critical fracture strength? To check this we replaced the epicenters by the intersections on the entire fault

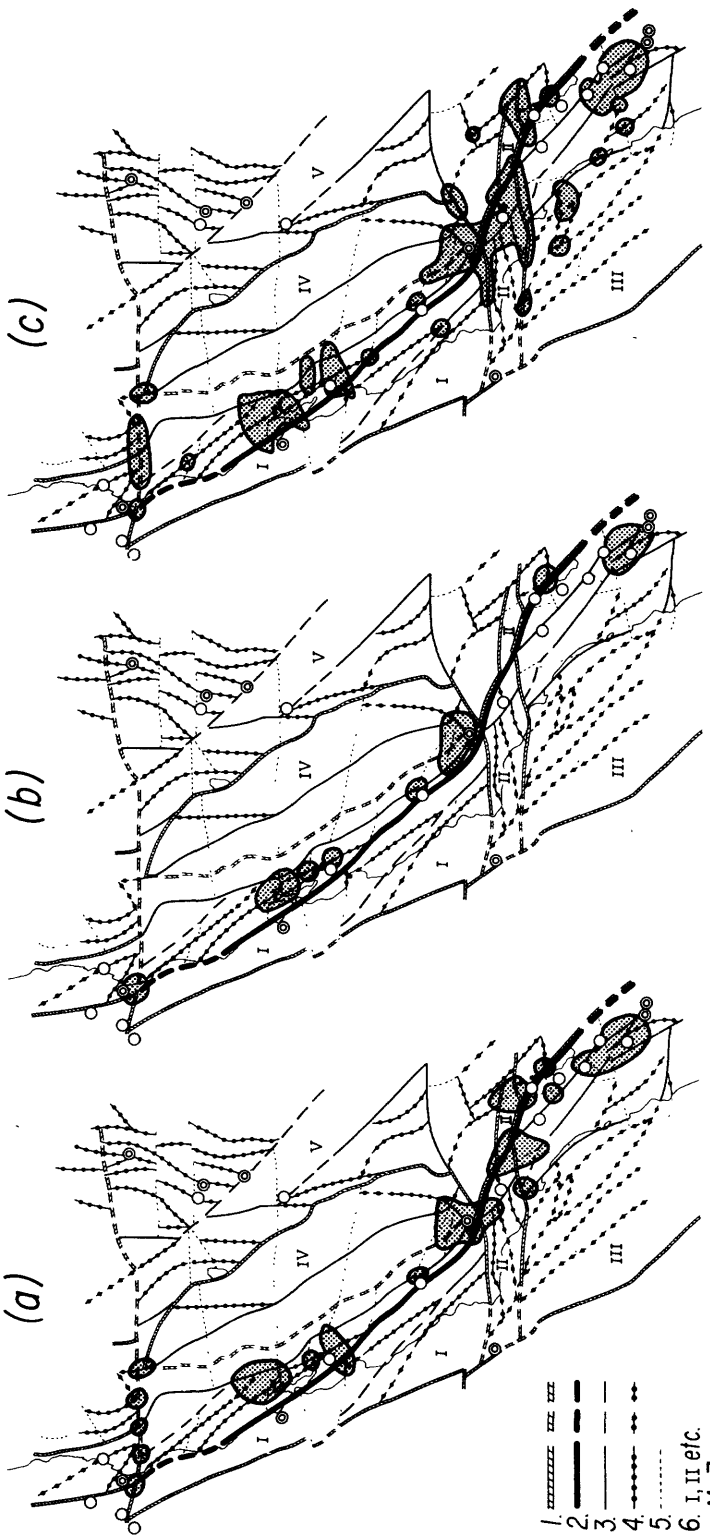

Fig. 7. Comparison of D areas for intersections of major lineaments for California, using different learning materials. Notation is the same as in Fig. 4.
(a) Main variant; same as Fig. 6b (see paragraph 4.3).
(b) Two dip-slip earthquakes eliminated (see paragraph 4.6).
(c) Learning for Anatolia (Table XXI).

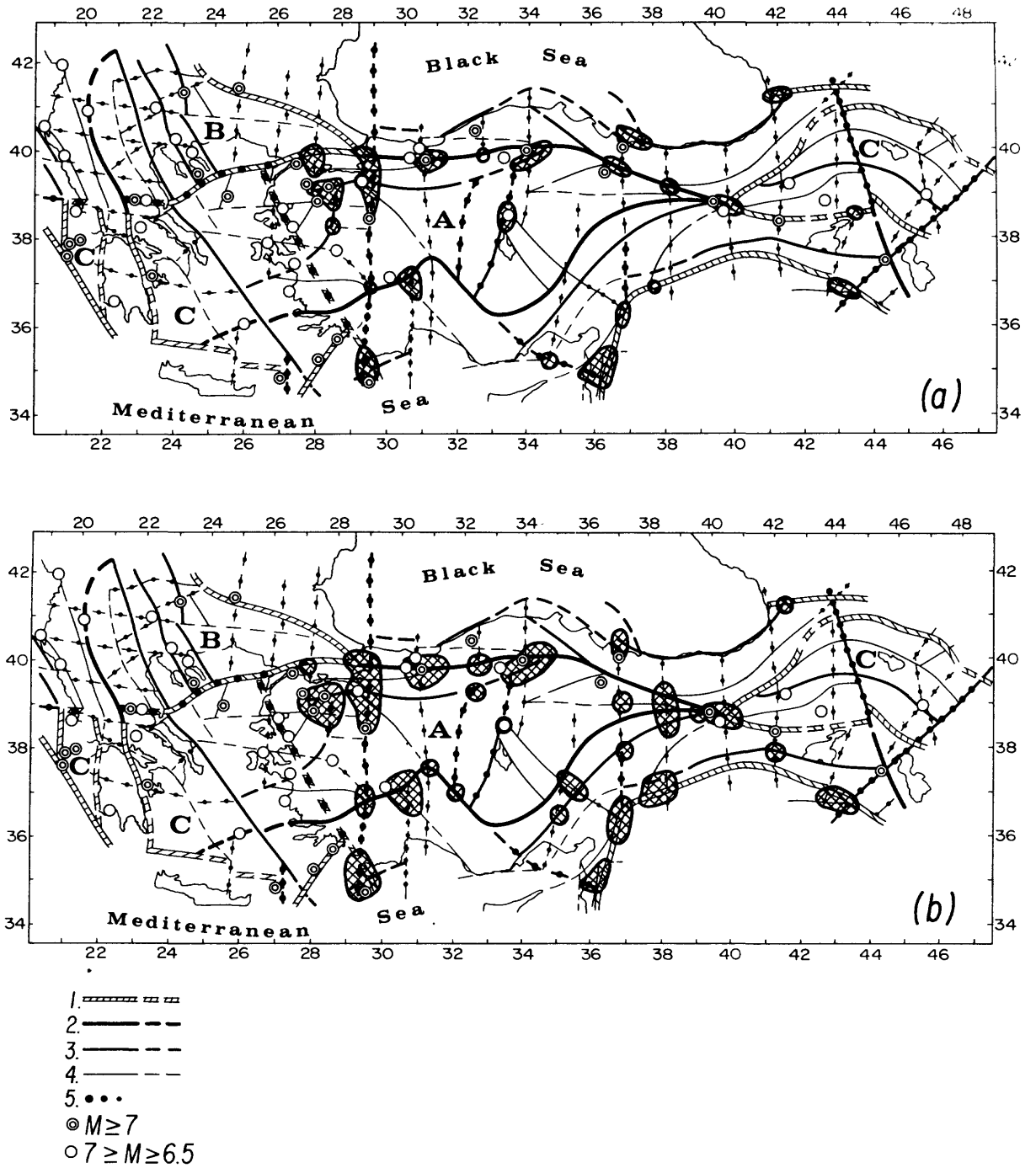

Fig. 8. Major lineaments of Anatolia.
(a) Recognition of D intersections with learning based on Anatolian data (Table XXI, after Gelfand et al. (1974a)).
(b) Recognition of D intersections by learning based on Californian data (Table XVIII).
Legend: lineaments (after Gelfand et al., 1974a): *1* = bounding the entire region (rank 1); *2* = bounding morphostructural countries (rank 1); *3* = bounding megablocks (rank 2); *4* = bounding blocks (rank 3); *5* = transverse.

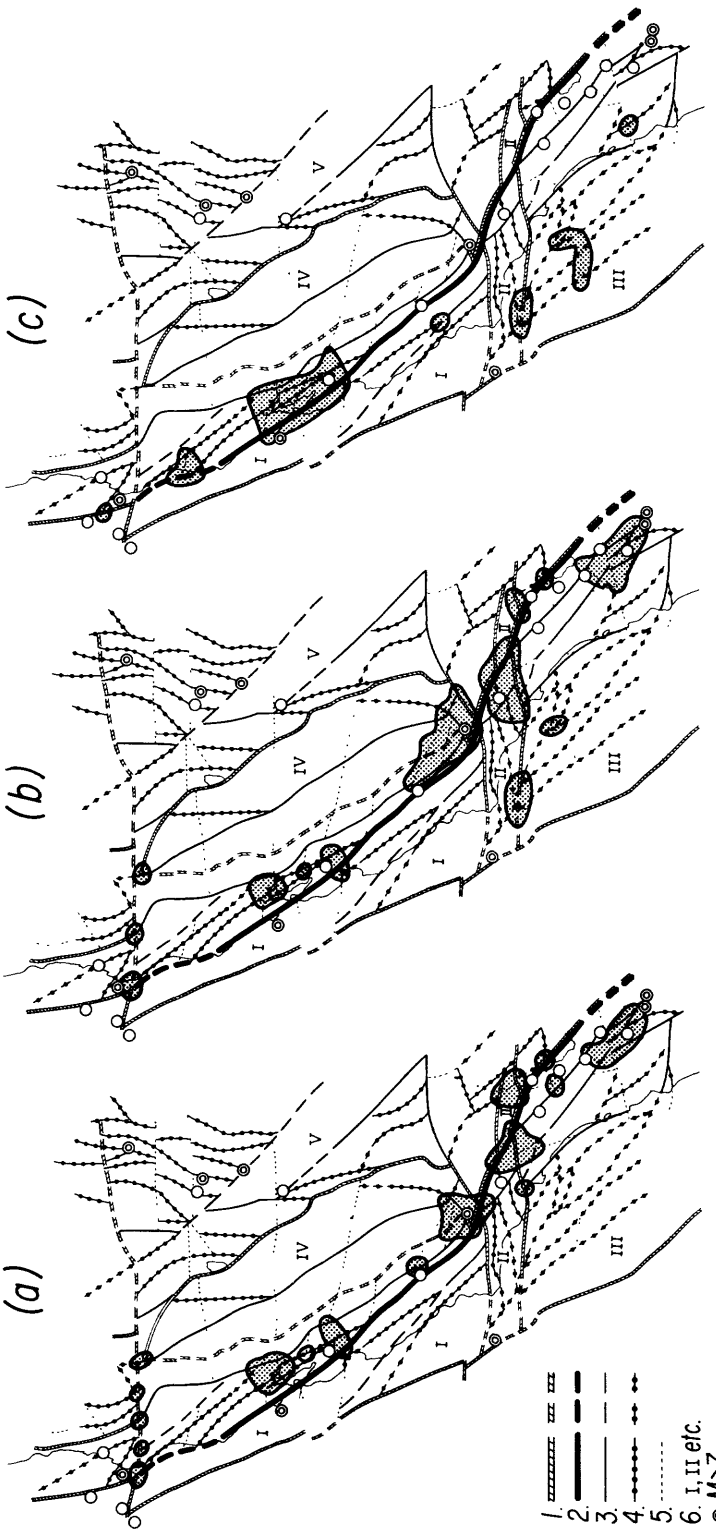

Fig. 9. Comparison of D areas for intersections of major lineaments for California. The notation is the same as Fig. 4.
(a) Main variant (same as Fig. 6b, see paragraph 4.3).
(b) Learning by CORA-3.
(c) Learning on fault breaks (paragraph 4.6).

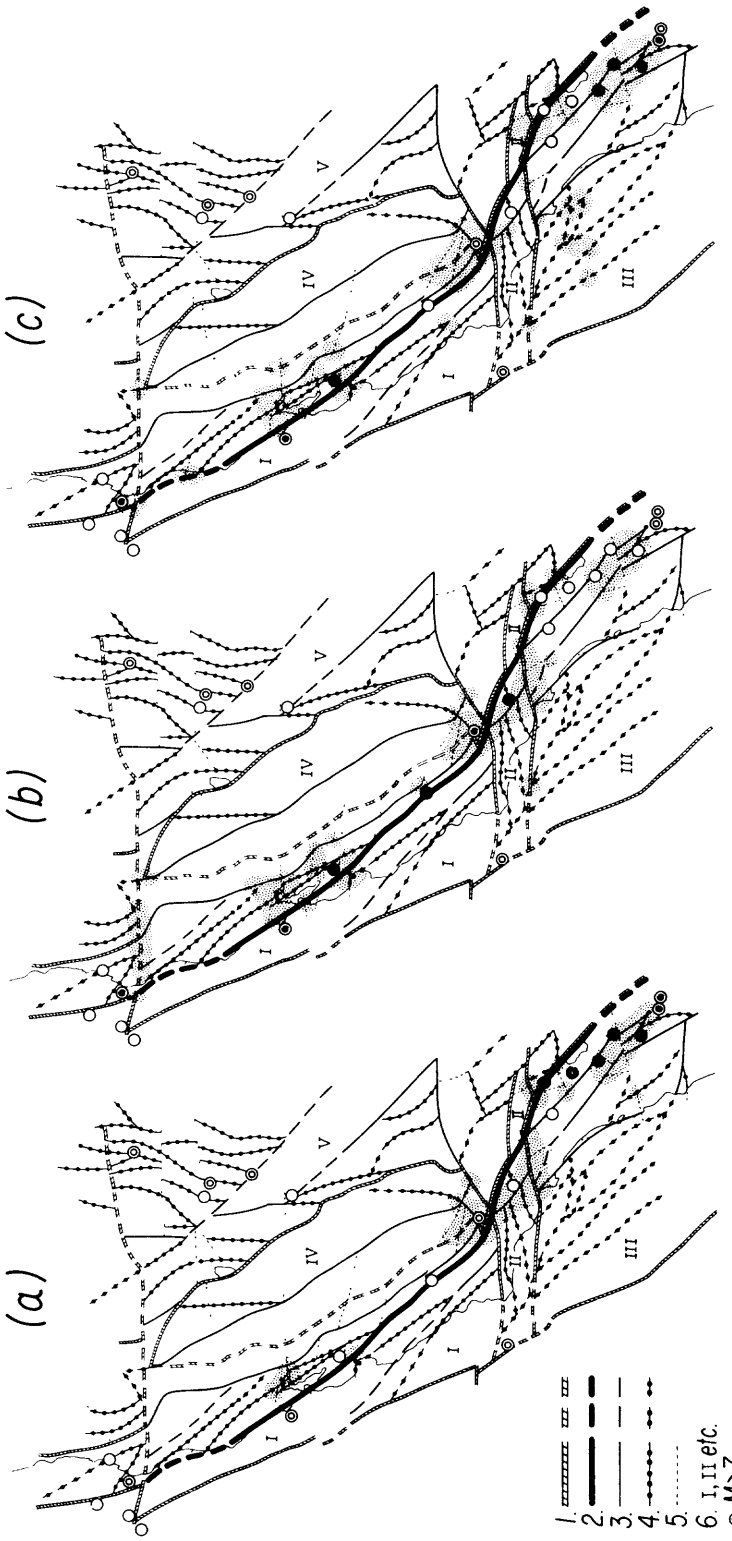

Fig. 10. Comparison of D areas for intersections of lineaments. Control experiment consists of eliminating groups of earthquakes. Epicenters eliminated from learning are filled in solid colors; the corresponding D areas are shaded. Lineaments defined in same way as Fig. 4. The experiment is aimed at recognition of intersections around the eliminated epicenters.

break of the San Francisco earthquake, 1906 (between intersections *13* and *89*). Clusters were formed around each of these intersections, exactly as was done around epicenters in the preceding sections. The results of recognition, shown in Fig. 9c, are unsuccessful. No intersections are recognized as D near 9 known epicenters out of 12. The three exceptions are the epicenters near the fault break, which are predetermined by learning. The next experiment indicates that this failure is due not to an uneven coverage of the territory by the objects of class I, but to the replacement of epicenters by the fault break.

4.6.2. Uniformity of the region

The analogous experiment was described in Section 3. The purpose is to see if we can recognize dangerous areas even if the epicenters in their vicinity are eliminated during the learning stage. Three cases were considered as shown in Fig. 10. The number of known strong earthquakes in the three cases is 6, 6 and 7, respectively. According to our experience with EH experiments, this number is marginal for successful learning. Nevertheless, the results shown in Fig. 10 are quite good in that at least one point was recognized as dangerous in almost all clusters not used in learning. The only exceptions are: two clusters near intersections *101* and *13* in Fig. 10b; one cluster near *158* in Fig. 10a. This confirms the conclusion reached in the analogous experiment in Section 3.

4.6.3. Effect of dip-slip earthquakes

Two of the earthquakes, used for learning, are of dip-slip variety (years 1952 and 1971; epicenters near intersections *165* and *119*). The clusters, corresponding to these earthquakes, were eliminated from learning in this experiment. The distinctive features did not change noticeably. The results of recognition (with the same threshold as in main variant, $\bar{\Delta} = \Delta^*$) are shown in Fig. 7b. We see that the number of D intersections decreased significantly, from 25 in the main variant to 17. Only three points outside of clusters are recognized as D (*72*, *73* and *104*), slightly expanding already known clusters. Fig. 6 shows that the main effect was the elimination of a group of D points in the Transverse Ranges, a geologically reasonable result.

4.7. Comparison with Section 3

D areas recognized for intersections and for points on major faults (Figs. 3 and 6) basically coincide in that the same five groups of D-points show up in both cases. The slight differences are due to the fact that the study of intersections covers a larger territory.

The characteristic features (Table XVII) show that D and N intersections are often characterized by low and high elevations (h_1, $H_{\min}$ and $H_{\max}$), respectively. This reinforces the idea derived from the results in Section 3 that D intersections are often associated with neotectonic subsidence against a background of weak uplift. Two more observations may be made.

(1) Additional evidence of the importance of vertical movements at D intersections are the large gradients ($\Delta H/\ell_4$) and the mountain–plain contacts which show up in many D features, with opposite conditions holding for N features.

(2) The fracturing of the crust is more pronounced for D than for N intersections. This is shown by the occurrence of lineaments of high rank in D features and low rank in N features. Also many N features show small values of n_2 – the number of intersections within 62.5-km distance.

5. Conclusions

Using pattern recognition, we have divided California into two types of areas: D areas where epicenters of strike-slip earthquakes with $M \geqslant 6.5$ can occur and N areas where these epicenters cannot occur. Distinctive features for each of these areas were identified. The D areas are characterized by proximity to intersections or ends of major faults and by relatively low elevation or subsidence against a background of weaker uplift. The N areas often show higher elevation or stronger uplift but less contrast in relief. D areas concentrate in five places. These results were tested against numerous control experiments and seem to be stable and reliable.

It is surprising that the relatively simple and crude parameters which make up the distinctive features suffice to achieve these results. Perhaps large earthquakes occur on faults which penetrate significantly into the lithosphere and fault movements on such a scale can be recognized in simple ways. Perhaps parameters based on systems of faults and other types of

lineaments summarize more geophysical and geological information than their simplicity implies. Perhaps the result that epicenter locations occur at identifiable places along faults and not at arbitrary locations on faults implies the existence of a special property or agent in the epicentral region which acts to initiate rupture. This special property might be one which concentrates stress to weaken rock, or to "lubricate" a fault.

Our results are not useful as they stand for earthquake hazard mitigation since they identify epicenters and not the entire length of fault rupture, which may extend well beyond a D area. However a search for short-term precursors may be promising in D areas and future efforts in earthquake control by fluid injection and withdrawal could make use of D and N information.

Over the years many efforts have been made to characterize earthquake-prone regions by the occurrence of certain relationships in the field. For example, "earthquake country" has been characterized by topographic and geomorphic forms, by intersecting faults and by other ways in the geological literature. Our procedure seems to be a more precise formulation of many ideas which have been vaguely recognized in the past. It allows one to get more definite results, providing a method for recognizing differences between geologically different areas rather than describing each area by itself. It employs past experience, intuition and/or hypotheses; but it uses a logical framework to formulate explicitly the pertinent and reliable parts of these elements. The procedure consists of five steps.

(1) Preliminary separation of objects into groups.

(2) Separation of promising parameters by histogram analysis.

(3) The combination of parameters into features, singlets to triplets, and the analysis of all possible features to identify distinctive ones.

(4) The use of distinctive features in recognition.

(5) The analysis of distinctive features for their geological or geophysical meaning.

(6) The design of control experiments to prevent self-deception.

Statistical procedures are alternative methods to pattern recognition but in this case they are difficult to apply because the number of strong earthquakes is inadequately small.

In the future we intend to apply pattern recognition to time prediction rather than space prediction and to other geophysical applications.

Acknowledgements

This study is a product of the U.S.A./U.S.S.R. Working Group on Earthquake Prediction. The participation of Drs. L. Knopoff and F. Press was supported by grants with the U.S. Geological Survey, Department of the Interior.

Appendix – Major morphostructures and lineaments of California and adjacent regions

1. Basic definitions

Morphostructures are structures in the earth's crust (or its upper part) expressed in present day topographic relief. Tectonic and geomorphic maps often describe structures, based only on either geological or geomorphic evidence. For the study of earthquakes, however, actively developing structures are important. These structures are expressed in topographic relief; geomorphic evidence may therefore be important for their reconstruction, together with geological data.

Rank of morphostructure. The following subdivision seems adequate for tectonically and seismically active regions. Each region is divided into morphostructural countries (I), countries into megablocks (II), and megablocks into blocks (III). The rank assigned to each type of morphostructure is indicated by brackets.

Countries differ by the type of orogenesis and/or by the large-scale tectonic features.

Megablocks inside a country differ either by the dominant type of relief, or by the average parameters of the relief (such as heights of peaks, dominant strikes, relative area occupied by basins and ranges, etc.); or by the pattern of the main elements of relief.

Blocks inside megablocks differ in neotectonic history; for example, large separate ranges or depressions in contrast to a complex of smaller ranges, depressions and valleys can be outlined as separate blocks.

Morphostructural provinces. In some large countries, such as the Pamir and Tien-Shan regions, where the history of relief is long and complicated, an intermediate morphostructure – a province – was introduced (Gelfand et al., 1973a). A province is a group of megablocks which have similar preorogenic histories, and accordingly, similar general features of relief. The same first rank, as for countries, was assigned to provinces. (For example, an internal depression inside a platform may be transformed after activation into a large intermountain basin and regarded as a province.)

Lineaments. The boundary zones between morphostructures are called lineaments. They have the same rank as the morphostructures which they separate. Lineaments of the first rank have widths from about 10 to 50 km, perhaps more; they may be thousands of kilometers in length. A lineament is the surface trace of an active fault (or flexure), penetrating deeply into the earth's crust and perhaps through the entire lithosphere. Different parts of a lineament may be expressed in different ways: geological, geomorphic or both; the evidence for a lineament may not necessarily be as direct as faults shown on a tectonic map. Let us describe some of the evidence for lineaments, which may differ for longitudinal and transverse lineaments.

Longitudinal lineaments are approximately parallel to the main elements of relief (such as ridges, basins, elongated intra-mountain depressions, etc.). Usually they form the boundaries between these elements. They are often expressed directly by zones of tectonic faults. Detailed tectonic maps show them as a system of narrow, elongated blocks. However, some parts of longitudinal lineaments are not traced by faults, but by geomorphic evidence: direct contact of contrasting forms of relief such as steep mountain front and flat plain, linear form of valley between ridges, etc.

Transverse lineaments form a large angle with the dominant strike of the main elements of relief and tectonics. They are traced mainly by terminations of these elements, en-echelon patterns, relative displacements of elements, sharp changes in height or strike, sharp changes in types of relief. A regular linear pattern of these features is evidence for a transverse lineament. Transverse lineaments may also show as patterns in the occurrence of volcanoes, the highest peaks or saddle points in parallel ridges, etc. Sometimes the evidence for transverse lineaments may show simply as a straight-line river on the slope of a ridge, which does not flow in the direction of steepest descent of the slope, or distinct, short ranges, or narrow intrusive bodies with transverse strike, or transverse faults of limited extent, shown on tectonic maps. Transverse lineaments are not always marked by the clear traditional evidence of long narrow ridges, valleys and tectonic faults. The evidence for these lineaments may be indirect, subtle and discontinuous. However, the general pattern of evidence allows one to draw transverse lineaments with reasonable certainty, especially with the aid of satellite photography. The name "transverse" could be misleading in that the main distinction is not the strike, but evidence of the kind just described. For example, the Transverse Ranges of California, though perpendicular to the dominant strike of the region, are nevertheless classified as a longitudinal lineament, since the structure carries its own faults, ridges and valleys.

Disjunctive knots. Specific morphostructures of disjunctive knots are formed around the intersections of lineaments. They are zones of especially intensive fracturing and contrasting neo-tectonic movements. Following along a lineament one can notice the appearance of a disjunctive knot by a set of specific phenomena, connected with a general increase of neo-tectonic activity and with manifestations of intersecting lineaments: the types of relief become more diverse (types corresponding to each lineament show up) and appear in new combinations; the heights of ridges and height differences change drastically; boundaries of contrasting forms of relief assume a broken-line form; rivers flow along faults and their valleys straighten; the orientation of valleys corresponds to the direction of both intersecting lineaments; fault activity increases; the lineaments inside the knots are usually expressed by faults; the topographic and geological maps show mosaic patterns; a grid of surface faults expressed tectonically or geomorphically is not uncommon.

As a rule a knot is wider than the lineaments from which it is formed. The linear dimensions of knots depend on the rank of the component lineaments and may vary from 20 to 200 km or more. One knot may include several intersections of lineaments.

It is clear from this description that though the knots have rather distinct boundaries the determination of these boundaries demands quite specialized research – in the field and on detailed maps. In the absence of such research we must consider in our problem "intersections" instead of knots. An intersection is the point of intersection of the axes of lineaments. It is a much more formal object than a knot but it is easier to handle. Each intersection belongs to some knot; but it is unknown a priori which intersections belong to the same knot. Algorithm CLUSTERS was especially devised to deal with this difficulty.

2. The scheme of major lineaments (Fig. 4)

The area of interest is divided into morphostructures of three ranks: countries, megablocks and blocks (see first paragraph of this Appendix). Their boundaries are the lineaments of corresponding rank, shown in Fig. 3. The five following countries are represented:

I = Coast Ranges; *II* = Transverse Ranges; *III* = southern California-northern end of the Peninsula Ranges and the entire Mexican section of the Cordilleras; *IV* = Sierra-Nevada; *V* = western part of the Basin and Range Province.

Country *I* belongs to the Pacific orogenic belt, with active Cenozoic folding. The four other countries belong to the Cordilleran orogenic belt where the folding was mostly finished in the Mesozoic area. These four countries differ in Pliocene–Quaternary orogenic development. Faults of the San Andreas system cross countries, *I, II* and *III.* Its width is about 60 km in the north, near San Francisco Bay and up to 160 km, if not more, in southern California. The details are described elsewhere (Ranzman, in preparation).

References

Atwood, W., 1940. The Physiographic Provinces of North America. Ginn, Boston, Mass., 535 pp.

Bongard, M.M., Vaintsveig, M.I., Guberman, Sh.A., Izvekova, M.L. and Smirnov, M.S., 1966. The use of self-learning

programs in the detection of oil containing layers. Geol. Geofiz., 6: 96–105 (in Russian).

Briggs, P. and Press, F., in preparation. Pattern recognition applied to earthquake epicenters in California and Nevada.

Coffman, J.L. and Von Hake, C.A., 1973. Earthquake history of the United States. Natl. Oceanic Atmos. Adm. (U.S.), Publ., 41-1, 208 pp.

Cook, K.L., 1966. Rift system in the basin and range province. In: The World Rift System, Proc. UMC Symp., Ottawa, Ont., September 6–8, 1965, Geol. Surv. Can., Pap., 66-14: 246–275.

Dickinson, W.R. and Grantz, A., 1968. Proc. Conf. on Geological Problems of San Andreas. In: Geological Sciences, Vol. XI, Stanford University, Palo Alto, Calif., 374 pp.

Gelfand, I.M., Guberman, Sh.A., Izvekova, M.L., Keilis-Borok, V.I. and Ranzman, E.Ia., 1972. Criteria of high seismicity, determined by pattern recognition. In: A.R. Ritsema (Editor), The Upper Mantle, Tectonophysics, 13(1/4): 415–422.

Gelfand, I.M., Guberman, Sh.A., Izvekova, M.L., Keilis-Borok, V.I. and Ranzman, E.Ia., 1973a. Recognition of places where strong earthquakes may occur, I. Pamir and Tien-Shan. In: Computational Seismology, Vol. 6 (in Russian).

Gelfand, I.M., Guberman, Sh.A., Kaletskaja, M.S., Keilis-Borok, V.I., Ranzman, E.Ia. and Zhidkov, M.P., 1973b. On the transfer of criteria of high seismicity from Central Asia to Anatolia and adjacent regions. Dokl. Akad. Nauk S.S.S.R., 20, N2 (in Russian).

Gelfand, I.M., Guberman, Sh.A., Kalezkaja, M.S., Keilis-Borok, V.I., Ranzman, E.Ia., Rotwain, I.M. and Zhidkov, M.P., 1974a. Recognition of places where strong earthquakes may occur, II. Four regions of Asia Minor and S-E Europa. In: Computational Seismology, Vol. 7 (in Russian).

Gelfand, I.M., Guberman, Sh.A., Keilis-Borok, V.I., Ranzman, E.Ia., Rotwain, I.M. and Zhidkov, M.P., 1974b. Recognition of places where strong earthquakes may occur, III. The case when the boundaries of disjunctive knots are unknown. In: Computational Seismology, Vol. 7 (in Russian).

Gutenberg, B. and Richter, C.F., 1954. Seismicity of the Earth and Associated Phenomena. Princeton University Press, Princeton, N.J., 310 pp.

Hain, W.Y., 1971. Regional Geotectonics, Vol. 1. Moscow University, Moscow (in Russian).

Hamilton, W. and Myers, W.B., 1966. Cenozoic tectonics of the Western United States. In: The World Rift System, Proc. UMC Symp., Ottawa, Ont., September 6–8, 1965, Geol. Surv. Can., Pap., 66-14: 291–306.

Hill, M.L., 1966. The San Andreas system, California and Mexico. In: The World Rift System, Proc. UMC Symp., Ottawa, Ont., September 6–8, 1965, Geol. Surv. Can., Pap., 66-14: 239–245.

King, F.B., 1969. The tectonics of North America. A discussion to accompany the *Tectonic Map of North America, Scale 1 : 5,000,000.* U.S. Geological Survey, Washington, D.C.

National Oceanic and Atmospheric Administration, 1965–1973. Bulletins of preliminary determination of epicenters. Boulder, Colo.

Ranzman, E. Ia., in preparation. Major morphostructures and lineaments of California.

Richter, C., 1958. Elementary Seismology. Freeman, San Francisco, Calif., 768 pp.

Rothe, J.P., 1969. The seismicity of the Earth. UNESCO, Paris, 336 pp.

Thompson, G.A., 1966. The rift system of the Western United States. In: The World Rift System, Proc. UMC Symp., Ottawa, Ont., September 6–8, 1965, Geol. Surv. Can., Pap., 66-14: 280–289.

USGS, no date. Topographic Map of the United States. Scale 1 : 1,000,000, Washington, D.C.

USGS, 1962. Tectonic Map of the United States. Scale 1 : 2,500,000, Washington, D.C.

USGS, 1965. Geologic Map of North America. Scale 1: 5,000,000, Washington, D.C.

Wright, H. and Frey, D., 1965. The Quaternary of the United States. Princeton University Press, Princeton, N.J., 922 pp.

(page 429 follows)

JOURNAL OF GEOPHYSICAL RESEARCH, VOL. 85, NO. B2, PAGES 813–820, FEBRUARY 10, 1980

Long-Term Premonitory Seismicity Patterns in Tibet and the Himalayas

V. KEILIS-BOROK

Institute of Physics of the Earth, Academy of Sciences of the USSR
Moscow, USSR

L. KNOPOFF

Institute of Geophysics and Planetary Physics, University of California
Los Angeles, California 90024

C. R. ALLEN

Seismological Laboratory, California Institute of Technology
Pasadena, California 91125

An attempt is made to identify seismicity patterns precursory to great earthquakes in most of Tibet as well as the central and eastern Himalayas. The region has considerable tectonic homogeneity and encompasses parts of China, India, Nepal, Bhutan, Bangladesh, and Burma. Two seismicity patterns previously described were used: (1) pattern Σ is a peak in the sum of earthquake energies raised to the power of about 2/3, taken over a sliding time window and within a magnitude range less than that of events we are trying to predict; and (2) pattern S (swarms) consists of the spatial clustering of earthquakes during a time interval when the seismicity is above average. Within the test region, distinct peaks in pattern Σ have occurred twice during the 78-year-long test period: in 1948–49, prior to the great 1950 Assam-Tibet earthquake ($M = 8.6$), and in 1976. Peaks in pattern S have occurred three times; in 1932–1933, prior to the great 1934 Bihar-Nepal earthquake ($M = 8.3$), in 1946, and in 1978. The 1934 and 1950 earthquakes were the only events in the region that exceeded $M = 8.0$ during the test period. On the basis of experience here and elsewhere, the current peaks in both Σ and S suggest the likelihood of an $M = 8.0$ event within 6 years or an $M = 8.5$ event within 14 years. Such a prognostication should be viewed more as an experimental long-term enhancement of the probability that a large earthquake will occur than as an actual prediction, in view of the exceedingly large area encompassed and the very lengthy time window. Furthermore, the chances of a randomly occurring event as large as $M = 8.0$ in the region are perhaps 21% within the next 6 years, and the present state of the art is such that we can place only limited confidence in such forecasts. The primary impact of the study, in our opinion, should be to stimulate the search for medium- and short-term precursors in the region and to search for similar long-term precursors elsewhere.

INTRODUCTION

The purpose of this study is to investigate long-term seismicity patterns in a region of frequent great earthquakes with the hope of identifying precursory phenomena. The area chosen for study (Figure 1) is basically that of the central and eastern Himalayas, including the great syntaxial bend at the eastern end of the mountain chain arc, together with most of Tibet to the north. It encompasses parts of China, India, Nepal, Bhutan, Bangladesh, and Burma. Many disastrous historic earthquakes have occurred in the region [*Richter*, 1958], and its high seismicity is associated with the continental collision between the Indian and the Eurasian plates [*Molnar and Tapponnier*, 1975]. Seismotectonic boundaries within the region are diffuse and necessarily somewhat arbitrary owing to the fact that the region north of the Himalayan frontal fault cannot be divided readily into a series of rigid sub-blocks or miniplates, but instead shows many aspects of continuous deformation extending far to the north into China [*Tapponnier and Molnar*, 1977]. Throughout the region the stress distributions are related to the impingement of the Indian plate, with its very sharp northeast corner, against the Eurasian plate; thus the study region includes both areas of dominant thrust faulting within the Himalayas, as well as the area of dominant strike slip faulting east and northeast of the syntaxial bend in Burma and southern China. It should be noted that the study region is very large indeed, encompassing an area equivalent to that of the entire conterminous United States west of the Rocky Mountain crest, or that of the combined areas of the Ukraine, Georgia, Turkmenia, Uzbek, Tadzhik, and Kirghiz republics. That there should be mechanical interconnection over this entire area associated with the 'preparation' for individual great earthquakes is perhaps surprising, but this is one of the conclusions of our study.

DEFINITIONS

We tested three premonitory patterns, Σ, S, and B [*Caputo et al.*, 1979; *Keilis-Borok and Malinovskaya*, 1964; *Keilis-Borok and Rotvain*, 1979; *Keilis-Borok et al.*, 1979. Their definitions are given in the work of *Keilis-Borok et al.* [1979] and will be summarized here only briefly. We seek precursors of events with magnitudes $M \geq M_0$; events of these magnitudes are called strong earthquakes.

Pattern Σ (sigma). This pattern was introduced by *Keilis-Borok and Malinovskaya* [1964] and is represented by a peak of the function

$$\sum(t) = \sum_i G(M_i)$$

Here M_i, $i = 1, 2 \cdots$, are the magnitudes of consecutive earthquakes. The summation is taken over all earthquakes in the

Paper number 9B1195.
0148-0227/80/009B-1195$01.00

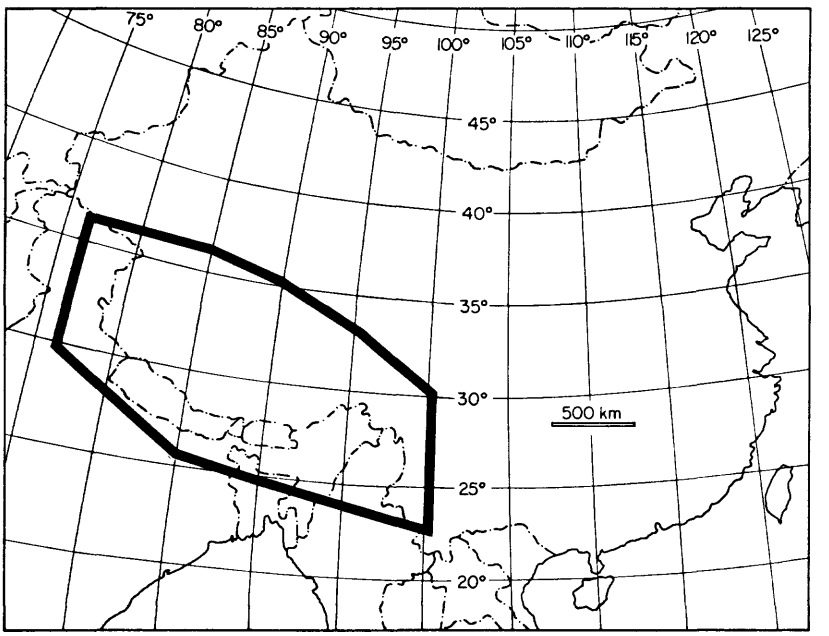

Fig. 1. Map showing area of study (heavy line).

region within the sliding time window of width s:

$$t - s \leq t_i \leq t$$

within the magnitude range

$$M_0 - d_2 \leq M_i \leq M_0 - d_1$$

and within the depth interval,

$$h_2 \leq h_i \leq h_1$$

The time of the ith earthquake is t_i, and h_i is its focal depth. Aftershocks of earthquakes with $M \geq M_0$ are eliminated from the summation in order to test the potential that earthquakes of intermediate magnitudes have for triggering larger events.

The function $G(M)$ is assumed to be

$$G = 10^{d(m-f)}$$

Pattern Σ is diagnosed when

$$\Sigma(t) \geq cG(M_0)$$

Pattern S ('swarms'). This pattern was introduced by *Caputo et al.* [1979] and consists of a clustering of earthquakes during a time interval when the seismicity is above average. The formal definition is as follows. We count earthquakes in the sliding time interval from $t - s$ to t and in the magnitude range $M_i \geq M_1$. $N(t)$ is the total number of such earthquakes in the whole region, $n(t)$ is obtained from $N(t)$ by the elimination of aftershocks of strong earthquakes. We determine $r(t)$, which is the maximum number of epicenters for which $n(t)$ has been calculated and which can be surrounded by a small rectangular area of size $\Delta\phi$ in latitude and $\Delta\lambda$ in longitude. Pattern S is diagnosed when

$$N(t) > c_1 \qquad n(t) > c_2\overline{N}(t) \qquad r(t) \geq c_3 n(t)$$

$\overline{N}(t)$ is the average value of $N(t)$ in the interval from the beginning of the catalog to t or in the sliding window extending from $t - c_4$ to t.

Pattern B ('burst of aftershocks'). This pattern was introduced by *Keilis-Borok et al.* [1979] and is represented by an earthquake with an abnormally large number of aftershocks at the beginning of its aftershock sequence. Aftershocks are identified as the earthquakes within a distance $R(M)$ from the main shock and time interval $T(M)$ after the main shock, M being its magnitude. The number b_i of aftershocks during the first e days after the ith main shock is estimated. Pattern B is diagnosed when b_i is abnormally large, $b_i \geq \bar{b}$.

The threshold $\bar{b}$ was determined as follows. Let $b(t)$ be the maximum value of b_i during the sliding time interval $t - s \geq t_i \geq t$. Then by analogy with $\overline{N}(t)$ the function $\bar{b}(t)$ is the running average value of $b(t)$ in the interval extending from t_0 to t; if this average is less than some constant, we replace it by this constant. Alternatively, a constant threshold may be used.

All three patterns are probably similar projections of a general pattern, which is the abnormal clustering of earthquakes in the time-space-energy domain. This general pattern was called 'burst of seismicity' by *Keilis-Borok et al.* [1979].

DATA ANALYSIS

We listed the earthquakes of the region under consideration from the revised catalog of earthquakes of China and adjacent regions [*Lee et al.*, 1976, 1978]. The catalog of historical earthquakes is, not unexpectedly, far less complete than the instrumental catalog which begins around 1900 (Table 1). We therefore confine our attention to the instrumental catalog. A list of all earthquakes in this region with $M \geq 7.0$ is given in Table 2.

Pattern Σ. Parametric values were assigned a priori, on the basis of previous studies, as follows: $s = 5$ years, $d = 0.91$, $f = 4.5$. Note that the choice of f plays no role in the determination of pattern Σ. No limits were imposed on focal depths, since the catalog shows unknown or normal depths for almost all earthquakes. The magnitudes and rates of occurrence of the largest earthquakes in the region (Table 2) indicate a choice of M_0 of between 8.0 and 8.5. We selected $M_0 = 8.0$ and $M_0 - d_1 = 7.8$ [*Keilis-Borok and Malinovskaya*, 1964]; the lower limit, $M_0 - d_2 = 6.0$ is dictated by the lack of reliability of the catalog below the cutoff. All earthquakes within a distance of 100 km from the epicenter of each of the three strong earthquakes with $M \geq 8.0$ and within one year after it were la-

TABLE 1. Statistics of Earthquakes in Tibet and the Himalayas, after *Lee et al.* [1976, 1978]

Date	Magnitude				
	<6.0	6.0–6.4	6.5–6.9	7.0–7.4	≥7.5
1450–1899	10	1	2	0	0
1900–1919	0	3	3	2	0
1920–1939	0	14	6	1	1
1940–1959	0	30	9	0	4
1960–1976	0	12	6	4	0

beled as aftershocks of these earthquakes and hence were eliminated from Σ. The thresholds for the definition of aftershocks are the same as in some of the previous studies. Generally, not all aftershocks will be identified by these thresholds after strong or main shocks. However, for this catalog an increase in the thresholds will not alter our conclusions and indeed will only make our results look better; Σ will be smaller except in the intervals preceding strong earthquakes.

The function $\Sigma(t)$ is shown in Figure 2, and the significant peak in the function Σ before the 1950 Assam-Tibet earthquake is evident. *Keilis-Borok and Malinovskaya* [1964] took the threshold value $c = 0.5$; if we take this value, we identify pattern Σ and declare a long-term alarm when $\Sigma\ (T) \geq 765$. This a priori threshold has thus far given no false alarms. On the other hand, we failed to detect pattern Σ prior to the 1934 earthquake, $M = 8.3$, which took place on the border of the region. We cannot establish pattern Σ prior to the 1951 earthquake with $M = 8.0$, since it occurs within too short a time after the Assam-Tibet earthquake.

Pattern S. We assumed $M_0 = 8$, $s = 5$, as before; the choice $M_1 = 6$ was dictated by the catalog; $c_2 = 1$, $c_3 = 0.5$, as in previous studies [*Caputo et al.*, 1979; *Keilis-Borok and Rotvain*, 1979]; $\Delta\phi = 0.4°$, $\Delta\lambda = 0.8°$. The results are inconclusive (Figures 3 and 4). Except for a brief interval around 1918, we do not consider the period before 1930, when $N < 5$ and is too small. After 1930, pattern S with both $n > \overline{N}$ and $r \geq 0.5n$ occurs twice, prior to both the 1934 and the 1950 earthquakes; the latter occurred contemporaneously with pattern Σ. The locations of the swarms are shown by stars in Figures 4*a*, and 4*b*. We believe the values of N are too small to use pattern S as an independent precursor, although it can be summoned as supporting evidence. Five earthquakes in 1976 near the southeast corner of our region are not diagnosed as pattern S because $n/\overline{N}$ is too small in the corresponding time window, 1972–1976. If the time window were chosen to be 3 years, pattern S would have been diagnosed (see last point on Figure 3) and would have been a result in correspondence with our observation of pattern Σ for this period.

Pattern B. Pattern B cannot be studied in this region because the catalog at our disposal has almost no aftershocks for most earthquakes.

Figures 2 and 3 imply the existence of premonitory patterns Σ and S in this region; the strongest earthquake, with $M = 8.6$ in 1950, is preceded by both patterns; the earthquake of $M = 8.3$ in 1934 is preceded by pattern S. Neither of the patterns has generated false alarms.

We discuss the danger of self-deception. Two decisions related to pattern Σ were not made in previous papers. One is the choice $M_0 = 8.0$. Nothing in the catalog dictates that we make this choice. If we had chosen $M_0 = 8.5$, we would take $M_0 - d_1 = 8.3$ [*Keilis-Borok and Malinovskaya*, 1964]. This would lead to the following changes. The $M = 8.3$ earthquake of 1934 is no longer a strong earthquake and hence would be included in Σ. This would generate a major maximum in Σ about 16 years prior to the 1950 Assam-Tibet earthquake. This maximum was described by *Keilis-Borok and Malinovskaya* [1964] on the basis of the Gutenberg-Richter catalog. The time interval of 16 years is consistent with a rough correlation between the magnitude of the forthcoming earthquake and its delay after the rise of Σ. We cannot reject the notion that the occurrence of pattern Σ in 1948 is not the first but the second in a sequence of precursors. Another consequence of the increase of M_0 and $M_0 - d_1$ would be that the earthquake of 1951 with $M = 8.0$ with its two aftershocks, $M = 6.2$ and 7.5, would also be included in Σ, and this would give a false alarm in 1951, immediately after the Assam-Tibet earthquake. The results are reasonably stable to the variation of the other numerical parameters.

In the investigation of pattern S we arbitrarily chose $M = 6$ and $s = 5$ years. These values are essentially predetermined by the catalog; any increase of M_1 or decrease of s would reduce N, which is already too small. We also assumed $\Delta\phi = 0.4°$, $\Delta\lambda = 0.7°$. The results remain the same if we increase these values, since the swarms, small as they are, are well concentrated in space. Hence pattern S is weak but reasonably stable.

More important was the decision by which the boundaries of the region were selected. These boundaries are generally nonunique, and for this part of the world the uncertainty is larger than usual, as was indicated in the introduction. We have been concerned that a change in the boundaries might lead to a significant change in the results. However, the test described below shows that our results are relatively stable to variations in the boundaries.

POSSIBLE TECTONIC IMPLICATIONS

There is so far no unique answer to the following question: What zones of active structure should be analyzed together in the study of the occurrence of strong earthquakes? Let us assume that pattern Σ, described in the previous section, is significant and discuss its possible meaning.

TABLE 2. Earthquakes with $M \geq 7$

Year	Date	M
1905	April 4	8.0*
1908	Aug. 20	7.0
1915	Dec. 3	7.0
1934	Jan. 15	8.3
1934	Dec. 15	7.1
1947	July 29	7.7
1950	Aug. 15	8.6
1951	Nov. 18	8.0
1952	Aug. 17	7.5
1973	July 14	7.0
1975	Jan. 19	7.1
1976	May 29	7.0
1976	May 29	7.1

*Located slightly outside of test area.

TABLE 3. Comparison of Catalogs, 1973–1976

Year	Date	*Lee et al.* [1978]	*Academia Sinica* [1976]
1973	July 14	7.0	7.3
	July 14	6.0	6.0
	Sept. 8	6.0	6.0
1975	Jan. 19	7.1	6.9
	March 18	6.3	6.0
	May 5	6.5	6.4
1976	May 29	7.0	7.5
	May 29	7.1	7.6
	May 29	not listed	6.0
	May 31	6.3	6.6
	June 1	not listed	6.1
	June 9	6.0	6.1
	July 4	not listed	6.0
	July 21	6.4	6.8

Nine earthquakes occurred during the period 1943–1947 that contributed to the marked peak of Σ in 1948. The positions of their epicenters are shown in Figure 4*a*. Sixty-four percent of the contribution to the peak was made by a single earthquake of magnitude 7.7 in 1948. The eight remaining events might be considered as normal random background except that seven of them occurred in the western part of the region, where the long-term seismicity is much lower than in the east; during the entire 1900–1976 period the numbers of events west and east of longitude 90° are 31 and 65, respectively (excepting aftershocks). The probability of getting 7 out of 8 of the 1944–1948 events west of 90° by a random binomial model is 0.002, which is small. Therefore we propose that there is a mechanical connection between these events, and, taken together with the larger magnitude 7.7 shock to the east, they represent systematic 'unlocking' of the plate boundary in this area preparatory to the great earthquake of 1950, which was centered still farther southeast. We recognize that the faulting associated with the 1950 earthquake did not extend over the entire 1500-km-long zone encompassed by the premonitory shocks, but we do suggest that the 'mechanical preparation' for this great earthquake was taking place over a very wide area in the years before the earthquake, with redistribution of stresses pointing toward the subsequent more localized epicentral area. This could be an a posteriori qualitative explanation of the premonitory pattern in Σ in 1948.

Let us now see whether this premonitory pattern could have been identified if the boundaries of the test region had been drawn on the basis of other seismotectonic considerations. Differences between solely tectonically and solely seismologically based regionalizations should be kept in mind. The purpose of the first is to outline areas with common features of historic tectonic development and makeup. The purpose of the second is to outline zones with interdependent stress-strength fields, which may form transition zones between tectonic provinces defined in the usual sense. That is, such seismic zones may show very diverse tectonic features and earthquake mechanisms, since earthquake-producing stresses do not necessarily terminate at tectonic boundaries. With this in mind, we repeat our analysis for four additional variations of the test area boundaries. These are shown in Figure 5.

Area A (Figure 5) simply represents a minor expansion in the boundaries of the original test area. Area B encompasses a somewhat larger area to the southeast, thereby including a considerably increased number of shocks from the very active southern Yunnan seismic area. The eastern boundary of the original test area at 100°E longitude was particularly arbitrary, so this additional test is significant. Area C includes an even greater number of shocks to the east, including those of northern Yunnan and southern Szechwan. Area D is an area more limited than that of the original test area, encompassing a large 'cloud' of epicenters but drawn without any tectonic basis; region D excludes territory lying to the west of longitude 90°.

Patterns Σ for each of these regions are compared in Figure 6. We indicate on this figure only those values of Σ which are greater than 750. The diagnosis of pattern Σ is evidently stable to the thresholds c and M_0. In all four cases a major maximum of $\Sigma \geq 1200$ precedes the 1950 earthquake. As might have been expected, with the expansion of the region some secondary maxima also increase. The maxima in the 1970's will be discussed separately.

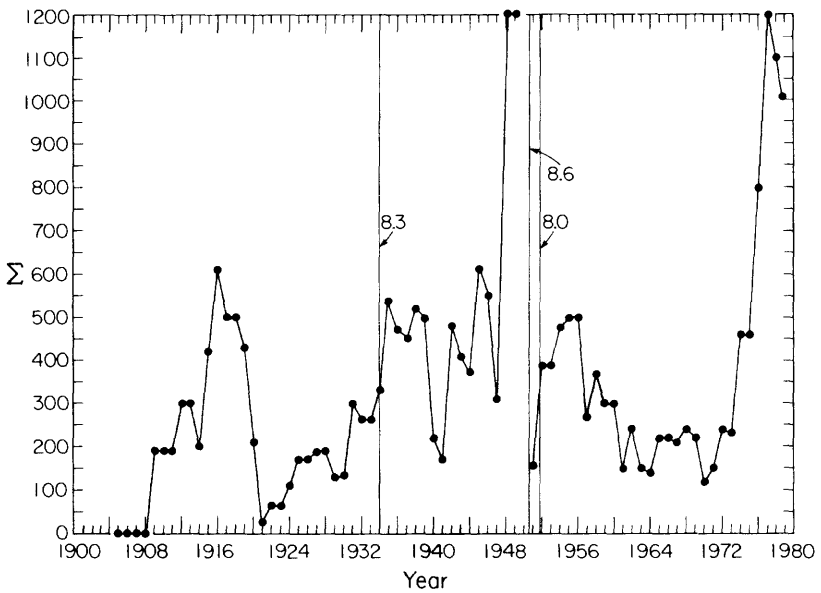

Fig. 2. Pattern Σ (solid circles) and strong earthquakes for the area of study (vertical lines, with magnitudes).

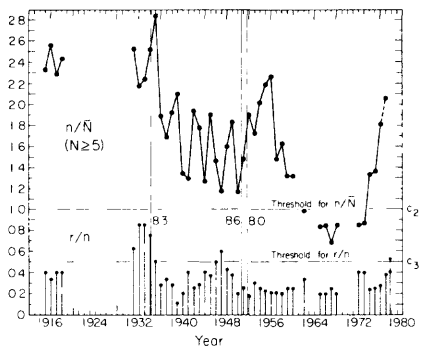

Fig. 3. Pattern S and the strongest earthquakes (vertical lines). Top curve shows $n(t)/\bar{N}(t)$ when $N \geq 5$, and bottom diagram shows $r(t)/n(t)$.

Pattern S before the 1934 ($M = 8.3$) earthquake persists through all the variations; pattern Σ appears 6 years and more before this same earthquake in variations A and C. Pattern Σ appears as a false alarm around 1940 in variations C and D. Patterns Σ and S both appear through all variations before the 1950 ($M = 8.6$) earthquake, with the exception that pattern S disappears in variations C and D. In region C it disappears because the swarms that produced pattern S in the other cases do not pass the increased threshold $\bar{N}$; in region D it disappears because the swarm is now outside the region. Finally, the occurrence of pattern Σ in the late 1970's vanishes in variation D and is replaced by pattern S. We note that variation D inflicts the greatest change on the original assignment to the region, since D describes only the eastern half of the entire region. The process of excluding earthquakes from the region west of longitude 90° from our count creates a strong instability in the appearance or disappearance of the two patterns.

A further expansion of the region may include other strong earthquakes, but we see no compelling reason to consider them here. If all of the boundaries of the region are extended by 500 km, for example, thereby more than doubling the test area, only two additional earthquakes with $M \geq 8$ are included. One of these, the 1905 Kangra (India) earthquake, occurred too close to the start of the instrumental catalog period to search for precursors; the other is a 1912 event of $M = 8.0$ in central Burma, an area for which our catalog is markedly deficient. The great 1897 Assam (India) earthquake with $M = 8.7$ occurred within the original test area, but catalogs for that time are too inadequate to search for precursors.

THE RECENT PATTERN Σ

We discuss the fact that $\Sigma(t)$ reached the same height, 1200, in 1976 as before the 1950 Assam-Tibet earthquake. This implies that another earthquake of $M \geq 8$ may occur within several years in the study region. We consider the similarity of this recent pattern to the pattern which preceded the earthquake of 1950 with $M = 8.6$. Thirteen earthquakes are listed in the catalog for the period 1972–1976 and generate the peak of $\Sigma(t)$ at the end of 1976. The locations of their epicenters and contributions to Σ are shown in Figure 4*b*. The major difference in the patterns of 1948 (Figure 4*a*) and 1976 is the following: the peak in 1948 was formed mainly by one earthquake, $M = 7.7$, which contributed 64% of Σ and was located relatively close to the earthquake of 1950 (see Figure 4*a*). The more recent peak is formed by several relatively weaker earthquakes, two with $M = 7.1$, three with $M = 7.0$, three with $M = 6.5$, and so on. The epicenters of these earthquakes are distributed over two regions, each contributing about one half of Σ. This difference may be important. However, we know of no reasons to withdraw the forecast of an enhanced probability of occurrence due to such a difference; indeed, the experience of *Keilis-Borok and Malinovskaya* [1964] suggests just the opposite, namely, that pattern Σ preceding a strong earthquake can be formed by several earthquakes, as well as by a single

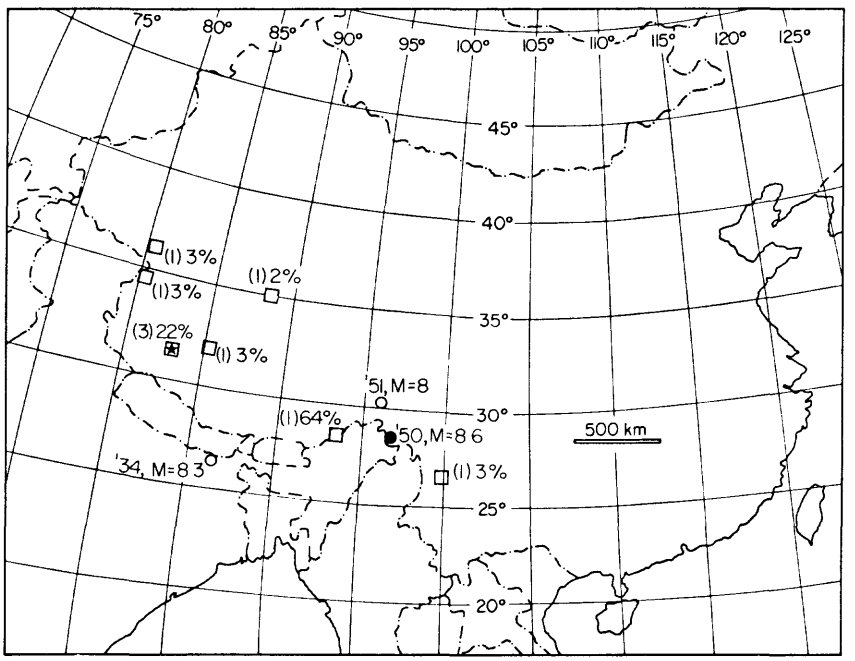

Fig. 4*a*. Epicenter of the 1950 Assam-Tibet earthquake (solid circle) and locations of the earthquakes which formed patterns Σ and S in 1943–1947 (squares). Parentheses indicate numbers of events at given locations, and percentages indicate individual contributions to Σ. The star indicates the location of the swarm which gave rise to pattern S. The 1934 and 1951 epicenters are indicated by open circles.

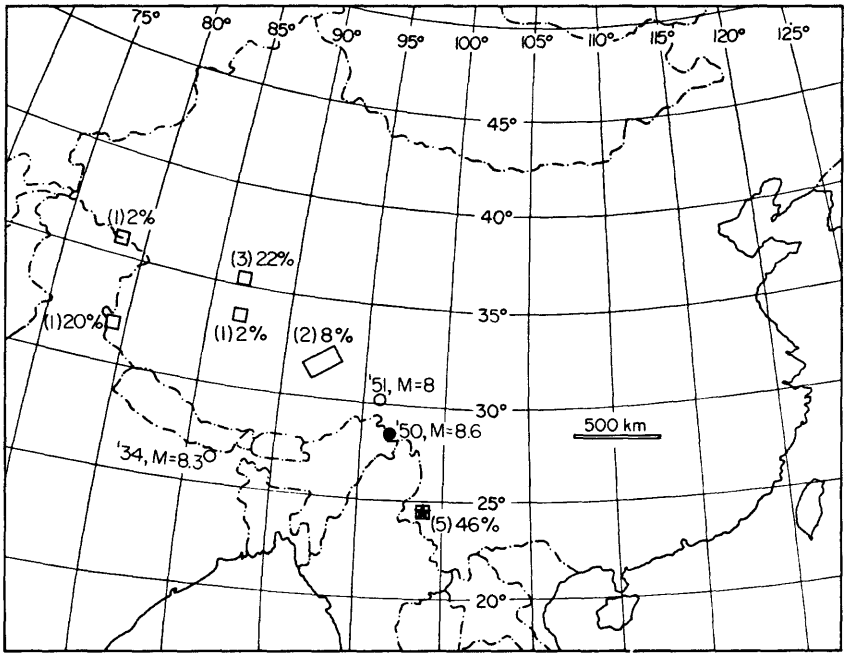

Fig. 4*b*. Pattern Σ in 1977. Symbols are the same as in Figure 4*a* except that squares indicate earthquakes in 1973–1976 contributing to peak of Σ.

one with larger magnitude. One might simply replace pattern Σ by the occurrence of a single earthquake with sufficiently large magnitude or, equivalently, by a peak of energy release. However, this would greatly increase the number of errors (both false alarms and failures to predict), since the correlation between strong and slightly smaller earthquakes, although positive, is too weak to be of value as a precursory criterion.

We discuss the corrections to the earthquake catalog introduced in *Academia Sinica* [1976]. For the region under consideration the only significant changes took place for the earthquakes of 1973–1976. These are summarized in Table 3. The corrections will lead to the following changes in our analysis: the peak of $\Sigma(t)$ in 1976 will increase to 2100; evidently the peak in 1948 will remain the same. In other words, pattern Σ in 1977 will become more pronounced. At the same time, 75% of the peak of Σ in 1976 will be contributed by the cluster of earthquakes at the southeast corner of the region, so that the above mentioned difference between pattern Σ in 1948 and 1976 will not be as great. Three additional earth-

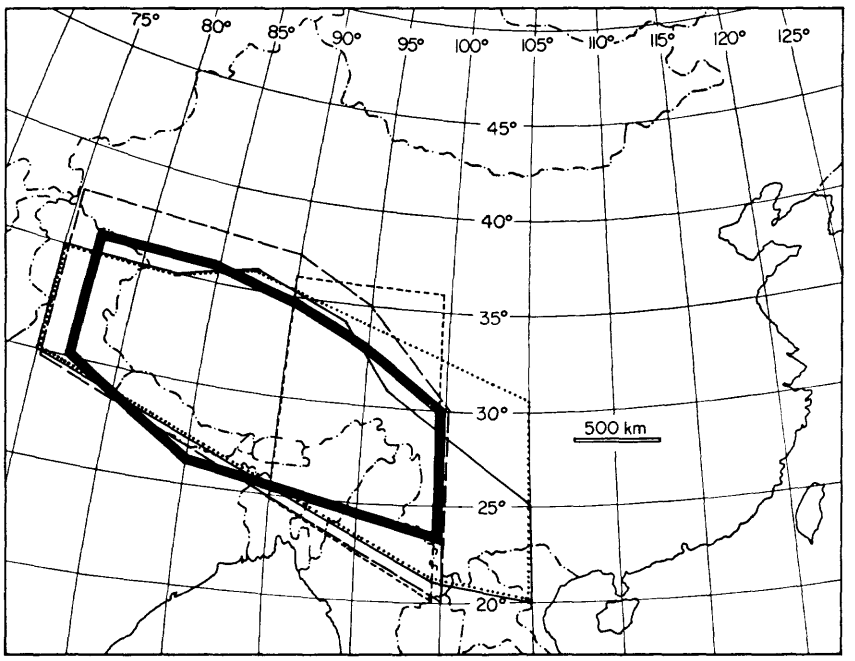

Fig. 5. Variations in the boundaries of the region. Original test area I is indicated by the heavy solid line. The long-dashed line indicates test area A; the thin solid line test area B; the dotted line test area C; and the short-dashed line test area D.

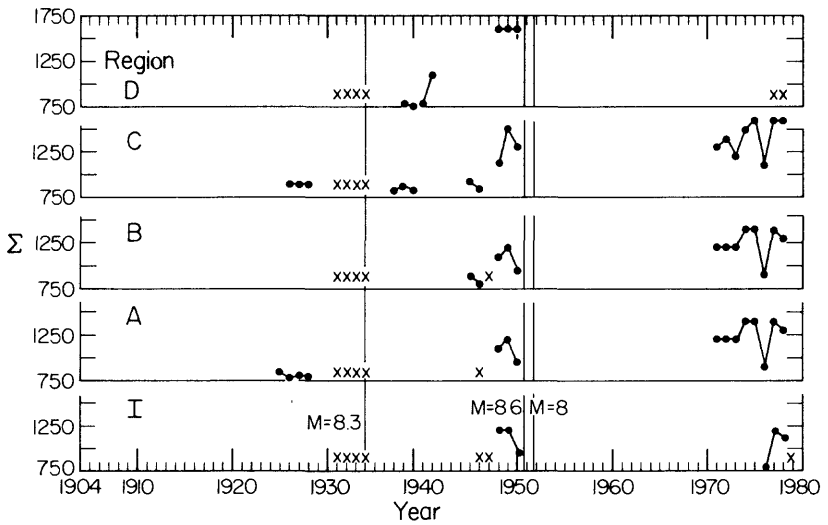

Fig. 6. Stability of patterns Σ and S to variations in the boundaries of the region. Solid circles represent values of Σ greater than 750; crosses indicate the identification of pattern S. Regions are as defined in Figure 5.

quakes in 1976 (May 29, June 1, July 4) will amplify the swarm of 1976 by producing an increase in both n and r by 3, so that both thresholds will be passed and pattern S diagnosed. Comparison of the catalog which we used with the NOAA catalog shows no differences which influence our conclusions. The only exception is the earthquake of 1934, M = 8.3, which we have taken into consideration.

If we consider the peak of Σ in 1976 to be a precursor to a strong earthquake with $M \geq 8$, the following questions arise: when is it expected, what is the probability of its occurrence, and where within the region may its epicenter be located? These questions have no exact answers, since our experience is too limited. Moreover, to narrow the place and time of a predicted earthquake, one should also study medium and short-term precursors. According to *Keilis-Borok and Malinovskaya* [1964] the time interval between the appearance of pattern Σ and the following strong earthquake is 8–16 years for magnitudes of strong earthquakes 8–8.6, respectively. Later experience with other patterns [*Caputo et al.*, 1979; *Keilis-Borok et al.*, 1979] suggests shorter intervals, so that it seems reasonable to expect an earthquake of magnitude about 8 in the study region some time before 1985 or of about 8.6 before 1993.

We estimate how informative this statement is by comparison with a Poissonian model of earthquake occurrence. We base our calculation on the assertion that three strong earthquakes have occurred in this century in or very close to the study region. These are 1905 (M = 8.0), 1934 (M = 8.3), and 1950 (M = 8.6). For our purposes we take the 1951 event (M = 8.0) as an aftershock of the stronger 1950 event, even though they occurred about 6° apart; in our analysis we are unable to forecast the second of two events occurring within such a short time span. Based on a model of occurrence in which 3 events with $M \geq 8$ occur randomly in 78 years, during the next 6 years, at least one earthquake with $M \geq 8$ will occur with a probability of about 21%; similarly, based on a random rate of occurrence of one event per 78 years, during the next 14 years, at least one earthquake with $M \geq 8.5$ will occur with a probability of 17%. We have arbitrarily chosen to start our calculation with the year 1900, thereby including the 1905 event but deleting the 1897 event from our list; this has represented to us a reasonable compromise between the extremes including both the 1897 and 1905 events or deleting them both according to choice of date of start of the catalog. The inclusion of events near the turn of the century, which was a period of unusually high world-wide seismicity, overestimates the probability of occurrence for the near future. In any case the expectation based on patterns Σ and S is statistically significant when compared with that of randomly occurring events. A defect of this calculation is that we have estimated the probability of occurrence of an event with $M \geq 8.5$ in the next 14 years from a Poisson rate of one earthquake with this magnitude per 78 years. The rate may be significantly different; if it is lower than 1/78, then our Poissonian comparison probability is reduced. Comparison models other than the Poissonian random model can be introduced at the reader's discretion; these may raise or lower the comparison probabilities compared with those given above, but such models are too numerous for us to anticipate on an individual basis.

It is difficult to estimate the probability of a false alarm. If was below 20% in the previous studies of the occurrence of pattern Σ before strong earthquakes, but our experience is much too limited to accept this figure for any consequential purpose. More accurate estimates will require that we study other medium-term patterns. Other patterns are also necessary for attempts to specify the places of future epicenters within the very large region.

CONCLUSIONS

Within the area of this study, which encompasses the central and eastern Himalayas, the seismicity pattern Σ has occurred only once during the 1900–1975 period, in 1948. This was followed in 1950 by the largest earthquake during the period, the Assam-Tibet event of M = 8.6. The seismicity pattern S also preceded the 1950 earthquake but was only marginally diagnostic; it also occurred once before, in 1933, prior to the only other earthquake with magnitude exceeding 8.0 during the test period, the 1934 Bihar-Nepal event of M = 8.3. Both premonitory patterns were generated by earthquakes that were widely distributed throughout the region, particularly near the northern and eastern borders, and were by no means limited to the specific areas of the major events and their aftershocks. A large contribution to the peak in Σ that preceded the 1950 event was in fact from earthquakes centered more than 1,000 km to the west, although the largest

single contribution came from a somewhat closer earthquake with $M = 7.7$. A possible qualitative explanation is that patterns Σ and S indicate that the plate boundary between the Indian and the Eurasian plates is becoming progressively unlocked; redistributions of stresses trigger the more localized large events.

A clear pattern Σ and a marginally diagnostic pattern S reappear for the Himalaya-Tibet region in 1976. In view of past experience regarding premonitory patterns in this region and others [*Keilis-Borok and Malinovskaya*, 1964] this pattern suggests the approach of an earthquake of at least $M = 8$ somewhere in the region and suggests that it should occur within the next 14 years if it is as large as $M = 8.5$. Such a prognostication should be regarded more as an experimental long-term forecast of an enhanced probability of occurrence than as an actual prediction, in view of the exceedingly large area encompassed (including parts of six countries) and the very lengthy time window. In our opinion it calls mainly for a vigorous scientific effort to identify medium- and short-term precursors in the region. Furthermore, we emphasize the following points. (1) Earthquakes of very large magnitude are relatively frequent in this region anyway, having occurred recently in 1897, 1905, 1934, and 1950. We estimate that the probability of a randomly occurring event of $M = 8.5$ during any given 14-year period is about 17%. (2) A clear possibility obviously exists that the allegedly precursory pattern is instead a false alarm, and the state of the art is such that we can at present have only limited confidence in such prognostications. On the basis of using this particular technique in other parts of the world, we estimate that the probability is perhaps 80% that the forecast of an enhanced probability of occurrence is in fact valid, although this estimate must to some degree be tempered by the fact that clear precursory patterns in Σ preceded only one of the two largest earthquakes in this particular region during the test period.

In summary, the primary impact of this study should, in our opinion, be to stimulate the search for medium- and short-term precursors in the Himalaya-Tibet area and to stimulate the search and evaluation elsewhere in the world for long-term precursors similar to those suggested in this paper.

Acknowledgments. The present study was carried out as a part of Project III of the program of Soviet-American cooperation in earthquake prediction while one of the US (V.I.K-B.) was a visiting scientist at the Seismological Laboratory of the California Institute of Technology, where he was a Sherman Fairchild Distinguished Scholar, and at the Institute of Geophysics and Planetary Physics of the University of California, Los Angeles. The visit of Keilis-Borok to the United States was supported by the Fairchild Foundation through Caltech and by the U.S. Geological Survey. W. Lee provided us with invaluable consultations on the seismicity of China. The assistance of M. French is gratefully acknowledged. E. R. Engdahl and W. Rihenhart helped us to obtain recent supplements to the NOAA earthquake file. We appreciate critical comments by D. L. Anderson. Contribution number 3177, Division of Geological and Planetary Sciences, California Institute of Technology, Pasadena, California 91125. Publication number 1876, Institute of Geophysics and Planetary Physics, University of California, Los Angeles, California 90024.

REFERENCES

Academia Sinica, Catalog of strong earthquakes in China, 780 B.C.–1976 A.D., $M \geq 6$, Peking, 1976.

Caputo, M., P. Gasperini, V. Keilis-Borok, N. Marcelli, and I. M. Rotvain, Earthquake swarms as forerunners of strong earthquakes in Italy, *Ann. Geofis. Rome*, in press, 1979.

Keilis-Borok, V., and L. N. Malinovskaya, On regularity in the occurrence of strong earthquakes, *J. Geophys. Res., 69*, 3019, 1964.

Keilis-Borok, V., and I. M. Rotvain, On soon-to-break seismic gaps, *Proceedings of the Conference on Seismic Gaps*, U.S. Geological Survey, Menlo Park, Calif., 1979.

Keilis-Borok, V., L. Knopoff, I. M. Rotvain, and T. M. Sidorenko, Bursts of seismicity as a long-term premonitory pattern, *J. Geophys. Res., 85*, this issue, 1980.

Lee, W. H. K., *Earthquakes and China*, U.S. Geological Survey, Menlo Park, Calif., 1976.

Lee, W. H. K., F. T. Wu, and C. Jacobsen, Catalog of historical earthquakes in China compiled from recent Chinese publications, *Bull. Seismol. Soc. Amer., 66*, 2003, 1976.

Lee, W. H. K., F. T. Wu, and S. C. Wang, A catalog of instrumentally determined earthquakes in China (magnitude ≥ 6) compiled from various sources, *Bull. Seismol. Soc. Amer., 68*, 383, 1978.

Molnar, P., and P. Tapponnier, Cenozoic tectonics of Asia: Effects of a continental collision, *Science, 189*, 419, 1975.

Richter, C. F., *Elementary Seismology*, 768 pp., W. H. Freeman, San Francisco, Calif., 1958.

Tapponier, P., and P. Molnar, Active faulting and tectonics in China, *J. Geophys. Res., 82*, 2905, 1977.

(Received March 6, 1979;
revised August 9, 1979;
accepted August 13, 1979.)

Formation of Coda Waves

V. A. Dubrovskiy
Institute of Physics of the Earth
Academy of Science, USSR

ABSTRACT

We studied two approaches to interpretation of the envelope of the coda wave. For a given wave length scattering may be described by the single-scattering theory for a certain type of inhomogeneity, when scattering is strong only along the direction of the primary wave (backscattering model). Diffusion theory deals with all other types of inhomogeneities. It is shown that the envelope of coda wave due to diffusion process decay exponentially with the decay constant decreasing with time. Then in a rough approximation we may express the coda envelope as the sum of two envelopes: back scattering envelope and diffusion envelope. The reciprocal of effective quality factor Q_{eff} becomes the sum of Q_d^{-1} responsible for scattering losses and Q^{-1} for irreversible nonelastic processes. In this case the rough evaluation gives rather high value of Q. The possibility of the earthquake prediction by the observations of the early part of the coda wave is discussed.

INTRODUCTION

The subject of coda wave formation is attracting more and more attention. Therefore, physical processes leading to long tails in seismograms should be investigated more carefully. Recent analysis of experimental data (Aki and Chouet, 1975; Rautian and Khalturin, 1978; Chouet, 1979; Aki, 1980) indicates that, first, the envelope of the coda wave constructed from peak to peak amplitude of the seismogram tails includes the factor

$$\exp(-\frac{\omega t}{Q}).$$

Secondly, the Q-factor turns out to be dependent on frequency: $Q \sim \omega^n$, where n varies, according to different reports, in a range of ~.5-1. This probably reflects differences in the properties of the crust and upper mantle in different areas. Moreover, for body waves in the crust and upper mantle there is also a frequency dependence of Q-factor (Fedotov and Boldyrev, 1969; Aki, 1980). The most striking fact is that the frequency dependence of the Q-factor for a propagating body S-wave and Q-factor for coda waves turn out to be identical or very close to each other (Aki, 1980).

In a number of works (Aki, 1969; Aki and Chouet, 1975; Kopnichev, 1975; H. Sato, 1977), theoretical analysis of formation of coda has been performed using model representations of weak scattering of both body waves and surface waves. Analysis has shown that the coda power at any time t (measured

from the earthquake origin time) in a given frequency band is given by (Aki and Chouet, 1975)

$$P(\omega,t) = S\, t^{-m}\, e^{-\omega t/Q} \qquad (1)$$

where source term S, which varies with earthquake magnitude, represents the effect of both primary and secondary wave sources. But within the scheme of single scattering theory in general use there is a serious conceptual difficulty concerning the physical meaning of Q introduced in (1). Should this Q include the loss by scattering in addition to the anelastic loss? The question is not trivial because the exponential factor in equation (1) was introduced at the early stage of obtaining equation (1) as if it is due to nonelastic dissipative losses. There is no obvious reason to include the loss by weak scattering. Analysis of a wide range of seismological data from completely different geological areas of the earth's crust and upper mantle indicates that formula (1), obtained from the weak scattering theory, agrees with observations if we allow the frequency dependence of Q. Here, we will attempt to discover the reasons for that and to clarify the physical meaning of the frequency dependence of Q.

The wave scattering model

Suppose that the scatterers are distributed randomly in space with the density n. Each one is characterized by a total cross-section defined as a ratio of scattered energy to incoming energy per unit area and differential cross-section defined as

a ratio of scattering energy into unit solid angle to incoming energy per unit area. The cross-section has the dimension cm^2 and is roughly proportional to the heterogeneity cross-section, and the proportionality factor is near unity in the range of wave length comparable with scattering size. In the case of a spherical wave generated at the origin, the change in energy due to scattering at the travel distance r is given by

$$J(r) = e^{-n\sigma r} J_o \qquad (2)$$

where $J(r)$ is the total energy carried by primary waves through the sphere of radius r, and J_o is the radiated source energy. In fact, the energy change of the spherical wave $J(r) - J(r+\Delta r)$ for distance Δr is equal, by definition of the cross-section, to $(\sigma J(r)/4\pi r^2)\ n4\pi r^2\ \Delta r$. Considering limit $\Delta r \to 0$ in $J(r) - J(r+\Delta r) = n\sigma J(r)\ \Delta r$ and integrating, we obtain equation (2). Thus, energy flows out due to scattering in the transverse direction to the propagation direction. The energy decreases according to equation (2).

We will now consider propagation from a source to an observation point. The wave conversion is neglected and only S-S scattering is considered. We will study below only single scattering, in which dissipation of the primary wave is described by equation (2). Strictly speaking, it is not correct to neglect the double scattering while assuming the equation (2) for primary waves, because both give rise to the term of second order in σ. It may be justified, however, when

the scattering is strong only in the forward and backward direction and weak otherwise. For example we may assume differential cross-section in the form

$$\sigma(\cos\eta) \sim a^2 \delta_\varepsilon (1-\cos\eta) \qquad (3)$$

where δ_ε is some smearing δ-function, η is angle between the direction of the scattering and the direction from a inhomogeneity to the source and a is proportional to a size of the inhomogeneity. It may be also a reflection on some discontinuities in the Earth's interior. But the input due to such reflections is rather small (Kopnichev, 1978). Consider an ellipsoidal rotation surface with foci at the source and receiver. The scatterers distributed on the surface contribute to coda at the same time. The greater (n) and the smaller (m) half-axes of the ellipse which forms the ellipsoidal rotation surface, are, respectively,

$$n = \frac{ct}{2} \qquad m = \frac{\sqrt{c^2 t^2 - \Delta^2}}{2}$$

where Δ is the epicentral distance. Let θ be the angle between a line from the epicenter to the observation point and a line from the epicenter and the scattering point of the ellipsoid. The distance from the epicenter to the scatterer is r. Then, the energy transmitted in the direction of the observation point is

$$\Delta J = \frac{\sigma(\cos\eta)}{4\pi r^2} J = \frac{\sigma(\cos\eta)}{4\pi r^2} e^{-n\sigma r} J_o \qquad (4)$$

where $\sigma(\cos\eta)$ is a differential cross-section (3), depending only on the angle between the direction of primary wave propagation

and the direction of scattered waves with $\cos\eta = (r^2 + (ct-r)^2-\Delta^2)/2r(ct-r)$. At the observation point, using equation (2) for attenuation, we have

$$J_s = \frac{a^2 e^{-n\sigma(ct-r)}}{(ct-r)^2}\,\Delta J = \frac{\sigma a^2}{4\pi r^2 (ct-r)^2}\; e^{-n\sigma ct} J_o \qquad (5)$$

where a is the effective radius of scatterer, proportional to $\sqrt{\sigma}$. Now we integrate (5) over the ellipsoidal shell which corresponds to the time interval t and t + δt, so we obtain the energy brought to the coda from all sources located inside the mentioned ellipsoidal layer

$$I = n\int J_s r^2 \sin\theta\, d\theta\, dr\, ds = \frac{-\omega t}{e^{Q}} e^{-n\sigma ct} \frac{2\pi n a^2}{2} J_o \int_0^{\pi} \sin\theta\, d\theta \int_{\frac{c^2 t^2-\Delta^2}{2(ct-\Delta\cos\theta)}}^{\frac{c^2(t+\delta t)^2-\Delta^2}{2(c(t+\delta t)-\Delta\cos\theta)}} \frac{\sigma\, dr}{(ct-r)^2} \qquad (6)$$

Here we used the equation $r = (c^2t^2-\Delta^2)/2(ct-\Delta\cos\theta)$ for the ellipse which forms the surface of the rotation. Also, the factor $e^{\frac{-\omega t}{Q}}$ has been added to describe nonelastic losses. The integration in (6) is rather simple if σ is constant (Kopnichev, 1975; Sato, 1977). We do not know with enough precision the dependence of the differential cross-section on a scattering angle. Moreover, this dependence can be rather unstable in the intermediate frequency band (ka~1). This is shown by numerical analysis performed for a complete cross-section of scattering on elastic spherical inclusion embedded in the elastic environment (Truell and others, 1969). However, we are interested in the envelope of the coda wave described by (6) in asymptotic case

$$\frac{\delta t}{t} << \frac{\Delta}{ct} << 1 \qquad (7)$$

The condition inequality (7) means that the time interval t between the wave pulse emission and observation is greater compared to the epicentral distance Δ and even greater compared to δt, time needed to form the scattered wave. Using the first of the inequalities in (7) and the average theorem one could estimate the second of the integrals in equation (6) up to the first order accuracy of $\delta t/t$. If $(\Delta/ct) \to 0$, the other integral is easily estimated. Now, under assumption (7), one can obtain an estimate of (6). In fact,

$$I \simeq \frac{2n\sigma_s a^2 C\delta t}{c^2 t^2} \; e^{-n\sigma ct} \; e^{-\frac{\omega t}{Q}} \; J_o \qquad (8)$$

where $\sigma_s = \sigma(\cos\eta = -1)$. This coincides closely with the expression which, after Aki, is used by all authors to interpret the envelope of coda waves. It would be exactly equal to (1) if the effective Q-factor (quality factor) were introduced.

$$\frac{1}{Q_{eff}} = \frac{1}{Q_d} + \frac{1}{Q} \qquad (9)$$

where Q_d has a form

$$Q_d = \frac{\omega}{n\sigma c} \qquad (10)$$

One should note that in (8) the factor independent of time is proportional to $\sigma^{5/2}$. Indeed, one can show that the quantities Q and $c\delta t$ introduced to obtain (8) are proportional to the effective scattering radius, i.e. each of them is proportional to $\sigma^{1/2}$.

Now the physical meaning of the frequency dependence of quality factor becomes clearer. The factor is used for analysis and interpretation of coda wave using (1). The effective Q^{-1} is a sum of Q^{-1} responsible for scattering losses and Q^{-1} for irreversible nonelastic processes.

The frequency dependence of Q appears to come from the frequency dependence of Q_d due to back-scattering. The frequency dependence of Q_d is not simple because it contains the total effective cross-section. The frequency dependence of total cross-section turns out to be unstable and sensitive to the contrast of elasticity and density between inclusion and matrix. As shown by model computations for the case of scattering by a spherical inclusion (Truell et al, 1969, Appendix M), the cross-section may oscillate around a value $\sigma_n = (\sigma/\pi b^2) \sim 1$ (b is the radius of spherical inclusion); or it may change smoothly or remain constant for different cases of contrast between inclusion and the matrix in a range of kb from one to ten. The oscillations of σ with change in frequency are due to a presence of eigenfrequencies of the spherical elastic scattering. Since the oscillator is in a matrix which consumes the oscillation energy as radiation, each spectrum line of the oscillation has a finite band width. In other words, each eigenfrequency has its own decrement factor (Dubrovsky, 1977). The decrement value may be very sensitive to interrelation between the parameters of inclusion and matrix. We will return to this problem later.

It is not surprising, then, that different authors give different degrees of the effective factor change for primary and coda waves. Naturally, due to the large samples of statistical data and the statistical character of addition of scattered waves, such details as oscillation of σ, (still important for geophysics) are being averaged.

It is interesting to note that if (9) is true then one can make an estimate for the frequency independent part of the quality factor at high frequencies. A summary of the frequency dependence of the quality factor is presented in Aki's paper (Aki, 1980, Fig. 1). It is easy to see that all the curves go to a level of approximately $.5\ 10^{-3}$ at high frequencies. It implies that the quality factor describing irreversible nonelastic losses must have a rather high value, about 2000. In other words, the scattering losses are much greater than nonelastic ones. So far, we have considered the single-scattering theory assuming that the scattered energy is concentrated only in forward and backward directions. If this is not the case, multiple scattering must be considered. It is, however, practically impossible to consider all segmented trajectories which connect the earthquake center and the observation point and have the same length ct. So, one should reconsider the simple scheme described above and try another, more realistic one. One possibility, and perhaps the only one at the present time, is the diffusion equation approach which we shall discuss in the next section.

Diffusion approach.

While propagating, the wave pulse meets scattering centers and loses part of its energy as a result of reemission by the scattering center. The energy will dissipate later through multiple scattering processes and nonelastic losses. It is known (Morse and Feshbach, 1961; Aki and Chouet, 1975; Dainty and Toksoz, 1977) that the process may be approximately described by the diffusion equation

$$\frac{\partial E}{\partial t} - D\Delta E - \frac{\omega}{Q} E = q \qquad (11)$$

where E is the density of scattered energy, D is a diffusion coefficient, Q is the quality factor of nonelastic losses and q is a source density.

The diffusion coefficient D is determined by the wave propagation speed c, total cross-section σ and the density n of scatterers in the following way:

$$D = \frac{c}{3n\sigma} \qquad (12)$$

Our approach differs from previous ones (for example, Aki and Chouet, 1975; Dainty and Toksoz, 1977) since we consider the scattering objects as energy sources, following the idea described by Morse and Feshbach (Morse and Feshbach, 1961). The wave intensity is determined by the total cross-section using as we did in the previous section, as follows:

$$q = \frac{n\sigma}{4\pi r^2} e^{-n\sigma r} \delta(t - \frac{r}{c}) J_o \qquad (13)$$

where delta-function $\delta(t - \frac{r}{c})$ fixes the moment when the

energy is lost to the matrix at point r.

Thus, we solve equation (11) for infinite space. Using a conventional Green function technique (Tikhonov and Samarski, 1967), we find from the three-dimensional Green function

$$Y(x,y,z,t) = \frac{1}{(4\pi Dt)^{3/2}} e^{-\frac{x^2+y^2+z^2}{4Dt} - \frac{\omega t}{Q}} \tag{14}$$

the solution of the above problem in the form

$$E = \frac{J_o \sigma n}{32\pi (\pi D)^{3/2}} \int_o^t \iiint_{-\infty}^{\infty} \frac{e^{-n\sigma r}}{r^2 (t-\tau)^{3/2}} e^{-\frac{(x-\zeta)^2+(y-\ell)^2+(z-\nu)^2}{4D(t-\tau)}} \tag{15}$$

$$\delta\left(t-\frac{r}{c}\right) d\tau d\zeta d\ell d\nu, \quad r = (\zeta^2+\eta^2+\nu^2)^{1/2}$$

The solution in (15) sums up the contribution of dissipating energy from all sources of scattering. The sources merge after the primary wave passes. Performing integration over y and θ and using the delta-function over r, we arrive at the expression

$$E = \left(\frac{3}{\pi}\right)^{1/2} \frac{(n\sigma)^{3/2} e^{-n\sigma ct}}{2(ct)^{1/2}\Delta} J_o \int_0^1 \frac{e^{n\sigma ct\alpha}}{(1-\alpha)\alpha^{1/2}} e^{-\frac{3}{4}\frac{\eta^2+(1-\alpha)^2}{\alpha} n\sigma ct} \left\{ e^{\frac{3}{2}\frac{1-\alpha}{\alpha}\eta n\sigma ct} - e^{-\frac{3}{2}\frac{1-\alpha}{\alpha}\eta n\sigma ct} \right\} d_\alpha \tag{16}$$

Expression (16) determines the time dependence of coda wave envelop at the observation point having epicentral distance Δ. One should note that the dependence itself varies with time due to complex behavior of the integral (16). Consequently, it cannot be represented in any simple analytical way at all times. Let us try to estimate (16) for different asymptotic cases using the saddle point method.

I. $\eta \lesssim 1$, when we observe the coda formation. For this time interval we have

$$E \simeq \frac{3}{\sqrt{2}} \frac{n^2\sigma^2}{\Delta} \frac{(ct)^2(ct-\Delta)\, J_o}{[c^2t^2-\frac{3}{2}(ct-\Delta)^2 n\sigma ct][2\Delta^2-6n\sigma\Delta(c\,t-\Delta)^2]^{1/2}} \qquad (18)$$
$$e^{-n\sigma\Delta-\frac{1}{6}} \quad e^{\frac{3}{8}[(ct-\Delta)n\sigma+\frac{2}{3}]^2}$$

An exponential growth with increasing $(ct-\Delta)$ occurs.

II. $\eta \ll 1$, $n\sigma ct \lesssim 1{,}5$ when the primary wave has passed a considerable distance as compared to Δ and we observe the very beginning of diffusion coda. This case takes place if $n\sigma\Delta \ll 1$.

$$E \simeq I\left(\frac{6}{\pi}\right)^{1/2} \frac{\sigma}{(ct)^2}\, e^{-n\sigma ct}\, e^{3\left(1-3\sqrt{1-\frac{(n\sigma ct)^2}{3}}\right)} \qquad (19)$$
$$\exp\left\{-\frac{(n\sigma ct)^2\left(1-\frac{3}{n\sigma ct}+\frac{3}{n\sigma ct}\sqrt{1-\frac{(n\sigma ct)^2}{3}}\right)}{4\left(1-\sqrt{1-\frac{(n\sigma ct)^2}{3}}\right)}\right.$$

where $I = \int_0^1 \exp\frac{3}{4\bar{\alpha}^2}\left(1-\frac{n\sigma ct}{2\bar{\alpha}}\right)(\alpha-\bar{\alpha})^2 d\alpha$ with $\bar{\alpha} = \frac{3}{n\sigma ct}\left(1-\sqrt{1-\frac{(n\sigma ct)^2}{3}}\right)$

There is a practically constant flow of energy into the diffusion part of the coda, since a small increase of the

exponential part with $\exp\{-2+(n\sigma ct+2)^2/8\}\sim e^{-3/2}$ at $n\sigma ct << 1$ to 1 at $n\sigma ct \sim 1,5$ may be compensated by a decreased exponent coefficient.

III. $\eta << 1$, $n\sigma ct > 1,5$ when the direct wave has passed a considerable distance and we observe only the coda. Since the integrated function in (16) in this case goes up smoothly from 0 at $\alpha = 0$ to $3\eta n\sigma ct \exp\{n\sigma ct\}$ we can evaluate approximately after expanding at $\eta \sim 0$ and take the integrated function at some $\alpha = \bar{\alpha}$ instead of the integral. After that, $\bar{\alpha}$ does not considerably differ from 1 if $n\sigma\Delta >> 1$, that is at big Δ. Then we have

$$E = \frac{3}{2}\left(\frac{3}{\pi}\right)^{1/2} \frac{\sigma^{5/2} n^{5/2}}{(ct)^{1/2}} J_o \frac{1}{\bar{\alpha}^{3/2}} e^{-\frac{4-(\bar{\alpha}+1)^2}{4\bar{\alpha}} n\sigma ct} \qquad (20)$$

The diffusion part of the coda goes to zero at large values of $n\sigma ct > 1$ very slowly. Namely, if $\bar{\alpha}$ differs from 1 by a value $\varepsilon << 1$ then the exponential decay is proportional to $\exp\{-\varepsilon n\sigma ct\}$, and ε becomes smaller when the time increases. It turns out to be less than in the case of single backscattering.

Discussion.

For a given wave length, scattering may be described by the single-scattering theory for a certain type of inhomogeneity and by the diffusion theory for another type. We may consider a given inhomogeneity as a sum of two types. Then, in a rough approximation, we may express the coda envelope as the sum of two envelopes obtained earlier.

Putting together formulae (8) and (20) and omitting unnecessary details, we can derive an expression for the coda envelope

$$J = A\{\frac{n_s(\sigma_s)^{5/2}}{c^2t^2} e^{-\frac{\omega t}{Q_d}} + B \frac{(n_d\sigma_d)^{5/2}}{(ct)^{1/2}} e^{-\varepsilon\frac{\omega t}{Q_d}}\} e^{-\frac{\omega t}{Q}} J_o \qquad (21)$$

where A and B are constants subject to experimental determination. The quality factor Q_d is given by (10), n is the number of each kind of scatterings per unit volume. Q is the quality factor due to nonelastic losses and ε is small as compared to 1 and slowly decreases with increasing time. Expression (21) implies that the general character of the decay due to single and multiple scattering will be determined by a successive entering in time of each of two terms in the parentheses (21). Thus we have shown that single and diffusion scattering each plays its own role under different frequencies and scattering sizes. Each one is related to its cross-section and quality factor Q_d is

$$Q_d = \frac{\omega}{n_d\sigma_d c} \qquad (22)$$

where σ_d is the diffusion scattering cross-section, which is close to the total cross-section. Both processes describe different phenomena and complement each other.

The coda wave and earthquake prediction

As is implies by (21), the coda wave is directly dependent on the scattering cross-section. Since the latter heavily depends on frequency (on the relation between scattering size

and wave length), the coda wave must depend on the frequency. Moreover, in the middle frequency range, when $ka = 2\pi a/\lambda \gtrsim 1$, there are resonance phenomena related to reemission of the oncoming wave mostly at resonance frequencies. As shown in a monograph by Truell et al (1969) on the example of spherical scattering, the resonance pattern is most obvious when the scattering and the environment are not very different in their elastic rates. From the physical point of view, it is obvious that the narrower a resonance, i.e. the higher the quality factor of the inhomogeneity, the more significant reemission we have, i.e. the greater cross-section at the corresponding resonance. On the other hand, the coda wave collects scattered or reemitted wave from a great volume, and it therefore carries integral information about the scattering features of the medium. The scattering information in the earthquake source area on the other hand is contained in the early part of coda if the observation station is located not far from the center of a small earthquake. Suppose now that as a result of tectonic stress increase (which can cause strong earthquakes), inhomogeneities are created in the area of a future earthquake. The scattering due to the inhomogeneities can be the volumes, filled by microcracks which usually lead to a reduction of the effective elastic moduli by 10-15% before the earthquake. In this case, the relative amplitude of early part and later part of the coda from small earthquakes can provide information

about changes in the stressed states of the earth's interior in the area of an anticipated major earthquake. Let us show using a spherical model of scatterer, how the quality factor of torsion vibrations changes, and scattering features as well, depending on changes in the contrast in shear modulus between the sphere and the matrix. In order to do that we need to obtain a solution for the sphere and for the matrix by specifying boundary conditions of displacement and stress continuity and emmission conditions at infinity. The result is similar to the case of radial vibrations (Dubrovsky, 1977) and leads to the following complex transcendent equation for the lowest mode (n=1) of the torsion vibrations

$$\frac{\chi}{\alpha} \operatorname{ctg} \frac{\chi}{\alpha} = 1 - \frac{\chi^2}{\eta} \frac{1+i\chi}{\chi^2 - i3\beta\chi - 3\beta} \qquad (23)$$

where $\chi = \omega \ell / c_{se}$ is a dimensionless frequency, ℓ is the radius of sphere, $\alpha = c_{si}/c_{se}$ is a ratio of shear wave velocity for sphere (C_{si} and matrix (C_{se}). $\eta = \rho_e/\rho_i$ is the corresponding ratio of densities and $\beta = (\mu_e - \mu_i)/\mu_e$ is dimensionless parameter characterizing a contrast of the shear modules. The solution of equation (23) is a set of complex frequencies $\chi^{(m)} = \chi_o^{(m)} + i\,\chi_1^{(m)}$ where the real part $\chi_o^{(m)}$ defines a spectrum of eigen-frequencies $\omega^{(m)} = \chi_o^m\, C_{se}/Q$ and the imaginary part defines corresponding decrements $\gamma^{(m)} = \chi_1^{(m)} c_{se}/Q$. The names are justified by the fact that the outside solution for r-dependence of the displacement is the Hankel function of a complex argument

$$u_e = A\left(\frac{c_{se}}{(\omega^{(m)}+i\gamma^{(m)})\tau} - i\,\frac{c_s^2}{(\omega^{(m)}+i\gamma^{(m)})^2\tau^2}\right)e^{i\omega^{(m)}\left(t-\frac{\tau}{c_{se}}\right)}e^{-\gamma^{(m)}\left(t-\frac{\tau}{c_{se}}\right)} \quad (24$$

It represents a moving spherical wave of frequency $\omega^{(m)}$ decaying at each fixed point according to law $\exp\{-\gamma^{(m)}t\}$. Separating real and imaginary parts in (23) and having in mind that we are looking for a solution with a high quality factor $Q_i = \omega^{(m)}/\gamma^{(m)} \equiv \chi_o^{(m)}/\chi_i^{(m)} >> 1$, we end up with the following system of transcendent equations:

$$\begin{aligned} &\frac{1}{\alpha}\,\mathrm{ctg}\,\frac{\chi_o}{\alpha}\,\frac{\mathrm{cth}\frac{2\chi_1}{\alpha}-1}{\mathrm{ctg}\frac{2\chi_o}{\alpha}+\mathrm{cth}^2\frac{\chi_1}{\alpha}} \sim \frac{3\beta}{\chi_o} \\ &\frac{1}{\alpha}\,\mathrm{cth}\,\frac{\chi_1}{\alpha}\,\frac{\mathrm{ctg}\,\frac{2\chi_o}{\alpha}+1}{\mathrm{ctg}\,\frac{2\chi_o}{\alpha}+\mathrm{cth}\frac{2\chi_1}{\alpha}} \sim 1 + 3\beta\,\frac{\chi_1+2}{\chi_o^2} \end{aligned} \quad (25)$$

Here we use this for the case $\eta \simeq 1$ and $\beta \lesssim 0,15$. Since the eigenfrequencies $\chi_o^{(m)}$ belong to small range near $\alpha m\pi$ and decrements are not so sensitive to the number m, the approximations $\chi_o >> \chi_1$ made in obtaining (24) turn out to be valid, at least for upper harmonics. An estimate using (25) shows that χ_1 changes with β from .05 through .01, .15 up to .20 from 1.71, 1.30, 1.06, up to .88; i.e. a change of contrast by 15% leads to reduction of χ_1 from infinity with $\beta = 0$ to 1.06 with $\beta = 15\%$. Thus, a stressed state change leading to such scatterings can be detected in the coda wave as quality factor $Q \simeq 0,85 \cdot m \cdot \pi$ with $\beta \sim 15\%$. It may affect an increased magnitude of the early part especially, if the observation

point is not far from the anticipated earthquake area. Naturally, the approach to the possibility of the earthquake prediction by coda wave observations presented here needs further analysis, which may uncover some additional precursors. At the present time this possibility seems to be quite feasible.

In conclusion, we would like to make one more comment. We have investigated propagation and scattering of a wave pulse. This is true if observation times greatly exceed pulse duration. However, in the case of resonance scattering, each resonating scatter is going to reemit at the resonant frequencies according to (25) and (24) with quality factor of each partial wavelet $Q_i = \omega^{(m)}/\gamma^{(m)}$ depending on the contrast between inclusion and matrix. The higher the contrast, the higher the cross-section and the longer the wavelet.

Acknowledgements

This work was carried out during the author's stay at MIT as a part of US-USSR Joint Cooperative Scientific Program on Earthquake Prediction in collaboration with K. Aki, to whom I am very grateful.

References

Aki, K., 1980, Scattering and Attenuation of Shear Waves in the Lithosphere, J. Geophys. Res., in press.

Aki, K., and B. Chouet, 1975, Origin of coda waves: source, attenuation and scattering effects, J. Geophys. Res. 80, 3322-3342.

Chouet, B., 1979, Temporal variation in the attenuation of earthquake coda near Stone Canyon, California, Geophys. Res. Lett., 6, 143-146.

Dainty, A. M. and Toksoz, M. N., 1977, Elastic wave propagation in a highly scattering medium - a diffusion approach, Jour. of Geophysics 43, 375-388.

Dubrovsky, V. A., 1977, Seismic oscillation of the inclusions, in the issue Problems of the vibrosounding of the Earth, publish. Science, in Russian.

Fedotov, S. A. and Boldyrev, S. A., 1969, Frequency dependence of the body-wave absorption in the crust and the upper mantle of the Kuril-Island chain, Izv., Earth Physics, No. 9, 17-33.

Kopnichev, Y. F., 1975, Modes of the formation of the coda part of seismograms, Reports of Academie of Science USSR, 222, N2, 333-335.

Kopnichev, Y. F., 1978, Seismic coda wave, Publisher Science, in Russian.

Morse, P. M. and Feshbach, H., 1961, Methods of theoretical physics, McGraw-Hill, New York.

Sato, M., 1977, Energy propagation including scattering effects single isotropic scattering approximation, J. Phys. Earth, 25, 27-41.

Truell, B., Elbaum, Ch. and Chick, B. B., 1969, Ultrasonic Methods in Solid State Physics, Acad. Press, New York-London.

Tychonov, A. N. and Samarski, A. A., 1970, Partial differential equations of mathematical physics, Holden-Day, Inc.

Rautian, T.G.and Khalturin,V.I. 1978. The Use of the Coda for Determination of the Earthquake Source Spectrum. Bull.Seismological Soc. Amer. Vol.68,Number 4, p923-948

AN EVALUATION OF THE RESPONSE OF AN EXPERIMENTAL FRAME AND PANEL BUILDING TO EARTHQUAKE LOADS*

by

S.Kh. Negmatullaev, C. Rojahn and A. I. Zolotarev

The goal of this investigation was to evaluate the response of an experimental, full-scale, frame and panel building to the simulated acceleration of strong earthquakes and, using this as an example, to develop methods of designing frame structures to withstand random seismic actions. The subject of the study is a type of frame building developed by designers of the Tadzhik-giprostroy Institute, termed the "Tadzhikskiy Frame" (TK), which was designed for construction in the ninth zone of seismic intensity (on the Soviet intensity scale). The experimental test building was erected at the experimental proving ground of the Institute of Seismic Resistant Construction and Seismology of the Academy of Sciences of Tadzhikskaya SSR.

1. Brief design features

Figure 1 shows the plan and section views of the experimental building, a three story frame building of precast and reinforced concrete, poured in place. The columns of the frame are precast, reinforced concrete ($f_w c'$=200Kg/cm^2) 35 x 35 cm in section. The precast columns extend the entire height of the building except for sections at each floor level that are poured in place.

The reinforced concrete ($f_w c'$=200 Kg/cm^2) are poured in place. The floor and roof decks are precast, reinforced-concrete ribbed plates, which are installed during assembly of the supporting columns. The plates are connected to one another by welding the reinforcing bars which extend from each plate. The lateral ribs of the plates serve as a concrete form for the poured-in-place beams, which are poured around the welded connections. Wall panels are made of precast, lightweight aggregate concrete ($f_w c'$=50Kg/cm^2) with panel thickness of 25 cm. The panels are suspended from the cast-in-place beams. The building is founded on spread footings, which are connected on the building perimeter by reinforced-concrete foundation girders. Sandy loam deposits with depths up to 180m serve as the base of the building.

2. Solution to the problem of eigenvalues and eigenvectors

Let us examine the dynamic model of a regular structure (Figure 2). We consider a model in which the compliance matrix **C**, the stiffness matrix **K**, and the mass matrix **M**, are sufficiently consistent. If the number of degrees of freedom **n**, the matrix **K**, and the diagonal matrix **M**, are given, then the problem of undamped, free vibrations is written in the form:

*Translated from the Russian: Further details are in reference 34.

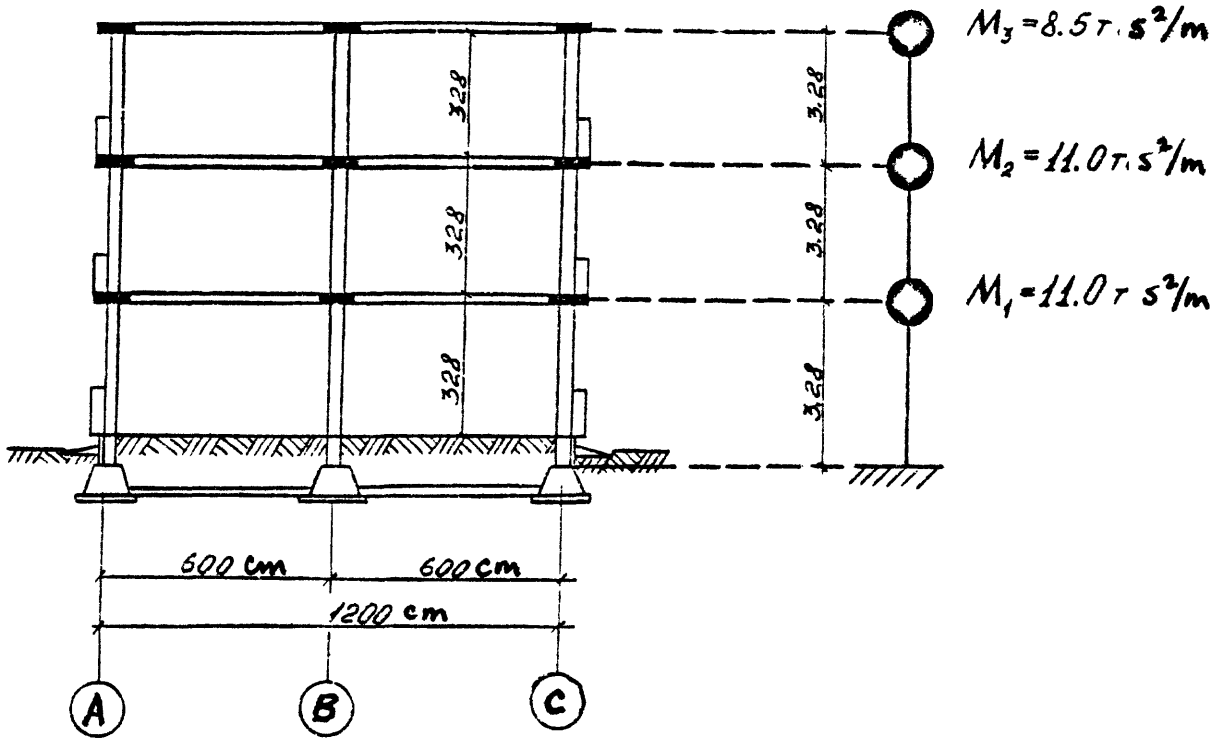

Figure 1. Plan and section views and floor masses of the experimental frame building

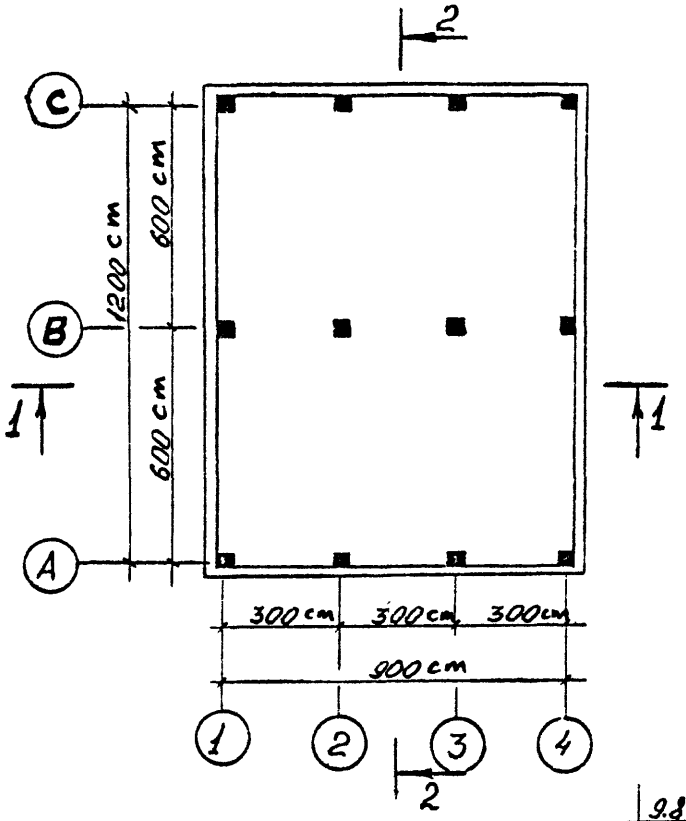

Plan

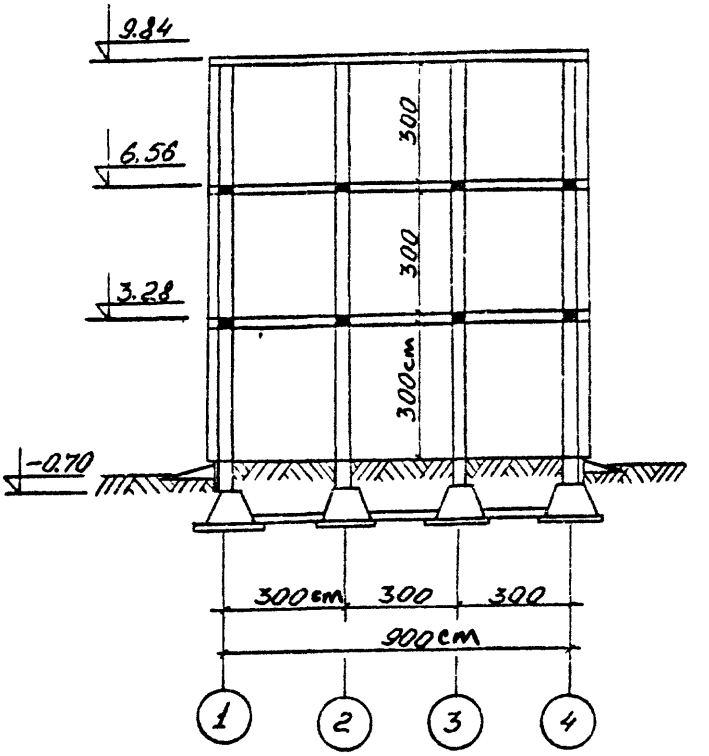

Section I-I

$$KY = -M\ddot{Y}, \qquad (1)$$

where the vector-function $Y(t)$ contains all of the degrees of freedom being examined $Y_1(t), Y_2(t), \ldots, Y_n(t)$.

If in (1) we substitute

$$y(t) = X \cdot \sin(pt + \varepsilon), \qquad (2)$$

where X - is an unknown numerical vector, and p - is an unknown frequency, then the problem reduces to a search for the eigenvalues of $\lambda = p^2$ for a homogeneous problem

$$KX = \lambda \cdot MX, \ (\lambda = p^2). \qquad (3)$$

In the general case the spectrum of eigenvalues $\lambda_1, \lambda_2, \ldots \lambda_n$ and the corresponding eigenvectors $X_1, X_2, \ldots X_n$, with the given specific matrices K and M can be found only by numerical methods, which are available in modern computers in the form of standard programs.

However, if the matrices K and M have a sufficiently regular structure, then we can try to solve the problem in the following manner: find the analytical function of three arguments i, k, and n $F(i,k,n)$ and the function of two arguments $f(i,n)$, which have the property that during substitution of a certain numerical value $i < n$ in place of the letter argument i and in place of n the specific number of the degrees of freedom of a regular calculated model being examined, the eigen number λ_i is derived, and the function (i,k,n)

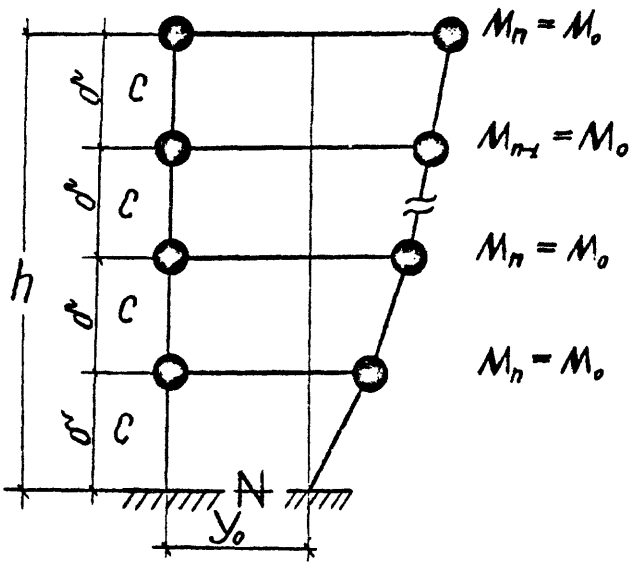

Fig. 2. Dynamic model of a regular structure.

when $k = 1, 2, 3, \ldots, n$ yields the corresponding components of the eigenvector X_i. In this case we can find all the eigenvalues λ_i and the eigenvectors X_i practically without errors.

For the model being examined we will assume that the cantilever is under only shear stress between the two masses. Such a simplified dynamic model corresponds with a sufficient degree of accuracy to a regular frame, in which all

the floors are absolutely rigid plates. In this case rigidity of a cantilever is determined from the formula:

$$c = \sum \frac{12 E_k J_k}{\delta^3}, \quad (4)$$

where the sum is spread over all the columns of a floor (all floors are identical).

If, in addition to the frame columns, one must consider certain more rigid end plates which are under shear stress, then to this total one should add the terms of the form $c_g = \frac{KG_g F_g}{\delta}$, which take into consideration the rigidity of these endplates.

The basic plan of the method of displacements is accomplished in the case being considered by introduction of horizontal forces, which are capable of securing the given static shifts $y_1, y_2, \ldots, y_n$ in a horizontal direction. The force $-M_0\ddot{y}_k$ acts on the mass which is k-th in order (all masses are identical and equal M.). We shall write the equilibrium condition for the k-th support force of a cantilever:

$$R_{k,k+1} + R_{k,k-1} = M_0\ddot{y}_k, \qquad (5)$$

where $R_{k,k+1} = c\cdot(y_{k+1} - y_k)$, $R_{k,k-1} = -c\cdot(y_k - y_{k-1})$.

By substituting the values $R_{k,k+1}$ and $R_{k,k-1}$ into (5) we obtain:

$$c\cdot(-y_{k-1} + 2y_k - y_{k+1}) = -M_0 y_k. \qquad (6)$$

Note that this equality is valid only when $k = 1, 2, 3 \ldots n-1$. The equilibrium of the n-th mass is written differently:

$$c(y_n - y_{n-1}) = -M_0\ddot{y}_n. \qquad (7)$$

In addition to this the equilibrium condition for the first mass has the form:

$$c\cdot(2y_1 - y_2) = -M_0 y_1. \qquad (8)$$

This expression coincides with the general formula (6) only in the case where $y_{k-1} = y_0 = 0$.

Thus, the matrix of rigidities has the following structure:

$$K = C\,X \begin{vmatrix} 1 & -1 & 0 & 0 & - & - & - & - & 0 \\ -1 & 2 & -1 & 0 & - & - & - & - & 0 \\ 0 & -1 & 2 & -1 & - & - & - & - & 0 \\ - & - & - & - & - & - & - & - & - \\ - & - & - & - & - & - & - & - & - \\ 0 & - & - & - & - & - & -1 & 2 & -1 \\ 0 & - & - & - & - & - & 0 & -1 & 2 \end{vmatrix}, \quad (9)$$

here it is assumed that the components of the vector Y are renumbered in the following order: $Y_n, Y_{n-1}, \ldots, Y_2, Y_1$.

Only the first and last lines have the specific structure in (9). Note that the last line also becomes typical, when in matrix K_n one more column is formally added, in which the last element equals -1, and all the remaining elements equal zero. In this case it is necessary to increase by one the number of components of the vector Y by formal introduction of the last component Y_0, but require in this case fulfillment of the condition

$$Y_0 = 0 \quad (10)$$

Let us examine a homogeneous system of equations (3) with such regular matrices K and M. We will try to represent the components of the vector $X\{x_n, x_{n-1}, \ldots, x_1, x_0\}$ by the general formula:

$$x_k = A\varepsilon_1^k + B\varepsilon_2^k, \quad (11)$$

where A, B, ε_1, ε_2 are unknown values.

The problem consists in selecting these values so that when $k=n$ the component x_n is obtained, and when $k=n-1$ the number x_{n-1} is obtained, etc. When $k=0$ in conformity with (10) formula (11) should be transformed into 0, i.e.

$$A + B = 0. \tag{12}$$

Consequently,

$$x_k = A(\varepsilon_1^k - \varepsilon_2^k); \quad k = n, n-1, \ldots, 1. \tag{13}$$

The vector X, which is formed by such components, during multiplication by the matrix K in form (9) yields an n-dimensional vector KX with the components $\{v_n, v_{n-1}, \ldots, v_1\}$. It is clear that

$$v_n = c(x_n - x_{n-1}) = cA\cdot[\varepsilon_1^n(1-\varepsilon_1^{-1}) - \varepsilon_2^n\cdot(1-\varepsilon_2^{-1})], \tag{14}$$

When $k = n-1, n-2, \ldots, 1$ we have:

$$v_k = c\cdot(-x_{k-1} + 2x_k - x_{k+1}) = cA\cdot[\varepsilon_1^k\cdot(-\varepsilon_1^{-1} + 2 - \varepsilon_1) - \varepsilon_2^k\cdot(-\varepsilon_2^{-1} + 2 - \varepsilon_2)]. \tag{15}$$

From this it is evident that in order to fulfill the vector equality (3) the following conditions are required:

$$v_k = p^2\cdot M_0\cdot A\cdot(\varepsilon_1^k - \varepsilon_2^k), \quad k = n-1, n-2, \ldots, 1, \tag{16}$$

$$v_n = p^2\cdot M_0\cdot A\cdot(\varepsilon_1^n - \varepsilon_2^n). \tag{17}$$

All equalities of the type (16) will be fulfilled, if

$$c\cdot(-\varepsilon_1^{-1} + 2 - \varepsilon_1) = p^2\cdot M_0; \quad c\cdot(-\varepsilon_2^{-1} + 2 - \varepsilon_2) = p^2 M_0. \tag{18}$$

In other words, the numbers ε_1 and ε_2 must be radicals of the equation

$$\xi^2+\left(\frac{p^2 M_0}{c}-2\right)\cdot\xi+1=0. \qquad (19)$$

Because $\xi_1 \times \xi_2 = 1$ and the discriminant of this equation is negative, then we can assume:

$$\xi_1=e^{i\varphi},\quad \xi_2=e^{-i\varphi} \qquad (20)$$

Note that the numerical value of the amount φ remains unknown, for the magnitude of p^2 in (19) is unknown.

By taking (20) into account both equalities of (18) lead to the same relationship: $$p^2=\frac{c}{M_0}\left(2-e^{i\varphi}-e^{-i\varphi}\right)=\frac{c}{M_0}\left(2-2\cos\varphi\right)=4\frac{c}{M_0}\sin^2\frac{\varphi}{2}. \qquad (21)$$

It still remains to satisfy equality (17). For its fulfillment, as is easy to see, one needs the condition:

$$c\cdot\left[e^{i\varphi n}-e^{-i\varphi n}-e^{i\varphi(n-1)}+e^{-i\varphi(n-1)}\right]=p^2 M_0\cdot\left(e^{i\varphi n}-e^{-i\varphi n}\right). \qquad (22)$$

From this we obtain:

$$p^2=\frac{c}{M_0}\cdot\frac{\sin n\varphi-\sin(n-1)\varphi}{\sin n\varphi}=2\frac{c}{M_0}\cdot\sin^2\frac{\varphi}{2}\cdot\left(1+\operatorname{ctg} n\varphi\cdot\operatorname{ctg}\frac{\varphi}{2}\right). \qquad (22)$$

Expressions (21) and (22) will give one and the same numerical value for p^2, if the unknown magnitude of φ will satisfy the condition:

$$\operatorname{tg}\frac{\varphi}{2}=\operatorname{ctg} n\varphi. \qquad (23)$$

Here we carried out a division with the multiplier $\sin^2\frac{\varphi}{2}$, which on the basis of (21) should be different from 0, for otherwise the frequency of p^2 would equal 0 (an unstable system).

The equality (1 - 1 - 22) is not hard to convert to the type:

$$\cos\left(n+\frac{1}{2}\right)\varphi=0. \qquad (24)$$

From this we determine:

$$\left(n+\frac{1}{2}\right)\cdot\varphi=\frac{\pi}{2}\cdot(2i-1),\quad i=1,2,3,\ldots,n.$$

Consequently, in place of one value for φ, which satisfies condition (24), we found n values:

$$\varphi_i = \frac{\pi}{2} \cdot \frac{2i-1}{n+\frac{1}{2}}, \quad i = 1, 2, 3, \ldots, n, \qquad (25)$$

which are determined on the basis of (21) n values of eigen frequencies

$$p_i^2 = 4\frac{C}{M_0} \cdot \sin^2\left(\frac{\pi}{4} \cdot \frac{2i-1}{n+\frac{1}{2}}\right), \quad i = 1, 2, \ldots, n. \qquad (26)$$

This is the required function $f(i, n)$, which determines n eigenvalues $\lambda_i = p_i^2$. Although we use formula (1 - 1- 24) only with whole-number values of i, it does carry meaning and the number of times it is differentiated is unlimited for any complex values of i and n, i. e. we have an analytical function.

Now, after determining the size of φ_i, we can determine the function $F(i, k, n)$ on the basis of (13) and (20), i.e.

$$x_{i,k} = 2A \cdot \sin\left(k \cdot \frac{\pi}{2} \cdot \frac{2i-1}{n+\frac{1}{2}}\right), \quad k = n, n-1, \ldots, 2, 1, \qquad (27)$$

where the symbol i designates the number of the eigen vector, and the symbol k determines the number of the component.

Consequently, the unstandardized vector X_i is determined with an accuracy up to the constant multiplier 2A and is determined by components of the type (27).

For dynamic models which contain only point masses M_K, which horizontal shifts $X_{i,K}$ correspond to, standardization of the shapes of vibrations of X_i reduces to conversion from unstandardized movements $X_{i,K}$ to the corresponding coefficients of standardized shapes of vibrations $\eta_{i,K}$. In this case in place of the unstandardized vector $X_i\{x_{in}, x_{in-1}, \ldots, x_{i1}\}$ a standardized vector $\eta_i\{\eta_{in}, \eta_{in-1}, \ldots, \eta_{i1}\}$

is produced. In this case the following relationship holds between the vectors X_i and η_i :

$$\eta_i = c_i \cdot X_i , \qquad (28)$$

where $c_i = \frac{\sum_{k=1}^{n} M_k \cdot X_{ik}}{\sum_{k=1}^{n} M_k \cdot X_{ik}^2}$ is the standardizing multiplier. (29)

By substituting the value of X_{ik} from formula (27) into (29) and by using the equations for the series $\sum_{k=1}^{n} \sin kx$ and $\sum_{k=1}^{n} \sin^2 kx$, and taking (23) into consideration while doing so, we obtain:

$$c_i = \frac{2}{2n+1} \cdot \operatorname{ctg} \frac{\varphi_i}{2} . \qquad (30)$$

Finally, for the standardized shapes of vibrations we have:

$$\eta_{ik} = \frac{2}{2n+1} \cdot \operatorname{ctg} \frac{\varphi_i}{2} \cdot \sin k\varphi_i , \qquad (31)$$

where φ_i is determined from formula (25).

Equations for determining the frequencies p_i (26) and the standardized shapes of the free vibrations η_{ik} turned out to be simple and convenient, which allows one to easily apply them in the practice of designing and calculating the seismic stability of structures. We must point out that such equations for frequencies and shapes of free vibrations of systems of a regular structure were derived also in works [1,2,3] and in others. In these works the problem was examined and solved by known methods of the theory of finite differences. Here we have only attempted to analyze this method as a solution of a certain matrix problem, when the matrices have regular structure.

It is worthwhile to examine the following formulation of the problem: insofar as the first and last lines of the matrix K are untypical anyway, it is thus sensible to make them (i.e. the corresponding equa-

tions of equilibrium) even more "dissimilar" to the remaining lines. Such a picture is obtained, for example, if the distance from the base to the first mass is made untypical, i.e., for example, by increasing it in comparison to the typical distance δ . One can also make the highest mass distinct from the remaining ones. Such changes are reflected only on the first and last components of the matrix equality (1). It is clear, that the general plan of the solution described above remains in force in this case.

Let us examine a similar model i.e. a model with distinct upper mass and lower columns, which we shall give the name of "partially regular". As before, we shall consider that the force between random k-th and k+1-th masses depends only on the differences of the horizontal movements of these masses, i.e.

$$R_{k,k+1} = -R_{k+1,k} = c\cdot(y_{k+1} - y_k). \qquad (32)$$

Of course, in the most general case the force $R_{k,k+1}$ depends on shifts of all the floor spans, i.e. $R_{k,k+1}$ is a linear combination of these shifts. However, the difference in shifts of the nearest floor spans plays the chief role in this linear combination. In other words, formula (32) is absolutely accurate for a framework with absolutely rigid floors.

Consequently, in discussing the conformity between a real building and the model being examined (Fig. 3), then a real building must satisfy the following conditions: 1) the shear force between k and k+1-th floor spans is <u>principally</u> determined by the difference in

the shifts of these floor spans; 2) the masses of all floor spans, with the exception of the highest one, equal one another $M_{n-1}=M_{n-2}= \ldots =M_1=M_0$; the mass of the upper floor span $M_n=\alpha M_0$; 3) the magnitude of rigidity C for all floors, with the exception of the first, is identical; 4) the force at the second floor is determined by the formula:

$$R_{1\phi}=c_0(y_1-y_\phi)=c_0\cdot y_1, \qquad (33)$$

where $y_\phi = 0$ - is the foundation shift.

We hasten to note that if we write down the equilibrium condition of the lower concentrated mass and make use of formula (33), then we obtain an untypical equation. In order to circumvent this difficulty we shall introduce a certain arbitrary shift y_0, which corresponds to a certain imaginary point, which lies on the broken line which connects the mass M_1 to the stationary foundation (Fig. 3). In this case the position of this point is selected so that the relationship

$$c_0y_1=c(y_1-y_0), \qquad (34)$$

or

$$y_0=(1-\rho)\cdot y_1, \quad \rho=\frac{c_0}{c}. \qquad (35)$$

is fulfilled for the given values of C and C_0.

Condition (35) enables us to make use of typical formula (32) in place of untypical (33) in determinations of the force R_{y0}. In this case the equilibrium equation for the first mass M_1 is derived according to the same plan as for the remaining floor spans (with the exception of the upper one).

Let us emphasize that an identical relationship of type (32) for

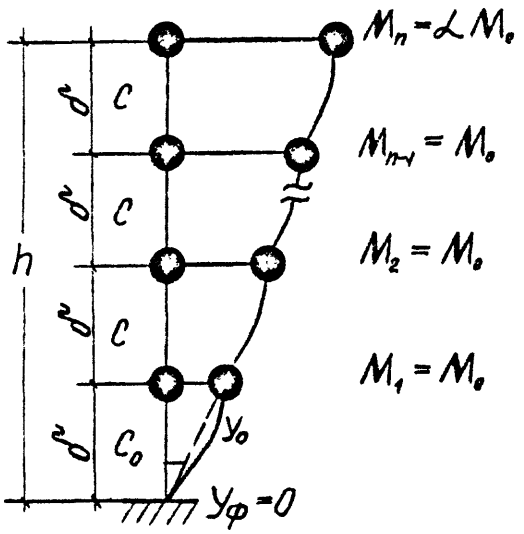

Fig. 3. Dynamic calculated plan of a partially regular structure.

all floors does not necessarily assume an identical height for all floors. The magnitude of C depends on the diameter of the bearing elements and of their height. It is possible to increase the diameter and increase the height so that the magnitude of C remains unchanged.

Thus, the general solution of the problem being considered, as before, is of type (11), where ξ_1 and ξ_2 as before are the radicals of equation (19). If we convert from the complex constants A and B to the real constants $\bar{A}$ and $\bar{B}$, then formula (11) is rewritten thus:

$$X_k = \bar{A} \cdot \cos k\varphi + \bar{B} \cdot \sin k\varphi. \qquad (36)$$

The random constants $\bar{A}$ and $\bar{B}$ are determined in this case from the following conditions. We start with condition (34). It signifies, that if from the general solution (36) we find

$$X_0 = \bar{A}, \qquad (37)$$

and then we find

$$X_1 = \bar{A}\cos\varphi + \bar{B}\sin\varphi, \qquad (38)$$

then the values of $\bar{A}$ and $\bar{B}$ must be such that during substitution of (37) and (38) into equality (35) this equality is satisfied, i.e.

$$\bar{A}=(1-\rho)\cdot(\bar{A}\cos\varphi+\bar{B}\sin\varphi).$$

From this

$$\bar{A}=\bar{B}\cdot\frac{(1-\rho)\cdot\sin\varphi}{1-(1-\rho)\cos\varphi}=g\bar{B}, \qquad (39)$$

where

$$g=\frac{(1-\rho)\sin\varphi}{1-(1-\rho)\cdot\cos\varphi}. \qquad (40)$$

Note that when $\rho = 1$ $\bar{A} = 0$ is produced, which corresponds to the case in which the rigidity of the ground floor C_0 does not differ from typical rigidity C, i.e. the system has a regular structure.

In conformity with (39) we can write (36) in the form:

$$x_k=D\cdot\sin(k\varphi+\psi), \qquad (41)$$

where

$$D=\sqrt{1+g^2}\cdot\bar{B}, \quad \psi=\operatorname{arctg}(g). \qquad (42)$$

Now we can convert to the second untypical equation, which expresses the equilibrium condition for the upper untypical mass $M_n=\alpha\cdot M_0$. This condition has the form:

$$c\cdot(x_n-x_{n-1})=\alpha\cdot M_0\rho^2x_n. \qquad (43)$$

In conformity with (41) we obtain:

$$\rho^2=\frac{c}{\alpha\cdot M_0}\cdot\left[1-\cos\varphi+\sin\varphi\cdot\operatorname{ctg}(n\varphi+\psi)\right]. \qquad (44)$$

In order to satisfy the typical equation

$$c\cdot(-x_{k-1}+2x_k-x_{k+1})=\rho^2M_0x_k, \qquad (45)$$

we also substitute (41) here, which leads to the relationship

$$\rho^2=4\frac{c}{M_0}\cdot\sin^2\frac{\varphi}{2} \qquad (46)$$

Equations (44) and (46) will yield identical numerical values for

frequency ρ , if

$$1-\cos\varphi+\sin\varphi\cdot\operatorname{ctg}(n\varphi+\psi)=4\alpha\cdot\sin\frac{\varphi}{2}\cdot$$

From this we obtain the following characteristic equation for determining φ:

$$(2\alpha-1)\cdot\operatorname{tg}\frac{\varphi}{2}-\operatorname{ctg}(n\varphi+\psi)=0\,, \quad (47)$$

where in conformity with (40) and (42) ψ also is a function of φ, and also depends on the parameter

It is not difficult to show that for each specific value of the parameters ρ and α we obtain from this equation n different (with accuracy to terms of the type $2j\pi$) radicals of $\varphi_1, \varphi_2, \varphi_3 \ldots, \varphi_n$. By substitution of φ_i into (46) and (41) we obtain the i-th characteristic frequency and the appropriate unstandardized shape of free vibrations. We obtain standardized shapes of vibrations on the basis of (28) and (29). By substituting (41) into these formulas we get:

$$\eta_{ik}=\sin(k\varphi_i+\psi)\frac{\alpha\cdot\sin(n\varphi_i+\psi_i)+\sin\left(\frac{n-1}{2}\varphi_i+\psi_i\right)\cdot\sin\frac{n}{2}\varphi_i\cdot\operatorname{cosec}\frac{\varphi_i}{2}-\sin\psi_i}{\frac{n-1}{2}+\alpha\cdot\sin^2(n\varphi_i+\psi)-\frac{1}{2}\cdot\cos[(n-1)\varphi_i+2\psi_i]\cdot\sin n\varphi_i\cdot\operatorname{cosec}\varphi_i+\frac{1}{2}\cos 2\varphi} \quad (48)$$

In order to find radicals of the characteristic equation (47) a program is compiled on a "MIR" type computer.

Now we can turn to the model of the frame building being investigated. We can take a cantilever under shear stress with rigid restraints in the base as a dynamic model. This is presented in Fig.1. The effect of give of the base on the dynamic characteristics of buildings in the given case is minor because the parameters n_1 and n_2 calculated for this building, which in a definite sense characterize the relationships of the shift K_x and angular K_φ rigidities of the base to the

rigidity C of the building itself, turned out to be equal to about 2, which, as follows from reference [4], indicates an insignificant influence of the give of the base.

From the model shown in Fig. 1 it is evident, that we are dealing with the plan of a partially regular structure, because the height of the ground floor is different from the others, and also the mass M_3, which is condentrated in the level of the floor span of the upper floor, is different from the masses M_1 and M_2. The rigidity of a typical floor, determined from formula (4), equals $C = 0.0135 \times 10^6$ t/m, and the rigidity of the ground floor $C_0 = 0.08 \times 10^6$ t/m. From this the value of the parameter $\rho = \frac{C_0}{C} = 0.6$. The value of the parameter $\alpha = \frac{M_n}{M_0} = 0.8$. On the basis of the calculated parameters ρ and α the radicals of the characteristic equation (47) were determined, which produced: $\varphi_1 = 0.380$, $\varphi_2 = 1.228$, $\varphi_3 = 2.168$. We determine the frequencies of the free vibrations of the building being studied from formula (46): $p_1 = 12.8 \frac{1}{\text{second}}$, $p_2 = 39.2 \frac{1}{\text{second}}$, $p_3 = 59.8 \frac{1}{\text{second}}$. In this manner the periods of the free vibrations of the building are -- $T_1 = 0.5$ sec, $T_2 = 0.16$ sec, $T_3 = 0.10$ sec. The coefficients of the standardized shapes of vibrations η_{ik} are calculated on the basis of (48). The standardized shapes of vibrations are presented in Fig. 4, where the values of the coefficients η_{ik} are also given.

It should be noted that in determining the dynamic parameters of a building we did not consider the rigidity of the wall panels, which, however, in the case of weak seismic actions can participate in the work

of the frame. By considering the rigidity of the wall panels, which is calculated from the formula $C_\eta = \frac{kG_\eta F_\eta}{\delta}$, the periods of free vibrations of a building, which are determined according to the methods presented above, yield: T_1 = 0.33 sec, T_2 = 0.11 sec, T_3 = o.07 sec.

3. Construction of a matrix of the damping forces for regular models.

A system of differential equations of induced vibrations in matrix form, as is known, has the form:

$$KY + \alpha H\dot{y} + M\ddot{y} = -y_o M a_o, \qquad (49)$$

where the matrices K, M and the vector Y have the same sense as in (1), but the N-dimensional vector a_o, in the general case, consists of unities and zeros [4]. The matrix H is the matrix of the damping forces, α is the measure of energy scattering.

Normally, in calculations, in place of a complex system of equations (49) a simpler system of second order N-differential equations of the following type is used

$$\ddot{a}_i(t) + \alpha p_i \dot{a}_i(t) + p_i^2 a_i(t) = -\ddot{y}_o(t), \quad i = 1, 2, \ldots, N. \qquad (50)$$

These quite simple differential equations correspond to the vibrations of linear oscillators with frequencies $p_i = \frac{2\pi}{T_i}$, where T_i is the i-th fundamental period of vibrations for the dynamic model plan under consideration. As is known, converting from the system of equations (49) to a system of type (50) can be accomplished when all shapes of vibrations η_i and the respective frequencies p_i are known. Conversion from (49) to (50) actually corresponds to replacement of the unknown

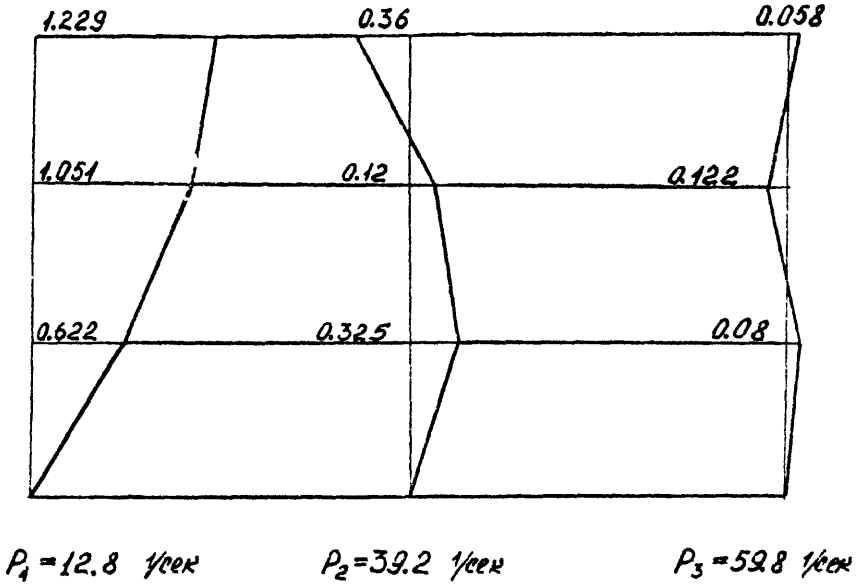

Fig. 4. Standardized shapes of vibrations of an experimental frame building.

$Y_n(t), Y_{n-1}(t), \ldots, Y_1(t)$ by the new unknowns $a_N(t), a_{N-1}(t), \ldots, a_1(t)$. In this case the relationship between the old and new unknowns in vector form is expressed in this way:

$$y(t) = a_1(t)\cdot\eta_1 + a_2(t)\cdot\eta_2 + \ldots + a_N(t)\cdot\eta_N . \qquad (5I)$$

The question arises: what should the matrix H be like, so that we can make use of equations of type (50).

It follows, for example, that if we want to solve the problem by aid of the electromechanical modeling method, then for real modeling of the system of equations (49) it is also necessary to know what the matrix H must be like. This problem was studied by A. A. Derkachev [5], V. T. Rasskazovskiy [6], A. I. Tseytlin [7] and others.

This problem of determining the matrix H reduces in this case to

extraction of the square root from a certain positively defined square matrix. It is known that if a certain positively defined matrix A has positive eigenvalues $\lambda_1, \lambda_2, \ldots, \lambda_N$, i.e.

$$Az_i = \lambda_i z_i, \qquad (52)$$

then matrix B, which satisfies condition $B^2 = A$, has the eigenvalues $\sqrt{\lambda_1}, \sqrt{\lambda_2}, \ldots, \sqrt{\lambda_N}$ and the same eigen vectors z_i, i.e.

$$Bz_i = \sqrt{\lambda_i} \cdot z_i, \qquad (53)$$

This feature of matrix $B = A^{1/2}$ is also made use of for solving the problem just set forth. However, in the general case the operation for finding the matrix $B = A^{1/2}$ from a given positively defined matrix A represents a quite complex problem in the case of a very large N. The calculation of the matrix $A^{1/2}$ is derived simply only in one partial case: when the matrix A is a diagonal, and along the diagonal are placed only non-negative numbers. In this case $A^{1/2}$ has an obvious meaning -- the square root is extracted from the diagonal elements.

The problem of extracting a square root is substantially simplified if matrix A is a Hermitian positively defined matrix [8]. Because we are dealing only with real matrices, a Hermitian matrix becomes a real symmetrical matrix. In this case matrix B is constructed in the following manner: 1) for each eigenvalue λ_i of problem (52) we construct a standardized vector

$$U_i = d_i z_i, \qquad (54)$$

such that $(U_i, U_i) = 1$; 2) we form the matrix U, whose columns are the vectors U_i; 3) we determine matrix B from the formula

$$B = U^T \Lambda^{\frac{1}{2}} U, \qquad (55)$$

where $\Lambda^{1/2}$ is a diagonal matrix in which the numbers $\sqrt{\lambda_1}, \sqrt{\lambda_2}, \ldots, \sqrt{\lambda_N}$ are located along the diagonal from top to bottom, and U^T is a transposed matrix, which as a consequence of orthostandardization of the vectors U_i satisfies the condition

$$U^T \times U = E,$$

where E is a unit matrix.

Such a method for determining the root of a square from a matrix is particularly convenient when the eigenvectors U_i, and the eigenvalues λ_i are determined not by the numerical method, but by aid of certain analytical formulas, as is done for the above examined regular plans.

In this manner, for solving the problem set forth the system of equations (49) must be rewritten so that in place of the diagonal matrix M there be a unit matrix E, and so that the remaining matrices remain symmetrical without fail. For example, if the entire equation (49) is again multiplied by M^{-1}, then we obtain

$$M^{-1}KY + \alpha \cdot M^{-1}H\dot{Y} + E\ddot{Y} = -\ddot{y}_0 a_0 .$$

However, in this case the method for extracting a square root described above for an unsymmetrical matrix $M^{-1}K$ is no longer applicable.

Therefore, we proceed in the following manner: 1) between the matrix K and the vector Y, and also between H and $\dot{Y}$ we insert $E = M^{-1/2}M^{1/2}$; 2) we make the substitution

$$M^{1/2}Y = Z; \qquad (56)$$

3) on the left we multiply the entire resulting equality by the matrix $M^{-1/2}$. As a result of these operations we obtain:

$$A z + \alpha \cdot B \cdot \dot{z} + \ddot{z} = -y_0 M^{\frac{1}{2}} a_0, \qquad (57)$$

where $$A = M^{-\frac{1}{2}} K M^{-\frac{1}{2}}, \quad B = M^{-\frac{1}{2}} H M^{-\frac{1}{2}}. \qquad (58)$$

The system of equations (57) leads to the type (50) by the help of replacement of

$$z(t) = a_1(t) \cdot \tilde{\eta}_1 + a_2(t) \cdot \tilde{\eta}_2 + \ldots + a_N(t) \cdot \tilde{\eta}_N, \qquad (59)$$

where $\tilde{\eta}_i = C_i z$, only in this case, if B is the square root of A, i.e.

$$B = M^{-\frac{1}{2}} H M^{-\frac{1}{2}} = U^T \Lambda^{\frac{1}{2}} U = A^{\frac{1}{2}}. \qquad (60)$$

We can demonstrate this. Let the vectors z_i be the eigenvectors of problem (52), where the matrix A is of the type (58), and the matrix $B = M^{-1/2} H M^{-1/2}$ is the square root from matrix A. We will standardize the eigenvectors z_i by the aid of the multiplier

$$C_i = \frac{(M^{\frac{1}{2}} a_0 z_i)}{(z_i, z_i)}, \quad \tilde{\eta}_i = C_i \cdot z_i. \qquad (61)$$

In this case the standardized vectors $\tilde{\eta}_i$ satisfy the condition

$$\tilde{\eta}_1 + \tilde{\eta}_2 + \ldots + \tilde{\eta}_N = M^{\frac{1}{2}} a_0. \qquad (62)$$

By substituting this sum into (57) in place of $M^{1/2} a_0$, and the expansion of (59) in place of $z(t)$ and by making use of the relationship

$$A\tilde{\eta}_i = \lambda_i \tilde{\eta}_i, \quad B\tilde{\eta}_i = \sqrt{\lambda_i}\, \tilde{\eta}_i$$

we obtain

$$\sum_{i=1}^{N} \tilde{\eta}_i \left[\lambda_i \cdot a_i + \alpha \sqrt{\lambda_i} \cdot \dot{a}_i + \ddot{a}_i\right] = -\sum_{i=1}^{N} \tilde{\eta}_i \cdot \ddot{y}_0. \qquad (63)$$

By equating on the left and on the right the coefficients when there are identical vectors $\tilde{\eta}_i$ we have:

$$\lambda_i \cdot a_i + \alpha \sqrt{\lambda_i} \cdot \dot{a}_i + \ddot{a}_i = -\ddot{y}_0. \qquad (64)$$

It remains merely to show that $\lambda_i = p_i^2$. For this we enter $A = M^{-1/2} K M^{-1/2}$ and $z_i = M^{1/2}$ into (52) and we multiply the entire equation on the left by $M^{1/2}$. Then we get

$$KX_i = \lambda_i M X_i, \quad z = M^{\frac{1}{2}} X_i. \qquad (65)$$

From this it follows that $\lambda_i = p_i^2$. In addition we showed that $Z_i = M^{1/2}X$ where X_i is the i-th shape of the vibrations. If we now substitute $Z_i = M^{1/2}X_i$ into (61), we obtain a normal standardizing multiplier (29). From this $\tilde{\eta}_i = M^{1/2}\eta$

Now we proceed to determination of matrix H. After multiplying the matrix equation (60) on the left and right by $M^{1/2}$ we get:

$$H = M^{\frac{1}{2}} U^T \Lambda^{\frac{1}{2}} U M^{\frac{1}{2}}. \qquad (66)$$

In order to construct matrix U in (66) we must construct the vectors Z_i from the eigenvectors X_i on the basis of (65). The vectors Z_i should then be standardized, i.e. we should find $U_i = d_i Z_i$ from the condition $(U_i, U_i) = 1$.

Thus, the matrix H is obtained in the system of equations (49) as a result of remultiplication of all matrices in (66). In such form a system of differential equations of induced vibrations with consideration of energy scattering can be directly realized on an analog computer.

For the frame building being considered the calculated matrices in (49) are of the type:

the matrix of rigidities K are

$$K = \begin{vmatrix} 1.35 & -1.35 & 0 \\ -1.35 & 2.70 & -1.35 \\ 0 & -1.35 & 2.70 \end{vmatrix} \times 10^4 \text{ t/m};$$

the matrix of scattering H

$$H = \begin{vmatrix} 0.456 & -0.167 & 0.04 \\ -0.167 & 0.483 & 0.19 \\ -0.04 & -0.19 & 0.333 \end{vmatrix} \times 10^{+3} \frac{T\ sec}{m}$$

the diagonal matrix of masses M

$$M = \begin{vmatrix} 8.5 & 0 & 0 \\ 0 & 11.0 & 0 \\ 0 & 0 & 11.0 \end{vmatrix} \frac{T\ sec^2}{m} .$$

4. Algorithm for determining the response of structures to random seismic action, given by an accelerogram of vibrations of the ground $\ddot{y}_0(t)$.

In the known method of calculating structural response from actual accelerograms, the seismic load at the k-th point being examined is presented in the form:

$$S_k(t) = M_k \cdot \sum_{i=1}^{n} \tau(T_i, \alpha, t) \cdot \eta_{ik} , \qquad (67)$$

where η_{ik} is the coefficient of the i-th standardized shape of vibrations for the k-th point, $\tau(T_i, \alpha, t)$ is the corrected seismic acceleration for the i-th shape which is determined from the formula:

$$\tau(T_i, \alpha, t) = p_i \int_0^t e^{-\frac{\alpha p_i (t-v)}{2}} \cdot \sin p_i (t-v) \cdot \ddot{y}_0(v)\, dv . \qquad (68)$$

The use of formula (67) for determining seismic loads entails a number of difficulties and inconveniences, which include above all the fact that the error rate which arises from not considering all the periods and shapes of the free vibrations is unknown (normally several predominant modes are considered). This is related to incorrectness of the pro-

blem of determining the vector of a seismic load $S\{S_1, S_2, \ldots, S_n\}$ from the given vector of the deformed state of $y\{y_1, y_2, \ldots, y_n\}$. The fact is that failure to consider the higher periods and shapes of free vibrations yields a low error rate for the vector of deformations Y; however, the very small variation of the deformed state sometimes causes a very substantial (and sometimes an impermissibly large) variation of the corresponding vector of static load [5].

In this connection there have been attempts not to make use of expansions from shapes in the form of (67) in determining seismic loads. One way to circumvent the difficulties, which are caused by an improper relationship between static deformation and static external forces, comes from the possibility in general of giving up the intermediate understanding of external forces, and immediately proceeding to determination of the internal stresses in buildings in the study of earthquakes.

One of the most advanced of such approaches, in our opinion, is the method of determining the internal stresses in a building during a random seismic action by the aid of a Duhamel integral (convolution integral) of the type:

$$R_K(t) = \int_0^t h_R(t-\upsilon)\cdot \ddot{y}_0(\upsilon)\,d\upsilon, \qquad (69)$$

where $R_K(t)$ is the response (internal stresses, displacements, accelerations) of a building to random seismic action, given by an accelerogram of the ground vibrations $\ddot{y}_0(t)$,

$h_R(t)$ is the response of a building to an "earthquake" in the form of a solitary instantaneous impulse $\ddot{y}_0(t) = \delta(t)$, the function $h_R(t)$ is still called a weighted function.

Determination of the response of structures by the aid of a convolution integral (69) also has a number of advantages over other methods. Firstly, producing weighted functions $h_R(t)$ is possible in the majority of cases in the closed type without previously finding the frequencies and shapes of the free vibrations of systems. Secondly, formula (69) has great universality: by substituting into the integral equation the weighted functions either for movements, or accelerations, or for internal stresses, in the left part of (69) we will produce respectively the response

of a system to random action either in the form of movements, or accelerations of point vibrations, or directly in the form of the process of change of the internal stresses in a certain section of the building being studied.

Calculation of the response of structures by the aid of weighted functions was examined in the works of Ya. M. Ayzenberg [9], A. A. Derkachev [5], V. T. Rasskazovskiy [6], Ye. Til, Dzh. Lord, K Meyyer [10], E. Rozen-Blyuet [11] and others.

Determination of the function $R(t)$, which describes the law of change of a certain response (internal stresses, displacements, accelerations) by the aid of a convolution integral of type (69) with the given accelerogram $\ddot{y}_0(t)$ is related to serious calculational difficulties. Thses difficulties arise because the argument of t in the right hand part of (69) is contained not only in the type of upper limit of the integral, but also in the type of parameter in the integral equation $h_R(t-\tau)$. Consequently, in changing the upper limit the

integral function is also changed. Therefore, in algorithms which were used for direct calculation of a convolution integral (69), for example, in works [6] and [10] a very large amount of computer time was needed.

Borel's theorem of convolution [12] is assumed as the basis for the algorithm for calculating a convolution integral which we developed:

$$F\left[f_1(t)\right]\cdot F\left[f_2(t)\right]=F\left[f_1(t)*f_2(t)\right], \qquad (70)$$

where

$$f_1(t)*f_2(t)=\int_{-\infty}^{\infty} f_1(\tau)\cdot f_2(t-\tau)\,d\tau=\int_{-\infty}^{\infty} f_1(t-\tau)\cdot f_2(\tau)\,d\tau,$$

here $F[f_1(t)]$ and $F[f_2(t)]$ are complex Fourier transformations respectively of the functions $f_1(t)$ and $f_2(t)$:

$$F[f_1(t)]=\int_{-\infty}^{\infty} f_1(t)\cdot e^{-i\omega t}dt,$$

$$F[f_2(t)]=\int_{-\infty}^{\infty} f_2(t)\cdot e^{-i\omega t}dt.$$

$F[f_1(t)*f_2(t)]$ are complex Fourier transformations of the function, which is determined by the convolution integral. In the given case we can designate the weighted function $h_R(t)$ by the function $f_1(t)$, and the random seismic action $\ddot{y}_0(t)$ is designated by $f_2(t)$

Convolution $f_1(t)*f_2(t)$ represents the sought after response of a structure R (t). By calculating the complex Fourier transformations for a weighted function h_R(t) and for the accelerogram $\ddot{y}_0$ (t) and by carrying out remultiplication of the conversions obtained we thereby determine the complex Fourier transformation C (ω) of the function R (t)

$$C(\omega)=\frac{1}{\sqrt{2\pi}}\cdot F[h_R(t)]\cdot F[\ddot{y}_0(t)]. \qquad (7I)$$

By making the operation of an inverse Fourier transformation we find the very function R (t):

$$R(t)=\frac{1}{\sqrt{2\pi}}\cdot\int_{-\infty}^{\infty}c(\omega)\cdot e^{i\omega t}d\omega. \qquad (72)$$

In work [13] we derived expressions for responses (weighted functions) of the models for a regular structure (which were there considered) on the external action in the form of a solitary horizontal pulse. In particular, the expression for a weighted function of internal stresses (of intersecting forces) has the form:

$$h_{k,k+1}(t)=\frac{2}{2n+1}\cdot\sqrt{CM_0}\cdot\sum_{i=1}^{n}e^{-\frac{\alpha p_i t}{2}}\cdot ctg\frac{\varphi_i}{2}\cdot\cos\left(k\varphi_i+\frac{\varphi_i}{2}\right)\cdot\sin p_i t, \qquad (73)$$

where φ_i is determined from formula (25).

Calculation of a complex Fourier transformation $H_k(i\omega)$ of a weighted function (73) has been set forth in sufficient detail in work [14]. Here we shall give the final result:

$$H_k(i\omega)=A(\omega)+i\cdot B(\omega),$$

where

$$\frac{A(\omega)}{\sqrt{CM_0}}=\frac{2}{\sqrt{2\pi}(2n+1)}\cdot\sum_{i=1}^{n}\frac{p_i\cdot\left(p_i^2+\frac{\alpha^2p_i^2}{2}-\omega^2\right)}{\left(p_i^2+\frac{\alpha^2p_i^2}{4}-\omega^2\right)^2+\alpha^2\cdot p_i^2\cdot\omega^2}\cdot ctg\frac{\varphi_i}{2}\cdot\cos\left(k\varphi_i+\frac{\varphi_i}{2}\right), \qquad (74)$$

$$\frac{B(\omega)}{\sqrt{CM_0}}=\frac{2}{\sqrt{2\pi}(2n+1)}\cdot\sum_{i=1}^{n}\frac{\alpha p_i^2\omega}{\left(p_i^2+\frac{\alpha^2p_i^2}{4}-\omega^2\right)^2+\alpha^2p_i^2\cdot\omega^2}\cdot ctg\frac{\varphi_i}{2}\cdot\cos\left(k\varphi_i+\frac{\varphi_i}{2}\right).$$

For the accelerogram $\ddot{y}_0$ (t) the complex Fourier transformation

$$W(\omega)=\frac{1}{\sqrt{2\pi}}\cdot\int_0^{t_n}\ddot{y}_0(\upsilon)e^{-i\omega\upsilon}d\upsilon=\frac{1}{\sqrt{2\pi}}\cdot[a_n(\omega)-ib_n(\omega)], \qquad (75)$$

where

$$a_n(\omega)=\int_0^{t_n}\ddot{y}_0(\upsilon)\cdot\cos\omega\upsilon d\upsilon,$$

$$b_n(\omega)=\int_0^{t_n}\ddot{y}_0(\upsilon)\cdot\sin\omega\upsilon d\upsilon,$$

is calculated on the basis of the algorithm set forth in work [15].

5. Analysis of derived numerical solutions

On the basis of the algorithm developed and the programs compiled (the programs were compiled in ALGOL-60 language on the "M-220M" computer) we calculated the response of an experimental model of a frame building to the action of accelerograms of two strong earthquakes -- the Gazli earthquake of May 17, 1976 and the San Fernando earthquake of February 9, 1971.

According to the data of the YESSN (Unified System of Seismic Observations) of the USSR the magnitude of the Gazli earthquake was 7.2, the depth of the focus was 20-25 km. The intensity of shaking at the installation point of the devices exceeded nine (on the Soviet intensity scale). Cracks formed in the ground as a result of the earthquake, and in a number of places ejections through the cracks to the surface of chunks of dense rock were noticed (16). In the settlement of Gazli, which is located at a distance of 30 km from the epicenter, the majority of brick buildings were completely or partially destroyed, and large-panel constructed buildings suffered serious damages (17), (18), (19).

The earthquake at San Fernando was estimated to have a magnitude of 6.6 (20). It also caused substantial damage to buildings and structures (21).

These earthquakes are characterized by significant amplitudes of ground vibration accelerations. For the Gazli earthquake the maximal values of accelerations were: in the N-S direction 0.69g, in the E-W direction 0.79g, and in the vertical direction 1.39g (16). For the San

Fernando earthquake the maximum amplitude of ground accelerations of the S74°W component was 1.25g, and the maximum velocity, 114 cm/s (20).

The accelerogram of the Gazli earthquake is distinguished by the high-frequency nature of the vibrations. Such a nature is typical for "close" earthquakes. The maximum amplitude of ground vibration accelerations in the N-S direction corresponded to a period T=0.12 s. For the accelerogram of the San Fernando earthquake, the frequencies of ground vibrations were slightly lower than for the Gazli earthquake (20).

From the point of view of methods of seismic regionalization (quantitative evaluation of seismic danger, shaking on the surface, engineering analysis of the destructive consequences etc.) these earthquakes were approximately identical with the maximum intensities slightly exceeding nine on the MSK-64 (Soviet intensity) scale.

An accelerogram of the N-S component of the Gazli earthquake and an accelerogram of the S74°W component of the San Fernando earthquake were chosen as time histories to be utilized in the calculation of the response of the experimental building. Ordinates of the tabulated accelerogram of the Gazli earthquake were taken from reference (22), and the ordinates of the San Fernando earthquake accelerogram were taken from reference (23). It should be noted that for the San Fernando earthquake, the most intensive part of the accelerogram with a duration of slightly more than 15 s was selected.

The calculated maximal values of the response -- the shear

forces, diplacements, accelerations -- of the experimental frame building are presented in table 1. It should be noted that in the calculation the value of the measure of energy scattering was taken as equal to α=0.2. Figures 5-10 show the time histories of shear force acceleration, and displacement response for both earthquakes.

Table 1

Accelerogram of Gazli earthquake	Accelerogram of San Fernando earthquake	Response of a building according to standard design calculations
1	2	3
	Shear Force	
$Q_{1,0}$ = 512 T	$Q_{1,0}$ = 666 T	$Q_{1,0}$ = 62.4 T
$Q_{2,1}$ = 415 T	$Q_{2,1}$ = 600 T	$Q_{2,1}$ = 50.8 T
$Q_{3,2}$ = 254 T	$Q_{3,2}$ = 354 T	$Q_{3,2}$ = 30.8 T
	Displacement	
Y_1 = 3.8 cm	Y_1 = 5.0 cm	Y_1 = 1.3 cm
Y_2 = 6.6 cm	Y_2 = 9.3 cm	Y_2 = 1.6 cm
Y_3 = 8.3 cm	Y_3 - 12.0 cm	Y_3 = 2.3 cm
	Acceleration in fractions of g	
Y_1 = 1.5 g	Y_1 = 1.7 g	Y_1 = 0.25 g
Y_2 = 1.7 g	Y_2 = 2.3 g	Y_2 = 0.28 g
Y_3 = 2.4 g	Y_3 = 3.3 g	Y_3 = 0.37 g

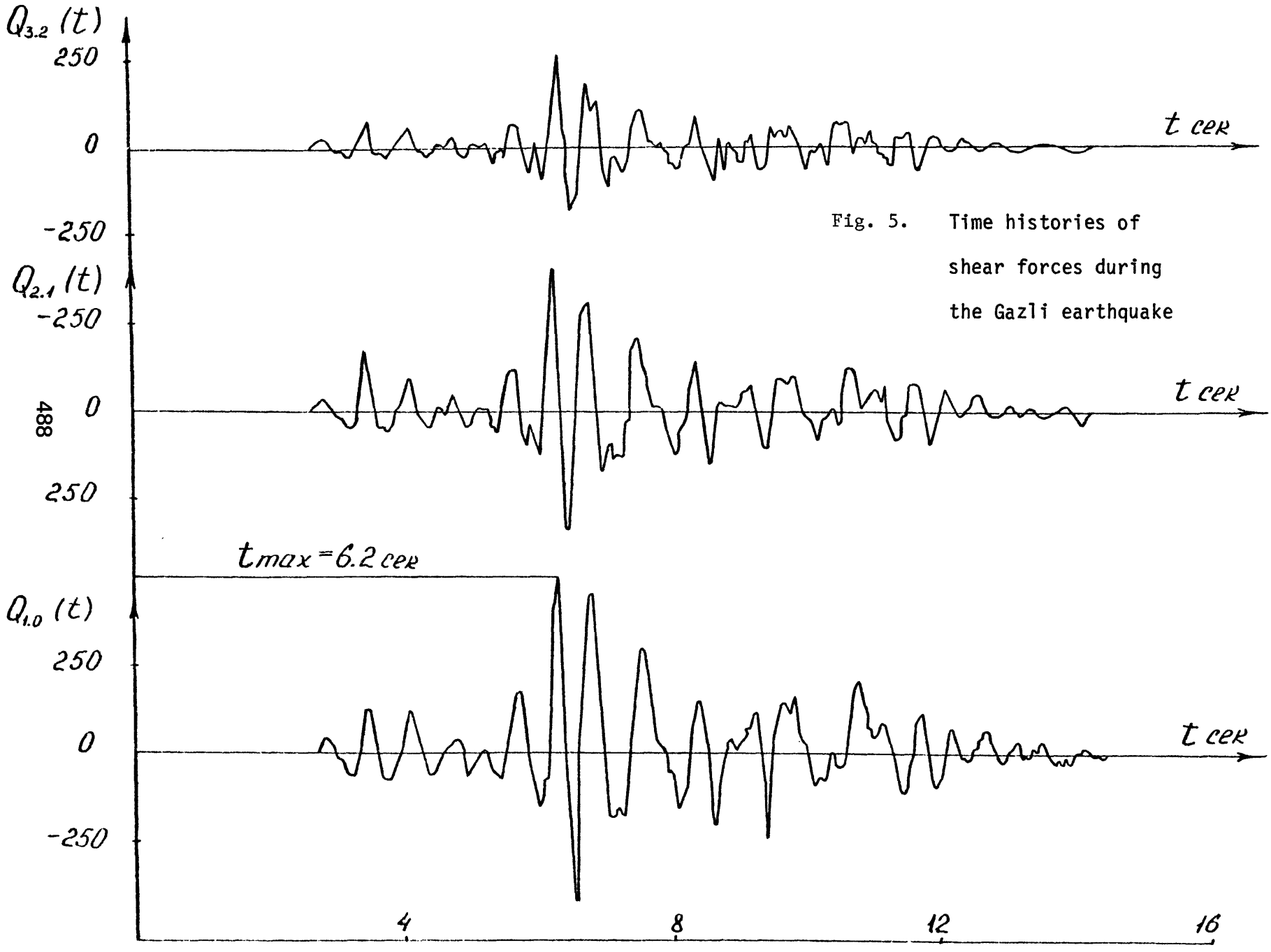

Fig. 5. Time histories of shear forces during the Gazli earthquake

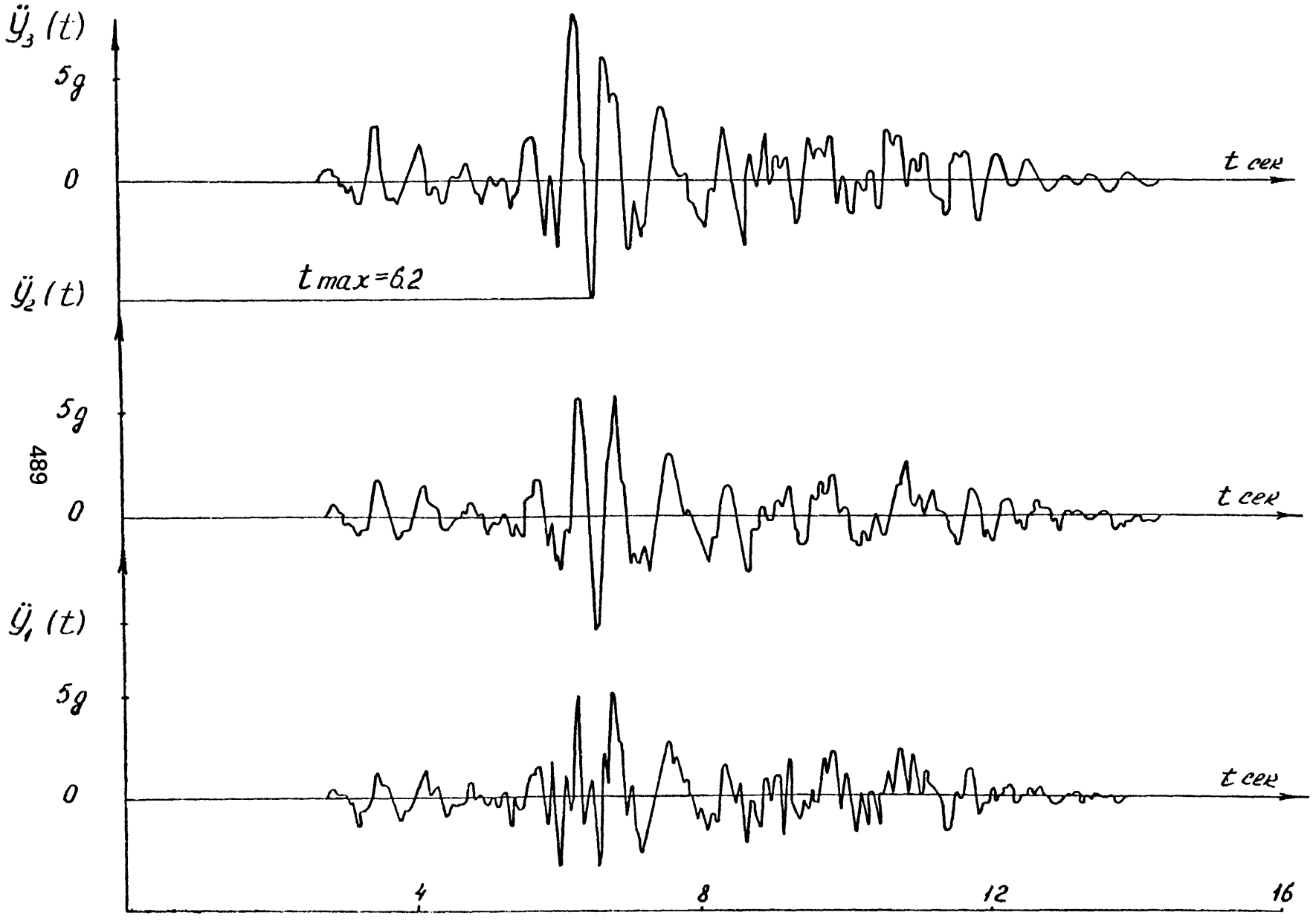

Fig. 6 Theoretical accelerograms from the Gazli earthquake

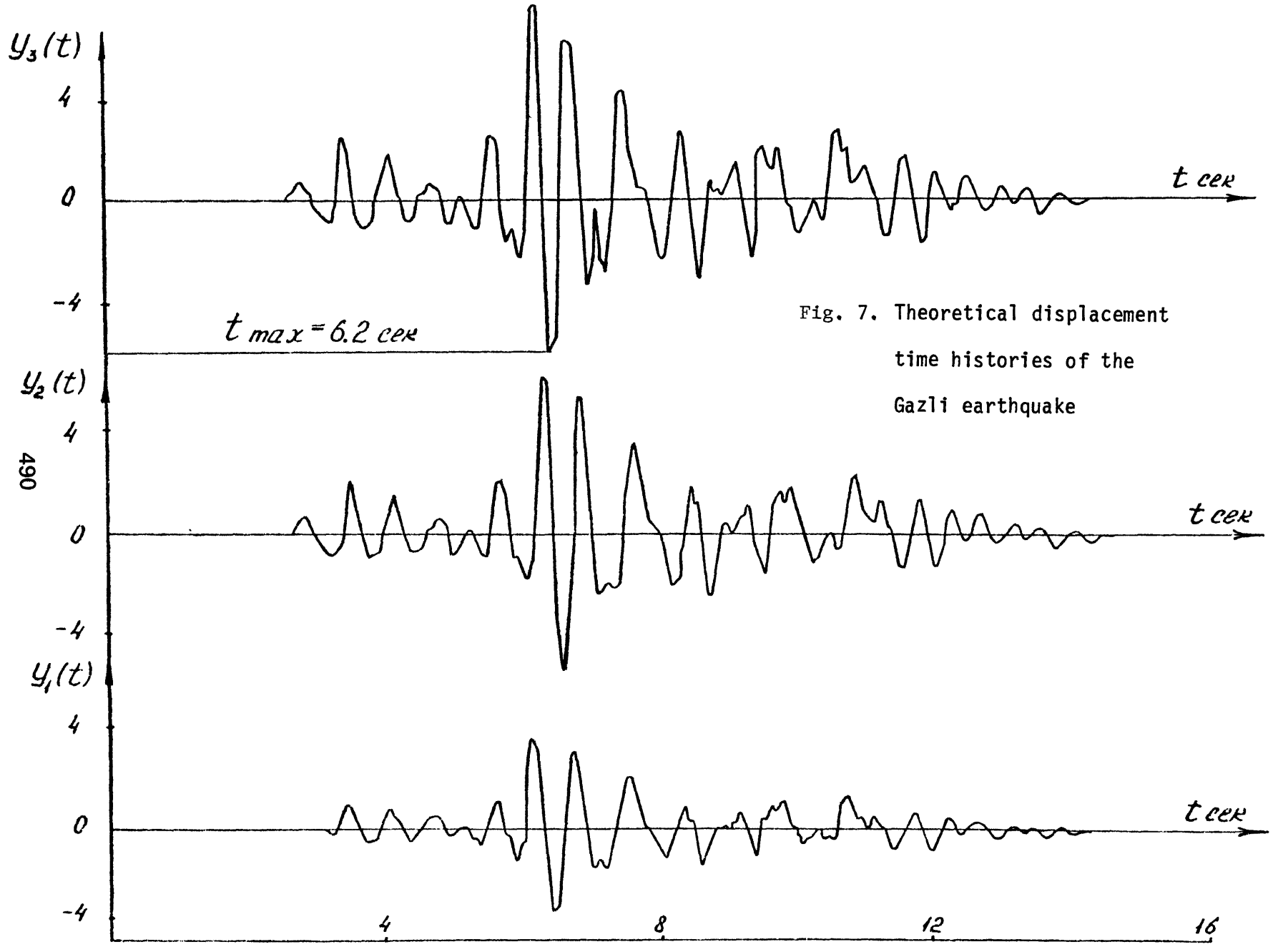

Fig. 7. Theoretical displacement time histories of the Gazli earthquake

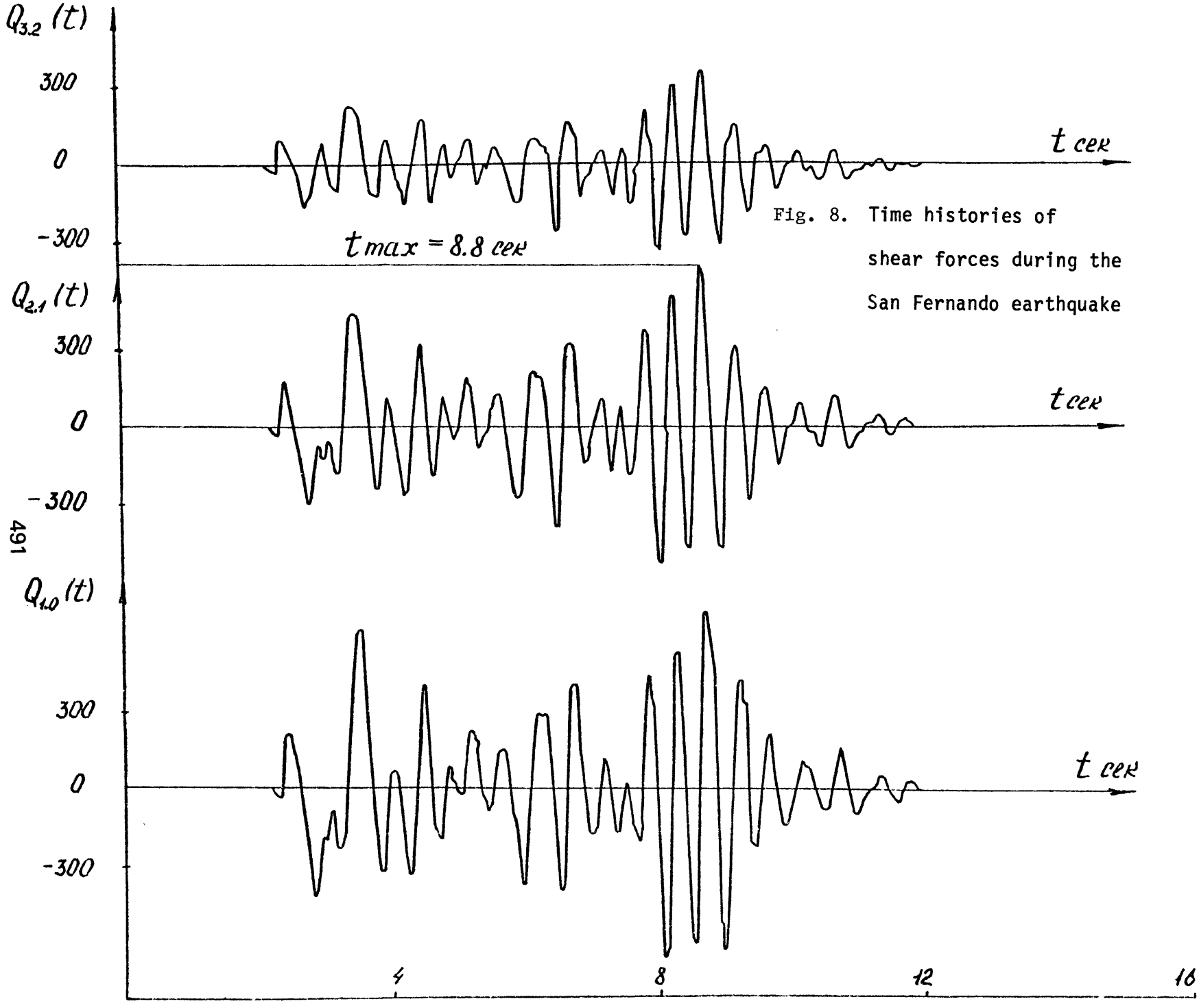

Fig. 8. Time histories of shear forces during the San Fernando earthquake

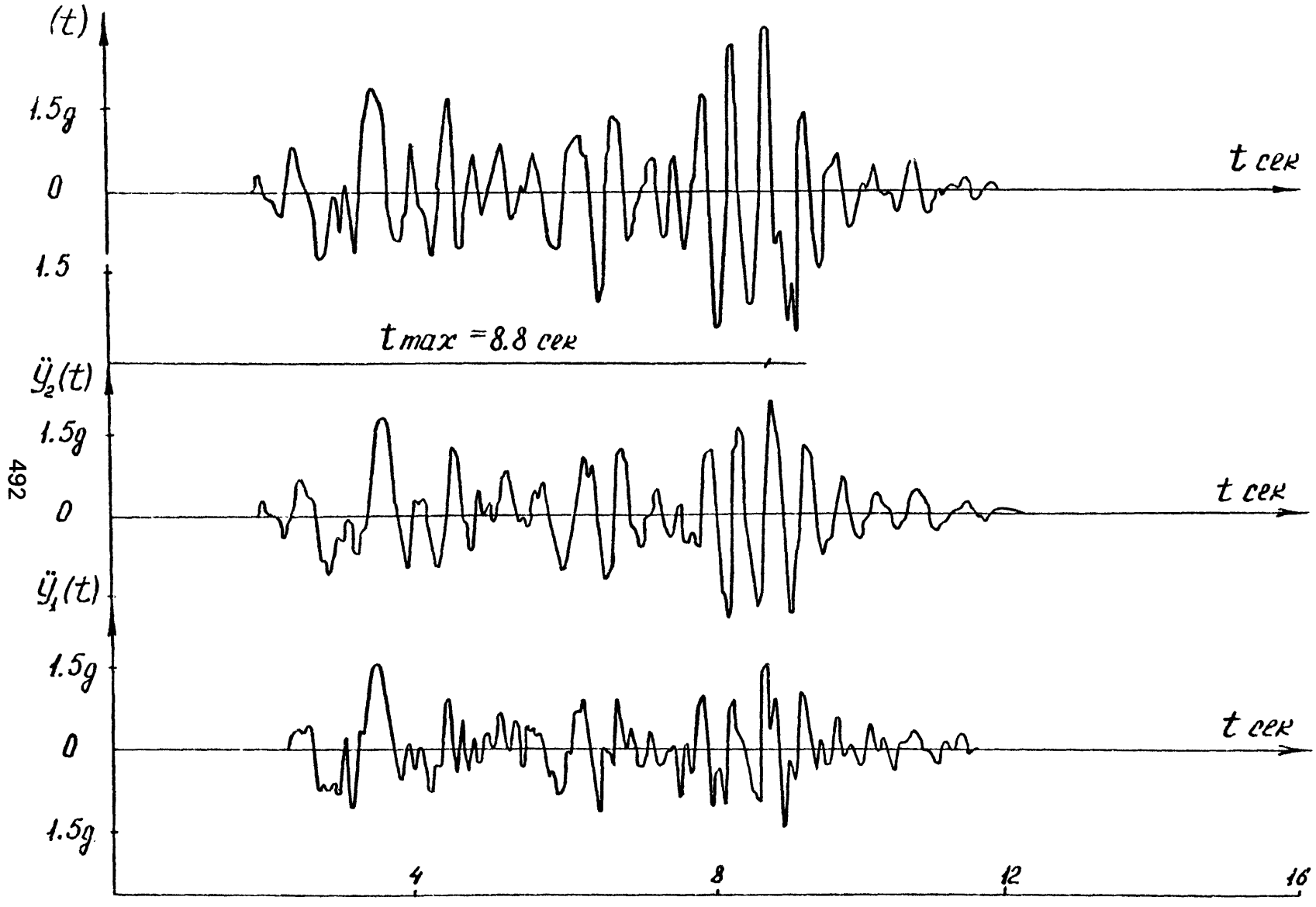

Fig. 9. Theoretical accelerograms of the San Fernando earthquake

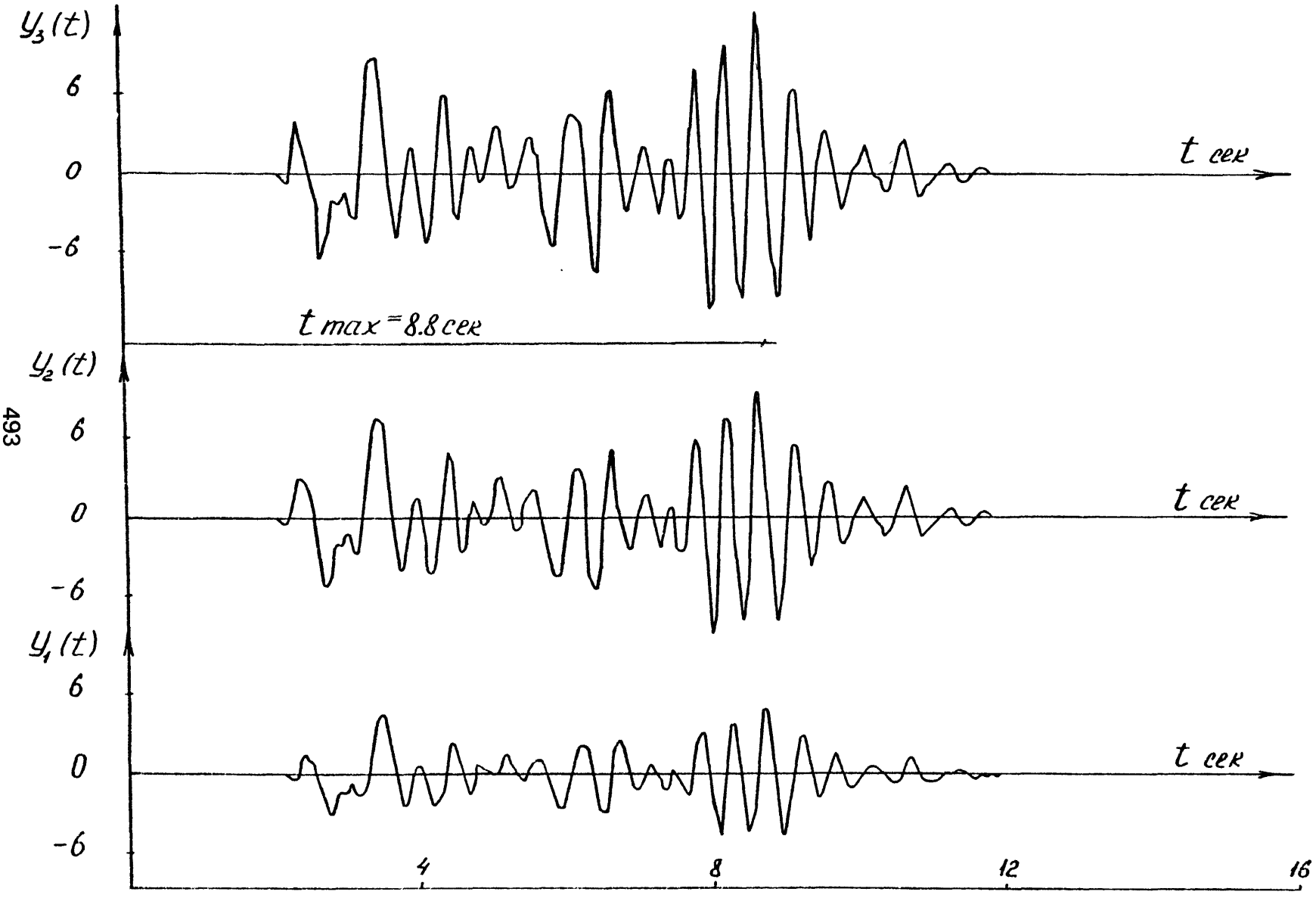

Fig. 10. Theoretical displacement time histories of the San Fernando earthquake.

In this table the amplitudes of the shear forces $Q_{K,K-1}$, which are determined according to standard calculations, were found from the formula:

$$Q_{K,K-1} = \sum_{i=1}^{3} \left| Q^{i}_{K,K-1} \right|,$$

where $Q^{i}_{K,K-1}$ is the shear force, which corresponds to the i-th shape of vibrations. Standard amplitudes of displacements of points along the height of a building were determined from the formula:

$$A_K \leq \left| \frac{K_c \beta(T_1) g}{p_1^2} \cdot \eta_{1K} \right| + \left| \frac{K_c \beta(T_2) g}{p_2^2} \cdot \eta_{2K} \right| + \left| \frac{K_c \beta(T_3) g}{p_3^2} \cdot \eta_{3K} \right|,$$

where p_i is the angular frequency of the fundamental vibrations of a building for the i-th shape, $p_i = \frac{2\pi}{T_i}$

From the theoretical acceleration and displacement time histories produced it is evident that a building experiences vibrations which are principally at a frequency close to the frequency of the first mode. The change in internal stresses occurs also at a frequency which is close to the fundamental frequency. However, higher modes are also clearly evident on the recordings of vibrations produced, especially on the accelerograms. The maximum responses produced for the building investigated occurred during the time of most intensive ground vibrations. The most intensive vibrations

of the building begin 6 s after the onset of the Gazli earthquake, but for the selected partion of the San Fernando earthquake accelerogram they began after 8 s. During the San Fernando earthquake accelerogram, the building vibrated slightly more intensively than during the action of the Gazli earthquake accelerogram.

At this point one should note the next important circumstance: although the maximum acceleration of the San Fernando earthquake exceeded the maximum acceleration of the Gazli earthquake by a factor of two, nevertheless, the amplitudes of the internal stresses in the building, and also the theoretical acceleration of the vibrating elements of the building were quite close. For example, according to standard methodology for calculating seismic actions, the internal stresses must increase by a factor of two during an increase of the coefficient of seismicity K_c.

As is evident from table 1, the calculated amplitudes of the response exceed by several times the amplitudes, which were determined using standard design calculations for the ninth intensity zone. Thus, the maximum amplitude of the shear forces at the level of the lower floor $Q_{1,0}^{max}$ during the action of the Gazli earthquake accelerogram exceed the respective standard amplitude by eight times and by ten times during the action of the San Fernando earthquake accelerogram. The extent to which amplitudes produced for the shear forces exceed standard forces is explained by the large

amplitude of the ground vibration accelerations $\ddot{Y}_0$ (t), which is $\ddot{Y}_{0\,max}$ = 0.6 g for the accelerogram of the Gazli earthquake and $\ddot{Y}_{0\,max}$ = 1.25 g for the accelerogram of the San Fernando earthquake. It should be noted in the standard calculations of the amplitude of the coefficient of seismicity K_c which corresponds in fractions of g up to the amplitude of ground vibration acceleration, for the ninth zone of intensity. One should also consider the fact that the maximum value of response in the transitional process, which is apparent in formula (69), exceeds by 1.3 to 1.4 times the corresponding value of a reaction under steady conditions (24).

There are numerous examples of cases in which calculations based on actual accelerograms of earthquakes yield amplitudes of the response several times greater than the standard design amplitudes. Thus according to reference (25) it is noted that the difference between the values of seismic loads, which are calculated from accelerograms of real earthquakes, and values, which are determined on the basis of standard situations, reaches a factor of three or four. In reference (6) it is also pointed out that this difference can reach a factor of four, a fact also noted in other studies (26). Here it should be noted that in the references cited, accelerograms of earthquakes utilized were of significantly less intensity than those used by us.

Theoretical values greater than standard design values should not be considered unusual or inexplicable. The fact is that the standard amplitudes of the internal seismic stresses are quite arbitrary

in the sense that they are calculated for equally arbitrary limiting values of these stresses in the designed supporting elements. The actual bearing capacity of these elements during brief-duration dynamic loads is significantly higher. In other words, the standard seismic stress R_H and the actual dynamic values R_g of these same stresses during real earthquakes approximately satisfy the ratio:

$$\frac{R_H}{[R]_H} \div \frac{R_g}{[R]_\varphi},$$

where $[R]_H$ signifies the permissible standard value of this stress during its static increase, $[R]_\varphi$ is the actual brief-duration maximum stress, which is still permissible. Of course, calculations made from separate modelling of strong earthquake cannot serve as the basis for a final solution of the problem of standardization of seismic loads: the problem is closely related to more detailed studies of the actual bearing capacity of the elements of a building under seismic conditions.

One must take into account a large variety of factors, which determine the actual behavior of structures during strong earthquakes. Such factors include the elastic-plastic efficiency of structural materials, in which a structural element absorbs significantly more energy than during elastic vibrations.

To a certain degree, consideration of the physical nonlinearity of the "stress-deformation" diagram can be compensated for by an artificial increase of the α coefficient, which figures in our calculations.

This point has been repeatedly noticed by various authors. A detailed study of the formal possibility of such an artificial increase of the coefficient by a factor of two or three for "compensation" of the unconsidered plastic deformations on the example of a linear oscillator was conducted by S. S. Larbinayn (27). In considering the high intensity of the earthquakes examined it is natural to increase the amplitude of the measure of energy scattering α.

The phenomenon of the actual operation of frame buildings during strong seismic action requires specially designed experiments.

6. Preliminary results from explosion studies

Preliminary results of testing the experimental model to seismic blasting are now described. One of the main parts of the investigation -- the study of the behavior of buildings in response to seismic blast action -- was preceeded by a series of specially conducted blasts. These were intended to show the wave picture of ground movement and produce empirical relationships, connecting the parameters of the explosions (quantity of blasting substance, number and depth of charges, their mutual positions) to the parameters of ground vibrations (kinematic amplitudes, periods, duration); this enables one to control the seismic effect of explosions.

It should be noted that conducting such investigations is required for each specific section using the engineering and geological circumstances peculiar to the sector, because the wave picture of ground movement is a "property" of a given section.

Study of the wave picture of ground movement was initially conducted

by placing charges in solitary and single-row linearly concentrated boreholes. Performing separate blasts permitted us to show the relationships between the kinematic parameters of the vibrations of ground particles and the quantity of blasting material, depth of charge and distance to recording site. By executing the blasts with linearly, single-row distributed charges creates the possibility of a smooth wave front at relatively short distances; thus the directionality and effectiveness of the blast action could be studied at the instant of blasting. The results of these investigations are set forth in references (28) and (29).

Investigations of the parameters of ground vibrations during solitary and linearly, single-row distributed blasts at the instant of the blast showed that it is possible to attain, depending on the parameters of the explosion, such a vibration intensity (in particular, speeds of vibrations of ground particles on the order of 30-40 cm/s), that buildings which experience significant overloads of the type which occur during quite strong earthquakes.

However, in this case the duration of ground vibrations does not exceed 1.5 s and dies out with a decrease of the distance to the recording points. A substantial contrast in the frequency composition of the explosions and real earthquakes was also observed.

In view of this, we conducted investigations at the Institute of Seismic Resistant Construction and Seismology of the Academy of Science of Tadzhikskaya SSR in order to show the possibility of earthquake modeling using explosions which would be sufficient for practical use.

Certain aspects of this problem were examined in references (30) and (31).

As the tests showed, the duration of ground vibrations can be increased by the aid of blasts with multi-row linearly distributed charges with a delay in blasting between rows. Such a type of six-row linearly distributed blast with a delay of blasts between rows of 0.5 s (the amount of delay was taken from (28) was conducted in 1975 at the experimental proving ground. The charge depth was 20 m. The overall weight of the blasting material was 12 t. The positioning layout of the charges is presented in Fig. 11. The blast wave progressed in the direction of the experiment frame building.

The tests and investigations, also described in reference 34, were conducted by a group of Soviet and American scientists in accordance with the Agreement on Cooperation in the Area of Protection of the Environment (problem 9, project 4, "Engineering and seismological investigations").

7. Registration of ground vibrations and vibrations of the experimental model of the frame building

The experimental model was equipped with Soviet (32) and American equipment for recording the kinematic parameters of the vibrations of the ground and the building itself. We used S5S and VBP-3 seismic receivers with five Hertz GB-SH galvanometers for recording displacements. The dynamic range of the S5S seismic receiver is 0.01 - 15 mm, and the frequency range is 02 -100 Hz. The range of the VBP-3 seismic receiver is 1-100 mm, and the frequency range is 1-100 Hz.

Recording of the accelerations of the vibrations was made by two types

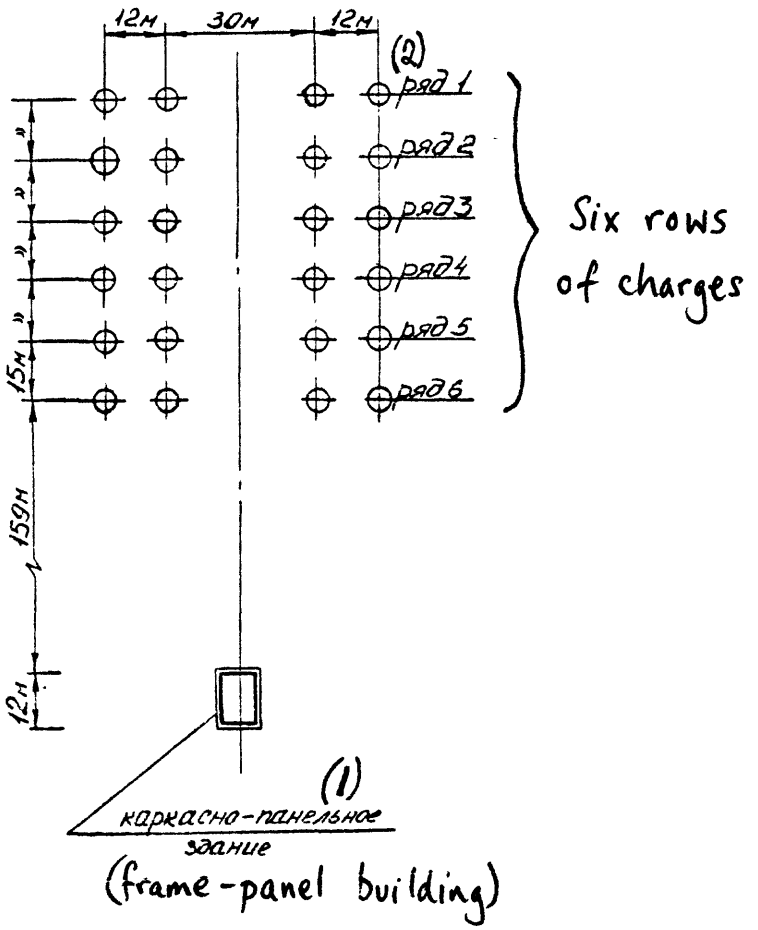

Fig. 11. Plan for location of charges.

Key: (1) Frame building.
(2) Charge.

of seismic receivers -- the OSP seismic receiver coupled with the 120 Hertz GB-1U galvanometer, whose frequency range is 0.17 - 30 Hz, and with the 50 Hertz "Kinemetrics" accelerometers. The vibrations registered by the Soviet equipment were recorded on photographic paper on the N-700 lightbeam oscillograph. The vibrations registered by the "Kinemetrics" accelerometers were recorded onto light-sensitive film of the "Kinemetrics CRA-1" analog recorder.

The seismic receivers for registering horizontal displacements and accelerations of building vibrations were installed along the two principal building directions at each floor level and on the foundation. Seismometers, which register vertical vibrations, were placed on the foundation and on the roof.

In order to detect possible torsional vibrations of the experimental model of the building relative to the vertical axis at three of its points (on the foundation, on the lst floor and third floor (roof)) double-pendulum SBGPP seismometers were installed in combination with five Hertz GB-SH galvanomometers. In addition, for the same purpose, two "Kinemetrics" accelerometers were installed on the east and west ends of the roof and oriented in the direction of the blast (north-south direction).

The layout plan of the seismic apparatus in the building is presented in Fig. 12 and 13.

Some of the seismic receivers for recording ground vibrations were placed at the base of one of the perimeter columns of the building, and the remaining ones were placed 25 m distant from it is pits at the level of the foundation basement (Fig. 12). Two kinematic amplitudes were

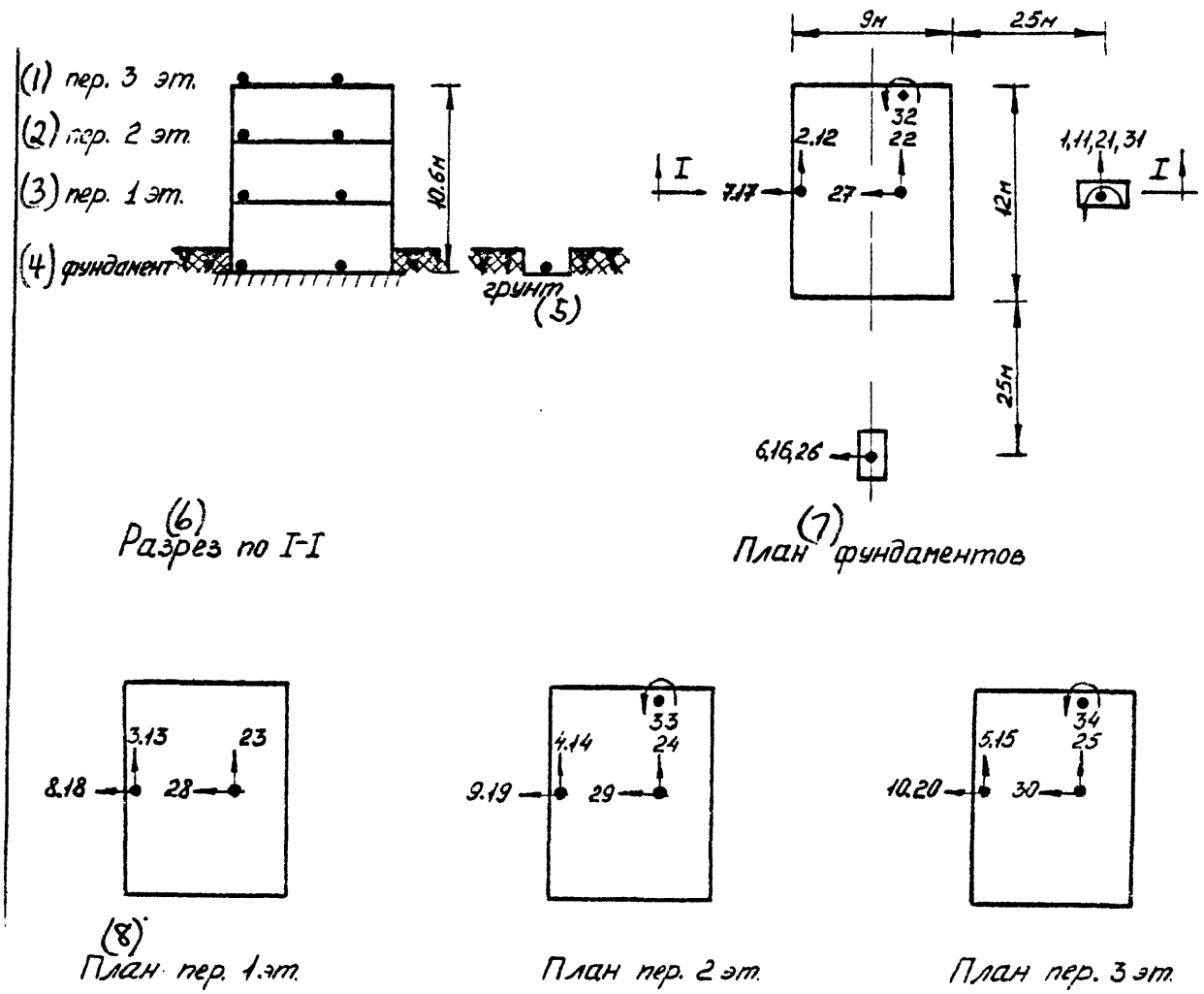

Fig. 12 Layout plan for seismic registering apparatus

1 - 10 SS S5S seismic receivers, 11-10 --

V5P-3, 21-30 —OSP, 31-34 -- SBGPP).

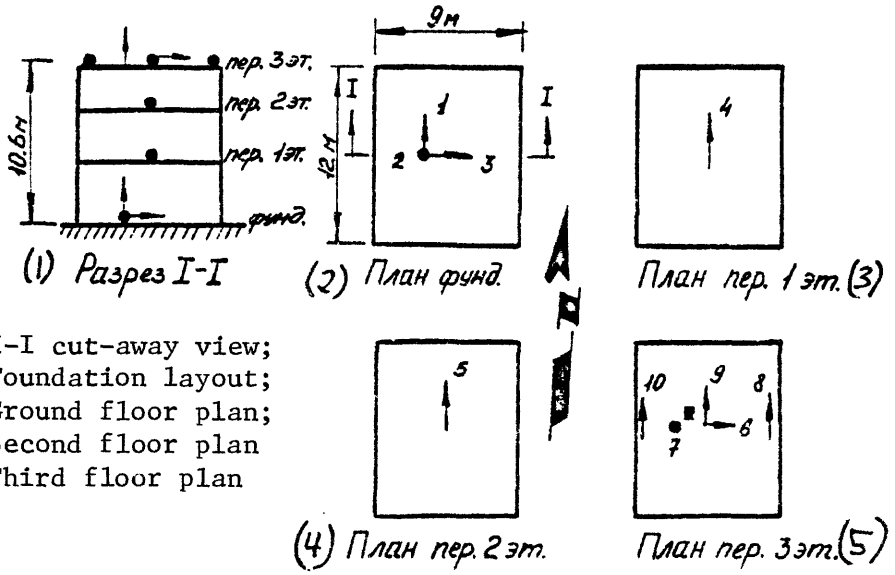

Key: (1) I-I cut-away view;
(2) Foundation layout;
(3) Ground floor plan;
(4) Second floor plan
(5) Third floor plan

Fig. 13. Layout plan for "Kinemetrics" accelerometers, registered -- acceleration and displacement of the three components which corresponded to the main axes of the building and the vertical axis Z.

8. Preliminary results of the investigations. In this work we present the primary analysis of vibrograms of vibrations of the ground and of the building of the component which corresponds to the direction of the formulation of the blast wave. Figures 14, 15, 16, 17 present the accelerograms obtained for vibrations of the ground and building, the maximal amplitudes of the kinematic parameters are given in table 2.

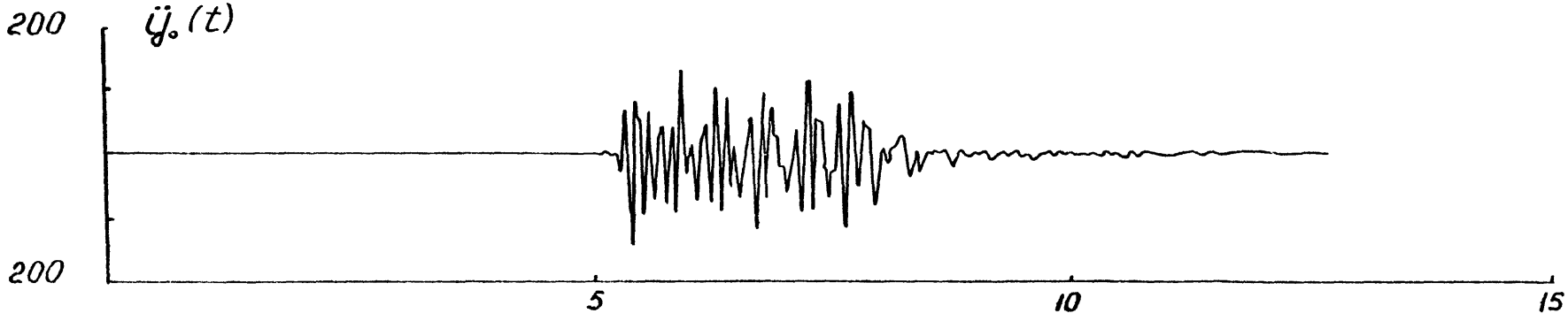

Fig. 14. Accelerogram of ground vibrations during blast action using 12 tons of explosives.

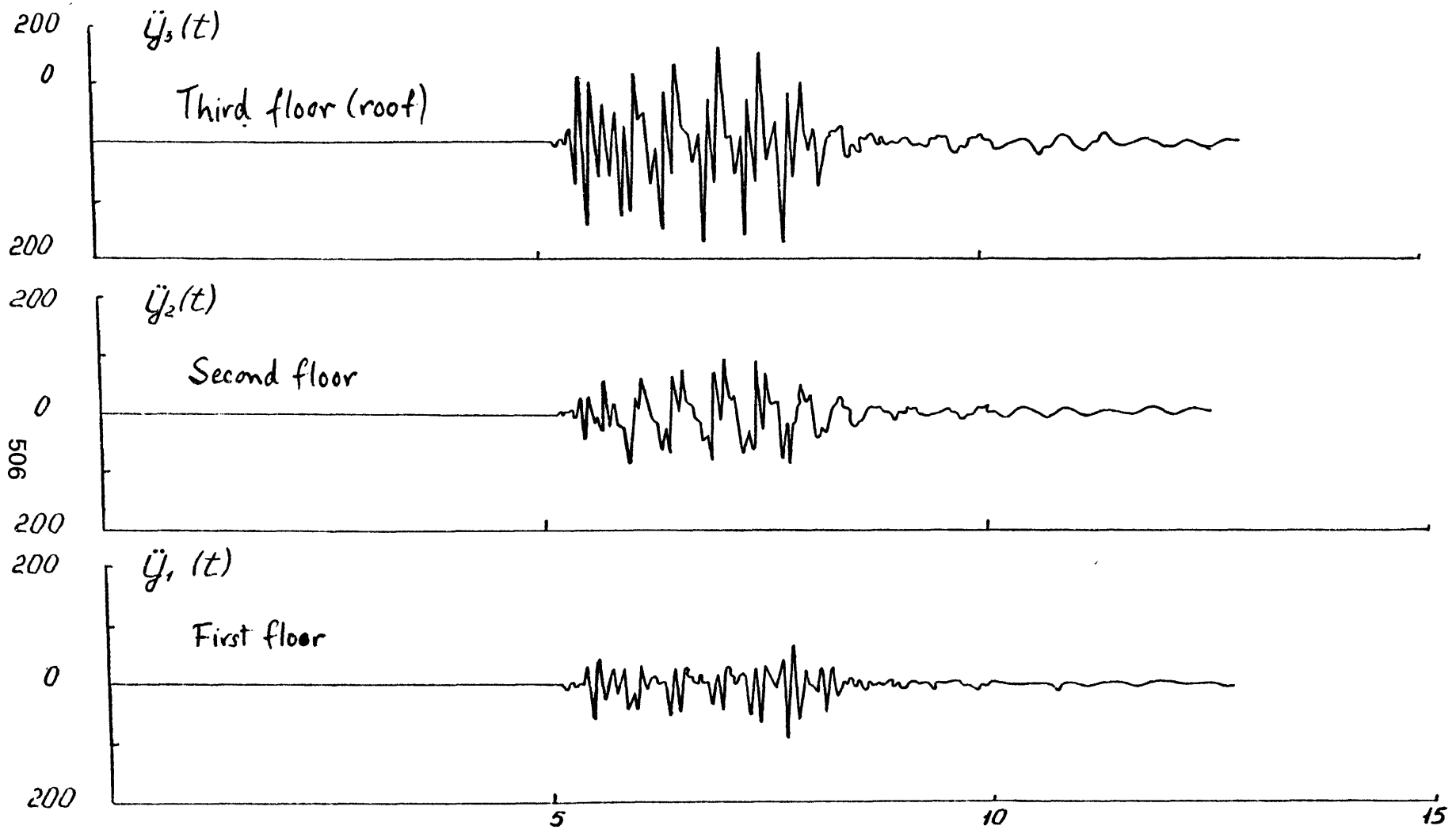

Fig. 15 Recorded (OSP accelerometers) accelerograms of vibrations at various floor levels of the experimental frame building

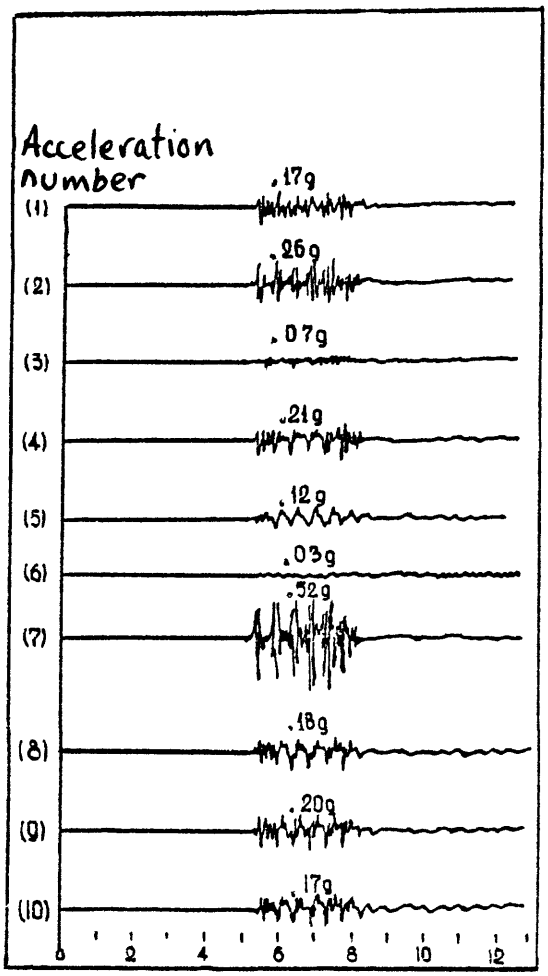

Fig. 16 Recorded (Kinemetrics accelerometers) accelerograms of vibrations of the ground and at several points within the experimental frame building

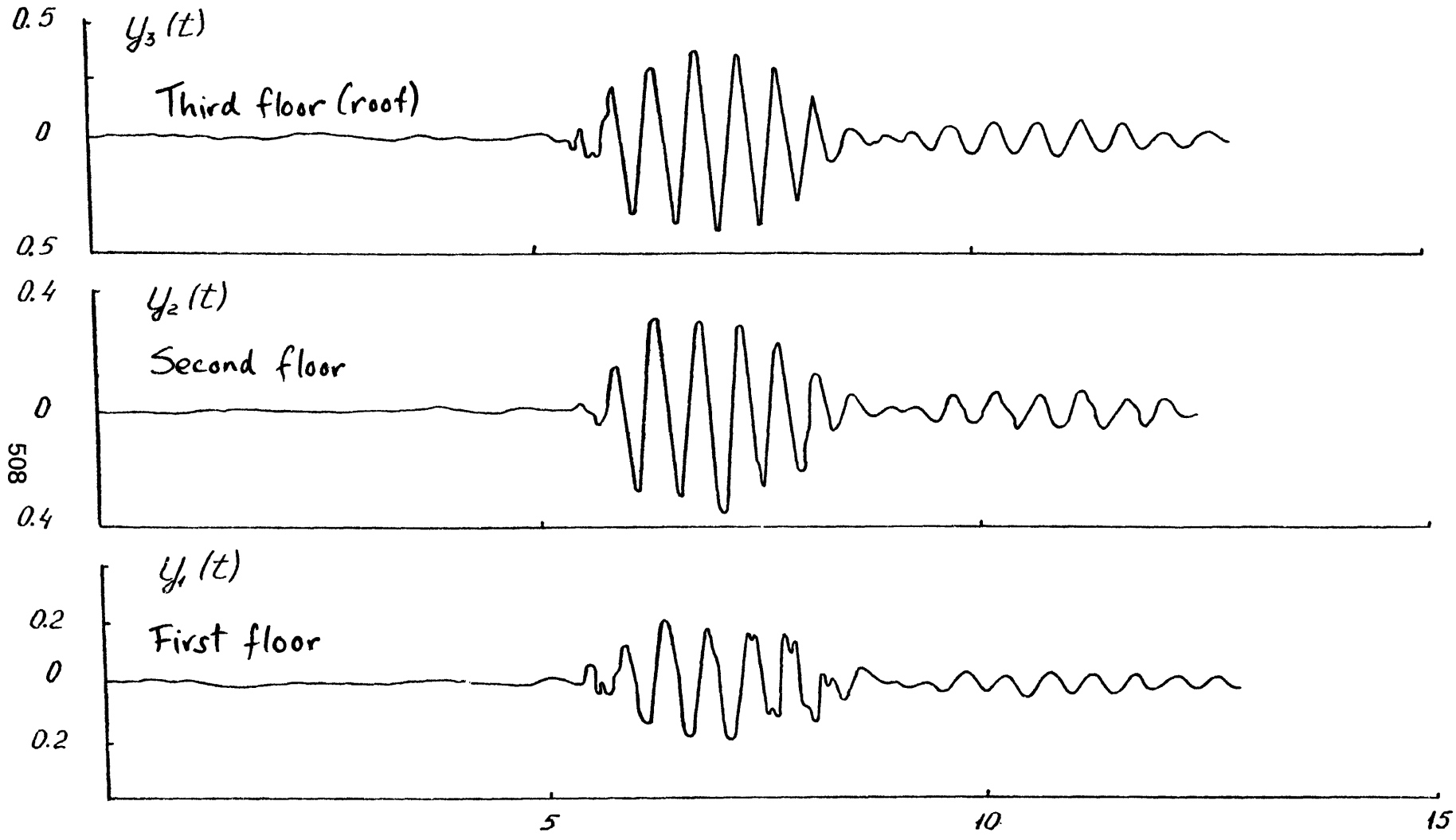

Fig. 17 Recorded (S 5 S seisometers) seismograms of vibrations at various floor levels of the experimental frame building

Table 2

Transducer location	Maximum amplitude of acceleration	Maximum amplitude of displacement
Ground (25 m from building	110 cm/s^2	0.10 cm
Ground (at base of outer column)	144 cm/s^2	-
Foundation	110 cm/s^2	0.20 cm
Frist floor	206 cm/s^2	0.26 cm
Second floor	150 cm/s^2	0.39 cm
Third floor	196 cm/s^2	0.47 cm

It should be noted that the accelerograms of the vibrations, which were registered by OSP seismic receivers and by the "Kinemetrics" accelerometers are nearly identical to one another. The maximal amplitudes of the accelerations of vibrations are also quite close to one another, with the exception of the amplitude obtained for the ground floor. The maximal amplitude recorded by the "Kinemetrics" accelerometer equals $\ddot{Y}_{2max} = 118$ cm/s^2, and by the seismic receiver OSP equals $\ddot{Y}_{2\,max} = 150\ cm/s^2$.

From the vibrograms generated, it is evident that the duration of intensive ground vibrations is approximately 3.5 s. The vibrations occur with a predominant perior $T_{rp} = 0.45$ s.

Let us consider the determination of the principal dynamic characteristics of the building. An analysis of the seismograms showed that its

basic period of free vibrations equals T = 0.47 s. Here it should be noted that with less weak actions (in the experiments conducted earlier) the amplitude of this period was equal to T = 0.30 s. This is explained by the fact that the wall panels also participate in the performance of a frame during weak actions; during stronger actions they cease to operate.

The resulting curves showing the displace shape of the fundamental mode of the building indicate that the vibrations of the building are of the shear-bed form. This mode shape is given in Fig. 18.

The approximate value of the logarithmic increment of dampening δ, defined as the natureal logarithm of the radio of the amplitude of the preceeding amplitude of vibrations to the subsequent one, being based on the last three cycles of intensive vibrations on the seismograms, was equal to $\delta = 0.3$. The measure of energy scattering was $\alpha = \frac{\delta}{\pi} = 0.096$, and damping in fractions of the critical $\xi_e = \frac{\alpha}{2}$ X 100% = 4.8%.

Fig. 19 presents the spectra of reactions, which were constructed on the basis of accelerogram generated by "Kinemetrics" accelerometers, which were placed in the ground at the base of the one of central support columns. The spectra are given in a tripartite diagram. In examining the spectra of the illustrated velocities we see that the maximal values basically fall within the interval of periods 0.1 to 0.5 s. Based on this and keeping in mind that the basic period of vibrations of the experimental model of a building equals $T_1 = 0.47$ s, we are led to the conclusion of the advantage of conducting tests on such kinds of buildings

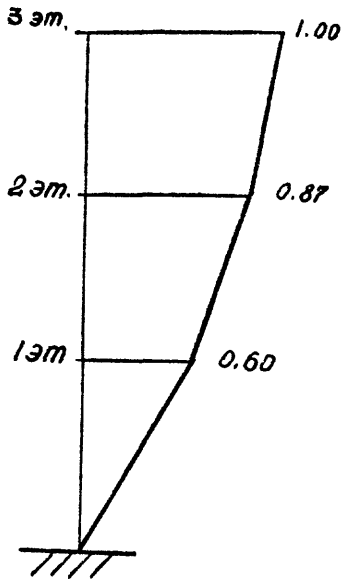

Fig. 18. Basic form of vibrations of an experimental frame building.

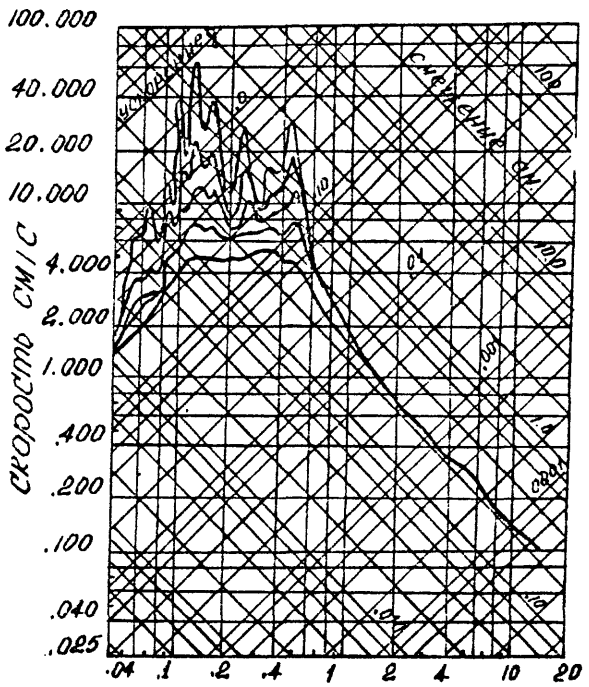

Fig. 19. Spectra of the reaction during seismic blast action.

using explosion studies, executed similarly to the one we carried out.

In concluding our preliminary analysis we should mention that we did not detect any kind of damage to the building in our experiment.

9. Comparison of calculated and observed response of the building. On the basis of the model described below we calculated the response of the building to the action which was given by the accelerogram of ground vibrations at the base of the one of the central support columns for a given blast. The digitization stop size for the accelerogram was

Δt = 0.018 s.

For the dynamic model of the building we used a cantilever under sheer stress, which was supporting concentrated masses at each floor; we assumed a rigid foundation condition.

The theoretical calculated maximal amplitudes of acceleration and displacement at various points are presented in table 3, and the time histories of theoretically determined response are given in Figs. 20 and 21.

Table 3

Location	Maximum amplitude of acceleration	Maximum amplitude of displacement
First floor	247 cm/s^2	0.4 cm
Second floor	220 cm/s^2	0.7 cm
Third floor	237 cm/s^2	0.9 cm

From the comparison of theoretical determined and recorded response grams of vibrations, it is evident that they agree quite well with each

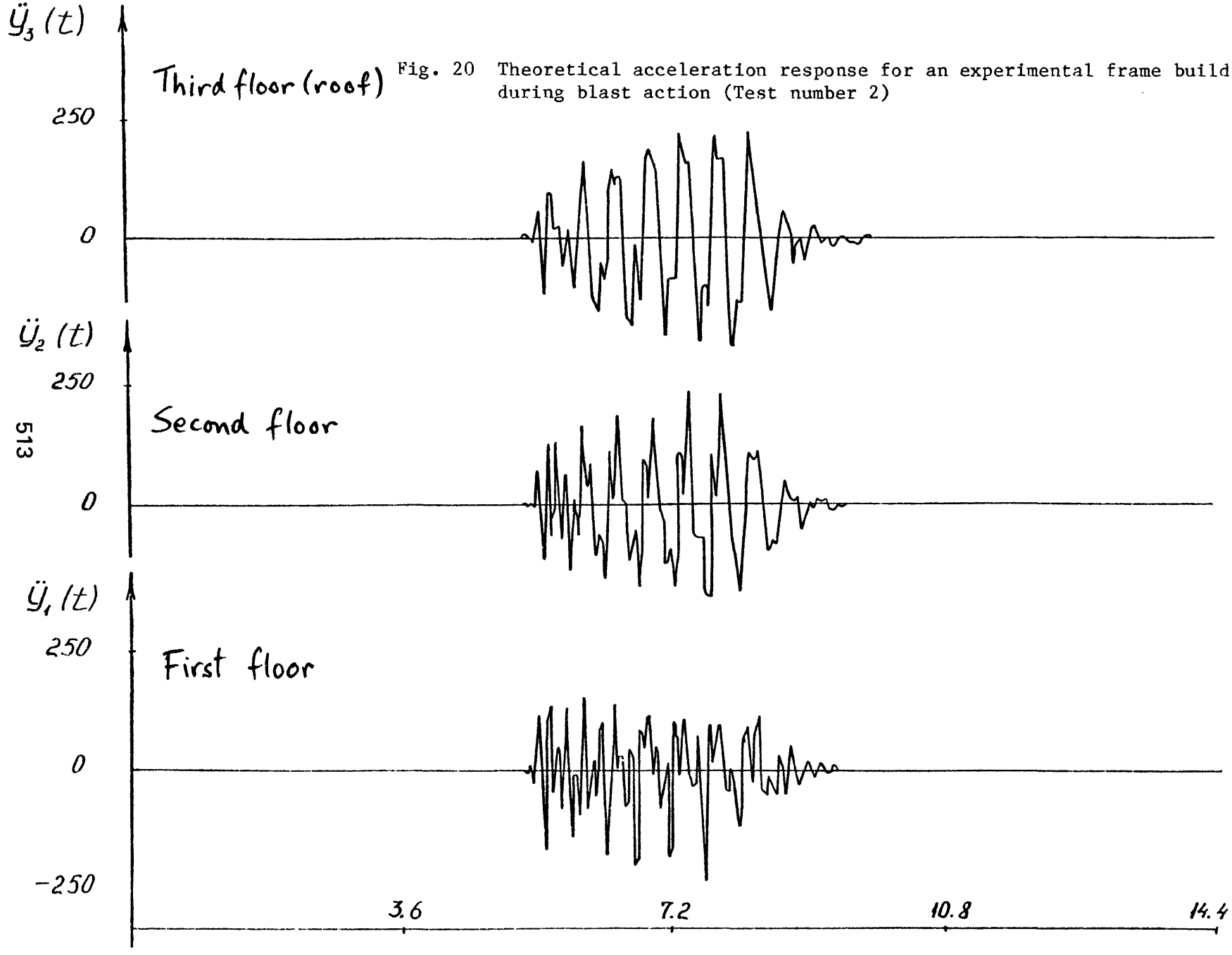

Fig. 20 Theoretical acceleration response for an experimental frame building during blast action (Test number 2)

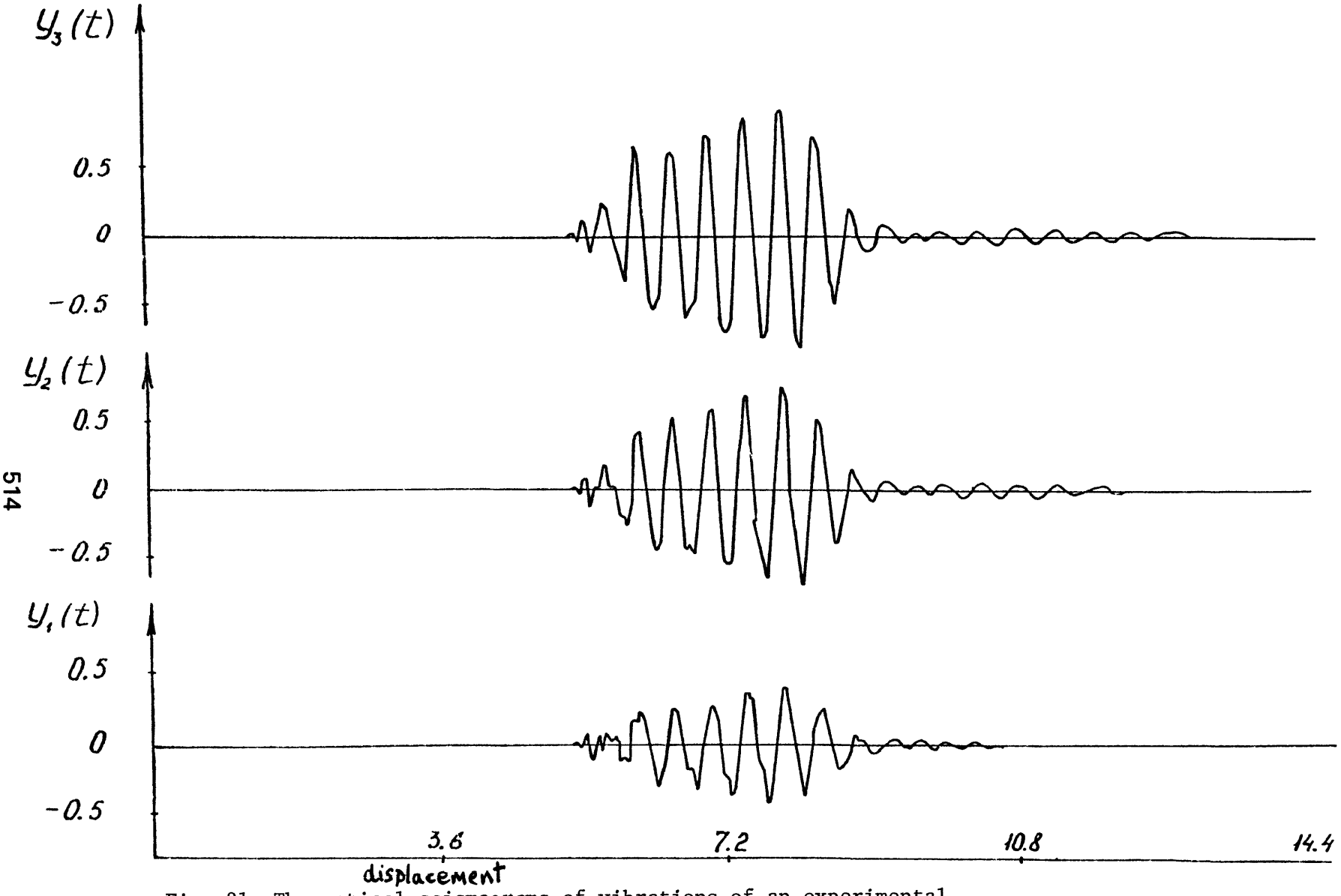

Fig. 21. Theoretical seismograms of vibrations of an experimental frame building during seismic blast action (test number 2).

other.

Regarding the comparison of the theoretically determined maximal amplitudes of response, the amplitudes of acceleration (allowing for the approximations of all our initial data, and of our initial hypotheses) turned out to be practically identical. The difference in amplitudes for the ground and 3rd floors was 20%, and for the second floor it was 46%; the difference in amplitudes of maximum displacements is more significant -- from 50 to 90%.

The theoretically determined response together with our comparisons shows the suitability of the algorithm used for an approximate evaluation of building response to random seismic actions.

With this algorithm we also determined the theoretical amplitudes of the internal stresses (shear forces), which arise in sections of the experimental model of a building during the explosion study that was made. The time histories of shed forces are presented in Fig. 22. The maximum amplitudes equaled: at the first floor, $Q_{1,0}^{max}$ = 58.6 T, at the second floor, $Q_{2,1}^{max}$ = 46.1 T, and at the third floor, $Q_{3,2}^{max}$ = 26.1 T. We shall compare these amplitudes with the amplitudes which are determined according to several current design standards.

10. Determination of calculated seismic loads according to the Unifed Building Code (UBC 1976) of the U.S.A.

The basis formula for determining seismic loads in this

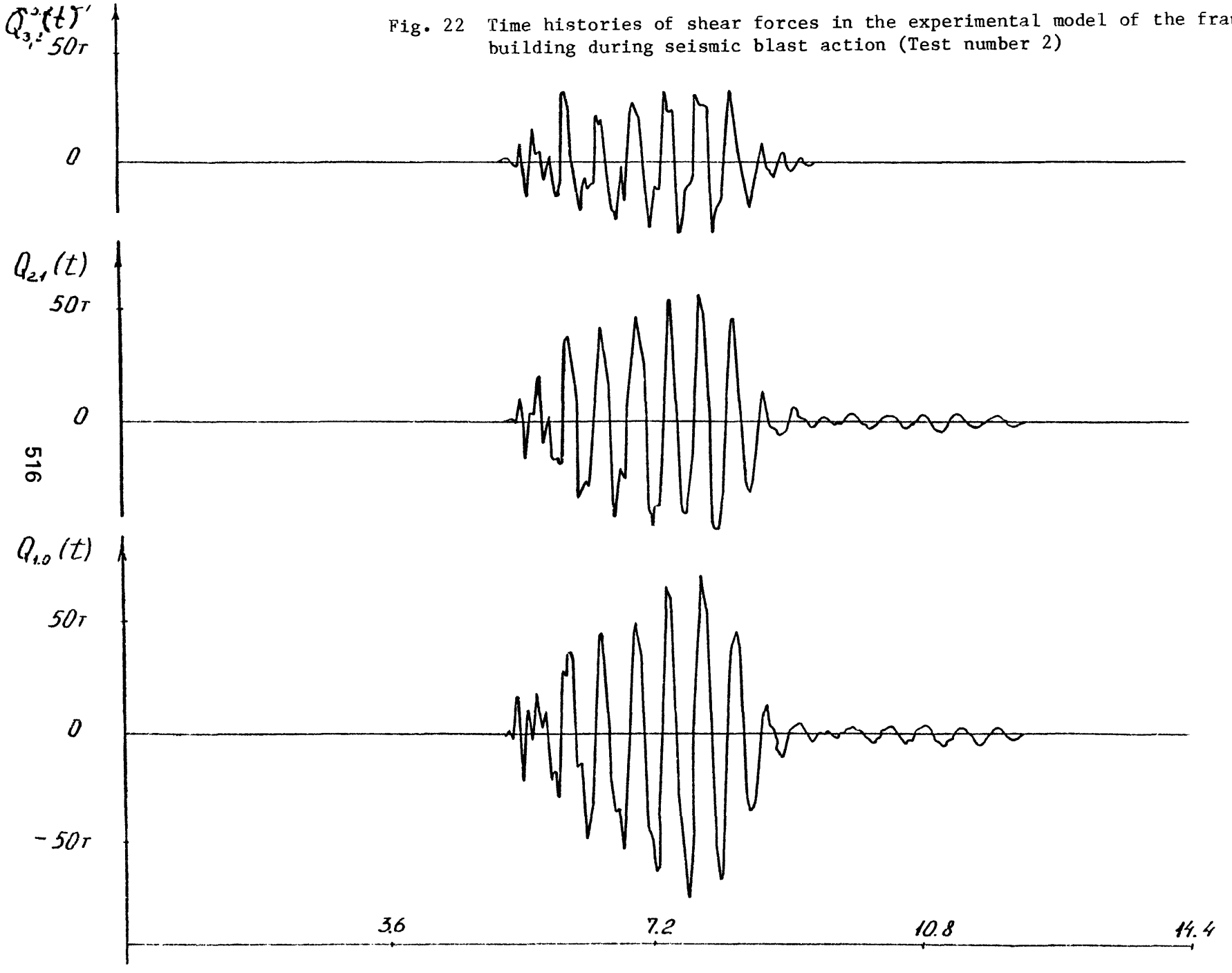

Fig. 22 Time histories of shear forces in the experimental model of the frame building during seismic blast action (Test number 2)

case is a formula of the type:

$$V=Z.i.K.C.S.W, \qquad (76)$$

where Z is the coefficient whose value is dependent on the seismicity of the region; for a region with high seismicity (zone 4) Z = 1.00;

(T=0.5s, C=0.094 in the case of the test building)

i is the occupancy importance factor; for non-essential low-occupancy structures i = 1.00;

K is the horizontal force factor which is assigned in relation to the kind of building; for buildings with a box system K - 1.33; for buildings with a dual bracing system consisting of a ductile moment resistant spacframe and shear walls or braced frames K = 0.80; for buildings with a ductile moment resisting space frame K = 0.67;

C is a numerical coefficient equal to $\frac{1}{15\sqrt{T}}$

T is the fundamental elastic period of vibration.

S is the coefficient for site-structure resonance; for unknown geological conditions S = 1.5;

W is the total dead load of the building ($W=W_1 + W_2 + W_3$ = 332.9T in the case of the test building).

Using formula (76) we can determine the complete seismic load: assuming K = 1.22,

$$V=1\cdot1\cdot1{,}33\cdot0{,}094\cdot1{,}5\cdot332{,}9=62{,}4T .$$

assuming K = 0.8,

$$V = 37.6\ T,$$

and assuming K = 0.67,

$$V = 31.4\ T.$$

The distribution of the complete seismic load over the height of the building is calculated on the basis of the formula:

$$F_x = \frac{(V - F_t) \cdot W_x \cdot h_x}{\sum_{i=1}^{n} W_i \cdot h_i}, \qquad (77)$$

where **Wi** is the weight, concentrated in the **i** -th level of the building;

hi is the height from the foundation to the **i** -th level;

$\mathbf{F_t}$ is the force on the upper part to account for higher mode behavior for flexible structures,

(when T_1 0.7 s F_t = 0).

For K = 1.33 the distribution of the complete seismic load over the height is as follows: F_1 = 11.8 T; F_2 = 24.0 T; F_3 = 26.6 T.

The calculated values of seismic loads $\mathbf{S_{iK}}$ for the experimental frame buildings, computed according to the Soviet code EPSN P-A.12-69, are presented in table 4. These values correspond to seismic intensity zone nine, and are the values of the coefficients for standardize mode shapes of vibration.

Table 4.

	First Mode		Second Mode		Third Mode	
Floor	T_1 = 0.5 s		T_2 = 0.16 s		T_3 = 0.11 s	
	η_{1K}	$S_{1K}T$	η_{2K}	$S_{2K}T$	η_{3K}	$S_{3K}T$
1.	0.622	13.7	0.325	10.7	0.080	2.6
2.	1.051	22.7	0.120	3.9	-0.122	-4.0
3.	1.229	20.4	-0.360	-9.0	0.058	1.4

If we determine the calculated values of the internal stresses R_k in the K-th section by the formula: where R_{ik} is the amplitude of the

$$R_k = \sum_{i=1}^{n} |R_{ik}|,$$

internal stress in the K-th section according to i-th shape, then the shear force in the lower section of the cantilever will equal

$$Q_{1,0} = \sum_{i=1}^{3} Q_{1,0} = 62.4\ T$$

As we see, the value of the intersecting force $Q_{1,0}$, which is determined according to Soviet code SN&P P P-A.12-69, coincides with a full seismic load V at the base of the building determined using the USA design code (UBC 1976) when K = 1.33. It should be noted that the distribution of seismic loads by height according to the USA code in this case coincides in the first approximation with the distribution of loads for the basic form of free vibrations of buildings according to the Soviet code, SN&P P-A.12-69.

On the basis of the foregoing one can see discrepancies in the distribution of seismic loads according to SN&P P-A.12-69 and (UBC 1976). The discrepancies exist, for example, in determining the coefficient C and in the distribution of the seismic loads by height.

In particular cases, for small and medium-size buildings, the calculations according to the SN&P P-A.12-69 and UBC 1976 can yield completely harmonious results, as happened in our case (when

K = 1.33).

It is interesting that the resulting theoretical amplitudes of the shear forces were close to the code-determined values, determined for intensity zone 9. (K_s = 0.1). If we consider that the recorded maximum amplitude of accelerations of vibrations of the $\ddot{Y}_{omax}$ equaled 144 cm/s^2 at the base of the column, 110 cm/s^2 at a distance 25 m away from the building, then it can be said that the experimental model of the building experienced loads corresponding to eight and ninth intensity zones (33).

There is no doubt about the advantage of using specially created explosion-tests when investigating the seismic stability of buildings and structures (34).

BIBLIOGRAPHY

1. Tishchenko, V. G., Abdurashidov, K. S., Shaalimov A. A. O dinamicheskikh kharakteristikakh mnogoetazhnykh zdaniy pri simmetrichnykh prostranstvennykh kolebaniyakh. [Dynamic Characteristics of Multistory Buildings During Symmetrical Spatial Vibrations]. Sb. "Voprosy inzhenernoy seysmologii," Vyp. 16, "Nauka," M., 1974.

2. Vol'fson, B. P. O sobstvennykh kolebaniyakh odnomernoy periodicheskoy sistemy. [Fundamental Vibrations of One Dimensional Periodic System]. Sb. ""Issledovaniya po teorii sooruzheniy." Vyp. XVII. Izd-vo literatury po str-vu, M., 1969.

3. Weigand, A. Die gedamphte homogene Schwiengunskette. Z. angew. Math., Band 38, heft 112, Jan/Febr., 1958.

4. Derkachev, A. A, Negmatullayev,S. Kh. Dinamicheskiye raschetnyye skhemy zdaniy i ikh svobodnyye kolebaniya. [Dynamic Calculated Plans of Buildings and Their Free Vibrations]. Izd-vo "DONISH," Dushanbe, 1970.

5. Derkachev, A. A. Metody regulyarizatsii nekorrektnykh zadach teorii seysmicheskikh nagruzok. [Methods for Regularization of Improper Problems of the Theory of Seismic Loads]. Vyp. 2. Izd-vo "DONISH," Dushanbe, 1972.

6. Rasskazovskiy, V. T. Osnovy fizicheskikh metodov opredeleniya seysmicheskikh vozdeystv[Principles of Physical Methods of Determination of Seismic Actions]. Izd-vo "FAN," Tashkent, 1973.

7. Tseytlin, A. I. Ob uchete zatukhaniya v raschetakh sooruzheniy na seysmicheskiye vozdeystviya. [Consideration of Dampening in Calculations of Structures for Seismic Actions]. Sb. "Sovershenstvovaniye metodov rascheta i konstruirovaniye zdaniy i sooruzheniy, vozvodimykh v seysmicheskikh rayonakh" TSNIISK, M. 1976.

8. Markus, M., Mink, Kh. Obzor po teorii matrits i matrichnykh neravenstv. [Review of the Theory of Matrices and Matrix Inequalities]. Izd-vo "Nauka," M., 1972.

9. Ayzenberg, L. M. Sooruzheniya s vyklyuchayushchimisya svyazyami dlay seysmicheskikh rayonov. [Structures With Break-Away Connections for Seismic Regions]. Stroyizdat, M., 1976.

10. Teal, E. J., Lord T., Meyer S. Multi-Degree of Freedom Response Spectra for Elastic Systems. Fifth World Conference on Earthquake Engineering, Rome, 1973.

11. Rozenblyut, E. Nekotoryye prilozheniya teorii veroyatnosti k raschetu na seysmichnost'. [Certain Applications of the Theory of Probability to Calculation of Seismicity[. Sb. "Mezhdunarodnaya konferentsiya po seysmostoykomu stroitel'stvu." Gosstroyizdat, M., 1961.

12. Korn, G., Korn, T. Spravochnik po matematike. [Handbook of Mathematics]. Izd-vo "Nauka,", M., 1968.

13. Derkachev, A. A., Zolotarev, A. I. Opredeleniye impul'snykh reaktsiy vnutrnnikh usiliy v nekotorykh regulyarnykh sooruzheniyakh. [Determination of Pulse Reactions of Internal Stresses in Certain Regular Structures]. DOKL. AN TADZH SSR, Vol. XIX, No 4, Izd-vo "DOINSH," Dushanbe, 1976.

14. Zolotarev, A. I. Opredeleniye chastotknkh kharakteristik nekotorykh regulyarnykh sistem. [Determination of Frequency Characteristics of Certain Regular Systems]. DOKL. AN TADZH SSR, Vol. XX., No 2, Izd-vo "DOINSH," Dushanbe, 1978.

15. Derkachev, A. A., Negmatullayev, S. Kh. Sovremennyye problemy inzhenernoy seysmologii i teorii seysmostoykosti. [Modern Problems of Engineering Seismology and of the Theory of Seismic Stability]. Izd-vo "DOINSH," Dushanbe, 1975.

16. Aleksin, P. A., Grayzer, V. I., Pletnev, K. G., Shteyberg V. V., Zaynutdinov, K. S. Kolebaniya grunta pri sil'nykh Gazliyskikh zemletryaseniyakh. Ref. Informatsii, Vyp. II, TSINIS, M., 1976.

17. Polyakov, S. V., Zharov, A. M. Otsenka sravnitel'noy povrezhdayemosti zdaniy razlichnykh konstruktivnykh skhem vo vremya Gazliyskikh (Kyzyl-Kumskikh) zemletryaseniy 8 aprelya i 17 maya 1976 g. Ref. Informatsiya, vyp. II, TSINIS, M., 1976.

18. Martem'yanov, A. I., Shirin, V. V. Otsenka stepeni povrezhdeniya zdaniy, postradavshikh v rezul'tate sil'nykh zemletryaseniy v Zapadnykh Kyzyl-Kumakh. Ref. Informatsiya, vyp. II, TSINIS, M., 1976.

19. Ashkinadze, G. N., Gendel'man, L. B. Sostoyaniye krupnopanel'nykh zdaniy pos. Gazli posle zemletryaseniy 8 aprelya i 17 maya 1976 g. Ref. Informatsiya, vyp. II, TSINIS, M., 1976.

20. Strong-Motion Instrumental Data on the San-Fernando Earthquake of Feb. 9, 1971. D. E. Hudson, Editor, 1971.

21. San-Fernando, California, Earthquake of February 9, 1971. V. 1, 2, Washington, D. C. 1973.

22. Shteynberg, V. V., Pletnev, K. G., Grayzer, V. M. Akselerogramma kolebaniy grunta pri razrushitel'nom Gazliyskom zemletryasenii 17 maya 1976. Ref. Informatsiya, vyp. I, TSINIS, M., 1977.

23. Strong Motion Earthquake Accelerograms, Digitized and Plotted Data. California Institute of Technology, Pasadena, California, 1973.

24. Barshteyn, M. F. Prilozhneiye veroyatnykh metodov i raschetu sooruzheniy na seysmicheskiye vozdeystviya. "Str. Mekh-ka i raschet sooruzheniy," No. 2, 1960.

25. Nazarov, A. G., Darbinyan, S. S. Osnovy kolichestvennogo opredeleniya intensivnosti sil'nykh zemletryaseniy. [Principles of Quantitative Determination of the Intensity of Strong Earthquakes]. Izd-vo AN Arm. SSR, Yerevan, 1974.

26. Begiyev, B. B. Seysmicheskiye sily i deformatsii v protsesse zemletryaseniy, vychislennyye s pomoshch'yu elektronnykh mashin. Byull. Soveta po seysmologii AN SSSR, No. 14, 1963.

27. Darbinyan, S. S. Statisticheskiy analiz parametrov kolebaniy grunta pri sil'nykh zemletryaseniyakh i ikh vozdeystviya na uprugo-plasticheskiye sistemy. [Statistical Analysis of the Parameters of Ground Vibrations During Strong Earthquakes and Their Actions on Elastic-Plastic Systems]. Doctoral Dissertation. Leninakan, 1974.

28. Rulev, B. G., Kharin, D. A. O napravlennom deystvii rassredotochennykh odnoryadnykh vzryvov. [Directional Action of Distributed Single-Row Blasts]. Vzryvnoye delo, sb. 64/21. Seysmika i voronki vybrosa pri podzemnykh vzryvakh. [Seismics and Ejection Cones During Underground Blasts]. Izd-vo "Nedra," M., 1968.

29. Negmatullayeva, S. Kh., Rulev, B. G., Kharin, D. A. Rezul'taty ispytaniya konstruktsiy razlichnykh tipov seysmovzryvnymi volnami. VOPROSY INZHENERNOY SEYSMOLOGII, vyp. 15, Izd-vo "Nauka," M., 1970.

30. Grib, S. I. Rabota svaynykh fundamentov na gorizontal'noye seysmicheskoye vozdeystviye. [Performance of Pile-Supported Foundations During Horizontal Seismic Action]. Candidate Dissertation. M., 1972.

31. Karapetyan, B. K., Karapetyan, N. K. Seysmicheskiye vozdeystviya na zdaniya i sooruzheniya. [Seismic Actions on Buildings and Structures]. Izd-vo "Nauka," M., 1978.

32. Apparatura i metodika seysmometricheskikh nablyudeniy v SSSR. [Equipment and Methods of Seismometric Observations in the USSR]. Izd-vo "Nauka," M., 1974.

33. Stroitel'nyye normy i pravila "Stroitel'stvo v seysmicheskikh rayonakh. Normy proyektirovaniya." [Construction Standards and Rules. "Construction in Seismic Regions. Design Standards."] SN and P P-A. 12-69. Gosstroyizdat, M., 1976.

34. Rojahn, C., Negmatullaev, S. H., Poland, C. D., Mork, P. N., and Pevez, V., 1979, Explosion-generated vibration test of a three-story reinforced concrete frame and precast panel building in Tadzhik, S. S. R.: Bulletin of the European Association for Earthquake Engineering, vol. 5, no. 2, p. 76-84.

(page 525 follows)

CRITERIA FOR THE OPTIMUM LOCATION OF STATIONS TO MEASURE STRONG MOTION FROM EARTHQUAKES

by

A. A. Lunëv
R. B. Matthiesen
K. M. Mirozoyev
S.Kh. Negmatullaev
C. Rojahn

In countries with high seismic activity, there has been an increasing development of special instrumentation to measure strong motion, particularly in the last 10 years. As a result of this increase in the number of instruments and expansion of the areas covered, records have been obtained of strong earthquakes in the United States, USSR, Japan, Chile, Peru, Yugoslavia, Romania, Italy and a number of other countries. The increased instrumentation resulted from the interest shown by engineers in broad-band records from strong earthquakes. Until recently, the effects of destructive earthquakes had been analyzed on the basis of the observed damage to structures and subsequent evaluation of the factors that could have been induced such damage. Currently, seismic parameters and an analysis of the behavior of buildings and structures are beginning to be evaluated on the basis of instrumental data. Further expansion and perfection of the instrument network for measuring strong earthquakes, accumulation of records, and their processing and analysis will provide new tasks for researchers.

It is necessary to create a unified system to obtain and use the records on an international scale. This is closely linked to the questions of standardizing instruments, as well as methods and algorithms for processing and analyzing the information, and storing, duplicating and exchanging records. An important aspect is the optimal location of recording stations in the seismically active zone in order to obtain the maximum number of records in the shortest possible time, to increase the reliable operation of the instruments, and to reduce the cost of operating the network.

A first step to unify efforts in this direction was made by the United States and the USSR on the basis of the intergovernmental agreement on "Environmental Protection" concluded in 1975. The project on "Earthquake Engineering Studies" provides for the organization in Tadzhikistan of a network of stations to record strong and destructive earthquakes: it was planned jointly by the staff of the U.S. Geological Survey and the Institute of Earthquake Engineering and Seismology of the Tadzhik Soviet Socialist Republic Academy of Sciences. This network was organized in 1976 by the joint efforts of Soviet and American specialists. Currently the network consists of 22 strong motion stations equipped with Soviet and American equipment. Although the project is not yet completed, as a result of the exchange of information and equipment, the first records have been obtained of perceptible earthquakes, and methods of processing and analyzing the records have been developed. Taking into account that a strong earthquake is a rare event and that creating a station network and its operation over a long period of time are expensive, serious attention must be given to the question of planning and locating stations for measuring strong motion.

The great diversity in the types of ground conditions, peculiarities in the geological structure of the different regions, and their topographic relief significantly affect the

nature of the strong motion. The urgent need for data for use in engineering design requires the accumulation of statistics from strong-motion records and their analysis in the shortest possible time. It is vital to have the most efficient deployment of the instruments in the places where strong earthquakes are most likely to occur.

In organizing the joint network of stations in Tadzhikistan two main principles were involved. The first was derived from the need to predict the characteristics of the strong ground motions in the given region for the purposes of structural design. Consequently, the special needs for development in the given region were considered as well as the outlook for development of the territory, construction of cities, industrial facilities, large hydraulic structures, and so forth.

The second principle taken into consideration was the seismic activity of the region. In this case, the pattern of seismic activity plays a role. At this stage, the geological and geophysical data of the region are evaluated, as well as the location of deep faults, and identification of zones of increased current tectonic activity.

Achievements in seismology now make it possible to identify the sites and zones of greatest seismic hazard. Modern charts of seismic microzoning define zones in which earthquakes of intensity (on the Soviet scale) seven, eight and nine can be expected with different recurrence intervals: the region of intensity-nine shocks is however fairly large. Furthermore, where the charts indicate the greatest frequency of earthquakes, these mainly reflect past events. Therefore, such charts cannot predict the most likely sites of strong earthquakes in the near future.

Further perfection and development of the network of stations for measuring strong motion can also be carried out in conjunction with theories of earthquake prediction, specifically a scientifically substantiated prediction of the site, time and magnitude of the earthquake.

S. A. Fedotov has advanced the idea of the cyclic recurrence of seismic energy release along uniformly active seismic zones (Fedotov, 1968) and has shown that successive strong earthquakes occur in the regions **between** the sites of strong earthquakes in the past. Based on the concepts of S. A. Fedotov, analogous work was carried out for the territory of Tadzhikistan along the main seismogenic structure of the Gissaro-Kokshaal fault and adjacent regions to reveal the probable sites at which strong earthquakes may occur. (Mirozoyev, 1976; Kulagin, Malamud, and Sirozheva, 1978). The basis of the idea is the following. If a strong earthquake (together with aftershocks) has already removed the high stresses inside the Earth's crust at some site along a uniform zone of activity, then the next strong earthquake must occur in another place where the stresses still remain high (seismic gap theory).

The latest data indicate that strong earthquake activity occurs simultaneously in large territories. The recent outburst of seismic activity in Central Asia can serve as an example where for 4 years, from 1974 to 1978, a series of strong earthquakes took place: Markansu with M = 7.2 (1974), Gazli with M = 7.3 (1974), Isfarin with M = 6.5 (1977), Alay with M = 6.7 (1978), as well as a number of other less strong, but perceptible earthquakes. The normal frequency of such earthquakes in the Central Asian region is considerably lower.

Seismotectonic activation of the Earth's crust and the upper mantle along a great segment which includes the entire seismogenic structure produces a release of seismic energy at points where its concentration is the greatest. Consequently, successive strong earthquakes must occur in those places where there has been no recurrence for a long

time. It is natural that the stresses in individual places along the uniform seismogenic structure could be released by means of intensive plastic deformations (creep). But these deformations must be large enough that they could be detected with the naked eye. Such deformations are unknown in the territory of Tadzhikistan both now and in the past. On the other hand, it is difficult to imagine that a seismogenic zone that is uniform in structure and activity would release stresses in the form of earthquakes at one site, while at another site only in the form of creep. Therefore, to expect successive strong earthquakes in places where they have not occurred for some time (these sections can be conditionally named "potential seismic gaps") seems to be reasonable. This conclusion is justified both on Kamchatka and in Tadzhikistan.

The most active epicentral zone of crustal earthquakes in the territory of Tadzhikistan is the south Tien Shan zone. In this zone, such destructive earthquakes as the Karatagskoye in 1907 with M = 7.2, Fayzabad in 1930 and 1943 with M = 6 and 6.5 respectively, Khayt in 1949 with M = 7.5, Markansu in 1974 with M = 7.4, Alay in 1978 with M = 6.7, and a number of others have occurred. This zone is clearly traced from the west to the east in figure 1. In the region of Faizabad, it is divided into western (less active) and eastern (more active) parts. The density of epicenters in each part differs by a factor of 5. In the limits of the south Tien Shan epicentral zone, four seismogenic zones (subzones) are isolated: the Gissaro-Kokshaal fault, the Ilyak fault, the Pamiro-Alay, and northern section of the Darvaz-Karakul fault (Mirozoyev, 1976).

Figure 2 shows the distribution in these zones of the earthquakes with intensity (on the Soviet scale) K≥12 (magnitude M ≥4). Earthquakes with intensity K=12 are included in the figure only where the strongest earthquakes have not yet occurred. For the strongest earthquakes, the year of occurrence is shown. It is apparent that with time there is a gradual filling of the intervals between the sites of past earthquakes.

The graph in figure 2 was constructed for the period from 1895 to 1972 and was published in 1976 (Mirozoyev, 1976); it was used to predict that an earthquake was expected in the near future within the limits of coordinates 71.3-72.9° longitude east. This earthquake occurred here on 1 November 1978 with magnitude M = 6.7 (Lat. =39.4°, Long. = 72.6°). From this same graph one could have predicted the Markans earthquake of 1974 (M = 7.3) with longitude 73.9°E in the seismogenic zone of the northern section of the Darvaz-Karakul fault (fig. 2).

Attention should be drawn to the lengthy absence of strong earthquakes in the zone of the Gissaro-Kokshaal fault within the coordinates 69.5°-69.2° longitude east, and in the zone of the Darvaz-Karakul fault within the coordinates 72.3°-72.9° and 70.0°-70.8° longitude east. The average time for recurrence of earthquakes with intensities K=15, 16 and 17 (M ≥6)in the seismogenic zone of the Gissaro-Kokshaal fault over its entire length is roughly equal to 10, 10 and 50 years, respectively, while for the Darvaz-Karaku zone of the fault (northern section), the recurrence time is 15, 40 and 130 years.

In the Pamiro-Alay seismogenic subzone, the release of energy occurs fairly uniformly. On figure 1, the dotted lines show the regions of expected strong earthquakes in the south Tien-Shan epicentral zone. The listed zones of possible occurrence of strong earthquakes are the most promising for locating stations for measuring strong motion.

Further expansion and modernization of the network of strong-motion stations in the territory of Tadzhikistan must be carried out with regard to the probable zones of occurrence of strong earthquakes in the near future. Analogous work to identify such zones for the purpose of locating instruments to record strong earthquakes should be carried out in other seismic regions of the world also.

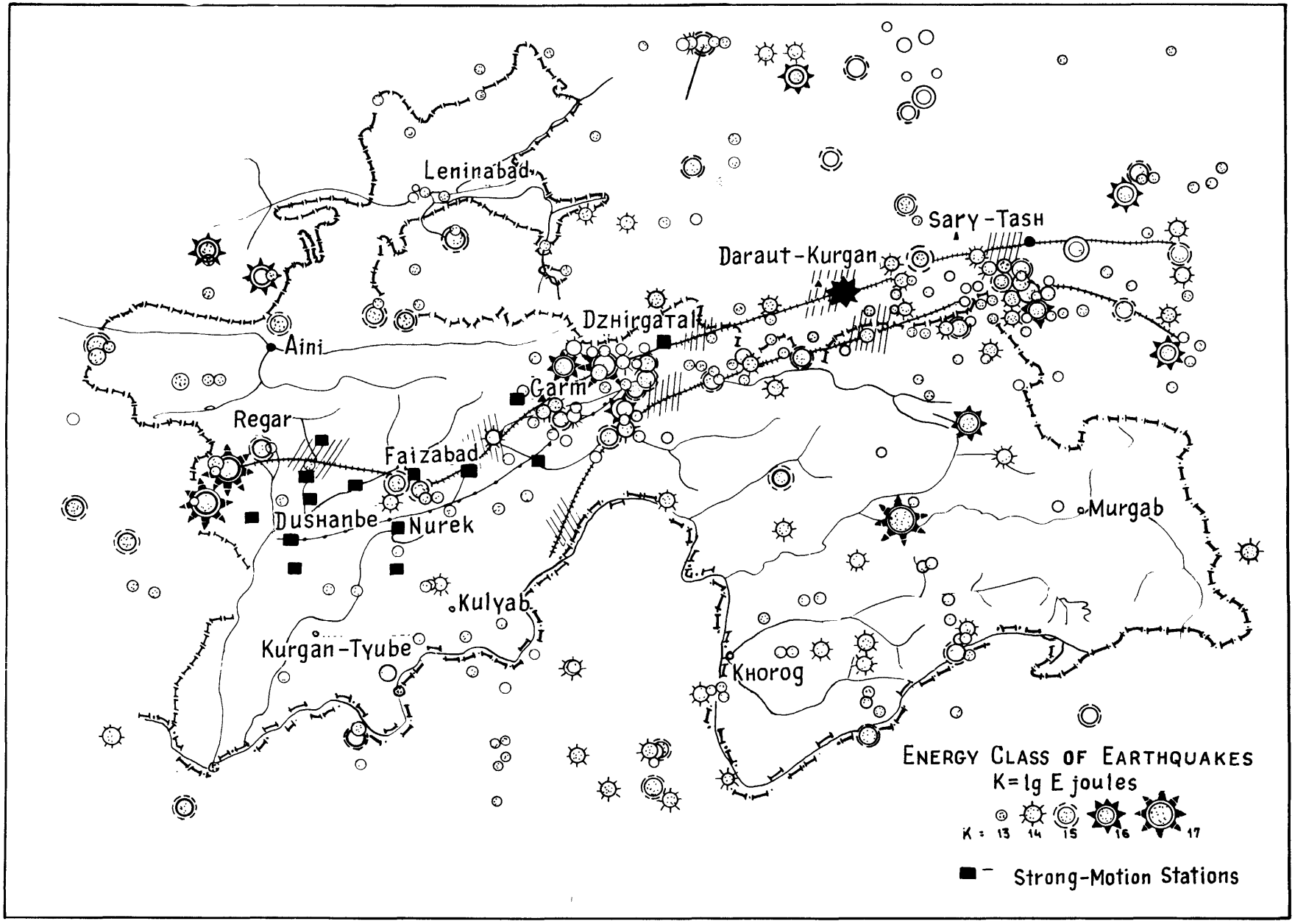

Figure 1. Map of strong earthquakes with identification of probable zones of their expected occurrence.

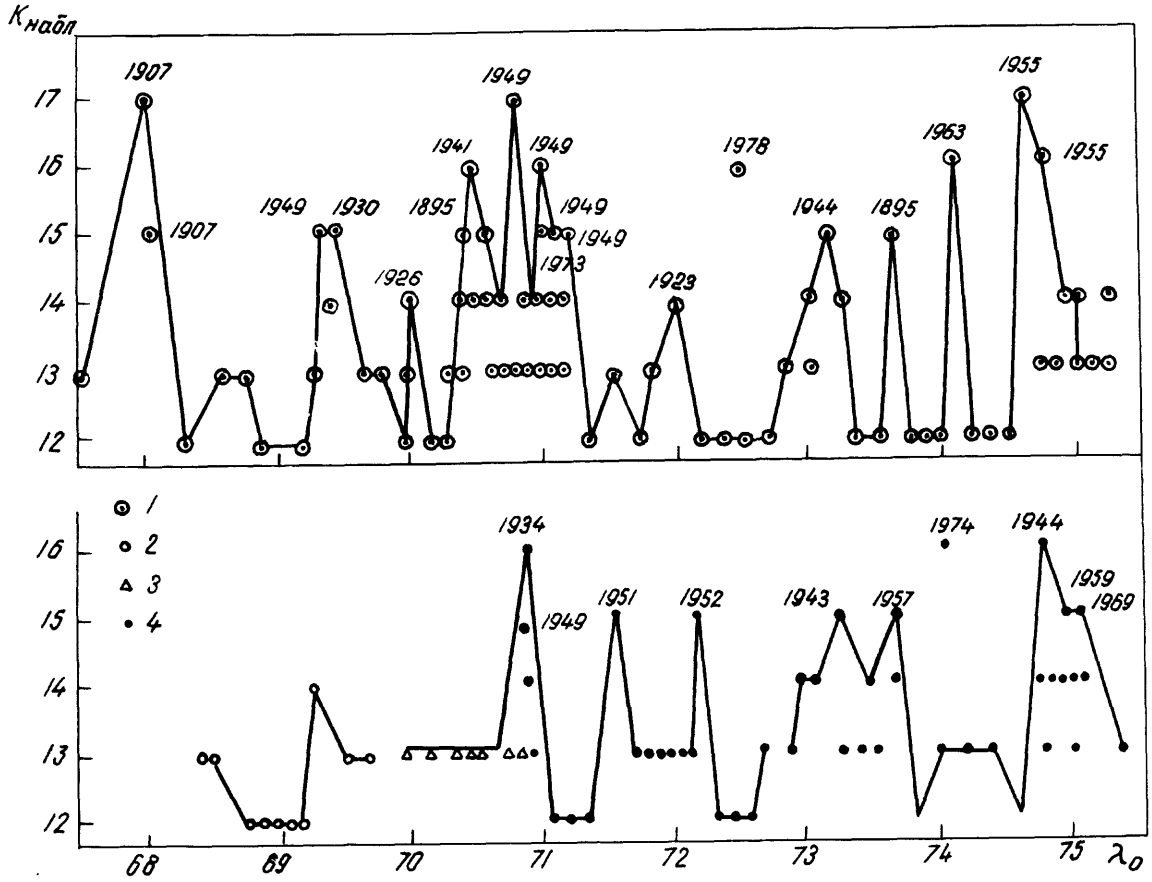

Figure 2. Strongest earthquakes in seismogenic zones of Tadzhikistan:

1. for Gissaro-Kokshaal zone in the period 1895-1972 (zone I)
2. Ilyak fault for 1931-1972 (zone II)
3. Cispamiro for 1914-1972 (subzone Vb)
4. northern section of Darvaz-Karakul zone for 1929-1972 (subzone IVb)

horizontal axis shows longitude east in degrees.

REFERENCES CITED

Fedotov, S. A. in "Seysmicheskoye rayonirovaniye SSSR" (Seismic Zoning of the USSR), Moscow, Nauka, 1968.

Kulagin, V. K.; Malamud, A. S.; and Sirozheva, Kh. Z. "Posledovatel'-nost' vysvobozhdeniya seysmicheskoy energii v kruphykh seysmogennykh zonakh i prognoz mest sil'nykh zemletryaseniy" (Sequence of Release of Seismic Energy in Major Seismogenic Zones and Prediction of Sites of Strong Earthquakes), Moscow, VINITI, No 2299-78, 1978.

Mirozoyev, K. M. "Main Characteristics of Seismicity of Seismogenic Zones Tadzhikistan," "Seysmotektonika nekotorykh rayonov yuga SSSR" (Seismotectonics of Certain Regions of Southern USSR), Moscow, Nauka, 1976.